frontiers | Research Topics

Deep-sea chemosynthetic ecosystems: Living in extreme environments

Edited by
Chaolun Li, Hao Chen, Raul Bettencourt, Dong Feng, Hongmei Jing, Jian-Wen Qiu, Jin Sun and Yong Wang

Published in
Frontiers in Marine Science

ISSN 1664-8714
ISBN 978-2-83252-104-5
DOI 10.3389/978-2-83252-104-5

About Frontiers

Frontiers is more than just an open access publisher of scholarly articles: it is a pioneering approach to the world of academia, radically improving the way scholarly research is managed. The grand vision of Frontiers is a world where all people have an equal opportunity to seek, share and generate knowledge. Frontiers provides immediate and permanent online open access to all its publications, but this alone is not enough to realize our grand goals.

Frontiers journal series

The Frontiers journal series is a multi-tier and interdisciplinary set of open-access, online journals, promising a paradigm shift from the current review, selection and dissemination processes in academic publishing. All Frontiers journals are driven by researchers for researchers; therefore, they constitute a service to the scholarly community. At the same time, the *Frontiers journal series* operates on a revolutionary invention, the tiered publishing system, initially addressing specific communities of scholars, and gradually climbing up to broader public understanding, thus serving the interests of the lay society, too.

Dedication to quality

Each Frontiers article is a landmark of the highest quality, thanks to genuinely collaborative interactions between authors and review editors, who include some of the world's best academicians. Research must be certified by peers before entering a stream of knowledge that may eventually reach the public - and shape society; therefore, Frontiers only applies the most rigorous and unbiased reviews. Frontiers revolutionizes research publishing by freely delivering the most outstanding research, evaluated with no bias from both the academic and social point of view. By applying the most advanced information technologies, Frontiers is catapulting scholarly publishing into a new generation.

What are Frontiers Research Topics?

Frontiers Research Topics are very popular trademarks of the *Frontiers journals series*: they are collections of at least ten articles, all centered on a particular subject. With their unique mix of varied contributions from Original Research to Review Articles, Frontiers Research Topics unify the most influential researchers, the latest key findings and historical advances in a hot research area.

Find out more on how to host your own Frontiers Research Topic or contribute to one as an author by contacting the Frontiers editorial office: frontiersin.org/about/contact

Deep-sea chemosynthetic ecosystems: Living in extreme environments

Topic editors

Chaolun Li — Key Laboratory of Marine Ecology and Environmental Sciences, Institute of Oceanology, Chinese Academy of Sciences (CAS), China

Hao Chen — Institute of Oceanology, Chinese Academy of Sciences (CAS), China

Raul Bettencourt — University of the Azores, Portugal

Dong Feng — Shanghai Ocean University, China

Hongmei Jing — Institute of Deep-Sea Science and Engineering, Chinese Academy of Sciences (CAS), China

Jian-Wen Qiu — Hong Kong Baptist University, SAR China

Jin Sun — Ocean University of China, China

Yong Wang — Tsinghua University, China

Citation

Li, C., Chen, H., Bettencourt, R., Feng, D., Jing, H., Qiu, J.-W., Sun, J., Wang, Y., eds. (2023). *Deep-sea chemosynthetic ecosystems: Living in extreme environments*. Lausanne: Frontiers Media SA. doi: 10.3389/978-2-83252-104-5

Table of contents

frontiers | Frontiers in Marine Science

TYPE Editorial
PUBLISHED 09 February 2023
DOI 10.3389/fmars.2023.1087465

OPEN ACCESS

EDITED BY
Ciro Rico,
Institute of Marine Sciences of Andalusia (CSIC), Spain

REVIEWED BY
Pierre Methou,
Japan Agency for Marine-Earth Science and Technology (JAMSTEC), Japan
Zongze Shao,
Third Institute of Oceanography, China

*CORRESPONDENCE
Hao Chen
chenhao@qdio.ac.cn
Hongmei Jing
hmjing@idsse.ac.cn

SPECIALTY SECTION
This article was submitted to Marine Molecular Biology and Ecology, a section of the journal Frontiers in Marine Science

RECEIVED 02 November 2022
ACCEPTED 03 February 2023
PUBLISHED 09 February 2023

CITATION
Chen H, Li C, Qiu J-W, Bettencourt R, Feng D, Wang Y, Jing H and Sun J (2023) Editorial: Deep-sea chemosynthetic ecosystems: Living in extreme environments.
Front. Mar. Sci. 10:1087465.
doi: 10.3389/fmars.2023.1087465

Editorial: Deep-sea chemosynthetic ecosystems: Living in extreme environments

Hao Chen[1]*, Chaolun Li[1,2], Jian-Wen Qiu[3], Raul Bettencourt[4], Dong Feng[5], Yong Wang[6], Hongmei Jing[7]* and Jin Sun[8]

[1]Center of Deep Sea Research, and CAS Key Laboratory of Marine Ecology and Environmental Sciences, Institute of Oceanology, Chinese Academy of Sciences, Qingdao, China, [2]South China Sea Institute of Oceanology, Chinese Academy of Sciences, Guangzhou, China, [3]Department of Biology and Hong Kong Branch of the Southern Marine Science and Engineering Guangdong Laboratory (Guangzhou), Hong Kong Baptist University, Hong Kong, Hong Kong SAR, China, [4]OKEANOS Marine Research Institute/Department of Oceanography and Fisheries, Faculty of Science and Technology, University of the Azores, Horta, Portugal, [5]Shanghai Engineering Research Center of Hadal Science and Technology, College of Marine Sciences, Shanghai Ocean University, Shanghai, China, [6]Institute for Ocean Engineering, Shenzhen International Graduate School, Tsinghua University, Shenzhen, China, [7]CAS Key Laboratory for Experimental Study under Deep-sea Extreme Conditions, Institute of Deep-sea Science and Engineering, Chinese Academy of Sciences, Sanya, China, [8]Institute of Evolution and Marine Biodiversity, Key Laboratory of Mariculture (Ministry of Education), Ocean University of China, Qingdao, China

KEYWORDS

deep-sea ecosystem, adaptation and evolution, chemosynthetic symbiosis, biodiversity and biogeochemistry, methane oxidation

Editorial on the Research Topic
Deep-sea chemosynthetic ecosystems: Living in extreme environments

Occurring in different geological settings, cold seep and hydrothermal vent systems are energy hotspots on the deep-sea seafloor, supporting the distribution and an abundance of chemosynthetic microorganisms and megafauna. With the advance in deep-sea exploration technology, we are now recognizing the greater habitat complexity and biodiversity of chemosynthetic ecosystems. We also recognize that the contribution of chemosynthetic production on the global carbon cycle may have been underestimated. Deep-sea chemosynthetic ecosystems in seeps and vents therefore are ideal system to study the interactions among the geosphere, hydrosphere and biosphere enabling a continued support of in chemosynthetic ecosystems. In Research Topic "*Deep-sea chemosynthetic ecosystems: living in the extreme environments*", we have presented updated information on the chemosynthetic ecosystems from cold seeps of South China Sea, and its role in the global biosphere with the help of state-of-the-art geochemical and molecular technologies.

Among the unsolved questions on deep-sea chemosynthetic ecosystems, how the systems have originated, evolved and supported the biota communities is fundamental to further our knowledge on the physical and chemical principles that sustain deep-sea chemosynthetic ecosystems and their thriving biological communities. A series of studies have been conducted on the biogeochemistry of deep-sea chemosynthetic ecosystems to answer these questions. It is now widely acknowledged that the high concentrations of reduced chemicals such as methane, sulfur, hydrogen, ammonia and even reduced metals could sustain distinct chemosynthetic microbiomes such as methanotrophs and thiotrophs. Meanwhile, heterotrophic communities such as hydrocarbon degraders are also divergent and

prosperous in some cold seep and hydrothermal vent fields, demanding high concentrations of dissolved organic carbon (DOC) as their nutrition. Reports showed that the DOC concentrations in seep sediments are higher than non-seep deep-sea sediments. Although methane-derived DOC could play important roles in the deep ocean carbon cycle, information on the reactivity of these seep DOC is yet quite limited. Here, with biogeochemical analysis, Hu et al. confirmed the significant contribution of methane-derived DOC at the seep cores and characterized the enhanced production of relatively labile dissolved organic matter (DOM) by anaerobic oxidation of methane (AOM) process in seep sediments. Their study suggested the lower degradation degree of these labile DOM, highlighting the indispensable role of methane derived DOC in supporting the heterotrophic microbial communities of deep-sea.

Though the deep-sea chemosynthetic ecosystems are featured by high concentrations of reduced chemicals, local environmental conditions of these ecosystems are also known to be dynamic in both time and space. The heterogeneity of deep-sea environments is recognized as a vital challenge and decisive factor for deep-sea organisms, shaping their community distribution and driving their environmental adaptations. Using cultivation dependent and independent methods, previous studies have investigated the diversity, adaptation and ecological significance of microorganisms in deep-sea chemosynthetic ecosystems. Corresponding to the environmental heterogeneity, Zhai et al. have observed both horizontal and vertical heterogeneity in microbial community in the cold seep sediments. Their results indicated that sulfate and methane were the main factors that structured the microbial community. While the microbial compositions from different sampling sites and depths were distinct, the microbial community cooperated closely to promote the overall community productivity. In addition, Zhang et al. has cultured a representative of *Lentisphaerae* bacteria from cold seep sediments, which is able to utilize polysaccharides for growth. Interestingly, the *Lentisphaerae* bacteria could significantly increase the environmental microbial diversity by metabolizing polysaccharides or other substances, demonstrating their unique physiological characterizations and ecological roles in the deep-sea habitats.

Besides the diverse microbial communities, a variety of megafauna inhabit in deep-sea chemosynthetic ecosystems. While continuous efforts are still being made to characterize novel megafauna species (e.g. the polyplacophoran *Thermochiton xui* by Wang et al., and the amphipods *Cyphocaris lubrica* and *Cyphocaris formosa* by Wang et al.), focuses on physiological novelty and diversity of megafauna are also growing. More so as for the case of mollusks, crustaceans and polychaetes, which are known to form symbiotic relationships with chemosynthetic bacteria that provide most of the organic carbon needed for the animal host's nutrition.

However, knowledge on the molecular basis of chemosynthetic symbiosis is yet still limited. Moreover, the reproductive strategies and the dispersal and connectivity of megafauna in deep-sea ecosystem are also of interest. In this Research Topic, Guan et al. investigated the lipid inventories of seep-dwelling bivalves and identified several lipids biomarkers reflecting symbiont types and local environments of bivalve hosts. The information derived from lipid biomarkers could also help interpret data from the rock record, providing valuable tools to investigate the nutrition strategies of ancestor chemosymbiotic hosts. Similarly, Wang et al. characterized the different nitrogen sources that fuel symbiotic mussels at cold seeps. This multifaceted study has provided important evidence on the mechanism of nitrogen acquisition in symbiotic mussels and a broad perspective for carbon and nitrogen transformations in cold seep systems. Diverged from their ancestors a few hundred million years ago, the deep-sea mussels have evolved an unique lifestyle that is distinct from their non-symbiotic relatives. How these deep-sea mussels reproduce and whether they share the same sex determination/differentiation mechanisms with non-symbiotic mussels are less investigated. Here, resorting to transcriptome and whole-genome DNA methylation analyses, Zhong et al. have characterized hundreds of genes that may participate in the sex determination of deep-sea mussel, and concluded that the sex determination mechanisms are conserved in mussels from different habitats. These studies have substantially advanced our knowledge on the chemosymbiotic molluscan hosts.

Although widely recognized as oases of life over the last four decades, deep-sea chemosynthetic ecosystems are still mysterious, with many hidden secrets awaiting discovery. Besides studies covered by our current Research Topic, more efforts are still needed to unravel the unique biological diversity, structure and ecological processes in these deep-sea chemosynthetic ecosystems. For instance, there is limited information about temporal and spatial changes of free-living chemosynthetic microbial community, let alone the individual/population changes of deep-sea megafauna in response to environmental changes and human activities (Wang et al.). Finally, interdisciplinary efforts and the application of state-of-the-art methods (such as single-cell sequencing [Li et al.], spatial transcriptomics, mass spectrometry imaging, *in situ* experiments and *in situ* detection) are also needed to reveal the adaptations of these deep-sea organisms. We expect to see more exciting discoveries in the years to come.

Author contributions

Writing—original draft: HC; Writing—review & editing: HC, CL, J-WQ, RB, DF, YW, HJ, and JS. All authors contributed to the article and approved the submitted version

Conflict of interest

The authors declare that the research was conducted in the absence of any commercial or financial relationships that could be construed as a potential conflict of interest.

Publisher's note

frontiers in Marine Science

ORIGINAL RESEARCH
published: 02 December 2021
doi: 10.3389/fmars.2021.797084

Production of Labile Protein-Like Dissolved Organic Carbon Associated With Anaerobic Methane Oxidization in the Haima Cold Seeps, South China Sea

Tingcang Hu[1], Min Luo[1,2], Yunping Xu[1], Shanggui Gong[1] and Duofu Chen[1]**

[1] Shanghai Engineering Research Center of Hadal Science and Technology, College of Marine Sciences, Shanghai Ocean University, Shanghai, China, [2] Laboratory for Marine Geology, Qingdao National Laboratory for Marine Science and Technology, Qingdao, China

OPEN ACCESS

Edited by:
Hao Chen,
Institute of Oceanology, Chinese Academy of Sciences (CAS), China

Reviewed by:
David C. Podgorski,
University of New Orleans, United States
Michael Thomas Montgomery,
Texas A&M University-Corpus Christi, United States

***Correspondence:**
Min Luo
mluo@shou.edu.cn
Duofu Chen
dfchen@shou.edu.cn

Specialty section:
This article was submitted to Deep-Sea Environments and Ecology, a section of the journal Frontiers in Marine Science

Received: 18 October 2021
Accepted: 17 November 2021
Published: 02 December 2021

Citation:
Hu T, Luo M, Xu Y, Gong S and Chen D (2021) Production of Labile Protein-Like Dissolved Organic Carbon Associated With Anaerobic Methane Oxidization in the Haima Cold Seeps, South China Sea. Front. Mar. Sci. 8:797084. doi: 10.3389/fmars.2021.797084

Cold seeps where methane-rich fluids escape from the seafloor generally support enormous biomass of chemosynthetic organisms and associated fauna. In addition to transporting a great amount of methane toward the seafloor, cold seeps also contribute to the aged, dissolved organic carbon (DOC) pool in the deep ocean. Here, two sediment cores from the "Haima cold seeps," northern South China Sea and a nearby reference core were analyzed for pore-water sulfate and DOC concentrations, $\delta^{13}C$ of DOC, and optical properties of dissolved organic matter (DOM). High DOC concentrations (0.9–3.7 mM) accompanied by extremely low $\delta^{13}C$ values (−43.9 to −76.2‰) suggest the conversion of methane into sedimentary DOC pool in the seep sediments. Parallel factor analysis (PARAFAC) of the fluorescence excitation-emission matrices shows higher fluorescent intensities of labile protein-like components (C2 and C4) and lower fluorescent intensities of refractory humic-like components (C1 and C3) in the seep cores compared to the reference core. The intensity of C2 is positively correlated with DOC concentrations and $\delta^{13}C$-DOC in the seep sediments, suggesting that the labile protein-like DOM was produced by the anaerobic oxidation of methane (AOM). Moreover, low humification index (HIX) and high biological index (BIX) values also indicate intensified production of relatively labile DOM with lower degradation degree in the seep cores compared to the reference core. Hence, we highlight that methane-derived DOC may serve as important carbon and energy sources for heterotrophic microbial communities due to its relatively labile nature.

Keywords: cold seeps, dissolved organic carbon, fluorescence spectrum, protein-like, AOM

INTRODUCTION

Dissolved organic carbon (DOC) in marine sediments represents an important by-product during the mineralization of particulate organic matter (POC; Aller, 1978; Berner, 1980; Komada et al., 2013; Burdige et al., 2016). Although the majority of POC is ultimately degraded to dissolved inorganic carbon (DIC), a varying fraction of POC is converted to DOC and accumulates in marine

sediments (Burdige, 2002; Komada et al., 2013). This net production of DOC results in significantly higher pore water DOC concentrations than bottom seawater (Martin and McCorkle, 1993; Alperin et al., 1994; Burdige et al., 1999). DOC release from continental margin sediments can supply ∼180 Tg C year $^{-1}$ to the deep ocean, roughly equivalent to the riverine DOC input (Burdige et al., 1999), thereby affecting the characteristics of DOC in the deep ocean. Pore-water DOC in the very surface sediments is more labile and younger than the deep-ocean DOC due to rapid turnover of the labile POC component (Bauer et al., 1995; Komada et al., 2012). With the ongoing POC degradation in the sediments, increasingly amount of highly degraded, low-molecular-weight refractory DOC is produced and accumulated in the pore water. Based on numerical modeling results, Burdige et al. (2016) concluded that refractory DOC accounted for > 95% of the total pore-water DOC except that in the sediments close to the seafloor.

Marine sediments hold ∼500–10,000 Gt carbon in the form of methane, predominantly occurred as gas hydrate (Kvenvolden, 1988; Buffet and Archer, 2004; Milkov, 2004). In the case of gas hydrate dissociation due to temperature and/or pressure changes, a large quantity of methane is released and transported toward the seafloor, forming cold seeps (Reeburgh, 2007). In addition to POC mineralization, DOC production in seep-impacted sediments is closely associated with the anaerobic oxidation of methane (AOM; Pohlman et al., 2011). As a result, significantly higher DOC concentrations have been observed in seep sediments compared to non-seep deep sea sediments (Hung et al., 2016; Amaral et al., 2021). Valentine et al. (2005) found that the proportion of methane-derived DOC increases with enhanced AOM rates and microbial activity in the cold seep sediments. Because of the influence of AOM, DOC is generally ^{13}C- and ^{14}C-depleted in seep sediments. Mass-balance calculation using δ^{13}C and Δ^{14}C data showed that up to 86% of pore water DOC in the Arctic cold seep sediments was derived from fossil methane. Furthermore, Pohlman et al. (2011) suggested that methane-derived DOC accounted for up to 28% of DOC pool in the overlying bottom water, thereby likely representing an important but previously unconsidered source of pre-aged, ^{13}C-depleted carbon into the deep ocean.

The potential impact of sediment-derived DOC on the deep ocean carbon cycle mainly depends on the reactivity of DOC. Optical property provides important insights into the source, composition, and reactivity of dissolved organic matter (DOM; Burdige et al., 2004; Coble, 2007; Dittmar and Stubbins, 2014; Chen et al., 2016; Wagner et al., 2020). Microbial metabolism sustained by deeply-sourced methane-rich fluids *via* mud volcanism has been documented to significantly contribute to the production of fluorescence dissolved organic matter (FDOM), ∼70% of which was characterized by labile, protein-like fluorescence components (Amaral et al., 2021). Apart from the microbe-derived FDOM, thermogenically altered FDOM transported from the deep subsurface has also been detected in mud volcano pore fluids (Brogi et al., 2019). Moreover, bottom water collected from methane seeps contained more protein-like and lipid-like DOM components than non-seep areas, suggesting that cold seep sediments can be an important source of DOM to the bottom water, thereby impacting bottom-water DOM composition and reactivity (Sert et al., 2020).

Even though cold seep sediments have been recognized as an important source of overlying water DOM, knowledge on the reactivity of methane-derived DOM is quite limited, which hinders the assessment of the potential impact of methane-derived, fossil DOC on the deep ocean DOC pool. Here, we analyzed pore-water concentrations of sulfate (SO_4^{2-}) and DOC, stable carbon isotopic compositions (δ^{13}C) of sedimentary DOC, and fluorescence properties of sedimentary DOM in the "Haima cold seeps," northern South China Sea (SCS). This work seeks to test the hypothesis that the majority of methane-derived DOC is relatively labile that could play an important role in sustaining heterotrophic metabolism in both the sediments and overlying bottom water.

MATERIALS AND METHODS

Study Area

The "Haima cold seeps" was discovered in the Qiongdongnan basin (QDNB), located in the extensional sector of the northern SCS passive margin, by the Guangzhou Marine Geological Survey in 2015. It consists of two active seep areas (ROV1 and ROV2; 7 km apart) with the water depth of ∼1,400 m (**Figure 1**). Geophysical imaging showed that the seeps were sustained by upward-migrating methane gas evidenced by the occurrence of gas chimney (Wang et al., 2008). Due to intense methane gas bubbling, methane hydrates were formed in shallow sediments, and living benthic fauna (e.g., tubeworms, clams, and mussels) were observed at the two seep sites by remotely operated vehicle (ROV) surveys (Liang et al., 2017).

Sample Collection

A gravity core (ROV1) and a push core (ROV5) were retrieved from the "Haima cold seeps" during the R/V Haiyang-6 cruise in September 2020. A reference core (QDN-C-S03) was collected from non-seep area using a gravity corer during R/V Haiyang-10 cruise in August 2019. The recovered cores were immediately brought to the onboard laboratory and sliced into 2–20 cm intervals for pore water collection using Rhizon samplers. Aliquots for DOM analysis were stored in pre-combusted (550°C for 4 h), 40 ml brown glass bottle and frozen at −20°C until further analysis. The aliquot for SO_4^{2-} analysis was acidified with HNO_3 and stored in a refrigerator (∼4°C). After pore water extraction was completed, sediment samples were kept frozen at −20°C.

Analytical Methods

The concentrations of SO_4^{2-} were determined using a Dionex ICS-900 ion chromatograph after a 500-fold dilution with Milli-Q water. Ion Pac AS23-type column for anion and a mixed solution of Na_2CO_3 and $NaHCO_3$ was used as eluent for SO_4^{2-} concentration measurements. The analytical precision for SO_4^{2-} is better than 2%. DOC concentrations were determined by a high-temperature catalytic combustion method after a proper

dilution with Milli-Q water using Shimadzu TOC-L analyzer with an analytical precision of ± 3%. The deep seawater provided by Hansell laboratory (University of Miami) was used as the DOC standard validation. For δ^{13}C-DOC analyses, pore water samples were acidified to pH ∼ 2 with 6 M HCl for 72 h to remove inorganic carbon and then analyzed by high-temperature combustion on a Vario Cube TOC analyser connected to an Isoprime 100 continuous flow isotope ratio mass spectrometer. The analytical precision for δ^{13}C-DOC is better than 0.2‰.

Absorption spectra were scanned from 200 to 800 nm on an ultraviolet-visible (UV-Vis) spectrophotometer (Shimadzu Inc., Japan). Fluorescence excitation-emission matrices (EEMs) were measured using a Hitachi F-7000 luminescence spectrometer (Hitachi Inc., Japan). Excitation ranged 240–450 nm with 5 nm interval, while emission encompassed between 250 and 550 nm with 1 nm interval. The EEMs correction process included blank subtraction, inner filter correction and scatter removal. Fluorescence data were converted to Raman intensity units (RU) by normalizing the fluorescence collected in arbitrary units to the Raman peak area at 350 nm. Subsequently, we used parallel factor analysis (PARAFAC) to determine the number of fluorescent components based on the split-half validation. The EEMs correction and PARAFAC modeling were performed using the MATLAB R2019a with the drEEM toolbox (Murphy et al., 2013). In addition, the optical indices, including the fluorescence index (FI), humification index (HIX) and biological index (BIX) were also analyzed. FI is a ratio of emission wavelengths at 470 and 520 nm, gained at excitation 370 nm, which is usually used to distinguish between autochthonous (microbial source) and allochthonous DOM (terrestrial source) (Mcknight et al., 2001; Cory et al., 2010). HIX is an area under the emission spectra 435–480 nm divided by the area 300–345 nm, at excitation wavelength 254 nm, which can be used to reflect the humic substance content and the degree of humification (Ohno, 2002). BIX is the ratio of emission intensity at 380 nm divided by 430 nm at excitation 310 nm, which is positively correlated with the contribution of the autotrophic produced, low-degradation degree FDOM (Huguet et al., 2009).

RESULTS

Downcore Profiles of SO_4^{2-}, Dissolved Organic Carbon, and δ^{13}C-DOC

The downcore variations in concentrations of SO_4^{2-} and DOC and δ^{13}C-DOC values are shown in **Figure 2**. At the reference core (QDN-C-S03), the SO_4^{2-} concentrations decrease slightly with depth from 26.0 to 22.4 mM. In contrast, the SO_4^{2-} concentrations decline rapidly with depth at both seep cores, forming shallow sulfate-methane transition zone (SMTZ) (∼120 cm for ROV1 and ∼30 cm for ROV5). Sedimentary DOC concentrations in all three cores (0.31 – 3.7 mM) are significantly higher than the average deep-ocean DOC concentration (∼40 μM) (Hansell and Carlson, 1998). The concentrations and δ^{13}C values of DOC generally remain constant throughout the reference core, whereas both seep cores exhibit significantly higher DOC concentrations and lower δ^{13}C values (**Figure 2**). In addition, the downcore profiles of DOC concentrations mirror that of δ^{13}C values at both seep cores, with higher DOC concentrations corresponding to lower δ^{13}C values and *vice versa*.

Optical Properties of Sedimentary Dissolved Organic Matter

Four fluorescent components (C1–C4) were identified based on the EEM-PARAFAC model. These components were matched to previous models in the OpenFluor database that had a 0.95 minimum similarity score for the identical match between spectra. C1 (Ex/Em maxima: 250(320)/410 nm) and C3 (Ex/Em maxima: 255(370)/472) were matched to several PARAFAC models in the OpenFluor database and assigned as relatively refractory marine/microbial humic-like and terrestrial humic-like components (Coble, 1996; Murphy et al., 2014; Chen et al., 2016; Loginova et al., 2016; **Figure 3**). A number of labile protein-like components were matched to C2 (Ex/Em maxima: 275/350) in the OpenFluor database, indicating that C2 is a ubiquitous component of natural organic matter (Murphy et al., 2014). C4 (Ex/Em maxima: 265/285), also identified as a labile protein-like component, was matched to four studies focusing on seawater (Coble, 1996; Burdige et al., 2004; Murphy et al., 2014; Loginova et al., 2016). More specifically, C2 and C4 were thought to represent tryptophan-like and tyrosine-like compounds, respectively, in a variety of natural environments (Murphy et al., 2008; Chen et al., 2018). In addition, these labile protein-like components were also likely associated with aliphatic hydrocarbons (Dvorski et al., 2016; Podgorski et al., 2018; Mirnaghi et al., 2019). However, given the biogenic origin of methane in the "Haima" cold seeps (Wei et al., 2020), we presume a negligible contribution of petroleum-derived aliphatic compounds to the labile protein-like components. The fluorescence intensity of protein-like components (C2 + C4) account for 63% ± 17% of the total FDOM intensity (C1 + C2 + C3 + C4) at the seep cores, which is significantly higher than those at the reference core (17% ± 8%). FI values (1.67–2.03) do not show significant differences between the seep cores and the reference core (**Figure 4**). In contrast, HIX values at the reference core (0.84–0.92) are higher than those at the seep cores (0.47–0.71), while BIX values show an opposite pattern with slightly higher values at the seep cores than at the reference core.

DISCUSSION

Sources of Dissolved Organic Carbon in the Seep Sediments

Dissolved organic carbon in continental margin sediments is generally produced during the process of POC mineralization (Komada et al., 2013; Burdige et al., 2016). In the seep sediments, in addition to POC mineralization, DOC production is also associated with AOM process (Valentine et al., 2005; Pohlman et al., 2011). DOC concentrations at both seep cores (ROV1 and

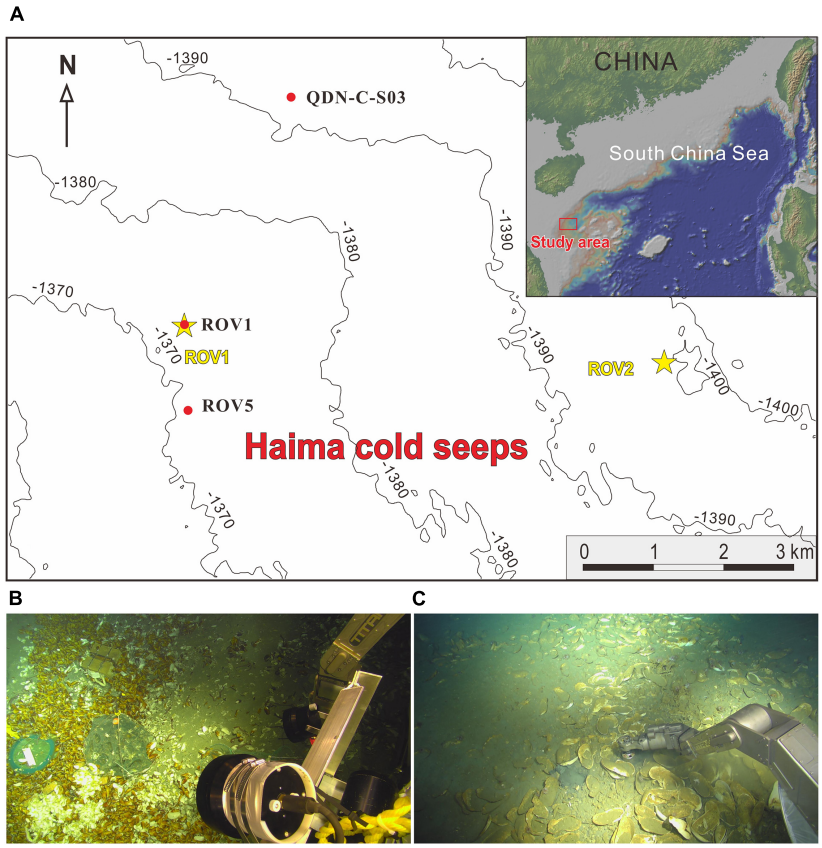

FIGURE 1 | (A) Locations of the three coring sites in the "Haima cold seeps" area. The yellow asterisks show the ROV1 and ROV2 seep areas. The red dots indicate the locations of coring sites. Cores ROV1 and ROV5 were taken from the active methane seep area and core QDN-C-S03 was collected from a non-seep area as a reference. Photos of seafloor where cores **(B)** ROV1 and **(C)** ROV5 were taken.

ROV5) are higher than those at the reference core (QDN-C-S03), and ROV5 with shallower SMTZ exhibits higher average pore-water DOC compared to ROV1 with deeper SMTZ. These observations suggest that seep sediments contribute to DOC production with elevated methane flux and resulting AOM rate corresponding to enhanced DOC production. Moreover, ^{13}C-depleted DOC measured at the seep cores (−43.9 to −76.2‰) also points to a predominately methane-derived DOC as methane collected from "Haima cold seeps" is mostly biogenic in origin with δ^{13}C values ranging between −72.3 and −71.5‰ (Wei et al., 2020). In contrast, at the reference core absent of methane seepage, the δ^{13}C values of DOC are significantly higher, exhibiting similar values of sedimentary TOC in the Qiongdongnan basin that receives both marine and terrestrial organic matter input (Cao et al., 2017). The slight decrease in SO_4^{2-} at the reference core points to the dominance of particulate organic carbon sulfate reduction (POCSR) rather than AOM in consuming SO_4^{2-}, which is consistent with the inference of sedimentary TOC-derived DOC. Pore-water DOC production dominated by POCSR has also been observed in the anoxic sediments of the Arctic Ocean (Chen et al., 2016).

In addition, the significant inverse correlation between DOC concentrations and δ^{13}C-DOC values at both seep cores was observed (**Figure 5**), which was explained as the coupling between AOM and DOC production (Pohlman et al., 2011). The extremely low δ^{13}C-DOC values and high DOC concentrations at the SMTZ of both seep cores are associated with AOM. Meanwhile similar phenomenon also observed above the current SMTZ at ROV1 (**Figure 2E**). This shallower depth interval featuring DOC and δ^{13}C-DOC anomalies may represent the paleo-SMTZ where intense AOM and resulting DOC production was occurring when upward methane flux was higher compared to the current conditions. Fluctuation of SMTZ due to the variations in methane seepage intensities has been suggested to take place in the "Haima cold seeps" (Hu et al., 2019) and other seep areas worldwide (e.g., Borowski et al., 1999; Peketi et al., 2012; Sultan et al., 2016).

Enhanced Production of Labile Dissolved Organic Carbon in the Seep Sediments

The positive linear correlations were observed for DOC concentrations and total FDOM intensities (**Figure 6**), indicating the coupled production mechanisms of DOC and FDOM at the study cores. The y-intercepts are 0.26 mM for QDN-C-S03, 0.39 mM for ROV1 and −0.70 mM for ROV5, respectively, which represent the non-fluorescence fraction of DOM. Because

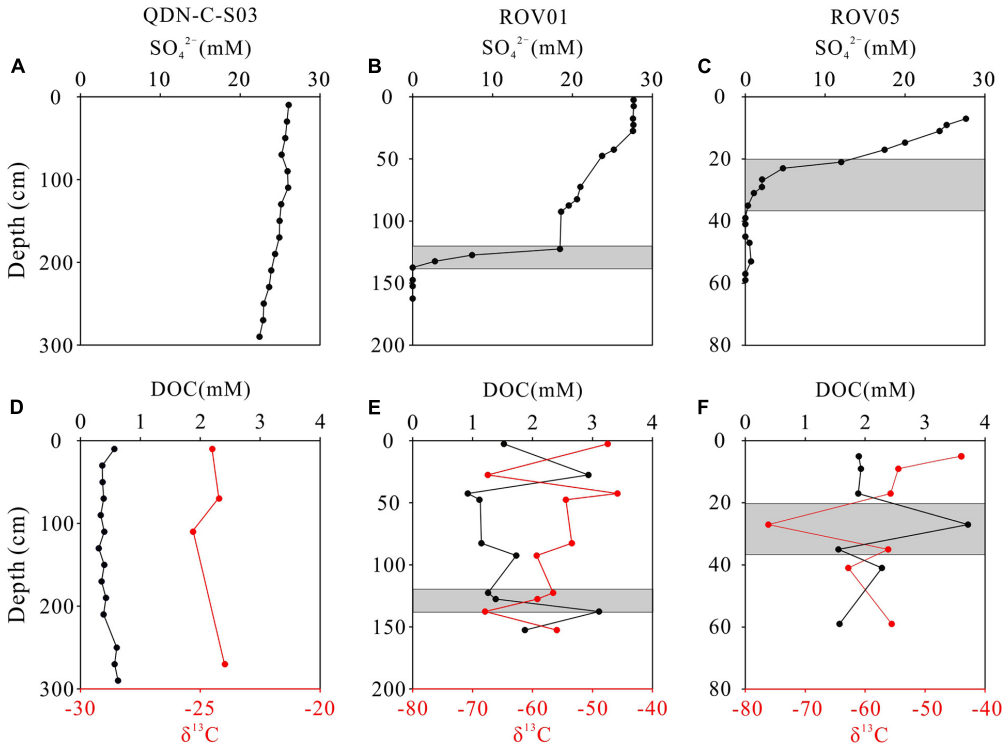

FIGURE 2 | Downcore profiles of pore-water SO_4^{2-}, dissolved organic carbon (DOC), and δ^{13}C-DOC at QDN-C-S03 **(A,D)**, ROV1 **(B,E)**, and ROV5 **(C,F)**. Shaded areas indicate the depths of the SMTZ.

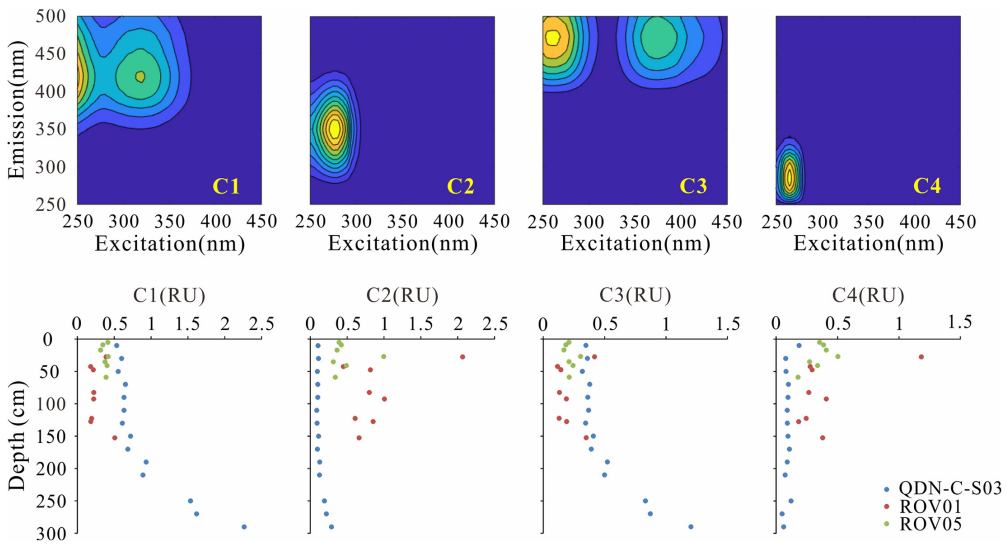

FIGURE 3 | Contour plots of the four components identified by EEM-PARAFAC (upper panel) and depth-profiles of the corresponding fluorescent intensities of fluorescence dissolved organic matter (FDOM) components (lower panel).

of the average DOC concentrations at QDN-C-S03 and ROV1 are 0.44 and 1.70 mM, we estimated that 41 and 77% of DOC pool are composed of fluorescence material at QDN-C-S03 and ROV1, respectively. The negative intercept value at ROV5 may imply a contribution of dissolved organic sulfur to FDOM pool. Sulfurization of organic matter is a common process during early diagenesis stage through reaction of polysulfide and bisulfide on C-C double bonds and oxo-groups (Schouten et al., 1994; Werne et al., 2008; Raven et al., 2015). HS^- produced by microbial sulfate reduction represents the major source for the

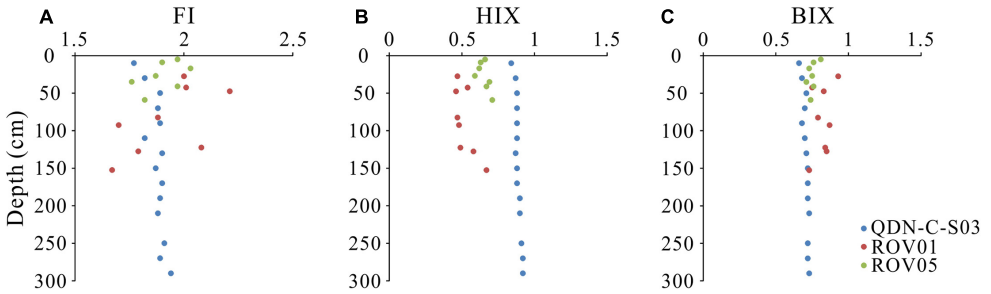

FIGURE 4 | Downcore variations in panel **(A)** fluorescence index (FI), **(B)** humification index (HIX), and **(C)** biological index (BIX) values at the seep cores (ROV1 and ROV5) and the reference core (QDN-C-S03).

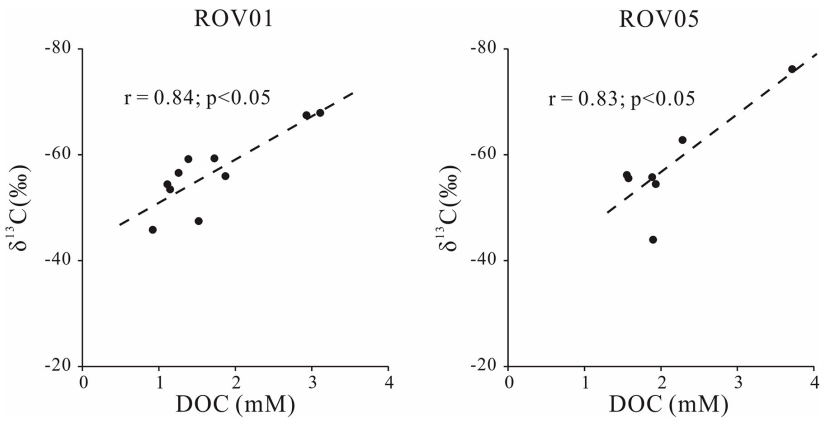

FIGURE 5 | Cross-plot of concentrations and $\delta^{13}C$ of DOC at seeps sites (ROV1 and ROV5).

S-bearing organic compounds in anoxic sediments (Schmidt et al., 2009; Seidel et al., 2014; Sleighter et al., 2014). Also, the amount of S-bearing molecular formulas formed in the sediments is dependent upon the HS^- concentrations in the pore water resulting from microbial sulfate reduction (Schmidt et al., 2017). Therefore, despite a lack of HS^- data for both seep cores, the much higher AOM rates suggested by considerably shallower SMTZ at ROV5 than ROV1 likely explain a significant production of dissolved organic sulfur.

Although the exact formation mechanism of methane-derived DOC is currently unclear, biochemical processes including methane-sourced carbon incorporation into acetate or larger biomoleculars, microbial excretion, and biomass degradation have been proposed (Hoehler et al., 1994; Yang et al., 2020). Here, greater amount of fluorescent protein-like components (C2 and C4) and correspondingly less amount of humic-like components (C1 and C3) at the seep cores (ROV1, ROV5) than those at the reference core (QDN-C-S03) suggests enhanced microbial activities and resulting release of more labile, protein-like components at the seep cores (**Figure 3**). These results are consistent with the observation of significantly elevated microbial abundance in the seep sediments (Levin, 2005; Niu et al., 2017). Meanwhile, low HIX values, large fraction of protein-like components (46–80%) and high BIX values also indicate intensified production of relatively labile FDOM with lower degradation degree associated with AOM at the seep cores compared to the reference core where sedimentary DOM is mostly produced by POCSR (**Figure 4**). Similar results have been reported at the mud volcanoes in the Gulf of Cádiz where the protein-like components accounted for ∼70% of the total FDOM (Amaral et al., 2021).

The positive correlations of C2 intensity with DOC concentrations and $\delta^{13}C$-DOC at both seep cores (**Figures 7**, **8**) also support our argument that labile protein-like DOM production is closely related to AOM. However, the correlation between the fluorescent intensity of the other protein-like component-C4 and DOC concentration as well as $\delta^{13}C$-DOC at both seep cores is less remarkable compared to C2, likely implying complicated sources and formation mechanism of C4. Although the specific chemical composition of methane-derived DOC has yet to be investigated, it has been suggested that methane could be converted to low-molecular-weight, labile organic materials (e.g., acetate) by AOM (Yang et al., 2020). This inference was demonstrated by the identification of a complete archaeal acetogenesis pathway in the ANME-2a genome and the activity of the key enzymes in acetate generation (Yang et al., 2020). Notably, the acetate may account for a small fraction of the methane-derived labile DOC pool, which can subsequently sustain the highly divergent heterotrophic communities in the seep sediments (Valentine et al., 2005).

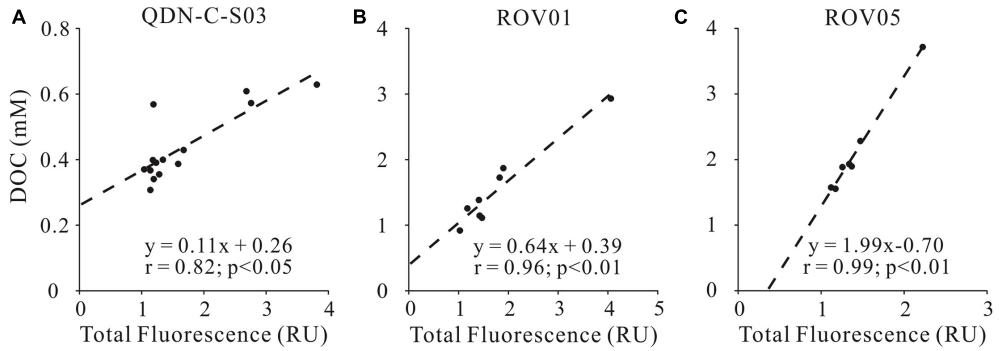

FIGURE 6 | Cross-plots of DOC concentrations and total fluorescence intensity at the sites ROV1 **(A)**, ROV5 **(B)**, and the QDN-C-S03 **(C)**.

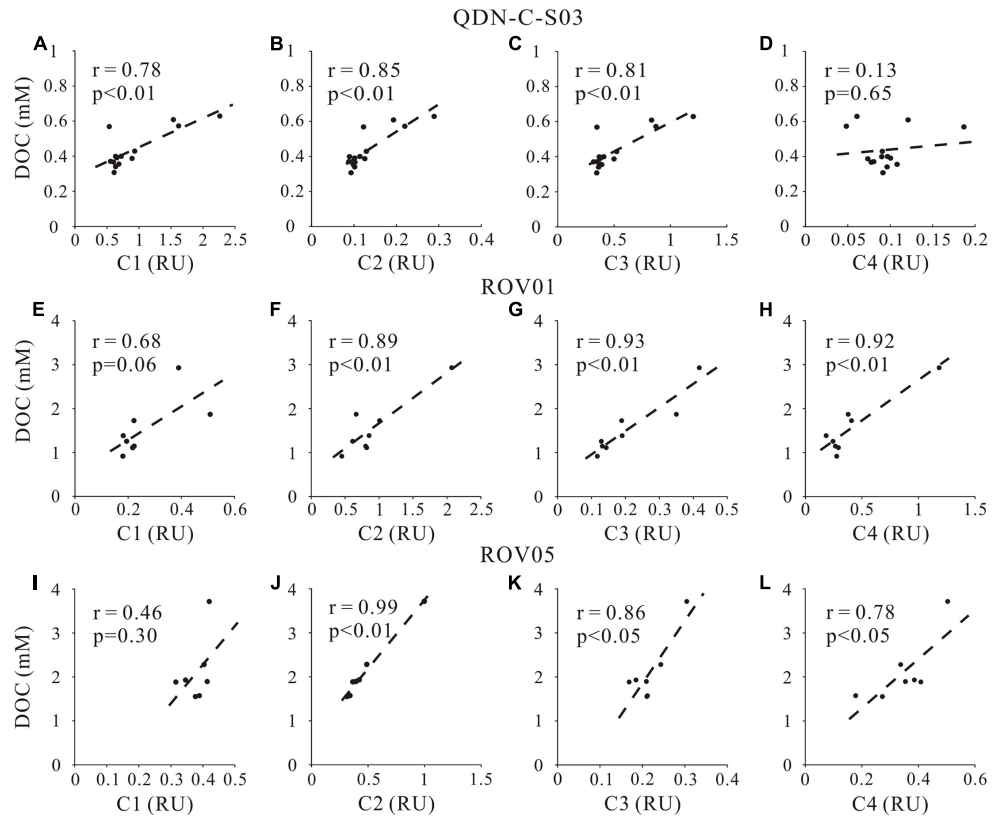

FIGURE 7 | Cross-plots of DOC concentrations and fluorescent intensity of FDOM components (C1, C2, C3, and C4) at cores QDN-C-S03 **(A–D)**, ROV1 **(E–H)** and ROV5 **(I–L)**.

In addition to producing protein-like components, AOM and accompanying microbial metabolism also produce humic-like refractory materials as shown by the positive correlations between humic-like component (C3) and DOC concentrations as well as δ^{13}C-DOC values at both seep cores (**Figures 7**, **8**). No significant correlations were found between marine/microbial humic-like (C1) and DOC concentrations or δ^{13}C-DOC values (**Figures 7**, **8**), indicating potential uncoupling of C1 production with AOM at seeps. However, the general positive correlations between C1 and DOC concentrations at the reference core may suggest a potential close relationship between C1 production and POC degradation (**Figure 7**). Indeed, higher C1 content at the reference core compared to the seep cores also suggests a greater contribution of POCSR at the reference core, likely reflecting inhibition of POCSR in the seep sediments (Niewohner et al., 1998; **Figure 3**). It is worth noting that the refractory property of the humic-like components in aquatic environments may not be necessarily associated with their chemical structures, but rather due to the environmental conditions such as their concentrations (Arrieta et al., 2015; Cerro-Gálvez et al., 2019a),

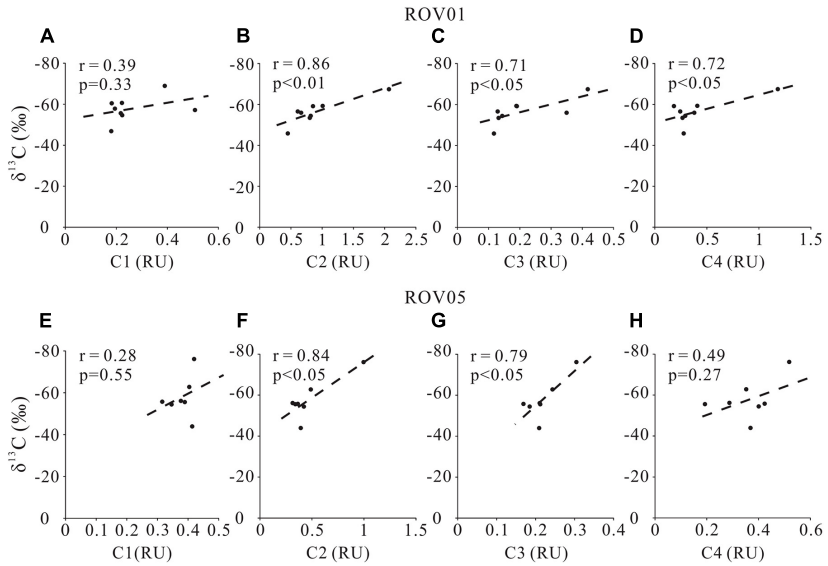

FIGURE 8 | Cross-plots δ^{13}C-DOC and FDOM components (C1, C2, C3, and C4) for the seeps sites ROV1 **(A–D)** and ROV5 **(E–H)**.

nutrient availability (Cerro-Gálvez et al., 2019b), microbial ecology, enzyme function, and steric hindrance (i.e., matrix protection) (Kleber, 2010). Therefore, it may be possible that the humic-like component would change and become less refractory to microbial metabolism when they enter the ocean (Arrieta et al., 2015).

Potential Impact of the Labile Dissolved Organic Carbon From Seep Sediments on the Deep Ocean Dissolved Organic Carbon Pool

In general, the lability of DOC in the ocean is thought to vary with its ages, with younger, unaltered DOC being more easily utilized by aquatic heterotrophs than older, heavily modified one (Bauer et al., 1995; Raymond and Bauer, 2001; Raymond et al., 2007). However, Hood et al. (2009) found the glaciers runoff can supply a considerable amount of labile but aged DOC to marine ecosystems. Also, recent studies suggested that the reactivity of DOC is not directly related to its age, but mainly affected by its intrinsic chemical composition and extrinsic environments (Jiao et al., 2010; Wagner et al., 2020; Dittmar et al., 2021). Likewise, in the seep-impacted sediments, methane-derived DOC is extremely depleted in ^{14}C because methane is mostly produced by microbial or thermal degradation of pre-aged organic matter (Kuivila et al., 1990). Valentine et al. (2005) speculated that DOC in seep sediments contained labile compounds that could feed the heterotrophic microbial community. In this study, our optical analyses of sedimentary DOM demonstrate an enhanced production of relatively labile protein-like materials at both seep cores compared to the reference core, thereby supplying additional food sources and energy for heterotrophic prokaryotes in the seep sediments. Indeed, the observation of highly ^{13}C-depleted lipid biomarkers in the seep carbonates likely suggested the uptake of AOM-derived OC by methane-oxidizing and sulfate-reducing consortia (Guan et al., 2019). In addition to supporting heterotrophic microbial activity in the seep sediments, DOC sourced from the seep sediments could also feed heterotrophy in the overlying seawater (Walker et al., 2017). The estimated ∼20.3 Tg C yr^{-1} methane-derived DOC from seep sediments to the global ocean represents an important carbon and energy source for the heterotrophic communities in the deep ocean (Pohlman et al., 2011; Hung et al., 2016; Fu et al., 2020). Although the labile methane-derived DOC in the seep sediments is rapidly recycled, it could have a significant impact on the deep ocean DOC pool as aged and refractory DOC can also be produced during microbial metabolism.

Furthermore, in the geological past when major methane release from sediments due to gas hydrate dissociation, e.g., during the Palaeocene-Eocene Thermal Maximum (PETM), methane-derived DOC efflux could be substantially greater than the present-day condition (Zachos et al., 2005). As a result, a large amount of methane-derived DOC was subsequently converted to microbial biomass and buried in the sediments. We postulate that an enhanced production of labile protein-like DOC in the seep sediments may help explain the carbon isotopic excursion of sedimentary organic matter in the geological history and have implications in understanding the global DOC cycle.

CONCLUSION

Analyses and comparison of pore-water SO_4^{2-}, DOC concentrations and δ^{13}C of DOC in the sediment cores taken from the "Haima cold seeps" regions (the northern SCS) suggest a significant contribution of methane-derived DOC at the seep cores. PARAFAC of the fluorescence excitation-emission matrices shows higher amount of protein-like fluorescent at the

seep cores than the reference core. The enhanced production of relatively labile, protein-like fluorescent component is associated with AOM, as also reflected by the extremely low $\delta^{13}C$ of DOC. We highlight that the methane-derived DOC could serve as important carbon and energy sources for the heterotrophic communities and that it may contribute to explaining the $\delta^{13}C$ excursion of sedimentary organic carbon in the geological history when major methane emission events took place.

DATA AVAILABILITY STATEMENT

The datasets presented in this study can be found in online repositories. The names of the repository/repositories and accession number(s) can be found below: https://doi.org/10.6084/m9.figshare.16802116.

AUTHOR CONTRIBUTIONS

TH: investigation, sample collection, methodology, data analysis, and writing—original manuscript. ML: conceptualization, methodology, data analysis, funding acquisition, and writing—review and editing. YX: methodology and writing—review and editing. SG: sample collection and methodology. DC: conceptualization, writing—review and editing, and funding acquisition. All authors contributed to manuscript preparation.

FUNDING

This study was supported by the National Natural Science Foundation of China (Grants: 41730528 and 42176069), National Key R&D Program of China (Grant: 2018YFC0310006), and Shanghai Rising-Star Program (21QA1403700).

ACKNOWLEDGMENTS

We thank the captains and crews of RVs *Haiyang-6* and *Haiyang-10* for their invaluable help with coring process during the expeditions. We also thank Urban J. Wünsch for helpful discussion on DOM optical data.

REFERENCES

Aller, R. C. (1978). Experimental studies of changes produced by deposit feeders on porewater, sediment, and overlying water chemistry. *Am. J. Sci.* 278, 1185–1234. doi: 10.2475/ajs.278.9.1185

Alperin, M. J., Albert, D. B., and Martens, C. S. (1994). Seasonal variations in production and consumption rates of dissolved organic carbon in an organic-rich coastal sediment. *Geochim. Cosmochim. Acta* 58, 4909–4929. doi: 10.1016/0016-7037(94)90221-6

Amaral, V., Romera-Castillo, C., and Forja, J. (2021). Submarine mud volcanoes as a source of chromophoric dissolved organic matter to the deep waters of the Gulf of Cádiz. *Sci. Rep.* 11:3200. doi: 10.1038/s41598-021-82632-3

Arrieta, J. M., Mayol, E., Hansman, R. L., Herndl, G. J., Dittmar, T., and Duarte, C. M. (2015). Dilution limits dissolved organic carbon utilization in the deep ocean. *Science* 348, 331–333. doi: 10.1126/science.aac7249

Bauer, J. E., Reimers, C. E., Druffel, E. R. M., and Williams, P. M. (1995). Isotopic constraints on carbon exchange between deep ocean sediments and sea water. *Nature* 373, 686–689. doi: 10.1038/373686a0

Berner, R. A. (1980). *Early Diagenesis: A Theoretical Approach*. Princeton, NJ: Princeton University Press.

Borowski, W. S., Paull, C. K., and Ussler, W. (1999). Global and local variations of interstitial sulfate gradients in deep-water, continental margin sediments: sensitivity to underlying methane and gas hydrates. *Mar. Geol.* 159, 131–154. doi: 10.1016/S0025-3227(99)00004-3

Brogi, S. R., Kim, J. H., Ryu, J. S., Jin, Y. K., Lee, Y. K., and Hur, J. (2019). Exploring sediment porewater dissolved organic matter (DOM) in a mud volcano: clues of a thermogenic DOM source from fluorescence spectroscopy. *Mar. Chem.* 211, 15–24. doi: 10.1016/j.marchem.2019.03.009

Buffet, B., and Archer, D. (2004). Global inventory of methane clathrate: sensitivity to changes in the deep ocean. *Earth Planet. Sci. Lett.* 227, 185–199. doi: 10.1016/j.epsl.2004.09.005

Burdige, D. J. (2002). "Sediment pore waters," in *Biogeochemistry of Marine Dissolved Organic Matter*, eds D. A. Hansell and C. A. Carlson (Cambridge, MA: Academic Press), 611–663.

Burdige, D. J., Berelson, W. M., Coale, K. H., McManus, J., and Johnson, K. S. (1999). Fluxes of dissolved organic carbon from California continental margin sediments. *Geochim. Cosmochim. Acta* 63, 1507–1515.

Burdige, D. J., Kline, S. W., and Chen, W. (2004). Fluorescent dissolved organic matter in marine sediment pore waters. *Mar. Chem.* 89, 289–311. doi: 10.1016/j.marchem.2004.02.015

Burdige, D. J., Komada, T., Magen, C., and Chanton, J. P. (2016). Modeling studies of dissolved organic matter cycling in Santa Barbara Basin (CA, USA) sediments. *Geochim. Cosmochim. Acta.* 195, 100–119.

Cao, M., Ma, Q., Wu, Y., and Zhang, J. (2017). Difference in organic matter distribution and degradation in surface sediment between Northern South China Sea and Hainan Island. *Oceanol. Limnol. Sin.* 48, 258–265.

Cerro-Gálvez, E., Casal, P., Lundin, D., Piña, B., Pinhassi, J., Dachs, J., et al. (2019a). Microbial responses to anthropogenic dissolved organic carbon in the Arctic and Antarctic coastal seawaters. *Environ. Microbiol.* 21, 1466–1481. doi: 10.1111/1462-2920.14580

Cerro-Gálvez, E., Sala, M. M., Marrasé, C., Gasol, J. M., Dachs, J., and Vila-Costa, M. (2019b). Modulation of microbial growth and enzymatic activities in the marine environment due to exposure to organic contaminants of emerging concern and hydrocarbons. *Sci. Total Environ.* 678, 486–498. doi: 10.1016/j.scitotenv.2019.04.361

Chen, M., Jung, J., Lee, Y. K., and Hur, J. (2018). Surface accumulation of low molecular weight dissolved organic matter in surface waters and horizontal off-shelf spreading of nutrients and humic-like fluorescence in the Chukchi Sea of the Arctic Ocean. *Sci. Total Environ.* 639, 624–632. doi: 10.1016/j.scitotenv

Chen, M., Kim, J. H., Nam, S. I., Niessen, F., Hong, W. L., Kang, M. H., et al. (2016). Production of fluorescent dissolved organic matter in Arctic Ocean sediments. *Sci. Rep.* 6:39213. doi: 10.1038/srep39213

Coble, P. G. (1996). Characterisation of marine and terrestrial DOM in seawater using excitation-emission matrix spectroscopy. *Mar. Chem.* 51, 325–346. doi: 10.1016/0304-4203(95)00062-3

Coble, P. G. (2007). Marine optical biogeochemistry: the chemistry of ocean color. *Chem. Rev* 107, 402–418. doi: 10.1021/cr050350

Cory, R. M., Mcneill, K., Cotner, J. P., Amado, A., Purcell, J. M., and Marshall, A. G. (2010). Singlet oxygen in the coupled photochemical and biochemical oxidation of dissolved organic matter. *Environ. Sci. Technol.* 44, 3683–3689. doi: 10.1021/es902989y

Dittmar, T., and Stubbins, A. (2014). "Dissolved organic matter in aquatic systems," in *Treatise on Geochemistry*, 2nd Edn, eds H. D. Holland and K. K. Turekian (Amsterdam: Elsevier Ltd), 125–156.

Dittmar, T., Lennartz, S. T., Wises, H. B., Hansell, D. A., Santinelli, C., Vanni, C., et al. (2021). Enigmatic persistence of dissolved organic matter in the ocean. *Nat. Rev. Earth Environ.* 2, 570–583. doi: 10.1038/s43017-021-00183-7

Dvorski, S. E. M., Gonsior, M., Hertkorn, N., Uhl, J., Muller, H., Griebler, C., et al. (2016). Geochemistry of dissolved organic matter in a spatially highly resolved groundwater petroleum hydrocarbon plume cross-section. *Environ. Sci. Technol.* 50, 5536–5546. doi: 10.1021/acs.est.6b00849

Fu, W., Qi, Y., Liu, Y., Wang, X., Druffel, E. R. M., Xu, X., et al. (2020). Production of ancient dissolved organic carbon in arctic ocean sediment: a pathway of carbon cycling in the extreme environment. *Geophys. Res. Lett* 47:e2020GL087119. doi: 10.1029/2020GL087119

Guan, H., Feng, D., Birgel, D., Peckmann, J., Roberts, H. H., Wu, N., et al. (2019). Lipid biomarker patterns reflect different formation environments of mussel- and tubeworm-dominated seep carbonates from the Gulf of Mexico (Atwater Valley and Green Canyon). *Chem. Geol.* 505, 36–47. doi: 10.1016/j.chemgeo.2018.12.005

Hansell, D. A., and Carlson, C. A. (1998). Deep-ocean gradients in the concentration of dissolved organic carbon. *Nature* 395, 263–266. doi: 10.1038/26200

Hoehler, T. M., Alperin, M. J., Albert, D. B., and Martens, C. S. (1994). Field and laboratory studies of methane oxidation in an anoxic marine sediment-evidence for a methanogen–sulfate reducer consortium. *Glob. Biogeochem. Cycles* 8, 451–463. doi: 10.1029/94GB01800

Hood, E., Fellman, J., Spencer, R., Hernes, P. J., Edwards, R., Amore, D. D., et al. (2009). Glaciers as a source of ancient and labile organic matter to the marine environment. *Nature* 462, 1044–1047. doi: 10.1038/nature08580

Hu, Y., Luo, M., Liang, Q., Chen, L., Feng, D., Yang, S., et al. (2019). Pore fluid compositions and inferred fluid flow patterns at the Haima cold seeps of the South China Sea. *Mar. Pet. Geol.* 103, 29–40. doi: 10.1016/j.marpetgeo.2019.01.007

Huguet, A., Vacher, L., Relexans, S., Saubusse, S., Froidefond, J. M., and Parlanti, E. (2009). Properties of fluorescent dissolved organic matter in the Gironde Estuary. *Org. Geochem.* 40, 706–719. doi: 10.1016/j.orggeochem.2009.03.002

Hung, C. W., Huang, K. H., Shih, Y. Y., Chen, H. H., Wang, C. C., Ho, C. Y., et al. (2016). Benthic fluxes of dissolved organic carbon from gas hydrate sediments in the northern South China Sea. *Sci. Rep.* 6:29597. doi: 10.1038/srep29597

Jiao, N., Herndl, G. J., Hansell, D. A., Benner, R., Kattner, G., Wilhelm, S. W., et al. (2010). Microbial production of recalcitrant dissolved organic matter: long-term carbon storage in the global ocean. *Nat. Rev. Microbiol.* 8, 593–599. doi: 10.1038/nrmicro2386

Kleber, M. (2010). What is recalcitrant soil organic matter? *Environ. Chem.* 7, 320–332. doi: 10.1071/EN10006

Komada, T., Burdige, D. J., Crispo, S. M., Druffel, E. R. M., Griffin, S., Johnson, L., et al. (2013). Dissolved organic carbon dynamics in anaerobic sediments of the Santa Monica Basin. *Geochim. Cosmochim. Acta* 110, 253–273. doi: 10.1016/j.gca.2013.02.017

Komada, T., Polly, J. A., and Johnson, L. (2012). Transformations of carbon in anoxic marine sediments: implications from $\Delta^{14}C$ and $\delta^{13}C$ signatures. *Limnol. Oceanogr.* 57, 567–581. doi: 10.4319/lo.2012.57.2.0567

Kuivila, K. M., Murray, J. W., and De Vol, A. H. (1990). Methane production in the sulfate-depleted sediments of two marine basins. *Geochim. Cosmochim. Acta* 54, 403–411. doi: 10.1016/0016-7037(90)90329-J

Kvenvolden, K. A. (1988). Methane hydrate-a major reservoir of carbon in the shallow geosphere? *Chem. Geol.* 71, 41–51. doi: 10.1016/0009-2541(88)90104-0

Levin, L. A. (2005). Ecology of cold seep sediments: interactions of fauna with flow, chemistry and microbes. *Oceanogr. Mar. Biol.* 43, 1–46. doi: 10.1201/9781420037449-3

Liang, Q., Hu, Y., Feng, D., Chen, L., Yang, S., Liang, J., et al. (2017). Authigenic carbonates from newly discovered active cold seeps on the northwestern slope of the South China Sea: constraints on fluid sources, formation environments, and seepage dynamics. *Deep Sea Res. Part I* 124, 31–41. doi: 10.1016/j.dsr.2017.04.015

Loginova, A. N., Thomsen, S., and Engel, A. (2016). Chromophoric and fluorescent dissolved organic matter in and above the oxygen minimum zone off Peru. *J. Geophys. Res. Oceans* 121, 7973–7990.

Martin, W. R., and McCorkle, D. C. (1993). Dissolved organic carbon concentrations in marine pore waters determined by high-temperature oxidation. *Limnol. Oceanogr.* 38, 1464–1479. doi: 10.2307/2838277

Mcknight, D. M., Boyer, E. W., Westerhoff, P. K., Doran, P. T., Kulbe, T., and Andersen, D. T. (2001). Spectrofluorometric characterization of dissolved organic matter for indication of precursor organic material and aromaticity. *Limnol. Oceanogr.* 46, 38–48.

Milkov, A. V. (2004). Global estimates of hydrate-bound gas in marine sediments: how much is really out there? *Earth Sci. Rev.* 66, 183–197. doi: 10.1016/j.earscirev.2003.11.002

Mirnaghi, F. S., Pinchin, N. P., Yang, Z., Hollebone, B. P., Lambert, P., and Brown, C. E. (2019). Monitoring of polycyclic aromatic hydrocarbon contamination at four oil spill sites using fluorescence spectroscopy coupled with parallel factor-principal component analysis. *Environ. Sci. Process. Impacts* 21, 413–426. doi: 10.1039/C8EM00493E

Murphy, K. R., Stedmon, C. A., Graeber, D., and Bro, R. (2013). Fluorescence spectroscopy and multi-way techniques. *PARAFAC Anal. Methods* 5, 6557–6566. doi: 10.1039/C3AY41160E

Murphy, K. R., Stedmon, C. A., Waite, T. D., and Ruiz, G. M. (2008). Distinguishing between terrestrial and autochthonous organic matter sources in marine environments using fluorescence spectroscopy. *Mar. Chem.* 108, 40–58. doi: 10.1016/j.marchem.2007.10.003

Murphy, K. R., Stedmon, C. A., Wenig, P., and Bro, R. (2014). OpenFluor- an online spectral583 library of auto-fluorescence by organic compounds in the environment. *Anal. Methods* 6, 658–661. doi: 10.1039/c3ay41935e

Niewohner, C., Hensen, C., Kasten, S., Zabel, M., and Schulz, H. D. (1998). Deep sulfate reduction completely mediated by anaerobic methane oxidation in sediments of the upwelling area off Namibia. *Geochim. Cosmochim. Acta* 62:455e464. doi: 10.1016/S0016-7037(98)00055-6

Niu, M., Fan, X., Zhuang, G., Liang, Q., and Wang, F. (2017). Methane-metabolizing microbial communities in sediments of the Haima cold seep area, northwest slope of the South China Sea. *FEMS Microbiol. Ecol* 93:9. doi: 10.1093/femsec/fix101

Ohno, T. (2002). Fluorescence inner-filtering correction for determining the humification index of dissolved organic matter. *Environ. Sci. Technol.* 36, 742–746.

Peketi, A., Mazumdar, A., Joshi, R. K., Patil, D. J., Srinivas, P. L., and Dayal, A. M. (2012). Tracing the paleo sulfate-methane transition zones and H_2S seepage events in marine sediments: an application of C-S-Mo systematics. *Geochem. Geophys. Geosyst.* 13:Q10007. doi: 10.1029/2012GC004288

Podgorski, D. C., Zito, P., McGuire, J. T., Martinovic-Weigelt, D., Cozzarelli, I. M., Bekins, B. A., et al. (2018). Examining natural attenuation and acute toxicity of petroleum-derived dissolved organic matter with optical spectroscopy. *Environ. Sci. Technol.* 52, 6157–6166. doi: 10.1021/acs.est.8b00016

Pohlman, J. W., Bauer, J. E., Waite, W. F., Osburn, C. L., and Chapman, N. R. (2011). Methane hydrate-bearing seeps as a source of aged dissolved organic carbon to the oceans. *Nat. Geosci.* 4, 37–41. doi: 10.1038/ngeo1016

Raven, M. R., Adkins, J. F., Werne, J. P., Lyons, T. W., and Sessions, A. L. (2015). Sulfur isotopic composition of individual organic compounds from Cariaco Basin sediments. *Org. Geochem.* 80, 53–59.

Raymond, P. A., and Bauer, J. E. (2001). Riverine export of aged terrestrial organic matter to the North Atlantic Ocean. *Nature* 409, 497–500. doi: 10.1038/35054034

Raymond, P. A., McClelland, J. W., Holmes, R. M., Zhulidov, A. V., Mull, K., Peterson, B. J., et al. (2007). Flux and age of dissolved organic carbon exported to the Arctic Ocean: a carbon isotopic study of the five largest arctic rivers. *Global. Biogeochem. Cycles* 21:GB4011. doi: 10.1029/2007GB002934

Reeburgh, W. S. (2007). Oceanic methane biogeochemistry. *Chem. Rev.* 107, 486–513. doi: 10.1021/cr050362v

Schmidt, F., Elvert, M., Koch, B. P., Witt, M., and Hinrichs, K.-U. (2009). Molecular characterization of dissolved organic matter in pore water of continental shelf sediments. *Geochim. Cosmochim. Acta* 73, 3337–3358. doi: 10.1016/j.gca.2009.03.008

Schmidt, F., Koch, B. P., Goldhammer, T., Elvert, M., Witt, M., Lin, Y. S., et al. (2017). Unraveling signatures of biogeochemical processes and the depositional setting in the molecular composition of pore water DOM across different marine environments. *Geochim. Cosmochim. Acta* 207, 57–80. doi: 10.1016/j.gca.2017.03.005

Schouten, S., De Graaf, W., Sinninghe Damste, J. S., van Driel, G. B., and de Leeuw, J. W. (1994). Laboratory simulation of natural sulphurization: II. Reaction of multi-functionalized lipids with inorganic polysulphides at low temperatures. *Org. Geochem.* 22, 825–834. doi: 10.1016/0146-6380(94)90142-2

Seidel, M., Beck, M., Riedel, T., Waska, H., Suryaputra, I. G. N. A., Schnetger, B., et al. (2014). Biogeochemistry of dissolved organic matter in an anoxic intertidal creek bank. *Geochim. Cosmochim. Acta* 140, 418–434. doi: 10.1016/j.gca.2014.05.038

Sert, M. F., D'Andrilli, J., Gründger, F., Niemann, H., Granskog, M. A., Pavlov, A. K., et al. (2020). Compositional differences in dissolved organic matter

between arctic cold seeps versus non-seep sites at the svalbard continental margin and the Barents Sea. *Front. Earth Sci.* 8:552731. doi: 10.3389/feart.2020.552731

Sleighter, R. L., Chin, Y.-P., Arnold, W. A., Hatcher, P. G., McCabe, A. J., McAdams, B. C., et al. (2014). Evidence of incorporation of Abiotic S and N into prairie wetland dissolved organic matter. *Environ. Sci. Technol. Lett.* 1, 345–350. doi: 10.1021/ez500229b

Sultan, N., Garziglia, S., and Ruffine, L. (2016). New insights into the transport processes controlling the sulfate-methane-transition-zone near methane vents. *Sci. Rep.* 6:26701. doi: 10.1038/srep26701

Valentine, D. L., Kastner, M., Wardlaw, G. D., Wang, X., Purdy, A., and Bartlett, D. H. (2005). Biogeochemical investigations of marine methane seeps, Hydrate Ridge, Oregon. *J. Geophys. Res.* 110:GO2005. doi: 10.1029/2005JG000025

Wagner, S., Schubotz, F., Kaiser, K., Hallmann, C., Waska, H., Rossel, P. E., et al. (2020). Soothsaying DOM: a current perspective on the future of oceanic dissolved organic carbon. *Front. Mar. Sci.* 7:341. doi: 10.3389/fmars.2020.00341

Walker, B. D., Druffel, E., Kolasinski, J., Roberts, B. J., Xu, X., and Rosenheim, B. E. (2017). Stable and radiocarbon isotopic composition of dissolved organic matter in the Gulf of Mexico. *Geophys. Res. Lett.* 44, 8424–8434. doi: 10.1002/2017GL074155

Wang, X. J., Wu, S. G., Dong, D., Gong, Y. H., and Chai, C. (2008). Characteristics of gas chimney and its relationship to gas hydrate in Qiongdongnan Basin. *Mar. Geol. Quat. Geol.* 28, 103–108.

Wei, J., Li, J., Wu, T., Zhang, W., Li, J., Wang, J., et al. (2020). Geologically controlled intermittent gas eruption and its impact on bottom water temperature and chemosynthetic communities-a case study in the "HaiMa" cold seeps, South China Sea. *Geol. J.* 55, 6066–6078.

Werne, J. P., Lyons, T. W., Hollander, D. J., Schouten, S., Hopmans, E. C., and Sinninghe Damsteé, J. S. (2008). Investigating pathways of diagenetic organic matter sulfurization using compoundspecific sulfur isotope analysis. *Geochim. Cosmochim. Acta* 72, 3489–3502. doi: 10.1016/j.gca.2008.04.033

Yang, S., Lv, Y., Liu, X., Wang, Y., Fan, Q., Yang, Z., et al. (2020). Genomic and enzymatic evidence of acetogenesis by anaerobic methanotrophic archaea. *Nat. Commun.* 11:3941. doi: 10.1038/s41467-020-17860-8

Zachos, J. C., Röhl, U., Schellenberg, S. A., Sluijs, A., Hodell, D. A., Kelly, D. C., et al. (2005). Rapid acidification of the ocean during the paleocene-eocene thermal maximum. *Science* 308, 1611–1615. doi: 10.1126/science.1109004

Conflict of Interest: The authors declare that the research was conducted in the absence of any commercial or financial relationships that could be construed as a potential conflict of interest.

Publisher's Note: All claims expressed in this article are solely those of the authors and do not necessarily represent those of their affiliated organizations, or those of the publisher, the editors and the reviewers. Any product that may be evaluated in this article, or claim that may be made by its manufacturer, is not guaranteed or endorsed by the publisher.

frontiers in Marine Science

ORIGINAL RESEARCH
published: 10 March 2022
doi: 10.3389/fmars.2022.831286

Lipid Biomarker Patterns Reflect Nutritional Strategies of Seep-Dwelling Bivalves From the South China Sea

Hongxiang Guan[1,2], Dong Feng[2,3], Daniel Birgel[4]*, Steffen Kiel[5], Jörn Peckmann[4], Sanzhong Li[1,2] and Jun Tao[6]*

[1] Frontiers Science Center for Deep Ocean Multispheres and Earth System, Key Lab of Submarine Geosciences and Prospecting Techniques, Ministry of Education and College of Marine Geosciences, Ocean University of China, Qingdao, China, [2] Laboratory for Marine Mineral Resources, Qingdao National Laboratory for Marine Science and Technology, Qingdao, China, [3] Shanghai Engineering Research Center of Hadal Science and Technology, College of Marine Sciences, Shanghai Ocean University, Shanghai, China, [4] Institute for Geology, Center for Earth System Research and Sustainability, Universität Hamburg, Hamburg, Germany, [5] Department of Paleobiology, Swedish Museum of Natural History, Stockholm, Sweden, [6] MLR Key Laboratory of Marine Mineral Resources, Guangzhou Marine Geological Survey, Guangzhou, China

OPEN ACCESS

Edited by:
Fengping Wang,
Shanghai Jiao Tong University, China

Reviewed by:
Wang Minxiao,
Institute of Oceanology (CAS), China
Xin Chen,
Shanghai Jiao Tong University, China
Solveig Irena Bühring,
University of Bremen, Germany

***Correspondence:**
Hongxiang Guan
guanhongxiang@ouc.edu.cn
Daniel Birgel
daniel.birgel@uni-hamburg.de

Specialty section:
This article was submitted to Marine Molecular Biology and Ecology, a section of the journal Frontiers in Marine Science

Received: *08 December 2021*
Accepted: *15 February 2022*
Published: *10 March 2022*

Citation:
Guan H, Feng D, Birgel D, Kiel S, Peckmann J, Li S and Tao J (2022) Lipid Biomarker Patterns Reflect Nutritional Strategies of Seep-Dwelling Bivalves From the South China Sea. Front. Mar. Sci. 9:831286. doi: 10.3389/fmars.2022.831286

Invertebrates living at methane seeps such as mussels and clams gain nutrition through symbiosis with chemosynthetic, chiefly methanotrophic and thiotrophic bacteria. Lipid biomarkers, including their compound-specific carbon stable isotope compositions, extracted from the host tissues are predestined for deciphering the various sources of diets and the associations among varying environments, endosymbionts, and hosts. Here, we investigated lipid inventories of soft tissues of two bathymodiolin mussel species hosting aerobic methanotrophic bacteria (*Gigantidas platifrons* from Site F and *Gigantidas haimaensis* from Haima seeps), one bathymodiolin mussel with thiotrophic bacteria (*Bathymodiolus aduloides* from Haima seeps), and one vesicomyid clam (*Archivesica marissinica* from Haima seeps) from the South China Sea. The gills of mussels hosting methanotrophic symbionts were found to contain high amounts of lipids of aerobic methanotrophic bacteria, such as the 4,4-dimethyl lanosterol, and other 4-methyl sterols, and the type I methanotroph-specific monounsaturated fatty acids (MUFAs) $C_{16:1\omega9}$ and $C_{16:1\omega8}$. Production of methyl-sterols is favored over fatty acids at low oxygen concentrations, as demonstrated in culture experiments with *Methylococcus capsulatus*. Since lesser fatty acids and abundant sterols are found in *G. haimaensis* compared to *G. platifrons*, *G. haimaensis* apparently lived at very low oxygen levels. Extremely high levels of MUFAs $C_{16:1\omega7}$ and $C_{18:1\omega7}$ were found in gill tissue of both *B. aduloides* and the vesicomyid clam *A. marissinica*. Given the absence of ω8 fatty acids, both *B. aduloides* and the vesicomyid clam contain thiotrophic bacteria only. The occurrence of ^{13}C-enriched 24-methylenecholesterol in *B. aduloides* indicates that the animal complemented its diet by filter-feeding (ca. 3% of the total sterol inventory) on photosynthetically derived carbon, whereas the majority of sterols are pointing to a diet relying on endosymbionts. Different types of 4-methyl

sterols were observed between the thiotroph-containing mussel and methanotroph-containing mussels, suggesting different biosynthetic steps are present from lanosterol to cholesterol between animal hosts and aerobic methanotrophs. Among the four bivalve species, specific lipid biomarker patterns diagnostic for either the symbionts or the hosts yielded similar $\delta^{13}C$ values in each species, indicating that the host obtained its nutrition either directly from the symbionts or derived at least most of its carbon in this way. The information derived from lipid biomarkers of bivalves and their corresponding symbionts in modern environments is vital to interpret data from the rock record, where most other methods to study microbial community composition are not applicable.

Keywords: chemosynthesis, symbiosis, aerobic methanotrophic bacteria, thiotrophic bacteria, lipid biomarkers, compound-specific carbon isotopes, South China Sea

INTRODUCTION

Chemosymbiotic invertebrates from hydrothermal vents and methane seeps, including mussels and clams, gain nutrition through chemosynthetic bacterial symbionts (Childress et al., 1986; Brooks et al., 1987; Fisher et al., 1987; Duperron et al., 2009, 2014). Such symbionts use either reduced sulfur compounds like hydrogen sulfide or methane as electron donors, with oxygen as electron acceptor, providing the invertebrate hosts with nutrition (Petersen and Dubilier, 2010). The host animal provides a stable environment, electron donors, and electron acceptors for the symbionts (Petersen and Dubilier, 2010).

The first report of mussels living in symbiosis with thiotrophic bacteria was from a hydrothermal vent site (Rau and Hedges, 1979), followed by reports from methane seeps, where mussels were found to harbor abundant intracellular methanotrophic bacteria in their gills (Childress et al., 1986). To date, more than 10 species of chemosymbiotic bathymodiolin mussels and clams have been reported from methane seep habitats and whale falls (Cordes et al., 2009; Faure et al., 2015; Duperron and Gros, 2016; Feng et al., 2018; Lan et al., 2019; Xu et al., 2019). It has been demonstrated that some bathymodiolin mussels host either thiotrophic (Cavanaugh, 1983; Distel et al., 1988) or aerobic methanotrophic bacteria, others harbor both types of symbionts, a phenomenon referred to as dual symbiosis (Childress et al., 1986; Fisher et al., 1993; Fiala-Médioni et al., 2002; Cordes et al., 2009; Xu et al., 2019). Putative chemosymbiotic invertebrates were also common at ancient seeps (Kiel, 2010; Kiel and Peckmann, 2019; Kiel et al., 2021).

The phylogeny of bacterial symbionts varies with chemosymbiotic invertebrate species, habitat characteristics, and locations (Nelson and Fisher, 2000; Thornhill et al., 2008; Lorion et al., 2013; Laming et al., 2015; Szafranski et al., 2015; Duperron and Gros, 2016), but can also vary with symbiont populations in response to environmental change (Kádár et al., 2005; Bettencourt et al., 2008). For example different clades of symbionts were found for *Escarpia laminata* from Alaminos Canyon and the Florida Escarpment, both Gulf of Mexico (Nelson and Fisher, 2000; Thornhill et al., 2008). Furthermore, gradual loss and re-establishment of symbiosis in the gills of *Bathymodiolus azoricus* was observed when keeping the host in sulfide-free or sulfide-containing seawater, respectively (Kádár et al., 2005; Bettencourt et al., 2008). Fiala-Médioni et al. (2002) suggested the existence of dual symbiosis, providing the host with greater environmental tolerance and increased niche space. Unfortunately, symbiotic bacteria from hydrothermal vents and hydrocarbon seeps have not been cultured successfully to date (Franke et al., 2021). Symbiotic bacteria and their symbiotic associations between hosts and symbionts are typically studied with electron microscopy, enzymatic analyses, 16*S* *r*RNA work, as well as lipid biomarkers and their carbon stable isotope compositions (Duperron et al., 2009; Petersen and Dubilier, 2010; Feng et al., 2015).

The analysis of lipid biomarkers is not only a powerful tool to identify bacterial signatures in symbiotic invertebrates, but also to quantify the abundance of bacterial symbionts. Typically, the most abundant lipids are fatty acids. The fatty acid inventory of aerobic methanotrophic bacteria is characterized by the monounsaturated fatty acid (MUFA) $C_{16:1\omega9}$, but especially by the group-specific MUFAs $C_{16:1\omega8}$, and $C_{18:1\omega8}$. In contrast, thiotrophic symbionts produce the ubiquitous MUFAs $C_{16:1\omega7}$ and $C_{18:1\omega7}$ (Jannasch, 1985; Nichols et al., 1985; Jahnke and Nichols, 1986; Bowman et al., 1991; Guezennec and Fiala-Medioni, 1996), which are common constituents of bacteria and eukaryotes, and are also produced or taken up by the host animals. Polyunsaturated fatty acids (PUFAs) *n*-C_{18}, *n*-C_{20}, and *n*-C_{22} are most likely taken up and stored by the host after heterotrophic consumption (Fullarton et al., 1995; Pond et al., 2000) rather than produced by endosymbiotic bacteria (Dunstan et al., 1993; Kawashima and Ohnishi, 2003). Besides fatty acids, chemosymbiotic mussels contain bacteriohopanepolyols (aminotriol and aminotetrol), and various 4,4-dimethyl sterols and 4-methyl sterols, exclusively derived from symbiotic aerobic methanotrophic bacteria (Fang et al., 1993; Jahnke et al., 1995; Pond et al., 1998; Riou et al., 2010; Kellermann et al., 2012).

Apart from the lipids of endosymbiotic bacteria, lipid biomarkers and compound-specific carbon stable isotope compositions of free-living aerobic methanotrophic bacteria have been studied intensively (Summons et al., 1994; Jahnke et al., 1999; Schouten et al., 2000; Talbot et al., 2001; Cordova-Gonzalez et al., 2020). In contrast to the ubiquitous occurrence of Type I and X methanotrophs in diverse natural environments, including the marine realm, type II methanotrophs seem to be confined to terrestrial habitats (Knief, 2015). The identification

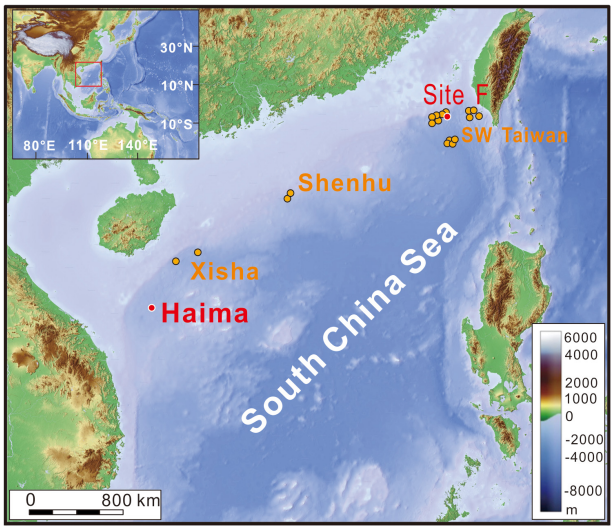

FIGURE 1 | Map showing the location of the sampling sites. Site F and Haima are active methane seeps (highlighted by red circles); orange circles indicate inactive methane seeps on the northern and western continental slope of the South China Sea.

of the different types of aerobic methanotrophs (Type I, X, and II) is commonly possible with biomarkers, since the different types of methanotrophs contain different biomarkers. For example, a high abundance of the MUFA $C_{16:1\omega8}$ was found in Type I and X methanotrophs, whereas MUFA $C_{18:1\omega8}$ tends to be predominant in Type II methanotrophs (Nichols et al., 1985; Bowman et al., 1991). On the other hand, 4-methyl steroids are highly specific biomarkers of Type I methanotrophs (e.g., Bouvier et al., 1976; Schouten et al., 2000). Information from lipid biomarkers can be complemented by their carbon stable isotope patterns, reflecting different carbon assimilation pathways of aerobic methanotrophs. Type-I and -X methanotrophs use the ribulose monophosphate (RuMP) pathway, whereas Type-II methanotrophs use the serine pathway (Anthony, 1982; Summons et al., 1994; Jahnke et al., 1999). The different assimilation pathways lead to distinct carbon isotopic fractionation (Jahnke et al., 1999; Cordova-Gonzalez et al., 2020). For example, Type I methanotrophs produce more highly ^{13}C-depleted lipids relative to Type II methanotrophs (Summons et al., 1994; Jahnke et al., 1999; Cordova-Gonzalez et al., 2020). Moreover, the δ^{13}C values of hopanoids and steroids synthesized by Type I methanotrophs are as much as 5–7‰ more negative than fatty acids, whereas in Type II methanotrophs, fatty acids are more depleted in ^{13}C than hopanoids (Summons et al., 1994; Jahnke et al., 1999). Therefore, lipid biomarkers alongside compound-specific carbon stable isotopes are primed to become part of the standard toolkit to discriminate the different types of symbionts and evaluate the nutritional status and associations between symbionts and hosts in chemosymbiosis.

We studied seep bivalves collected from two active seep sites of the South China Sea (**Figures 1**, **2**). The mussel *Gigantidas platifrons* was collected at Site F seep (also called Formosa ridge) at 1120 m water depth (Feng et al., 2015). One of the mussels and a clam retrieved from the Haima seep at 1390 m water depth were identified as new species and described as *G. haimaensis* and *A. marissinica* (Liang et al., 2017). The other mussel, *Bathymodiolus aduloides,* was collected at the Haima seep at 1390 m water depth. Transmission electron microscopy and 16S *r*RNA-encoding gene sequence analyses indicated that *G. platifrons* and *G. haimaensis* contain mainly aerobic methanotrophic bacteria as symbionts in their gills (Barry et al., 2002; Xu et al., 2019), whereas *B. aduloides* and *A. marissinica* were reported to live in symbiosis with thiotrophic bacteria (Feng et al., 2018; Lan et al., 2019). In this study, lipid biomarkers and compound-specific carbon stable isotope compositions were used to examine carbon assimilation pathways, nutritional status, and different host–symbiont associations in various environments, hosts, and symbionts of the four species of seep-dwelling bivalves from the South China Sea.

MATERIALS AND METHODS

Sample Collection and Storage

Specimens of *G. platifrons* were collected in May 2018 using the ROV *ROPOS* during a cruise with the Research Vessel "*Tan Kah Kee*" to Site F. Specimens of *G. haimaensis*, *A. marissinica*, and *B. aduloides* were retrieved in April 2018 and May 2019 from the Haima seep using the ROV *Haima* (**Table 1**). At the sampling sites, dense *G. platifrons*, *G. haimaensis*, and *A. marissinica* clusters were observed, respectively, covering large areas of the seabed. Several *B. aduloides* were scattered among carbonate blocks. Bottom water temperatures at both Site F and Haima seep were 3.0 to 3.5°C. After sampling, bivalves were stored onboard at −80°C and shipped to the home laboratory and kept at −25°C. The bivalves were dissected into gill, foot, and remaining tissue, immediately freeze-dried, ground, homogenized and kept at −25°C until further analysis.

Lipid Extraction and Analysis

Lipids were extracted from the gill and foot tissues of *G. platifrons*, *G. haimaensis*, *A. marissinica*, and *B. aduloides*. The homogenate was extracted with the solvents dichloromethane (3×), methanol:dichloromethane (1:1, v:v) (3×), and methanol (3×) using an ultrasonic bath to obtain the total lipid extracts (TLE). An aliquot of the TLE was saponified after addition of internal standards (19-methylarachidic acid, and tridecyl alcohol) with 6% KOH (w/v) in methanol (2 h at 70°C). Unfortunately, the concentration of the 19-methylarachidic acid standard in the fatty acid fraction was too low in comparison with the target compounds, resulting in a potential error in the quantification of fatty acids. The absolute contents of fatty acids should consequently not be taken at face value. Therefore, the relative portions of carboxylic acids and alcohols of the overall compound inventory of the respective fractions are provided in **Tables 2**, **3** in addition to absolute contents. The neutral fractions were extracted from the saponified TLE with *n*-hexane. To obtain carboxylic acids, the residuals were treated with 10% HCl to pH = 2 and extracted using *n*-hexane. It needs to be stressed

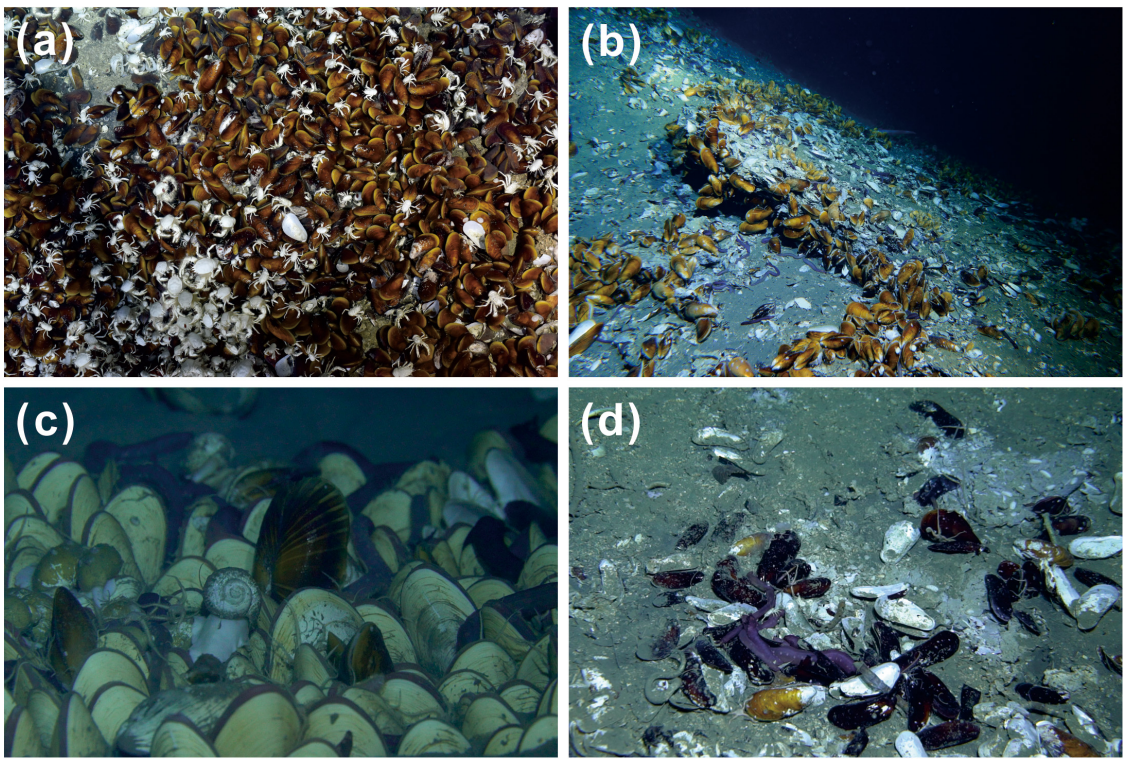

FIGURE 2 | Seafloor images from Site F **(a)** and Haima **(b–d)** methane seeps and the four species of bivalves *Gigantidas platifrons* **(a)**, *Gigantidas haimaensis* **(b)**, *Archivesica marissinica* **(c)**, and *Bathymodiolus aduloides* **(d)**.

TABLE 1 | Information on the four studied seep bivalves.

Host species	Sampling location	Habitat	Gammaproteobacterial endosymbionts	Associated Epsilonproteobacterial bacteria	References for symbionts
Gigantidas platifrons	South China Sea/Sagami Bay/Okinawa Trough	Hydrothermal vents/methane seeps	Methanotrophic bacteria	Yes	Duperron et al., 2009; Feng et al., 2015; Assié et al., 2016
Gigantidas haimaensis	South China Sea	Methane seeps	Methanotrophic bacteria	Yes	Xu et al., 2019
Archivesica marissinica	South China Sea	Methane seeps	Thiotrophic bacteria	n.d.	Lan et al., 2019 and this study
Bathymodiolus aduloides	South China Sea	Methane seeps	Thiotrophic bacteria	n.d.	Feng et al., 2018 and this study

n.d., not detected.

that bacteriohopanepolyols (BHPs) are commonly present in aerobic methanotrophic bacteria; however, we decided to focus on fatty acids and sterols and did not analyze BHPs in this study. The neutral fractions were silylated with bis(trimethylsilyl) trifluoroacetamide (BSTFA) for 3 h at 70°C, and the acid fractions were methylated with 14% BF_3-methanol in a screwcap vial (2 h at 60°C). To determine double bond positions of monounsaturated fatty acids, fatty acid methyl esters in *n*-hexane (50 μl) were treated with dimethyl disulfide (DMDS, 100 μ1) and iodine solution (500 μl; 6% w/v in diethyl ether), filled with argon and stored at 50°C for 48 h. After cooling, iodine was removed by shaking with drops of 5% (w:v) aqueous sodium thiosulfate (Nichols et al., 1986; Guan et al., 2021). The organic phase was removed and the aqueous phase was extracted with *n*-hexane to obtain the DMDS adducts. All fractions were analyzed with a Thermo Electron Trace GC–MS equipped with a 60-m DB-5 MS fused silica capillary column (0.32 mm i.d., 0.25 μm film thickness). Helium was used as carrier gas at a flow rate of 1.2 ml/min. Compound-specific carbon stable isotope analysis was performed on a GV Isoprime system interfaced to a Hewlett-Packard 6890 gas chromatograph at the Guangzhou Institute of Geochemistry, Chinese Academy of Sciences (GIG, CAS). The same chromatographic column was used for GC-MS analysis. The following GC temperature program was applied for GC-MS and GC-IRMS: initial temperature was held at 60°C for 2 min, from 60°C to 160°C at a ramp of 10°C/min; from 160

TABLE 2 | Contents and isotopic compositions of fatty acids (FAs) from bivalve tissues.

	Gigantidas platifrons				*Gigantidas haimaensis*				*Archivesica marissinica*				*Bathymodiolus aduloides*			
	Gill		Foot		Gill		Foot		Gill		Foot		Gill		Foot	
	Content (mg/g dw), %	$\delta^{13}C$ (‰)	Content (mg/g dw), %	$\delta^{13}C$ (‰)	Content (mg/g dw), %	$\delta^{13}C$ (‰)	Content (mg/g dw), %	$\delta^{13}C$ (‰)	Content (mg/g dw), %	$\delta^{13}C$ (‰)	Content (mg/g dw), %	$\delta^{13}C$ (‰)	Content (mg/g dw), %	$\delta^{13}C$ (‰)	Content (mg/g dw), %	$\delta^{13}C$ (‰)
Fatty acids																
$nC_{14:0}$	0.03 (<1)	n.d.	0.01 (<1)	n.d.	0.01 (<1)	n.d.	0.01 (<1)	n.d.	19.71 (9)	−45	0.13 (2)	−44	0.37 (1)	n.d.	<0.01	−44
$nC_{15:0}$	0.03 (<1)	n.d.	0.01 (<1)	n.d.	n.d.	n.d.	n.d.	n.d.	n.d.	n.d.	n.d.	n.d.	n.d.	n.d.	0.01 (<1)	n.d.
$nC_{16:1\omega9}$	n.d.	n.d.	n.d.	n.d.	n.d.	n.d.	n.d.	n.d.	n.d.	n.d.	0.06 (1)	n.d.	n.d.	n.d.	n.d.	n.d.
$nC_{16:1\omega8}$	5.64 (12)	−75[a]	n.d.	n.d.	0.93 (9)	−72[a]	n.d.	n.d.	n.d.	n.d.	n.d.	n.d.	n.d.	n.d.	n.d.	n.d.
$nC_{16:1\omega7c}$	11.17 (24)	n.d.	0.71 (8)	−70	0.94 (9)	n.d.	0.49 (5)	−65	92.81 (43)	−41	0.76 (10)	−43	13.08 (30)	−44	0.77 (4)	−46
$nC_{16:1\omega7t}$	n.d.	n.d.	n.d.	n.d.	n.d.	n.d.	n.d.	n.d.	7.62 (4)	n.d.	n.d.	n.d.	n.d.	n.d.	n.d.	n.d.
$nC_{16:1\omega5}$	n.d.	n.d.	n.d.	n.d.	n.d.	n.d.	n.d.	n.d.	0.99 (<1)	n.d.	n.d.	n.d.	0.62 (1)	−50	0.04 (<1)	n.d.
$nC_{16:2}$	4.19 (9)	n.d.	0.03 (<1)	n.d.	0.06 (1)	n.d.	n.d.	n.d.	n.d.	n.d.	n.d.	n.d.	n.d.	n.d.	n.d.	n.d.
$nC_{16:0}$	7.71 (16)	−74	1.54 (17)	−64	1.30 (12)	−67	1.62 (16)	−63	15.74 (7)	−40	0.88 (12)	−41	4.44 (10)	−41	2.63 (14)	−42
$nC_{17:0}$	0.14 (<1)	n.d.	0.15 (2)	−68	0.09 (1)	−68	0.06 (1)	−66	n.d.	n.d.	n.d.	n.d.	0.27 (1)	−40	0.20 (1)	−52
$nC_{18:3}$	1.79 (4)	n.d.	0.39 (4)	−59	0.05 (<1)	−58	0.15 (1)	n.d.	n.d.	n.d.	n.d.	n.d.	1.42 (3)	n.d.	1.07 (6)	n.d.
$nC_{18:4}$	1.73 (4)	n.d.	0.31 (3)	n.d.	n.d.	n.d.	n.d.	n.d.	n.d.	n.d.	n.d.	n.d.	3.19 (7)	−44	1.48 (8)	n.d.
$nC_{18:2}$	0.15 (<1)	n.d.	0.04 (<1)	n.d.	0.04 (<1)	n.d.	0.03 (<1)	n.d.	n.d.	n.d.	n.d.	n.d.	0.52 (1)	n.d.	0.17 (1)	n.d.
$nC_{18:2}$	0.62 (1)	n.d.	0.02 (<1)	n.d.	0.02 (<1)	n.d.	0.02 (<1)	n.d.	3.52 (2)	n.d.	0.10 (1)	−50	0.57 (1)	n.d.	0.19 (1)	n.d.
$nC_{18:1\omega9}$	n.d.	n.d.	n.d.	n.d.	0.04 (<1)	n.d.	0.04 (<1)	n.d.	n.d.	n.d.	n.d.	n.d.	0.34 (1)	n.d.	0.22 (1)	n.d.
$nC_{18:1\omega8}$	1.21 (3)	n.d.	n.d.	n.d.	0.08 (1)	n.d.	n.d.	n.d.	n.d.	n.d.	n.d.	n.d.	n.d.	n.d.	n.d.	n.d.
$nC_{18:1\omega7c}$	3.09 (7)	−72	0.72 (8)	−62	0.46 (4)	−65	0.51 (5)	−56.	4.30 (2)	n.d.	0.16 (2)	−45	3.12 (7)	−37	1.11 (6)	−46
$nC_{18:1\omega7t}$[b]	1.59 (3)	n.d.	0.11 (1)	n.d.	0.06 (1)	n.d.	n.d.	n.d.	n.d.	n.d.	n.d.	n.d.	n.d.	n.d.	n.d.	n.d.
$nC_{18:1\omega5}$	n.d.	n.d.	n.d.	n.d.	n.d.	n.d.	n.d.	n.d.	n.d.	n.d.	n.d.	n.d.	0.44 (1)	−39	0.45 (2)	−46
$nC_{18:0}$	1.25 (3)	−75	0.93 (10)	−67	0.53 (5)	−64	0.56 (5)	−61	5.34 (2)	−41	0.37 (5)	−37	1.40 (3)	−40	1.38 (7)	−40
$nC_{19:1\omega7}$	n.d.	n.d.	n.d.	n.d.	0.08 (1)	n.d.	0.06 (1)	n.d.	2.79 (1)	n.d.	0.10 (1)	−45	n.d.	n.d.	n.d.	n.d.
$nC_{20:4}$	n.d.	n.d.	n.d.	n.d.	n.d.	n.d.	n.d.	n.d.	n.d.	n.d.	n.d.	n.d.	1.31 (3)	n.d.	1.30 (7)	n.d.
$nC_{20:3}$	0.12 (<1)	n.d.	0.09 (1)	n.d.	0.06 (1)	n.d.	0.18 (2)	−54	n.d.	n.d.	n.d.	n.d.	0.23 (1)	n.d.	0.39 (2)	n.d.
$nC_{20:3}$	0.90 (2)	n.d.	0.39 (4)	−71	n.d.	n.d.	n.d.	n.d.	n.d.	n.d.	n.d.	n.d.	0.52 (1)	n.d.	0.39 (2)	n.d.
$nC_{20:2}$	1.37 (3)	−75	0.80 (9)	−71	0.70 (7)	−64	n.d.	−61	28.09 (13)	−41	0.14 (2)	−37	2.17 (5)	n.d.	1.61 (8)	n.d.
$nC_{20:2}$	1.35 (3)	n.d.	0.44 (5)	−76	0.40 (4)	n.d.	0.38 (4)	n.d.	9.79 (5)	−51	0.90 (12)	−47	3.96 (9)	−42	1.74 (9)	−43
$nC_{20:2}$	0.45 (1)	n.d.	0.06 (1)	−71	n.d.	n.d.	n.d.	n.d.	2.47 (1)	n.d.	n.d.	n.d.	0.16 (<1)	n.d.	0.03 (<1)	n.d.
$nC_{20:1\omega9}$	0.30 (1)	n.d.	0.42 (5)	n.d.	0.36 (3)	n.d.	0.47 (5)	−72	n.d.	n.d.	n.d.	n.d.	0.59 (1)	−36	0.67 (4)	−37
$nC_{20:1\omega7}$	1.73 (4)	−68	0.49 (5)	−68	1.09 (10)	−61	0.89 (9)	−61	18.82 (9)	−40	1.13 (16)	−44	3.03 (7)	−44	1.26 (7)	−46
$nC_{22:4}$	n.d.	n.d.	n.d.	n.d.	n.d.	n.d.	n.d.	n.d.	n.d.	n.d.	n.d.	n.d.	0.03 (<1)	n.d.	0.08 (<1)	n.d.

(Continued)

TABLE 2 | (Continued)

	Gigantidas platifrons				*Gigantidas haimaensis*				*Archivesica marissinica*				*Bathymodiolus aduloides*			
	Gill		Foot		Gill		Foot		Gill		Foot		Gill		Foot	
	Content (mg/g dw), %	$\delta^{13}C$ (‰)	Content (mg/g dw), %	$\delta^{13}C$ (‰)	Content (mg/g dw), %	$\delta^{13}C$ (‰)	Content (mg/g dw), %	$\delta^{13}C$ (‰)	Content (mg/g dw), %	$\delta^{13}C$ (‰)	Content (mg/g dw), %	$\delta^{13}C$ (‰)	Content (mg/g dw), %	$\delta^{13}C$ (‰)	Content (mg/g dw), %	$\delta^{13}C$ (‰)
$nC_{22:3}$	0.04 (<1)	n.d.	0.13 (1)	n.d.	0.05 (<1)	n.d.	0.10 (1)	n.d.	n.d.	n.d.	n.d.	n.d.	0.06 (<1)	n.d.	0.13 (1)	n.d.
$nC_{22:3}$	0.07 (<1)	n.d.	0.08 (1)	n.d.	n.d.	n.d.	n.d.	n.d.	n.d.	n.d.	n.d.	n.d.	0.04 (<1)	n.d.	0.05 (<1)	n.d.
$nC_{22:2}$	0.11 (<1)	n.d.	0.16 (2)	n.d.	0.06 (1)	n.d.	0.25 (2)	n.d.	n.d.	n.d.	0.20 (3)	n.d.	n.d.	n.d.	n.d.	n.d.
$nC_{22:2}$	0.47 (1)	n.d.	1.13 (12)	−69	2.46 (23)	−66	2.82 (27)	−65	n.d.	n.d.	0.59 (8)	−48	1.32 (3)	−44	1.40 (7)	−47
$nC_{22:1\omega9}$	n.d.	n.d.	n.d.	n.d.	0.77 (7)	n.d.	1.58 (15)	n.d.	n.d.	n.d.	0.35 (5)	n.d.	0.06 (<1)	n.d.	0.15 (1)	n.d.
$nC_{22:1\omega7}$	n.d.	n.d.	n.d.	n.d.	n.d.	n.d.	n.d.	n.d.	3.33 (2)	n.d.	1.42 (19)	−44	0.08 (<1)	n.d.	0.04 (<1)	n.d.
$nC_{22:0}$	n.d.	n.d.	n.d.	n.d.	0.03 (<1)	n.d.	0.07 (1)	n.d.	n.d.	n.d.	n.d.	n.d.	n.d.	n.d.	n.d.	n.d.
Sum	47.24		9.16		10.59		10.24		215.30		7.29		42.56		18.76	
Average $\delta^{13}C$ value		−73		−68		−62		−61		−43		−44		−41		−43

[a] $C_{16:1\omega8}$ + $C_{16:1\omega7}$.
[b] $C_{18:1\omega7t}$ co-eluted with $C_{18:2}$.
n.d., not detected.

to 320°C at a ramp of 1°C/min, and then held at 320°C for 30 min. The analytes were identified by their retention times and comparison with published mass spectra. The carbon isotopic composition is expressed in the standard δ notation in per mil (‰) relative to Vienna-PeeDee Belemnite (V-PDB) standard. The fatty acid methyl esters (FAMEs) and trimethylsiloxyl (TMS) derivatives were corrected for the addition of carbon during the derivatization. The fatty acids were measured as FAMEs and were corrected for the addition of an extra carbon due to the derivatization according to the following equation:

$$\delta^{13}C_{FA} = [(C_{n+1})\delta^{13}C_{FAME} - \delta^{13}C_{MEOH}]/C_n$$

The $\delta^{13}C_{FA}$ indicates the $\delta^{13}C$ value of the fatty acid, C_n represents the number of carbons in the fatty acid, $\delta^{13}C_{FAME}$ is the $\delta^{13}C$ value of the FAME, and $\delta^{13}C_{MEOH}$ is the $\delta^{13}C$ value of the methanol used for the methylation reaction.

The sterols or *n*-alcohols were measured as TMS-derivatives and were corrected for the addition of three extra carbons according to the following equation:

$$\delta^{13}C_{alcohol} = [(C_{n+3})\delta^{13}C_{TMS-derivatives} - 3\delta^{13}C_{TMS}]/C_n$$

The $\delta^{13}C_{alcohol}$ and C_n denotes the $\delta^{13}C$ value and the number of carbons in the target biomarker, respectively; $\delta^{13}C_{TMS}$ is the $\delta^{13}C$ value of the TMS in BSTFA, and $\delta^{13}C_{TMS-derivatives}$ is the $\delta^{13}C$ value for the TMS-derivative.

Each sample was measured at least in duplicate and the average values were used. Measurements were calibrated by several pulses of carbon dioxide with known $\delta^{13}C$ value before and after each run. An *n*-alkane mixture (C_{12} to C_{35}) of known isotopic composition was used to check instrument precision. All measured fractions and their compounds were diluted to concentrations of about 20 μg/ml. The injection volume was 1 to 2 μl. Generally, $\delta^{13}C$ values of target compounds were only collected when peak heights were higher than one third of the reference carbon dioxide peaks (see **Supplementary Figure S1**). The standard deviation of the compound-specific carbon isotope measurement was <0.8‰.

RESULTS

Fatty Acids

Generally, the net contents of fatty acids were much higher in gill than in foot tissues of *G. platifrons, A. marissinica*, and *B. aduloides*. Only for *G. haimaensis*, the contents of fatty acids were similar in gill and foot tissues. In foot tissues, PUFAs C_{18}, C_{20}, and C_{22} were the most abundant fatty acids of *G. platifrons*, *G. haimaensis*, and *B. aduloides* with contents varying from 4 to 10 mg/g dry weight (dw). In contrast, both gill and foot tissues of *A. marissinica* were dominated by MUFAs. Among the MUFAs, $C_{16:1\omega7}$ was the most abundant fatty acid, corresponding to 24% of total fatty acids in the gill tissues of *G. platifrons*, 30% of total fatty acids in *B. aduloides*, and 43% of total fatty acids in *A. marissinica*. However, PUFA $C_{22:2}$,

TABLE 3 | Contents and isotopic compositions of sterols, hopanoid, and *n*-alcohols from bivalve tissues.

	Gigantidas platifrons				***Gigantidas haimaensis***				***Archivesica marissinica***				***Bathymodiolus aduloides***			
	Gill		**Foot**		**Gill**		**Foot**		**Gill**		**Foot**		**Gill**		**Foot**	
	Content (mg/g dw), (%)	**$\delta^{13}C$ (‰)**	**Content (mg/g dw), (%)**	**$\delta^{13}C$ (‰)**	**Content (mg/g dw), (%)**	**$\delta^{13}C$ (‰)**	**Content (mg/g dw), (%)**	**$\delta^{13}C$ (‰)**	**Content (mg/g dw), (%)**	**$\delta^{13}C$ (‰)**	**Content (mg/g dw), (%)**	**$\delta^{13}C$ (‰)**	**Content (mg/g dw), (%)**	**$\delta^{13}C$ (‰)**	**Content (mg/g dw), (%)**	**$\delta^{13}C$ (‰)**
Sterols																
Cholesterol (I)	1.15 (44)	−78	0.44 (54)	−78	12.76 (21)	−74	11.64 (48)	−75	0.01 (17)	n.d.	0.02 (4)	n.d.	0.16 (46)	−40	0.21 (53)	−41
Cholestanol (II)	0.05 (2)	−81	0.24 (29)	−81	3.19 (5)	−75	2.39 (10)	n.d.	<0.01	n.d.	<0.01	n.d.	0.02 (6)	−46	0.05 (13)	−45
Cholesta-5,24-*dien*-3β-ol (III)	0.32 (12)	−84	n.d.	n.d.	9.47 (16)	−76	4.83 (20)	−78	n.d.	n.d.	n.d.	n.d.	n.d.	n.d.	n.d.	n.d.
24-Methylenecholesterol (IV)	n.d.	n.d.	n.d.	n.d.	n.d.	n.d.	n.d.	n.d.	n.d.	n.d.	n.d.	n.d.	0.01 (3)	−32	0.01 (3)	−30
cholest-7-*en*-3β-ol (V)	0.13 (5)	−80	n.d.	n.d.	7.16 (12)	−78	3.39 (14)	−76	n.d.	n.d.	n.d.	n.d.	0.01 (3)	−40	0.01 (3)	−40
4α-Methylcholesta-8(14),24-*dien*-3β-ol (VI)	0.41 (16)	−79	n.d.	n.d.	8.91 (15)	−80	0.55 (2)	n.d.	n.d.	n.d.	n.d.	n.d.	n.d.	n.d.	n.d.	n.d.
4α-Methylcholesta-8(14)-*en*-3β-ol (VII)	0.04 (2)	n.d.	0.14 (17)	−79	2.48 (4)	n.d.	0.78 (3)	n.d.	n.d.	n.d.	n.d.	n.d.	n.d.	n.d.	n.d.	n.d.
Lanost-8(9)-*en*-3β-ol (VIII)	n.d.	n.d.	n.d.	n.d.	n.d.	n.d.	n.d.	n.d.	n.d.	n.d.	n.d.	n.d.	0.07 (20)	−45	0.07 (18)	−45
Lanosterol (IX)	0.38 (15)	−82	n.d.	n.d.	15.20 (25)	−76	n.d.	n.d.	n.d.	n.d.	n.d.	n.d.	0.06 (17)	−43	0.02 (5)	−42
Nor-lanosterol (X)	0.11 (4)	−83	n.d.	n.d.	0.78 (1)	n.d.	n.d.	n.d.	n.d.	n.d.	n.d.	n.d.	n.d.	n.d.	n.d.	n.d.
Stigmast-5-en-3β-ol (XI)	n.d.	n.d.	n.d.	n.d.	n.d.	n.d.	n.d.	n.d.	<0.01	n.d.	0.01 (2)	n.d.	n.d.	n.d.	n.d.	n.d.
Sum	2.57		0.82		59.94		23.58		0.01		0.03		0.33		0.39	
Average $\delta^{13}C$ value		−81		−79		−77		−76						−41		−41
$\Delta\delta^{13}C_{sterols-FAs}$		−8.0		−11		−13		−13						0		2
Hopanoid																
Diplopterol	0.02 (1)	n.d.	n.d.	n.d.	n.d.	n.d.	n.d.	n.d.	n.d.	n.d.	n.d.	n.d.	n.d.	n.d.	n.d.	n.d.
n-Alcohols																
$nC_{22:0}$	n.d.	n.d.	n.d.	n.d.	0.31 (1)	n.d.	0.33 (1)	n.d.	0.03 (50)	n.d.	0.40 (77)	n.d.	0.02 (6)	−35	0.03 (8)	−38
$nC_{28:0}$	n.d.	n.d.	n.d.	n.d.	0.19 (<1)	n.d.	0.13 (1)	n.d.	0.01 (17)	n.d.	0.07 (13)	n.d.	n.d.	n.d.	n.d.	n.d.
$nC_{30:0}$	n.d.	n.d.	n.d.	n.d.	n.d.	n.d.	0.32 (1)	n.d.	0.01 (17)	n.d.	0.02 (4)	n.d.	n.d.	n.d.	n.d.	n.d.
Sum	n.d.				0.50		0.77		0.06		0.52		0.02		0.03	

n.d., not detected.

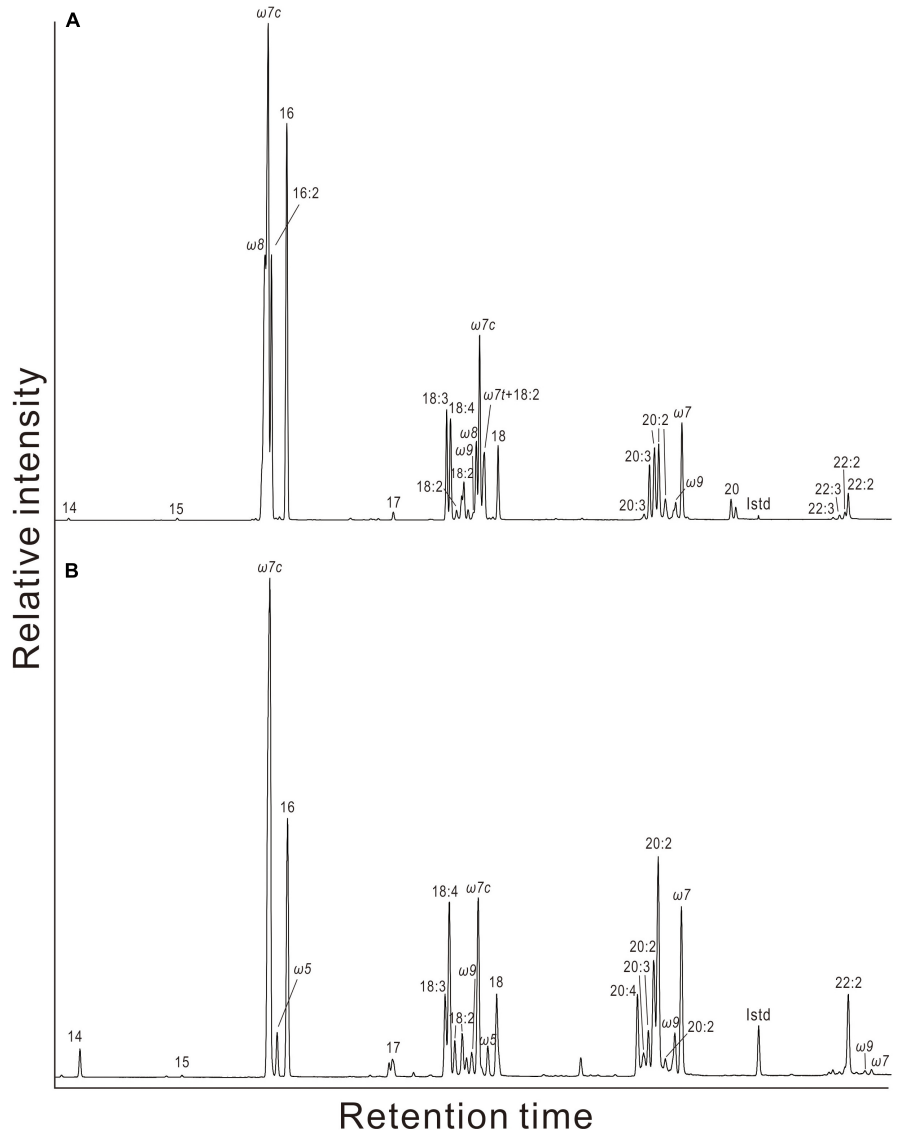

FIGURE 3 | Partial gas chromatograms of fatty acids in gill tissues of **(A)** *Gigantidas platifrons* and **(B)** *Bathymodiolus aduloides*. The ω indicates the double bond position of monounsaturated fatty acids (MUFAs), the suffix c is for *cis* and t for *trans*, referring to stereoisomers of MUFAs. Double bond positions of polyunsaturated fatty acids (PUFAs) have not been determined.

accounting for 23% of total fatty acids, dominated in the gill tissue of *G. haimaensis*. The fatty acids $C_{16:1\omega8}$ (12% and 9% of total fatty acids, respectively) and $C_{18:1\omega8}$ (3% and 1% of total fatty acids, respectively) were only observed in the gill tissues of *G. platifrons* and *G. haimaensis*. Generally, the fatty acids $C_{16:1\omega7}$, $C_{18:1\omega7}$, and $C_{20:1\omega7}$ were among the most abundant compounds of total fatty acids in gill and foot tissues of the four species, making up 32% and 22% for *G. platifrons*, 24% and 19% for *G. haimaensis*, and 58% and 28% for *A. marissinica*, and 44% and 17% for *B. aduloides*, respectively, with significantly higher relative abundances in gill tissues than in foot tissues. All relative percentages are referring to total fatty acids. Furthermore, $C_{16:1\omega5}$ was found in the gill tissue of *A. marissinica* in trace amounts (<1% of total fatty acids), while $C_{16:1\omega5}$ and $C_{18:1\omega5}$ were present in both gill and foot tissues of *B. aduloides* (**Figures 3**, **4**).

The fatty acids from the gill and foot tissues of *G. platifrons* and *G. haimaensis* were strongly depleted in ^{13}C, with $\delta^{13}C$ values ranging from −75‰ to −59‰ and −72‰ to −54‰, respectively. Compared to *G. platifrons* and *G. haimaensis*, *A. marissinica* and *B. aduloides* yielded moderately negative $\delta^{13}C$ values for fatty acids from −51‰ to −37‰ and −52‰ to −36‰, respectively (**Table 2**).

Lipid Biomarkers in the Alcohol Fractions

Various sterols were found in the gill and foot tissues of *G. platifrons*, *G. haimaensis*, *A. marissinica*, and *B. aduloides* (**Table 3** and **Figure 5**). Even though the inventory of sterols

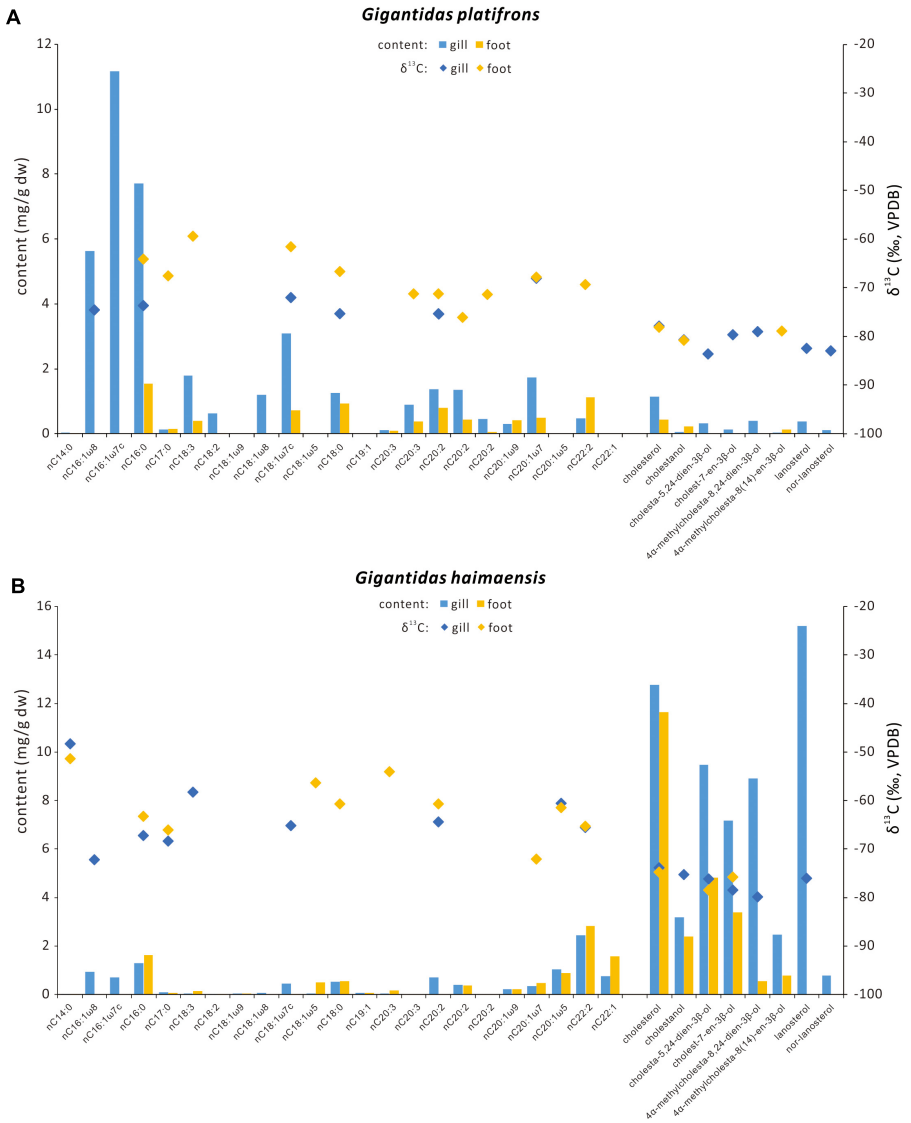

FIGURE 4 | Contents and carbon isotopic compositions of selected fatty acids and sterols for **(A)** *Gigantidas platifrons* and **(B)** *Gigantidas haimaensis*. Blue bars = contents of gill tissues; orange bars = contents of foot tissues; blue diamonds = δ^{13}C values of biomarkers from gill tissues; orange diamonds = δ^{13}C values of biomarkers from foot tissues.

was generally similar for *G. platifrons* and *G. haimaensis*, the contents of individual compounds varied significantly between the two species and types of tissues (**Figure 4**). The total content of sterols in the gill tissue of *G. haimaensis* was 60 mg/g dw, whereas the gill tissue content of sterols of *G. platifrons* was very low (2.6 mg/g dw). In *B. aduloides*, the sterol contents were even below 2 mg/g dw. Lanosterol (IX, see **Figure 6** for structure) and cholesterol (I) were the most abundant sterols in the gill tissue of both *G. haimaensis* (16 mg/g dw) and *G. platifrons* (1.1 mg/g dw), representing 25% and 44% of the total alcohols, respectively. In *B. aduloides*, cholesterol (I) was the most abundant sterol, accounting for 46% and 53% of the total alcohols in gill and foot tissues, respectively, followed by lanost-8(9)-*en*-3β-ol (VIII), lanosterol, cholestanol, 24-methylenecholesterol (IV), and cholest-7-*en*-3β-ol (**Table 3** and **Figure 7**). In the foot tissue, cholesterol (I) was most abundant in *G. platifrons* and *G. haimaensis* (0.4 mg/g dw and 12 mg/g dw, respectively), but was slightly more abundant in the gills (1.1 mg/g dw and 13 mg/g dw, respectively). Lanosterol, though, was not found in any of the foot tissue samples.

Other sterols, such as *nor*-lanosterol (X), cholestanol (II), cholesta-5,24-*dien*-3β-ol (III), cholest-7-*en*-3β-ol (V), 4α-methylcholesta-8(14),24-*dien*-3β-ol (VI), and 4α-methylcholesta-8(14)-*en*-3β-ol (VII), were as well more prominent in the gill tissues than in foot tissues of *G. platifrons* and *G. haimaensis*. In *B. aduloides*, the composition and contents of sterols in the foot tissue are similar to gill tissue. The single

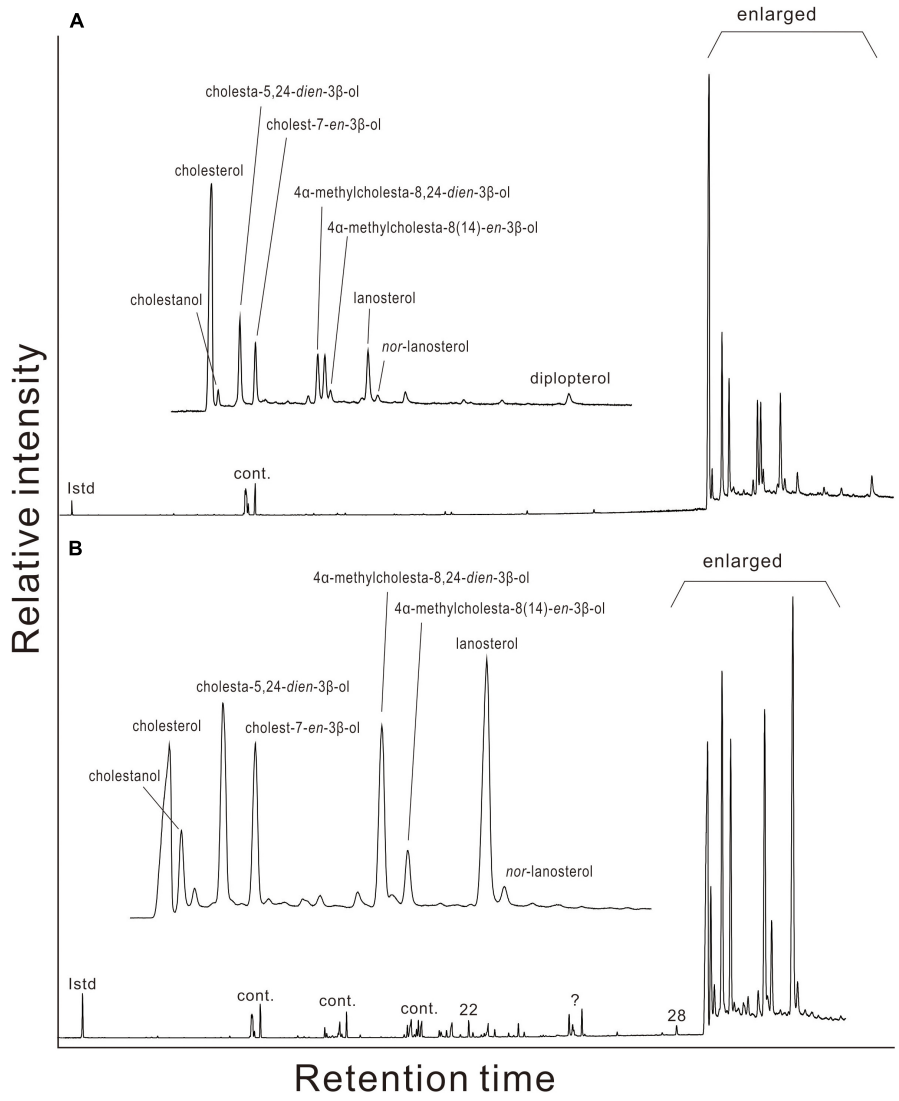

FIGURE 5 | Gas chromatograms of alcohols in gill tissues of **(A)** *Gigantidas platifrons* and **(B)** *Gigantidas haimaensis*. Roman numerals indicate *n*-alcohols; ? denotes presently unknown; Cont. = contaminant.

hopanoid, found only in traces in the gills of *G. platifrons*, was diplopterol (**Figure 5**). Minute amounts of cholesterol (I), cholestanol (II), and stigmast-5-en-3β-ol (XI) were found in *A. marissinica*. The total sterols accounted for 17% and 6% of all alcohols in the gill and foot tissues, respectively, with relatively higher contents in the foot than in the gill.

The *n*-alcohols $C_{22:0}$, $C_{28:0}$, and $C_{30:0}$ were found in gill and foot tissues of *G. haimaensis*, *A. marissinica*, and *B. aduloides*. The gill and foot tissues revealed similar ^{13}C depletion for sterols, with $\delta^{13}C$ values varying from −84‰ to −78‰ and −80‰ to −74‰ for *G. platifrons* and *G. haimaensis*, respectively. For *B. aduloides*, cholesterol, cholestanol, cholest-7-*en*-3β-ol, and the 4,4-dimethyl sterols (lanosterol and lanost-8(9)-*en*-3β-ol) in both gill and foot tissues yielded $\delta^{13}C$ values from −46‰ to −40‰, whereas the $\delta^{13}C$ values of 24-methylenecholesterol in gill and foot tissues ranged from −32‰ to −30‰.

DISCUSSION

Lipid Biomarker Signatures of Aerobic Methanotrophic Symbionts and Carbon Assimilation of *Gigantidas platifrons* and *Gigantidas haimaensis*

Both *G. platifrons* (Site F) and *G. haimaensis* (Haima seeps) were referred to as *B. platifrons* previously (Feng et al., 2015, 2018) and were reported to host methanotrophs (Duperron et al., 2009; Feng et al., 2015; Assié et al., 2016; Xu et al., 2019). Xu et al. (2019) analyzed the microbial 16S *r*RNA genes in gill tissue of *G. haimaensis* collected from the Haima seep site, and found that the bacteria were dominated by three phylotypes of symbiotic Gammaproteobacteria and three phylotypes of symbiotic Epsilonproteobacteria. The most

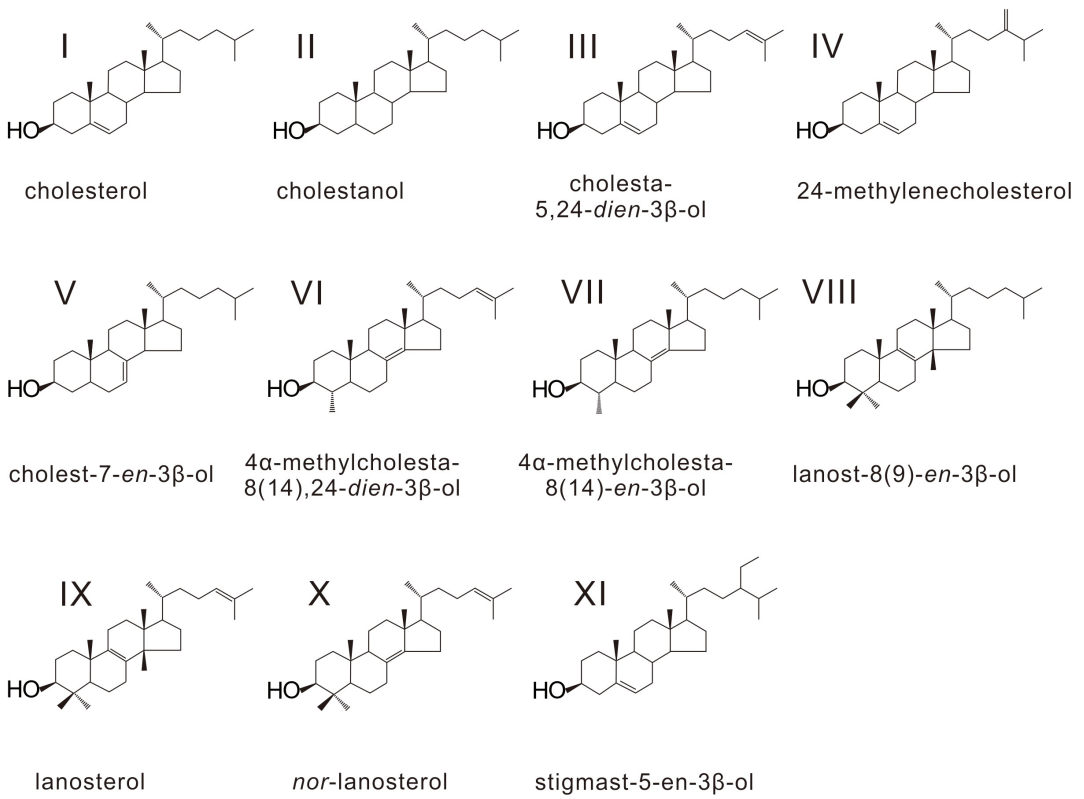

FIGURE 6 | Structures of sterols found in soft tissues of seep bivalves in the South China Sea.

abundant gammaproteobacterial phylotype of *G. haimaensis* clustered close to methanotrophic Gammaproteobacteria of other *Gigantidas* species and were assigned to Type I aerobic methanotrophic bacteria (Xu et al., 2019). Given Type II methanotrophs have never been reported in the marine realm (Knief, 2015), the symbionts harbored in *G. platifrons* are likely to be Type I methanotrophs too. Type I methanotrophs are the most prominent symbionts in the gills of both *G. platifrons* and *G. haimaensis*, which is supported by characteristic fatty acid inventories, including *cis* and *trans* isomers of $C_{16:1}$ with double bonds at ω6, ω7, ω8, and ω9 (Bowman et al., 1993) and a predominance of $C_{16:1\omega8}$ fatty acid over $C_{18:1\omega8}$ fatty acid (cf. Nichols et al., 1985; Bowman et al., 1991; Niemann et al., 2006; Riou et al., 2010).

In addition to fatty acids, 4,4-dimethyl sterols (lanosterol and *nor*-lanosterol), 4-methyl sterols (4α-methylcholesta-8(14),24-*dien*-3β-ol and 4α-methylcholesta-8(14)-*en*-3β-ol), and desmethyl sterols (cholesterol, cholestanol, cholesta-5,24-*dien*-3β-ol, and cholest-7-*en*-3β-ol) were observed in soft tissues of *G. platifrons* and *G. haimaensis*. The absolute and relative contents of sterols are generally different, for example lanosterol accounted for 15% and 25% of the total alcohols in gills of *G. platifrons* and *G. haimaensis*, respectively. However, the overall inventory of sterols of *G. platifrons* and *G. haimaensis* is similar (**Table 3**). Cholesterol is the most abundant sterol in the gill of *G. platifrons* (44%), whereas in *G. haimaensis* lanosterol dominates (25%; **Figure 4**). Cholesterol and other desmethyl sterols are common in eukaryotes, but lanosterol-like 4,4-dimethyl sterols and 4-methyl sterols are only present in free-living (Jahnke and Nichols, 1986; Cordova-Gonzalez et al., 2020) and endosymbiotic aerobic methanotrophs among bacteria (Jahnke et al., 1995; Kellermann et al., 2012). Both 4,4-dimethyl sterols and 4-methyl sterols are demethylation products of lanosterol in aerobic methanotrophic bacteria (*Methylococcus capsulatus*; Bouvier et al., 1976; Summons et al., 1994). Based on similar ^{13}C-depletions and the co-occurrence of 4-methyl sterol intermediates and desmethylated cholesterol in soft tissues other than gills, cholesterol was supposed to be synthesized by the animal host using bacterial 4-methyl sterols as diet (Jahnke et al., 1995). For *G. platifrons* and *G. haimaensis*, 4-methyl sterols and cholesterol occurred in both gill and foot tissues and yielded similar $\delta^{13}C$ values, indicating that 4-methyl sterols are most likely biosynthetic intermediates and represent metabolic precursors in cholesterol biosynthesis. The high abundance of 4,4-dimethyl sterols and 4-methyl sterols agrees with the presence of Type I methanotrophs, which are the only bacteria known to synthesize these source-specific compounds in noteworthy amounts (Bird et al., 1971; Schouten et al., 2000; Wei et al., 2016; Cordova-Gonzalez et al., 2020). In culture, *Methylococcus capsulatus* biosynthesizes fatty acids with significant ^{13}C-depletion compared to methane, with Δ values ranging from −25‰ to −17‰ (Jahnke et al., 1999), whereas the

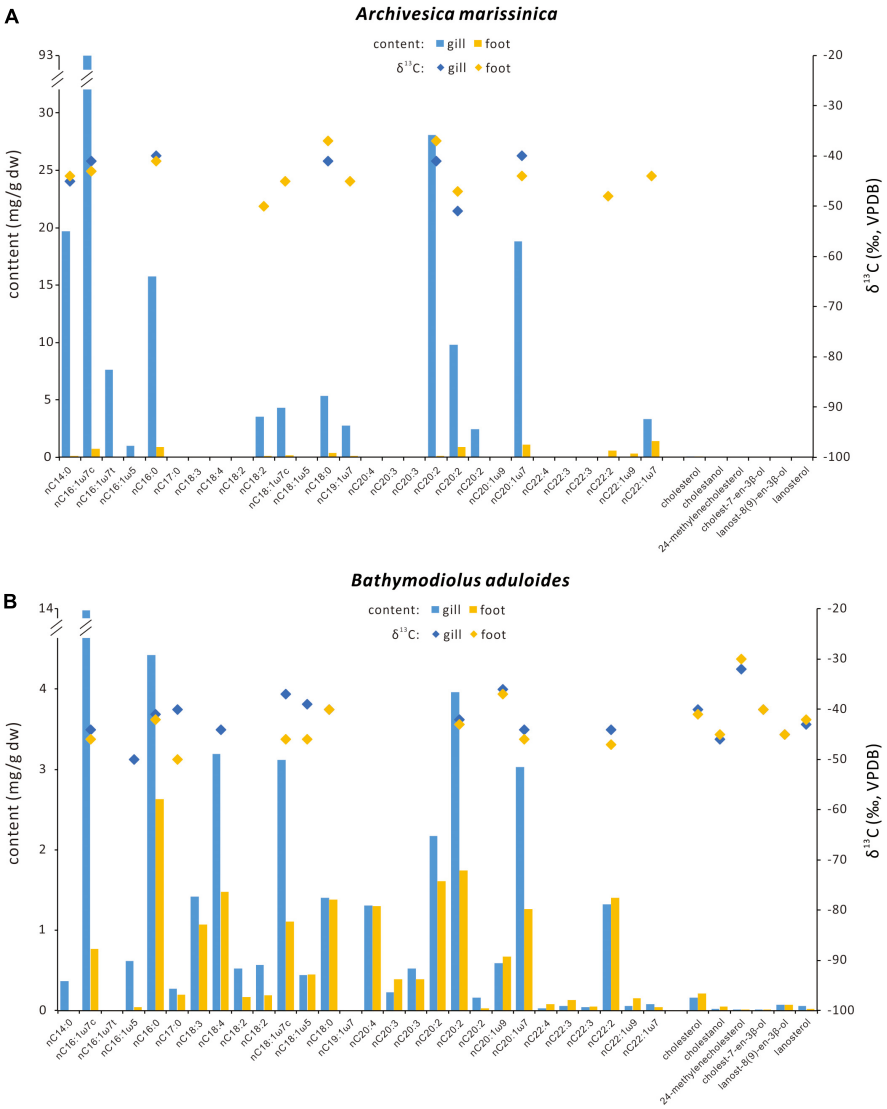

FIGURE 7 | Contents and carbon isotopic compositions of selected fatty acids and sterols for **(A)** *Archivesica marissinica* and **(B)** *Bathymodiolus aduloides*. Blue bars = contents of gill tissues; orange bars = contents of foot tissues; blue diamonds = $\delta^{13}C$ values of biomarkers from gill tissues; orange diamonds = $\delta^{13}C$ values of biomarkers from foot tissues.

fatty acids in the gills of type I methanotroph-containing mussels were more ^{13}C-depleted by ca. −16‰ (Jahnke et al., 1995). At site F and Haima seeps, available $\delta^{13}C$ values of methane approximately correspond to −60‰ (Feng et al., 2015; Fang et al., 2019). In the gills of *G. platifrons* and *G. haimaensis*, the symbiont-specific $C_{16:1\omega8}$ fatty acid and most fatty acids yielded $\delta^{13}C$ values from −75‰ to −72‰ and −75‰ to −65‰, respectively, which is consistent with fractionation patterns of fatty acids in type I/X methanotrophs and mussels that live in symbiosis with type I methanotrophs (Jahnke et al., 1995; Kellermann et al., 2012). Further, both 4,4-dimethyl sterols and 4-methyl sterols were more ^{13}C-depleted than fatty acids, with an average $\Delta\delta^{13}C_{sterols-fatty\ acids}$ between −13‰ and −8‰, similar to values reported from laboratory cultures (Summons et al., 1994; Jahnke et al., 1999; Cordova-Gonzalez et al., 2020). As for fatty acids, the isotopic pattern of sterols confirms a predominance of Type I and/or X methanotrophs (cf. Cordova-Gonzalez et al., 2020).

Although $\delta^{13}C$ values of fatty acids and sterols were uniform for *G. platifrons* and *G. haimaensis*, contents of the various lipids varied in the two mussels. While the same fatty acid inventory was found in gill and foot tissues of both mussels, contents of fatty acids were much higher in *G. platifrons* (see **Figure 4**), whereas both 4,4-dimethyl and 4-methyl sterols were more abundant in *G. haimaensis*. The strong variation in the membrane lipid composition, especially the ratio of fatty acids over sterols, is most likely caused by variation of oxygen levels in the environment. Such an effect was shown by

Jahnke and Nichols (1986) for *Methylococcus capsulatus* grown under varying oxygen tensions, revealing that sterols (4-methyl and 4,4-dimethyl sterols) and phospholipids were most abundant in cells grown with 0.5 and 1.1% oxygen. As oxygen was reduced, the amount of MUFA $C_{16:1}$ decreased but the 4,4-dimethyl sterols were predominantly produced at very low oxygen tensions (0.1%). Except for type X methanotrophs, oxygen level affecting membrane lipid composition was also reported for *Methylobacterium organophilum* (Type II methanotroph; Patt and Handon, 1978). Bathymodiolin mussels acquire symbionts horizontally and may take up various types and different amounts of symbionts in response to varying environmental conditions (Won et al., 2003; Kádár et al., 2005; Franke et al., 2021), which may also affect the biosynthesis of membrane lipids. In the present study, *G. platifrons* yielded significantly higher contents of MUFA $C_{16:1}$ than *G. haimaensis*, which may reflect a higher oxygen level for *G. platifrons*. Although no oxygen concentrations have been reported for the study sites, applying these observations to the biomarker patterns in *G. haimaensis* suggests that *G. haimaensis* most likely lived at a low level of dissolved oxygen.

Apart from the symbiont-specific fatty acids, the MUFAs C_{20} and C_{22}, as well as PUFAs C_{20} and C_{22} of the animal host (Conway and McDowell-Capuzzo, 1991; Pond et al., 1998) were present in both *G. platifrons* and *G. haimaensis*. In chemotrophic symbioses, some bivalves are highly dependent on the metabolic intermediates transferred by the symbionts, which leads to a similar range of $\delta^{13}C$ values for the lipids produced by hosts and symbionts (Jahnke et al., 1995; Pond et al., 1998; Kellermann et al., 2012). With respect to the seep-dwelling bivalves from the South China Sea, most symbiont- and host-specific fatty acids of *G. platifrons* and *G. haimaensis* yielded $\delta^{13}C$ values from −75‰ to −68‰ and −72‰ to −60‰, respectively, indicating that the host obtained most of its nutrition either directly from the symbionts or consumes symbiont-derived carbon.

Nutritional Signatures in *Archivesica marissinica* and *Bathymodiolus aduloides*

Membrane lipids of free-living sulfide-oxidizing bacteria are usually characterized by prominent ω7 fatty acids with either $C_{16:1\omega7}$ or $C_{18:1\omega7}$ predominating (Jannasch, 1985; Guezennec and Fiala-Medioni, 1996; Arning et al., 2008). These compounds were also found to be abundant in thiotrophic bacteria living in mussels (Pond et al., 1998; Kellermann et al., 2012) and mussels cultured in the presence of hydrogen sulfide (Riou et al., 2010). The high abundance of MUFAs $C_{16:1\omega7}$ and $C_{18:1\omega7}$ and the absence of 4-methyl sterols in *A. marissinica* (yielding cholesterol, cholestanol, and stigmast-5-en-3β-ol instead) agrees with thiotrophic bacteria as only endosymbionts.

For *B. aduloides*, in addition to the abundant MUFAs $C_{16:1\omega7}$ and $C_{18:1\omega7}$, a range of sterols, including cholesterol, cholestanol, 24-methylenecholesterol, cholest-7-*en*-3β-ol, lanost-8(9)-*en*-3β-ol, and lanosterol, were found in both gill and foot tissues. It has been demonstrated that some mussels are capable of synthesizing sterols (Teshima and Kanazawa, 1974; Teshima and Patterson, 1981). Sterols in soft tissues of symbiont-containing mussels may originate from its symbionts, diets from ingested plant and algal material, or synthesis by the animal host. For *B. aduloides*, a derivation of sterols except for 24-methylenecholesterol from filter-feeding is unlikely, because sterols synthesized by plants and algae are characterized by high abundance of sterols alkylated at C-24 containing either a methyl group or ethyl group (Jarzebski and Popov, 1985; Volkman, 2003, 2005). Furthermore, such photosynthetically derived carbon reveals $\delta^{13}C$ values around −30‰ to −20‰ (Conway and McDowell-Capuzzo, 1991; Kellermann et al., 2012), which is inconsistent with the carbon stable isotopic pattern of the *B. aduloides* sterols (from −46‰ to −40‰). Feng et al. (2018) reported $\delta^{13}C_{biomass}$ values (−37‰ to −33‰) in soft tissues of *B. aduloides* from Site F of the South China Sea and concluded that the mussels host thiotrophic bacteria. However, the thiotrophic symbionts are not a potential source candidate for sterols, since no sulfide-oxidizing bacteria have been shown to synthesize sterols to date (McCaffrey et al., 1989; Conway and McDowell-Capuzzo, 1991). Given the absence of ω8 fatty acids, a derivation of 4,4-dimethyl sterols (lanosterol and lanost-8(9)-*en*-3β-ol) from aerobic methanotrophic bacteria is highly unlikely as well.

Apart from the bacterial domain, eukaryotes including animals are known to produce lanosterol. Using ^{14}C-labeling in cultures revealed that the oyster *Crassostrea virginica* incorporated acetate to form squalene, 4,4-dimethylsterols, and 4-methylsterols, which can also convert lanosterol to cholesterol (Teshima and Patterson, 1981). These results suggest that the lanosterol in *B. aduloides* was most likely synthesized by the animal host. However, the lanost-8(9)-*en*-3β-ol as an intermediate has never been reported in aerobic methanotrophs and symbiont-containing invertebrates before, but it was found to co-occur with lanosterol in hyperlipidemic serum and rat livers (Gray et al., 1969; Scallen et al., 1971). As one of the intermediates in the conversion from lanosterol to cholesterol, the production of lanost-8(9)-*en*-3β-ol may occur as the first step when the side chain of lanosterol is reduced (Gray et al., 1969; Scallen et al., 1971). Although uncertainties are present, the absence of lanost-8(9)-*en*-3β-ol in aerobic methanotrophs is most likely caused by differences in biosynthetic steps from lanosterol to cholesterol between aerobic methanotrophs and animals.

In addition to nutrients supplied by the endosymbionts, *B. aduloides* complemented its diet by filter-feeding on photosynthetically derived carbon, as indicated by the presence of ^{13}C-enriched 24-methylenecholesterol ($\delta^{13}C$ values from −32‰ to −30‰) in both gill and foot tissues. Since consumers are generally ^{13}C-enriched by only 0.4‰ to 1‰ compared to their diet (McCutchan et al., 2003), these $\delta^{13}C$ values suggest higher plants or marine phytoplankton as sources (Goericke et al., 1994). Similar observations were made for the Pacific-Antarctic Ridge and the Gulf of Mexico. At the Pacific-Antarctic Ridge, a chemosynthesis-based community was observed to progressively shift its nutritional lifestyle to filter-feeding when diffuse hydrothermal venting vanished (Stecher et al., 2002). Reduction in symbiont abundances and changes in energy sources induced by decrease of hydrogen sulfide

concentration were also reflected by very low contents of symbiont-specific lipids and relatively ^{13}C-enriched cholesterol (−22‰) in *Bathymodiolus* cf. *thermophilus* from seeps of the Gulf of Mexico (Kellermann et al., 2012). Although both *A. marissinica and B. aduloides* contain thiotrophic bacteria, there are major differences when it comes to their symbionts. *A. marissinica* transmits the symbionts from parent to offspring (Ohishi et al., 2016; Lan et al., 2019), whereas *B. aduloides* acquires symbionts from the ambient environments for each new generation (Franke et al., 2021). Such differences in symbiont clades and amounts may lead to variations in the biomarker inventories of both hosts and symbionts. The above findings including our study confirm that lipid biomarkers and their isotope signatures are excellent tracers to decode varying environmental conditions and carbon and energy pathways in chemosynthesis-based ecosystems.

CONCLUSION

Four species of seep bivalves collected from Site F (*Gigantidas platifrons*) and Haima seeps (*Gigantidas haimaensis*, *Bathymodiolus aduloides*, and *Archivesica marissinica*) in the South China Sea were analyzed for lipid biomarkers and compound-specific carbon stable isotope patterns. *Gigantidas platifrons* and *Gigantidas haimaensis* were demonstrated to live in symbioses with methanotrophic bacterial symbionts as revealed by abundant ^{13}C-depleted lanosterol, *nor*-lanosterol, 4-methylsterols, and monounsaturated fatty acids $C_{16:1\omega9}$ and $C_{16:1\omega8}$ extracted from gill tissues. The relatively higher abundance of $C_{16:1\omega8}$ relative to $C_{18:1\omega8}$ and the occurrence of 4,4-dimethylsterols and 4-methylsterols agree with an assignment to type I methanotrophs. The much higher sterol contents and the less abundant fatty acids in *G. haimaensis* compared to *G. platifrons* probably reflect low oxygen levels during the growth of *G. haimaensis*. The gill tissues of both *B. aduloides* and *A. marissinica* contained significant amounts of $C_{16:1\omega7}$ and $C_{18:1\omega7}$ fatty acids, and their nutritional status was found to be different from *G. platifrons* and *G. haimaensis*. *A. marissinica* apparently contains only thiotrophic bacteria, indicated by the lack of ω8 fatty acids, 4,4-dimethylsterols, and 4-methylsterols. Based on the biomarker patterns, *B. aduloides* is also suggested to contain thiotrophic bacteria, but the animal host complemented its diet through filter-feeding as revealed by relatively ^{13}C-enriched 24-methylenecholesterol. The different types of 4-methyl sterols between the thiotroph-containing mussel (*B. aduloides*) and the methanotroph-containing mussels (*G. platifrons* and *G. haimaensis*) are likely caused by different biosynthetic steps from lanosterol to cholesterol between animal hosts and aerobic methanotrophs. Furthermore, the host-specific polyunsaturated fatty acids C_{20} and C_{22} in all four bivalve species yielded δ^{13}C values close to those of symbiont-specific fatty acids, suggesting that the hosts acquired most of their nutrition from the symbionts.

DATA AVAILABILITY STATEMENT

The original contributions presented in the study are included in the article/**Supplementary Material**, further inquiries can be directed to the corresponding authors.

ETHICS STATEMENT

Ethical review and approval was not required for the animal study because invertebrate studies at seeps are common.

AUTHOR CONTRIBUTIONS

HG, DF, and JT collected the samples. HG did the experiments. HG, DB, and JP analyzed the biomarker data. All authors contributed to the preparation of the manuscript.

FUNDING

This research was supported by NSF of China (Grant Number 91958105) and the Shandong Special Fund of Pilot National Laboratory for Marine Science and Technology (Qingdao; Grant Number 2021QNLM020002).

ACKNOWLEDGMENTS

We express our sincere appreciation to the crews of the *Haima*, *ROPOS*, *Haiyang-06*, and "*Tan Kah Kee*" Cruises for their professionalism in sampling. We thank S. Gao (GIG, CAS) for sample preparation and technical assistance. The manuscript benefited from insightful comments of the reviewers.

SUPPLEMENTARY MATERIAL

The Supplementary Material for this article can be found online at: https://www.frontiersin.org/articles/10.3389/fmars.2022.831286/full#supplementary-material

REFERENCES

Anthony, C. (1982). *The Biochemistry of Methylotrophs*. London: Academic Press.

Arning, E. T., Birgel, D., Schulz-Vogt, H. N., Holmkvist, L., Jørgensen, B. B., Larson, A., et al. (2008). Lipid biomarker patterns of phosphogenic sediments from upwelling regions. *Geomicrobiol. J.* 25, 69–82.

Assié, A., Borowski, C., van der Heijden, K., Raggi, L., Geier, B., Leisch, N., et al. (2016). A specific and widespread association between deep-sea Bathymodiolus mussels and a novel family of Epsilonproteobacteria. *Environ. Microbiol. Rep.* 8, 805–813. doi: 10.1111/1758-2229.12442

Barry, J. P., Buck, K. R., Kochevar, R. K., Nelson, D. C., Fujiwara, Y., Goffredi, S. K., et al. (2002). Methane-based symbiosis in a mussel, *Bathymodiolus platifrons*, from cold seeps in Sagami Bay, Japan. *Invertebrate Biol.* 121, 47–54. doi: 10.1111/j.1744-7410.2002.tb00128.x

Bettencourt, R., Dando, P., Rosa, D., Riou, V., Colaço, A., Sarrazin, J., et al. (2008). Changes of gill and hemocyte-related bio-indicators during long term

maintenance of the vent mussel *Bathymodiolus azoricus* held in aquaria at atmospheric pressure. *Comparat. Biochem. Physiol. Part A* 150, 1–7. doi: 10.1016/j.cbpa.2008.02.020

Bird, C. W., Lynch, J. M., Pirt, S. J., and Reid, W. W. (1971). Steroids and squalene in *Methylococcus capsulatus* grown on methane. *Nature* 230, 473–474. doi: 10.1038/230473a0

Bouvier, P., Rohmer, M., Benveniste, P., and Ourisson, G. (1976). Δ8(14)-Steroids in the bacterium *Methylococcus capsulatus*. *Biochem. J.* 159, 267–271. doi: 10.1042/bj1590267

Bowman, J. P., Skerrat, J. H., Nichols, P. D., and Sly, L. I. (1991). Phospholipid fatty acid and lipopolysaccharide fatty acid signature lipids in methane-utilizing bacteria. *FEMS Microbiol. Lett.* 85, 15–21.

Bowman, J. P., Sly, L. I., Nichols, P. D., and Hayward, A. C. (1993). Revised taxonomy of the methanotrophs: description of *Methylobacter gen*. nov., emendation of *Methylococcus*, validation of *Methylosinus* and *Methylocystis* species, and a proposal that the family *Methylococcaceae* includes only the group I methanotrophs. *Int. J. Systematic Evol. Microbiol.* 43, 735–753.

Brooks, J. M., Kennicutt, M. C., Fisher, C. R., Macko, S. A., Cole, K., Childress, J. J., et al. (1987). Deep-sea hydrocarbon seep communities: evidence for energy and nutritional carbon sources. *Science* 238, 1138–1142. doi: 10.1126/science.238.4830.1138

Cavanaugh, C. M. (1983). Symbiotic chemoautotrophic bacteria in marine invertebrates from sulfide-rich habitats. *Nature* 302, 58–61. doi: 10.1016/j.scitotenv.2021.150054

Childress, J. J., Fisher, C. R., Brooks, J. M., Kennicutt, M. C., Bidigare, R., and Anderson, A. E. (1986). A methanotrophic marine molluscan (Bivalvia: Mytilidae) symbiosis: mussels fueled by gas. *Science* 233, 1306–1308. doi: 10.1126/science.233.4770.1306

Conway, N., and McDowell-Capuzzo, J. (1991). Incorporation and utilization of bacterial lipids in the *Solemya velum* symbiosis. *Mar. Biol.* 108, 277–291.

Cordes, E. E., Bergquist, D. C., and Fisher, C. R. (2009). Macro-ecology of Gulf of Mexico cold seeps. *Annual Rev. Mar. Sci.* 1, 143–168. doi: 10.1146/annurev.marine.010908.163912

Cordova-Gonzalez, A., Birgel, D., Kappler, A., and Peckmann, J. (2020). Carbon stable isotope patterns of cyclic terpenoids: a comparison of cultured alkaliphilic aerobic methanotrophic bacteria and methane-seep environments. *Organ. Geochem.* 139:103940.

Distel, D., Lane, D., Olsen, G., Giovannoni, S., Pace, B., Pace, N., et al. (1988). Sulfur-oxidizing bacterial endosymbionts–analysis of phylogeny and specificity by 16S ribosomal RNA sequences. *J. Bacteriol.* 170, 2506–2510.

Dunstan, G. A., Volkman, J. K., and Barrett, S. M. (1993). The effect of lyophilization on the solvent extraction of lipid classes, fatty acids and sterols from the oyster *Crassostrea gigas*. *Lipids* 28, 937–944. doi: 10.1007/bf02537504

Duperron, S., and Gros, O. (2016). *Colwellia* and sulfur-oxidizing bacteria: an unusual dual symbiosis in a Terua mussel (Mytilidae: Bathymodiolinae) from whale falls in the Antilles arc. *Deep-Sea Res. Part I* 115, 112–122. doi: 10.1016/j.dsr.2016.05.012

Duperron, S., Gaudron, S. M., Lemaitre, N., and Bayon, G. (2014). A microbiological and biogeochemical investigation of the cold seep tubeworm *Escarpia southwardae* (Annelida: Siboglinidae): symbiosis and trace element composition of the tube. *Deep-Sea Res. Part I* 90, 105–114.

Duperron, S., Lorion, J., Samadi, S., Gros, O., and Gaill, F. (2009). Symbioses between deep-sea mussels (Mytilidae: Bathymodiolinae) and chemosynthetic bacteria: diversity, function and evolution. *C. R. Biol.* 332, 298–310. doi: 10.1016/j.crvi.2008.08.003

Fang, J., Abrajano, T. A., Comet, P. A., Brooks, L. M., Sassen, R., and MacDonald, I. R. (1993). Gulf of Mexico hydrocarbon seep communities XI. Carbon isotopic fractionation during fatty acid biosynthesis of seep organisms and its implication for chemosynthetic processes. *Chem. Geol.* 109, 271–279.

Fang, Y., Wei, J., Lu, H., Liang, J., Lu, J., Fu, J., et al. (2019). Chemical and structural characteristics of gas hydrates from the Haima cold seeps in the Qiongdongnan Basin of the South China Sea. *J. Asian Earth Sci.* 182:103924. doi: 10.1016/j.jseaes.2019.103924

Faure, B., Schaeffer, S. W., and Fisher, C. R. (2015). Species distribution and population connectivity of deep-sea mussels at hydrocarbon seeps in the Gulf of Mexico. *PLoS One* 10:e0118460. doi: 10.1371/journal.pone.0118460

Feng, D., Cheng, M., Kiel, S., Qiu, J.-W., Yang, Q., Zhou, H., et al. (2015). Using *Bathymodiolus* tissue stable carbon, nitrogen and sulfur isotopes to infer biogeochemical process at a cold seep in the South China Sea. *Deep-Sea Res. Part I* 104, 52–59. doi: 10.1016/j.dsr.2015.06.011

Feng, D., Peckmann, J., Li, N., Kiel, S., Qiu, J.-W., Liang, Q., et al. (2018). The stable isotope fingerprint of chemosymbiosis in the shell organic matrix of seep-dwelling bivalves. *Chem. Geol.* 479, 241–250. doi: 10.1016/j.chemgeo.2018.01.015

Fiala-Médioni, A., McKiness, Z. P., Dando, P., Boulegue, J., Mariotti, A., Alayse-Danet, A. M., et al. (2002). Ultrastructural, biochemical, and immunological characterization of two populations of the mytilid mussel *Bathymodiolus azoricus* from the Mid-Atlantic Ridge: evidence for a dual symbiosis. *Mar. Biol.* 141, 1035–1043. doi: 10.1007/s00227-002-0903-9

Fisher, C. R., Brooks, J. M., Vodenichar, J. S., Zande, J. M., Childress, J. J., and Burke, R. A. Jr. (1993). The co-occurrence of methanotrophic and chemoautotrophic sulfur-oxidizing bacterial symbionts in a deep-sea mussel. *Mar. Ecol.* 14, 277–289.

Fisher, C. R., Childress, J. J., Oremland, R. S., and Bidigare, R. R. (1987). The importance of methane and thiosulfate in the metabolism of the bacterial symbionts of two deep-sea mussels. *Mar. Biol.* 96, 59–71. doi: 10.1007/bf00394838

Franke, M., Geier, B., Hammel, J. U., Dubilier, N., and Leisch, N. (2021). Coming together—symbiont acquisition and early development in deep-sea bathymodioline mussels. *Proc. R. Soc. B* 288:20211044. doi: 10.1098/rspb.2021.1044

Fullarton, J. G., Dando, P. R., Sargent, J. G., Southward, A. J., and Southward, E. C. (1995). Fatty acids of hydrothermal vent *Ridgeia piscesae* and inshore bivalves containing symbiotic bacteria. *J. Mar. Biol. Assoc. U K.* 75, 455–468. doi: 10.1017/s0025315400018300

Goericke, R., Montoya, J. P., and Fry, B. (1994). "Physiology of isotopic fractionation in algae and cyanobacteria," in *Stable Isotopes in Ecology and Environmental Science*, eds K. Lajtha and R. H. Michener (Oxford: Blackwell). doi: 10.1073/pnas.70.10.2727

Gray, M. F., Morrison, A., Farish, E., Lawrie, T. D. V., and Brooks, C. J. W. (1969). Characterization of 5α-lanost-8(9)-en-3β-ol in hyperlipaemic serum. *Biochim. Biophys. Acta* 187, 163–165. doi: 10.1016/0005-2760(69)90147-7

Guan, H., Birgel, D., Feng, D., Peckmann, J., Liu, L., Liu, L., et al. (2021). Lipids and their $\delta^{13}C$ values reveal carbon assimilation and cycling in the methane-seep tubeworm *Paraescarpia echinospica* from the South China Sea. *Deep–Sea Res. I* 174:103556. doi: 10.1016/j.dsr.2021.103556

Guezennec, J., and Fiala-Medioni, A. (1996). Bacterial abundance and diversity in the Barbados Trench determined by phospholipid analysis. *FEMS Microbiol. Ecol.* 19, 83–93. doi: 10.1111/j.1574-6941.1996.tb00201.x

Jahnke, L. L., and Nichols, P. D. (1986). Methyl sterol and cyclopropane fatty acid composition of *Methylococcus capsulatus* grown at low oxygen tensions. *J. Bacteriol.* 167, 238–242. doi: 10.1128/jb.167.1.238-242.1986

Jahnke, L. L., Summons, R. E., Dowling, L. M., and Zahiralis, K. D. (1995). Identification of methanotrophic lipid biomarkers in cold seep mussel gills: chemical and isotopic analysis. *Appl. Environ. Microbiol.* 61, 576–582. doi: 10.1128/aem.61.2.576-582.1995

Jahnke, L. L., Summons, R. E., Hope, J. M., and Des Marais, D. J. (1999). Carbon isotopic fractionation in lipids from methanotrophic bactria II: the effects of physiology and environmental parameters on the biosynthesis and isotopic signatures of biomarkers. *Geochimica Cosmochimica Acta* 63, 79–93. doi: 10.1016/s0016-7037(98)00270-1

Jannasch, H. W. (1985). The chemosynthetic support of life and the microbial diversity at deep-sea hydrothermal vents. *Proc. R. Soc. London* 225, 277–297.

Jarzebski, A., and Popov, S. (1985). Comparison of sterol composition of some Baltic Sea and Black Sea mussels. *Mar. Biol.* 86, 159–161.

Kádár, E., Bettencourt, R., Costa, V., Serrão Santos, R., Lododa-Cunha, A., and Dando, P. R. (2005). Experimentally induced endosymbiont loss and re-acquirement in the hydrothermal vent bivalve *Bathymodiolus azoricus*. *J. Exp. Mar. Biol. Ecol.* 318, 99–110.

Kawashima, H., and Ohnishi, M. (2003). Fatty acid compositions of various tissue lipids in the marine bivalves, *Megangulus venulosus* and *Megangulus zyonoensis*, from coastal waters of Hokkaido, Northern Japan. *J. Oleo Sci.* 52, 309–315.

Kellermann, M. Y., Schubotz, F., Elvert, M., Lipp, J. S., Birgel, D., Prieto-Mollar, X., et al. (2012). Symbiont–host relationships in chemosynthetic mussels: a comprehensive lipid biomarker study. *Organ. Geochem.* 43, 112–124.

Kiel, S. (2010). "The fossil record of vent and seep mollusks," in *The Vent and Seep Biota. Topics in Geobiology*, ed. S. Kiel (Heidelberg: Springer), 255–278. doi: 10.1098/rspb.2014.2908

Kiel, S., and Peckmann, J. (2019). Resource partitioning among brachiopods and bivalves at ancient hydrocarbon seeps: a hypothesis. *PLoS One* 14:e0221887. doi: 10.1371/journal.pone.0221887

Kiel, S., Birgel, D., Lu, Y., Wienholz, D., and Peckmann, J. (2021). A thyasirid-dominated methane-seep deposit from Montañita, southwestern Ecuador, from the Oligocene-Miocene boundary. *Palaeogeography Palaeoclimatol. Palaeoecol.* 575:110477.

Knief, C. (2015). Diversity and habitat preferences of cultivated and uncultivated aerobic methanotrophic bacteria evaluated based on pmoA as molecular marker. *Front. Microbiol.* 6:1346. doi: 10.3389/fmicb.2015.01346

Laming, S. R., Szafranski, K. M., Rodrigues, C. F., Gaudron, S. M., Cunha, M. R., Hilário, A., et al. (2015). Fickle or faithful: the roles of host and environmental context in determining symbiont composition in two bathymodioline mussels. *PLoS One* 10:e0144307. doi: 10.1371/journal.pone.0144307

Lan, Y., Sun, J., Zhang, W., Xu, T., Zhang, Y., Chen, C., et al. (2019). Host–symbiont interactions in deep-sea chemosymbiotic vesicomyid clams: insights from transcriptome sequencing. *Front. Mar. Sci.* 6:680. doi: 10.3389/fmars.2019.00680

Liang, Q., Hu, Y., Feng, D., Peckmann, J., Chen, L., Yang, S., et al. (2017). Authigenic carbonates from newly discovered active cold seeps on the northwestern slope of the South China Sea: constraints on fluid sources, formation environments, and seepage dynamics. *Deep-Sea Res. Part I* 124, 31–41. doi: 10.1016/j.dsr.2017.04.015

Lorion, J., Kiel, S., Faure, B. M., Kawato, M., Ho, S. Y. W., Marshall, B. A., et al. (2013). Adaptive radiation of chemosymbiotic deep-sea mussels. *Proc. R. Soc. B* 280:20131243. doi: 10.1098/rspb.2013.1243

McCaffrey, M. A., Farrington, J. W., and Repeta, D. (1989). Geochemical implications of the lipid composition of *Thioploca spp*. from the Peru upwelling region–15°S. *Organ. Geochem.* 14, 61–68.

McCutchan, J. H., Lewis, W. M., Kendall, C., and McGrath, C. C. (2003). Variation in trophic shift for stable isotope ratios of carbon, nitrogen, and sulfur. *Oikos* 102, 378–390. doi: 10.1034/j.1600-0706.2003.12098.x

Nelson, K., and Fisher, C. R. (2000). Absence of cospeciation in deep-sea vestimentiferan tube worms and their bacterial endosymbionts. *Symbiosis* 28, 1–15. doi: 10.1002/jmor.1054

Nichols, P. D., Guckert, J. B., and White, D. C. (1986). Determination of monounsaturated fatty acid double-bond position and geometry for microbial monocultures and complex consortia by capillary GC–MS of their dimethyl disulphide adducts. *J. Microbiol. Methods* 5, 49–55.

Nichols, P. D., Smith, G. A., Antworth, C. P., Hanson, R. S., and White, D. C. (1985). Phospholipid and lipopolysaccharide normal and hydroxy fatty acids as potential signatures for methane-oxidizing bacteria. *FEMS Microbiol. Ecol.* 31, 327–335.

Niemann, H., Lösekann, T., de Beer, D., Elvert, M., Nadalig, T., Knittel, K., et al. (2006). Novel microbial communities of the Haakon Mosby mud volcano and their role as a methane sink. *Nature* 443, 854–858. doi: 10.1038/nature05227

Ohishi, K., Yamamoto, M., Tame, A., Kusaka, C., Nagai, Y., Sugimura, M., et al. (2016). Long-term cultivation of the deep-sea clam Calyptogena okutanii: changes in the abundance of chemoautotrophic symbiont, elemental sulfur, and mucus. *Biol. Bull.* 230, 257–267. doi: 10.1086/BBLv230n3p257

Patt, T. E., and Handon, R. S. (1978). Intracytoplasmic membrane, phospholipid, and sterol content of *Methylobacterium organophilum* cells grown under different conditions. *J. Bacteriol.* 134, 636–644.

Petersen, J. M., and Dubilier, N. (2010). "Symbiotic methane oxidizers," in *Handbook of Hydrocarbon and Lipid Microbiology*, ed. K. N. Timmis (Berlin and Heidelberg: Springer-Verlag).

Pond, D. W., Bell, M. V., Dixon, D. R., Fallick, A. E., Segonzac, M., and Sargent, J. R. (1998). Stable-carbon-isotope composition of fatty acids in hydrothermal vent mussels containing methanotrophic and thiotrophic bacterial endosymbionts. *Appl. Environ. Microbiol.* 64, 370–375. doi: 10.1128/AEM.64.1.370-375.1998

Pond, D. W., Gebruk, A., Southward, E. C., Southward, A. J., Fallick, A. E., Bell, M. V., et al. (2000). Unusual fatty acid composition of storage lipids in the bresiloid shrimp, *Rimicaris exoculata*, couples the photic zone with MAR hydrothermal vent sites. *Mar. Ecol. Prog. Series* 198, 171–179.

Rau, G. H., and Hedges, J. I. (1979). Carbon-13 depletion in a hydrothermal vent mussel: suggestion of a chemosynthetic food source. *Science* 203, 648–649. doi: 10.1126/science.203.4381.648

Riou, V., Bouillon, S., Serrão Santos, R., Dehairs, F., and Colaco, A. (2010). Tracing carbon assimilation in endosymbiotic deep-sea hydrothermal vent mytilid fatty acids by ^{13}C-fingerprinting. *Biogeosci. Discussions* 7, 3453–3475.

Scallen, T. J., Dhar, A. K., and Loughran, E. D. (1971). Isolation and characterization of C-4 methyl intermediates in cholesterol biosynthesis after treatment of rat liver in vitro with cholestan-3β,5α,6β-triol. *J. Biol. Chem.* 246, 3168–3174.

Schouten, S., Bowman, J. P., Irene, W., Rijpstra, C., and Sinninghe-Damsté, J. S. (2000). Sterols in a psychrophilic methanotroph, *Methylosphaera hansonii*. *FEMS Microbiol. Lett.* 186, 193–195. doi: 10.1111/j.1574-6968.2000.tb09103.x

Stecher, J., Türkay, M., and Borowski, C. (2002). Faunal assemblages on the Pacific–Antarctic ridge near the foundation seamount chain (37 30'S, 110 30'W). *Cahiers Biol. Mar.* 43, 271–274.

Summons, R. E., Jahnke, L. L., and Rocsandic, T. (1994). Carbon isotopic fractionation in lipids from methanotrophic bacteria: relevance for interpretation of the geochemical record of biomarkers. *Geochimica Cosmochimica Acta* 58, 2853–2863. doi: 10.1016/0016-7037(94)90119-8

Szafranski, K. M., Piquet, B., Shillito, B., Lallier, F. H., and Duperron, S. (2015). Relative abundances of methane- and sulfur-oxidizing symbionts in gills of the deep-sea hydrothermal vent mussel *Bathymodiolus azoricus* under pressure. *Deep-Sea Res. Part I* 101, 7–13. doi: 10.1016/j.dsr.2015.03.003

Talbot, H. M., Watson, D. F., Murrel, J. C., Carter, J. F., and Farrimond, P. (2001). Analysis of intact bacteriohopanepolyols from methanotrophic bacteria by reversed-phase high-performance liquid chromatography–atmospheric pressure chemical ionization mass spectrometry. *J. Chromatogr. A* 921, 175–185. doi: 10.1016/s0021-9673(01)00871-8

Teshima, S.-I., and Kanazawa, A. (1974). Biosynthesis of sterols in abalone, *Haliotis gurneri*, and mussel, *Mytilus edulis*. *Comp. Biochem. Physiol. Part B: Comp. Biochem.* 47B, 555–561. doi: 10.1016/0305-0491(74)90004-2

Teshima, S.-I., and Patterson, S. W. (1981). Sterol biosynthesis in the oyster *Crassostrea virginica*. *Lipids* 16, 234–239.

Thornhill, D. J., Wiley, A. A., Campbell, A. L., Bartol, F. F., Teske, A., and Halanych, K. M. (2008). Endosymbionts of *Siboglinum fiordicum* and the phylogeny of bacterial endosymbionts in Siboglinidae (Annelida). *Biol. Bull.* 214, 135–144. doi: 10.2307/25066670

Volkman, J. K. (2003). Sterols in microorganisms. *Appl. Microbiol. Biotechnol.* 60, 495–506.

Volkman, J. K. (2005). Sterols and other triterpenoids: source specificity and evolution of biosynthetic pathways. *Organ. Geochem.* 36, 139–159.

Wei, J. H., Yin, X. C., and Welander, P. V. (2016). Sterol synthesis in diverse bacteria. *Front. Microbiol.* 7:990. doi: 10.3389/fmicb.2016.00990

Won, Y.-J., Hallam, S. J., O'Mullan, G. D., Pan, I. L., Buck, K. R., and Vrijenhoek, R. C. (2003). Environmental acquisition of thiotrophic endosymbionts by deep-sea mussels of the genus *Bathymodiolus*. *Appl. Environ. Microbiol.* 69, 6785–6792. doi: 10.1128/AEM.69.11.6785-6792.2003

Xu, T., Feng, D., Tao, J., and Qiu, J.-W. (2019). A new species of deep-sea mussel (Bivalvia: Mytilidae: Gigantidas) from the South China Sea: morphology, phylogenetic position, and gill-associated microbes. *Deep-Sea Res. Part I* 146, 79–90.

Conflict of Interest: The authors declare that the research was conducted in the absence of any commercial or financial relationships that could be construed as a potential conflict of interest.

Publisher's Note: All claims expressed in this article are solely those of the authors and do not necessarily represent those of their affiliated organizations, or those of the publisher, the editors and the reviewers. Any product that may be evaluated in this article, or claim that may be made by its manufacturer, is not guaranteed or endorsed by the publisher.

frontiers | Frontiers in Marine Science

ORIGINAL RESEARCH
published: 07 April 2022
doi: 10.3389/fmars.2022.849449

Two New Species of *Cyphocaris* (Amphipoda, Amphilochidea, Cyphocarididae) From Water Columns Above a Methane Seep in the South China Sea

Yanrong Wang[1,2,3], *Zhongli Sha*[1,2,3,4]* *and Xianqiu Ren*[1]

[1] Department of Marine Organism Taxonomy and Phylogeny, Institute of Oceanology, Chinese Academy of Sciences, Qingdao, China, [2] Laboratory for Marine Biology and Biotechnology, Qingdao National Laboratory for Marine Science and Technology, Qingdao, China, [3] College of Biological Sciences, University of Chinese Academy of Sciences, Beijing, China, [4] Shandong Province Key Laboratory of Experimental Marine Biology, Institute of Oceanology, Chinese Academy of Sciences, Qingdao, China

OPEN ACCESS

Edited by:
Jian-Wen Qiu,
Hong Kong Baptist University, Hong Kong SAR, China

Reviewed by:
Wonchoel Lee,
Hanyang University, South Korea
Johanna N. J. Weston,
Newcastle University, United Kingdom
Yu Zhao,
Xiamen University, China

***Correspondence:**
Zhongli Sha
shazl@qdio.ac.cn

Specialty section:
This article was submitted to Deep-Sea Environments and Ecology, a section of the journal Frontiers in Marine Science

Received: 06 January 2022
Accepted: 08 March 2022
Published: 07 April 2022

Citation:
Wang Y, Sha Z and Ren X (2022) Two New Species of Cyphocaris (Amphipoda, Amphilochidea, Cyphocarididae) From Water Columns Above a Methane Seep in the South China Sea. Front. Mar. Sci. 9:849449. doi: 10.3389/fmars.2022.849449

The Formosa Ridge methane seep is one of three known active methane seepage areas discovered on the northern slope of the South China Sea. *Cyphocaris* is a genus of pelagic amphipods. Two new species of *Cyphocaris* collected from water columns above the Formosa Ridge methane seep are reported in the present study. *Cyphocaris lubrica* sp. nov. collected at a depth of 1,118 m is characterized by pereonite 1 dorsal projection not extending beyond head, and the pereopod 5 having a spur beyond pereonite 7. *Cyphocaris formosa* sp. nov. collected at a depth of 500–800 m is characterized by well-developed pereonite 1 dorsal projection extending beyond head and pereopod 5 without spur. The present work describes these two new species and compares them with closely related species, and provides a modified key of world Cyphocarididae species.

Keywords: Amphipoda, *Cyphocaris*, taxonomy, deep sea, new species

INTRODUCTION

The Formosa Ridge is an active methane seep on the northern South China Sea continental slope (Feng and Chen, 2015; Feng et al., 2018; Kuo et al., 2019), located in the passive China continental margin about 100 km southwest of Taiwan (Lin et al., 2007a; Lin et al., 2007b; Machiyama et al., 2007). The community of the Formosa Ridge methane seep is dominated by two epibenthic species: the bathymodioline mussel *Gigantidas platifrons* (Hashimoto and Okutani, 1994) and the galatheid squat lobster *Shinkaia crosnieri* (Baba and Williams, 1998; Zhao et al., 2020). Although a number of studies have been conducted to understand the biodiversity of the epifauna of this methane seep (Li, 2017; Zhao et al., 2020), and the connectivity of such epifauna with those of the open western Pacific (Xu et al., 2022), nothing is known about the zooplankton in the water columns above the seep.

Amphipoda is one of the largest orders of the Crustacea and the most widespread crustacean taxa, occurring in almost all aquatic environments, some subterranean habitats and some terrestrial habitats (Barnard and Karaman, 1991; Lowry and Myers, 2017). Cyphocaridids are pelagic amphipods found throughout the oceans of the world from 90 m to thousands of meters deep (Hughes and Lowry, 2015). The Cyphocarididae is characterized by having reduced coxae 1–3, a well-developed lacinia mobilis, outer plate of maxilla 1 with an unmodified 6/5 setal-tooth arrangement, and a deeply cleft telson (Lowry and Stoddart, 1997). Cyphocarididae contains two genera *Cyphocaris* (Boeck, 1871) and *Procyphocaris* J.L. (Barnard, 1961). *Procyphocaris* is a monotypic genus that can be morphologically distinguished from *Cyphocaris* by the basis of pereopod 7 having smooth, rather than serrate posterior margin, and by having only coxae 1–2 reduced and covered by coxa 3 (Hughes and Lowry, 2015).

The genus *Cyphocaris* was reviewed by Hughes and Lowry (2015), and updated by Andrade et al. (2021). The genus, currently containing 18 species, includes members that are widely reported from the Pacific, the Atlantic, the Indian Ocean, the Arctic and the Antarctic Oceans. Six *Cyphocaris* species (*C. anonyx*, *C. bouvieri*, *C. challengeri*, *C. faurei*, *C. Polaris*, and *C. richardi*) have been reported from more than one ocean (Hughes and Lowry, 2015). For instance, *C. anonyx* (Boeck, 1871) has been reported from the Indian Ocean (Barnard, 1937; Birstein & Vinogradov, 1964; Vinogradov, 2004), the South and North Pacific (e.g. Schellenberg, 1929; Pirlot, 1933; Shoemaker, 1945; Birstein and Vinogradov, 1963; Barnard, 1967; Sanger, 1974; Vinogradov, 1990), the South and North Atlantic (e.g. Schellenberg, 1955; Thurston, 1976; Gislason and Astthorsson, 1992), the Great Australian Bight (Birstein and Vinogradov, 1962), and the Subantarctic (Kane, 1962). The rest of the *Cyphocaris* species have been reported from just one ocean, namely, two species (*C. boecki* and *C. pedroi*) from the South Atlantic (Sorrentino et al., 2016; Andrade et al., 2021); two species (*C. geyserensis* and *C. cornuta*) form the Indian Ocean (Ledoyer, 1978; Ledoyer, 1986; Vinogradov, 2004); two species (*C. johnsoni* and *C. tunicola*) from the North Atlantic (Shoemaker, 1934; Lowry and Stoddart, 1997); two species(*C. latirama* and *C. ohtsukai*) from the North Pacific (Hendrycks and Conlan, 2003; Tomikawa, 2009); and four species (*C. ananke*, *C. bellona*, *C. nesoi*, and *C. tartaros*) from the South Pacific (Lowry and Stoddart, 1994; Hughes and Lowry, 2015).

During research cruises on board the Chinese research vessel KEXUE to survey the biodiversity of the Formosa Ridge methane seep (**Figure 1**) in the South China Sea in 2020 and 2021, two individual of Cyphocarididae were collected at different depths by using MultiNet. The two specimens are identified to *Cyphocaris* on the basis of pereopod 7 having serrate posterior margin, and reduced coxae 1–3 partly covered by coxa 4. These two individuals exhibit some characteristics distinct from other described *Cyphocaris* species, so they are identified as new species, described morphologically and compared with other similar congeneric species. The provided key is modified from Hughes and Lowry (2015) and Sorrentino et al. (2016).

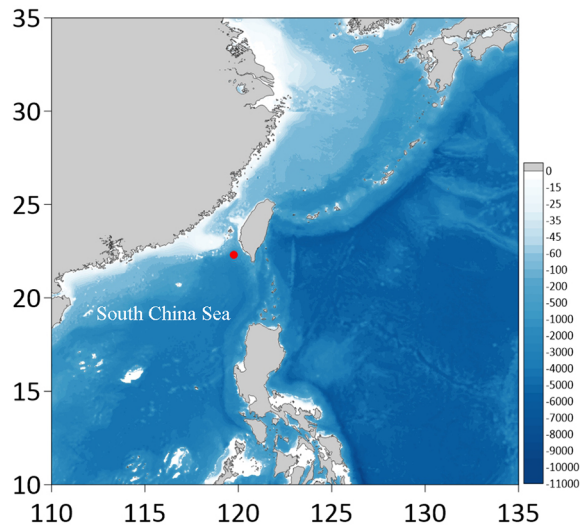

FIGURE 1 | A map showing the location of sampling site (red circle) in the South China Sea.

MATERIAL AND METHODS

Zooplankton samples were taken on board the research vessel KEXUE by MultiNet (Multi Plankton Sampler XL MPS XL, 200-mesh sieve, sampling for about 3 h), during expeditions to the Formosa Ridge methane seep by the Institute of Oceanology, Chinese Academy of Sciences (IOCAS) in May 2020 and June 2021, respectively. Type material of C. *lubrica* sp. nov. was collected at 1,118 m depth [temperature (4.1°), salinity (34.63‰) and oxygen (4.9 mg/l)], and was sorted on board and fixed in 96% ethanol, then transferred to 75% ethanol in the laboratory; type material of *C. formosa* sp. nov. was collected at 500–800 m depth [temperature (6–9°), salinity (34.56–34.63‰) and oxygen (5.25–5.15 mg/l)] and was sorted on board and fixed in 10% formalin, then transferred to 75% ethanol in the laboratory. Both specimens were deposited in the Marine Biological Museum (MBM), Chinese Academy of Sciences (CAS), Qingdao, China.

The individuals were examined and dissected with a ZEISS Discovery V20dissecting microscope. Scanning electron microscope (SEM) observation of the distal part of the outer plate and palp of maxilla 1 of C. *lubrica* sp. nov., was conducted using Hitachi S-3400N SEM at an accelerating voltage of 5 kV. Line drawings were first created from images from the dissecting microscope, and then completed using the software Adobe Photoshop CS6 with a graphics tablet (Wacom PTH-851; Coleman, 2003). Length measurements were made by using a LINKS caliper along the outline of the animal, beginning from the rostrum to the posterior margin of telson.

The following abbreviations were used in **Figures 2–6**: A, antenna; G, gnathopod; H, head; L, left; LL, lower lip; Md, mandible; Mx1, maxilla 1; Mx2; maxilla 2; Mxp,

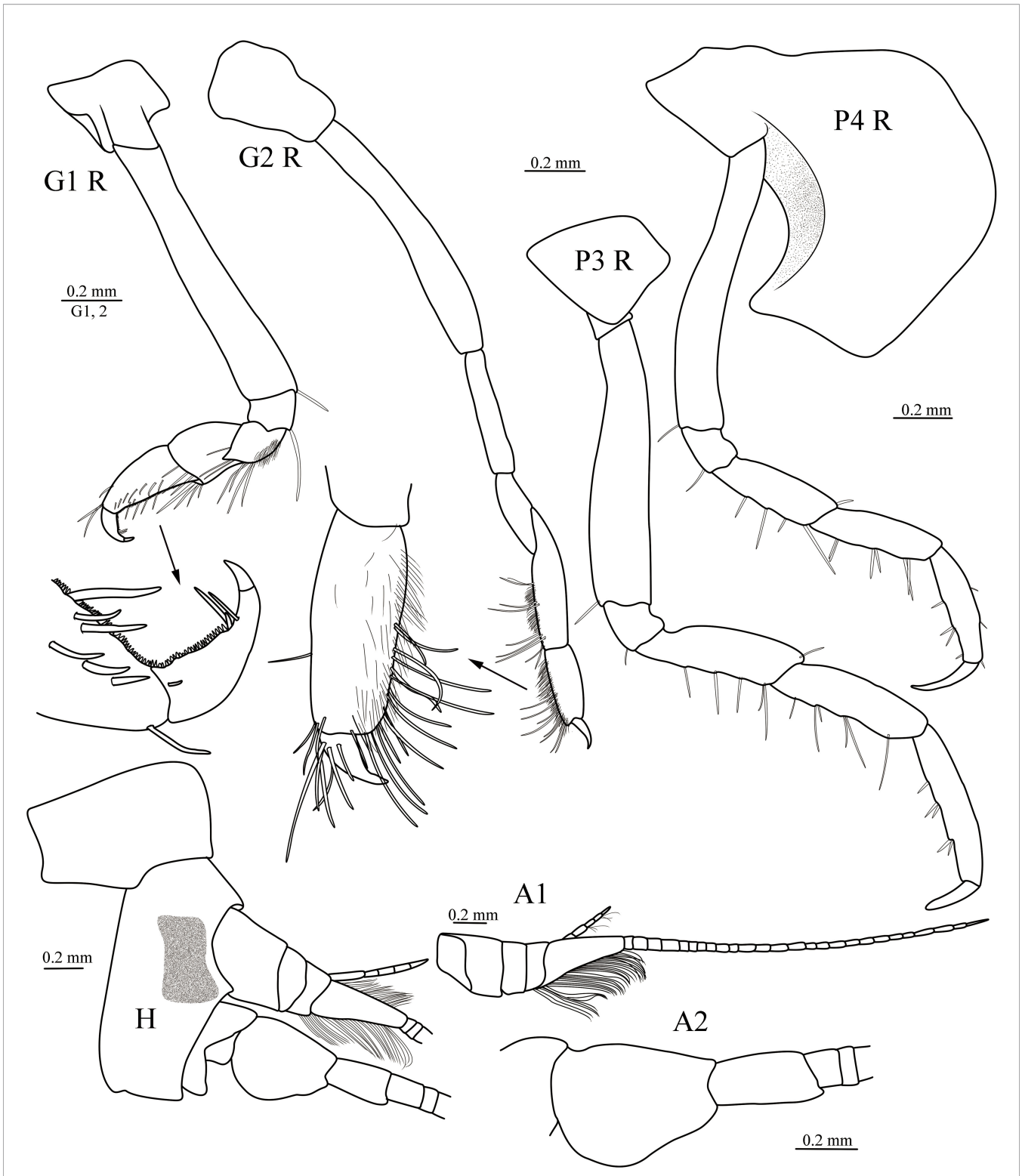

FIGURE 2 | *Cyphocaris lubrica* sp. nov., MBM 286819, male holotype (9.1 mm), showing head, antenna 1 and 2, gnathopod 1 and 2 and pereopod 3 and 4. For abbreviations, see text.

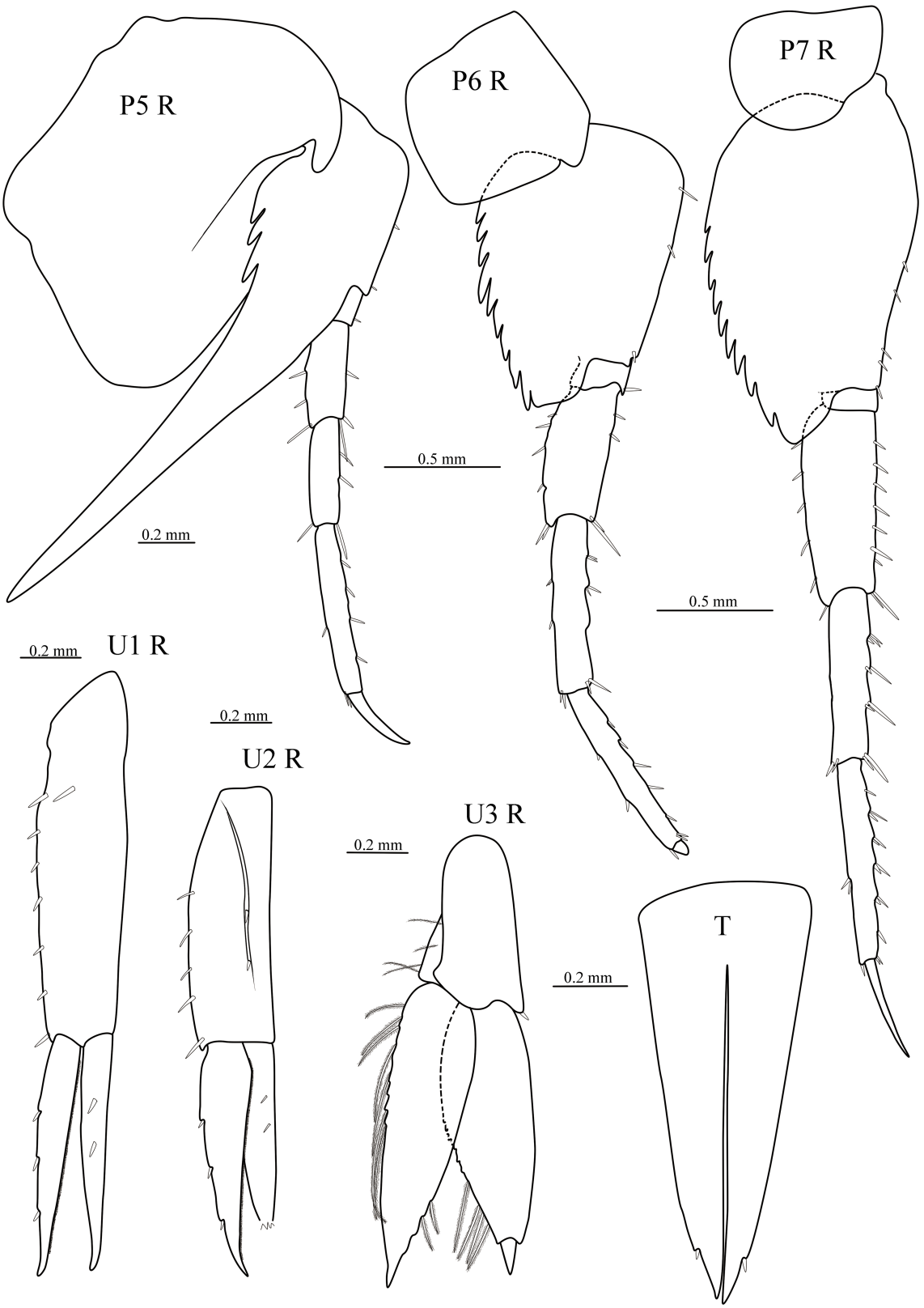

FIGURE 3 | *Cyphocaris lubrica* sp. nov., MBM 286819, male holotype (9.1 mm), showing pereopod 5–7, uropod 1–3 and telson. For abbreviations, see text.

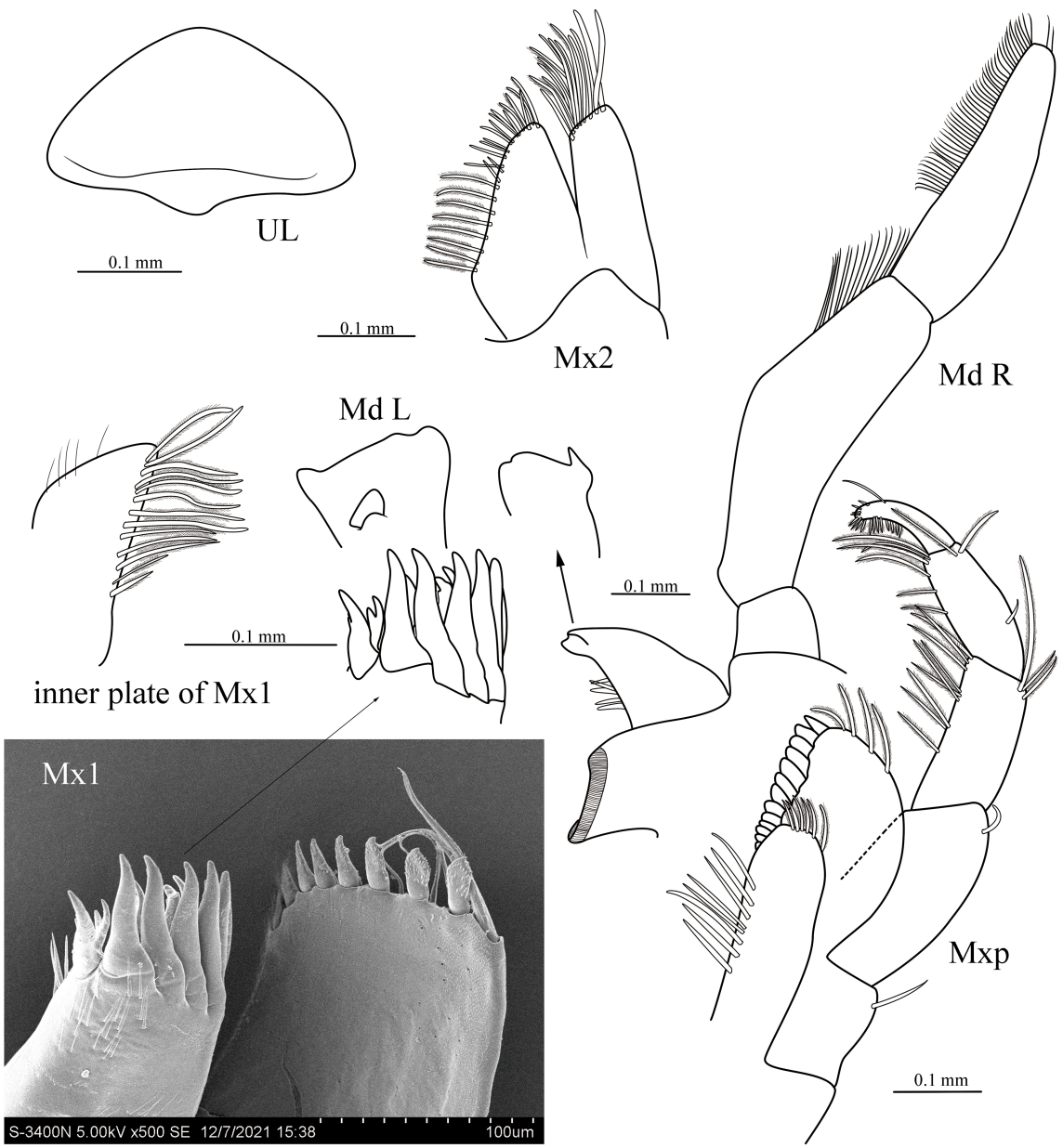

FIGURE 4 | *Cyphocaris lubrica* sp. nov., MBM 286819, male holotype (9.1 mm), showing mouthparts, SEM picture showing outer plate of distal part of outer plate and palp of maxilla 1. For abbreviations, see text.

maxilliped; P, pereopod; R, right; T, telson; U, uropod; UL, upper lip.

RESULTS

We described two new species of *Cyphocaris*, and each new species was described based on one individual. The classification system follows that of Lowry and Myers (2017).

Order Amphipoda (Latreille, 1816).

Suborder Amphilochidea (Boeck, 1871).

Superfamily Lysianassoidea (Dana, 1849).

Family Cyphocarididae (Lowry and Stoddart, 1997).

Genus *Cyphocaris* (Boeck, 1871).

Diagnosis: Head deeper than long. Flagella of antennae long; first peduncular article of antenna 1 with callynophore, accessory flagellum present. Mouthparts forming quadrate bundle; upper lip and epistome separate; mandible incisor ordinary, molar triturative, palp well setose, attached opposite molar; inner plate

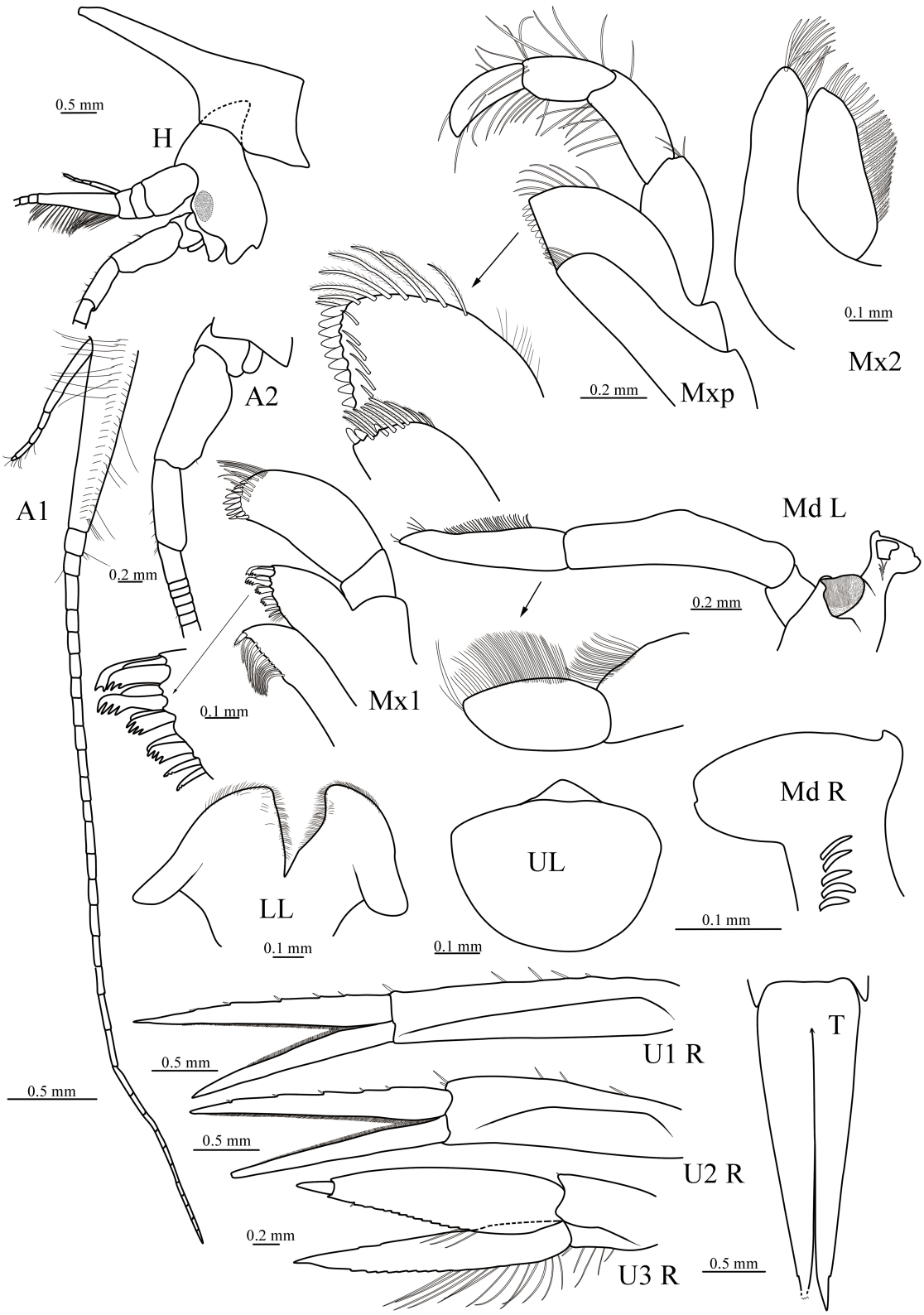

FIGURE 5 | *Cyphocaris formosa* sp. nov., MBM 286820, male holotype (19 mm), showing head, antenna 1 and 2, mouthparts, uropod 1–3 and telson. For abbreviations, see text.

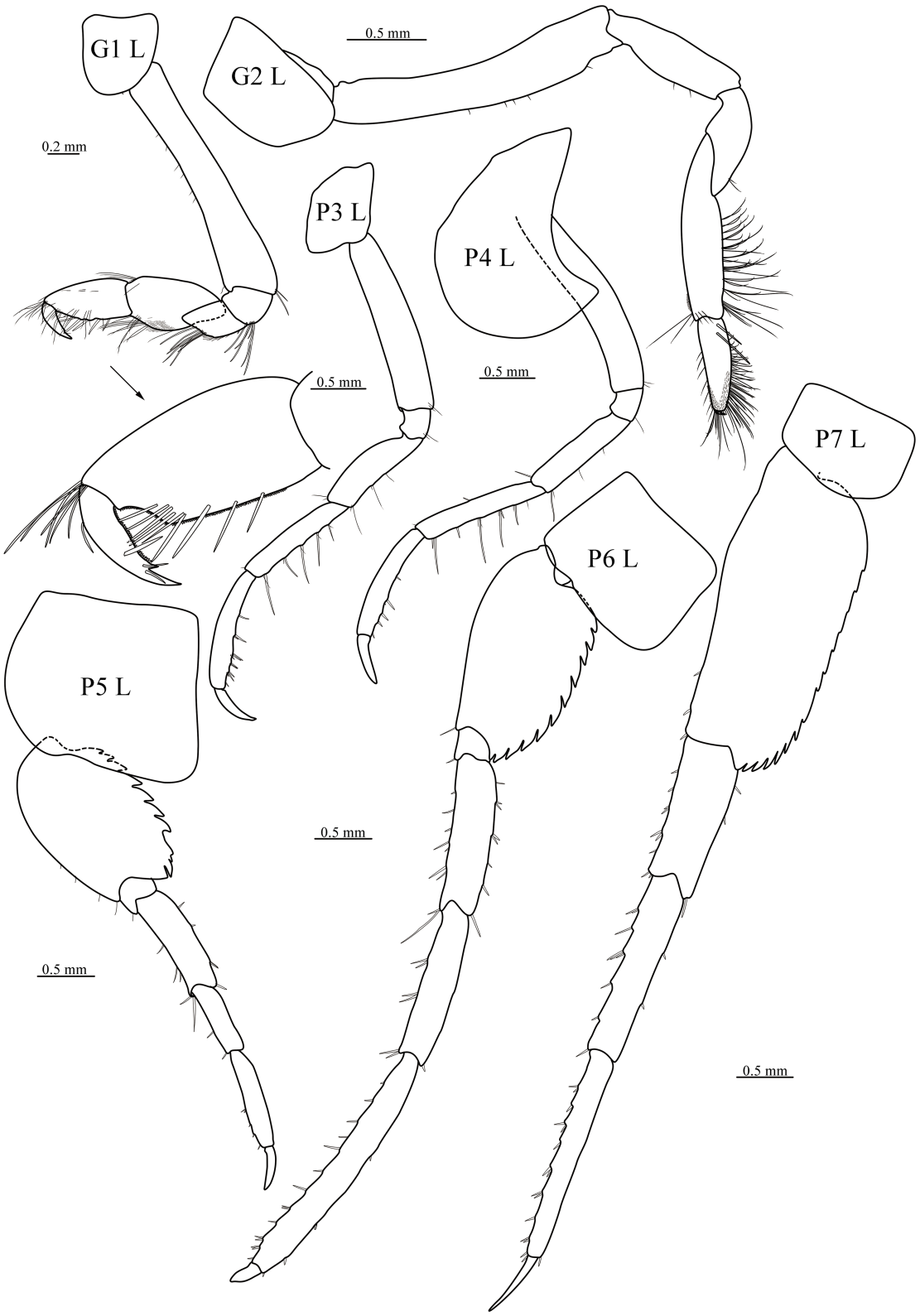

FIGURE 6 | *Cyphocaris formosa* sp. nov., MBM 286820, male holotype (19 mm), showing gnathopod 1 and 2, pereopod 3–7. For abbreviations, see text.

of maxilla 1 strongly setose; palp 2-articulate, large; inner and outer plates of maxilliped well-developed, plap strongly exceeding outer plate, dactylus well-developed. Coxae 1–3 small, strongly shortened and partly covered by coxa 4; coxa 4 large and visible, strongly lobate and excavate; coxa 5 usually large. Gnathopod 1 simple, carpus and propodus subequal in length, dactylus large. Propodus of gnathopod 2 slightly to greatly shorter than carpus, often both very elongate and linear, propodus minutely subchelate. Uropod 3 ordinary to elongate, peduncle elongate, aequiramous, outer ramus uni- or 2-articulate. Telson elongate, deeply cleft (Barnard and Karaman, 1991).

Cyphocaris lubrica sp. nov. (**Figures 1**, **2**, **6**, **7**)

lsid:zoobank.org:act:B7BECCC6-0681-4E32-A36F-75E00CB68311

Type Material: Holotype: MBM 286819, ♂ (9.1 mm), dissected, the Formosa Ridge methane seep, coll. No. TXNLQ044, 22°07′N 119°17′E, depth 1118 m, 19 June 2021, MultiNet, collected by Min Hui and Ziming Yuan.

Description

Holotype, male, 9.1 mm. *Body* smooth, without setae. *Pereonite 1* conspicuously produced anterodorsally, length subequal to basal width. *Head* narrow than long, eyes present, dumbbell-shaped; rostrum absent; lateral cephalic lobe acute, anteroventral corner produced rounded, ventral margin convex. *Antenna 1* much shorter than antenna 2; peduncular article 1 longer than articles 2 and 3 combined; accessory flagellum short, 5-articulate, have tufts of setae, almost reaching to end of primary flagellum first article; primary flagellum article 1 very long, ventrally with well-developed callynophore in two fields, calceoli absent. *Antenna 2* slightly shorter than body, peduncular article 4 strongly broadened, nearly as long as body, flagellum calceoli absent.

Epistome and upper lip separate, unequally produced. *Mandible* incisor smooth, toothed laterally; right lacinia mobilis absent, left one smooth, blade-like; right accessory setal with 5 setae; molar well-developed, triturative; palp 3-articulate, article 1 shortest, article 2 longer than article 3, posterior margin nearly straight, anterior margin with medial bulge, with dense row of submarginal setae distally, article 3 anterior margin with dense row of setae. *Maxilla 1* outer plate with 11 setal teeth; inner plate tapering distally, inner margin with 13 plumose setae; palp with 8 robust dentate setae and 5 slender plumose setae. *Maxilla 2* inner plate broad, triangular, with marginal plumose setae and slender setae; outer plate with apical setae. *Maxilliped* inner plate rectangular, with 3 nodular apical robust setae, distal margin lined with 6 plumose setae; outer plate subovate, apicolateral margin with long setae, medial margin with 13 nodular robust setae; palp 4-articulate, article 2 subequal in length to article 1, mesial margin with row of plumose setae, distal of lateral margin with three plumose setae; dactylus slightly shorter than article 3, mesial margin with short dense plumose setae.

Gills present on Gnathopod 2 to pereopod 7, gill on pereopod 7 not reduced.

Gnathopod 1 weakly subchelate; coxa small; basis long, slightly widened distally; merus posteriorly produced, acute, posterior surface with short setae; carpus length 0.6 × propodus; propodus with palm finely serrate; dactylus posterior margin serrated, with one and a pair distal robust setae, nail present. *Gnathopod 2* minutely subchelate; coxa small, deeper than long; basis elongate, margins naked; ischium elongate, margins naked; merus length 0.7 × ischium subtriangular; carpus length 1.1 × merus, anterior margin setose; propodus length 0.8 × carpus, subrectangular, posterior and distal margins with slender setae, palm reduced, palmer corner not defines by stout seta; dactylus small, curved, reaching to palmar corner. *Pereopod 3* slender; coxa subquadrate; basis elongate, posterodistal corner with one long seta; ischium short; merus and carpus subequal in length, posterior margins with long setae; propodus subequal in length to carpus, posterior margin with one and two pairs of robust setae; dactylus slightly curved, apical rounded. *Pereopod 4* slender, coxa large, expanded and round anteriorly, posteroventral corner forming subacute projection, partially overlapping coxae 2–3; basis elongate, posterodistal corner with one long seta; ischium to propodus similar to that of pereopod 3, but propodus subequal in length to carpus; dactylus slender, longer than 1/2 length of propodus. *Pereopod 5–7* increasing in length. *Pereopod 5* coxa large, subrectangular, anterodistal corner forming an elongate subacute projection, posteroventral corner expanded and rounded; basis anterior margin broadly rounded, with two small setae, posterior margin with large subacute spur, straight, beyond pereonite 7, ventral margin smooth, dorsal margin proximal with three teeth; ischium short, anterior margin with one seta; merus and carpus subequal in length, anterior and posterior margins with robust setae; propodus elongate; dactylus slightly curved, nearly 1/2 length of propodus. *Pereopod 6* coxa small, subquadrate; basis suboval, anterior margin with several small setae, posterior margin expanded, serrated, posteroventral lobe truncatus; merus slightly expanded posteriorly; carpus longer than merus, posterior and anterior margins with small setae; propodus slender; dactylus small, only 1/10 length of propodus, rounded. *Pereopod 7* coxa small, ventral margin convex; basis suboval, anterior margin with several small robust setae, posterior margin serrated, posteroventral lobe subacute; merus and carpus subequal in length, merus slightly expanded posteriorly, anterior and posterior margins with robust setae; propodus slender, anterior margin with several pairs of robust setae; dactylus slender, nearly straight, longer than 1/2 length of propodus.

Uropod 1 elongate, peduncle much longer than rami, with 8 marginal robust setae; rami subequal in length margins with robust setae. *Uropod 2* peduncle slightly longer than outer ramus, with 7 marginal robust setae; inner ramus broken, margins with robust setae. *Uropod 3* peduncle short, marginal with 4 short plumose setae, ventrodistally with one robust seta; outer ramus slightly longer than inner ramus, outer margin with several long plumose setae, inner margin with two short plumose setae; inner ramus 2-articulate, inner margin with four short plumose setae. *Telson* elongate, deeply cleft to 87%, lobes tapering distally, each with one subapical robust seta.

Etymology

From the Latin *lubric* (=smooth), referring to the spur of pereopod 5 having smooth ventral margin and dorsal margin only having three teeth at base.

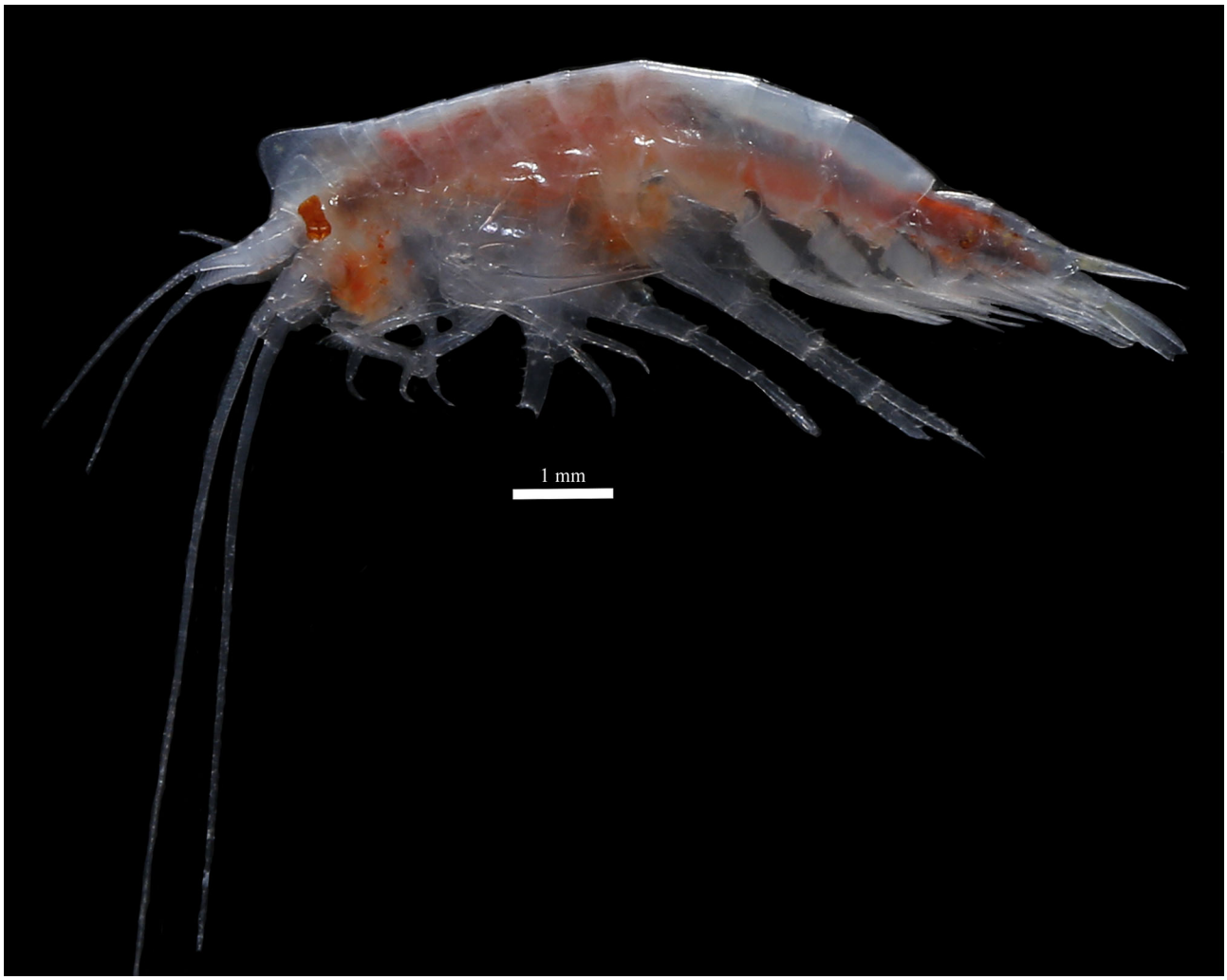

FIGURE 7 | *Cyphocaris lubrica* sp. nov., MBM 286819, male holotype (9.1 mm), photographed immediately after sorting from the zooplankton samples by Ziming Yuan.

Distribution

Northwest Pacific, South China Sea, the Formosa Ridge methane seep at a depth of 1118 m.

Remarks

Cyphocaris lubrica sp. nov. is most similar to *C. bouvieri*, but can be easily distinguished from the latter by pereonite 1 having well-developed dorsal projection, which is absent in *C. bouvieri* (Gurjanova, 1962, Figure 7; Hughes and Lowry, 2015, Figure 9); the spur of pereopod 5 beyond pereonite 7, and dorsal margin of it having only three large teeth, while the dorsal margin of spur having more than 7 teeth in *C. bouvieri* (Gurjanova, 1962, Figure 7; Tencati and Geiger, 1968, Figure 4; Hughes and Lowry, 2015, Figure 12); eyes absent in *C. bouvieri* (Gurjanova, 1962, Figure 7; Hughes and Lowry, 2015, Figure 9).

C. lubrica sp. nov. is similar to five species: *C. ananke* (Hughes and Lowry, 2015), *C. anonyx* (Boeck, 1871), *C. bouvieri* (Chevreux, 1916), *C. challengeri* (Stebbing, 1888), *C. faurei* (Barnard, 1916) and *C. pedroi* (Sorrentino et al., 2016) for the spur of pereopod 5 not beyond pleonite 1. The new species differs from *C. challengeri*, *C. faurei* and *C. pedroi* by the produced pereonite 1 (Stebbing, 1888; Hughes and Lowry, 2015; Sorrentino et al., 2016); differs from *C. ananke* and *C. anonyx* the posterior margin of basis of pereopod 5 not completely serrate, and the spur of pereopod reaching to middle length of pleonite (Hughes and Lowry, 2015).

Cyphocaris formosa sp. nov. (**Figures 3**, **4**, **8**)

lsid:zoobank.org:act:337E3D54-C517-446A-9811-0FD4E05C9F0C

Type material: Holotype: MBM 286820, ♂ (19 mm), dissected, the Formosa Ridge methane seep, coll. No. CS051, 22°07′N 119°17′E, depth 500–800 m, 17 May 2020, MultiNet, collected by Min Hui and Ziming Yuan.

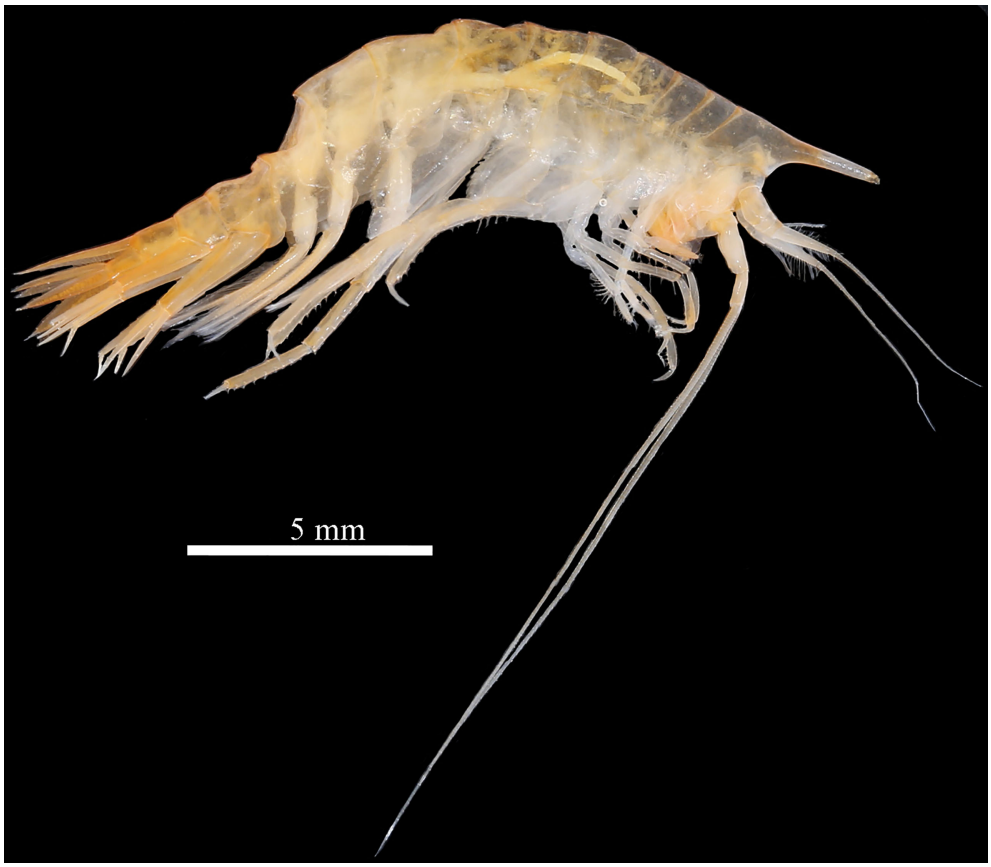

FIGURE 8 | *Cyphocaris formosa* sp. nov., MBM 286820, male holotype (19 mm), photographed immediately after sorting from the zooplankton samples by Ziming Yuan.

Description

Holotype, male, 19 mm. *Body* smooth, without setae. *Pereonite 1* conspicuously produced anterodorsally. *Head* narrow, much deeper than long, eyes present, subovate; rostrum absent; lateral cephalic lobe rounded, anteroventral corner produced acute, ventral margin convex. *Antenna* 1 much shorter than antenna 2; peduncular article 1 longer than articles 2 and 3 combined; accessory flagellum short, 5-articulate, having tufts of setae, not reaching end of primary flagellum first article; primary flagellum article 1 very long, ventrally with well-developed callynophore in two fields, calceoli absent. *Antenna 2* length slightly longer than body, peduncular article 4 not strongly broadened; flagellum calceoli absent.

Epistome and upper lip separate, unequally produced. *Mandible* incisor smooth, toothed laterally; right lacinia mobilis absent, left one smooth, boot-shaped; accessory setal row with 4 (left) and 5 (right) setae; molar well-developed, triturative; palp 3-articulate, article 1 much shorter than 2 and 3, article 2 posterior margin nearly straight, anterior margin with medial bulge, with dense row of submarginal setae distally, article 3 shorter than 2, anterior margin with dense row of setae. *Maxilla 1* inner plate triangular, tapering distally, inner margin lined with 1 robust plumose seta and 11 slender plumose setae; outer plate with 11 setal teeth; palp 2-articulate, with 9 robust setae and with 9 slender setae in two rows. *Maxilla 2* inner plate triangular, lined with 9 slender setae and 21 slender plumose setae; outer plate with 13 apical setae. *Maxilliped* inner rectangular, with 3 nodular apical robust setae, distal margin lined with 9 plumose setae; outer plate subovate, apicolateral margin with long plumose setae, medial margin with 9 nodular robust setae and row of submarginal slender setae; palp 4-articulate, article 1 longest, article 2 longer than article 3, inner margin with row of plumose setae, article 2 margins with dense plumose, dactylus subequal to article 3, margins have plumose.

Gnathopod 1 subchelate; coxa small, ventrally rounded; basis long, slightly widened distally; merus posteriorly produced, acute, posterior surface with short setae; carpus length 1.2 × propodus; propodus with palm finely serrate, defined by weak corner; dactylus curved, posterior margin finely serrate, with 3 subapical slender setae, with nail and subterminal spine. *Gnathopod 2* minutely subchelate; coxa tapering ventrally; basis with triangular lobe anterodistally; ischium elongate; merus length 0.8 × ischium, subtriangular; carpus twice longer than propodus, posterior margin lined with long setae, surface without short setae; propodus with palm smooth; dactylus small. *Pereopod 3* slender;

coxa subquadrate; basis straight; merus to propodus gradually increasing in length; dactylus shorter than 1/2 length of propodus. *Pereopod 4* coxa anterior margin rounded, posteroventral lobe produced acute. *Pereopod 5* shorter than pereopods 6 and 7; coxa subquadrate; basis posterior margin not produced, serrate, posterodistal lobe not much beyond distal margin of ischium; merus distinctly longer than carpus; propodus subequal in length to merus; dactylus length 0.45 × propodus. *Pereopod 6* distinctly shorter than pereopod 7; coxa subquadrate; basis posterior margin serrate, posterodistal lobe not beyond distal margin of ischium; merus and carpus subequal in length, and much shorter than propodus; dactylus recurved. *Pereopod 7* coxa small, subquadrate; basis subrectangular, posterior margin nearly straight, serrate, posterodistal lobe beyond distal margin of ischium, corner serrate; merus shorter than carpus; propodus longer than carpus; dactylus slender, straight.

Uropod 1 elongate, peduncle longer than inner ramus, with 5 marginal robust setae; outer ramus shorter than inner one. *Uropod 2* reaching end of uropod 3; peduncle shorter than inner ramus; outer ramus shorter than inner one. *Uropod 3* slightly beyond posterior margin of telson; peduncle much shorter than rami; rami subequal in length; outer ramus 2-articulate. *Telson* elongate, deeply cleft to 87%, lobes tapering distally, distal of right lobe broken.

Etymology

The species is named after the type locality "the Formosa Ridge methane seep".

Distribution

Northwest Pacific, South China Sea, the Formosa Ridge methane seep at a depth of 500–800 m.

Remarks

Cyphocaris formosa sp. nov. is most similar to *C. nesoi* (Hughes and Lowry, 2015) and *C. richardi* (Chevreux, 1905) for having the peduncular article 4 of antenna 2 not strongly broadened; the pereonite 1 having slender dorsal projection extending well beyond bead and the basis of pereopod 5 without spur. The new species differs from *C. nesoi* by the dactylus of gnathopod 1 having subterminal spine; the accessory flagellum 5-articulate; only outer ramus of uropod 3 2-articulate, but both rami having two articles in *C. nesoi* (Hughes and Lowry, 2015, Figure 19); lateral margin of telson without setae. With the limited original illustration of *C. richardi*, *C. formosa* sp. nov. differs from it by the posterior margin of basis of pereopod 5 not strongly serrate, and not beyond distal margin of ischium, while the posterodistal corner of basis far beyond distal margin of ischium (Chevreux, 1905, Figure 2); the shape of dorsal projection of pereonite 1 columned, not triangular (Chevreux, 1905, Figure 1; Birstein and Vinogradov, 1955, Figure 2).

Key to World Cyphocarididae Species

1. Pereopod 7 basis posterior margin smooth; coxae 1–2 reduced, covered by coxa 3 *Procyphocaris indurata* (Barnard, 1925).

–Pereopod 7 basis posterior margin serrate; coxae 1–3 all small, partly covered by coxa 4 2 (*Cyphocaris*).

2. Pereopod 5 basis posterior margin with spur 3

–Pereopod 5 basis posterior margin without spur 16

3. Pereopod 5 basis posterior margin spur extremely elongate, reaching beyond pleonite 1 4

–Pereopod 5 basis posterior margin spur not reaching beyond pleonite 1 10

4. Pereopod 5 basis posterior margin spur ventral margin with serrations 5

–Pereopod 5 basis posterior margin spur ventral margin smooth, without serration 8

5. Pereopod 5 basis posterior margin spur ventral margin with single serration 6

–Pereopod 5 basis posterior margin spur ventral margin with multiple serrations 7

6. Pereonite 1 dorsal projection short, not extending beyond head *C. geyserensis* (Ledoyer, 1986).

–Pereonite 1 dorsal projection long, extending well beyond head *C. tartaros* (Hughes and Lowry, 2015).

7. Gnathopod 2 coxa sub-triangular; epimeron 2 posteroventral corner quadrate; telson almost reaching posterior end of uropod 3 *C. ohtsukai* (Tomikawa, 2009).

–Gnathopod 2 coxa sub-quadrate; epimeron 2 posteroventral corner rounded; telson not reaching mid-length of inner ramus of uropod 3 *C. cornuta* (Ledoyer, 1978).

8. Head eye not greatly enlarged, length twice as long as wide; telson reaching posterior end of uropod 3. *C. bellona* (Lowry and Stoddart, 1994).

–Head eye greatly enlarged, length at least 3 times longer than wide; telson exceeding posterior end of uropod 3 9

9. Pereonite 1 forming long, narrow, slightly up-turned process in male, not developed in female. Telson 1.5 × as long as uropod 3 *C. johnsoni* (Shoemaker, 1934).

–Pereonite 1 forming long, narrow, slightly down-turned process in both sexes. Telson 1.8 × as long as uropod 3 *C. tunicola* (Lowry and Stoddart, 1997).

10. Pereopod 5 basis posterior margin spur margins serrate 11

–Pereopod 5 basis posterior margin spur margins smooth 12

11. Pereopod 4 coxa anterior margin is subacute; telson short not reaching the end of uropod 3 *C. anonyx* (Boeck, 1871).

–Pereopod 4 coxa anterior margin is broadly rounded; telson long reaching end of uropod 3 *C. ananke* (Hughes and Lowry, 2015).

12. Pereopod 5 basis proximal posterior margin smooth 13

–Pereopod 5 basis proximal posterior margin serrate 14

13. Gnathopod 1 merus with subtrapezoid serrated structure on the posterodistal corner; pereopod 5 coxa well-developed lobe on anterodistal margin, broadly rounded and apically reverted backwards *C. pedroi* (Sorrentino et al., 2016).

–Gnathopod 1 merus anterodistal margin tapered; pereopod 5 coxa, anterodistal margin expanded posteriorly, rounded *C. faurei* (Barnard, 1916).

14. Pereopod 5 basis posterior margin spur exceeding length of merus 15

–Pereopod 5 basis posterior margin spur not exceeding merus *C. challengeri* (Stebbing, 1888).

15. Eyes absent; pereonite 1 dorsal projection absent; spur of pereopod 5 not beyond pereonite 7 *C. bouvieri* (Chevreux, 1916).

–Eyes present; pereonite 1 dorsal projection present; spur of pereopod 5 beyond pereonite 7 *C. lubrica* sp. nov.

16. Pereonite 1 dorsal projection extending well beyond head 17

–Pereonite 1 dorsal projection absent or extending slightly beyond head 19

17. Pereopod 5 basis posterior margin weakly serrate (or strongly in male), posterodistal corner rounded 18

–Pereopod 5 basis posterior margin strongly serrate, posterodistal corner subacute *C. richardi* (Chevreux, 1905).

18. Accessory flagellum 7-articulate; dactylus of gnathopod 1 without subterminal spine; inner ramus of uropod 3 2-articulate *C. nesoi* (Hughes and Lowry, 2015).

–Accessory flagellum 5-articulate; dactylus of gnathopod 1 with subterminal spine; inner ramus of uropod 3 uniarticulate *C. formosa* sp. nov.

19. Head lateral cephalic lobe concave *C. latirama* (Hendrycks and Conlan, 2003).

–Head lateral cephalic lobe subacute *C. polaris* (Gurjanova, 1951).

DISCUSSION

The amphipod fauna described from methane seeps comprises, up to now, 22 species spread over 12 families (**Table 1**). Moreover, 23 species were reported from oil and methane seep at a large freshwater lake, Lake Baikal (Mekhanikova and Sitnikova, 2014). The present two new species were collected by MultiNet, which means they are pelagic amphipods. Among all species reported from methane seeps (**Table 1**), *Harpiniopsis fulgens* (Barnard, 1960), *Harpiniopsis naiadis* (Barnard, 1960), *Paraphoxus oculatus* (Sars, 1879) and *Ampelisca romigi*

TABLE 1 | Worldwide list of amphipods known from methane seep fields.

Family/species	Ocean	Site	Depth (m)	References
Caprellidae				
Abyssododecas styx (Takeuchi et al., 2016)	Pacific	Japan Trench	5,695–5,793	Takeuchi et al., 2016
Ischyroceridae				
Bonnierella californica (Barnard, 1966)	Pacific	East·Pacific Rise: 21° N	2,590	Vinogradov, 1994; Vinogradov, 1995
Pleustidae				
Mesopleustes abyssorumi (Stebbing, 1888)	Pacific	Monterey Canyon	694–3,040	Vinogradov, 1994; Vinogradov, 1995
Leucothoidae				
Leucothoe ayrtonia (Bellan-Santini, 1997)	Atlantic	Barbados trench	1,947	Bellan-Santini, 1997
Eusiridae				
Sennaia bidactyla (Bellan-Santini, 1997)	Atlantic	Barbados trench	1,654	Bellan-Santini, 1997
Infraorder Lysianassida				
Phoxocephalidae				
Harpinia intermedia (Bellan-Santini, 1997)	Atlantic	Barbados trench	1,947	Bellan-Santini, 1997
Harpiniopsis fulgens (Barnard, 1960)	Pacific	Guaymas Basin	128–1,934	Vinogradov, 1993; Vinogradov, 1995
Harpiniopsis naiadis (Barnard, 1960)	Pacific	Guaymas Basin	320–2,026	Vinogradov, 1994; Vinogradov, 1995
Paraphoxus oculatus (Sars, 1879)*	Pacific	Guaymas Basin	30–1,150	Vinogradov, 1993; Vinogradov, 1995
Proharpinia barbada (Bellan-Santini, 1997)	Atlantic	Barbados trench	1,947	Bellan-Santini, 1997
Endevouridae				
Ensayara ursus (Kilgallen, 2009)	Pacific	Omakere Ridge	1,055–1,102	Kilgallen, 2009
Lysianassidae				
Hippomedon keldyshi (Vinogradov, 1994)	Pacific	Monterey Canyon	3,041	Vinogradov, 1994; Vinogradov, 1995
Orchomene kaikoi (Bellan-Santini, 1990)	Pacific	near Japan Islands	5,640–5,695	Bellan-Santini, 1990; Vinogradov, 1995
Tryphosidae				
Orchomene stocki (Bellan-Santini, 1990)	Atlantic	Barbados trench	4,935	Bellan-Santini, 1990
Orenoqueia serrata (Bellan-Santini, 1997)	Atlantic	Barbados trench	1,947	Bellan-Santini, 1997
Tryphosella uristesi (Bellan-Santini, 1997)	Atlantic	Barbados trench	1,947	Bellan-Santini, 1997
Galathella solivagus (Kilgallen, 2009)	Pacific	Omakere Ridge	1,124	Kilgallen, 2009
Uristidae				
Stephonyx carinatus (Bellan-Santini, 1997)	Atlantic	Barbados trench	1,947	Bellan-Santini, 1997
Stephonyx incertus (Bellan-Santini, 1997)	Atlantic	Barbados trench	1,947	Bellan-Santini, 1997
Ampeliscidae				
Ampelisca romigi (Barnard, 1954)	Pacific	Guaymas Basin	813	Vinogradov, 1993; Vinogradov, 1995
Byblis frigidus (Coyle and Highsmith, 1989)	Pacific	Bering Sea: Pyipa Volcano	492	Vinogradov, 1994; Vinogradov, 1995
Pardaliscidae				
Halice hesmonectes (Martin et al., 1993)	Pacific	East·Pacific Rise	2,520	Martin et al., 1993; Vinogradov, 1995

**According to Jarrett and Bousfield (1994), the material of "Paraphoxus oculatus" from the California region represents another species (Vinogradov, 1995).*

(Barnard, 1954) are also pelagic amphipods and found in trawls (Vinogradov, 1995).

Excepting for the present two new species, only two *Cyphocaris* species have been reported from NW Pacific: *C. polaris* and *C. ohtsukai*. *C. lubrica* sp. nov. can be distinguished from *C. polaris* by the presence of spur on pereopod 5, and from *C. ohtsukai* by dorsal projection of pereonite 1 not exceeding beyond head. *C. formosa* sp. nov. can be distinguished from *C. polaris* by the presence of acute dorsal projection of pereonite 1 exceedingly well beyond head, and from *C. ohtsukai* by the absence of spur of pereopod 5.

DATA AVAILABILITY STATEMENT

The datasets presented in this study can be found in online repositories. The names of the repository/repositories and accession number(s) can be found below: ZooBank [urn:lsid:zoobank.org:pub:F5856D5A-4A03-4E80-9A16-08B74516D507].

AUTHOR CONTRIBUTIONS

Data curation: YW. Funding acquisition: ZS. Illustrations: YW. Writing original draft: YW. Writing review & editing: YW, ZS, XR and XR. All authors listed have made a substantial, direct, and intellectual contribution to the work and approved it for publication.

FUNDING

This work was supported by the National Science Foundation for Distinguished Young Scholars (42025603), Key Research Program of Frontier Sciences, CAS (QYZDBSSW-DQC036), the Strategic Priority Research Program of the Chinese Academy of Sciences (XDA22050302; XDB42000000), the National Key R&D Program of China (2018YFC0310802), and the Special Research Assistant Project of Chinese Academy of Sciences (E2KY031).

ACKNOWLEDGMENTS

We would like to express our sincere thanks to the crews of KEXUE for their assistance during the survey. We are very grateful to Dr. Min Hui and Ziming Yuan for collecting the specimens. Many thanks to Dr. Charles Oliver Coleman from the Museum für Naturkunde—Leibniz Institute for Research on Evolution and Biodiversity, Berlin, Germany, for providing some references.

REFERENCES

Andrade, L. F., Alves-Júnior, F. A., Bertrand, A., and Senna, A. R. (2021). A New Species of *Cyphocaris* Boec(Amphipoda: Lysianassoidea: Cyphocarididae): Found Off the Rocas Atoll, Northeastern Brazil. *Taxonomy* 1 (4), 360–373. doi: 10.3390/taxonomy1040027

Baba, K., and Williams, A. B. (1998). New Galatheoidea (Crustacea, Decapoda, Anomura) From Hydrothermal Systems in the West Pacific Ocean Bismarck Archipelago and Okinawa Trough. *Zoosystema* 20, 143–156.

Barnard, J. L. (1961). Gammaridean Amphipoda from Depths of 400-6000 Meters. *Galathea Report* 5, 23–128.

Barnard, K. H. (1916). Contributions to the Crustacean Fauna of South Africa n° 5. The Amphipoda. *Ann. S. Afr. Mus.* 15 (3), 105–302.

Barnard, K. H. (1925). Contributions to the Crustacean Fauna of South Africa n° 8. Further Additions to the List of Amphipoda. *Ann. S. Afr. Mus.* 20 (5), 319–380.

Barnard, K. H. (1937). Amphipoda. *Sci. Rep. John Murray Expedition* 4, 131–201.

Barnard, J. L. (1954). Amphipoda of the Family Ampeliscidae Collected in the Eastern Pacific Ocean by the Velero III an Velero IV. *Allan Hancock Pacific Expeditions* 18 (1), 1–137.

Barnard, J. L. (1960). The Amphipod Family Phoxocephalidae in the Eastern Pacific Ocean With Analyses of Other Species and Notes for a Revision of the Family. *Allan Hancock Pacific Expeditions* 18 (3), 175–368.

Barnard, J. L. (1966). Submarine canyons of southern California. Part V. Systematics: Amphipoda. *Allan Hancock Pacific Expeditions* 27 (5), 1–166.

Barnard, J. L. (1967). Bathyal and Abyssal Gammaridean Amphipoda of Cedros Trench, Baja California. *US Natl. Mus. Bull.* 260, 1–205. doi: 10.5479/si.03629236.260.1

Barnard, J. L., and Karaman, G. S. (1991). The Families and Genera of Marine Gammaridean Amphipoda (Except Marine Gammaroids). *Rec. Aust. Mus.* 13 (2), 1–866.

Boeck, A. (1871). Crustacea Amphipoda Borealia et Arctica. *Forhandlinger fra Videnskabernes Selskab Christiania 1871*, 83–280. doi: 10.5962/bhl.title.2056

Bellan-Santini, D. (1990). Nouvelles Espèces D'*Orchomene* s.L. (Crustacea - Amphipoda) Des Fonds Abyssaux. Affinités Avec Les Autres *Orchomene Profonds*. *Beaufortia* 41 (3), 15–23.

Bellan-Santini, D. (1997). Amphipods of the Cold Seep Community on the South Barbados Accretionary Prism. *Crustaceana* 70 (1), 1–30. doi: 10.1163/156854097X00311

Birstein, J. A., and Vinogradov, M. E. (1955). [Pelagic Gammarideans (Amphipoda-Gammaridea) From the Kurile-Kamchatka Trench]. *Akademya Nauk SSSR Trudy Inst. Okean* 12, 210–287.

Birstein, J. A., and Vinogradov, M. E. (1962). [Pelagic Gammaridea (Amphipoda, Gammaridea) Collected by the Soviet Antarctic Expedition on the M/V "Ob", South of 40°s]. *Akademya Nauk SSSR Issled. Fauny Morei* 1, 33–56.

Birstein, J. A., and Vinogradov, M. E. (1963). [The Deep Sea Pelagic Amphipods of the Philippine Trench]. *Akademya Nauk SSSR Trudy Inst. Okean* 71, 81–93.

Birstein, J. A., and Vinogradov, M. E. (1964). [Pelagic Gammarid Amphipods of the Northern Part of the Indian Ocean]. *Akademya Nauk SSSR Trudy Inst. Okean* 65, 152–195.

Coyle, K. O., and Highsmith, R. C. (1989). Arctic Ampeliscid Amphipods: Three New Species. *J. Crustacean Biol.* 9 (1), 157–175. doi: 10.1163/193724089X00296

Chevreux, E. (1905). Description D'un Amphipode (*Cyphocaris Richardi* Nov. Sp.) Provenant Des Pêches Au Filet À Grande Ouverture De La Dernière Campagne Du Yacht Princesse-Alic). *Bull. Mus. Océanogr. Monaco* 24, 1–5.

Chevreux, E. (1916). Sur les amphipodes du genre Cyphocaris Boeck recueillis par la "Princesse Alice" au moyen du filet Richard à grande ouverture. *Bull. Mus. Océanogr. Monaco* 319, 1–6.

Coleman, C. O. (2003). " Digital Inking": How to Make Perfect Line Drawings on Computers. *Org. Divers. Evol.* 3 (4), 303. doi: 10.1078/1439-6092-00081

Dana, J. D. (1849). Synopsis of the genera of Gammaracea. *Am J Sci Arts (ser. 2)* 8 (22), 135–140.

Feng, D., and Chen, D. (2015). Authigenic Carbonates From an Active Cold Seep of the Northern South China Sea: New Insights Into Fluid Sources and Past Seepage Activity. *Deep-Sea Res. Part II*, 122, 74–83. doi: 10.1016/j.dsr2.2015.02.003

Feng, D., Qiu, J. W., Hu, Y., Peckmann, J., Guan, H., Tong, H., et al. (2018). Cold Seep Systems in the South China Sea: An Overview. *J. Asian Earth Sci.*, 168, 3–16. doi: 10.1016/j.jseaes.2018.09.021

Gislason, A., and Astthorsson, O. S. (1992). Zooplankton Collected by Sediment Trap Moored in Deep Water South of Iceland. *Sarsia* 77, 219–224. doi: 10.1080/00364827.1992.10413507

Gurjanova, E. F. (1951). Bokoplavy morei SSSR i sopredelnykh vod (Amphipoda, Gammaridea). [Amphipods of the seas of USSR and adjacent waters (Amphipoda, Gammaridea)]. *Opredeliteli po faune SSSR, Akademiya Nauk SSSR* 41, 1–1029.

Gurjanova, E. F. (1962). [Amphipods of the Northern Part of the Pacific Ocean (Amphipoda-Gammaridea). Part 1]. *Akademya Nauk SSSR Opredeliteli po Faune SSSR* 74, 1–440.

Hashimoto, J., and Okutani, T. (1994). Four New Mytilid Mussels Associated With Deepsea Chemosynthetic Communities Around Japan. *Venus* 53, 61–83.

Hendrycks, E. A., and Conlan, K. E. (2003). New and Unusual Abyssal Gammaridean Amphipoda From the North-East Pacific. *J. Nat. Hist.* 37, 2303–2368. doi: 10.1080/00222930210138926

Hughes, L. E., and Lowry, J. K. (2015). A Review of the World Cyphocarididae With Description of Three New Species (Crustacea, Amphipoda, Lysianassoidea). *Zootaxa* 4058 (1), 1–40. doi: 10.11646/zootaxa.4058.1.1

Jarrett, N. E., and Bousfield, E. L. (1994). The Amphipod Superfamily Phoxocephalidea on the Pacific Coast of North America. Family Phoxocephalidae. Part H. Subfamilies Pontharpiniidae, Parbarpiniinae, Brolginae, Phoxocephalinae and Harpiniinae. Systematics and Distributional Ecology. *Amphipacifica* 1, 71–150.

Kane, J. E. (1962). Amphipoda From Waters South of New Zealand. *NZ J. Sci.* 5, 295–315.

Kilgallen, N. M. (2009). New Species of Lysianassoid Amphipoda (Crustacea) Associated With Seamounts, Marine Canyons and Cold Seeps of New Zealand. *Zootaxa* 2298, 1–30. doi: 10.11646/zootaxa.2298.1.1

Kuo, M. Y., Kang, D. R., Chang, C. H., Chao, C. H., Wang, C. C., Chen, H. H., et al. (2019). New Records of Three Deep-Sea *Bathymodiolus* Mussels (Bivalvia: Mytilida: Mytilidae) From Hydrothermal Vent and Cold Seeps in Taiwan. *J. Mar. Sci. Technol.* 27 (4), 6. doi: 10.6119/JMST.201908_27(4).0006

Latreille, P. A. (1816). Amphipoda. Nouveau Dictionaire d'Histoire naturelle, appliquée aux Arts, à l'Agriculture, à l'Économie rurale et domestique, à la Médecine, etc. Par une société de Naturalistes et d'Agriculteurs (2nd ed.) Tome 1. Deterville, Paris, 467–469. doi: 10.5962/bhl.title.20211

Ledoyer, M. (1978). Contribution À L'étude Des Amphipodes Gammariens Profonds De Madagascar (Crustacea). *Téthys* 8, 365–382.

Ledoyer, M. (1986). Crustacés Amphipodes Gammariens. Familles Des Haustoriidae À Vitjazianidae. *Faune Madag.* 59, 599–1112.

Li, X. (2017). Taxonomic Research on Deep-Sea Macrofauna in the South China Sea Using the Chinese Deep-Sea Submersible Jiaolong. *Integr. Zool.* 12, 270–282. doi: 10.1111/1749-4877.12254

Lin, S., Lim, Y. C., Liu, C. S., Yang, T. F., Chen, Y. G., Machiyama, H., et al. (2007a). Formosa Ridge, a Cold Seep With Densely Populated Chemosynthetic Community in the Passive Margin, Southwest of Taiwan. *Geochim. Cosmochim. Acta* 71 (Supplement 1), A582.

Lin, S., Machiyama, H., Chen, Y. G., Soh, W., Yang, T. F., Wang, Y., et al. (2007b). Near Sea Floor Gas Hydrate Formation and Influence on Pore Water Chemistry and Authigenic Carbonate at the Formosa Ridge, South China Sea. *EOS Trans. AGU* 88 (52), OS21A–OS205.

Lowry, J., and Myers, A. (2017). A Phylogeny and Classification of the Amphipoda With the Establishment of the New Order Ingolfiellida (Crustacea: Peracarida). *Zootaxa* 4265 (1), 1–89. doi: 10.11646/zootaxa.4265.1.1

Lowry, J. K., and Stoddart, H. E. (1994). Crustacea Amphipoda: Lysianassoids From the Tropical Western South Pacific Ocean. *Mém. Mus. Nutt. Hist. Nut* 161, 127–223.

Lowry, J. K., and Stoddart, H. E. (1997). Amphipoda Crustacea IV. Families Aristiidae, Cyphocarididae, Endevouridae, Lysianassidae, Scopelocheiridae, Uristidae. *Mem. Hourglass Cruises* 10 (1), 1–148.

Machiyama, H., Lin, S., Fujikura, K., Huang, C. Y., Ku, C. Y., Lin, L. H., et al. (2007). Discovery of "Hydrothermal" Chemosynthetic Community in a Cold Seep Environment, Formosa Ridge: Seafloor Observation Results From First ROV Cruise, Off Southwestern Taiwan. *EOS Trans. AGU* 88 (52), OS23A–O1041.

Martin, J. W., France, S. C., and Van Dover, C. L. (1993). Halice Hesmonectes, a New Species of Pardaliscid Amphipod (Crustacea, Peracarida) From Hydrothermal Vents in the Eastern Pacific. *Can. J. Zool.* 71, 1724–1732. doi: 10.1139/z93-244

Mekhanikova, I. V., and Sitnikova, T. Y. (2014). Amphipods (Amphipoda, Gammaridea) at the Gorevoy Utes Oil and Methane Seep, Lake Baikal. *Crustaceana* 87 (13), 1500–1520. doi: 10.1163/15685403-00003367

Pirlot, J. M. (1933). Les Amphipodes De L'expédition Du Siboga. Deuxième Partie: Les Amphipodes Gammarides, II: - Les Amphipodes De La Mer Profonde. 1. (Lysianassidae, Stegocephalidae, Stenothoidae, Pleustidae, Lepechinellidae). *Siboga-Expeditie Monogr.* 33c, 114–167.

Sanger, G. A. (1974). Pelagic Amphipod Crustaceans From the Southeastern Bering Sea, June 1971. *NOAA Tech. Rep.* NMFS SSRF-580, iii and 1–8.

Sars, G. O. (1879). Crustacea et Pycnogonida nova in itinere 2do et 3tio expeditionis Norvegicae anno 1877 & 78 collecta (prodromus descriptionis). *Arch. Math. Naturvidensk* 4, 427–476.

Schellenberg, A. (1929). Die Abyssale Und Pelagische Gammariden. *Bul. Mus. Comp. Zool.* 69, 191–201.

Schellenberg, A. (1955). Amphipoda. Rep. Swed. Deep-Sea Exped. *Ser. 2 Zool.* 14, 181–195.

Shoemaker, C. R. (1934). Reports on the Collections Obtained by the First Johnson-Smithsonian Deep-Sea Expedition to the Puerto Rican Deep. Three New Amphipods. *Smithson. Misc. Collect.* 91, 1–6.

Shoemaker, C. R. (1945). The Amphipoda of the Bermuda Oceanographic Expedition–1931. *Zoologica* 30, 185–266.

Sorrentino, R., Alves, J., Johnsson, R., and Senna, A. R. (2016). A New Species of Cyphocarididae (Crustacea, Amphipoda, Lysianassoidea) From Off the Northeastern Brazilian Coast. *Zootaxa* 4161, 3, 345–356. doi: 10.11646/zootaxa.4161.3.3

Stebbing, T. R. R. (1888). Report on the Amphipoda Collected by H.M.S. Challenger During the Years 1873-1876. *Rep. Sci. Voyage H.M.S. Challenger Zool.* 29, 1–1737.

Takeuchi, I., Lindsay, D., and Tomikawa, K. (2016). A New Genus and Species of Phtisicidae (Crustacea: Amphipoda) From Abyssal Depths in the Japan Trench, With Special Reference to Similarities With Southern Ocean Genera. *J. Crust. Biol.* 36 (4), 495–506. doi: 10.1163/1937240x-00002457

Tencati, J. R., and Geiger, S. R. (1968). Pelagic Amphipods of the Slope Waters of Northeast Greenland. *J. Fish. Res. Bd. Canada* 25, 1637–1650. doi: 10.1139/f68-147

Thurston, M. H. (1976). The Vertical Distribution and Diurnal Migration of the Crustacea Amphipoda Collected During the SOND Cruise I. *J. Mar. Biol. Ass. U.K.* 56, 143–159. doi: 10.1017/S002531540001897X

Tomikawa, K. (2009). A New Species of the Genus *Cyphocaris* (Crustacea: Amphipoda: Cyphocarididae) From Japan. *Bull. Natl. Mus. Nat. Sci. Ser. A* Suppl. 3, 37–46.

Vinogradov, G. M. (1990). [Pelagic Amphipods (Amphipoda, Crustacea) From the South-Eastern Pacific]. *Akademya Nauk SSSR Trudy Inst. Okean* 124, 27–104.

Vinogradov, G. M. (1993). Amfipody (Crustacea) s "Černych Kuril'ščikov" Iz Rajonov Gidrotermal'noj Aktivnosti Vostočnoj Časti Tichogo Okeana [Amphipods (Crustacea) From the "Black Smokers" From Hydrothermal Vents Areas of the Eastern Pacific]. *Zool. Zh* 72 (2), 40–53.

Vinogradov, G. M. (1994). Amphipods From the Seeps Fields and Nearby Benthic Communities From Hydrothermal-Active Areas of the Northern and Eastern Pacific Ocean. *Trudy Inst. Okean* 131, 100–125.

Vinogradov, G. M. (1995). Colonization of Pelagic and Hydrothermal Vent Habitats BY Gammaridean Amphipods: An Attempt of Reconstruction. *Pol. Arch. Hydrobiol.* 42 (4), 417–430.

Vinogradov, G. M. (2004). Near-Bottom and Pelagic Gammaridean Amphipods in the Western Indian Ocean. *Ann. S. Afr. Mus.* 112, 39–88.

Xu, T., Wang, Y., Sun, J., Chen, C., Watanabe, H. K., Chen, J., et al. (2022). Hidden Historical Habitat-Linked Population Divergence and Contemporary Gene Flow of a Deep-Sea Patellogastropod Limpet. *Mol. Biol. Evol.* 38 (12), 5640–5654. doi: 10.1093/molbev/msab278

Zhao, Y., Xu, T., Law, Y. S., Feng, D., Li, N., Xin, R., et al. (2020). Ecological Characterization of Cold-Seep Epifauna in the South China Sea. Deep-Sea Res. Part I-Oceanogr. *Res. Pap.* 163, 103361. doi: 10.1016/j.dsr.2020.103361

Conflict of Interest: The authors declare that the research was conducted in the absence of any commercial or financial relationships that could be construed as a potential conflict of interest.

this article, or claim that may be made by its manufacturer, is not guaranteed or endorsed by the publisher.

frontiers | Frontiers in Marine Science

ORIGINAL RESEARCH
published: 14 April 2022
doi: 10.3389/fmars.2022.848136

Cultivation and Functional Characterization of a Deep-Sea *Lentisphaerae* Representative Reveals Its Unique Physiology and Ecology

Tianhang Zhang[1,2,3,4], *Rikuan Zheng*[2,3,4], *Rui Liu*[2,3,4], *Ronggui Li*[1*] and *Chaomin Sun*[2,3,4*]

[1] College of Life Sciences, Qingdao University, Qingdao, China, [2] CAS Key Laboratory of Experimental Marine Biology & Center of Deep Sea Research, Institute of Oceanology, Chinese Academy of Sciences, Qingdao, China, [3] Laboratory for Marine Biology and Biotechnology, Qingdao National Laboratory for Marine Science and Technology, Qingdao, China, [4] Center of Ocean Mega-Science, Chinese Academy of Sciences, Qingdao, China

As a member of *Planctomycetes–Verrucomicrobia–Chlamydia* (PVC) superphylum, the phylum *Lentisphaerae* is broadly distributed in various environments. *Lentisphaerae* members have been recognized as being typically difficult to isolate in pure culture—only five strains belonging to this phylum were cultured up to now—and therefore their major physiology and ecology are largely unknown. Here, using a polysaccharide degradation-driven strategy, we successfully cultured a representative of *Lentisphaerae* bacteria (*Candidatus* Coldseepensis marina zth2) from the deep-sea cold seep. Based on physiological and phylogenetic analyses, strain zth2 is identified as a type strain of a novel family. Notably, strain zth2 divides by a budding manner and a unique feature seen in ultrathin-section electron microscopic observation is the occurrence of narrow protrusions, namely, both cell wall and cytoplasm on the surface of strain zth2. Through growth assays and transcriptomic analyses, strain zth2 was verified to efficiently utilize polysaccharides, phosphate, and iron for growth. Strikingly, the utilization of polysaccharide, phosphate, and iron is correlative and jointly contributes to carbon, phosphorus, and iron metabolisms and thereby facilitating the production of energy. By mimicking the ocean environment and using operational taxonomic units (OTUs) analysis, we demonstrated that strain zth2 significantly enrich the microbial diversity by metabolizing polysaccharides or other substances. Overall, we propose that *Lentisphaerae* members are potential contributors to the cycling of nutrient, carbon, phosphorus, and other elements in the deep biosphere.

Keywords: ***Lentisphaerae*, cold seep, polysaccharide, phosphorus, cultivation, deep-sea**

OPEN ACCESS

Edited by:
Jian-Wen Qiu,
Hong Kong Baptist University,
Hong Kong SAR, China

Reviewed by:
Hideyuki Tamaki,
National Institute of Advanced Industrial Science and Technology (AIST), Japan
Stefan M. Sievert,
Woods Hole Oceanographic Institution, United States

***Correspondence:**
Chaomin Sun
sunchaomin@qdio.ac.cn
Ronggui Li
lrg@qdu.edu.cn

Specialty section:
This article was submitted to Deep-Sea Environments and Ecology, a section of the journal Frontiers in Marine Science

Received: *04 January 2022*
Accepted: *14 March 2022*
Published: *14 April 2022*

Citation:
Zhang T, Zheng R, Liu R, Li R and Sun C (2022) Cultivation and Functional Characterization of a Deep-Sea Lentisphaerae Representative Reveals Its Unique Physiology and Ecology. Front. Mar. Sci. 9:848136. doi: 10.3389/fmars.2022.848136

INTRODUCTION

The PVC superphylum gathers bacteria from seven phyla: namely, the three founder phyla (*Planctomycetes*, *Verrucomicrobia*, *Chlamydiae*) that it is named after, *Lentisphaerae* and *Kirimatiellaeota* and also some uncultured candidate phyla, such as the *Candidatus* Omnitrophica (previously known as *OP3* and *WWE2*) (Pinos et al., 2016; Rivas-Marin and Devos, 2018). Members within the PVC superphylum present different lifestyles, cell plans, and environments (Pinos et al., 2016), and show diverse interesting characteristics (Pilhofer et al., 2008), such as, some *Planctomycetes* are implicated in carbon and nitrogen cycles (Strous et al., 2006), or synthesize special sterols (Pearson et al., 2003), numerous *Chlamydiae* are pathogens of mammals (Corsarol and Greub, 2006), some members of *Chlamydiae* and *Verrucomicrobiae* are symbionts (Horn, 2008). With the superphylum status now broadly accepted, it is clear that PVC bacteria are fascinating new model organisms for bacterial and evolutionary cell biology (Rivas-Marin et al., 2016), biogeochemical cycles (Strous et al., 2006), biotechnology (Devos and Ward, 2014; Wiegand et al., 2020), and human health (Devos and Ward, 2014).

Among the PVC superphylum, the *Lentisphaerae* phylum was proposed in 2004 after the isolation of two marine strains (Cho et al., 2004). Members belonging to the phylum *Lentisphaerae* have been recognized as being typically difficult to isolate in pure culture, therefore only five pure cultures are available at the time of writing (Choi et al., 2015) and few progresses except taxonomic characteristics associated with the pure culture of this phylum have been disclosed. Nevertheless, the phylum *Lentisphaerae* bacteria are ubiquitously distributed, such as seawater (Cho et al., 2004; Choi et al., 2013) and sediments (Polymenakou et al., 2009), anaerobic sludge (Qiu et al., 2013), landfill leachate (Limam et al., 2010), and animal and human gut (Peng et al., 2015; Liu et al., 2018). In addition, *Lentisphaerae* bacteria are predicted to be closely associated with biogeochemical cycles (Jiang et al., 2015), bioremediation (Das and Kazy, 2014), polysaccharide degradation (Yan et al., 2012), and human health issues, namely, type 2 diabetes (T2D) (Maskarinec et al., 2021), inflammation in the terminal ileum (Fan et al., 2020), and autoimmune hepatitis (Lou et al., 2020). However, the majority of above achievements associated with *Lentisphaerae* bacteria were predicted based on the results of metagenomic. Despite the surge of microbial metagenome data, experimental testing is necessary to confirm inferences about the cell biology, ecological roles, and evolution of *Lentisphaerae* bacteria. Therefore, cultivation of more *Lentisphaerae* members is a priority to understand the unique biology of this kind of difficult-to-culture bacteria.

To date, the phylum *Lentisphaerae* is classified into two classes, namely, *Lentisphaeria* (Choi et al., 2015) and *Oligosphaeria* (Qiu et al., 2013). There are two orders (*Lentisphaerales* and *Victivallales*) and two families (*Lentisphaeraceae* and *Victivallaceae*) (Zoetendal et al., 2003; Choi et al., 2013) within the *Lentisphaeria* class, and there are only one order (*Oligosphaerales*) and one family (*Oligosphaeraceae*) within the *Oligosphaeria* class (Qiu et al., 2013). Correspondingly, three genera (*Victivallis*, *Lentisphaera*, and *Oligosphaera*) have been proposed. The five cultured species include *Victivallis vadensis* ATCC BAA-548^T (Zoetendal et al., 2003), *Lentisphaera araneosa* HTCC2155^T (Cho et al., 2004), *Lentisphaera marina* IMCC11369^T (Choi et al., 2013), *Oligosphaera ethanolica* 8KG-4^T (Qiu et al., 2013), and *Lentisphaera profundi* SAORIC-696^T (Choi et al., 2015). Notably, among these five pure cultures, *V. vadensis* ATCC BAA-548^T was a strictly anaerobic cellobiose-degrading strain (Zoetendal et al., 2003); *L. marina* IMCC11369^T was found to have a capability of degrading starch (Choi et al., 2013); and *O. ethanolica* 8KG-4^T could grow fermentatively on glucose, ribose, xylose, galactose, and sucrose (Qiu et al., 2013). Therefore, *Lentisphaerae* bacteria possess potentials of degrading polysaccharides as those reported in other PVC superphylum members (van Vliet et al., 2019).

As the primary biomass production, polysaccharides are a ubiquitous energy source for microbes in both terrestrial and marine ecosystems including the deep ocean (Zheng et al., 2021a). Many members of the *Bacteroidetes* phylum are specialized in polysaccharide degradation and contribute to the carbon and nutrient cycling of the deep biosphere (Zheng et al., 2021a). Notably, many PVC superphylum bacteria also evolved prominent polysaccharides degradation capabilities: two novel *Kiritimatiellales* strains isolated from Black Sea sediment could anaerobically degrade sulfated polysaccharides; and *Verrucomicrobia* use hundreds of enzymes to digest the algal polysaccharide fucoidan (Sichert et al., 2020). Up to now, it is obscure whether *Lentisphaerae* members possess the polysaccharide degradation capability. When we enriched microorganisms with deep-sea cold seep samples using a basal medium supplemented with various polysaccharides (Zheng et al., 2021a), we found a small amount of *Lentisphaerae* bacterial 16S rRNA gene sequences in addition to *Bacteroidetes* bacteria based on the operational taxonomic units (OTUs) analysis of the bacterial community within the enrichment. However, the potentials of these deep-sea *Lentisphaerae* members toward polysaccharides degradation were unknown due to the lack of pure cultures.

Here, we successfully cultured a novel *Lentisphaerae* strain zth2 from deep-sea cold seep samples by using a polysaccharide-degradation approach. Using growth assay and transcriptomic methods, we further investigated the degradative details of two polysaccharides (starch and laminarin) by strain zth2. We also found the metabolism of polysaccharide and the utilization of phosphorus and iron were closely correlative. Lastly, its contribution to the environmental micro-biodiversity and oceanic carbon/phosphorus cycling were also investigated and discussed.

MATERIALS AND METHODS

Sampling and Isolation of Deep-Sea Bacteria

The deep-sea samples were collected by the *RV KEXUE* from a typical cold seep at the Formosa Ridge (Site F) in the South China

Sea (E119°17'07.322", N22°06'58.598") as described by Cao et al. (2021). The relevant chemical parameters of the cold seep are shown in **Supplementary Table 1**. The temperature, salinity, and underwater depth of sampling sites were recorded in real time by an SBE 25plus Sealogger CTD (SBE, USA). Concentrations of CO_2 and CH_4 in surface sediments were measured *in situ* with CONTROSHydroCO_2 (CONTROS, Norway) and HydroCH_4 (CONTROS, Norway) sensors, respectively. All sensors were mounted on the Discovery *ROV* (Cao et al., 2021). Dissolved oxygen was measured above the vent site and the measurement method of dissolved oxygen can refer to the article of Cao et al. (2021) and more details can be found in *Materials and Methods*. Specific site information is shown in **Supplementary Table 2**. To enrich the polysaccharide degrading bacteria, the sediment needs to be suspended with seawater sterilized three times to ensure that the sediment is not contaminated. A temperature gradient is then set before the culture is carried out, with the aim of slowly reviving the microbes in the sediment, which is very important for the whole isolation and culture process. Later, the sediment samples were cultured at 28°C for 6 months in an anaerobic inorganic medium supplemented with 1.0 g/L of mixed seaweed polysaccharides, namely, porphyra polysaccharide (PP), agar, carrageenan, laminarin, fucoidan, starch, alginate, ulvan, and enteromorpha polysaccharide (EP). The compositions of inorganic medium are 1.0 g NH_4Cl, 1.0 g $NaHCO_3$, 1.0 g CH_3COONa, 0.5 g KH_2PO_4, 0.2 g $MgSO_4$, 0.7 g cysteine hydrochloride, 500 μl 0.1% (w/v) resazurin in 1 L filtered seawater, pH 7.0. This medium was prepared anaerobically as previously described (Fardeau et al., 1997). After the 6-month enrichment, 50 μl dilution portions were spread on Hungate tubes covered by a modified organic medium (1.0 g NH_4Cl, 1.0 g $NaHCO_3$, 1.0 g CH_3COONa, 0.5 g KH_2PO_4, 0.2 g $MgSO_4$, 1.0 g yeast extract, 1.0 g peptone, 0.7 g cysteine hydrochloride, 500 μl 0.1% (w/v) resazurin in 1 L filtered seawater, pH 7.0) supplemented with 15.0 g/L agar. The Hungate tubes were anaerobically incubated at 28°C for 7 days. Individual colonies with distinct morphology were selected using sterilized bamboo sticks and then cultured in the anaerobic liquid 2216E medium (5.0 g/L yeast extract, 1.0 g/L peptone, 0.7 g cysteine hydrochloride, 500 μl 0.1% (w/v) resazurin, 1 L filtered seawater, pH 7.0). Strain zth2 was isolated and purified with 2216E medium by repeated use of the Hungate roll-tube methods for several rounds until it was considered to be pure. The purity of strain zth2 was conventionally confirmed repeated partial sequencing of the 16S rRNA gene. Strain zth2 is preserved at −80°C in 2216E medium supplemented with 20% (v/v) glycerol.

Transmission Electron Microscope (TEM) Observation

To observe the morphological characteristics of strain zth2, its cell pellets were washed with 10 mM phosphate buffer solution (PBS, pH 7.4) and then centrifuged at 5,000 *g* for 5 min, and taken by immersing copper grids coated with a carbon film for 20 min, washed for 10 min in PBS and dried for 20 min at room temperature (Buchan et al., 2014). Ultrathin-section electron microscopic observation was performed as described previously (Sekiguchi et al., 2003; Graham and Orenstein, 2007). Briefly, the samples were firstly preserved in 2.5% (v/v) glutaraldehyde overnight at 4°C and then washed three times using PBS in the next day. Later, samples were dehydrated in ethanol solutions of 30, 50, 70, 90, and 100% for 10 min each time, and then the dehydrated samples were embedded in a plastic resin. Ultrathin sections (50–70 nm) of cells were prepared with an ultramicrotome (Leica EM UC7, Germany), stained with uranyl acetate and lead citrate. All samples were examined using TEM (HT7700, Hitachi, Japan) with a JEOL JEM 12000 EX (equipped with a field emission gun) at 100 kV.

Studies on Physiological Traits of Strain zth2

The temperature, pH, and NaCl concentration ranges for the growth of strain zth2 were determined in the anaerobic liquid 2216E medium incubated for 5 days. Growth assays were performed at different temperatures (4, 28, 30, 37, and 60°C). The pH range for growth was tested from pH 2.0 to 10.0 with increments of 1 pH unit. Salt tolerance was tested with 0–10% (w/v) NaCl (1.0% intervals) in 2216E medium prepared with sterile water instead of sea water. Substrates utilization of strain zth2 was tested in the medium consisting of (L^{-1}): 1.0 g NH_4Cl, 1.0 g $NaHCO_3$, 1.0 g CH_3COONa, 0.5 g KH_2PO_4, 0.2 g $MgSO_4$, 0.7 g cysteine hydrochloride, 500 μl 0.1% (w/v) resazurin in 1 L filtered seawater, pH 7.0. Single substrate (namely, glucose, mannitol, laminarin, fructose, dextrin, fucoidan, maltose, mannose, glycine, pullulan, lactose, polyethylene glycol, butyrate, sucrose, acetate, formate, starch, trehalose, galactose, cellulose, xylose, lactate, ethanol, D-mannose, glycerin, phosphate, and sorbitol) was added from sterile filtered stock solutions to the final concentration at 1.0 g/L, respectively. Cell culture containing basic medium without adding any other substrates was used as a control. For each substrate, three biological replicates were performed.

Genome Sequencing and Analysis

According to the instructions of the manufacturer, genomic DNA of strain zth2 was extracted using a QIAGEN Genomic-tip (QIAGEN Biotech Co., Ltd., Germany). For genome sequencing, 15 ml strain zth2 culture was inoculated in a 2 L anaerobic bottle containing 1.5 L anaerobic 2216E medium. After cell growth reached the logarithmic phase, the culture solution was centrifuged at 8,000 *g* for 10 min to obtain cell pellets.

Its cell pellets were washed with 10 mM phosphate buffer solution (PBS, pH 7.4) and then centrifuged at 8,000 *g* for 5 min. Then the supernatant was poured out and the cell pellets were preserved at −80°C for sequencing. Quality inspection of DNA purity, concentration, and integrity was performed by NanoDrop (Thermo Scientific, USA), and 0.35% agarose gel electrophoresis, respectively. Then, a genomic DNA library for Nanopore sequencing was constructed by using a ligation sequencing kit (Oxford Nanopore Technologies Ltd., UK). The library was sequenced using a Promethion sequencer 48. Canu v1.5 (Koren et al., 2017) was used to assemble the filtered subreads

and Pilon v1.22 (Walker et al., 2014) was used to correct the assembly sequence with higher accuracy. Sequencing work was conducted by Biomarker Technologies Co., Ltd. (Beijing, China).

Genome related values are calculated by several methods: Average Nucleotide Identity (ANI) based on the MUMMER ultra-rapid aligning tool (ANIm), ANI based on the BLASTN algorithm (ANIb), the tetra-nucleotide signatures (Tetra), and *in silico* DNA–DNA similarity. ANIm, ANIb, and Tetra frequencies were calculated using JSpecies WS (http://jspecies.ribohost.com/jspeciesws/). The recommended species criterion cut-offs for the ANIb and ANIm were respectively used as 95% and 0.99 for the Tetra signature. The calculation of *in silico* DNA–DNA similarity values was performed by the Genome-to-Genome Distance Calculator (GGDC) (http://ggdc.dsmz.de/) (Meier-Kolthoff et al., 2013). The isDDH results were calculated based on the recommended formula 2.

Phylogenetic Analysis

The 16S rRNA gene based tree was constructed with the full-length 16S rRNA sequences by the maximum likelihood method. In short, the full-length 16S rRNA (1,361 bp) gene sequence of strain zth2 was obtained from its whole genome (accession number MW729759), and other 16S rRNA sequences of related taxa used for phylogenetic analysis were obtained from NCBI (www.ncbi.nlm.nih.gov/). The multiple sequence alignment of sequences was performed by MAFFT ver.7 (https://mafft.cbrc.jp/alignment/server/). The method of Gappyout was used to trim sequences. Phylogenetic trees were constructed using W-IQ-TREE web server (http://iqtree.cibiv.univie.ac.at/) (Trifinopoulos et al., 2016) with GTR + F + I + G4 model. The edition of the phylogenetic tree was performed by the online tool Interactive Tree of Life (iTOL v4) (Letunic and Bork, 2019).

The genome tree was constructed from a concatenated alignment of 37 protein-coding genes (Wu et al., 2013) that extracted from each genome by Phylosift (v1.0.1) (Darling et al., 2014) with automated setting. The genomes used to construct the genome tree included both draft and finished genomes from NCBI. Aligned sequences were trimmed using TrimAl (version 1.2) with gappyout function. The phylogenetic trees were constructed using W-IQ-TREE web server (http://iqtree.cibiv.univie.ac.at) (Trifinopoulos et al., 2016) with GTR + F + I + G4 model, and the online tool Interactive Tree of Life (iTOL v6) was used for the tree edition (Letunic and Bork, 2019).

Growth Assays of Strain zth2 Cultured in Different Media

Growth assays of strain zth2 were performed at atmospheric pressure. To detect the effect of polysaccharides on the growth of strain zth2, the modified 1/5 2216E medium (containing 1 g/L yeast extract, 0.2 g/L peptone, 0.7 g cysteine hydrochloride, 500 μl 0.1% (w/v) resazurin, 1 L seawater, pH 7.0) supplemented either with or without 1 g/L of different polysaccharides, namely, PP (porphyra polysaccharide), carrageenan, laminarin, starch or ulvan. For all the growth assays, 100 μl strain zth2 culture was inoculated in 15 ml Hungate tubes containing 10 ml medium. All of the Hungate tubes were anaerobically incubated at 28°C. Bacterial growth status was monitored by measuring the OD_{600} value *via* a microplate reader (Infinite M1000 Pro; Tecan, Mannedorf, Switzerland) every day until cell growth reached the stationary phase.

To explore the effects of phosphate and iron on bacterial growth, strain zth2 was grown in basic medium (containing 10 g/L glucose, 0.3 g/L NaCl, 0.5 g/L $(NH_4)_2SO_4$, 0.3 g/L $MgSO_4$, 0.2 g/L KCl, 0.03 g/L $MnSO_4$, 0.2 g/L peptone, 0.7 g cysteine hydrochloride, 500 μl 0.1% (w/v) resazurin, 1 L seawater, pH 6.0–6.5) supplemented with Na_3PO_4 (2.6 mM), or $FeSO_4$ (0.03 g/L), or both $FeSO_4$ (0.03 g/L) and $Ca_3(PO_4)_2$(1.0 g/L), or both $FeSO_4$ (0.03 g/L) and Na_3PO_4 (2.6 mM). Similarly, the growth assays were performed as described above.

Transcriptomic Analysis

Transcriptomic analysis was performed by Novogene (Tianjin, China). For the transcriptomic analysis of the effects of polysaccharides on the growth of strain zth2, strain zth2 was cultured in the above modified 1/5 2216E medium supplemented either with or without 1 g/L of polysaccharides (laminarin or starch) in 2 L anaerobic bottles for 4 days. For the transcriptomic analysis of the effects of phosphate and iron on the growth of strain zth2, cells suspension of strain zth2 was cultured in the above basic medium supplemented with Na_3PO_4 (2.6 mM), or $FeSO_4$ (0.03 g/L), or both $FeSO_4$ (0.03 g/L) and Na_3PO_4 (2.6 mM) in 2 L anaerobic bottles for 5 days. After incubation, the cells were collected by centrifugation at 8,000 *g*, 4°C, 10 min. For transcriptomic analyses, total RNAs of strain zth2 were extracted using TRIzol reagent (Invitrogen, USA) and DNA contamination was removed using the MEGA clear^{TM}Kit (Life technologies, USA). Detailed protocols of the following procedures, namely, library preparation, clustering and sequencing and data analyses were described in the **Supplementary Information**.

Operational Taxonomic Units (OTUs) Analysis

To better understand the ecological role of strain zth2, we mimicked the ocean environment in the anaerobic bottles. Briefly, dialysis bags (containing 50 ml sterilized seawater, named SW; 50 ml sterilized seawater with strain zth2 cells, named SWL; 50 ml sterilized seawater with 1 g/L of laminarin, named SWP; 50 ml sterilized seawater with 1 g/L of laminarin and strain zth2 cells, named SWLP) were respectively put into four anaerobic bottles filled with filtered sea water using medium speed double circle qualitative filter paper from the First Sea Bathing Beach, Qingdao, China. After a month of cultivation, bacterial cells grown outside of the dialysis bags were respectively collected and used for OTUs sequencing that was performed by Novogene (Tianjin, China). Total DNAs from the above four samples were extracted by the CTAB/SDS method (Murray and Thompson, 1980) and were diluted to 1 ng/μl with sterile water and used for PCR template. 16S rRNA genes of distinct regions (16S V3/V4) were amplified using specific primers (341F: 5′-CCTAYGGGRBGCASCAG and 806R: 5′-GGACTACNNGGGTATCTAAT) with the barcode. The PCR products were purified with a Gel Extraction Kit (Qiagen, Germany) and prepared to construct libraries. Sequencing libraries

were generated using a TruSeq® DNA PCR-Free Sample Preparation Kit (Illumina, USA) following the instructions of the manufacturer. The library quality was assessed on the Qubit@ 2.0 Fluorometer (Thermo Scientific, USA) and Agilent Bioanalyzer 2100 system (Agilent, USA). The library was sequenced on an Illumina NovaSeq platform. Paired-end reads (250 bp) were merged using FLASH (V1.2.7, http://ccb.jhu.edu/software/FLASH/) (Magoc and Salzberg, 2011). Quality filtering on the raw tags was performed according to the QIIME (V1.9.1, http://qiime.org/scripts/split_libraries_fastq.html) quality controlled process (Bokulich et al., 2013).

The tags were compared with the reference database (Silva database, release 111-2012_07, https://www.arbsilva.de/) using UCHIME algorithm (UCHIME Algorithm, http://www.drive5.com/usearch/manual/uchime_algo.html) (Edgar et al., 2011) to detect chimera sequences, and then the chimera sequences were removed (Haas et al., 2011). Sequence analyses were performed by Uparse software (Uparse v7.0.1001, http://drive5.com/uparse/) (Edgar, 2013). Sequences with ≥97% similarity were assigned to the same OTUs. The representative sequence for each OTU was screened for further annotation. For each representative sequence, the Silva Database (release 111-2012_07, http://www.arb-silva.de/) (Quast et al., 2013) was used based on Mothur algorithm to annotate taxonomic information

RESULTS

Isolation, Genome and Phylogeny of a Cultured *Lentisphaerae* Representative From the Deep-Sea Cold Seep

In our previous work, we successfully isolated a novel *Bacteroidetes* species through a polysaccharide degradation-driven strategy from the deep-sea cold seep (Zheng et al., 2021a). Beyond our expectation, we found there was a small amount of *Lentisphaerae* bacteria within the enrichment based on the OTUs analysis. Given that members of *Lentisphaerae* are typical difficult-to-culture microbes (Choi et al., 2015), we spent much effort for a couple of rounds of purification and 16S rRNA sequencing confirmation and eventually obtained the pure culture of a *Lentisphaerae* bacterium (strain zth2) (**Figure 1A**). Under the TEM observation, strain zth2 possessed an irregular coccoid cell (~400–500 nm in size, no flagellum) with the extracellular slime layer (**Figure 1B**), which was very similar to the morphologies of other *Lentisphaerae* members reported previously (Zoetendal et al., 2003; Cho et al., 2004).

To gain more insights into strain zth2, the whole genome was sequenced and analyzed. The genome size of strain zth2 is 3,198,720 bp with a DNA G+C content of 43.77% and it is complete (**Supplementary Figure S1A** and **Supplementary Table 3**). Annotation of the genome of strain zth2 revealed 2,683 predicted genes that included 66 RNA genes (6 rRNA genes, 52 tRNA genes and 8 ncRNAs). The genome contains 146 CAZymes that may be related to its capability of polysaccharides degradation (**Supplementary Figure S1B**). The genome relatedness values were calculated by the average nucleotide identity (ANI), *in silico* DNA–DNA similarity (*is*DDH) and the tetranucleotide signatures (Tetra), against two available genomes of type strains of *Lentisphaerae* bacteria: *V. vadensis* ATCC BAA-548^T (Zoetendal et al., 2003) and *L. araneosa* HTCC2155^T (Cho et al., 2004) (**Supplementary Table 3**). The average nucleotide identities (ANIb) of strain zth2 with BAA-548^T and HTCC2155^T were 65.32 and 65.45%, respectively. The average nucleotide identities (ANIm) of strain zth2 with BAA-548^T and HTCC2155^T were 89.31 and 83.99%, respectively. The tetra values of strain zth2 with BAA-548^T and HTCC2155^T were 0.69176 and 0.48857, respectively. Based on digital DNA–DNA hybridization employing the Genome-to-Genome Distance Calculator GGDC, the *in silico* DDH estimates for strain zth2 with BAA-548^T and HTCC2155^T were 26.1 and 25.5%, respectively. These results together demonstrated the genome of strain zth2 to be clearly below established 'cut-off' values (ANIb: 95%, ANIm: 95%, AAI: 95%, *is*DDH: 70%, Tetra: 0.99) (Goris et al., 2007; Meier-Kolthoff et al., 2013) for defining bacterial species (**Supplementary Table 3**), suggesting it represents a novel taxon of *Lentisphaerae*.

To clarify the taxonomic status of strain zth2, we further performed the phylogenetic analysis with 16S rRNA genes of some cultured and uncultured representatives of PVC superphylum. The maximum likelihood tree of 16S rRNA placed strain zth2 as a distinct cluster separating from other three identified families, namely, *Victivallaceae* (from order *Victivallales*), *Lentisphaeraceae* (from order *Lentisphaerales*) and *Oligosphaeraceae* (from order *Oligosphaerales*) (**Figure 1C**). Consistently, a genome-based tree (**Supplementary Figure S2**) further confirmed the position of strain zth2, located between the branches of families of *Victivallaceae* and *Lentisphaeraceae*. Moreover, based on the 16S rRNA gene sequence of strain zth2, a sequence similarity calculation using the NCBI server indicated that the closest relatives of strain zth2 were *V. vadensis* ATCC BAA-548^T (88.77%, family *Victivallaceae*), *L. araneosa* HTCC2155^T (86.09%, *Lentisphaeraceae*), *L. marina* IMCC11369^T (85.73%, *Lentisphaeraceae*), *L. profundi* SAORIC-696^T (85.72%, *Lentisphaeraceae*), and *O. ethanolica* 8KG-4^T (83.87%, *Oligosphaeraceae*). Recently, the proposed median and minimum sequence identity values of 16S rRNA sequence for a new family have been revealed as 92.25 and 87.65% (Yarza et al., 2014), respectively. Therefore, combining the results of 16s rRNA phylogenetic tree, a genome-based tree and ANI analysis, we propose that strain zth2 is classified as the type strain of a novel family. Given its isolated site, we proposed the name *Candidatus* Coldseepensis marina gen. nov., sp. nov. for strain zth2. In addition, we also proposed the associated genus and family as *Candidatus* Coldseepensis gen. nov. and *Candidatus* Anaerobicaceae fam. nov., respectively.

Ultrathin-Section Electron Microscopic Observation of Cell Division and the Special Protrusions of Strain zth2

As previously reported, members of the PVC superphylum have very complex and specific cytoarchitectural features (Rivas-Marin and Devos, 2018). Ultrathin TEM sections showed that strain zth2 possessed distinctive membrane and compartmentalization

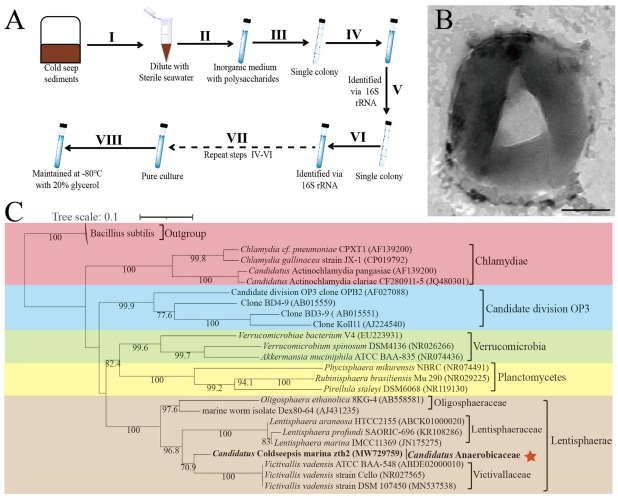

FIGURE 1 | Isolation, morphology and phylogeny of *Candidatus* Coldseepensis marina zth2. **(A)** Diagram of enrichment and isolation of strain zth2 through a polysaccharide degradation-driven strategy. **(B)** Observation of the cell morphology of strain zth2 through the transmission electron microscopy. Bar is 250 nm. **(C)** Maximum likelihood 16S rRNA phylogenetic tree showed the positions of the phylum *Lentisphaerae* (including strain zth2 and other cultured type strains) together with other members within the PVC superphylum. The numbers on the node indicate statistical support for bootstrap values, respectively. The position of *Candidatus* Coldseepensis marina zth2 and its attributive family *Candidatus* Anaerobicaceae is indicated with red star. Some *Bacillus* members were used as outgroup. The accession number of each 16S rRNA is shown in the parentheses after corresponding strain name. Scale bar, 0.1 substitutions per nucleotide position.

systems (**Figures 2A, B**). In particular, its outer membrane possessed a lot of twists and turns (**Figure 2A**), which effectively increased the surface area of the cell membrane. Notably, strain zth2 divided by budding (**Figure 2A**) but not the usual binary fission manner that adopted by most bacteria. In the division process, daughter cells always originated from one site of the mother cell (**Figure 2A**, panel I), and then the bud became bigger and bigger along with the cellular content distributing into the daughter cell (**Figure 2A**, panels II to VI). Once the content and size of daughter cell were equal to those of mother cell, the daughter cell would separate from the mother cell (**Figure 2A**, panels VII to VIII), and a cell division cycle was finished.

Another dramatic feature of strain zth2 was that there were several narrow protrusions around the cells (**Figure 2B**, panels I–IV, the red arrow points). These protruded 80–114 nm from the cell and were 40–80 nm in diameter measured at the base of the structure preserved slender shape. They seemed to be coincided with the definition of prosthecae as cellular appendages or extensions of the cell containing cytoplasm (Staley, 1968).

Strain zth2 Possesses a Prominent Capability to Degrade and Utilize Different Polysaccharides

Based on our enrichment and isolation strategy of strain zth2 (**Figure 1A**), this strain was proposed to possess a prominent capability of degrading polysaccharides. To test the potential polysaccharide substrate spectra of strain zth2, we checked the growth status of strain zth2 in the medium supplemented with different kinds of polysaccharides at a final concentration of 1 g/L. The results showed the supplementation of porphyra polysaccharide (PP), carrageenan and ulvan could only modestly promote the growth of strain zth2 (**Figure 3A**). In contrast, the supplement of starch or laminarin could significantly facilitate the growth of strain zth2, resulting in an almost 4-fold increased growth compared to the control group (**Figure 3A**).

To further validate the mechanism of polysaccharides degradation mediated by strain zth2, we performed transcriptomic analysis of strain zth2 grown in the medium supplemented with starch or laminarin. Indeed, the expression of many genes encoding glycan degradation was evidently upregulated when 1 g/L of starch was added in the medium. These included genes encoding amylase, glycosyl hydrolases (GH families 3, 9, 18, and 32), glycosyl transferases (GT1, GT2, and GT41), and glucanases (**Figure 3B**). Meanwhile, many proteins associated with ATP production (namely, ATP corrinoid adenosyltransferase, NAD/NADPH binding domain proteins, electron transfer flavoprotein, etc.) were also significantly upregulated in the presence of starch (**Figure 3C**), which might contribute to the growth promotion of strain zth2. Out of our expectation, the supplementation of starch could also dramatically upregulate the expression of many proteins responsible for phosphorus and iron metabolisms (**Figure 3D**). These included phosphoadenosine phosphosulfate reductase, PhoU, Fe–S binding protein and so on. Similarly, the supplement of 1 g/L of laminarin in the medium also markedly upregulated the expression of proteins responsible for glycan degradation (**Figure 3E**), ATP production (**Figure 3F**) and phosphorus and iron metabolisms (**Figure 3G**). Significantly, GH9 family proteins were annotated as laminarinase in CAZy database, which may play the key role in the degradation of laminaria.

Utilization of Polysaccharide, Phosphate and Iron by Strain zth2 is Correlative and Mutually Promoted

Based on the above transcriptomic results of polysaccharide utilization, we speculate that the utilization of polysaccharide could promote phosphorus and iron metabolisms (**Figure 3D**). Therefore, we next sought to explore the effects of the supplementation of phosphorus and iron on the growth of strain zth2. First, we analyzed the growth status of strain zth2 in a basic medium supplemented with Na_3PO_4 (2.6 mM), or $FeSO_4$ (0.03 g/L), or both $FeSO_4$ (0.03 g/L) and $Ca_3(PO_4)_2$ (1 g/L), or both $FeSO_4$ (0.03 g/L) and Na_3PO_4 (2.6 mM). The growth curves showed that strain zth2 could only grow to an OD_{600} value about 0.06 in the basic medium amended with $FeSO_4$ after two weeks incubation (**Figure 4A**). In contrast, in the presence of $FeSO_4$, the growth of strain zth2 could be significantly promoted to OD_{600} values about 0.20 and 0.68 (about 11-fold increase) when insoluble $Ca_3(PO_4)_2$ or soluble Na_3PO_4 was added into the basic medium (**Figure 4A**). These results indicated the soluble phosphate was necessary for the growth of strain zth2 and this bacterium could transform insoluble

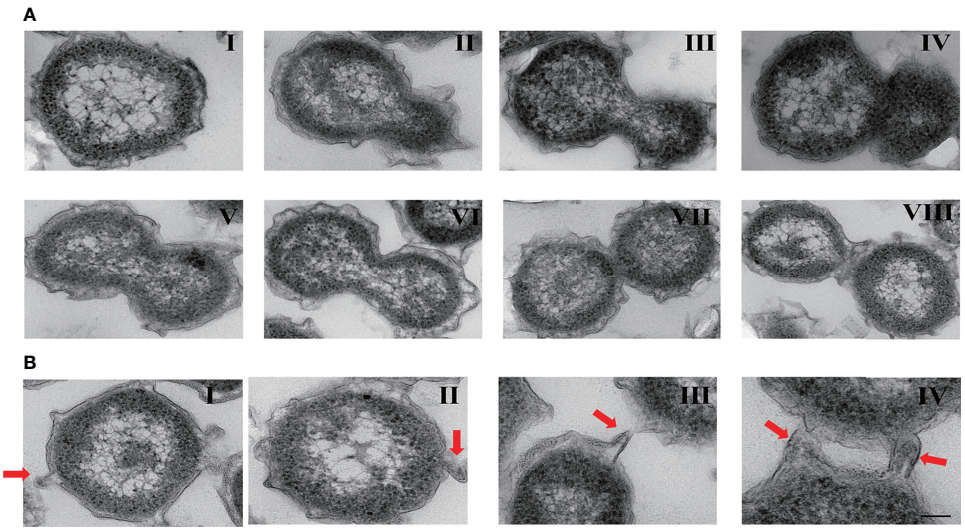

FIGURE 2 | Ultrathin-section electron microscopic observation of cell biological characteristics of strain zth2. **(A)** Ultrathin TEM sections showing the process of polar budding division (panels I–VIII) conducted by strain zth2. **(B)** Ultrathin TEM sections showing the narrow protrusions around the cell (panels I–IV, the red arrow indicates).

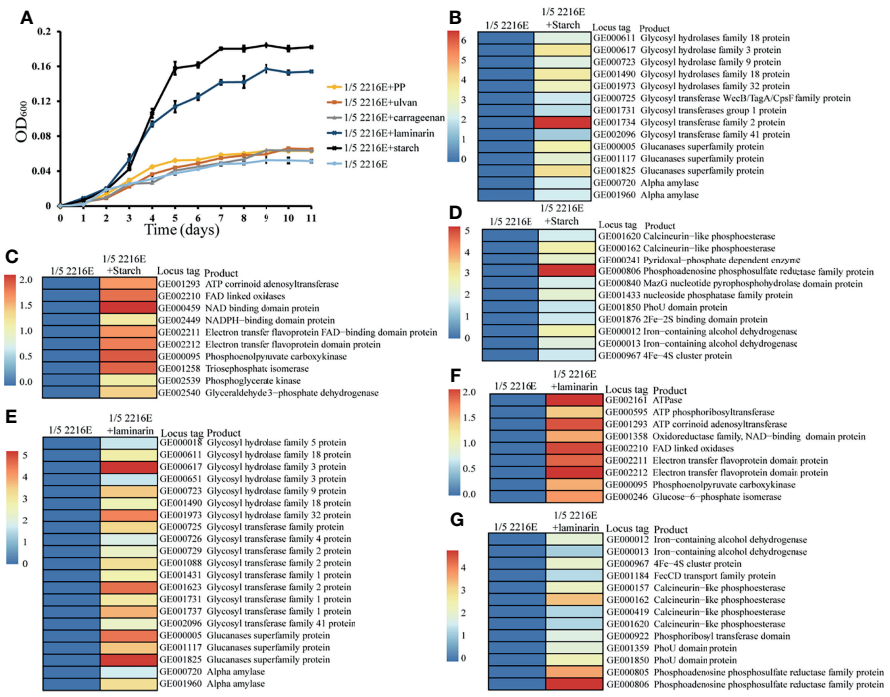

FIGURE 3 | Strain zth2 could effectively degrade and utilize starch and laminarin for growth. **(A)** Growth assays of strain zth2 in the 1/5 2216E medium supplemented either without or with 1 g/L of laminarin, starch, PP (porphyra polysaccharide), carrageenan, and ulvan, respectively. **(B–D)** Transcriptomics based heat map showing all upregulated genes encoding proteins associated with polysaccharide degradation **(B)**, energy generation **(C)**, phosphorus and iron metabolisms **(D)** supplemented with 1 g/L of starch. **(E–G)** Transcriptomics based heat map showing all upregulated genes encoding proteins associated with polysaccharide degradation **(E)**, energy generation **(F)**, phosphorus and iron metabolisms **(G)** supplemented with of 1 g/L of laminarin.

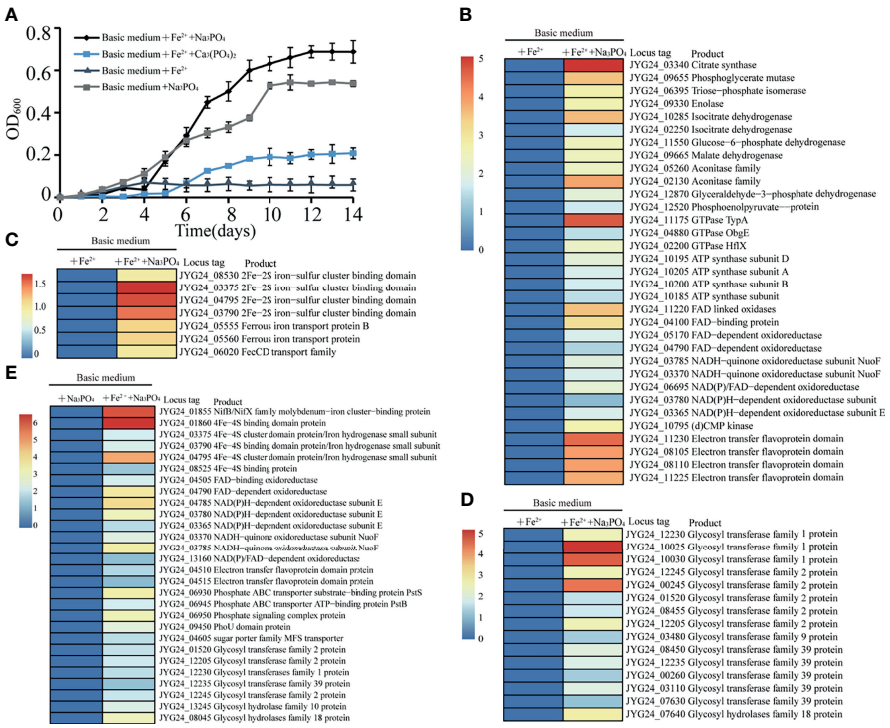

FIGURE 4 | Strain zth2 could effectively utilize phosphate and iron for growth. **(A)** Growth assays of strain zth2 in basic medium supplemented with $FeSO_4$ (0.03 g/L), or Na_3PO_4 (2.6 mM), or both $FeSO_4$ (0.03 g/L) and $Ca_3(PO_4)_2$ (1 g/L), or both $FeSO_4$ (0.03 g/L) and Na_3PO_4 (2.6 mM). **(B, C, D)** Transcriptomics based heat map showing all upregulated genes encoding proteins associated with energy generation **(B)**, iron metabolism **(C)**, polysaccharide degradation **(D)** when compared the growth of strain zth2 in basic medium added both $FeSO_4$ (0.03 g/L) and Na_3PO_4 (2.6 mM) with that in basic medium added only $FeSO_4$ (0.03 g/L). **(E)** Transcriptomics based heat map showing all upregulated genes encoding proteins associated with iron metabolism, energy generation, phosphorus metabolism and polysaccharide degradation when compared the growth of strain zth2 in basic medium added both $FeSO_4$ (0.03 g/L) and Na_3PO_4 (2.6 mM) with that in basic medium added only Na_3PO_4 (2.6 mM).

$Ca_3(PO_4)_2$ to soluble phosphate for utilization to some extent. On the other hand, in the presence of Na_3PO_4, the absence of $FeSO_4$ in the medium could decrease about a quarter of the growth rate (from OD_{600} value 0.68 to 0.53) (**Figure 4A**), suggesting that iron is also a key factor for the growth of strain zth2.

We next analyzed the effects of Na_3PO_4 or $FeSO_4$ on the growth of strain zth2 through a transcriptomic approach. The results showed that, compared to the medium only amended with $FeSO_4$, the supplement of both Na_3PO_4 and $FeSO_4$ could upregulate the expression of proteins responsible for energy production, such as citrate synthase, malate dehydrogenase, GTPase, ATP synthase, FAD/NADH dependent enzymes and electron transfer flavoprotein (**Figure 4B**). This result was well consistent with the growth cure shown in **Figure 4A**. Strikingly, many proteins associated with iron metabolisms (**Figure 4C**) and polysaccharide degradation (**Figure 4D**) were also evidently upregulated when Na_3PO_4 was supplemented in the medium beside $FeSO_4$, suggesting the presence of soluble phosphate could facilitate iron metabolisms and polysaccharide degradation. On the other hand, the absence of $FeSO_4$ in the medium indeed weakened the metabolisms of phosphorus, iron, and polysaccharide and the eventual energy generation even though Na_3PO_4 was present in the medium (**Figure 4E**). This result is a good explanation that the absence of $FeSO_4$ in the medium could decrease a half of growth rate as shown in **Figure 4A**. In the combined growth assay and transcriptomics results, we conclude that the utilization of polysaccharide, phosphate, and iron by strain zth2 is correlative and mutually promoted, and these three nutrient sources are essential factors supporting the best growth of strain zth2.

Strain zth2 Evidently Increases the Environmental Microbial Diversity

Given its prominent capability of polysaccharide degradation and acquiring phosphorus and iron, we next sought to ask whether strain zth2 could provide extra nutrient to other bacteria and thereby promote microbial diversity as shown in the previous report of the ecological function of *Bacteroides* (Zheng et al., 2021a). We therefore mimicked the natural ecological environment for bacterial growth and survival in the laboratory (**Figure 5A**). Correspondingly, four anaerobic dialysis bags (namely, SW, SWL, SWP, and SWLP) were respectively incubated in different anaerobic bottles filled with filtered but non-sterilized sea water using medium speed double circle qualitative filter paper for one month (**Figure 5A**). After 30-day incubation, the cells growing in the non-sterilized sea water were collected and used for OTUs analysis to determine the

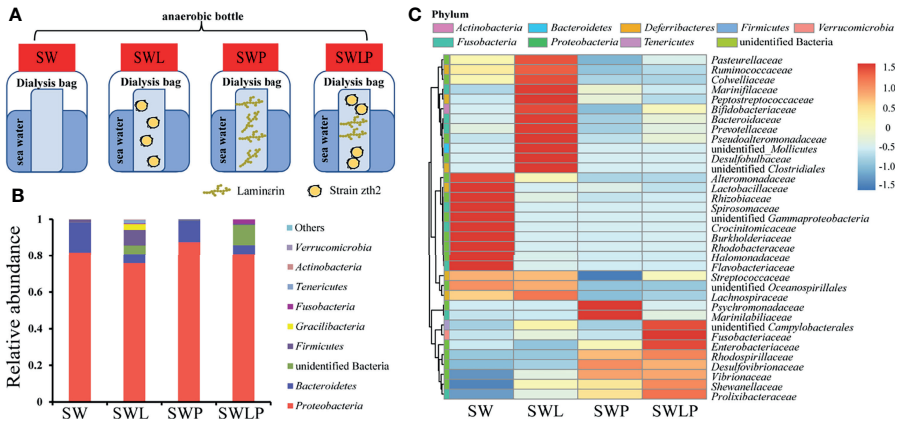

FIGURE 5 | Strain zth2 evidently increases marine microbial diversity in a system that mimics natural environment. **(A)** Diagrammatic scheme of the experimental design for analyzing the ecological role of strain zth2 in a system that mimics natural environment. Briefly, four anaerobic dialysis bags (containing sterile sea water, named SW; sterile sea water supplemented with strain zth2 cells, named SWL; sterile sea water supplemented with 1 g/L of laminarin, named SWP; sterile sea water supplemented with both strain zth2 cells and 1 g/L of laminarin, named SWLP) were respectively incubated in different anaerobic bottles filled with filtered but non-sterilized sea water. **(B, C)** The relative abundances of operational taxonomic units (OTUs) representing different bacteria in the sea water are shown at the phylum **(B)** and family **(C)** levels.

variety and abundance of bacteria in each sample. The OTUs analysis results revealed that the bacterial diversity of samples SW and SWP was very low: at the phylum level, only 3–4 phyla including *Proteobacteria*, *Bacteroides* and *Firmicutes* (or *Gracilibacteria*) were identified in the sea water (**Figure 5B**). In contrast, the bacterial diversity of samples SWL and SWPL was significantly increased (**Figure 5B**). Especially, the bacterial variety was increased to 8–9 phyla in sample SWL, and many bacteria belonging to unidentified bacteria and different known phyla (namely, *Tenericutes*, *Fusobacteria*, *Actinobacteria*, and *Verrucomicrobia*) were enriched, indicating that strain zth2 is indeed able to increase the environmental bacteria diversity. Similarly, at the family level, the abundance and variety of novel members belonging to other phyla rather than *Proteobacteria* were obviously enhanced in both SWL and SWLP samples, further confirming the proposal that strain zth2 contributes to the increase and maintainance of microbial diversity regardless of the presence of polysaccharide.

In the combined data on the utilization of polysaccharide, phosphate and iron, and also the contribution to the microbial diversity conducted by strain zth2, we proposed a model representing the central metabolism and ecological function of strain zth2 (**Figure 6**). In this model, different polysaccharides were degraded and then transported into the cells by special transporters; then the oligosaccharide could be further transformed into glucose (or other simple sugar) and enters into the Embden–Meyerhof–Parnas (EMP) glycolysis pathway, which thereby joining to the tricarboxylic acid cycle (TCA pathway) and producing energy; the degradation products can also promote the growth of other microorganisms; on the other hand, different kinds of phosphate could be effectively obtained and utilized as a nutrient source for phosphorus cycling and ATP production; meanwhile, iron could be acquired and transported into the cells to activate essential iron-associated enzymes (e.g., Fe–Fe hydrogenase and Fe–S protein) for various metabolic pathways and thereby generating energy. As mentioned above, the utilization of polysaccharide, phosphate, and iron by strain zth2 is correlative and jointly contributes to carbon, phosphorus, and iron metabolisms and cycling, which thereby supports bacterial growth and promotes the environmental microbial diversity.

Description of *Candidatus* Anaerobicaceae fam.nov.

Candidatus Anaerobicaceae (An.ae'ro.bica.ce.ae. N.L. fem. adj. *Candidatus* Coldseepensis type genus of the family; suff. -aceae, ending to denote a family; N.L. fem. pl. adj. *Candidatus* Anaerobicaceae the family of the genus *Candidatus* Coldseepensis.) The type genus is *Candidatus* Coldseepensis.

Description of *Candidatus* Coldseepensis gen.nov.

For the genus name *Candidatus* Coldseepensis, cold.seep'ensis. N.L. fem. n. Given its isolated site, we proposed this name. The type and only species of the genus is *Candidatus* Coldseepensis marina.

Description of *Candidatus* Coldseepensis Marina sp. nov.

Candidatus Coldseepensis marina (ma.ri'na. L. fem. adj. marina of the sea, marine). Cells are coccoid, ~400–700 nm in size, and have no flagellum; strictly anaerobic; the temperature range for growth is 28–37°C with an optimum at 28°C (**Supplementary Figure S3A**); growing at pH values of 6.0–8.0 (optimum, pH 7.0) (**Supplementary Figure S3B**); growth occurs at NaCl concentrations between 2.0 and 4.0% with an optimum growth

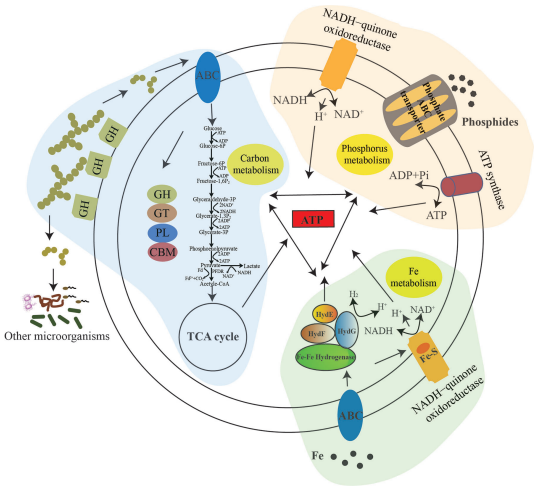

FIGURE 6 | A proposed model showing the utilization of polysaccharide, phosphate and iron for energy production and growth of strain zth2, and also its contribution to the promotion of microbial diversity. In this model, three different pathways for ATP generation are shown: tricarboxylic acid cycle (TCA pathway) driven by the polysaccharides degradation and the Embden–Meyerhof–Parnas (EMP) glycolysis pathway; utilization of phosphate as a nutrient source for phosphorus cycling and ATP production; acquisition of iron to activate essential iron-associated enzymes (e.g., Fe–Fe hydrogenase and Fe–S protein) for various metabolic pathways and thereby generating energy. Meanwhile, the cycling of carbon, phosphorus and iron is activated to facilitate the central metabolism of strain zth2. Obviously, the utilization of polysaccharide, phosphate and iron by strain zth2 is correlative and jointly contributes to promote bacterial growth and environmental microbial diversity.

at 3% NaCl (**Supplementary Figure S3C**); growth is stimulated by using glucose, maltose, fructose, sucrose, mannose, starch, cellulose, laminarin, dextrin, lactose, galactose, xylose, mannitol or sorbitol as a sole carbon source (**Supplementary Table 4**). The type strain, zth2^{T}, was isolated from the sediment of deep-sea cold seep, P.R. China.

DISCUSSION

Microbial communities in marine sediments are known to play a key role in global elemental and nutrient cycling (Zhang et al., 2020; Baker et al., 2021). However, the vast majority of microbes present in sediments have not been successfully cultured in a laboratory setting (Baker et al., 2021). In fact, the large proportion of uncultured strains is estimated to account for more than 75% of sediment genera (Lloyd et al., 2018), impacting that our understanding of marine sediment microbiology is limited. However, a detailed comparison of the metabolic potential of uncultured strains suggests that these new microbes are capable of directing previously undescribed fundamental pathways in elemental and nutrient cycling (Baker et al., 2021; Zheng et al., 2021a; Zheng et al., 2021b). Given the important role that uncultured communities play in the oceans, there is an urgent need to better resolve the diversity and ecological roles of these uncultured taxa (Baker et al., 2021). It is accepted that members belonging to the phylum *Lentisphaerae* are typically difficult to obtain in pure culture in the laboratory condition (Choi et al., 2015). In the present study, we developed an innovative approach by using a polysaccharide degradation-directed approach to enrich and purify *Lentisphaerae* bacteria (**Figure 1A**). With this, the first representative (*Candidatus* Coldseepensis marina zth2) belonging to a novel family (*Candidatus* Anaerobicaceae) was cultured in laboratory from a deep-sea cold seep sedimentary sample (**Figure 1C**). Actually, we also obtained a novel species belonging to *Bacteroidetes* phylum through the same enrichment method from deep-sea cold seep sediments, and the prominent polysaccharide degradation capability of this *Bacteroidetes* strain was verified (Zheng et al., 2021a). Therefore, it will be a promising approach to isolate more uncultured microbes from deep-sea samples that enriched in an inorganic medium supplemented with different polysaccharides given that polysaccharides are deemed to be ubiquitously distributed in deep-sea sediments (Gao et al., 2017).

The phylum *Lentisphaerae* is one of the members of PVC superphylum. With the superphylum status now amply accepted, it is clear that PVC bacteria are fascinating new model organisms for bacterial and evolutionary cell biology (Rivas-Marin and Devos, 2018). For example, they have features that separate them from other bacteria, such as extensive bacterial endomembrane systems and atypical modes of cell division (Rivas-Marin et al., 2016). Consistently, strain zth2 divided by budding (**Figure 2A**) but not the usual binary fission manner that is adopted by most bacteria. Actually, budding is also employed by some species of *Planctomycetes* phylum (another important PVC member) (Wiegand et al., 2018; Wiegand et al., 2020). To our knowledge, this is the first report that *Lentisphaerae* bacterium performs budding fission, suggesting the budding division might be an alternative manner adopted by many PVC bacteria besides binary fission. However, the universal bacterial cell division protein FtsZ was found to exist in strain zth2, indicating that strain zth2 might conduct a different budding division pathway compared to *Planctomycetes* bacteria which lack FtsZ-like proteins (Wiegand et al., 2020). Another distinct cell biological trait of strain zth2 is that there were several narrow protrusions around the cells like appendages or prosthecae as previously reported (Butler et al., 2002). This similar structure has been found in some members of *Planctomycetes* and *Verrucomicrobia*. Butler et al. found strain ATCC 35122 belonging to membership of the *Planctomycetales* possessed a unique feature seen in both negatively stained cells and in thin-sectioned cells that was described as the occurrence of 'hump' protrusions (Butler et al., 2002). Kulichevskaya et al. reported the presence of crateriform pits and numerous fibrillar appendages on the cell surface and an unusual spur-like projection on one pole of the cell by phase-contrast micrographs of strain MPL7 belonging to the *Planctomycetales* (Kulichevskaya et al., 2007). Also, Dobro et al. observed novel extracellular appendages along the prosthecae on the cell surface of *Prosthecobacter debontii* belonging to *Verrucomicrobia* through using electron cryotomography (ECT) (Dobro et al., 2017). However, the specific function of this prosthecae structure is not clear. Notably,

Wagner et al. showed that prosthecae, cylindrical extensions of the *Caulobacter crescentus* cell envelope, could take up and hydrolyze organic phosphate molecules (Wagner et al., 2006), which indicated that strain zth2 may be capable of phosphate uptake through the protrusions of its cells. Taken together, it will be interesting to understand its unusual cell division and disclose the detailed function of this narrow structure on the cell of strain zth2 in the future.

It is well accepted that nutrient and element cycling driven by microbes is essential for the whole deep-sea ecological system (Baker et al., 2021). Various polysaccharides (e.g., glycogen, starch, laminarin) are stored as energy reserve by animals, plants and microorganisms (van Vliet et al., 2019), and the degradation and utilization of algal polysaccharides greatly contribute to the deep-sea element and nutrient cycling (Zheng et al., 2021a). Through growth assays and transcriptomic analysis, we found that strain zth2 was able to efficiently utilize not only polysaccharides (**Figure 3**) but also phosphate and iron (**Figure 4**) for growth, indicating its potentials to drive diverse element and nutrient cycles. Phosphorus is an essential element to all life, being a structural and functional component of all organisms inhabiting across the ocean surface to the sediments (Paytan and McLaughlin, 2007). Previous studies indicated a coupling between iron cycling and phosphate cycling in suboxic environments (Paytan and McLaughlin, 2007). Indeed, in strain zth2, the utilization and metabolisms of phosphate and iron are correlative (**Figure 4**), moreover, this coupling process was also demonstrated to be closely associated with polysaccharides metabolism (**Figure 4**), highlighting contributions of strain zth2 to the cycling of nutrient, carbon, phosphorus, and iron (**Figures 3**, **4**, and **6**). With this, we speculate that the metabolisms of organic (like polysaccharide) and inorganic (e.g., phosphate, iron) substances are correlated and more complicated than our present cognitive.

Given that strain zth2 possesses versatile metabolic pathways and is a potential contributor to the nutrient and element cycling (**Figure 6**), it is not a surprise to observe that it significantly increased the microbial diversity in a simulative natural ecological system (**Figure 5**). Therefore, we propose that *Lentisphaerae* members might play underestimated roles toward the cycling of nutrient, carbon, phosphorus, iron, and other elements in the deep biosphere. In summary, this study extends our understanding of the cultivation and unique physiological characterizations and also ecological roles of *Lentisphaerae* bacteria.

DATA AVAILABILITY STATEMENT

The whole 16S rRNA sequence and complete genome sequence of strain zth2 have been respectively deposited in the GenBank database under accession numbers MW729759 and CP071032. The raw sequencing reads for transcriptomic analysis and OTUs analysis of microbial diversity have been respectively deposited to NCBI Short Read Archive under accession numbers PRJNA756144, PRJNA754499 and PRJNA756866 Strain zth2 has been preserved in the Third Institute of Oceanography, Ministry of Natural Resources, Xiamen, China (accession number: MCCC1K06937).

AUTHOR CONTRIBUTIONS

TZ and CS conceived and designed the study. TZ conducted most of the experiments. RZ helped to isolate and identify the *Lentisphaerae* strain, RL (Rui Liu) collected the samples from the deep-sea cold seep. RL (Ronggui Li) provided suggestions for the experiments design. TZ and CS lead the writing of the manuscript. All authors listed have made a substantial, direct, and intellectual contribution to the work and approved it for publication.

FUNDING

This work is funded by the Key Deployment Projects of Center of Ocean Mega-Science of the Chinese Academy of Sciences (Grant No. COMS2020Q04), China Ocean Mineral Resources R&D Association Grant (Grant No. DY135-B2-14), Shandong Provincial Natural Science Foundation (Grant No.ZR2021ZD28), Strategic Priority Research Program of the Chinese Academy of Sciences (Grant No. XDA22050301), Major Research Plan of the National Natural Science Foundation (Grant No. 92051107) and Taishan Young Scholar Program of Shandong Province (Grant No. tsqn20161051) for CS.

SUPPLEMENTARY MATERIAL

The Supplementary Material for this article can be found online at: https://www.frontiersin.org/articles/10.3389/fmars.2022.848136/full#supplementary-material

REFERENCES

Baker, B. J., Appler, K. E., and Gong, X. Z. (2021). New Microbial Biodiversity in Marine Sediments. *Annu. Rev. Mar Sci.* 13, 161–175. doi: 10.1146/annurev-marine-032020-014552

Bokulich, N. A., Subramanian, S., Faith, J. J., Gevers, D., Gordon, J. I., Knight, R., et al. (2013). Quality-Filtering Vastly Improves Diversity Estimates From Illumina Amplicon Sequencing. *Nat. Methods* 10, 57–59. doi: 10.1038/NMETH.2276

Buchan, A., LeCleir, G. R., Gulvik, C. A., and Gonzalez, J. M. (2014). Master Recyclers: Features and Functions of Bacteria Associated With Phytoplankton Blooms. *Nat. Rev. Microbiol.* 12, 686–698. doi: 10.1038/nrmicro3326

Butler, M. K., Wang, J., Webb, R. I., and Fuerst, J. A. (2002). Molecular and Ultrastructural Confirmation of Classification of ATCC 35122 as a Strain of *Pirellula Staleyi*. *Int. J. Syst. Evol. Microbiol.* 52, 1663–1667. doi: 10.1099/ijs.0.02167-0

Cao, L., Lian, C., Zhang, X., Zhang, H., Wang, H., Zhou, L., et al. (2021). *In Situ* Detection of the Fine Scale Heterogeneity of Active Cold Seep Environment of

the Formosa Ridge, the South China Sea. *J. Mar. Syst.* 218, 611–21. doi: 10.1016/j.jmarsys.2021.103530

Choi, A., Song, J., Joung, Y., Kogure, K., and Cho, J. C. (2015). *Lentisphaera Profundi* Sp Nov., Isolated From Deep-Sea Water. *Int. J. Syst. Evol. Microbiol.* 65, 4186–4190. doi: 10.1099/ijsem.0.000556

Choi, A., Yang, S. J., Rhee, K. H., and Cho, J. C. (2013). *Lentisphaera Marina* Sp Nov., and Emended Description of the Genus *Lentisphaera*. *Int. J. Syst. Evol. Microbiol.* 63, 1540–1544. doi: 10.1099/ijs.0.046433-0

Cho, J. C., Vergin, K. L., Morris, R. M., and Giovannoni, S. J. (2004). *Lentisphaera Araneosa* Gen. Nov., Sp Nov, a Transparent Exopolymer Producing Marine Bacterium, and the Description of a Novel Bacterial Phylum, *Lentisphaerae*. *Environ. Microbiol.* 6, 611–621. doi: 10.1111/j.1462-2920.2004.00614.x

Corsarol, D., and Greub, G. (2006). Pathogenic Potential of Novel *Chlamydiae* and Diagnostic Approaches to Infections Due to These Obligate Intracellular Bacteria. *Clin. Microbiol. Rev.* 19, 283–297. doi: 10.1128/CMR.19.2.283-297.2006

Darling, A. E., Jospin, G., Lowe, E., Matsen, F. I. V., Bik, H. M., and Eisen, J. A. (2014). PhyloSift: Phylogenetic Analysis of Genomes and Metagenomes. *Peerj* 2, e243. doi: 10.7717/peerj.243

Das, R., and Kazy, S. K. (2014). Microbial Diversity, Community Composition and Metabolic Potential in Hydrocarbon Contaminated Oily Sludge: Prospects for *in Situ* Bioremediation. *Environ. Sci. Pollut. R.* 21, 7369–7389. doi: 10.1007/s11356-014-2640-2

Devos, D. P., and Ward, N. L. (2014). Mind the PVCs. *Environ. Microbiol.* 16, 1217–1221. doi: 10.1111/1462-2920.12349

Dobro, M. J., Oikonomou, C. M., Piper, A., Cohen, J., Guo, K., Jensen, T., et al. (2017). Uncharacterized Bacterial Structures Revealed by Electron Cryotomography. *J. Bacteriol.* 199, e00100–e00117. doi: 10.1128/JB.00100-17

Edgar, R. C. (2013). UPARSE: Highly Accurate OTU Sequences From Microbial Amplicon Reads. *Nat. Methods* 10, 996–998. doi: 10.1038/NMETH.2604

Edgar, R. C., Haas, B. J., Clemente, J. C., Quince, C., and Knight, R. (2011). UCHIME Improves Sensitivity and Speed of Chimera Detection. *Bioinformatics* 27, 2194–2200. doi: 10.1093/bioinformatics/btr381

Fan, H. N., Zhu, P., Lu, Y. M., Guo, J. H., Zhang, J., Qu, G. Q., et al. (2020). Mild Changes in the Mucosal Microbiome During Terminal Ileum Inflammation. *Microb. Pathog.* 142, 104104. doi: 10.1016/j.micpath.2020.104104

Fardeau, M. L., Ollivier, B., Patel, B. K., Magot, M., Thomas, P., Rimbault, A., et al. (1997). *Thermotoga Hypogea* Sp. Nov., a Xylanolytic, Thermophilic Bacterium From an Oil-Producing Well. *Int. J. Syst. Bacteriol.* 47, 1013–1019. doi: 10.1099/00207713-47-4-1013

Gao, B. L., Jin, M., Li, L., Qu, W., and Zeng, R. Y. (2017). Genome Sequencing Reveals the Complex Polysaccharide-Degarding Ability of Novel Deep-Sea Bacterium *Flammeovirga Pacifica* WPAGA1. *Front. Microbiol.* 8. doi: 10.3389/fmicb.2017.00600

Goris, J., Konstantinidis, K. T., Klappenbach, J. A., Coenye, T., Vandamme, P., and Tiedje, J. M. (2007). DNA-DNA Hybridization Values and Their Relationship to Whole-Genome Sequence Similarities. *Int. J. Syst Evol Microbiol.* 57, 81–91. doi: 10.1099/ijs.0.64483-0

Graham, L., and Orenstein, J. M. (2007). Processing Tissue and Cells for Transmission Electron Microscopy in Diagnostic Pathology and Research. *Nat. Protoc.* 2, 2439–2450. doi: 10.1038/nprot.2007.304

Haas, B. J., Gevers, D., Earl, A. M., Feldgarden, M., Ward, D. V., Giannoukos, G., et al. (2011). Chimeric 16s rRNA Sequence Formation and Detection in Sanger and 454-Pyrosequenced PCR Amplicons. *Genome Res.* 21, 494–504. doi: 10.1101/gr.112730.110

Horn, M. (2008). *Chlamydiae* as Symbionts in Eukaryotes. *Annu. Rev. Microbiol.* 62, 113–131. doi: 10.1146/annurev.micro.62.081307.162818

Jiang, X. X., Dang, H. Y., and Jiao, N. Z. (2015). Ubiquity and Diversity of Heterotrophic Bacterial *nasA* Genes in Diverse Marine Environments. *PloS One* 10, e0117473. doi: 10.1371/journal.pone.0137817

Koren, S., Walenz, B. P., Berlin, K., Miller, J. R., Bergman, N. H., and Phillippy, A. M. (2017). Canu: Scalable and Accurate Long-Read Assembly *via* Adaptive *K*-Mer Weighting and Repeat Separation. *Genome Res.* 27, 722–736. doi: 10.1101/gr.215087.116

Kulichevskaya, I. S., Ivanova, A. O., Belova, S. E., Baulina, O. I., Bodelier, P. L. E., Rijpstra, W. I. C., et al. (2007). *Schlesneria Paludicola* Gen. Nov., Sp. Nov., the First Acidophilic Member of the Order *Planctomycetales*, From *Sphagnum*-Dominated Boreal Wetlands. *Int. J. Syst. Evol. Microbiol.* 57, 2680–2687. doi: 10.1099/ijs.0.65157-0

Letunic, I., and Bork, P. (2019). Interactive Tree Of Life (iTOL) V4: Recent Updates and New Developments. *Nucleic Acids Res.* 47, 256–259. doi: 10.1093/nar/gkz239

Limam, R. D., Bouchez, T., Chouari, R., Li, T. L., Barkallah, I., Landoulsi, A., et al. (2010). Detection of WWE2-Related *Lentisphaerae* by 16S rRNA Gene Sequencing and Fluorescence *in Situ* Hybridization in Landfill Leachate. *Can. J. Microbiol.* 56, 846–852. doi: 10.1139/W10-065

Liu, Y. H., Song, X. B., Zhou, H. M., Zhou, X., Xia, Y. L. , Dong, X., et al. (2018). Gut Microbiome Associates With Lipid-Lowering Effect of Rosuvastatin in *Vivo*. *Front. Microbiol.* 9, 0530. doi: 10.3389/fmicb.2018.00530

Lloyd, K. G., Steen, A. D., Ladau, J., Yin, J. Q., and Crosby, L. (2018). Phylogenetically Novel Uncultured Microbial Cells Dominate Earth Microbiomes. *mSystems* 3, e00055–e00018. doi: 10.1128/mSystems.00055-18

Lou, J., Jiang, Y., Rao, B., Li, A., Ding, S., Yan, H., et al. (2020). Fecal Microbiomes Distinguish Patients With Autoimmune Hepatitis From Healthy Individuals. *Front. Cell Infect. Microbiol.* 10. doi: 10.3389/fcimb.2020.00342

Magoc, T., and Salzberg, S. L. (2011). FLASH: Fast Length Adjustment of Short Reads to Improve Genome Assemblies. *Bioinform* 27, 2957–2963. doi: 10.1093/bioinformatics/btr507

Maskarinec, G., Raquinio, P., Kristal, B. S., Setiawan, V. W., Wilkens, L. R., Franke, A. A., et al. (2021). The Gut Microbiome and Type 2 Diabetes Status in the Multiethnic Cohort. *PloS One* 16, e0250855. doi: 10.1371/journal.pone.0250855

Meier-Kolthoff, J. P., Auch, A. F., Klenk, H. P., and Goker, M. (2013). Genome Sequence-Based Species Delimitation With Confidence Intervals and Improved Distance Functions. *BMC Bioinf.* 14, 60. doi: 10.1186/1471-2105-14-60

Murray, M. G., and Thompson, W. F. (1980). Rapid Isolation of High Molecular-Weight Plant DNA. *Nucleic Acids Res.* 8, 4321–4325. doi: 10.1093/nar/8.19.4321

Paytan, A., and McLaughlin, K. (2007). The Oceanic Phosphorus Cycle. *Chem. Rev.* 107, 563–576. doi: 10.1021/cr0503613

Pearson, A., Budin, M., and Brocks, J. J. (2003). Phylogenetic and Biochemical Evidence for Sterol Synthesis in the Bacterium *Gemmata Obsuriglobus*. *PNAS* 100, 15352–15357. doi: 10.1073/pnas.2536559100

Peng, S., Yin, J. G., Liu, X. L., Jia, B. Y., Chang, Z. G., Lu, H. J., et al. (2015). First Insights Into the Microbial Diversity in the Omasum and Reticulum of Bovine Using Illumina Sequencing. *J. Appl. Genet.* 56, 393–401. doi: 10.1007/s13353-014-0258-1

Pilhofer, M., Rappl, K., Eckl, C., Bauer, A. P., Ludwig, W., Schleifer, K. H., et al. (2008). Characterization and Evolution of Cell Division and Cell Wall Synthesis Genes in the Bacterial Phyla *Verrucomicrobia*, *Lentisphaerae*, *Chlamydiae*, and *Planctomycetes* and Phylogenetic Comparison With rRNA Genes. *J. Bacteriol.* 190, 3192–3202. doi: 10.1128/Jb.01797-07

Pinos, S., Pontarotti, P., Raoult, D., Baudoin, J. P., and Pagnier, I. (2016). Compartmentalization in PVC Super-Phylum: Evolution and Impact. *Biol. Direct* 11, 38. doi: 10.1186/s13062-016-0144-3

Polymenakou, P. N., Lampadariou, N., Mandalakis, M., and Tselepides, A. (2009). Phylogenetic Diversity of Sediment Bacteria From the Southern Cretan Margin, Eastern Mediterranean Sea. *Syst. Appl. Microbiol.* 32, 17–26. doi: 10.1016/j.syapm.2008.09.006

Qiu, Y. L., Muramatsu, M., Hanada, S., Kamagata, Y., Guo, R. B., and Sekiguchi, Y. (2013). *Oligosphaera Ethanolica* Gen. Nov., Sp Nov., an Anaerobic, Carbohydrate-Fermenting Bacterium Isolated From Methanogenic Sludge, and Description of *Oligosphaeria* Classis Nov in the Phylum *Lentisphaerae*. *Int. J. Syst. Evol. Microbiol.* 63, 533–539. doi: 10.1099/ijs.0.039545-0

Quast, C., Pruesse, E., Yilmaz, P., Gerken, J., Schweer, T., Yarza, P., et al. (2013). The SILVA Ribosomal RNA Gene Database Project: Improved Data Processing and Web-Based Tools. *Nucleic Acids Res.* 41, 590–596. doi: 10.1093/nar/gks1219

Rivas-Marin, E., Canosa, I., and Devos, D. P. (2016). Evolutionary Cell Biology of Division Mode in the Bacterial *Planctomycetes-Verrucomicrobia-Chlamydiae* Superphylum. *Front. Microbiol.* 7. doi: 10.3389/fmicb.2016.01964

Rivas-Marin, E., and Devos, D. P. (2018). The Paradigms They Are a-Changin': Past, Present and Future of PVC Bacteria Research. *Anton Leeuw Int. J. G* 111, 785–799. doi: 10.1007/s10482-017-0962-z

Sekiguchi, Y., Yamada, T., Hanada, S., Ohashi, A., Harada, H., and Kamagata, Y. (2003). *Anaerolinea Thermophila* Gen. Nov., Sp. Nov. And *Caldilinea Aerophila* Gen. Nov., Sp. Nov., Novel Filamentous Thermophiles That Represent a Previously Uncultured Lineage of the Domain *Bacteria* at the Subphylum Level. *Int. J. Syst. Evol. Microbiol.* 53, 1843–1851. doi: 10.1099/ijs.0.02699-0

Sichert, A., Corzett, C. H., Schechter, M. S., Unfried, F., Markert, S., Becher, D., et al. (2020). *Verrucomicrobia* Use Hundreds of Enzymes to Digest the Algal Polysaccharide Fucoidan. *Nat. Microbiol.* 5, 1026–1039. doi: 10.1038/s41564-020-0720-2

Staley, J. T. (1968). Prosthecomicrobium and Ancalomicrobium - New Prosthecate Freshwater Bacteria. *J. Bacteriol.* 95, 1921–1942. doi: 10.1128/Jb.95.5.1921-1942.1968

Strous, M., Pelletier, E., Mangenot, S., Rattei, T., Lehner, A., Taylor, M. W., et al. (2006). Deciphering the Evolution and Metabolism of an Anammox Bacterium From a Community Genome. *Nature* 440, 790–794. doi: 10.1038/nature04647

Trifinopoulos, J., Nguyen, L. T., von Haeseler, A., and Minh, B. Q. (2016). W-IQ-TREE: A Fast Online Phylogenetic Tool for Maximum Likelihood Analysis. *Nucleic Acids Res.* 44, 232–235. doi: 10.1093/nar/gkw256

van Vliet, D. M., Palakawong Na Ayudthaya, S., Diop, S., Villanueva, L., Stams, A. J. M., and Sanchez-Andrea, I. (2019). Anaerobic Degradation of Sulfated Polysaccharides by Two Novel *Kiritimatiellales* Strains Isolated From Black Sea Sediment. *Front. Microbiol.* 10. doi: 10.3389/fmicb.2019.00253

Wagner, J. K., Setayeshgar, S., Sharon, L. A., Reilly, J. P., and Brun, Y. V. (2006). A Nutrient Uptake Role for Bacterial Cell Envelope Extensions. *PNAS* 103, 11772–11777. doi: 10.1073/pnas.0602047103

Walker, B. J., Abeel, T., Shea, T., Priest, M., Abouelliel, A., Sakthikumar, S., et al. (2014). Pilon: An Integrated Tool for Comprehensive Microbial Variant Detection and Genome Assembly Improvement. *PloS One* 9, e112963. doi: 10.1371/journal.pone.0112963

Wiegand, S., Jogler, M., Boedeker, C., Pinto, D., Vollmers, J., Rivas-Marin, E., et al. (2020). Cultivation and Functional Characterization of 79 *Planctomycetes* Uncovers Their Unique Biology. *Nat. Microbiol.* 5, 126–140. doi: 10.1038/s41564-019-0588-1

Wiegand, S., Jogler, M., and Jogler, C. (2018). On the Maverick *Planctomycetes*. *FEMS Microbiol. Rev.* 42, 739–760. doi: 10.1093/femsre/fuy029

Wu, D. Y., Jospin, G., and Eisen, J. A. (2013). Systematic Identification of Gene Families for Use as "Markers" for Phylogenetic and Phylogeny-Driven Ecological Studies of Bacteria and Archaea and Their Major Subgroups. *PloS One* 8, e77033. doi: 10.1371/journal.pone.0077033

Yan, L., Gao, Y. M., Wang, Y. J., Liu, Q., Sun, Z. Y., Fu, B. R., et al. (2012). Diversity of a Mesophilic Lignocellulolytic Microbial Consortium Which is Useful for Enhancement of Biogas Production. *Bioresour Technol.* 111, 49–54. doi: 10.1016/j.biortech.2012.01.173

Yarza, P., Yilmaz, P., Pruesse, E., Glockner, F. O., Ludwig, W., Schleifer, K. H., et al. (2014). Uniting the Classification of Cultured and Uncultured Bacteria and Archaea Using 16S rRNA Gene Sequences. *Nat. Rev. Microbiol.* 12, 635–645. doi: 10.1038/nrmicro3330

Zhang, J., Liu, R., Xi, S. C., Cai, R. N., Zhang, X., and Sun, C. M. (2020). A Novel Bacterial Thiosulfate Oxidation Pathway Provides a New Clue About the Formation of Zero-Valent Sulfur in Deep Sea. *ISME J.* 14, 2261–2274. doi: 10.1038/s41396-020-0684-5

Zheng, R. K., Cai, R. N., Liu, R., Liu, G., and Sun, C. M. (2021a). *Maribellus Comscasis* Sp. Nov., A Novel Deep-Sea *Bacteroidetes* Bacterium, Possessing a Prominent Capability of Degrading Cellulose. *Environ. Microbiol.* 23, 4561-4575. doi: 10.1111/1462-2920.15650

Zheng, R. K., Liu, R., Shan, Y. Q., Cai, R. N., Liu, G., and Sun, C. M. (2021b). Characterization of the First Cultured Free-Living Representative of *Candidatus Izemoplasma* Uncovers its Unique Biology. *ISME J.* 15, 2676–2691. doi: 10.1038/s41396-021-00961-7

Zoetendal, E. G., Plugge, C. M., Akkermans, A. D. L., and de Vos, W. M. (2003). *Victivallis Vadensis* Gen. Nov., Sp Nov., a Sugar-Fermenting Anaerobe From Human Faeces. *Int. J. Syst. Evol. Microbiol.* 53, 211–215. doi: 10.1099/ijs.0.02362-0

Conflict of Interest: The authors declare that the research was conducted in the absence of any commercial or financial relationships that could be construed as a potential conflict of interest.

Publisher's Note: All claims expressed in this article are solely those of the authors and do not necessarily represent those of their affiliated organizations, or those of the publisher, the editors and the reviewers. Any product that may be evaluated in this article, or claim that may be made by its manufacturer, is not guaranteed or endorsed by the publisher.

frontiers | Frontiers in Marine Science

ORIGINAL RESEARCH
published: 28 April 2022
doi: 10.3389/fmars.2022.856291

Gonad Transcriptome and Whole-Genome DNA Methylation Analyses Reveal Potential Sex Determination/Differentiation Mechanisms of the Deep-Sea Mussel *Gigantidas platifrons*

Zhaoshan Zhong[1,2,3], *Minxiao Wang*[1,2,3], *Hao Chen*[1,2,3], *Hao Wang*[1,2,3], *Huan Zhang*[1,2,3], *Li Zhou*[1,2,3], *Yan Sun*[1,2,3], *Lei Cao*[1,2,3], *Chao Lian*[1,2,3], *Mengna Li*[1,2,3,4] *and Chaolun Li*[1,2,3,4]*

[1] Center of Deep Sea Research, Chinese Academy of Sciences Key Laboratory of Marine Ecology and Environmental Sciences, Institute of Oceanology, Chinese Academy of Sciences, Qingdao, China, [2] Laboratory for Marine Ecology and Environmental Science, Qingdao National Laboratory for Marine Science and Technology, Qingdao, China, [3] Center for Ocean Mega-Science, Chinese Academy of Sciences, Qingdao, China, [4] University of Chinese Academy of Sciences, Beijing, China

Gigantidas platifrons is one of the most dominant deep-sea mussels in cold seeps ecosystems in the South China sea. Studies have shown that deep-sea mussels are a gonochoristic species, however, little is known about the molecular mechanisms of sex determination in *G. platifrons*. In this study, RNA-seq and WGBS methylation analysis were performed on adult *G. platifrons* gonads to identify potential sex-related genes and generate a comprehensive analysis of sex determination in deep-sea mussels. A total of 5923 genes were identified as differentially expressed between the ovaries and testes, of which 2711 were female-biased and 3212 were male-biased. Among them, 161 genes may participate in the sex determination, and we found that *DMRT2* may play an important role in male sex determination, and *FOXL2*, *Wnt7*, and *β-catenin* may have impact on female sex determination. Moreover, common expression patterns were found in majority of the sex-related genes such as *FOXL2*, *β-catenin*, and genes in *SOX* family, suggesting the sex determination mechanisms of mussels in different habitats were conserved. The 5mC levels of transcription start sites (TSS2K) were significantly higher in sex-related genes than other DEGs in both gonads. Positive correlation was observed between sex-related genes expression and methylation in male, however, the effects of the DNA methylation on gene expression were complex in female. In short, we argue that sex determination mechanisms of deep-sea mussel *G. platifrons* is mainly controlled by genetic, and the methylation may have a regulation role on male sex determination or differentiation.

Keywords: deep-sea mussel, *Gigantidas platifrons*, gonad transcriptome, methylation, sex determination and differentiation

OPEN ACCESS

Edited by:
Taewoo Ryu,
Okinawa Institute of Science and Technology Graduate University, Japan

Reviewed by:
Dafni Anastasiadi,
The New Zealand Institute for Plant and Food Research Ltd, New Zealand
Kazue Nagasawa,
Tohoku University, Japan

****Correspondence:***
Chaolun Li
lcl@qdio.ac.cn

Specialty section:
This article was submitted to Deep-Sea Environments and Ecology, a section of the journal Frontiers in Marine Science

Received: *17 January 2022*
Accepted: *30 March 2022*
Published: *28 April 2022*

Citation:
Zhong Z, Wang M, Chen H, Wang H, Zhang H, Zhou L, Sun Y, Cao L, Lian C, Li M and Li C (2022) Gonad Transcriptome and Whole-Genome DNA Methylation Analyses Reveal Potential Sex Determination/Differentiation Mechanisms of the Deep-Sea Mussel Gigantidas platifrons. Front. Mar. Sci. 9:856291. doi: 10.3389/fmars.2022.856291

INTRODUCTION

Deep-sea mussels belonging to the subfamily Bathymodiolinae (Mytilidae) are the dominant species in deep-sea chemosynthetic ecosystems such as cold seeps and hydrothermal vents (Jones et al., 2005). The population dynamics of deep-sea mussels and how they can thrive in these extreme environments have received much attention (Carney et al., 2006; Laming et al., 2018). The sex ratio of a species is one of the most important factors that could affect population dynamics (Dyson and Hurst, 2004). For mollusks for which sex determination can be influenced by the environment, the sex ratio has been observed to change with temperature and the seasons in shallow-water species (Stenyakina et al., 2009; Collin, 2013; Villamor and Yamamoto, 2015; Xu et al., 2016). In contrast to shallow-water ecosystems, the deep-sea environment has a stable and low temperature and no seasonal changes through the year (Boutet et al., 2008). Therefore, previously, deep-sea mussels were not expected to exhibit sex ratio changes, but from relatively recent investigations into deep-sea chemosynthetic ecosystems, many deep-sea mussels have been observed to have changed sex ratios with increasing age and sampling time in different seasons (Tyler et al., 2007; Laming et al., 2014; Zhong et al., 2020). Nonetheless, studies have shown that the sex determination mechanisms could change rapidly between phylogenetically closely-related species (Gempe and Beye, 2011). Based on phylogenetic studies and fossil evidence, it appears that deep-sea mussels entered that environment more than 85 million years ago (Lorion et al., 2013). Consequently, the mechanisms of sex determination or differentiation in deep-sea mussels may have differences from those for shallow water species. However, the same sex ratio changes observed in deep-sea mussels suggest that some sex determination or differentiation mechanisms are conserved between deep-sea mussels and their shallow water relatives. The similarities and differences between deep and shallow species need to be further researched.

Sex determination is the process that establishes the sex of an individual and regulates the differentiation of sex characteristics (Smith et al., 2009; Capel, 2017; Du et al., 2017; Lin et al., 2021). The sex determination mechanism is typically considered to include two sex-determining strategies, namely genetic sex determination (GSD) and environmental sex determination (ESD) (Conover and Heins, 1987). The sex of an individual is complex. The sex of most vertebrates was determined by sex chromosomes. However, the situation is much more complex in lower vertebrates like fishes and reptiles whose sex could be determined by multiple loci from different autosomal chromosomes or even by environments only (ESD) (Nagahama et al., 2021). As to mollusca, only gastropods have been reported with sex chromosomes and others including the bivalves which have not found sex chromosomes, and their sex can be determined by genetics or environment, or both (Breton et al., 2018). Bathymodioline mussels have been studied for over 40 years, and although various reproductive strategies have been observed such as hermaphroditism in the genus *Idas* (Tyler et al., 2009), gonochorism in the genera *Bathymodiolus* and *Gigantidas* (Pennec and Beninger, 1997; Comtet et al., 1999; Eckelbarger and Young, 1999; Kádár et al., 2006; Tyler et al., 2007; Rossi and Tunnicliffe, 2017; Zhong et al., 2020), the molecular mechanisms that determine hermaphroditism or gonochorism are not well understood.

With the development of sequencing technology, RNA sequencing (RNA-Seq) of the gonadal samples has also been used to examine sex determination or differentiation in bivalves (Teaniniuraitemoana et al., 2014; Li et al., 2016; Chen et al., 2017; Ghiselli et al., 2018; Li et al., 2018). Moreover, a set of conserved transcription factors which determine the direction of sex differentiation in bivalves has previously been identified, such as *FOXL2* (forkhead box L2) in female-determining pathways and *DMRT* (double-sex- and mab3-related transcription factor) and *SOX* gene family (Sry-related HMG-box genes) in male-determining pathways (Naimi et al., 2009; Ghiselli et al., 2012; Teaniniuraitemoana et al., 2014; Li et al., 2016; Li et al., 2018). For shallow water mytilid species, through gonadal transcriptome of males *Perumytilus purpuratus*, some sperm-related transcripts have been found (Briones et al., 2018); by the comparison of female and male gonadal transcriptomes in *Limnoperna fortunei*, 187 sex-related genes including *DMRT*, *SOX*, and *FOX* were identified, which revealed target genes for sex determination or differentiation in *L. fortunei* (Afonso et al., 2019). Furthermore, DNA methylation has been shown to play an important role in gene expression, especially 5-methylcytosine (5mC) in the genome which have a regulative role in the transcription of sex-related genes and ultimately affect sex determination (Wittkopp et al., 2004; Feng et al., 2010; Tachibana, 2015; Li et al., 2021; Lin et al., 2021). For example, different 5mC levels have been determined for the two sexes of many animals including reptiles (turtles and alligators), fishes (half-smooth tongue sole and hybrid tilapia) and mollusca (oysters), by bisulfite sequencing (BS-Seq) (Olson and Roberts, 2014; Shao et al., 2014; Wan et al., 2016; Radhakrishnan et al., 2018; Lin et al., 2021). Through integrated analysis of transcriptome and methylome, (Lin et al., 2021) found some important sex maintenance and gonadal development pathways in adult alligators (e.g., *DMRT1-SOX9-AMH* pathway for males and oocyte meiotic maturation pathway for females). They also observed that DNA methylation density (calculated by the number of methylated C in a region divided by the C covered by more than 5X reads in that region) and level (calculated by the number of methylated C in a region divided by the sum of methylated C and unmethylated C) were higher in testes than in ovaries, and the hypermethylation in the gene bodies enhanced the expression of male-biased genes in the testes. All these findings indicate that gonadal transcriptome and methylome integrated analysis would be an effective tool for addressing sex determination in animals (Lin et al., 2021). Therefore, to better elucidate the sex determination or differentiation of deep-sea mussels, integrated transcriptome and methylome studies are urgently needed.

Gigantidas platifrons is an endemic and gonochoric species of the hydrothermal vents and cold seeps in the Northwest Pacific, and mainly gets nutrition from the methanotrophic endosymbionts in its gills (Barry et al., 2002; Sun et al., 2017b; Zhong et al., 2020). The genomic information of *G. platifrons* has been sequenced which make it a model species for investigating

adaptations to extreme environments in deep sea (Sun et al., 2017a). In our study, we applied RNA-seq and whole-genome bisulfite (WGBS) methylation analysis on the gonad tissue of the adult deep-sea mussel *G. platifrons* to investigate the molecular mechanisms of sex determination. Further, through the comparison with shallow water relatives we investigate whether sex determination is conserved in deep-sea mussels.

MATERIALS AND METHODS

Animal Material and Tissue Sampling

Deep-sea mussel *G. platifrons* specimens were obtained from Site F (22°06′N, 119°17′E), a cold seep which located at a depth of 1100m in the South China Sea (**Figure 1A**). The environmental temperatures of Site F are about 4°C and other physiochemical parameters were documented by (Cao et al., 2021). The mussel materials were captured using the TITAN 4 manipulator of the ROV *Faxian*, operated from the R/V *Kexue* during September 2017, and the mussels were transported in an isothermal bio-box (**Figure 1B**) in the underframe of the ROV, which kept the water temperature around 8–9°C. The gonads of adult *G. platifrons* were dissected immediately after ROV retrieval on deck and then split into two pieces. Each gonad sample was fixed in 4% paraformaldehyde (PFA) overnight, washed twice with 0.01 M phosphate-buffered saline (1 × PBS) and then stored in 70% ethanol for sex identification. The remainder were flash-frozen in liquid nitrogen and stored at -80°C for RNA and DNA extraction. RNA and DNA were extracted from the testes and ovaries using Trizol (Thermo, Waltham, USA) and E.Z.N.A.® Mollusc DNA kit (Omega, Norcross, USA), according to the manufacturer's instructions, respectively.

Sex Identification of *G. platifrons*

The gonad samples were dehydrated with serial ethanol (80, 90, 100, and then 100%) and then transferred to xylene and embedded in paraffin wax. The 7 μm sections of gonad samples were cut on a Leica microtome and tiled on glass slides. Gonad sections were deparaffinized with xylene, hydrated with serial ethanol (100, 100, 90, 80, and then 70%), and stained with hematoxylin-eosin (HE) to determine the sex and development stages of the gonads (**Figures 1E, F**, other gonad sections of males and females are shown in **Supplementary Figure 1**).

RNA-Seq of *G. platifrons* Gonads

After sex identification, 12 female gonads and 12 male gonads were chosen for RNA extraction. RNA degradation and contamination were monitored on 1% agarose gels. RNA quality and integrity were checked using an Agilent 2100 Bioanalyzer, and the concentration of total RNA was quantified using a Nanodrop 1000 spectrophotometer. Qualified RNA was subsequently used for RNA-seq analysis. The RNA of each four female gonads was mixed in equal amounts to obtain three RNA pools of 12 female gonads and similar operation was performed for 12 male gonads. Herein, three female and three male gonadal RNA pools were prepared for RNA-seq. Six RNA samples were sent to Novogene Corporation (Beijing, China) for cDNA library construction. Then, library preparations were sequenced on an Illumina Hiseq 2500 platform and 125 bp paired-end reads were generated.

Gonad WGBS of *G. platifrons*

The WGBS sample scheme was same as RNA seq, and three female and three male gonadal DNA pools were obtained. For each DNA pool, 5.2 μg of genomic DNA spiked with 26 ng

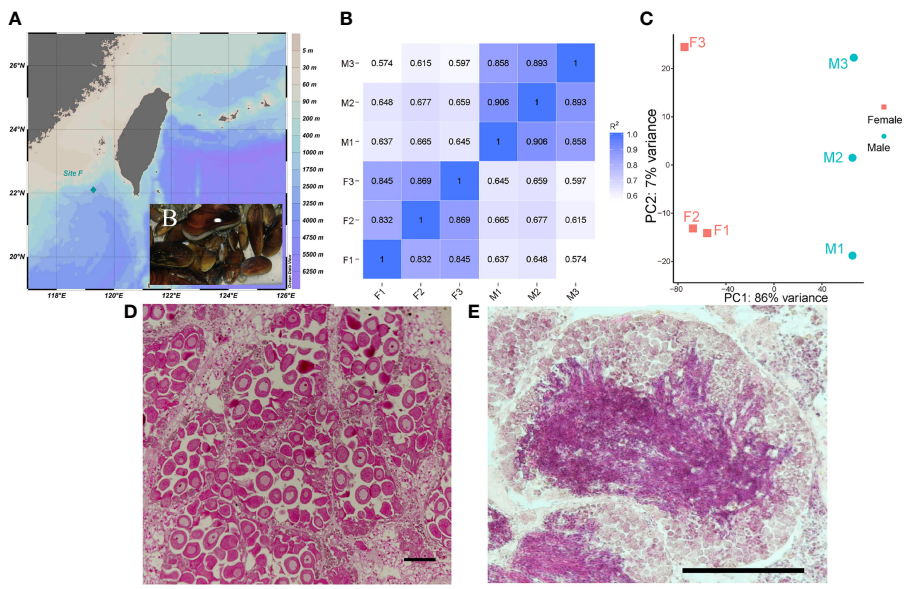

FIGURE 1 | Sample site **(A)** and captured *G. platifrons* [insert picture **(B)**]; Person correlation between samples **(C)**; PCA analysis of samples **(D)**; Representative female ovary, scale bar=100 μm **(E)** and male testis, scale bar=100 μm **(F)** of deep-sea mussel *G. platifrons*.

lambda DNA were fragmented by sonication to 200—300 bp with Covaris S220, followed by end repair and adenylation. These DNA fragments were treated twice with bisulfite using EZ DNA Methylation-GoldTM Kit (Zymo Research), before the resulting single-strand DNA fragments were PCR amplified using KAPA HiFi HotStart Uracil + ReadyMix (2X). Library concentration was quantified using Qubit® 2.0 Flurometer (Life Technologies, CA, USA) and quantitative PCR, and the insert size was assayed on an Agilent Bioanalyzer 2100 system. The clustering of the index-coded samples was performed on a cBot Cluster Generation System using TruSeq PE Cluster Kit v3-cBot-HS (Illumia) according to the manufacturer's instructions. After cluster generation, the library preparations were sequenced on an Illumina Hiseq 2500 platform and 125 bp paired-end reads were generated. Image analysis and base calling were performed with Illumina CASAVA pipeline, and generating 125bp paired-end reads.

Quality Control

Raw sequencing data were processed using fastp (version 0.20.0) with default parameters (Chen et al., 2018) to remove the adaptor sequences and low-quality reads of the RNA-seq and WGBS raw reads. Then the clean reads of RNA-seq and WGBS were prepared for downstream analysis.

RNA-Seq Data Analysis

The clean reads were mapped with an updated reference genome for *G. platifrons* (unpublished genome version, updated by Dr. Minxiao Wang) using HISAT2 (version 2.2.1). The mapped genes for *G. platifrons* were annotated in Nr, Swissprot, InterProscan, KEGG and the COG database. The transcripts of all the identified genes were quantified with featureCounts software (Version 2.0.1). Person correlation (**Figure 1C**) and principal component analysis (PCA) (**Figure 1D**) were then performed using custom-written R scripts to assess the relationships between gonad samples (**Figure 1B**). To identify sex-biased genes, the DESeq2 R package (version 1.10.1) was used. Only genes with $|\log_2(\text{fold change})| > 1$ and a corrected p value (q value) < 0.05 were regarded as differentially expressed genes (DEGs). Gene ontology (GO) and KEGG enrichment analysis of DEGs were conducted using Blast2GO and KOBAS software, GO terms and KEGG pathways with q values less than 0.05 were considered as significantly enriched. The results of enrichment analysis were visualized using ggplot2 R package (version 3.2.1) and OmicShare tools (www.omicshare.com/tools). Genes with GO annotation of 0007530 (sex determination) and 0007548 (sex differentiation) terms were selected as sex-related gene sets.

To find the similarities and differences in the gonadal transcriptomes and sex-related genes of deep-sea and shallow water mussels, the published transcriptome data of shallow water mussel gonads were selected for comparative transcriptome analysis. Transcriptome data for female and male gonads of only one shallow water mussel *L. fortunei* are published. The transcriptome and genome data for *L. fortunei* were downloaded from NCBI (https://www.ncbi.nlm.nih.gov/bioproject/587212) and GIGADB (https://ftp.cngb.org/pub/gigadb/pub/10.5524/100001_101000/100386/), respectively. All data were reanalyzed in line with the method mentioned previously. In short, first, the DEGs among the two sexes of *L. fortunei* were determined by DESeq2 and the GO and KEGG enrichment analysis were conducted using Blast2GO and KOBAS software. We then used OrthoFinder (version 2.5.2) to find the homologous protein sequences of *G. platifrons* and *L. fortunei*. Next, we used the *G. platifrons* sex-related genes and screened out single copy orthologous genes to obtain the orthologue sex-related genes in both *G. platifrons* and *L. fortunei*. Finally, we compared the expression pattern of shared sex-related genes in female and male gonads between *G. platifrons* and *L. fortunei*.

WGBS Data Analysis

Bismark software (version 0.16.1) was used to perform alignments of bisulfite-treated reads to a reference genome with the default parameters. The *G. platifrons* reference genome was first transformed to a bisulfite-converted version (C-to-T and G-to-A converted) and then indexed using bowtie2. Sequence reads were also transformed into fully bisulfite-converted versions (C-to-T and G-to-A converted) before they are aligned to similarly converted versions of the genome in a directional manner. Sequence reads that produce a unique best alignment from the two alignment processes (original top and bottom strand) were then compared to the *G. platifrons* genomic sequence and the methylation state of all cytosine positions in the read was inferred. Read pairs that shared the same coordinates in the genome were regarded as duplicated, and removed before calling methylation state, thus avoiding potential methylation level calculation bias. The bisulfite non-coversion rate was calculated as the percentage of cytosines sequenced at cytosine reference positions in the lambda genome. To identify the methylation site, we modeled the sum of 5mC of methylated counts as a binomial (Bin) random variable with methylation rate (r), as $5mC \sim Bin(5mC + umC^*r)$. To calculate the methylation level of the sequence, we divided the sequence into multiple bins, with each bin size at 10 kb. The sum of methylated and unmethylated read counts in each window were calculated. The 5mC level (ML) for each window or C site shows the fraction of methylated Cs, and is defined as: ML (5mC) =reads (5mC)/(reads (5mC) + reads (umC)). The relative proportion of 5mCs in the three regions including 2kb upstream of the genes' transcription start sites (TSS2K), the gene body, and 2kb downstream of transcription termination sites (TTS2K) were calculated as the proportion of mCG, mCHG, and mCHH of the total 5mC sites, respectively. Differentially methylated regions (DMRs) of the two sexes were identified using the DSS software (version 2.12.0). The regions with a p value less than 1e-05, length more than 50, average methylation level difference between groups greater than or equal to 20%, and at least three CpG sites were retained as a final DMR. We defined the genes related to DMRs as genes whose gene body region (from TSS to TTS) or TSS2K have an overlap (> 1bp) with the DMRs. Moreover, genes that were DEGs and had differential methylated promoter (DMP) regions were selected for the further analysis.

Integrative Analysis of the Expression Levels of Sex-Related Genes and Methylation

The average methylation level of all DEGs and sex-related genes in the three sequence regions (TSS2K, Gene body and TTS2K) were calculated and then compared between females and males. Conventionally, the major region of focus is promoter, so analyzed the 5mC level in the promoter of these genes between females and males.

Statistical Analyses

Statistical analyses of DEGs and sex-related genes methylation level between females and males were undertaken in GraphPad (version 7.04). The p values were calculated using non-parametric tests. $P < 0.05$ was considered statistically significant.

RESULTS

Summary of Gonadal Transcriptome of *G. platifrons*

To provide a global view of transcriptional differentiation and determine the molecular mechanisms underlying sex maintenance between male and female *G. platifrons*, six cDNA libraries were constructed and utilized for Illumina paired-end sequencing to generate representative transcripts of a wide range of biological processes. As shown in **Table 1**, after eliminating the primer and adapter sequences as well as the low-quality reads by fastp, the number of clean reads ranged between 38391192–50489378 with a relatively high base quality (Q30 > 92.63% for all samples). The unique mapping rate of all samples ranged from 63.35 to 69.20% when mapped against the updated *G. platifrons* reference genome (unpublished data). We obtained a total of 32,918 expressed genes in female and male gonads according to featureCounts (**Supplementary Table 1**, genes with expression).

Enrichment Analysis of DEGs Between Ovaries and Testes

DEG analysis revealed 5923 sex-biased genes which were differentially expressed between the ovaries and testes (**Figure 1B**), 2711 of which were up-regulated in the ovaries (female-biased genes) and 3212 were up-regulated in the testes (male-biased genes) (**Supplementary Table 1**, all DEGs). To investigate the functions of DEGs, GO and KEGG analysis were implemented. For GO enrichment analysis, the results showed that 434 GO terms were enriched to 257 biological processes (BP), 96 to cellular components (CC) and 81 to molecular functions (MF) (q value < 0.05, **Supplementary Table 2**; GO_BP, GO_MF, and GO_CC). Among them, 3318 DEGs were enriched to BP, and most of the BP were enriched within single-organism processes and multicellular organismal processes. Altogether, 2995 DEGs were enriched to CC. In terms of CC, cell related terms contributed the greatest proportion. A total of 3738 DEGs were enriched within MF. For MF, protein binding and catalytic activity represented the most universal terms. 3318 DEGs assigned to BP and the top 20 enriched BP are showed in **Figure 2A**. The processes related to cell growth and development were extensively enriched, especially those related to cytoskeleton and cell motility. Additionally, 600, 116, and 11 DEGs were assigned to "reproduction", "sex differentiation", and "sex determination", respectively, which account for 18.08, 3.5, and 0.33% of all BP terms, respectively. Furthermore, 2711 female-biased genes and 3212 male-biased genes were selected for separate GO enrichment analysis. We chose the top 10 enriched GO terms in BP, CC and MF for analyzing females and males (**Supplementary Table 2**, Top10 GO terms). Among them, nutrient metabolism related processes were the most enriched GO terms for female-biased genes while cytoskeletal correlation processes accounted for the dominant GO terms enriched for male-biased genes.

For KEGG enrichment analysis, a total of 1120 candidate genes in DEGs were noted from KEGG. Of these, 470 DEGs were significantly mapped onto 15 pathways (q value < 0.05, **Supplementary Table 2**, KEGG). The KEGG enrichment results were comparable with GO results, nine were related to metabolism, including carbon, glutathione, cytochrome P450, amino acids, and glycometabolism, which indicated that metabolic process related pathways play a vital role in sex determination and differentiation (**Figure 2B**). We found that pathways of microbial metabolism in diverse environments were the most enriched pathways, the other 20 related microbial metabolism pathways are shown in **Figure 2C**. We also found that 17 DEGs mapped onto the WNT signaling pathway (**Supplementary Table 2**, WNT), including Wnt6 (CSbapl.23381) and Wnt7 (CSbapl.46743) which function as signaling molecules in sexually dimorphic development. Wnt6 and Wnt7 were up-regulated in female *G. platifrons* gonads and the canonical WNT signaling mediator, *β-catenin*, was also detected in transcriptome and up-regulated in female gonads, which indicated the conservatism of sex determination in the deep-sea mussel *G. platifrons*.

TABLE 1 | Summary of clean reads of the transcriptome samples.

Groups	Samples	Raw reads	Clean reads	Q30 (%)	Total mapped reads	Uniquely mapped reads
Female	F1	47122044	46987368	95.02	41930387 (89.24%)	30000250 (63.85%)
	F2	38505308	38391192	93.82	34755377 (90.53%)	24320248 (63.35%)
	F3	39386960	39269710	93.33	35418171 (90.19%)	25777431 (65.64%)
Male	M1	41952996	41812412	94.58	36515133 (87.33%)	28562204 (68.31%)
	M2	50735082	50489378	94.11	44207999 (87.56%)	34941070 (69.20%)
	M3	48448844	48179296	92.63	41316657 (85.76%)	32489809 (67.44%)

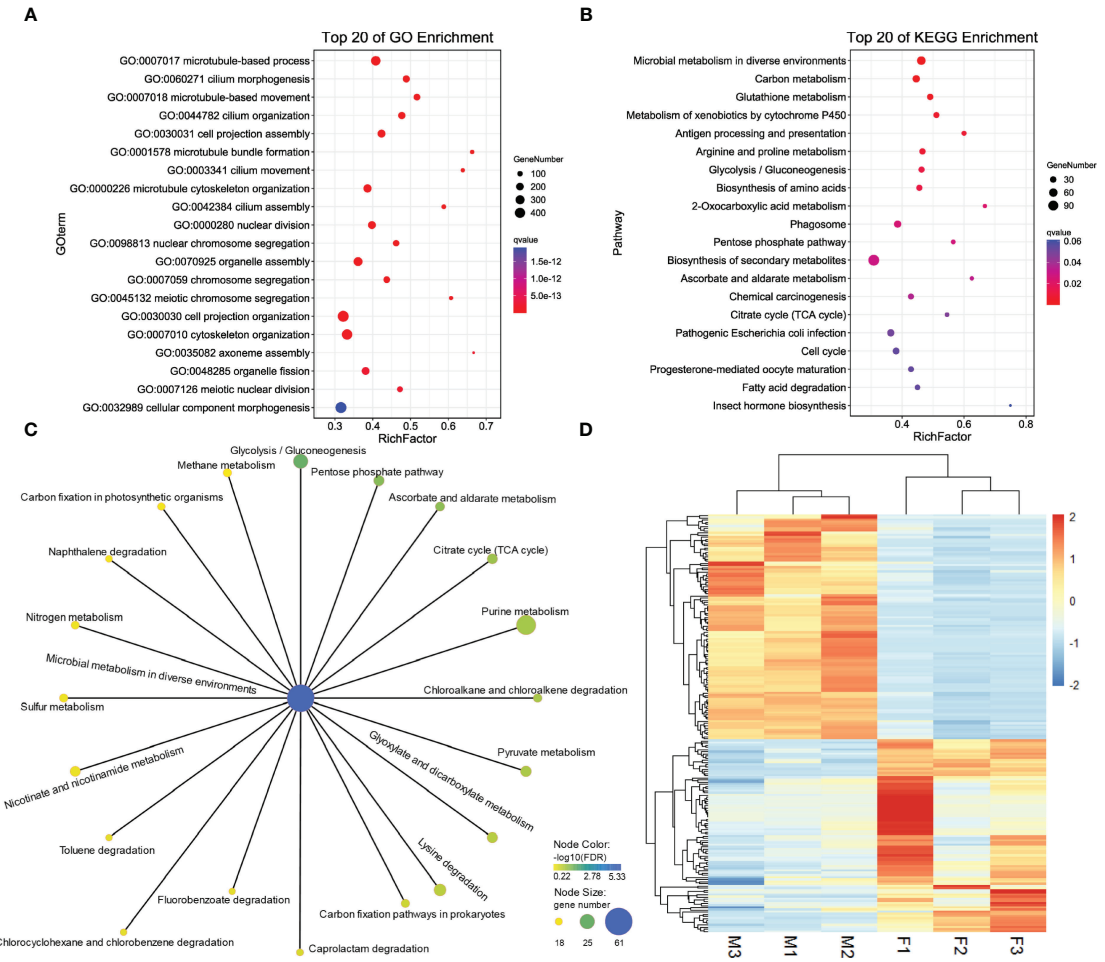

FIGURE 2 | Top 20 enriched GO terms in BP of DEGs **(A)**. Top 20 enriched KEGG pathways of DEGs **(B)**. Pathways related microbial metabolism in diverse environments that have been enriched for DEGs **(C)**. Expression patterns of 161 sex-related genes between two sexes of G. platifrons **(D)**. For **(A, B)**, the color represents the -log10 (q value), the bubble size represents the number of genes enriched into this term or pathway, and Rich Factor represents the ratio of the number of genes located in this term or pathway in the differentially expressed genes to the total number of genes located in this term or pathway in all the annotated genes. For **(D)**, the heatmap were draw by "pheatmap" package (version 1.0.12) of R software. Each column represents a sample, each row represents a gene, the gene expression level was normalization by each row, red represents up-regulated while blue represents down-regulated.

Search and Identification of Sex-Related Genes in *G. platifrons*

Of the total candidate genes, 161 were identified as sex-related genes generated using the "sex determination" and "sex differentiation" terms (**Supplementary Table 2**, sex-related genes). These genes could be categorized into transcriptional regulatory genes including the transcription factor, steroid hormone biosynthesis related genes, ovary and testis specific genes, gametogenesis related genes, some kinase genes related to cell differentiation, and development and other genes involved in sex determination or differentiation were mentioned in the literature. The expression patterns of 161 sex-related genes are shown in **Figure 2D** and **Supplementary Table 2**. Among these candidate genes, six vitelline envelope zona pellucida genes (*VEZP type 6/9/14/17/24*), one vitelline membrane outer layer protein 1 (*VMO1*), and one vitellogenin (*VTG*) were classified as ovary or oocyte-specific genes which were expressed more in females than males. Twenty-one genes had testis-specific expressions and 17 were sperm-specific genes such as testis-specific serine kinase (*TSSK*), testis-expressed protein (*TEX*), spermatogenesis-associated protein (*SPATA*), and sperm surface protein (*SP*); all of these genes were more highly expressed in males. Additionally, four genes annotated as the *SOX* gene family were found, including *SOX2* in the *SOXB1* group, *SOX4* in the *SOX C* group, *SOX5* in the *SOX D* group, and *SOX9* in the *SOX E* group. The main transcription factors such as *FOXL2* and *DMRT2* involved in female and male sex determination, respectively were also identified, and the *FOXL2* were expressed more in females, while *DMRT2* were high expression in males. Moreover, sex steroidogenesis-related genes such as estradiol 17β-dehydrogenase (*E2DH*), 17β-hydroxysteroid dehydrogenase (17β-HSD type 6/10/12/14) and CYP17a were all significantly

high expressed in females. The roles of these genes need further study in *G. platifrons*, but most of them have been identified as playing important roles in sex-determination/differentiation or gametogenesis in other animals and molluscan species.

Comparative Transcriptome Analysis Between Deep-Sea and Shallow Water Mussels

To find the similarities and differences between deep-sea mussels and shallow water relatives, we first used OrthoFinder (version 2.5.2) to screen the homologous genes of deep-sea mussel *G. platifrons* and shallow water mussel *L. fortunei*. A total of 2543 orthogroups were documented (**Supplementary Table 3**, othogroups), uncovering 35 shared sex-related genes by intersection with 161 sex-related genes in *G. platifrons*. Then, we compared the shared expression patterns of 35 sex-related genes between a deep-sea mussel and shallow water mussel. Thirty-five shared sex-related genes contained most of the genes that play an important role in sex determination and differentiation, such as *SOX* gene family, *FOXL2*, *β-catenin* and some testis-specific genes. For female high expressed genes, such as *SOX2*, *FOXL2* and *β-catenin*, SOX2 high expressed in female than male about 10 times in both two species, *FOXL2* were about 100 times more expressed in females than males of *G. platifrons*, and about 900 times more expressed in females than males of *L. fortunei*. The same expression patterns also found in *β-catenin* which were all more than 2 times expressed in females than males in both species. As similar expression pattern was observed in male-upregulated genes in both shallow water and deep-sea mussels, such as TEX36 and TEX47, which about 2-10 times more expressed in males than females (**Figure 3** and **Supplementary Table 3**, shared sex-related genes).

Summary Gonadal Methylome of *G. platifrons*

To examine the roles of DNA methylation in sex maintenance and gonad development in adult *G. platifrons*, the methylation patterns and levels of gonads for female and male *G platifrons* were detected with WGBS analysis (**Supplementary File 1**). We found that the 5mC levels of all genomic C sites for males (3.22%) were slightly higher than for females (3.09%) and the 5mC levels for the CG site (>96%) were higher than for the CHG (<1%) and CHH (~2%) sites. For the GC site, the average 5mC levels in the gene body (30-40%) were higher than that in other sequence regions such as promoter (~20%) and repeat regions (~10%) in the genome. We also found that the 5mC level showed a weak positive correlation with gene expression level (Spearman correlation r range from 0.313 to 0.543) at the three sequence regions (TSS2K, Gene body, TTS2K) and in both sexes (**Supplementary Table 4**, F_TTS2K_5mC_vs_gene_express, M_TTS2K_5mC_vs_gene_express, F_genebody_5mC_vs_gene_express, M_genebody_5mC_vs_gene_express, F_TSSK2k_5mC_vs_gene_express, and M_TSSK2k_5mC_vs_gene_express).

Integrative Analysis of Transcriptome and Methylome

The differential 5mC level of DEGs has the same trend with all genes being detected in the three sequence regions, and the

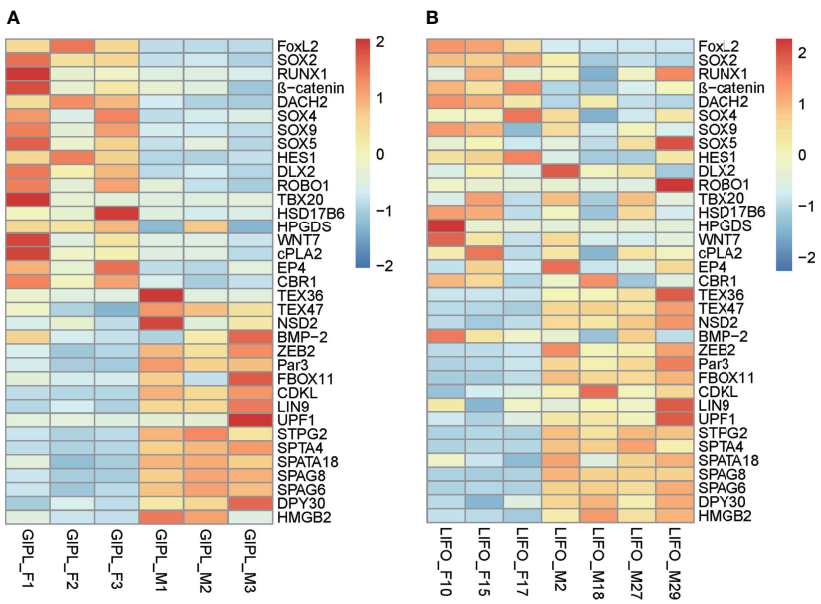

FIGURE 3 | Expressed pattern of shared sex-related genes in female and male between G. platifrons (GIPL_F1, GIPL_F2, GIPL_F3 versus GIPL_M1, GIPL_M2, GIPL_M3) **(A)** and L. fortunei (LIFO_F10, LIFO_F15, LIFO_F17 versus LIFO_M2, LIFO_M18, LIFO_M27, LIFO_M29) **(B)** The heatmap were draw by "pheatmap" package (version 1.0.12) of R software. Each column represents a sample, each row represents a gene, the gene expression level was normalization by each row, red represents up-regulated while blue represents down-regulated.

methylation levels were all significantly higher in males than females (**Figure 4A** and **Supplementary Table 4**, 5mC_DEGs). To identify the role of methylation more clearly in sex determination or sex differentiation, we screened the 1903 shared genes of DMRs and DEGs for further analysis (**Figure 4B**, **Supplementary Table 4**, DMRs_vs_DEGs). GO functional enrichment analysis showed that 1180 shared genes were enriched in the BP category, and 256 BP GO terms were significantly enriched (q value < 0.05). The top 20 enriched BP terms are shown in **Figure 4C**. Additionally, BP terms related to "sex differentiation" and "male sex differentiation" were all significantly enriched (**Supplementary Table 4**, BP_shared_genes_ DMRs_vs_DEGs). For KEGG analysis, 419 shared genes between DMRs and DEGs were associated with 335 pathways. The top 20 enriched pathways are shown in **Figure 4D**. A total of 128 shared genes were significantly enriched in metabolism and hormone biosynthesis related pathways (q value < 0.05). Some of the shared genes were enriched in the "WNT signaling pathway", "oocyte meiosis", and "FoxO signaling pathway", which play important roles in sex determination or differentiation and germ cell development.

Comparing the 5mC Levels of Sex-Related Genes With Other DEGs, and the Different 5mC Level of Sex-Related Genes Between the Two Sexes

The 5mC levels of each sex-related gene and DEG were documented in **Supplementary Table 4**. In total, 59 of 161 (36.65%) sex-related genes in *G. platifrons* displayed significantly differential methylation patterns between females and males (**Supplementary Table 4**, DMR_vs_sex-related genes), which contrasts to ~ 20.97% (6904/32,918) over whole genome (Fisher's exact test, $p < 0.0001$). To find out if the 5mC levels of sex-related genes were different from other DEGs, the 5mC levels of the TSS2K, the gene body and the TTS2K regions of 161 sex-related genes were compared with the other DEGs (5762 genes) using Kolmogorov-Smirnov tests. We defined the OF and OM as the other DEGs in females and other DEGs in males. The result shows that for the TSS2K region, the 5mC levels of sex-related genes for females (F) were significantly higher than for the other DEGs in females (OF) (**Figure 5A,** F vs OF, p=0.0169) while no significantly differences were found in males (**Figure 5A**, M vs OM, p=0.0977). For the gene body region, the 5mC levels of sex-related genes were not significantly different from OF (**Figure 5B**, F vs OF, p=0.0582), while 5mC levels of sex-related genes were significantly higher than OM (**Figure 5B**, M vs OM, p=0.0273). For the TTS2K region, 5mC levels of sex-related genes were not significantly different from OF (**Figure 5C**, F vs OF, p=0.2180) and OM (**Figure 5C**, M vs OMp=0.1567), respectively. Moreover, the 5mC levels of 161 sex-related genes for males were all significantly higher than for females in the gene body and TTS2K regions (**Figure 5D**, Gene body and TTS2K, $p < 0.0001$). However, for the TSS2K region, there were no significant differences between females and males (**Figure 5D**, TSS2K, $p = 0.2113$).

We then divided 161 sex-related genes into 73 female-biased sex-related genes (FBSGs) and 88 male-biased sex-related genes (MBSGs) according to expression levels. We found that 5mC levels were all significantly higher in MBSGs than FBSGs for the

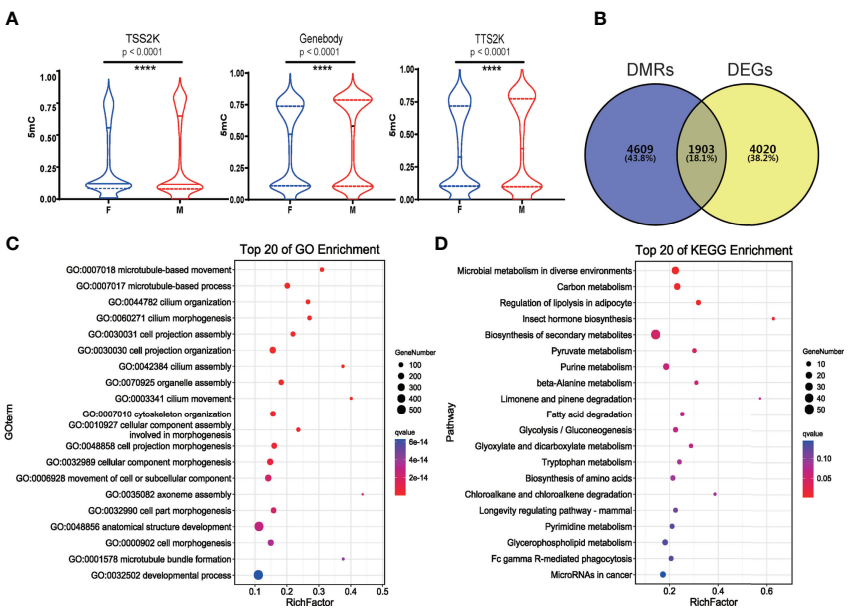

FIGURE 4 | 5mC levels of all genes in 3 sequence regions (TSS2K, Gene body and TTS2K) between female and male G. platifrons (Wilcoxon test, and $p < 0.0001$ (****) for all 3 sequence regions) **(A)**; 1903 shared genes between DMRs and DEGs of two sexes **(B)**; Top 20 enriched BP GO terms of shared genes between DMRs and DEGs **(C)**; Top 20 enriched KEGG pathways of shared genes between DMRs and DEGs **(D)**.

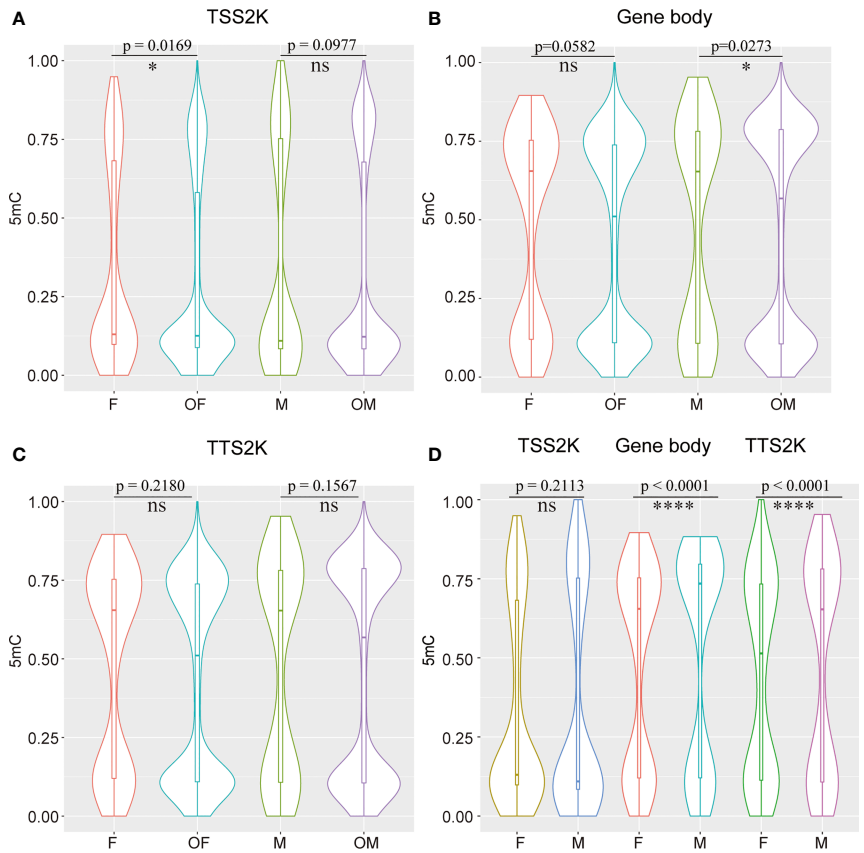

FIGURE 5 | Compare 5mC levels between 161 sex-related genes and the other DEGs in two sexes among TSS 2K, Gene body, and TTS 2K regions **(A–C)** and compare 5mC levels of 161 sex-related genes between females and males in TSS 2K, Gene body, and TTS 2K regions **(D)**; Kolmogorov-Smirnov test for **(A, C)**, and Wilcoxon test for **(D)**, ns, *, and **** represent $p > 0.05$, $p < 0.05$ and $p < 0.0001$ respectively, OF and OM represent the other DEGs in female and the other DEGs in male.

two sexes and the three regions (**Figure 6**, $p < 0.0001$). To find if the 5mC levels of FBSGs and MBSGs were significantly different in females and males, we conducted Wilcoxon matched-pairs signed rank tests for the three regions (**Figure 6**). The results showed that, except for the levels of FBSG 5mC levels in the gene body regions, there were no significant differences between the two sexes (**Figure 6**, $p = 0.0554$). Other 5mC levels of FBSGs and MBSGs were all higher in males than females in all three regions ($p < 0.0001$).

We subsequently investigated whether the sex-related genes overlapped with the DMPs (**Supplementary Table 4**, DMP_vs_sex-related genes). Only 12 sex-related genes were found by transcriptome and methylation associated analysis. These genes include male-biased genes such as testis-specific serine kinase (CSbapl.702), a WNT pathway gene *β-catenin* (CSbapl.3788) which is believed to be essential for female sex determination, and the transcription factor *SOX* family gene *SOX5*. Except for gene *Prx*, all 5mC levels of females were lower than those of males, which is in line with the trend of 5mC levels of all sex-related genes. For five female-biased genes, the hypomethylation of promoter regions corresponded with high methylation levels in promoter regions, which would suppress gene expression. However, for six male-biased genes except *Prx*, the hypermethylation of promoter regions resulted in high gene expression.

DISCUSSION

Sex determination mechanisms are widely divergent in animals and they can evolve rapidly (Bachtrog et al., 2014; Beukeboom and Perrin, 2014). Genetic and environmental sex determination systems are now considered as two ends of a continuum rather than separate mechanisms in vertebrate temperature-dependent sex determination species (Sarre et al., 2004; Quinn et al., 2011). As for bivalve species, sex may be determined by genes in combination with environment (Breton et al., 2018). Deep-sea mussels entered the deep-sea chemosynthetic environment at least 85 million years ago (Lorion et al., 2013), therefore the mechanisms of sex determination or differentiation may not be the same as for shallow water species. Sex determination or sex differentiation are intricate processes not always clearly distinguishable because their signaling cascades can be integrated in invertebrates (Matson and Zarkower, 2012;

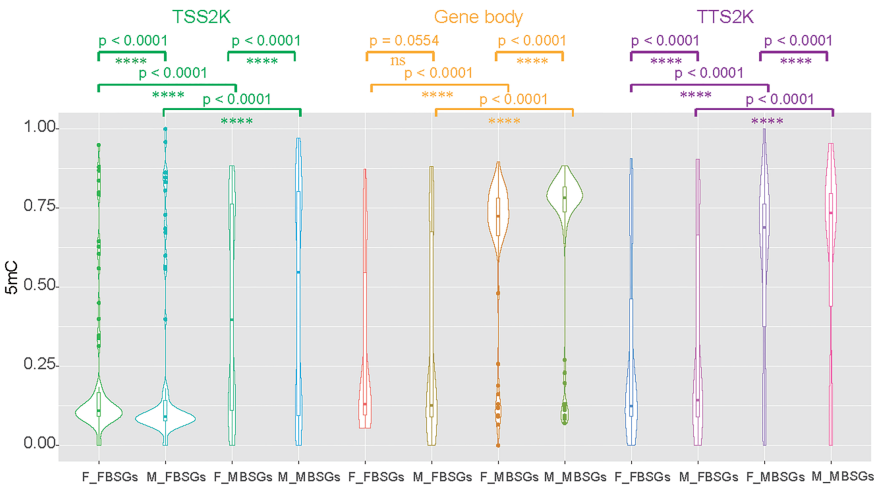

FIGURE 6 | Compare 5mC levels between female-biased sex-related genes (FBSGs) and male-biased sex-related genes (MBSGs) in the TSS 2K, Gene body, and TTS 2K regions by Kolmogorov-Smirnov test and compare 5mC levels of FBSGs and MBSGs in two sexes by Wilcoxon test. ns and **** represent $p > 0.05$ and $p < 0.0001$ respectively.

Huang et al., 2017). As with previous studies, in the present study the genes involved in sex determination or sex differentiation are described as 'sex-related genes' (Li et al., 2016; Chen et al., 2017; Gonzalez-Castellano et al., 2019; Yao et al., 2021). In the present work we used transcriptomic analysis to unravel sex-related genes featured in sex determination or differentiation, and we also tried to find out if epigenetics would affect the expression levels of sex-related genes. This is the first integrated analysis of the gonads of deep-sea mussels, providing data about sex-related genes and to study the correlation between gene methylation levels and expression levels.

Putative Mechanisms of Sex Determination or Differentiation in *G. platifrons*

Many genes related to sex determination are transcription factors, especially in terms of the *DMRT*, *FOX* and *SOX*, gene families (Smith et al., 2009; Matson et al., 2011; Huang et al., 2017; Li et al., 2018). By analyzing the female and male gonad transcriptome of *G. platifrons*, we identified at least 161 sex-related genes which were all belonged to DEGs and annotated to sex determination or sex differentiation GO term. Sixteen transcription factors were detected, including the common genes *DMRT2*, *FOXL2*, and *SOX9*, which were shown to be deeply conserved in sex determination or differentiation in animals (Liu et al., 2012; Li et al., 2018; Afonso et al., 2019).

The *DMRT* family of genes contains a highly conserved DNA binding domain called the DM domain. There are seven *DMRT* genes that have been shown to play critical roles in sexual regulation, including sex differentiation, sexual dimorphism, and spermatogenesis in a broad variety of metazoans, including nematodes, insects, and vertebrates (Zarkower, 2013). Another famous sex determination transcription factor is *FOXL2*. *FOXL2* is one of the *FOX* gene family members and preferentially expressed in the ovary of vertebrates, controlling ovarian differentiation and maintenance by repression of testis-specific genes from the early embryonic gonad throughout adult life (Uhlenhaut et al., 2009). Therefore, *FOXL2* and *DMRT* are the key genes for female and male sex determination and maintenance, respectively. In addition, they are mutually antagonistic in determining the sex of mammals (Matson et al., 2011). In *G. platifrons*, the *DMRT*2 gene was examined and found to be up-regulated in male gonads ($q < 0.05$), and *FOXL2* was at higher levels in females than males ($q < 0.05$). As in mammals, the balance between *FOXL2* and *DMRT*2 is suggested to be important for sex determination in *G. platifrons*. This phenomenon was also reported in other mollusca species such as the blacklip pearl oyster *Pinctada margaritifera*, Pacific oyster *Crassostrea gigas*, Yesso scallop *Patinopecten yessoensis* and razor clam *Sinonovacula constricta*, although the genes in the *DMRT* family and *FOX* family are not always the same among different species, for example *DMRT2* and *FOXL2* in *P. margaritifera*, *Dsx* and *FOXL2* in *C. gigas*, DMRT1L and *FOXL2* in *P. yessoensis*, *FOXA1*, *FOXD2*, and *DMRT*A2 in *S. constricta* (Teaniniuraitemoana et al., 2014; Zhang et al., 2014; Li et al., 2018; Yao et al., 2021).

The male-determining gene in mammals is the *SRY* gene. *SRY* is a member of the SOX gene family of DNA-binding proteins. *SRY* complexed with the *SF1* protein would upregulate other transcription factors including the important *SOX9* which is the up-stream regulator of male sex determination (Sinclair et al., 1990; Kashimada and Koopman, 2010). *SOX9* is one gene in the *SOXE* group that has an expression in the Sertoli cells necessary for testis determination, and is reinforced by *FGF9* and *DMRT*1 which are thus essential to this network (Matson and Zarkower, 2012). In mammals, once *SRY* expression begins, other genes start to express only in one sex, so the *SOX9* would not be active in female gonads (Gross, 2006). However, in our study, although no *SRY* was detected, the downstream gene *SOX9* was found in

the gonad transcriptome, and *SOX9* was not only active in male testes but also in female ovaries. Moreover, *SOX9* was not only highly expressed in males but also female. High expression in females may explain the phenomenon of hermaphroditism previously discovered in *G. platifrons* (Zhong et al., 2020). For other gonadal transcriptomes of shallow water bivalves, *SOX9* expression levels were also determined, such as in *P. yessoensis*, *C. gigas* and *L. fortunei*, but for these bivalves the *SOX9* expression levels were not significantly different between males and females (Zhang et al., 2014; Li et al., 2016; Afonso et al., 2019). Overall, we suggest that *SOX9* could be a key factor in sex determination or differentiation in *G. platifrons*, but it may not function in the way that it does in mammals or indeed other shallow bivalves.

We also identified the *β-catenin* gene in *G. platifrons*. In mammals, *β-catenin*, the center in the canonical WNT signaling pathway, is a key transcriptional regulator and is essential for ovarian development and maintenance (Liu et al., 2009). *RSPO1-WNT4-β-catenin* in the canonical WNT signaling pathway is independent and complementary to the *FOXL2*-leading pathway (Kocer et al., 2008). *β-catenin* presents in the gonads of both sexes of *G. platifrons* but was expressed significantly higher in ovaries, while *RSPO1* was not found, and *Wnt4* was not a DEG in the transcriptome of *G. platifrons*. Therefore, the existence and specific function of *β-catenin* for female sex determination needs further investigation.

In non-mammalian vertebrates, sterol hormones play an important role in sex determination and sex differentiation (Navarro-Martin et al., 2011). Aromatase CYP19a (Cytochrome P450 family 19) can irreversibly converts androgens into estrogens, which influences the ratio of androgen-to-estrogen, and the different ratio then determines undifferentiated gonad sexually differentiates into a testis or ovary. Sixteen Cytochrome P450 family genes were found in the deep-sea mussel gonadal transcriptome and eight were found in females and males' DEGs, however, CYP19a were not found in these data, but another important Cytochrome P450 family 17, one of the sex-related genes CYP17a was found both in two sexes of *G. platifrons* which were high expression in female. CYP17a has been shown to play important roles in female sex determination and male fertility by regulating sex steroid biosynthesis in fish (Yang et al., 2021). For *G. platifrons*, 9.88% were methylated in the testes and 8.21% were methylated in the ovaries for the TSS2K region of CYP17a, however, CYP17a was not defined as a DMR. So, the effect of methylation on CYP17a is not as pronounced as it is on CYP19a which hypermethylation occurs in testis and gene high expression in ovaries of fish (Wen et al., 2014), and it also possible that the mechanism of sterol hormones in mollusks is obviously different from that in vertebrates.

Specifically, we compared the sex-related genes between the deep-sea mussel *G. platifrons* and the shallow water mussel *L. fortunei*. The results showed that the common expression pattern of the male-biased sex-related genes and the expression level of those genes were all coincident among male samples, while for female-biased sex-related genes, the expression pattern and gene expression levels were inconsistent in *L. fortunei*. We suggest that the common expression pattern for female *G. platifrons* may be caused by the stable deep sea environment or the same development stages of gonads. Therefore, there are two factors that may lead to differences in the expression patterns of female-biased sex-related genes between *G. platifrons* and *L. fortunei*. First, the development cycle is different at the time of sampling for female gonads of *L. fortunei*. Second, the shallow water environment is not stable, and the maternal immunity may be influential, given that the *SOX* family genes are important genes that cause differential expression patterns in female individuals of *L. fortunei*, and the *SOX* family genes are reported to be related to immunity (Furukawa et al., 2021). The ovary is an important source of maternal immunity, therefore the differential expression between individuals may be caused by their different responses to the changing environment (Wang et al., 2015). In addition, the other important sex determination genes like *FOXL2*, *β-catenin*, and *Wnt7* all have same the expression patterns between *G. platifrons* and *L. fortunei* (**Figure 3**), suggesting some conserved sex determination mechanisms between these two mussels.Based on previous studies and our transcriptome data, all the aforementioned genes which are shared among *G. platifrons* and other animals are thought to be involved in sex determination, and thus we speculate that the sex determination or differentiation mechanism may be conserved in some degree among deep-sea mussels and shallow water species or other vertebrates, but there are also significant differences in the male and female expression patterns of specific sex-related genes. As for *G. platifrons*, based on sequence homology and functions inferred from transcriptome data, we suggest that although traditionally identified sex-related genes are not strictly expressed in male and female gonads, the expression of these genes or homologues, especially *SOX*, *FOXL2*, and *DMRT* genes, which are commonly referred to in other mollusks, are significantly different between males and females. We suggest that *SOX* may have high expression in the early developmental stage before *G. platifrons* gonadal maturation and in the up-stream regulator leading to male sex determination. However, in the gonadal maturation stage, the *SOX* gene would not highly express in testes. Thus, *SOX* would directly or indirectly activate *DMRT*2 for testis development in early stages and *DMRT2* may keep testis functional through a life. *FOXL2* may be highly expressed in ovaries and complemented by *β-catenin* leading to female sex-determination pathways in *G. platifrons*.

The Relationship Between DNA Methylation and Sex-Related Genes Expression

In the present study, we have shown that *G. platifrons* has some sex determination or differentiation mechanisms common with the shallow water mussel *L. fortunei* and other bivalves. Additionally, *G. platifrons* is shown to be a gonochoric species (Zhong et al., 2020), while the sex ratio is not coincident among groups of different shell lengths. Additionally, while hermaphroditism was observed in our samples, this was only the case in two large individuals, so we suspect that this species may not exhibit large-scale sex-reversal and sex maintenance. We recorded higher levels of global DNA methylation level in the

testis (3.22%) than ovary (3.09%), suggesting that male germ cells may be more heavily methylated than female germ cells, which concurs with findings reported for *P. yessoensis* (Li et al., 2019). Additionally, we also found that 5mC is predominantly in the gene body (30-40%) in both sexes, which is in agreement with previous studies of *C. gigas* (Gavery and Roberts, 2013; Olson and Roberts, 2014; Wang et al., 2014). Through enrichment analysis of the intersection of DMRs and DEGs in two sexes of *G. platifrons*, we found that methylation mainly affects metabolic processes and morphological differentiation of organisms (**Figure 4C, D**). Therefore, we hypothesize that methylation plays an important role in the differential metabolism of males and females in deep-sea mussels, in particular high 5mC levels may have a vital effect on male sex determination.

To further explore the effect of methylation on sex determination or differentiation, we chose to study mainly the sex-related genes. The methylation levels presented negative correlations with expression levels of sex-related genes in the ovaries of *G. platifrons*, which corroborates the concept that increased methylation corresponds to decreased gene expression (Riviere et al., 2013). In males, our results indicated the positive correlation between 5mC and sex-related gene expression, where genes with high expression levels had high 5mC levels (**Supplementary Figure 2**). This is similar to the observations reported for oyster male gamete (Gavery and Roberts, 2013; Olson and Roberts, 2014). We also found that the tendency for 5mC levels of all sex-related genes and MBSGs or FBSGs were all higher in males than females in the three sequence regions, although some comparisons were not statistically significantly different (**Figures 5D** and **6**). Moreover, similar patterns were found at the level of the single sex-related gene (**Supplementary Table 4**, 5mC_sex-related genes) indicating that females present more hypomethylation than males, but in males hypermethylation correlated with high levels of gene expression in all sequence regions (**Supplementary Figure 2**). We hypothesize that DNA methylation may act as an enhancer rather than a repressor in testis development. As show in **Figure 7**, we integrated the differential methylation of several key sex-related genes to speculate the sex-determining mechanism of deep-sea mussel *G. platifrons*.

For the result stated above, we suggest that the different methylation levels of sex-related genes in the two sexes and the inconsistent correlation between methylation level and sex-related genes expression level may play an important role for sex determination or differentiation of *G. platifrons* in the deep-sea.

CONCLUSION

In this study, we offer the first report of the gonadal transcriptome and methylome underlying sex determination or differentiation of *G. platifrons* which is the representative deep-sea bivalve in chemosynthetic ecosystem. We identified 161 sex-related genes

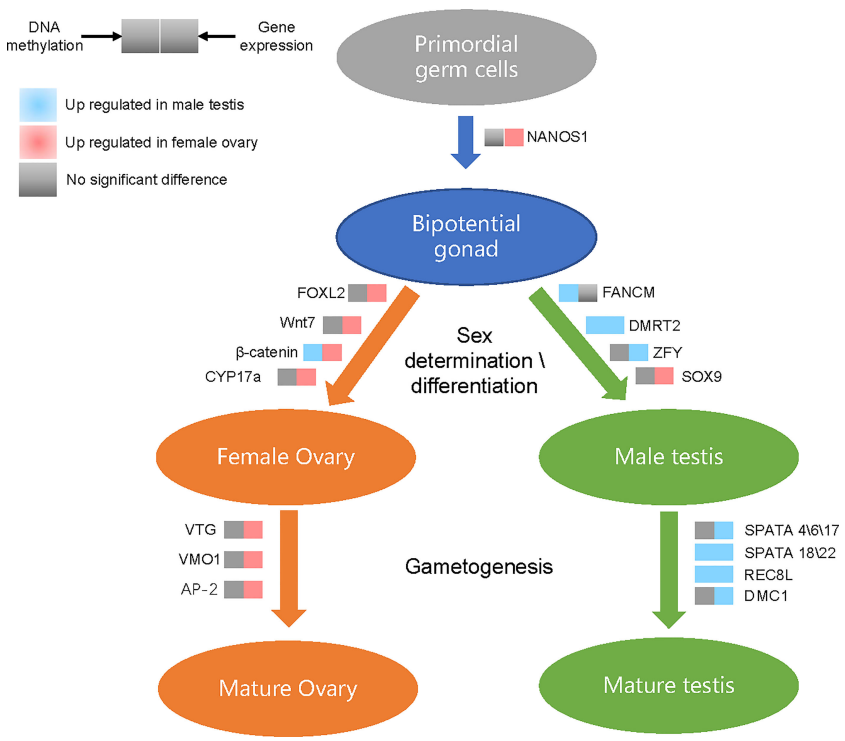

FIGURE 7 | Differentially methylated and differentially expressed genes in the putative sex determination pathway of *G. platifrons*. For each gene presented in the pathway, the methylation (left square) or expression (right square) changes when comparing testes with ovaries are shown by different colors.

that could be involved in sex determination or differentiation, along with the molecular mechanisms of sex determination in *G. platifrons*. Moreover, through the 5mC levels of genes detected, we suggest that hypermethylation phenomenon of male-biased genes are important for male sex differentiation and keeping the sex ratio balanced in deep-sea chemosynthetic ecosystems.

DATA AVAILABILITY STATEMENT

The datasets presented in this study can be found in online repositories. The names of the repository/repositories and accession number(s) can be found below: https://www.ncbi.nlm.nih.gov/, PRJNA789090.

AUTHOR CONTRIBUTIONS

ZZ and MW, conceptualization, methodology, investigation, formal analysis, and writing – original draft. HC, HW, HZ, LZ, LC, CL and ML, samples collection, inverstigation. CLL, conceptualization, supervision, project administration, funding acquisition, writing – review and editing. All authors gave their final approval for publication. All authors contributed to the article and approved the submitted version.

FUNDING

This work was supported by the National Natural Science Foundation of China (grant No. 42106100, 42076091 and 42030407), the Open Research Project of National Major Science and Technology infrastructure (RV KEXUE) (NMSTI-KEXUE2017K01), the Key Research Program of Frontier Sciences, CAS, (No. QYZDB-SSW-DQC036), the Senior User Project of R/V Kexue (No. KEXUE2019GZ02) and the Strategic Priority Research Program of the Chinese Academy of Sciences (XDB42000000).

ACKNOWLEDGMENTS

We thank all the crews onboard the *R/V* Kexue for their assistance in sample collection and all the laboratory staff for continuous technical advice and helpful discussions.

SUPPLEMENTARY MATERIAL

The Supplementary Material for this article can be found online at: https://www.frontiersin.org/articles/10.3389/fmars.2022.856291/full#supplementary-material

REFERENCES

Afonso, L. F., Americo, J. A., Soares-Souza, G. B., Torres, A. L. Q., Wajsenzon, I. J. R., and de Freitas Rebelo, M. (2019). Gonad Transcriptome of Golden Mussel Limnoperna Fortunei Reveals Potential Sex Differentiation Genes. *bioRxiv* doi: 10.1101/818757

Bachtrog, D., Mank, J. E., Peichel, C. L., Kirkpatrick, M., Otto, S. P., Ashman, T. L., et al. (2014). Sex Determination: Why So Many Ways of Doing It? *PloS Biol.* 12 (7), e1001899. doi: 10.1371/journal.pbio.1001899

Barry, J. P., Buck, K. R., Kochevar, R. K., Nelson, D. C., Fujiwara, Y., Goffredi, S. K., et al. (2002). Methane-Based Symbiosis in a Mussel, Bathymodiolus Platifrons, From Cold Seeps in Sagami Bay, Japan. *Invertebrate Biol.* 121 (1), 47–54. doi: 10.1111/j.1744-7410.2002.tb00128.x

Beukeboom, L. W., and Perrin, N. (2014). *The Evolution of Sex Determination* (USA: Oxford University Press).

Boutet, I., Tanguy, A., Le Guen, D., Piccino, P., Hourdez, S., Jollivet, D., et al. (2008). Transcriptomic Approach to Study the Response to Rapid Changes of Temperature in the Hydrothermal Vent Mussel Bathymodiolus Azoricus. *Comp. Biochem. Physiol. Part A.: Mol. Integr. Physiol.* 151, S38–S39. doi: 10.1016/j.cbpa.2008.05.143

Breton, S., Capt, C., Guerra, D., and Stewart, D. (2018). "Sex-Determining Mechanisms in Bivalves," in *Transitions Between Sexual Systems: Understanding the Mechanisms of, and Pathways Between, Dioecy, Hermaphroditism and Other Sexual Systems*. Ed. J. L. Leonard (Cham, Switzerland: Springer International Publishing), 165–192.

Briones, C., Nuñez, J. J., Pérez, M., Espinoza-Rojas, D., Molina-Quiroz, C., and Guiñez, R. (2018). *De Novo* Male Gonad Transcriptome Draft for the Marine Mussel Perumytilus Purpuratus With a Focus on its Reproductive-Related Proteins. *J. Genomics* 6, 127–132. doi: 10.7150/jgen.27864

Cao, L., Lian, C., Zhang, X., Zhang, H., Wang, H., Zhou, L., et al. (2021). *In Situ* Detection of the Fine Scale Heterogeneity of Active Cold Seep Environment of the Formosa Ridge, the South China Sea. *J. Mar. Syst.* 218, 103530. doi: 10.1016/j.jmarsys.2021.103530

Capel, B. (2017). Vertebrate Sex Determination: Evolutionary Plasticity of a Fundamental Switch. *Nat. Rev. Genet.* 18 (11), 675–689. doi: 10.1038/nrg.2017.60

Carney, S. L., Formica, M. I., Divatia, H., Nelson, K., Fisher, C. R., and Schaeffer, S. W. (2006). Population Structure of the Mussel "Bathymodiolus" Childressi From Gulf of Mexico Hydrocarbon Seeps. *Deep Sea Res. Part I: Oceanographic Res. Papers* 53 (6), 1061–1072. doi: 10.1016/j.dsr.2006.03.002

Chen, H., Xiao, G., Chai, X., Lin, X., Fang, J., and Teng, S. (2017). Transcriptome Analysis of Sex-Related Genes in the Blood Clam Tegillarca Granosa. *PloS One* 12 (9), e0184584. doi: 10.1371/journal.pone.0184584

Chen, S., Zhou, Y., Chen, Y., and Gu, J. J. B. (2018). Fastp: An Ultra-Fast All-in-One FASTQ Preprocessor. *Bioinformatics* 34, 17, i884–i890. doi: 10.1093/bioinformatics/bty560

Collin, R. (2013). Phylogenetic Patterns and Phenotypic Plasticity of Molluscan Sexual Systems. *J. Integr. Comp. Biol.* 53 (4), 723–735. doi: 10.1093/icb/ict076

Comtet, T., Le Pennec, M., and Desbruyères, D. (1999). Evidence of a Sexual Pause in Bathymodiolus Azoricus (Bivalvia: Mytilidae) From Hydrothermal Vents of the Mid-Atlantic Ridge. *J. Marine Biol. Assoc. U. K.* 79 (6), 1149–1150. doi: 10.1017/S0025315499001514

Conover, D. O., and Heins, S. W. J. N. (1987). Adaptive Variation in Environmental and Genetic Sex Determination in a Fish 326 (6112), 496–498. doi: 10.1038/326496a0

Du, X., Wang, B., Liu, X., Liu, X., He, Y., Zhang, Q., et al. (2017). Comparative Transcriptome Analysis of Ovary and Testis Reveals Potential Sex-Related Genes and Pathways in Spotted Knifejaw Oplegnathus Punctatus. *Gene* 637, 203–210. doi: 10.1016/j.gene.2017.09.055

Dyson, E. A., and Hurst, G. D. D. (2004). Persistence of an Extreme Sex-Ratio Bias in a Natural Population. *Proc. Natl. Acad. Sci. U.S.A.* 101 (17), 6520–6523. doi: 10.1073/pnas.0304068101

Eckelbarger, K. J., and Young, C. M. (1999). Ultrastructure of Gametogenesis in a Chemosynthetic Mytilid Bivalve (Bathymodiolus Childressi) From a Bathyal, Methane Seep Environment (Northern Gulf of Mexico). *Mar. Biol.* 135 (4), 635–646. doi: 10.1007/s002270050664

Feng, S., Cokus, S. J., Zhang, X., Chen, P.-Y., Bostick, M., Goll, M. G., et al. (2010). Conservation and Divergence of Methylation Patterning in Plants and Animals. *Proc. Natl. Acad. Sci.* 107 (19), 8689–8694. doi: 10.1073/pnas.1002720107

Furukawa, F., Doshimo, Y., Sodeyama, G., Adachi, K., Mori, K., Mori, Y., et al. (2021). Hemocyte Migration and Expression of Four Sox Genes During

Wound Healing in Pacific Abalone, Haliotis Discus Hannai. *Fish & Shellfish Immunology* 117, 24–35. doi: 10.1016/j.fsi.2021.07.011

Gavery, M. R., and Roberts, S. B. (2013). Predominant Intragenic Methylation Is Associated With Gene Expression Characteristics in a Bivalve Mollusc. *PeerJ* 1, e215. doi: 10.7717/peerj.215

Gempe, T., and Beye, M. (2011). Function and Evolution of Sex Determination Mechanisms, Genes and Pathways in Insects. *BioEssays: News Rev. Mol. Cell. Dev. Biol.* 33 (1), 52–60. doi: 10.1002/bies.201000043

Ghiselli, F., Iannello, M., Puccio, G., Chang, P. L., Plazzi, F., Nuzhdin, S. V., et al. (2018). Comparative Transcriptomics in Two Bivalve Species Offers Different Perspectives on the Evolution of Sex-Biased Genes. *Genome Biol. Evol.* 10 (6), evy082–evy082. doi: 10.1093/gbe/evy082

Ghiselli, F., Milani, L., Chang, P. L., Hedgecock, D., Davis, J. P., Nuzhdin, S. V., et al. (2012). *De Novo* Assembly of the Manila Clam Ruditapes Philippinarum Transcriptome Provides New Insights Into Expression Bias, Mitochondrial Doubly Uniparental Inheritance and Sex Determination. *Mol. Biol. Evol.* 29 (2), 771–786. doi: 10.1093/molbev/msr248

Gonzalez-Castellano, I., Manfrin, C., Pallavicini, A., and Martinez-Lage, A. (2019). *De Novo* Gonad Transcriptome Analysis of the Common Littoral Shrimp Palaemon Serratus: Novel Insights Into Sex-Related Genes. *BMC Genomics* 20 (1), 757. doi: 10.1186/s12864-019-6157-4

Gross, L. (2006). Male or Female? It Depends on the Dose. *PloS Biol.* 4 (6), e211–e211. doi: 10.1371/journal.pbio.0040211

Huang, S., Ye, L., and Chen, H. (2017). Sex Determination and Maintenance: The Role of DMRT1 and FOXL2. *Asian J. Androl.* 19 (6), 619–624. doi: 10.4103/1008-682X.194420

Jones, W. J., Won, Y. J., Maas, P. A. Y., Smith, P. J., Lutz, R. A., and Vrijenhoek, R. C. (2005). Evolution of Habitat Use by Deep-Sea Mussels. *Marine Biol.* 148 (4), 841–851. doi: 10.1007/s00227-005-0115-1

Kádár, E., Lobo-da-Cunha, A., Santos, R. S., and Dando, P. (2006). Spermatogenesis of Bathymodiolus Azoricus in Captivity Matching Reproductive Behaviour at Deep-Sea Hydrothermal Vents. *J. Exp. Marine Biol. Ecol.* 335 (1), 19–26. doi: 10.1016/j.jembe.2006.02.016

Kashimada, K., and Koopman, P. (2010). Sry: The Master Switch in Mammalian Sex Determination. *Development* 137 (23), 3921–3930. doi: 10.1242/dev.048983

Kocer, A., Pinheiro, I., Pannetier, M., Renault, L., Parma, P., Radi, O., et al. (2008). R-Spondin1 and FOXL2act Into Two Distinct Cellular Types During Goat Ovarian Differentiation. *BMC Dev. Biol.* 8 (1), 36. doi: 10.1186/1471-213X-8-36

Laming, S. R., Duperron, S., Cunha, M. R., and Gaudron, S. M. (2014). Settled, Symbiotic, Then Sexually Mature: Adaptive Developmental Anatomy in the Deep-Sea, Chemosymbiotic Mussel Idas Modiolaeformis. *Mar. Biol.* 161 (6), 1319–1333. doi: 10.1007/s00227-014-2421-y

Laming, S. R., Gaudron, S. M., and Duperron, S. (2018). Lifecycle Ecology of Deep-Sea Chemosymbiotic Mussels: A Review. *Front. Mar. Sci.* 5 (282). doi: 10.3389/fmars.2018.00282

Li, S. F., Lv, C. C., Lan, L. N., Jiang, K. L., Zhang, Y. L., Li, N., et al. (2021). DNA Methylation Is Involved in Sexual Differentiation and Sex Chromosome Evolution in the Dioecious Plant Garden Asparagus. *Hortic. Res.* 8 (1), 198. doi: 10.1038/s41438-021-00633-9

Lin, J. Q., Yu, J., Sun, L., and Fang, S. G. (2021). Genome-Wide DNA Methylation and Transcriptome Analyses Reveal Epigenetic and Genetic Mechanisms Underlying Sex Maintenance of Adult Chinese Alligator. *Front. Genet.* 12. doi: 10.3389/fgene.2021.655900

Liu, C. F., Bingham, N., Parker, K., and Yao, H. H. (2009). Sex-Specific Roles of Beta-Catenin in Mouse Gonadal Development. *Hum. Mol. Genet.* 18 (3), 405–417. doi: 10.1093/hmg/ddn362

Liu, X.-L., Zhang, Z.-F., Shao, M.-Y., Liu, J.-G., and Muhammad, F. (2012). Sexually Dimorphic Expression of Foxl2 During Gametogenesis in Scallop Chlamys Farreri, Conserved With Vertebrates. *Dev. Genes Evol.* 222 (5), 279–286. doi: 10.1007/s00427-012-0410-z

Li, Y., Zhang, L., Li, Y., Li, W., Guo, Z., Li, R., et al. (2019). Dynamics of DNA Methylation and DNMT Expression During Gametogenesis and Early Development of Scallop Patinopecten Yessoensis. *Mar. Biotechnol. (NY)* 21 (2), 196–205. doi: 10.1007/s10126-018-09871-w

Li, R., Zhang, L., Li, W., Zhang, Y., Li, Y., Zhang, M., et al. (2018). FOXL2 and DMRT1L Are Yin and Yang Genes for Determining Timing of Sex Differentiation in the Bivalve Mollusk Patinopecten Yessoensis. *Front. Physiol.* 9, 1166. doi: 10.3389/fphys.2018.01166

Li, Y., Zhang, L., Sun, Y., Ma, X., Wang, J., Li, R., et al. (2016). Transcriptome Sequencing and Comparative Analysis of Ovary and Testis Identifies Potential Key Sex-Related Genes and Pathways in Scallop Patinopecten Yessoensis. *Marine Biotechnol.* 18 (4), 453–465. doi: 10.1007/s10126-016-9706-8

Lorion, J., Kiel, S., Faure, B., Kawato, M., Ho, S. Y., Marshall, B., et al. (2013). Adaptive Radiation of Chemosymbiotic Deep-Sea Mussels. *Proc. Biol. Sci.* 280 (1770), 20131243. doi: 10.1098/rspb.2013.1243

Matson, C. K., Murphy, M. W., Sarver, A. L., Griswold, M. D., Bardwell, V. J., and Zarkower, D. (2011). DMRT1 Prevents Female Reprogramming in the Postnatal Mammalian Testis. *Nature* 476 (7358), 101–104. doi: 10.1038/nature10239

Matson, C. K., and Zarkower, D. (2012). Sex and the Singular DM Domain: Insights Into Sexual Regulation, Evolution and Plasticity. *Nat. Rev. Genet.* 13 (3), 163–174. doi: 10.1038/nrg3161

Nagahama, Y., Chakraborty, T., Paul-Prasanth, B., Ohta, K., and Nakamura, M. (2021). Sex Determination, Gonadal Sex Differentiation, and Plasticity in Vertebrate Species. *Physiol. Rev.* 101 (3), 1237–1308. doi: 10.1152/physrev.00044.2019

Naimi, A., Martinez, A.-S., Specq, M.-L., Diss, B., Mathieu, M., and Sourdaine, P. (2009). Molecular Cloning and Gene Expression of Cg-Foxl2 During the Development and the Adult Gametogenetic Cycle in the Oyster Crassostrea Gigas. *Comp. Biochem. Physiol. Part B.: Biochem. Mol. Biol.* 154 (1), 134–142. doi: 10.1016/j.cbpb.2009.05.011

Navarro-Martin, L., Vinas, J., Ribas, L., Diaz, N., Gutierrez, A., Di Croce, L., et al. (2011). DNA Methylation of the Gonadal Aromatase (cyp19a) Promoter Is Involved in Temperature-Dependent Sex Ratio Shifts in the European Sea Bass. *PloS Genet.* 7 (12), e1002447. doi: 10.1371/journal.pgen.1002447

Olson, C. E., and Roberts, S. B. (2014). Genome-Wide Profiling of DNA Methylation and Gene Expression in Crassostrea Gigas Male Gametes. *Front. Physiol.* 5. doi: 10.3389/fphys.2014.00224

Pennec, M. L., and Beninger, P. G. (1997). Ultrastructural Characteristics of Spermatogenesis in Three Species of Deep-Sea Hydrothermal Vent Mytilids. *Can. J. Zool.* 75 (75), 308–316. doi: 10.1139/z97-039

Quinn, A. E., Sarre, S. D., Ezaz, T., Marshall Graves, J. A., and Georges, A. (2011). Evolutionary Transitions Between Mechanisms of Sex Determination in Vertebrates. *Biol. Lett.* 7 (3), 443–448. doi: 10.1098/rsbl.2010.1126

Radhakrishnan, S., Literman, R., Neuwald, J. L., and Valenzuela, N. (2018). Thermal Response of Epigenetic Genes Informs Turtle Sex Determination With and Without Sex Chromosomes. *Sex Dev.* 12 (6), 308–319. doi: 10.1159/000492188

Riviere, G., Wu, G.-C., Fellous, A., Goux, D., Sourdaine, P., and Favrel, P. J. M. B. (2013). DNA Methylation is Crucial for the Early Development in the Oyster C. *Gigas* 15 (6), 739–753. doi: 10.1007/s10126-013-9523-2

Rossi, G. S., and Tunnicliffe, V. (2017). Trade-Offs in a High CO2 Habitat on a Subsea Volcano: Condition and Reproductive Features of a Bathymodioline Mussel. *Marine Ecol. Prog. Ser.* 574, 49–64. doi: 10.3354/meps12196

Sarre, S. D., Georges, A., and Quinn, A. (2004). The Ends of a Continuum: Genetic and Temperature-Dependent Sex Determination in Reptiles. *Bioessays* 26 (6), 639–645. doi: 10.1002/bies.20050

Shao, C., Li, Q., Chen, S., Zhang, P., Lian, J., Hu, Q., et al. (2014). Epigenetic Modification and Inheritance in Sexual Reversal of Fish. *Genome Res.* 24 (4), 604–615. doi: 10.1101/gr.162172.113

Sinclair, A. H., Berta, P., Palmer, M. S., Hawkins, J. R., Griffiths, B. L., Smith, M. J., et al. (1990). A Gene From the Human Sex-Determining Region Encodes a Protein With Homology to a Conserved DNA-binding Motif. *Nature* 346 (6281), 240–244. doi: 10.1038/346240a0

Smith, C. A., Roeszler, K. N., Ohnesorg, T., Cummins, D. M., Farlie, P. G., Doran, T. J., et al. (2009). The Avian Z-linked Gene DMRT1 Is Required for Male Sex Determination in the Chicken. *Nature* 461 (7261), 267–271. doi: 10.1038/nature08298

Stenyakina, A., Walters, L., Hoffman, E., and Calestani, C. (2009). Food Availability and Sex Reversal in Mytella Charruana, an Introduced Bivalve in the Southeastern United States. *Mol. Reprod. Dev.* 77, 222–230. doi: 10.1002/mrd.21132

Sun, Y., Wang, M., Li, L., Zhou, L., Wang, X., Zheng, P., et al. (2017b). Molecular Identification of Methane Monooxygenase and Quantitative Analysis of Methanotrophic Endosymbionts Under Laboratory Maintenance in

Bathymodiolus Platifrons From the South China Sea. *PeerJ* 5, e3565. doi: 10.7717/peerj.3565

Sun, J., Zhang, Y., Xu, T., Zhang, Y., Mu, H., Zhang, Y., et al. (2017a). Adaptation to Deep-Sea Chemosynthetic Environments as Revealed by Mussel Genomes. *Nat. Ecol. Evol.* 1 (5). doi: 10.1038/s41559-017-0121

Tachibana, M. (2015). Epigenetic Regulation of Mammalian Sex Determination. *J. Med. Invest.* 62 (1-2), 19–23. doi: 10.2152/jmi.62.19

Teaniniuraitemoana, V., Huvet, A., Levy, P., Klopp, C., Lhuillier, E., Gaertner-Mazouni, N., et al. (2014). Gonad Transcriptome Analysis of Pearl Oyster Pinctada Margaritifera: Identification of Potential Sex Differentiation and Sex Determining Genes. *BMC Genomics* 15 (1), 491. doi: 10.1186/1471-2164-15-491

Tyler, P. A., Marsh, L., Baco-Taylor, A., and Smith, C. R. (2009). Protandric Hermaphroditism in the Whale-Fall Bivalve Mollusc Idas Washingtonia. *Deep Sea Res. Part II: Topical Stud. Oceanography* 56 (19-20), 1689–1699. doi: 10.1016/j.dsr2.2009.05.014

Tyler, P., Young, C. M., Dolan, E., Arellano, S. M., Brooke, S. D., and Baker, M. (2007). Gametogenic Periodicity in the Chemosynthetic Cold-Seep Mussel "Bathymodiolus" Childressi. *Marine Biol.* 150 (5), 829–840. doi: 10.1007/s00227-006-0362-9

Uhlenhaut, N. H., Jakob, S., Anlag, K., Eisenberger, T., Sekido, R., Kress, J., et al. (2009). Somatic Sex Reprogramming of Adult Ovaries to Testes by FOXL2 Ablation. *Cell* 139 (6), 1130–1142. doi: 10.1016/j.cell.2009.11.021

Villamor, S., and Yamamoto, T. (2015). Reproductive Seasonality of Monetaria Annulus (Linnaeus 1758) (Mollusca: Gastropoda: Cypraeidae) in a Temperate Area. *Molluscan Res.* 35 (2), 95–101. doi: 10.1080/13235818.2014.954660

Wang, X., Li, Q., Lian, J., Li, L., Jin, L., Cai, H., et al. (2014). Genome-Wide and Single-Base Resolution DNA Methylomes of the Pacific Oyster Crassostrea Gigas Provide Insight Into the Evolution of Invertebrate CpG Methylation. *BMC Genomics* 15 (1), 1–12. doi: 10.1186/1471-2164-15-1119

Wang, L., Yue, F., Song, X., Song, L. J. D., and Immunology, C. (2015). Maternal Immune Transfer in Mollusc 48, 2, 354–359. doi: 10.1016/j.dci.2014.05.010

Wan, Z. Y., Xia, J. H., Lin, G., Wang, L., Lin, V. C., and Yue, G. H. (2016). Genome-Wide Methylation Analysis Identified Sexually Dimorphic Methylated Regions in Hybrid Tilapia. *Sci. Rep. Developmental & Comparative Immunology* 6, 35903. doi: 10.1038/srep35903

Wen, A. Y., You, F., Sun, P., Li, J., Xu, D. D., Wu, Z. H., et al. (2014). Cpg Methylation of Dmrt1 and cyp19a Promoters in Relation to Their Sexual Dimorphic Expression in the Japanese Flounder Paralichthys Olivaceus. *J. Fish Biol.* 84 (1), 193–205. doi: 10.1111/jfb.12277

Wittkopp, P. J., Haerum, B. K., and Clark, A. G. (2004). Evolutionary Changes in Cis and Trans Gene Regulation. *Nature* 430 (6995), 85–88. doi: 10.1038/nature02698

Xu, M., Fang, M., Yang, Y., Dick, J. T. A., Song, H., Luo, D., et al. (2016). Spatial Variation in Adult Sex Ratio Across Multiple Scales in the Invasive Golden Apple Snail, Pomacea Canaliculata. *Ecol. Evol.* 6 (8), 2308–2317. doi: 10.1002/ece3.2043

Yang, L., Zhang, X., Liu, S., Zhao, C., Miao, Y., Jin, L., et al. (2021). Cyp17a1 is Required for Female Sex Determination and Male Fertility by Regulating Sex Steroid Biosynthesis in Fish. *Endocrinology* 162 (12). doi: 10.1210/endocr/bqab205

Yao, H., Lin, Z., Dong, Y., Kong, X., He, L., and Xue, L. (2021).). Gonad Transcriptome Analysis of the Razor Clam (Sinonovacula Constricta) Revealed Potential Sex-Related Genes. *Front. Mar. Sci.* 8. doi: 10.3389/fmars.2021.725430

Zarkower, D. (2013). ""Chapter Twelve - DMRT Genes in Vertebrate Gametogenesis,"," in *Current Topics in Developmental Biology*. Ed. P. M. Wassarman (San Diego, CA, USA: Academic Press), 327–356.

Zhang, N., Xu, F., and Guo, X. (2014). Genomic Analysis of the Pacific Oyster (Crassostrea Gigas) Reveals Possible Conservation of Vertebrate Sex Determination in a Mollusc. *G3 (Bethesda Md)* 4 (11), 2207. doi: 10.1534/g3.114.013904

Zhong, Z., Wang, M., Chen, H., Zheng, P., and Li, C. (2020). Gametogenesis and Reproductive Traits of the Cold-Seep Mussel Gigantidas Platifrons in the South China Sea. *J. Oceanol. Limnol.* 38 (4), 1304–1318. doi: 10.1007/s00343-020-0027-4

Conflict of Interest: The authors declare that the research was conducted in the absence of any commercial or financial relationships that could be construed as a potential conflict of interest.

Publisher's Note: All claims expressed in this article are solely those of the authors and do not necessarily represent those of their affiliated organizations, or those of the publisher, the editors and the reviewers. Any product that may be evaluated in this article, or claim that may be made by its manufacturer, is not guaranteed or endorsed by the publisher.

frontiers | Frontiers in Marine Science

REVIEW
published: 21 June 2022
doi: 10.3389/fmars.2022.906267

Single-Cell Sequencing on Marine Life: Application and Future Development

Jing Li[1,2†], *Hao Wang*[1†] *and Chaolun Li*[1,2,3*]

[1] Center of Deep-Sea Research, Institute of Oceanology, Chinese Academy of Sciences, Qingdao, China, [2] University of Chinese Academy of Sciences, Beijing, China, [3] Laboratory for Marine Ecology and Environmental Science, Qingdao National Laboratory for Marine Science and Technology, Qingdao, China

Single-cell RNA-sequencing (scRNA-seq) is the genomic approach that directly examines gene expression information from individual cells and provides a higher resolution of cellular differences than bulk RNA-seq. In the past decade, with the rapid development of microfluid, barcoding, and next-generation sequencing (NGS) technologies, scRNA-seq has revolutionized transcriptomic studies and gained great success and broad prospects. However, compared with the wide use in the few model animals, the application of scRNA-seq in marine organisms is limited due to the high cost of early scRNA-seq and the immature of single-cell methods for marine organisms. Recently, with the increase of genomic data, maturation of scRNA-seq platform and downstream bioinformatics algorithms, the scRNA-seq has been successfully applied in several marine model animals with great success, which demonstrated that the scRNA-seq could be the ideal and powerful tool to extend our understanding of marine organisms' evolutionary and physiological processes and their adaptation to ecological niches. Here, we review the state-of-the-art improvements of single-cell sequencing techniques and new studies that apply single-cell methods to marine organisms. We also summarize the opportunities and challenges scientists may face in further single-cell research and propose several appealing prospects that may benefit from the combination of single-cell techniques and marine organisms.

Keywords: scRNA-seq, marine organism, snRNA-seq, future directions, cell isolation method

OPEN ACCESS

Edited by:
Taewoo Ryu,
Okinawa Institute of Science and Technology Graduate University, Japan

Reviewed by:
Yi Lan,
Hong Kong University of Science and Technology, Hong Kong, SAR China
Jack Chi-Ho Ip,
Hong Kong Baptist University, Hong Kong, SAR China

***Correspondence:**
Chaolun Li
lcl@qdio.ac.cn

[†]*These authors share first authorship*

Specialty section:
This article was submitted to Marine Biology, a section of the journal Frontiers in Marine Science

Received: *28 March 2022*
Accepted: *18 May 2022*
Published: *21 June 2022*

Citation:
Li J, Wang H and Li C (2022) Single-Cell Sequencing on Marine Life: Application and Future Development. Front. Mar. Sci. 9:906267. doi: 10.3389/fmars.2022.906267

1 INTRODUCTION

Single-cell sequencing examines the sequence information from individual cells, provding a higer resolution of cellular differences and a better understanding of the function of an individual cell in its microenvironment (Eberwine et al., 2014). With the advances in molecular biology, microfluidics and nanotechnology, single-cell sequencing methods have experienced rapid development (Stuart and Satija, 2019). From the in-depth analysis of gene expressions in only a few precious cells (Tang et al., 2009), to the establishment of high-throughput single-cell sequencing platforms (Zheng et al., 2017), the single-cell sequencing technology has gradually become a practical and efficient way to unravel the gene expression shifts among different cell subpopulations and was selected as the

"Method of the Year for 2013" by *Nature Methods* for its potential in understanding life one cell at a time (Nature Method Editorial Board, 2014). Among the single-cell techniques (**Figure 1A**), single-cell RNA sequencing (scRNA-seq) is one of the most widely used, with a range of protocols for sensitive and accurate sequencing being introduced in the last decade (Svensson et al., 2017). The unique advantage of scRNA-seq over typical RNA sequencing methods is the ability to eliminate the influence of averaging signals caused by the cell homogenate procedures and distinguish expression changes due to gene regulations from those due to shifts among cell types as well (Trapnell, 2015).

Typical RNA sequencing methods generally inform about the average gene expression across the overall cell population and this expression level of RNA is estimated across all cells of each subpopulation. Hence, this approach has missed the fact that individual cells could have patterns of expression that are very different from the average expression (Hong et al., 2020). Such cell-to-cell variability have important biological implications that can be deciphered by scRNA-seq data, which provide information about the degree of significance and meaning of a specific proportion of cells with a specific gene expression pattern (Gupta and Kuznicki, 2020).Therefore, scRNA-seq is an ideal method to better understand the function of multicellular tissues or organisms.

Understanding the cellular heterogeneity in diseased tissue can significantly promote the identification of precise drug targets and possibly develop new therapeutic approaches, single-cell sequencing was first put into practice in pharmaceutical and medical science (Tang et al., 2009). The possible applications of scRNA-seq are wide-ranging, including identifying stem cells, discovering new biomarkers, and detecting transcriptomic trajectories within the cell population. Consequently, numbers of articles concerning the application of scRNA-seq have greatly increased. Hitherto, scRNA-seq has been widely used not only in medicine, but also in biology, ecology and other fields (**Figure 1B**).

Compared to these disciplines above, marine biology has remained a brand new area for single-cell studies. As the ocean covers 70% of the earth surface and provides about 90% of the living space on the planet, marine lives are characterized by the incomparable diversity of both species and genes (Poore and Wilson, 1993). Recently, with the rapid development of scRNA-seq techniques, single-cell sequencing on marine organisms has promising perspectives,such as the application on studying marine life evolutionalry-development, symbiosis, stem cell and cell regeneration mechanism (Cao et al., 2019; Siebert et al., 2019; Hu et al., 2020; Zhang et al., 2020; Chari et al., 2021; Levy et al., 2021). Here, we review the development of scRNA-seq techniques, the single-cell data analysis methods, and highlight some recent improvements. We then discuss the opportunities of applying scRNA-seq techniques on marine organisms by summarizing the recent subcellular studies of marine multicellular organisms. Furthermore, we also argue

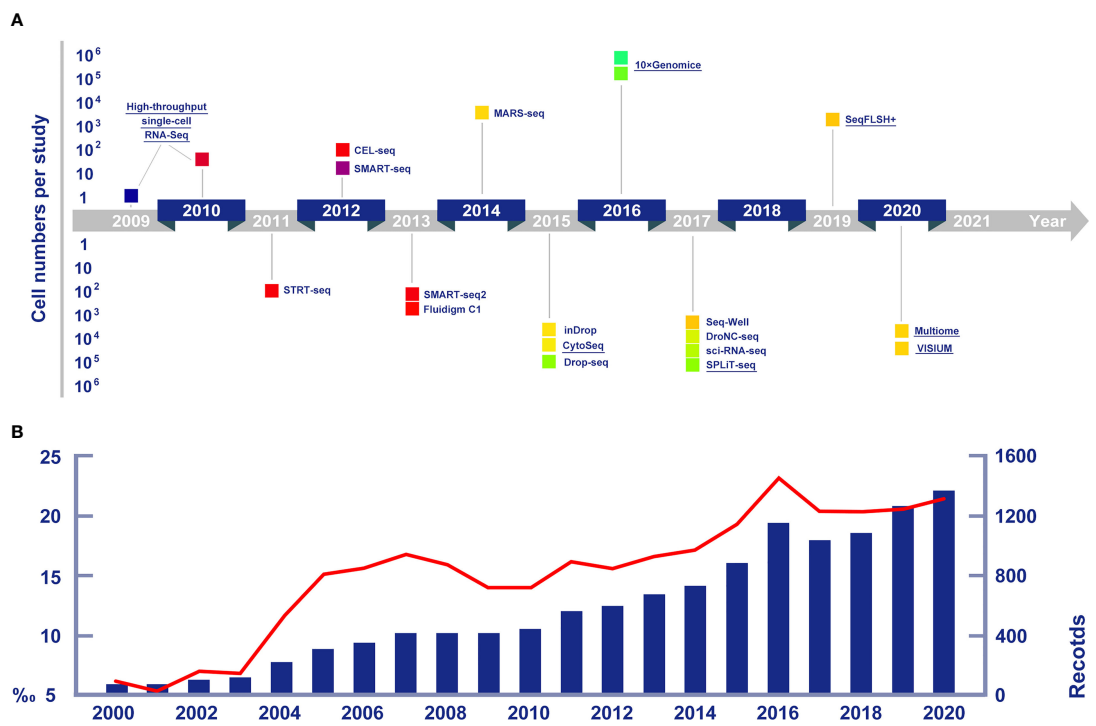

FIGURE 1 | **(A)** Cell numbers reported in publications and crucial single cell sequencing technologies in chronological arrangement. Technologies mentioned in detail in this article are highlighted by underlines. Data of new technologies are collected from Eng et al. (2019, seqFISH+), Bravo et al. (2020, 10x Multiome) and Longo et al. (2021, VISIUM). **(B)** The increasing trends of publications on marine life RNA sequencing research (the blue histogram), and the growing proportions of marine life research among all RNA sequencing studies (the red line chart).

the perspectives and possible challenges scientists might face in further studies of single-cell sequencing of marine organisms.

2 PROGRESSES OF SINGLE-CELL SEQUENCING

2.1 Development of Single-Cell Sequencing Techniques

The expression of individual genes from single cells was measured for the first time in 1992 by Eberwine et al. (1992). This study uses a sophisticated approach based on *in vivo* reverse transcription (RT) followed by amplification through *in vitro* transcription (IVT). Subsequently, simpler methods based on polymerase chain reaction (PCR) emerged, leading to scaling up of the number of cells and genes assayed over the years (Lambolez et al., 1992; Sheng et al., 1994; Peixoto et al., 2004). Eventually, untargeted single-cell mRNA amplification techniques were developed, which allowed researchers to perform transcriptome-wide studies using microarrays (Kurimoto et al., 2006; Esumi et al., 2008; Kurimoto et al., 2007; Tietjen et al., 2003). Building upon this, Tang et al. (2009) adapted the technologies to make them compatible with high-throughput DNA sequencing, which allowed a completely unbiased transcriptome-wide investigation of the mRNA in a single cell for the first time. During the past decade, advances in molecular biology, microfluidics and nanotechnology have given rise to a multitude of single-cell sequencing technologies.

2.1.1 Single-Cell Sequencing Methods

The scRNA-seq is one of the most widely used single-cell sequencing approaches, with a range of technologies for sensitive, highly multiplexed, or combinatorically barcoded profiling (Hashimshony et al., 2012; Ramsköld et al., 2012; Jaitin et al., 2014; Macosko et al., 2015). The collection of single cells is fundamental to scRNA-seq, and the cell separation techniques are becoming increasingly convenient and efficient thanks to the developments in molecular biology, microfluidics and nanotechnology (Stuart and Satija, 2019). Meanwhile, scRNA-seq has inspired a variety of complementary single-cell genomic, epigenomic and proteomic profiling technologies (Shapiro et al., 2013). Recently, scRNA-seq techniques have been widely used to differentiate cell populations (Plass et al., 2018; Koiwai et al., 2021), explore the dynamics of developmental biological processes (Farrell et al., 2018; Cao et al., 2019; Pijuan-Sala et al., 2019; Soria et al., 2020), and identify gene regulatory networks (Wagner et al., 2018). Alternatively, Grindberg et al. (2013) have promoted another set of single-cell sequencing technical procedures called the single-nuclei RNA-seq (snRNA-seq). This method focuses on the transcriptomic expression in single nuclei instead of whole cells, in order to solve the problem that some cells are too large to be manipulated by microfluids. In addition, the advantage of snRNA-seq is the application of a rapid dissociation protocol. This protocol can reduce the likelihood of aberrant transcription, and minimize abnormal gene expression due to the absence of ribosomes that are located in the cytoplasm (Lacar et al., 2016).

Besides single cell transcriptome sequencing, epigenomes of cells can also be obtained by sequencing the non-coding genomic regions in chromatins (Baek and Lee, 2020). An assay for Transposase Accessible Chromatin with high-throughput sequencing (ATAC-seq) was designed to identify open chromatin regions in the genome and to depict the epigenomes of cell bulks (Buenrostro et al., 2013). Using a novel sequencing method named single-cell ATAC-seq (scATAC-seq), the chromatin accessibility landscape at the single-cell level is profiled. The sequencing result can be used to uncover the mechanisms regulating cell-to-cell heterogeneity (Chen et al., 2019). Conventional ATAC-seq is an ensemble measure of open chromatin that uses the prokaryotic Tn5 transposase to tag regulatory regions by inserting sequencing adapters into accessible regions of the genome (Buenrostro et al., 2013). In scATAC-seq, individual cells are captured and assayed using a programmable microfluidics platform, and after being amplified and sequenced, the DNA accessibility maps of each individual cell can be generated. In contrast to bulk ATAC-seq data, data from scATAC-seq include more information, such as the fragment-size periodicity corresponding to integer multiples of nucleosomes and strong enrichment of fragments within regions of accessible chromatin (Buenrostro et al., 2015). Combined with scRNA-seq, scATAC-seq has been launched on a new single cell manipulation platform called 10x Multiome®. Multiomic studies based on the conjoint analysis of transcriptomic and epigenetic data have become practical since then, and recently, Bravo González-Blas et al. (2020) firstly used this platform to achieve multiomic analysis of *Drosophila* eye-antennal disc cells.

2.1.2 Single-Cell Sequencing Platforms

The most challenging issue in successful application scRNA-seq is to isolate high quality single cells with minimal disruption of the cell's native expression profile (Valihrach et al., 2018). As a result, many cell isolation protocols were introduced to isolate individual cells for sample preparation, after which the cells should become well dispersed and intact. Traditional single cell isolation technologies include micromanipulation (Woyke et al., 2009), fluorescence-activated cell sorting (FACS, Stepanauskas and Sieracki, 2007), and laser capture microdissection (LCM) (Ishii et al., 2010). Micromanipulation is the most conventional method of isolating single cells and relies on visual control to obtain pure cell populations. The main obstacle of micromanipulation is its inefficiency and low magnification due to limited resolution (Hohnadel et al., 2018). FACS measures the interactions of light with characteristics such as cell size, granularity and fluorescent structures or stains. LCM can isolate single cells, not in fluid suspension but cutting single cells in tissue sample sections.

In the past decade, many high-throughput platforms implementing single-cell sequencing have emerged (**Figure 2**), leading to an exponential increase in the number of cells assayed in one experiment and the expected boost of single-cell multi-omics data (Svensson et al., 2018).The most widely used modern

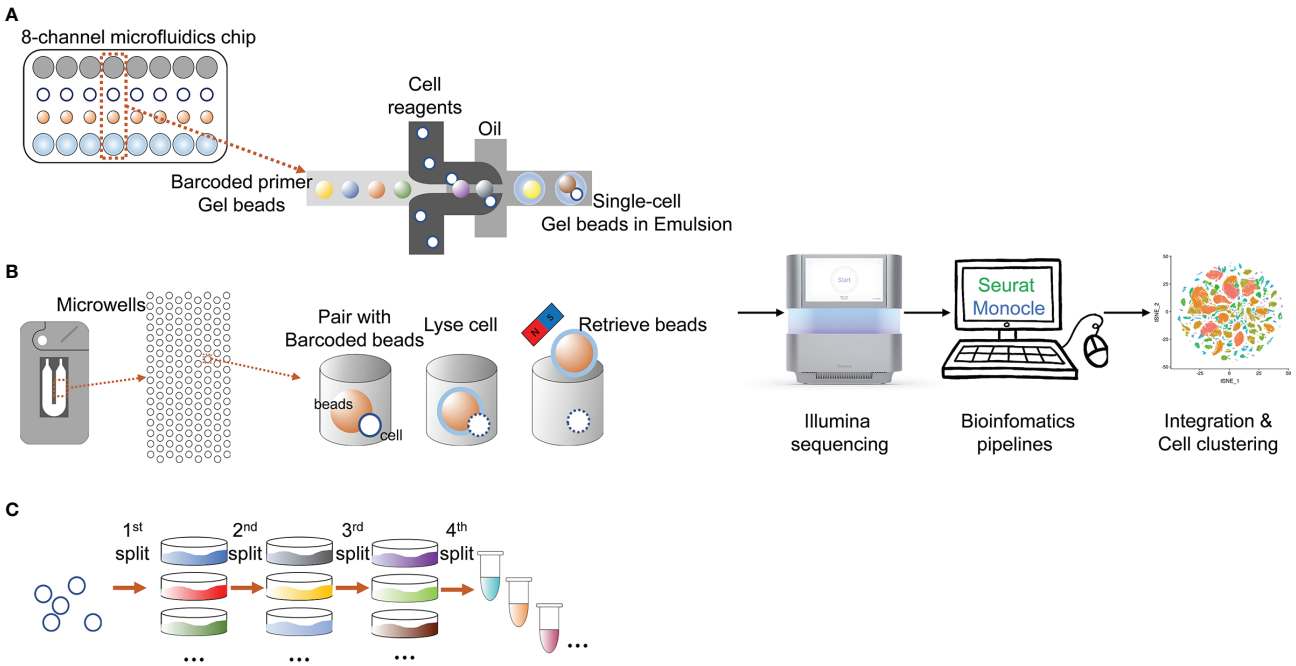

FIGURE 2 | State-of-the-art cell isolation methods and the main procedures of different scRNA-seq technologies. **(A)** microfluids; **(B)** microchips; **(C)** SPLiT-seq.

cell isolation method is the droplet microfluidic technology. This technology typically involves the steps of encapsulating single cells in droplets in an inert carrier oil. The usage of carrier oil allows the droplets to be moved, merged and stored (Hwang et al., 2018). Performing on up to thousands of cells in seconds, the high-throughput and efficiency of this technology make it ideal for large-scale application (Choi et al., 2020). Based on this droplet microfluidic technology, the Chromium System (10x Genomics®) was launched in 2016 as a scalable platform for the characterization and profiling of hundreds to millions of cells (Zheng et al., 2017). The gel beads contain barcoded oligonucleotides that are mixed with reversed transcription (RT) reagents and cells in oil environment that create the droplets, wherein the cDNA is synthesized. Droplets are then pooled, dissolved, and a cDNA library containing unique molecular identifiers (UMI) is prepared. It is currently the most popular instrument for high-throughput single-cell analysis judging from the high number of publications on its application.

Another modern cell isolation method is derived from nanowell technologies. Compared to droplet multifluidic technologies, nanowell technologies have advantages including a short cell-loading period, low reagent and sample volumes and compatibility with optical imaging (Valihrach et al., 2018). The ability to perform optical imaging allows users to examine and tune cell loading density, identify multiplets, and determine cell viabilities (Choi et al., 2020). The Rhapsody Single-Cell Analysis System (BD®) is a new instrument based on nanowell technologies, and is currently the only commercial high-throughput system that is not based on droplet technology (Valihrach et al., 2018). The Rhapsody system is based on arrays of 200,000 microwells with UMI-barcoded magnetic beads capable of capturing up to 20,000 single cells. Captured cells are lysed, and mRNA is bound to the beads. Due to the optical imaging ability, it can help users to decide how many beads are optimal for library preparation and if the quality of the sample is sufficient for downstream analysis. The remaining beads may be stored for later use (Valihrach et al., 2018).

Split-pool is an efficient and economical tool to isolate and individually barcode cells. Accordingly, Split-Pool Ligation-based Transcriptome sequencing (SPLiT-seq) is a low-cost, scRNA-seq platform that enables transcriptional profiling of hundreds of thousands of fixed cells or nuclei in a single experiment (Rosenberg et al., 2018). The most representative feature of SPLiT-seq is that no other instruments are required when applying this technique (Rosenberg et al., 2018). SPLiT-seq was recently introduced by Rosenberg et al. (2018) in their research on the development of the mouse brain and spinal cord. In SPLiT-seq, individual transcriptomes are uniquely labelled by passing a suspension of formaldehyde-fixed cells or nuclei through four rounds of combinatorial barcoding. After sequencing, each transcriptome is assembled by combining reads containing the same four-barcode combination. Four rounds of combinatorial barcoding can yield about 2×10^7 barcode combinations, enough to uniquely label over 1 million cells. By applying SPLiT-seq rather than conventional scRNA-seq platforms, the cellular origin of RNA in multicellular systems was successfully labelled.

The past decades witnessed the sustained efforts that have been made in developing single-cell sequencing techniques and single cell manipulating platforms, which has greatly enhanced

researchers' ability to handle a large number of single cells from diverse sources. Integrating these advancements together, single-cell sequencing achieves breakthroughs in numerous research areas and finally draws great public attention. As a result, the application of scRNA-seq or other substitute single-cell sequencing techniques in marine organisms is pressing and promising.

2.2 Development of ScRNA-Seq Data Analysis Methods

Recent advances in single-cell isolation and barcoding technologies have enabled DNA and mRNA profiles to be measured at single-cell resolution. The boost of single-cell transcriptome and genome databases calls for multiple analysis methods to characterize cell types and their functions regarding pathophysiological processes based on molecular signatures (Lee and Hwang, 2020). ScRNA-seq analysis provides abundant information of cell populations, regulatory networks, and cellular trajectories at the single-cell level (Hwang et al., 2018, **Figure 3**). Different methods have been developed for each kind of information to achieve diverse goals based on the corresponding information.

First, for cell population characterization, the methods cluster cells based on the similarity of the expression profile and identify marker genes that are predominantly expressed in each cell cluster. Cell population characterization is based on the combination of dimensionality reduction and clustering analysis. As for dimensionality reduction methods, a linear method, principal component analysis (PCA, Wold et al., 1987), and a nonlinear method, t-distributed stochastic neighbour embedding (t-SNE, Van der Maaten and Hinton, 2008), have both been widely used. Similar to t-SNE, uniform manifold approximation and projection (UMAP) is another nonlinear dimensionality reduction method, with more preservation of the global data structure and faster computing runtime (Becht et al., 2019). Recently, methods dealing with zero-inflated data or based on neural network models have also been developed (Qi et al., 2020).

Clustering methods aim to group data objects into multiple classes or clusters so that objects in the same cluster are similar and different from objects in other clusters. They are categorized into two types based on the quantification of similarity. Clustering based on distance, such as K-means (Wong and Hartigan, 1979) and X-means (Ishioka, 2000), clusters similar objects close to each other, while clustering based on a probability distribution model (EM algorithm, Dempster et al., 1977) finds a set of objects in a group of objects that conform to a specific distribution model. Popular clustering analysis methods include Seurat (Pollen et al., 2014), BackSPIN70 (Guo and Xu, 2018), and SNN-cliq (Guo et al., 2015).

Second, another set of methods are able to infer regulatory networks. By delineating regulatory relationships among marker genes, this set of methods can show co-expression across different cells in a cell population. The analysis of gene

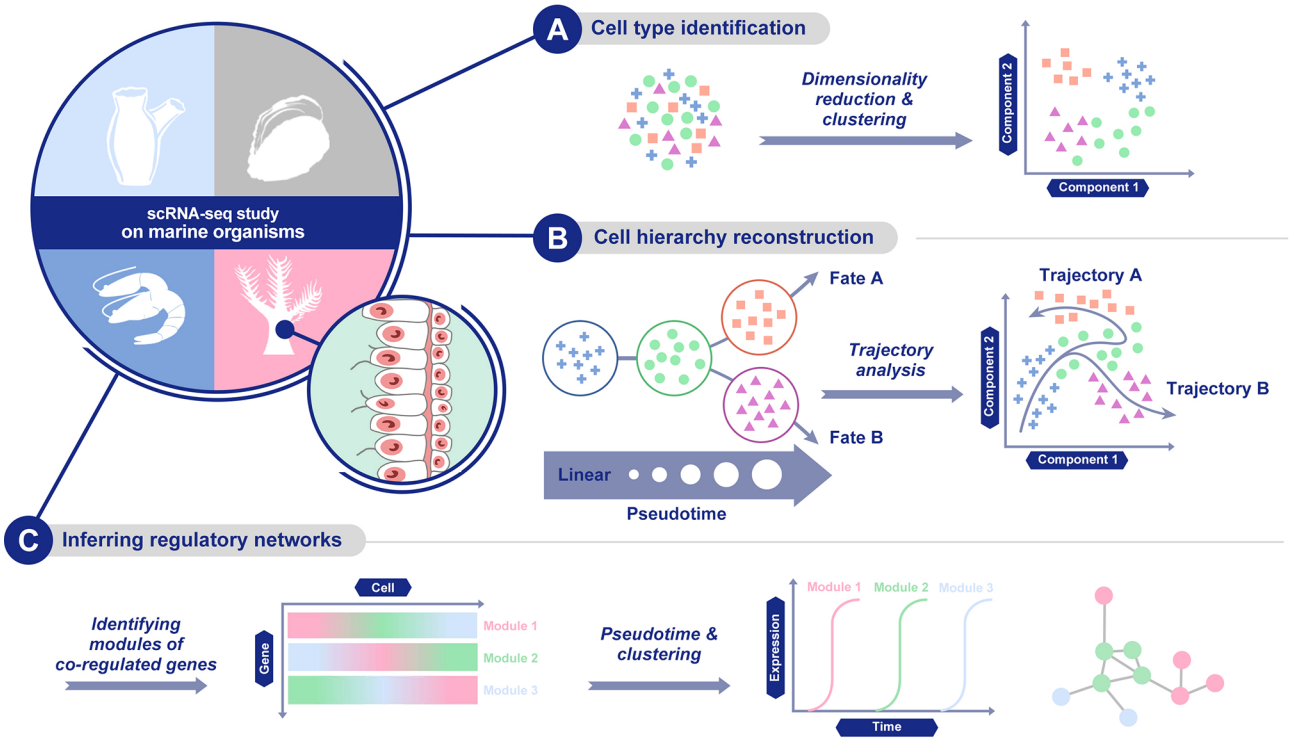

FIGURE 3 | Main scRNA-seq data analysis methods. **(A)** cell population characterization *via* dimensionality reduction and clustering; **(B)** cellular trajectory reconstruction by trajectory analysis; and **(C)** gene regulatory network establishment.

expression and the establishment of regulatory networks in a single cell come with a variety of computational challenges (Chen and Mar, 2018). Compared with bulk sample data, single-cell gene expression data has higher rates of zero values. This can be attributed to both the true biological effects that a transcript of a gene is not expected to be produced in every cell and to technical variations, which are associated with single cell assays due to the limited amounts of biological material. Recently, several methods specialized in the inference of regulatory networks were developed, such as SCENIC (Aibar et al., 2017), SCODE (Matsumoto et al., 2017) and PIDC (Chan et al., 2017).

Finally, there is a set of methods for building the cellular trajectory describing the temporal evolution of cells, which is estimated through the transition analysis of expression profiles. Early trajectory inference methods fixed the topology of the trajectory and focused on correctly ordering the cells along with the fixed topology, but recently developed methods infer the topology of the trajectory and the order of cells on the individual branches at the same time (Lee and Hwang, 2020). When picking up suitable analysis methods for the cellular trajectory, the accuracy, scalability, stability and usability of each method should be considered carefully (Saelens et al., 2019). Nowadays, frequently-used methods include Monocle (Qiu et al., 2017), DPT (Haghverdi et al., 2016) and Wishbone (Setty et al., 2016).

2.3 Applying ScRNA-Seq on Marine Organisms

The scRNA-seq technique has been attached to significant meaning and promising perspectives once it was developed in the last century due to its unique ability to provide a detailed understanding of spatial organization and transcriptomic programs of individual cells. Especially in the last five years, numerous studies applying single-cell methods on multicellular organisms were accomplished to reveal the genome expression of individual cells, quantify the relative abundance of different cell types, and understand the cellular lineages across the life cycle (Farrell et al., 2018; Plass et al., 2018; Wagner et al., 2018; Pijuan-Sala et al., 2019; Soria et al., 2020). Predictably, because of both the rapid growth of whole-genome sequencing data and the rapid development of single cell RNA-seq technologies, the implementation of single-cell sequencing on marine multicellular organisms remains in its ascendant, and shall catch the attention of more biological scientists in the near future. Hence, here we focused on the up-to-date research about the application of scRNA-seq on marine multicellular organisms, in order to discuss the opportunities and challenges that may be encountered in future single-cell related studies (**Figure 4**).

2.3.1 ScRNA-Seq Study of Evolutionalry-Development in Marine Organisms

As one of the closest living relatives of vertebrates, the ascidian serves a valuable model in understanding developmental and physiological processes that are comparable to those of vertebrates (Delsuc et al., 2006). Ascidian embryos are simple with fewer cells, making them the perfect subject to study the developmental processes of vertebrate embryos. Using a droplet-based high-throughput scRNA-seq method, Cao et al. (2019)

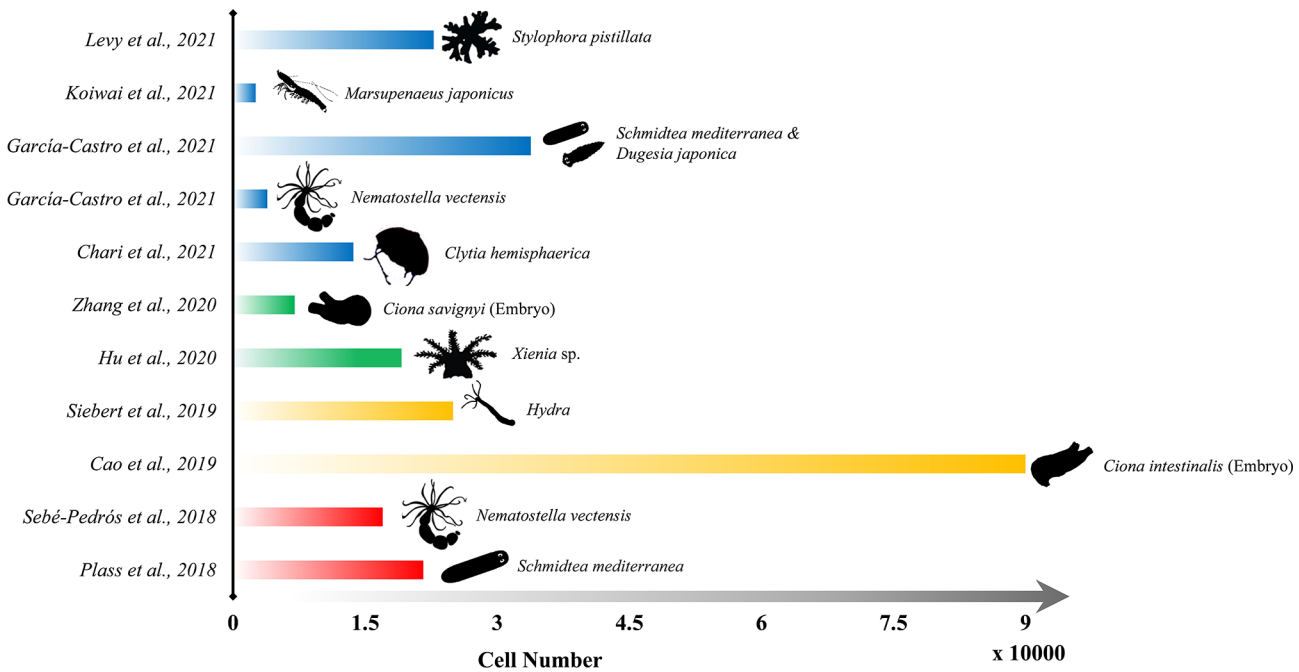

FIGURE 4 | Representative publications of the application of scRNA-seq on marine organisms since 2018. Length of each bar refers to the sequenced cell numbers, and the outline of each species are shown on the right end of the bar.

obtained comprehensive coverage of every cell population during the development of ascidian embryos. Single-cell transcriptomes for more than 90,000 cells spanning the entire development stage (from the onset of gastrulation to swimming tadpoles) in the ascidian *Ciona* intestinalis were determined, and the comprehensive transcriptome trajectories, as well as the gene regulatory networks, for over 60 cell types (including nearly 40 neuronal subtypes) comprising the *Ciona* tadpole were presented. This study revealed the dual properties of the *Ciona* notochord and the expansion of the vertebrate forebrain, providing insights into the evolutionary transition between invertebrates and vertebrates.

Furthermore, Zhang et al. (2020) applied scRNA-seq on embryos of the ascidian *Ciona savignyi* and acquired comparable cell population clustering results. Their work systematically examined the lineage specification in early *Ciona* embryogenesis. 47 cell types over eight cell cycles in the wild-type embryo were identified. And by building gene regulatory networks (GRN) of embryonic lineage development, the research indicates that *Brachyury* mutants, a key regulator of notochord fate in Ciona, might not be a strictly defined master regulator, and that *Brachyury* together with *Brachyury*-independent genes act in parallel in notochord GRN for notochord specification. Moreover, by matching to mouse embryo cell types, their study discovered conserved expression of a limited number of transcription factors, similar to the results between *Ciona* and zebrafish, or *Ciona* and *Xenopus*.

2.3.2 ScRNA-Seq Analysis of Symbiosis in Marine Organisms

Inhabitating ologotrophic tropical or subtropical oceans, many corals take up dinoflagellate algae of the Symbiodiniaceae family into their gastrodermis to maintain metabolic processes (Baker, 2003). The dinoflagellate alga resides within a lysosomal-like organelle inside the host cell and transfers diverse photosynthetic products to the coral, which in turn provides the symbiont with inorganic carbon (Davy et al., 2012). Based on single-cell sequencing technologies, it becomes practical to derive cell types and depict differentiated gene expression of the symbiotic cells in corals. Hu et al. (2020) identified 16 cell clusters out of 19,134 individual *Xenia* sp. cells, including gastrodermal cells and cnidocytes. Cluster 16 was attached to the endosymbiotic cells and its marker genes were predicted to encode proteins like receptors, extracellular matrix proteins, immune response proteins, phagocytosis and/or endocytosis proteins, or nutrient transporters. The cellular lineage dynamics of Cluster 16 were also examined by surgically cutting away all tentacles from *Xenia* polyps and observing the regeneration. The result indicated five progressive states between homeostatic conditions and the regeneration process, showing substantial changes of gene expression along pseudotime.

Recently, Levy et al. (2021) reported similar alga-hosting cell types in *Stylophora pistillata*, a stony coral species, and compared them to *Xenia* sp., both highlighted by positive gene expressions related to lipid metabolism. In this research, more than 40 cell types across the life cycle (larva, primary polyp and adult colony) of *S. pistillata* were identified by scRNA-seq. Among these cell types, one cell type in polyps related to skeleton-producing and two putative immune cell types were characterized by specialized gene overexpression. Moreover, comparative analysis with other cnidarian organisms provided systematic evidence of the evolutionary conservation of major cnidarian cell type programs, as well as novelties of calicoblasts and alga-hosting cell types in the stony coral.

2.3.3 ScRNA-Seq Study of Stem Cell and Cell Regeneration Mechanism in Marine Organisms

Due to the continual self-renewal and the capability of whole-body regeneration from a small piece of tissue, the cnidarian polyp *Hydra* keeps attracting researchers' attention. Siebert et al. (2019) have recently generated 24,985 single-cell transcriptomes from *Hydra* using Drop-seq, clustered the cells and annotated cell states from stem cells to terminally differentiated cells. Three previously uncharacterized subtypes of 12 neuronal cell populations were identified: two in the ectoderm and one in the endoderm, likely composed of ganglion neurons connected throughout the *Hydra* body. Also, in studies on the differentiation trajectories, a new marker gene specific to the multipotent stem cell population was identified, and a previously omitted cell state was discovered to be shared by the neuron and gland cell trajectory, indicating a shared evolutionary history of these cell types.

In contrast to the research on the cnidarian polyp, new scRNA-seq applications focused on the cnidarian hydrozoan medusa (Chari et al., 2021). A new workflow, so called whole animal multiplexed single-cell sequencing (WHAM-seq), was proposed and applied on *Clytia hemisphaerica*, and the *Clytia* cell types' response to starvation was determined. The results indicate that there is greater cell type diversity in the *Clytia* medusa than in its polyp-only hydrozoan cousin *Hydra*. The starvation experiment analysis reveals that the gastrodermal cell populations related to digestive compartments were maintained operationally as distinct 'cell types' rather than 'cell states' between starved and controlled conditions.

2.3.4 ScRNA-Seq Analysis of Marine Invertebrate's Cellular and Molecular Immunity

Another up-to-date research using scRNA-seq focused on the subpopulation of penaeid shrimp hemocytes in order to achieve more comprehensive understanding of its immune system (Koiwai et al., 2021). ScRNA-seq was performed on *Marsupenaeus japonicus* hemocytes using the custom-built Drop-seq platform. Six hemocyte types (Hem1-6) were classified and their functions in cell differentiation and immune system were characterized. The result indicates that Hem1 can be categorized into oligopotent hemocytes and located upstream in the differentiation process due to the strong expression of TGase, cell proliferation, and G2/M state-related genes, while Hem1 only accounts for a very small fraction of the analyzed cells. By analyzing the expression patterns of Antimicrobial peptide (AMP) and virus responsible protein- (VRP) encoding genes, Hem3-4 was attached to importance of maintaining immune

response against viruses whereas Hem5-6 are thought to be responsible for bacterial defense.

3 FUTURE DIRECTIONS OF SINGLE-CELL SEQUENCING ON MARINE ORGANISMS

Single-cell sequencing has been regarded as among the most remarkable biological technique enhancements in the 21st century, and especially in the past decade, the rapidly-increasing sequencing scales and the great success in commercial scRNA-seq technologies have accelerated the application of single-cell sequencing in various research fields. The total number of marine oganism species reaches about 226,000, occupying a large part in the zoology (Appeltans et al., 2012). Hot research fields, such as evolutionary-developmental studies of transitional species and the environmental adaptation studies of organisms, also have urgent needs in single cell sequencing data (Jager and Manuel, 2016; Cao et al., 2019; Schenkelaars et al., 2019; Zhang et al., 2020). As a result, the single-cell studies on marine organisms, focusing on either the cell type recognition or mapping cell lineage and gene regulatory networks, are just unfolding.

New techniques capable of controlling cell quality before analysis, such as the application of optical imaging systems and user-interfaces in sequencing platforms, will improve the reliability of scRNA-seq results (Valihrach et al., 2018). Applying multiomic single-cell sequencing is also a future direction for scRNA-seq further developing as well as integrative analyzing for multiomic data. Measurements of multiomes (genome, transcriptome, epigenome and proteome) are valuebale to describe the complexity of cells (Macaulay et al., 2017; Yuan et al., 2017). However, technologies for single-cell isolation, barcoding and sequencing to measure multiomes from the same cell, as well as integrative analysis methods for multiomic data, are altoghter in urgent need to be perfected (Lee and Hwang, 2020).

Furthermore, the analysis of single-cell gene expression variations in the special context of tissue is also a crucial perspective in the development of scRNA-seq technology, since the spatial variations of transcriptomic expressions in single cells throughout certain tissues are important evidence to unravel how cellular expressions change in response to the presence and proximity to other cells (Ståhl et al., 2016). The spacial analysis could be achieved by gene expression patterning technologies such as the application of *in situ* hybridization (ISH) or fluorescence *in situ* hybridization (FISH) to highlight marker genes and visualize cell morphology and gene expression locations (Horie et al., 2018; Soria et al., 2020; Chari et al., 2021; García-Castro et al., 2021). New techniques merging scRNA-seq and marker gene localization (e.g., spatial transcriptome techniques like SeqFISH+ and VISIUM) are urgently needed in the study of marine organisms (Ståhl et al., 2016; Longo et al., 2021).

4 CONCLUSION

The last decade has witnessed the vigorous development of single-cell sequencing technologies, and the application of these state-of-the-art techniques on marine organisms has both vital scientific significance and promising prospects. With the improvements of whole-genome amplification methods, automated cell isolation and barcoding strategies, commercial single-cell manipulation platforms met great success, bringing high efficiency, high accuracy and relatively low costs to the application of single-cell sequencing. The development of single-cell data analysis methods has made it possible to differentiate cell groups, map cell lineage history and decipher gene regulatory networks of target organisms. Hitherto, applications of single-cell sequencing mainly focused on marine microorganisms due to the smaller gene capacity and convenience of sampling, but creative single-cell studies on marine multicellular organisms have rapidly emerged.

While the advancement of sequencing techniques and the ongoing establishment of gene reference libraries have expedited the application of single-cell sequencing on marine organisms, challenges also exist due to the difficulties in sampling and preserving marine organism samples and the scarcity of high-quality genome sequencing databases. However, three prospects of applying single-cell sequencing (cell population characterization, regulatory network establishment and cellular trajectory analysis) on marine organisms are still appealing.

AUTHOR CONTRIBUTIONS

JL wrote all sections of the manuscript. HW and CL contributed to manuscript revision, read, and approved the submitted version. All authors contributed to the article and approved the submitted version.

FUNDING

This study was supported by the National Key RandD Program of China (Project Number 2018YFC0310702) and National Natural Science Foundation of China (Grant No. 42030407).

REFERENCES

Aibar, S., González-Blas, C. B., Moerman, T., Imrichova, H., Hulselmans, G., Rambow, F., et al. (2017). SCENIC: Single-Cell Regulatory Network Inference and Clustering. *Nat. Methods* 14 (11), 1083–1086. doi: 10.1038/nmeth.4463

Appeltans, W., Ahyong, S. T., Anderson, G., Angel, M. V., Artois, T., Bailly, N., et al. (2012). The Magnitude of Global Marine Species Diversity. *Curr. Biol.* 22 (23), 2189–2202. doi: 10.1016/j.cub.2012.09.036

Baek, S., and Lee, I. (2020). Single-Cell ATAC Sequencing Analysis: From Data Preprocessing to Hypothesis Generation. *Comput. Struct. Biotechnol. J.* 18, 1429–1439. doi: 10.1016/j.csbj.2020.06.012

Baker, A. C. (2003). Flexibility and Specificity in Coral-Algal Symbiosis: Diversity, Ecology, and Biogeography of Symbiodinium. *Annu. Rev. Ecol Evolution System* 34 (1), 661–689. doi: 10.1146/annurev.ecolsys.34.011802.132417

Becht, E., McInnes, L., Healy, J., Dutertre, C.-A., Kwok, I. W., Ng, L. G., et al. (2019). Dimensionality Reduction for Visualizing Single-Cell Data Using UMAP. *Nat. Biotechnol.* 37 (1), 38–44. doi: 10.1038/nbt.4314

Bravo González-Blas, C., Quan, X. J., Duran-Romaña, R., Taskiran, I. I., Koldere, D., Davie, K., et al. (2020). Identification of Genomic Enhancers Through Spatial Integration of Single-Cell Transcriptomics and Epigenomics. *Mol. Syst. Biol.* 16 (5), e9438. doi: 10.15252/msb.20209438

Buenrostro, J. D., Giresi, P. G., Zaba, L. C., Chang, H. Y., and Greenleaf, W. J. (2013). Transposition of Native Chromatin for Fast and Sensitive Epigenomic Profiling of Open Chromatin, DNA-Binding Proteins and Nucleosome Position. *Nat. Methods* 10 (12), 1213. doi: 10.1038/nmeth.2688

Buenrostro, J. D., Wu, B., Litzenburger, U. M., Ruff, D., Gonzales, M. L., Snyder, M. P., et al. (2015). Single-Cell Chromatin Accessibility Reveals Principles of Regulatory Variation. *Nature* 523 (7561), 486–490. doi: 10.1038/nmeth.2688

Cao, C., Lemaire, L. A., Wang, W., Yoon, P. H., Choi, Y. A., Parsons, L. R., et al. (2019). Comprehensive Single-Cell Transcriptome Lineages of a Proto-Vertebrate. *Nature* 571(7765), 349–354. doi: 10.1038/s41586-019-1385-y

Chan, T. E., Stumpf, M. P., and Babtie, A. C. (2017). Gene Regulatory Network Inference From Single-Cell Data Using Multivariate Information Measures. *Cell Syst.* 5 (3), 251–267.e253. doi: 10.1016/j.cels.2017.08.014

Chari, T., Weissbourd, B., Gehring, J., Ferraioli, A., Leclère, L., Herl, M., et al. (2021). Whole Animal Multiplexed Single-Cell RNA-Seq Reveals Plasticity of Clytia Medusa Cell Types. *bioRxiv* doi: 10.1101/2021.01.22.427844

Chen, H., Lareau, C., Andreani, T., Vinyard, M. E., Garcia, S. P., Clement, K., et al. (2019). Assessment of Computational Methods for the Analysis of Single-Cell ATAC-Seq Data. *Genome Biol.* 20 (1), 241. doi: 10.1186/s13059-019-1854-5

Chen, S., and Mar, J. C. (2018). Evaluating Methods of Inferring Gene Regulatory Networks Highlights Their Lack of Performance for Single Cell Gene Expression Data. *BMC Bioinf.* 19 (1), 1–21. doi: 10.1186/s12859-018-2217-z

Choi, J. R., Yong, K. W., Choi, J. Y., and Cowie, A. C. (2020). Single-Cell RNA Sequencing and Its Combination With Protein and DNA Analyses. *Cells* 9 (5), 1130. doi: 10.3390/cells9051130

Davy, S. K., Allemand, D., and Weis, V. M. (2012). Cell Biology of Cnidarian-Dinoflagellate Symbiosis. *Microbiol. Mol. Biol. Rev.* 76 (2), 229–261. doi: 10.1128/MMBR.05014-11

Delsuc, F., Brinkmann, H., Chourrout, D., and Philippe, H. (2006). Tunicates and Not Cephalochordates Are the Closest Living Relatives of Vertebrates. *Nature* 439 (7079), 965–968. doi: 10.1038/nature04336

Dempster, A. P., Laird, N. M., and Rubin, D. B. (1977). Maximum Likelihood From Incomplete Data *via* the EM Algorithm. *J. R. Stat. Society: Ser. B (Methodological)* 39 (1), 1–22. doi: 10.1111/j.2517-6161.1977.tb01600.x

Eberwine, J., Sul, J. Y., Bartfai, T., and Kim, J. (2014). The Promise of Single-Cell Sequencing. *Nat. Methods* 11, 25–27. doi: 10.1038/nmeth.2769

Eberwine, J., Yeh, H., Miyashiro, K., Cao, Y., Nair, S., Finnell, R., et al. (1992). Analysis of Gene Expression in Single Live Neurons. *Proc. Natl. Acad. Sci.* 89 (7), 3010–3014. doi: 10.1073/pnas.89.7.3010

Eng, C. H. L., Lawson, M., Zhu, Q., Dries, R., Koulena, N., Takei, Y., et al. (2019). Transcriptome-Scale Super-Resolved Imaging in Tissues by RNA seqFISH+. *Nature* 568 (7751), 235–239. doi: 10.1038/s41586-019-1049-y

Esumi, S., Wu, S.-X., Yanagawa, Y., Obata, K., Sugimoto, Y., and Tamamaki, N. (2008). Method for Single-Cell Microarray Analysis and Application to Gene-Expression Profiling of GABAergic Neuron Progenitors. *Neurosci. Res.* 60 (4), 439–451. doi: 10.1016/j.neures.2007.12.011

Farrell, J. A., Wang, Y., Riesenfeld, S. J., Shekhar, K., Regev, A., and Schier, A. F. (2018). Single-Cell Reconstruction of Developmental Trajectories During Zebrafish Embryogenesis. *Science* 360 (6392), eaar3131. doi: 10.1126/science.aar3131

García-Castro, H., Kenny, N. J., Iglesias, M., Alvarez-Campos, P., Mason, V., Elek, A., et al. (2021). ACME Dissociation: A Versatile Cell Fixation-Dissociation Method for Single-Cell Transcriptomics. *Genome Biol.* 22 (1), 89. doi: 10.1186/s13059-021-02302-5

Grindberg, R. V., Yee-Greenbaum, J. L., McConnell, M. J., Novotny, M., O'Shaughnessy, A. L., Lambert, G. M., et al. (2013). RNA-Sequencing From Single Nuclei. *Proc. Natl. Acad. Sci.* 110 (49), 19802–19807. doi: 10.1073/pnas.1319700110

Guo, M., Wang, H., Potter, S. S., Whitsett, J. A., and Xu, Y. (2015). SINCERA: A Pipeline for Single-Cell RNA-Seq Profiling Analysis. *PLoS Comput. Biol.* 11 (11), e1004575. doi: 10.1371/journal.pcbi.1004575

Guo, M., and Xu, Y. (2018). "Single-Cell Transcriptome Analysis Using SINCERA Pipeline," in *Transcriptome Data Analysis* (Cham, Switzerland: Springer), 209–222.

Gupta, R. K., and Kuznicki, J. (2020). Biological and Medical Importance of Cellular Heterogeneity Deciphered by Single-Cell RNA Sequencing. *Cells* 9 (8), 1751. doi: 10.3390/cells9081751

Haghverdi, L., Büttner, M., Wolf, F. A., Buettner, F., and Theis, F. J. (2016). Diffusion Pseudotime Robustly Reconstructs Lineage Branching. *Nat. Methods* 13 (10), 845. doi: 10.1038/nmeth.3971

Hashimshony, T., Wagner, F., Sher, N., and Yanai, I. (2012). CEL-Seq: Single-Cell RNA-Seq by Multiplexed Linear Amplification. *Cell Rep.* 2 (3), 666–673. doi: 10.1016/j.celrep.2012.08.003

Hohnadel, M., Maumy, M., and Chollet, R. (2018). Development of a Micromanipulation Method for Single Cell Isolation of Prokaryotes and Its Application in Food Safety. *PLoS One* 13 (5), e0198208. doi: 10.1371/journal.pone.0198208

Hong, M., Tao, S., Zhang, L., Diao, L. T., Huang, X., Huang, S., et al. (2020). RNA Sequencing: New Technologies and Applications in Cancer Research. *J. Hematol. Oncol.* 13 (1), 166. doi: 10.1186/s13045-020-01005-x

Horie, R., Hazbun, A., Chen, K., Cao, C., Levine, M., and Horie, T. (2018). Shared Evolutionary Origin of Vertebrate Neural Crest and Cranial Placodes. *Nature* 560 (7717), 228–232. doi: 10.1038/s41586-018-0385-7

Hu, M., Zheng, X., Fan, C. M., and Zheng, Y. (2020). Lineage Dynamics of the Endosymbiotic Cell Type in the Soft Coral *Xenia*. *Nature* 582 (7813), 534–538. doi: 10.1038/s41586-020-2385-7

Hwang, B., Lee, J. H., and Bang, D. (2018). Single-Cell RNA Sequencing Technologies and Bioinformatics Pipelines. *Exp. Mol. Med.* 50 (8), 1–14. doi: 10.1038/s12276-018-0071-8

Ishii, S., Tago, K., and Senoo, K. (2010). Single-Cell Analysis and Isolation for Microbiology and Biotechnology: Methods and Applications. *Appl. Microbiol. Biotechnol.* 86 (5), 1281–1292. doi: 10.1007/s00253-010-2524-4

Ishioka, T. (2000). Extended K-Means With an Efficient Estimation of the Number of Clusters. *Ouyou toukeigaku* 29 (3), 141–149. doi: 10.5023/jappstat.29.141

Jager, M., and Manuel, M. (2016). Ctenophores: An Evolutionary-Developmental Perspective. *Curr. Opin. Genet. Dev.* 39, 85–92. doi: 10.1016/j.gde.2016.05.020

Jaitin, D. A., Kenigsberg, E., Keren-Shaul, H., Elefant, N., Paul, F., Zaretsky, I., et al. (2014). Massively Parallel Single-Cell RNA-Seq for Marker-Free Decomposition of Tissues Into Cell Types. *Science* 343 (6172), 776–779. doi: 10.1126/science.1247651

Koiwai, K., Koyama, T., Tsuda, S., Toyoda, A., Kikuchi, K., Suzuki, H., et al. (2021). Single-Cell RNA-Seq Analysis Reveals Penaeid Shrimp Hemocyte Subpopulations and Cell Differentiation Process. *Elife* 10, e66954. doi: 10.7554/eLife.66954

Kurimoto, K., Yabuta, Y., Ohinata, Y., Ono, Y., Uno, K. D., Yamada, R. G., et al. (2006). An Improved Single-Cell cDNA Amplification Method for Efficient High-Density Oligonucleotide Microarray Analysis. *Nucleic Acids Res.* 34 (5), e42. doi: 10.1093/nar/gkl050

Lambolez, B., Audinat, E., Bochet, P., Crépel, F., and Rossier, J. (1992). AMPA Receptor Subunits Expressed by Single Purkinje Cells. *Neuron* 9 (2), 247–258. doi: 10.1016/0896-6273(92)90164-9

Lacar, B., Linker, S. B., Jaeger, B. N., Krishnaswami, S. R., Barron, J. J., Kelder, M. J. E., et al. (2016). Nuclear RNA-Seq of Single Neurons Reveals Molecular Signatures of Activation. *Nat. Commun.* 7, 11022. doi: 10.1038/ncomms11022

Lee, J., and Hwang, D. (2020). Single-Cell Multiomics: Technologies and Data Analysis Methods. *Exp. Mol. Med.* 52 (9), 1428–1442. doi: 10.1038/s12276-020-0420-2

Levy, S., Elek, A., Grau-Bové, X., Menéndez-Bravo, S., Iglesias, M., Tanay, A., et al. (2021). A Stony Coral Cell Atlas Illuminates the Molecular and Cellular Basis of Coral Symbiosis, Calcification, and Immunity. *Cell* 184 (11), 2973–2987. doi: 10.1016/j.cell.2021.04.005

Longo, S. K., Guo, M. G., Ji, A. L., and Khavari, P. A. (2021). Integrating Single-Cell and Spatial Transcriptomics to Elucidate Intercellular Tissue Dynamics. *Nat. Rev. Genet.* 22 (10), 1–18. doi: 10.1038/s41576-021-00370-8

Macaulay, I. C., Ponting, C. P., and Voet, T. (2017). Single-Cell Multiomics: Multiple Measurements From Single Cells. *Trends Genet.* 33 (2), 155–168. doi: 10.1016/j.tig.2016.12.003

Macosko, E. Z., Basu, A., Satija, R., Nemesh, J., Shekhar, K., Goldman, M., et al. (2015). Highly Parallel Genome-Wide Expression Profiling of Individual Cells Using Nanoliter Droplets. *Cell* 161 (5), 1202–1214. doi: 10.1016/j.cell.2015.05.002

Matsumoto, H., Kiryu, H., Furusawa, C., Ko, M. S., Ko, S. B., Gouda, N., et al. (2017). SCODE: An Efficient Regulatory Network Inference Algorithm From Single-Cell RNA-Seq During Differentiation. *Bioinformatics* 33 (15), 2314–2321. doi: 10.1093/bioinformatics/btx194

Mosmann, T. R., Cherwinski, H., Bond, M. W., Giedlin, M. A., and Coffman, R. L. (1986). Two Types of Murine Helper T Cell Clone. I. Definition According to Profiles of Lymphokine Activities and Secreted Proteins. *J. Immunol.* 136 (7), 2348–2357.

Nature Method Editorial Board (2014). Method of the Year 2013. *Nat. Methods* 11 (1), 1–1. doi: 10.1038/nmeth.2801

Peixoto, A., Monteiro, M., Rocha, B., and Veiga-Fernandes, H. (2004). Quantification of Multiple Gene Expression in Individual Cells. *Genome Res.* 14 (10a), 1938–1947. doi: 10.1101/gr.2890204

Pijuan-Sala, B., Griffiths, J. A., Guibentif, C., Hiscock, T. W., Jawaid, W., Calero-Nieto, F. J., et al. (2019). A Single-Cell Molecular Map of Mouse Gastrulation and Early Organogenesis. *Nature* 566 (7745), 490–495. doi: 10.1038/s41586-019-0933-9

Plass, M., Solana, J., Wolf, F. A., Ayoub, S., Misios, A., Glažar, P., et al. (2018). Cell Type Atlas and Lineage Tree of a Whole Complex Animal by Single-Cell Transcriptomics. *Science* 360 (6391), eaaq1723. doi: 10.1126/science.aaq1723

Pollen, A. A., Nowakowski, T. J., Shuga, J., Wang, X., Leyrat, A. A., Lui, J. H., et al. (2014). Low-Coverage Single-Cell mRNA Sequencing Reveals Cellular Heterogeneity and Activated Signaling Pathways in Developing Cerebral Cortex. *Nat. Biotechnol.* 32 (10), 1053. doi: 10.1038/nbt.2967

Poore, G. C. B., and Wilson, G. D. F. (1993). Marine Species Richness. *Nature* 361 (6413), 597–598. doi: 10.1038/361597a0

Qi, R., Ma, A., Ma, Q., and Zou, Q. (2020). Clustering and Classification Methods for Single-Cell RNA-Sequencing Data. *Briefings Bioinf.* 21 (4), 1196–1208. doi: 10.1093/bib/bbz062

Qiu, X., Mao, Q., Tang, Y., Wang, L., Chawla, R., Pliner, H. A., et al. (2017). Reversed Graph Embedding Resolves Complex Single-Cell Trajectories. *Nat. Methods* 14 (10), 979. doi: 10.1038/nmeth.4402

Ramsköld, D., Luo, S., Wang, Y.-C., Li, R., Deng, Q., Faridani, O. R., et al. (2012). Full-Length mRNA-Seq From Single-Cell Levels of RNA and Individual Circulating Tumor Cells. *Nat. Biotechnol.* 30 (8), 777–782. doi: 10.1038/nbt.2282

Rosenberg, A. B., Roco, C. M., Muscat, R. A., Kuchina, A., Sample, P., Yao, Z., et al. (2018). Single-Cell Profiling of the Developing Mouse Brain and Spinal Cord With Split-Pool Barcoding. *Science* 360 (6385), 176–182. doi: 10.1126/science.aam8999

Saelens, W., Cannoodt, R., Todorov, H., and Saeys, Y. (2019). A Comparison of Single-Cell Trajectory Inference Methods. *Nat. Biotechnol.* 37 (5), 547–554. doi: 10.1038/s41587-019-0071-9

Schenkelaars, Q., Vernale, A., Fierro-Constaín, L., Borchiellini, C., and Renard, E. (2019). "A Look Back Over 20 Years of Evo-Devo Studies on Sponges: A Challenged View of Urmetazoa," in *Evolution, Origin of Life, Concepts and Methods* (Springer), 135–160.

Setty, M., Tadmor, M. D., Reich-Zeliger, S., Angel, O., Salame, T. M., Kathail, P., et al. (2016). Wishbone Identifies Bifurcating Developmental Trajectories From Single-Cell Data. *Nat. Biotechnol.* 34 (6), 637–645. doi: 10.1038/nbt.3569

Shapiro, E., Biezuner, T., and Linnarsson, S. (2013). Single-Cell Sequencing-Based Technologies Will Revolutionize Whole-Organism Science. *Nat. Rev. Genet.* 14 (9), 618–630. doi: 10.1038/nrg3542

Sheng, H. Z., Lin, P. X., and Nelson, P. G. (1994). Analysis of Multiple Heterogeneous mRNAs in Single Cells. *Analytical Biochem.* 222 (1), 123–130. doi: 10.1006/abio.1994.1463

Siebert, S., Farrell, J. A., Cazet, J. F., Abeykoon, Y., Primack, A. S., Schnitzler, C. E., et al. (2019). Stem Cell Differentiation Trajectories in Hydra Resolved at Single-Cell Resolution. *Science* 365 (6451), eaav9314. doi: 10.1126/science.aav9314

Soria, C. L. D., Lee, J., Chong, T., Coghlan, A., Tracey, A., Young, M. D., et al. (2020). Single-Cell Atlas of the First Intra-Mammalian Developmental Stage of the Human Parasite Schistosoma Mansoni. *Nat. Commun.* 11 (1), 1–16. doi: 10.1038/s41467-020-20092-5

Ståhl, P. L., Salmén, F., Vickovic, S., Lundmark, A., Navarro, J.F., Magnusson, J., et al. (2016). Visualization and Analysis of Gene Expression in Tissue Sections by Spatial Transcriptomics. *Science* 353 (6294), 78–82. doi: 10.1126/science.aaf2403

Stepanauskas, R., and Sieracki, M. E. (2007). Matching Phylogeny and Metabolism in the Uncultured Marine Bacteria, One Cell at a Time. *Proc. Natl. Acad. Sci.* 104 (21), 9052. doi: 10.1073/pnas.0700496104

Stuart, T., and Satija, R. (2019). Integrative Single-Cell Analysis. *Nat. Rev. Genet.* 20 (5), 257–272. doi: 10.1038/s41576-019-0093-7

Svensson, V., Natarajan, K. N., Ly, L.-H., Miragaia, R. J., Labalette, C., Macaulay, I. C., et al. (2017). Power Analysis of Single-Cell RNA-Sequencing Experiments. *Nat. Methods* 14 (4), 381–387. doi: 10.1038/nmeth.4220

Svensson, V., Vento-Tormo, R., and Teichmann, S. A. (2018). Exponential Scaling of Single-Cell RNA-Seq in the Past Decade. *Nat. Protoc.* 13 (4), 599–604. doi: 10.1038/nprot.2017.149

Tang, F., Barbacioru, C., Wang, Y., Nordman, E., Lee, C., Xu, N., et al. (2009). mRNA-Seq Whole-Transcriptome Analysis of a Single Cell. *Nat. Methods* 6 (5), 377–382. doi: 10.1038/nmeth.1315

Tietjen, I., Rihel, J. M., Cao, Y., Koentges, G., Zakhary, L., and Dulac, C. (2003). Single-Cell Transcriptional Analysis of Neuronal Progenitors. *Neuron* 38 (2), 161–175. doi: 10.1016/S0896-6273(03)00229-0

Trapnell, C. (2015). Defining Cell Types and States With Single-Cell Genomics. *Genome Res.* 25 (10), 1491–1498. doi: 10.1101/gr.190595.115

Valihrach, L., Androvic, P., and Kubista, M. (2018). Platforms for Single-Cell Collection and Analysis. *Int. J. Mol. Sci.* 19 (3), 807. doi: 10.3390/ijms19030807

Van der Maaten, L., and Hinton, G. (2008). Visualizing Data Using T-SNE. *J. Mach. Learn. Res.* 9 (11). doi: 10.48550/arXiv.2108.01301

Wagner, D. E., Weinreb, C., Collins, Z. M., Briggs, J. A., Megason, S. G., and Klein, A. M. (2018). Single-Cell Mapping of Gene Expression Landscapes and Lineage in the Zebrafish Embryo. *Science* 360 (6392), 981–987. doi: 10.1126/science.aar4362

Weigand, H., Beermann, A. J., Čiampor, F., Costa, F. O., Csabai, Z., Duarte, S., et al. (2019). DNA Barcode Reference Libraries for the Monitoring of Aquatic Biota in Europe: Gap-Analysis and Recommendations for Future Work. *Sci. Total Environ.* 678, 499–524. doi: 10.1016/j.scitotenv.2019.04.247

Wold, S., Esbensen, K., and Geladi, P. (1987). Principal Component Analysis. *Chemometrics Intelligent Lab. Syst.* 2 (1-3), 37–52. doi: 10.1016/0169-7439(87)80084-9

Wong, M. A., and Hartigan, J. (1979). Algorithm as 136: A K-Means Clustering Algorithm. *J. R. Stat. Society Ser. C (Applied Statistics)* 28 (1), 100–108. doi: 10.2307/2346830

Woyke, T., Xie, G., Copeland, A., Gonzalez, J. M., Han, C., Kiss, H., et al. (2009). Assembling the Marine Metagenome, One Cell at a Time. *PLoS One* 4 (4), e5299. doi: 10.1371/journal.pone.0005299

Yuan, G.-C., Cai, L., Elowitz, M., Enver, T., Fan, G., Guo, G., et al. (2017). Challenges and Emerging Directions in Single-Cell Analysis. *Genome Biol.* 18 (1), 1–8. doi: 10.1186/s13059-017-1218-y

Zhang, T., Xu, Y., Imai, K., Fei, T., Wang, G., Dong, B., et al. (2020). A Single-Cell Analysis of the Molecular Lineage of Chordate Embryogenesis. *Sci. Adv.* 6 (45), eabc4773. doi: 10.1126/sciadv.abc4773

Zheng, G. X., Terry, J. M., Belgrader, P., Ryvkin, P., Bent, Z. W., Wilson, R., et al. (2017). Massively Parallel Digital Transcriptional Profiling of Single Cells. *Nat. Commun.* 8 (1), 1–12. doi: 10.1038/ncomms14049

Conflict of Interest: The authors declare that the research was conducted in the absence of any commercial or financial relationships that could be construed as a potential conflict of interest.

Publisher's Note: All claims expressed in this article are solely those of the authors and do not necessarily represent those of their affiliated organizations, or those of the publisher, the editors and the reviewers. Any product that may be evaluated in this article, or claim that may be made by its manufacturer, is not guaranteed or endorsed by the publisher.

frontiers | Frontiers in Marine Science

ORIGINAL RESEARCH
published: 15 July 2022
doi: 10.3389/fmars.2022.869226

Different Nitrogen Sources Fuel Symbiotic Mussels at Cold Seeps

Fuqiang Wang[1,2], *Ying Wu*[1]* *and Dong Feng*[3]

[1]State Key Laboratory of Estuarine and Coastal Research, East China Normal University, Shanghai, China, [2]Multidisciplinary Research Center for the Deep Sea, Pilot National Laboratory for Marine Science and Technology (Qingdao), Qingdao, China, [3]Shanghai Engineering Research Center of Hadal Science and Technology, College of Marine Sciences, Shanghai Ocean University, Shanghai, China

Cold seeps globally host dense unique oasis-type ecosystems, mainly fuelled by chemosynthetic microorganisms via reduced gases such as methane and hydrogen sulfide. However, the origin and pathway of nitrogen chemosynthesis in this widely distributed symbiont ecosystem remain poorly understood. Here, we explore biomarker methods (bulk stable isotope, amino acid (AA), fatty acid (FA) and compound-specific isotope analyses in gill tissues of mussels) to demonstrate the relative contributions of inorganic and organic nitrogen to symbiotic mussels at cold seeps in the South China Sea and their impact on the synthesis and metabolism of amino acids. *Gigantidas platifrons (G. platifrons)* symbioses with type II methanotrophs ***via*** the Serine pathway, and *Bathymodiolus aduloides (B. aduloides)* thrives with sulfur-oxidizing bacteria ***via*** the Calvin pathway, as revealed by bulk $\delta^{13}C$ and $\delta^{13}C$ of FAs. Based on the $\delta^{15}N$ values in gill tissues of mussels, organic nitrogen from sediment is estimated as the dominant nitrogen source for *B. aduloides* (97-98%), in contrast, NH_4^+ was the main nitrogen source for *G. platifrons.* Different dominant nitrogen sources result in the $\delta^{15}N$ of AAs in the gills of two mussel species having opposite trends, which might be related to synthesis and metabolism of AAs in symbiotic bacteria and host, respectively. Our findings reveal that the mechanism of nitrogen acquisition in cold seep systems is plastic and related to DIN sources/uptake and changing environmental conditions. These findings uncover novel biosynthesis of nitrogen in the deep sea, typically at cold seeps, and may have important implications for nitrogen biogeochemistry and deep-sea conservation.

Keywords: symbiotic mussels, cold seeps, nitrogen sources, biomarker methods, $\delta^{13}C$ of fatty acids, $\delta^{15}N$ of amino acids

OPEN ACCESS

Edited by:
Clara F. Rodrigues, University of Aveiro, Portugal

Reviewed by:
Ulisse Cardini, Stazione Zoologica Anton Dohrn Napoli, Italy
Emanuela Fanelli, Marche Polytechnic University, Italy

***Correspondence:**
Ying Wu
wuying@sklec.ecnu.edu.cn

Specialty section:
This article was submitted to Deep-Sea Environments and Ecology, a section of the journal Frontiers in Marine Science

Received: *04 February 2022*
Accepted: *13 June 2022*
Published: *15 July 2022*

Citation:
Wang F, Wu Y and Feng D (2022) Different Nitrogen Sources Fuel Symbiotic Mussels at Cold Seeps. Front. Mar. Sci. 9:869226. doi: 10.3389/fmars.2022.869226

INTRODUCTION

Cold seeps are widespread seafloor ecosystems supported by the emission of reduced gases from seabed reservoirs (Ruff et al., 2015; Goffredi et al., 2020). Symbioses associated with bacteria have played a central role in shaping the ecosystem surrounding invertebrates in cold seeps (Rubin-Blum et al., 2019). Among the dominant animals in these ecosystems are symbiotic mussels, which live in symbiosis with thiotrophic and/or methanotrophic symbionts and derive the vast majority of their nutrition from these symbionts (Feng et al., 2015; Rubin-Blum et al., 2017). Since their first discovery, cold seeps have been recognized as important pathways of element cycling on Earth (Paull et al., 1984; Feng et al., 2018). Many studies on symbiotic relationships, especially related to

carbon chemosynthetic processes, have been conducted. These findings have led to a basic understanding of seep ecosystems in terms of biodiversity and community composition (Suess, 2014) and energy and nutritional carbon sources (Brooks et al., 1987; Orphan et al., 2001). However, much more work has been focused on the carbon-fuelled symbiont system between bacteria and mussels than the nitrogen-fuelled system (Macavoy et al., 2002; Raggi et al., 2013; Rubin-Blum et al., 2017). Evidence that methane and CO_2 are the main carbon sources to the symbiont ecosystem suggests that different carbon sources result in distinct $\delta^{13}C$ values in the gills of mussels (Brooks et al., 1987), yet the nitrogen cycles in this widely distributed symbiont ecosystem remain largely unexplored (Vokhshoori et al., 2021). The nitrogen cycles can not only reveal the synthesis and metabolism of amino acids (AAs) in symbiotic mussels but also help to elucidate the interactions between fatty acids (FAs) and AAs and to understand the adaption of mussels to extreme environments and their interactions in cold seep ecosystems. Thus, understanding the nitrogen cycles in symbiotic mussels is vital to shed light on deep sea conservation.

Biochemical tracers, such as bulk stable isotopes ($\delta^{13}C$ and $\delta^{15}N$), FAs, and compound-specific isotope analysis (CSIA), have been applied to bacteria and symbionts. Because of the limited kinetic isotope fractionation of carbon associated with methanotrophs, bulk $\delta^{13}C$ values have successfully indicated the various carbon source contributions (Orphan et al., 2001; Michaelis et al., 2002). The varied $\delta^{15}N$ values also suggest that symbionts are capable of using different nitrogen sources (Petersen et al., 2016). FA composition analysis demonstrated that type II methanotrophs were the predominant microorganism responsible for methane oxidation (Bull et al., 2000; Kellermann et al., 2012), especially in high-methane or low combined-nitrogen environments (Jahnke et al., 1999). The analysis of $\delta^{15}N$ in AAs, however, has rarely been applied to quantitatively estimate the nutritive nitrogen sources used by symbionts in cold seeps but has emerged as a powerful approach for tracing the origins and fate of nitrogen in ecological and biogeochemical studies (Ohkouchi et al., 2017). Moreover, the combination of multiple isotope analyses, including bulk stable isotopes and stable isotopes in FAs and AAs, can help to elucidate the interactions between AAs and FAs (Riou et al., 2010; Takano et al., 2018).

In this study, we explored the biomarker methods previously used to investigate the trophic interactions of fishes (Gerringer et al., 2017; Wang et al., 2019) to delineate the biogeochemistry and nitrogen dynamics of symbiotic mussels in the Formosa Ridge (Site F) of the South China Sea (SCS). Site F is located in the northeast region of the continental slope of the SCS. It is a NNW–SSE oriented ridge that is nearly 2 km in length and rises over 100 m above the surrounding seabed (**Figure 1A**) (Feng et al., 2015). At site F, *Gigantidas platifrons* and *Bathymodiolus aduloides* were the most common and abundant taxa (**Figure 1B**) and symbiosed with methanotrophs and sulfur-oxidizing bacteria in their gills, respectively (Feng et al., 2015; Xu et al., 2019). Therefore, a comparative study of the gills of *G. platifrons* and *B. aduloides* is conducted in this research.

Based on the observation that *G. platifrons* and *B. aduloides* have obviously different biological composition characteristics, such as bulk stable isotopes and CSIA, we tested the hypothesis that *G. platifrons* and *B. aduloides* have different nitrogen-fuelled systems—fuelled by inorganic and organic nitrogen-influenced by the surrounding environment, in turn resulting in different symbiotic bacteria (Feng et al., 2015). We identified the type of methanotrophs and carbon biogeochemical cycles in mussels based on the bulk $\delta^{13}C$ and $\delta^{13}C$ of FAs. We also estimated the relative contributions of different nitrogen sources from $\delta^{15}N$ values. To clarify the synthesis of AAs, we measured the $\delta^{15}N$ of AAs and described the conversion between AAs and FAs. This multifaceted study provides a broad perspective for carbon and nitrogen transformations in symbiotic mussels in cold seeps and lays the foundation for their origin and adaptation to extreme environments.

METHODS

Study Site and Mussels

As described in other studies (Feng et al., 2015; Sun et al., 2017), our study site, called Site F (Formosa Ridge), is located at 22°06.922′N and 119°17.130′E at a depth of 1120 m. It is an oriented ridge above the surrounding seabed and has active methane seepage on the northeastern corner of the continental slope of the South China Sea (**Figure 1A**). Two mussel species were collected using the manned submersible Jiaolong during the Dayang-31 expedition in July 2013 (**Figure 1B**). The mussels were identified as *Gigantidas platifrons* and *Bathymodiolus aduloides* by the National Center for Biotechnology Information's gene sequence database at http://www.ncbi.nlm.nih.gov and http://www.marinespecies.org/aphia.php?p=taxdetails&id=1346726 (Wong et al., 2015; Xu et al., 2019). *G. platifrons* was numerically dominant and occurred mostly on carbonate pavement (**Figure 1C**), while *B. aduloides* was rare and occurred mainly on muddy sediment (**Figure 1D**). *G. platifrons* and *B. aduloides* harboured methanotrophic and thiotrophic symbionts, respectively. All mussels were placed in the sample baskets of the submersible. Once the deck of the ship returned, twelve individuals of *G. platifrons* and five individuals of *B. aduloides* were dissected into the mantle, gill, viscera, and foot tissue. All samples were stored at -20°C and transferred to the laboratory. In this study, the gill tissues were used to conduct the following experiments.

To compare the bulk isotopic contents in the symbiotic mussels at cold seep, the shallow-water mussels *M. edulis* and *M. coruscus* were bought from Sanggou Bay (in July 2014, 37°08′N and 122°30′E) and the aquaculture areas of Zhoushan (in June 2015, 30°32′N and 121°25′E), respectively. The species names were confirmed based on their morphological description.

Abbreviations: AA, amino acid; Ala, alanine; Arg, arginine; Asn, asparaginate; Asp, aspartic acid; CSIA, compound-specific isotope analysis; FA,fatty acid; FAME, fatty acid methyl ester; Glu,glutamic; Gly, glycine; Ile, isoleucine; Leu, leucine; Lys, lysine; Met, methionine; OM, organic matter; Phe, phenylalanine; POM, particulate organic matter; PUFA, polyunsaturated fatty acid; SCS,South China Sea, Ser, serine; Thr, threonine; Tyr, tyrosine; Val, valine.

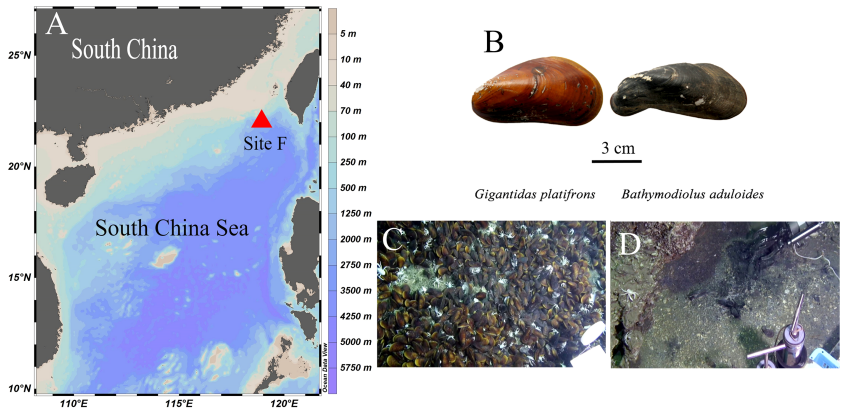

FIGURE 1 | Study site and mussel beds. **(A)** Site F location; **(B)** shells of the two mussels; **(C)** Gigantidas platifrons lives on carbonate pavement; **(D)** Bathymodiolus aduloides lives on muddy sediment; **(B–D)** were cited from Feng et al.[4]

Stable Isotope Analysis

All gill tissues were lyophilized in a freeze-dryer (LOC-1; Christ, Germany) and powdered using a mortar and pestle. Dried powdered samples (~0.2 mg for $\delta^{13}C$, ~1 mg for $\delta^{15}N$, three replicates) were weighed into tin cups, and stable isotopes ($\delta^{13}C$, $\delta^{15}N$) were measured using an isotope ratio mass spectrometer (Finnegan Delta plus XP; Thermo, Germany). The results were normalized to the Vienna Pee Dee Belemnite standard (V-PDB) for $\delta^{13}C$ and to atmospheric N (N_2) for $\delta^{15}N$. The stable isotope ratios are expressed in δ notation of units per mille as follows (Bond and Hobson, 2012):

$$\delta X(‰) = \left(\left(R_{sample} / R_{standard}\right) - 1\right) \times 1000 \quad (1)$$

where $X = {}^{13}C$ *or* ${}^{15}N$ and $R = {}^{13}C/{}^{12}C$ *or* ${}^{15}N/{}^{14}N$. The precision of the stable isotope analyses was ±0.1‰.

FA Analysis

FAs were extracted using a modified Folch method (Folch et al., 1957; Wang et al., 2019). Approximately 100 mg of the gill tissues was extracted by dichloromethane/methanol (2:1 v/v, including 0.01% BHT) and then centrifuged (3000 rpm, 10 min). The upper organic solvent layer was transferred to a flask using a pipette and evaporated to dryness under a stream of N_2 at room temperature. The dried FAs were transesterified to FA methyl esters (FAMEs) in a mixture of methanol (containing 5% HCl) and n-hexane at 50 for 12 h.

The FAMEs were analysed using gas chromatography (7890A GC; Agilent, United States) equipped with a DB-FFAP capillary column (30 m in length, 0.25 mm i.d., 0.25 mm film thickness; Agilent, United States). As an internal recovery standard, 21:0 was added to the samples, and 19:0 methyl ester was added as an internal quantification standard. The injector and detector temperatures were both 250°C. Injections (1 mL) were made at 60°C, and the temperature was increased to 170°C at a rate of 30°C/min. The temperature was held constant for 5 min, increased to 220°C at 1°C/min and held at this temperature for 10 min. Nitrogen (N_2) was used as the carrier gas at a flow rate of 1 mL/min. FAMEs were identified by comparing retention times with those of commercial standards (37 Component FAME Mix; Sigma, United States). The individual FAs were expressed as percentages of the total FA content based on peak areas. The FA recoveries in the analysis were >85%. If more than one sample was analysed, the data were reported as the mean ± standard deviation (SD).

Compound-Specific ^{13}C FA Analysis

To investigate the synthetic pathways of FAs from carbon sources, the $\delta^{13}C$ values of FAs in *B. aduloides* and *G. platifrons* were measured. The compound-specific ^{13}C FA values were analysed using a Trace Ultra GC coupled to a Delta V mass spectrometer *via* a GC combustion interface using helium (He) as the carrier gas (Thermo Scientific, Germany). The FAMEs were separated on a DB-5MS column (50 m, 0.32 mm i.d., 0.25 mm film thickness). The $\delta^{13}C$ values of the FAMEs were calibrated by analysing an 18:0 FAME certified standard (certified: -23.24‰, measured: -23.34‰ ± 0.1‰) supplied by Indiana University, and the analytical precision was ≤0.3‰ (Wang et al., 2019). All samples were analysed in triplicate.

To obtain isotope data for the FAs, FAME isotopes were corrected for the isotopes of the methyl moiety originating from methanol using the following formula:

$$\delta^{13}C_{FA} = \left[\left(n+1\right) \times \delta^{13}C_{FAME} - \delta^{13}C_{MeOH}\right] / n \quad (2)$$

where $\delta^{13}C_{FA}$ is the isotope of the FA, $\delta^{13}C_{FAME}$ is the isotope of the FAME, $\delta^{13}C_{MeOH}$ is the isotope of the methanol derivatization reagent (-37.4 ± 0.1‰), and n is the number of C atoms in the FAs.

AA Analysis

AAs were extracted from all the samples *via* HCl hydrolysis. Briefly, 1 mg of gill tissues was hydrolysed with 6 M HCl at 110°C for 20 h in precombusted sealed glass ampoules. After hydrolysis, the solution was neutralized to pH 8.5 with NaOH (Fitznar et al., 1999). The AAs were determined by high-performance liquid chromatography equipped with a Phenomenex™ Hyperclone column (5 μm particle diameter, BDS C18, 250 mm length, 4 mm inner diameter) (Wu et al., 2007). Eluent A was 125 mM sodium acetate with 2% methanol adjusted to pH 6.8 with acetic acid, and eluent B was 100% methanol. Gradient elution was used to separate all AAs, and external standards of the AAs (Sigma-Aldrich, Merck, USA) were used for calibration. The relative standard deviation triplicate analysis of the individual AAs was <3.5%.

Compound-Specific ^{15}N AA Analysis

The δ^{15}N of AAs was measured by coupling instrumental analysis (ion chromatography and Precon-GC-IRMS) and oxidation-reduction of AAs (Zhang et al., 2021; Wang et al., 2022). Briefly, AAs were separated using an IC system (Dionex, ICS-5000$^+$, Thermo Scientific, USA) equipped with an autosampler (Dionex, AS-AP) with an adjustable injection volume and coupled to an automated fraction collector (Dionex, UltiMate 3000). For the separation of AAs, the IC was equipped with an IC column (Dionex™ AminoPac™PA10, Thermo Scientific, USA), and a solvent ramp programme was used. At the end of each sample, 1 M sodium acetate was used to wash the column to remove any residue (Zhang et al., 2021). IC procedural blanks were collected after AA fractions, and were re-injected in IC system to ensure that all AAs has been collected completely. Meanwhile, the solvent blanks were also collected between Phe and Glu. These blanks were used to correct the isotopic interference from any nitrogenous compounds introduced by the analytical procedure up to this point that could be potentially converted to nitrite by NaClO [more details showed in Zhang et al. (2021)] Purified AAs were oxidized to NO_2^- by Strecker degradation (Schonberg and Moubacher, 1952; Zhang and Altabet, 2008). The next step was the conversion of NO_2^- to N_2O; here, $NH_2OH{\bullet}HCl$ was used as an alternative reductant (Bothner-By and Friedman, 1952; Liu et al., 2014). The stable nitrogen isotopes of the produced N_2O were analysed by a Precon-GC-IRMS (Trace GC 2000, Delta-V advantage, Thermo Scientific, USA) equipped with an autosampler (Precon Automated, Thermo Scientific, USA). Standard AAs (Merck, USA; Glu, USGS40, Gly, USGS64, the Reston Stable Isotope Laboratory of the U.S. Geological Survey) were treated with the same protocol as the samples and were used to calibrate the δ^{15}N value of the AAs. The results from this method were compared with the general GC-IRMS analysis with two lab standards (McCarthy Lab AA mixture and cyanobacteria) and only 0.6‰ deviations were found (Zhang et al., 2021).

Statistical Analysis

SPSS 23.0, Primer 7.0 and MATLAB were used to perform data analysis. By SPSS 23.0, the data were tested for normality by using Shapiro–Wilk test and homogeneity of variance using Levene's test. Cross validation using a discriminant analysis was applied to test the efficiency of FA and AA data, and linear regression was used to examine the relationship between N content and δ^{15}N of AAs in SPSS 23.0. A cluster analysis (K-Means) based on FAs was performed using Primer 7.0. Based on the coefficients in the linear combinations of variables making up the principal components (PCs), the dominant parameters were chosen to characterize the different mussel groups. To illustrate the reliability of the data, the Spearman correlation coefficient and the p value (two-tailed) were used to evaluate the significance of the correlation.

As described in previous studies, NH_4^+ was the main inorganic nitrogen source to *G. platifrons* and methane-oxidizing bacteria (Sun et al., 2017), and particulate organic matter (POM) only supply 5% of food sources to *G. platifrons* by filter-feeding (Wang, 2018). Thus, we assume that NH_4^+-derived nitrogen is considered the sole inorganic nitrogen source in the mussel gill of *G. platifrons* and contribute 95% of nitrogen, thereby particulate organic matter (POM)-derived nitrogen contributing 5% by the filter feeding of *G. platifrons*. A simple two-source mixing model in MATLAB was used to calculate the $\delta^{15}N_{ammonium}$ values in the surrounding environment. The following equations were used for this calculation:

$$f_{ammonium} + f_{POM} = 1 \tag{3}$$

$$\begin{aligned}&\left(\delta^{15}N_{ammonium} + \Delta^{15}N_{ammonium}\right)\times f_{ammonium}\\&+\left(\delta^{15}N_{OM} + \Delta^{15}N_{POM}\right)\times f_{POM} = \delta^{15}N_{gill}\end{aligned} \tag{4}$$

where $f_{ammonium}$ is the relative contribution of NH_4^+ (95%), f_{OM} is the relative contribution of OM (5%), $\delta^{15}N_{ammonium}$ is the δ^{15}N of NH_4^+, $\Delta^{15}N_{ammonium}$ is the ^{15}N enrichment of ammonium assimilation, $\delta^{15}N_{POM}$ is the δ^{15}N of POM, $\Delta^{15}N_{POM}$ is the δ^{15}N enrichment of POM assimilation, and $\delta^{15}N_{gill}$ is the δ^{15}N of mussel gill.

The $\Delta^{15}N_{ammonium}$ of ammonium assimilation is supposed as -4‰ when ambient ammonium is low (<1 mM) at the cold seeps (Liao et al., 2014). In site F, the concentration of NH_4^+ in sediment is about 10 mg/kg (Jing et al., 2020), which is lower than 1 mM. Thus, the $\Delta^{15}N_{ammonium}$ is estimated as -4‰ in this study. As measured in previous study, the δ^{15}N of sediment at site F was 3.7‰ (Jing et al., 2020). Based on the δ^{15}N relationship between the bulk sediment and organic nitrogen in the SCS, we estimated that $\delta^{15}N_{POM}$ was 3.7‰ (Kienast et al., 2005). In symbiotic organisms, the host ingested particulate detrital or living nitrogen sources (PON), there was no δ^{15}N enrichment observed (Ferrier-Pages and Leal, 2019), in turn $\Delta^{15}N_{OM}$ is supposed as zero. By the two-source mixing model, the δ^{15}N of NH_4^+ was then calculated (4.5 ± 0.4‰). Furthermore, we applied $\delta^{15}N_{ammonium}$ value to calculate the relative contributions of inorganic and organic nitrogen sources in *B. aduloides*. There are no genomics studies of *B. aduloides* so far. Thus, the relative contributions of inorganic nitrogen (including nitrate and ammonium) are unknown. We

assume that nitrate, ammonium and POM jointly determine the $\delta^{15}N_{gill}$ of *B. aduloides*. The following equations were used for this calculation:

$$f_{ammonium} + f_{nitrate} + f_{POM} = 1 \quad (5)$$

$$\begin{aligned}&\left(\delta^{15}N_{ammonium} - 4‰\right) \times ‰\, f_{ammonium} \\ &+\left(\delta^{15}N_{nitrate} + \Delta^{15}N_{nitrate}\right) \times f_{nitrate} \\ &+\delta^{15}N_{OM} \times f_{POM} = \delta^{15}N_{gill}\end{aligned} \quad (6)$$

where $f_{nitrate}$ is the relative contribution of nitrate, $\delta^{15}N_{nitrate}$ is the $\delta^{15}N$ of nitrate, $\Delta^{15}N_{nitrate}$ is the $\delta^{15}N$ enrichment of nitrate assimilation.

RESULTS

To investigate the symbiotic relationship of cold seep mussels with their symbiotic bacteria and the turnover of organic and inorganic nitrogen between the mussels and the surrounding environment, we collected 47 samples (gill tissues) from cold seeps and shallow water and analysed them for FAs, AAs, bulk $\delta^{13}C$ and $\delta^{15}N$, $\delta^{13}C$ of FAs, and $\delta^{15}N$ of AAs (**Supplementary Data**).

FA Biomarkers

In the principal component analysis (PCA) of FAs, all gill tissues of mussels were separated into four groups (**Figure 2**). PC1 (79.2%) distinguished mussels into cold seep areas and shallow water areas. 16:1n-7, 18:1n-7, 20:4n-6, 20:5n-3, and 22:6n-3 were the main loading factors contributing to PC1. PC2 (5.3%) also separated the mussels, and the main loading factors were 18:1n-7 and 20:4n-6. The PCA results revealed that symbiotic mussels and filter-feeding mussels had different FA components (**Supplementary Figures 1, 2**). The filter-feeding mussels (*Mytilus edulis*, n=15; *M. coruscus*, n=15) had higher n-3 polyunsaturated fatty acids (n-3 PUFAs) than symbiotic mussels in cold seeps. *B. aduloides* (n=5) harbouring sulfur-oxidizing bacteria had a low n-3 PUFA percentage, and *G. platifrons* (n=12), which thrived with methanotrophs, was not detected (**Supplementary Figure 1**). In contrast, *B. aduloides* and *G. platifrons* had higher 16:1n-7 and 18:1n-7 levels than filter-feeding mussels (**Supplementary Figure 2**). Moreover, 18:1n-7 was not detected in *M. edulis* and *M. coruscus*.

Bulk $\delta^{13}C$ and $\delta^{15}N$ of Gill Tissues in Mussels

The bulk stable isotopes of mussels in cold seeps and shallow water differed (**Figure 3**). *G. platifrons* had more negative $\delta^{13}C$ (-69.8 ± 1.7‰) and $\delta^{15}N$ (0.7 ± 0.5‰) values than other mussel species, which was similar with symbiotic mussels in the cold seeps (Vokhshoori et al., 2021). The $\delta^{13}C$ and $\delta^{15}N$ values of *B. aduloides* were -34.7 ± 2.0‰ and 3.6 ± 0.3‰, respectively. *M. edulis* and *M. coruscus* had similar $\delta^{13}C$ (-20.7 ± 0.8‰, -21.2 ± 0.5‰; $P<0.05$) values; however, the $\delta^{15}N$ values significantly differed (9.7 ± 0.3‰, 2.8 ± 1.0‰; $P<0.01$).

$\delta^{13}C$ of FAs

δB. *aduloides* (-49.2 to -38.5‰) had more positive $\delta^{13}C$ of FAs than *G. platifrons* (-78.4 to -70.4‰). Considering the carbon content of FAs, the average $\delta^{13}C$ values of FAs in *B. aduloides* and *G. platifrons* were -41.3 ± 0.6‰ and -76.8 ± 0.4‰, respectively (**Figure 4**). However, the $\delta^{13}C$ of 18:0 and 18:1n-7 in *G. platifrons* was more positive than other FAs, which was inconsistent with the results for *B. aduloides* (**Figure 4** and **Supplementary Figures 3, 4**).

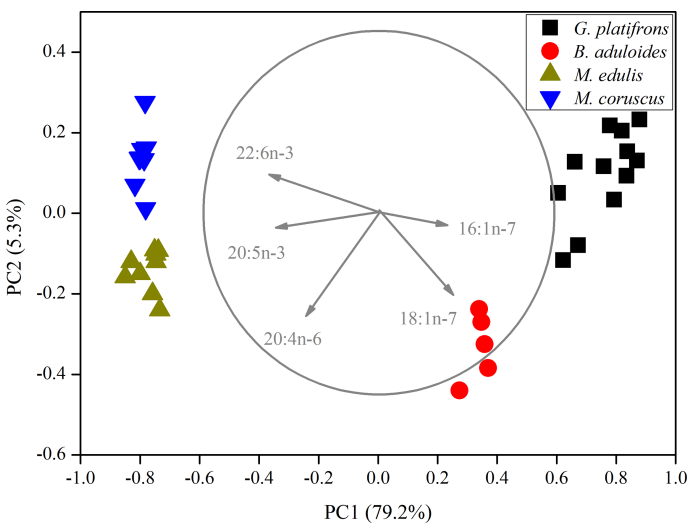

FIGURE 2 | Principal component analysis of mussels based on fatty acids. The length of vectors represents their contributions to axis.

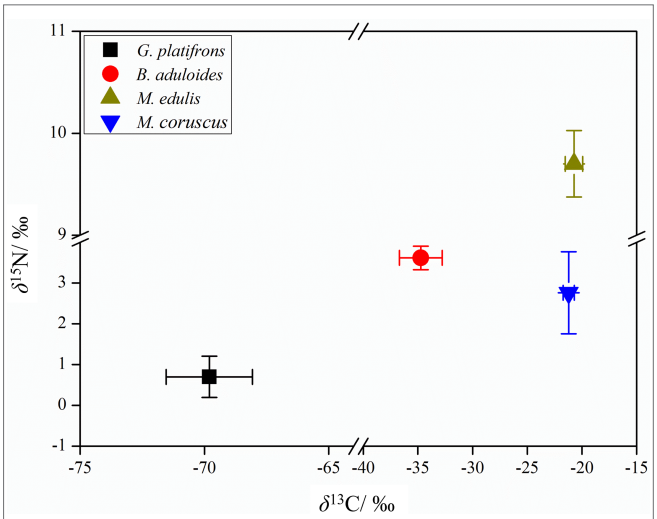

FIGURE 3 | Carbon and nitrogen stable isotope ratios (‰) of symbiotic and filter-feeding mussels.

δ^{15}N of AAs

To characterize the turnover of organic and inorganic nitrogen in cold seep mussels, the δ^{15}N values of AAs in *B. aduloides* and *G. platifrons* were used to trace the nitrogen flow between the symbiont and host. In *G. platifrons*, the N content was positively related to the δ^{15}N of AAs (y=0.25x+6.52, R^2 = 0.67, p<0.05) (**Figure 5**). In contrast, the N content in *B. aduloides* was negatively related to the δ^{15}N of AAs (y=-0.35x+12.36, R^2 = 0.64, p<0.05), which has not been reported to our knowledge. Glycine (Gly) and threonine (Thr) were also measured in this study (**Supplementary Figures 5, 6**) but these results are not shown in **Figure 5** due to the Gly cleavage system (Yamaguchi et al., 2017).

DISCUSSION

Characteristics of Carbon Sources and FAs in Gill Tissues of Symbiotic Mussels

G. platifrons mainly use methane-based energy sources as their carbon sources (Orphan et al., 2001; Michaelis et al., 2002), and in support of this, the δ^{13}C of *G. platifrons* is consistent with the δ^{13}C of methane (Michaelis et al., 2002; Feng et al., 2015). In contrast, the δ^{13}C values of *B. aduloides* indicate a -25‰ fractionation from the measured δ^{13}C of CO_2 in seawater, which reveals that sulfur-oxidizing bacteria utilize the Calvin cycle for carbon dioxide fixation (Ponnudurai et al., 2017). Meanwhile. this species was consistent with the chemosymbiotic species from the Gulf of Cadiz, which inferred a thiotrophic mode of nutrition (Rodrigues et al., 2013). Moreover, the low content of n-3 PUFAs and high contents of 16:1n-7 and 18:1n-7 in symbiotic mussels also demonstrate that energy derived from photosynthesis has an extremely low impact on the symbiotic mussels (Ackman, 1989). The high contents of 16:1n-7 and 18:1n-7 in the mussels indicate that *G. platifrons* and *B. aduloides* symbiose with type II methanotrophs (Serine pathway) and sulfur-oxidizing bacteria, respectively **(Supplementary Figure 2)**, which is consistent with the genome analysis (Sun et al., 2017). Type II methanotrophs are favoured in high-methane environments and utilize methane as the sole carbon and energy source (Jahnke et al., 1999). This is also the reason why *G. platifrons* occurs mostly on carbonate pavement, where methane is abundant. In the muddy sediment of cold seeps, sulfate reduction is achieved by sedimentary microbial mats with high metabolic rates (Tobler et al., 2016). Thus, sulfur-oxidizing bacteria provide *B. aduloides* with nutrition through the fixation of CO_2 into biomass using produced sulfide compounds as an energy source (Volland et al., 2018).

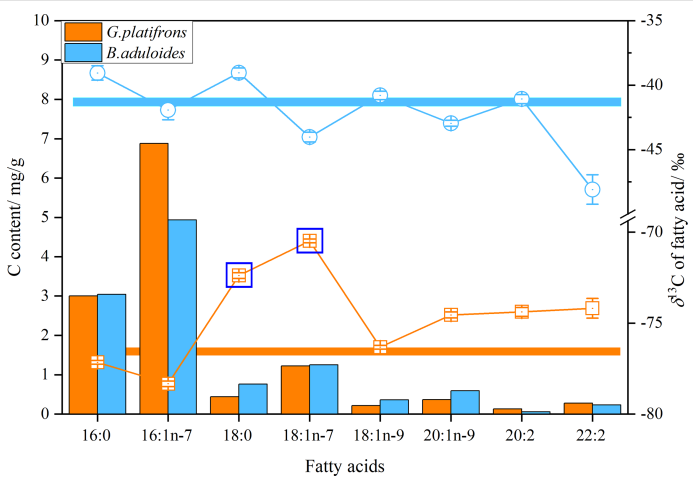

FIGURE 4 | δ^{13}C and carbon content of fatty acids in symbiotic mussels. Histograms represent the carbon content of fatty acids in tissues (dry weight), points represent the δ^{13}C of a single fatty acid, and straight lines represent the average δ^{13}C of fatty acids

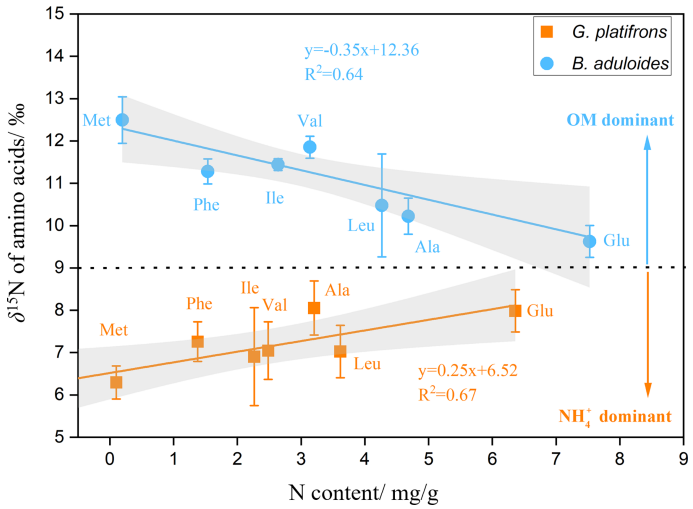

FIGURE 5 | Nitrogen content and $\delta^{15}N$ of amino acids in symbiotic mussels. OM, organic matter; above the black dotted line represents OM as the main nitrogen source for mussels; below the black dotted line represents nitrate as the main nitrogen source for mussels; the grey area represents the 95% confidence interval

These factors result in *B. aduloides* living mainly on muddy sediment.

The bulk $\delta^{13}C$ and $\delta^{13}C$ of FAs differed substantially between the two symbiotic mussels, which is consistent with the assimilation of different carbon sources, as discussed above. Compared with the bulk $\delta^{13}C$, the average $\delta^{13}C$ values of FAs were depleted by approximately 7–9‰ in *B. aduloides* and 2–7‰ in *G. platifrons*, suggesting *de novo* synthesis from dietary carbon sources (Deniro and Epstein, 1977). However, the different carbon isotope fractionation of $\delta^{13}C$ in mussels might be a result of the energy supply, with ^{12}C being the more favourable carbon source when energy is limited (Hugler and Sievert, 2011). In carbonate pavement, the abundant methane supplies enough energy to the type II methanotrophs symbiosing with *G. platifrons*, even though Serine pathway organisms operate in a less energetically favourable way (Anthony, 1982; Jahnke et al., 1999). Different from type II methanotrophs, sulfur-oxidizing bacteria use reduced sulfide from the anaerobic oxidation of methane as the energy source (Feng et al., 2015; Tobler et al., 2016). Instead of methane, *B. aduloides* use seawater CO_2 fixed *via* sulfur-oxidizing bacteria, which agrees well with the measured $\delta^{13}C$ values of CO_2 dissolved in seawater above the mussel beds (Feng et al., 2015). Thus, different carbon sources result to various carbon isotope fractionations. In addition, in both specimens, the differences in the $\delta^{13}C$ of FAs are also indicative of different biochemical pathways (Macavoy et al., 2002; Riou et al., 2010). In *B. aduloides*, unsaturated FAs are depleted relative to saturated FAs, indicating *de novo* transformations (Fang et al., 1993). In contrast, 18:1n-7 in *G. platifrons* shows more positive $\delta^{13}C$ values than 18:0, which provides additional evidence for a biochemical pathway involving FAs in the symbiosis of type II methanotrophs and mussels. A previous study suggested that host cells can assimilate AAs directly into FAs (Riou et al., 2010). Thus, the positive $\delta^{13}C$ of 18:1n-7 in type II methanotrophs demonstrates that this process might occur in bacteria (Bull et al., 2000; Takano et al., 2018).

Relative Contributions of Inorganic and Organic Nitrogen in *B. aduloides*

Bulk nitrogen isotopes, similar to bulk carbon isotopes, reflect the nitrogen diet sources of mussels. For example, the high $\delta^{15}N$ values of *M. edulis* illustrate their trophic interaction with POM in Sanggou Bay (Mahmood et al., 2016), while the low $\delta^{15}N$ values of *M. coruscus* suggest that their diets different with *M. edulis*. In a previous study, the lower $\delta^{15}N$ values of phytoplankton suggested that the primary producer in the East China Sea depend mainly on atmospheric nitrogen fixation (Minagawa and Wada, 1984). Thus, the low $\delta^{15}N$ values of *M. coruscus* might be caused by atmospheric nitrogen indirectly. In extreme environments, these aspects have not been sufficiently explored; however, it is clear that the symbiotic mussels in cold seeps must use alternative nitrogen sources, such as ammonium, nitrate or organic nitrogen, in the sediment (Petersen et al., 2016; Ferrier-Pagès and Leal, 2018), which are rarely quantitatively estimated.

In order to estimate the various sources of nitrogen to *B. aduloides*, we have to delineate the contribution of ammonia, nitrate and organic nitrogen. $\delta^{15}N_{inorg}$ in the SCS had a range of 3.1-4.8‰, and with the $\delta^{15}N$ of N_{inorg} generally being significantly isotopically lighter than bulk sedimentary $\delta^{15}N$ (3.7‰ in this study) (Kienast et al., 2005; Jing et al., 2020). Thus, the $\delta^{15}N_{nitrate}$ in this study was assumed between 3.1and 3.7‰. The average values of $\delta^{15}N_{nitrate}$ were used in this study (3.4 ± 0.3‰). During assimilation of nitrate by microbes, $\Delta^{15}N_{nitrate}$ is supposed as 5‰ when nitrate is not limiting (Liao et al., 2014). In the three-source mixing model, the relative contributions of NH_4^+, NO_3^-, and OM cannot be calculated directly. Thus, we calculated the ranges of inorganic nitrogen contributions when we assumed NH_4^+or NO_3^- had the contribution to *B. aduloides*. When the NH_4^+ was the inorganic nitrogen source to *B. aduloides*, the OM had a relative contribution of 97%. Otherwise, the NO_3^- was the inorganic nitrogen source to *B. aduloides*, the OM had a relative contribution of 98%. In other words, POM was the main nitrogen

source to *B. aduloides* (97-98%). As suggested in another study, filter feeding selectively on a nitrogen-rich suspension might be an important component of the nutritional requirements of *B. childressi*, which is consistent with our results (Pile and Young, 1999). This observation is also consistent with the regional differences, in which *G. platifrons* lives mainly on carbonate pavement and *B. aduloides* occurs mainly on muddy sediment. Moreover, these results illustrated that the limited sulfide might not satisfy their energy needs for the synthesis of all types of matter, and filter feeding OM from the surrounding environment might play a more prominent role in *B. aduloides* (Ponnudurai et al., 2020).

Synthesis and Metabolism of AAs in Symbiotic Mussels Using δ^{15}N of AAs

Based on the different contributions of inorganic and organic nitrogen to the symbiotic mussels, more details about the synthesis and metabolism of AAs can be revealed. The large ^{15}N depletion of Gly relative to other AAs is caused by the Gly cleavage system in organisms, which favours ^{15}N degradation and causes ^{14}N depletion in the remaining Gly molecules (Yamaguchi et al., 2017). Thr is also impacted by the Gly cleavage system because of irreversible transamination reactions (Mcmahon and Mccarthy, 2016). The peculiar fractionation patterns of Thr and Gly are completely different from those of other AAs, routinely exhibiting significant depletion of ^{15}N (Mccarthy et al., 2013; Mcmahon and Mccarthy, 2016). The degradation pattern of "heavy" AAs might produce metabolic fuel for *de novo* FA biosynthesis (Berg et al., 2002). Thus, the products of Thr and Gly degradation might result in positive $\boldsymbol{\delta}^{13}$C values in 18:1n-7 in *G. platifrons*. However, the degradation pathways of nitrogen in AAs are independent of the synthesis of carbon in FAs. The complex carbon flows in symbiotic mussels might cause the differences in the δ^{13}C of FAs between *G. platifrons* and *B. aduloides* (Riou et al., 2010).

In addition to Gly and Thr, the δ^{15}N values of AAs can illustrate the conversion between AAs. The opposite linear relationships between δ^{15}N values of AAs and nitrogen content of AAs might indicate the different synthesis and degradation of AAs in two symbiotic mussels. δIn a previous study, the nitrogen contents of AAs in bacteria show increases in the abundance of less energetically costly AAs (Akashi and Gojobori, 2002). Thus, Glu is the less energetically costly AA and have high content, Met, Phe is the highest energetic cost for biosynthesis and have low content, and other AAs (including Ile, Leu, Val, Ala) occupy the middle position (Yamaguchi et al., 2017). In *G. platifrons*, NH_4^+ was used as the inorganic nitrogen to *de novo* Glu synthesis. Glu, which is typically the most abundant AA in organisms, is often considered a "Glu pool" to form other AAs (Bender, 2012). In *G. platifrons*, both transamination and deamination favour the lighter stable isotope (^{14}N) and leave the residual "Glu pool" ^{15}N-enriched (Macko et al., 1986; Mcmahon and Mccarthy, 2016). Compared with that of Glu, the biosynthesis of other AAs requires more energy and favours lighter nitrogen (Wagner, 2005; Yamaguchi et al., 2017). Thus, the δ^{15}N values of AAs in *G. platifrons* reflected the order of the energy cost required to form different AAs. A previous study showed that the order of the energy cost was Ile>Leu> Val> Ala. The different order in *G. platifrons* (Ile>Val>Ala>Leu) may be caused by the mixture of *de novo* AA synthesis from inorganic nitrogen coupled with AA incorporation from OM (Ohkouchi et al., 2017). Met is considered as the high energetic cost for biosynthesis, it may be reasonable for the microbes to use incorporated Met directly *via* salvage incorporation and not to degrade it (Yamaguchi et al., 2017). Thus, Met had lowest δ^{15}N values in *G. platifrons*.

In contrast, *B. aduloides* has a negative correlation between N content and δ^{15}N values of AAs, which is consistent with the assimilation of different nitrogen sources. The filter feeding of *B. aduloides* might play a prominent role in its ingestion of POM from the surrounding sediment (97-98% from surrounding POM) (Ponnudurai et al., 2020). *B. aduloides* assimilates OM and degrades it into small molecules such as free AAs (Hoppe et al., 2002) and then transports the Glu to symbiotic bacteria (Hosie et al., 2002; Ponnudurai et al., 2020). Bacteria can use Glu by metabolizing it as carbon and nitrogen sources for resynthesis of AAs or by salvage incorporation (Davies and Humphrey, 1978; Ponnudurai et al., 2020). This process results in the remaining AAs being theoretically enriched in ^{15}N relative to the reacting AAs (Chikaraishi et al., 2007). However, the ^{14}N of metabolized AAs is not excreted as a waste product but is recycled by the symbiont and as resynthesized AAs (Ferrier-Pagès and Leal, 2018). Of the AAs, the Glu in the "Glu pool" was most affected in terms of its ^{14}N levels, as it incurred the lowest energy cost and was most abundant. Compared with Glu, Met is the most expensive AAs in terms of consumed moles of ATP per molecule (Kaleta et al., 2013). The symbiotic mussels use incorporated Met directly *via* salvage incorporation and not to degrade it as discussed above (Yamaguchi et al., 2017). Meanwhile, Met is rarely affected by the ^{14}N of metabolized AAs, and retain the highest δ^{15}N values in AAs.

Such kind of knowledge is the first time to be explored in seep ecosystem (**Figure 6**), it will better constrain the synthesize and metabolism of key elements governing the carbon, nitrogen and other element cycles in extreme environment. These studies will propose relationships between groups of fatty acids and amino acids, which allow testable predictions about biogeochemical processing in symbiotic mussels. An enhanced understanding of genomes and metabolic processes of microbials involved in those organic matter production and consumption in symbiotic mussels will contribute a significant relevance to this topic.

CONCLUSION

The biomarker evidence from this study supports the hypothesis that inorganic and organic nitrogen make different contributions to the nitrogen sources of *G. platifrons* and *B. aduloides*, respectively (**Figure 6**). We demonstrate that methane and CO_2 from the surrounding environment are the main carbon sources for *G. platifrons* and *B. aduloides* and impact the δ^{13}C values of FAs in these mussels. Their unique symbiotic relationships lead to obvious bacterial FA signatures in the mussels, which can represent methanotrophic and thiotrophic symbionts, respectively (Bull et al., 2000; Kellermann et al., 2012). The

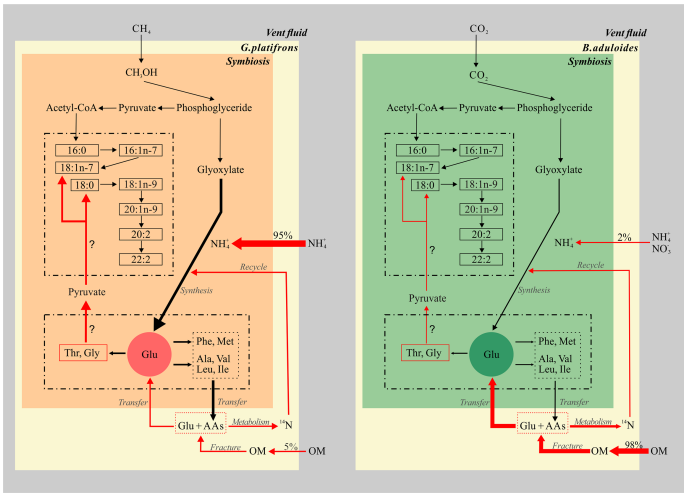

FIGURE 6 | Conceptual model of fatty acids and amino acids in symbiotic mussels. The left part represents the symbiont of *Gigantidas platifrons*, and the right part represents the symbiont of *Bathymodiolus aduloides*; OM, organic matter; the thickness of arrows represents the relative contributions of inorganic and organic nitrogen sources.

differences in AA $\delta^{15}N$ values, which showed opposite trends in the symbiotic mussels, might provide some evidence that the symbiotic mussels use different nitrogen sources. Inorganic nitrogen is the dominant nitrogen source for *G. platifrons* and OM is the dominant nitrogen source for *B. aduloides*, which are consistent with the nitrogen contributions from inorganic nitrogen and OM. The simple mixing model presented here provides baseline information for future studies aiming to quantify the different contributions of dietary sources in unique oasis-type ecosystems on the seafloor and to reveal the carbon and nitrogen flows in symbionts that are impacted by their surrounding environment in cold seeps.

DATA AVAILABILITY STATEMENT

The original contributions presented in the study are included in the article/**Supplementary Material**. Further inquiries can be directed to the corresponding author.

AUTHOR CONTRIBUTIONS

FW and YW contributed for conceptualization, and writing original draft preparation. DF contributed for sample preparation, data management, and draft modification. All authors contributed to the article and approved the submitted version.

FUNDING

This work was supported by the Natural Science Foundation of China (41876074, 42106049) and National Key Program for Basic Research (973 program, Grant No. 2014CB441502), and funded by Pilot National Laboratory for Marine Science and Technology (Qingdao) (No. JCZX202007). The authors declare no competing financial interests.

ACKNOWLEDGMENTS

We greatly appreciate help of the crews of the Xiangyanghong 09 as well as the Jiaolong team in helping us during the cruise, J. Sun (Hong Kong Baptist University) for help with mussel identification, L. Zhang (SCSIO, CAS) for sample preparation. This work was supported by the Natural Science Foundation of China (41876074, 42106049) and National Key Program for Basic Research (973 program, Grant No. 2014CB441502), and funded by Pilot National Laboratory for Marine Science and Technology (Qingdao) (No. JCZX202007). The authors declare no competing financial interests.

SUPPLEMENTARY MATERIAL

The Supplementary Material for this article can be found online at: https://www.frontiersin.org/articles/10.3389/fmars.2022.869226/full#supplementary-material

REFERENCES

Ackman, R. G. (1989). "Fatty Acids" in Marine Biogenic Lipids, Fats and Oils, ed. R. G. Ackman, CRC press (Basel: Marcel Dekker), 103-138.

Akashi, H. and Gojobori, T. (2002). Metabolic Efficiency and Amino Acid Composition in the Proteomes of Escherichia Coli and Bacillus Subtilis. *P. Natl. Acad. Sci.* 99, 3695–3700. doi: 10.1073/pnas.062526999

Anthony, C. (1982). The Biochemistry of Methylotrophs (London: Academic press London).

Bender, D. A. (2012). *Amino Acid Metabolism* (New York: John Wiley & Sons).

Berg, J., Tymoczko, J. and Stryer, L. (2002). Carbon Atoms of Degraded Amino Acids Emerge as Major Metabolic Intermediates. *Biochemistry* 2002, 5

Bond, A.L., and Hobson, K.A. (2012). Reporting Stable-Isotope Ratios in Ecology: Recommended Terminology, Guidelines and Best Practices. *Waterbirds* 35. doi: 10.1675/063.035.0213

Bothner-By, A. and Friedman, L. (1952). The Reaction of Nitrous Acid With Hydroxylamine. *J. Chem. Phys.* 20, 459–462. doi: 10.1063/1.1700442

Brooks, J. M., Kennicutt, M., Fisher, C., Macko, S., Cole, K., Childress, J., et al. (1987). Deep-Sea Hydrocarbon Seep Communities: Evidence for Energy and Nutritional Carbon Sources. *Science* 238, 1138–1142. doi: 10.1126/science.238.4830.1138

Bull, I. D., Parekh, N. R., Hall, G. H., Ineson, P. and Evershed, R. P. (2000). Detection and Classification of Atmospheric Methane Oxidizing Bacteria in Soil. *Nature* 405, 175–178. doi: 10.1038/35012061

Chikaraishi, Y., Kashiyama, Y., Ogawa, N. O., Kitazato, H. and Ohkouchi, N. (2007). Metabolic Control of Nitrogen Isotope Composition of Amino Acids in Macroalgae and Gastropods: Implications for Aquatic Food Web Studies. *Mar. Ecol. Prog. Ser.* 342, 85–90. doi: 10.3354/meps342085

Davies, D. D. and Humphrey, T. J. (1978). Amino Acid Recycling in Relation to Protein Turnover. *Plant Physiol.* 61, 54–58. doi: 10.1104/pp.61.1.54

Deniro, M. J. and Epstein, S. (1977). Mechanism of Carbon Isotope Fractionation Associated With Lipid Synthesis. *Science* 197, 261–263. doi: 10.1126/science.327543

Fang, J., Abrajano, T. A., Comet, P. A., Brooks, J. M., Sassen, R. and Macdonald, I. R. (1993). Gulf of Mexico Hydrocarbon Seep Communities: XI. Carbon Isotopic Fractionation During Fatty Acid Biosynthesis of Seep Organisms and its Implication for Chemosynthetic Processes. *Chem. Geo.* 109, 271–279. doi: 10.1016/0009-2541(93)90074-S

Feng, D., Cheng, M., Kiel, S., Qiu, J.-W., Yang, Q., Zhou, H., et al. (2015). Using Bathymodiolus Tissue Stable Carbon, Nitrogen and Sulfur Isotopes to Infer Biogeochemical Process at a Cold Seep in the South China Sea. *Deep-Sea Res. Pt I.* 104, 52–59. doi: 10.1016/j.dsr.2015.06.011

Feng, D., Qiu, J.-W., Hu, Y., Peckmann, J., Guan, H., Tong, H., et al. (2018). Cold Seep Systems in the South China Sea: An Overview. *J. Asian Earth Sci.* 168, 3–16. doi: 10.1016/j.jseaes.2018.09.021

Ferrier-Pagès, C. and Leal, M. C. (2018). Stable Isotopes as Tracers of Trophic Interactions in Marine Mutualistic Symbioses. *Ecol. Evol.* 9, 723–740. doi: 10.1002/ece3.4712

Ferrier-Pages, C. and Leal, M. C. (2019). Stable Isotopes as Tracers of Trophic Interactions in Marine Mutualistic Symbioses. *Ecol. Evol.* 9, 723–740. doi: 10.1002/ece3.4712

Fitznar, H. P., Lobbes, J. M. and Kattner, G. (1999). Determination of Enantiomeric Amino Acids With High-Performance Liquid Chromatography and Pre-Column Derivatisation With O-Phthaldialdehyde and N-Isobutyrylcysteine in Seawater and Fossil Samples (Mollusks). *J.Chromatogr. A.* 832, 123–132. doi: 10.1016/S0021-9673(98)01000-0

Folch, J., Lees, M. and Sloane Stanley, G. H. (1957). A Simple Method for the Isolation and Purification of Total Lipids From Animal Tissues. *J. Biol. Chem.* 226, 497–509. doi: 10.1016/S0021-9258(18)64849-5

Gerringer, M. E., Popp, B. N., Linley, T. D., Jamieson, A. J. and Drazen, J. C. (2017). Comparative Feeding Ecology of Abyssal and Hadal Fishes Through Stomach Content and Amino Acid Isotope Analysis. *Deep Sea Res. I Oceanogr. Res. Pap.* 121, 110–120. doi: 10.1016/j.dsr.2017.01.003

Goffredi, S. K., Tilic, E., Mullin, S. W., Dawson, K. S., Keller, A., Lee, R. W., et al. (2020). Methanotrophic Bacterial Symbionts Fuel Dense Populations of Deep-Sea Feather Duster Worms (Sabellida, Annelida) and Extend the Spatial Influence of Methane Seepage. *Sci. Adv.* 6, eaay8562. doi: 10.1126/sciadv.aay8562

Hoppe, H. G., Arnosti, C., and Herndl, G. F. (2001). "Ecological significance of bacterial enzymes in the marine environment," in Enzymes in the Environment, eds R. G. Burns and R. P. Dick (Basel: Marcel Dekker), 73–107.

Hosie, A. H., Allaway, D., Galloway, C. S., Dunsby, H. A. and Poole, P. S. (2002). Rhizobium Leguminosarum has a Second General Amino Acid Permease With Unusually Broad Substrate Specificity and High Similarity to Branched-Chain Amino Acid Transporters (Bra/LIV) of the ABC Family. *J. Bacteriol.* 184, 4071–4080. doi: 10.1128/jb.184.15.4071-4080.2002

Hugler, M. and Sievert, S. M. (2011). Beyond the Calvin Cycle: Autotrophic Carbon Fixation in the Ocean. *Anuu. Rev. Mar. Sci.* 3, 261–289. doi: 10.1146/annurev-marine-120709-142712

Jahnke, L. L., Summons, R. E., Hope, J. M. and Des Marais, D. J. (1999). Carbon Isotopic Fractionation in Lipids From Methanotrophic Bacteria II: The Effects of Physiology and Environmental Parameters on the Biosynthesis and Isotopic Signatures of Biomarkers. *Geochim. Cosmochim. Ac.* 63, 79–93. doi: 10.1016/S0016-7037(98)00270-1

Jing, H., Wang, R., Jiang, Q., Zhang, Y. and Peng, X. (2020). Anaerobic Methane Oxidation Coupled to Denitrification is an Important Potential Methane Sink in Deep-Sea Cold Seeps. *Sci. Total Environ.* 748, 142459. doi: 10.1016/j.scitotenv.2020.142459

Kaleta, C., Schauble, S., Rinas, U. and Schuster, S. (2013). Metabolic Costs of Amino Acid and Protein Production in Escherichia Coli. *Biotechnol. J.* 8, 1105–1114. doi: 10.1002/biot.201200267

Kellermann, M. Y., Schubotz, F., Elvert, M., Lipp, J. S., Birgel, D., Prieto-Mollar, X., et al. (2012). Symbiont–host Relationships in Chemosynthetic Mussels: A Comprehensive Lipid Biomarker Study. *Org. Geochem.* 43, 112–124. doi: 10.1016/j.orggeochem.2011.10.005

Kienast, M., Higginson, M. J., Mollenhauer, G., Eglinton, T. I., Chen, M. T. and Calvert, S. E. (2005). On the Sedimentological Origin of Down-Core Variations of Bulk Sedimentary Nitrogen Isotope Ratios. *Paleoceanography* 20, 2. doi: 10.1029/2004pa001081

Liao, L., Wankel, S. D., Wu, M., Cavanaugh, C. M. and Girguis, P. R. (2014). Characterizing the Plasticity of Nitrogen Metabolism by the Host and Symbionts of the Hydrothermal Vent Chemoautotrophic Symbioses Ridgeia Piscesae. *Mol. Ecol.* 23, 1544–1557. doi: 10.1111/mec.12460

Liu, D., Fang, Y., Tu, Y. and Pan, Y. (2014). Chemical Method for Nitrogen Isotopic Analysis of Ammonium at Natural Abundance. *Anal. Chem.* 86, 3787–3792. doi: 10.1021/ac403756u

Macavoy, S., Macko, S. and Joye, S. (2002). Fatty Acid Carbon Isotope Signatures in Chemosynthetic Mussels and Tube Worms From Gulf of Mexico Hydrocarbon Seep Communities. *Chem. Geo.* 185, 1–8. doi: 10.1016/S0009-2541(01)00394-1

Macko, S. A., Estep, M. L. F., Engel, M. H. and Hare, P. (1986). Kinetic Fractionation of Stable Nitrogen Isotopes During Amino Acid Transamination. *Geochim. Cosmochim. Ac.* 50, 2143–2146. doi: 10.1016/0016-7037(86)90068-2

Mahmood, T., Fang, J., Jiang, Z. and Zhang, J. (2016). Carbon and Nitrogen Flow, and Trophic Relationships, Among the Cultured Species in an Integrated Multi–Trophic Aquaculture (IMTA) Bay. *Aquacult. Env. Interac.* 8, 207–219. doi: 10.3354/aei00152

Mccarthy, M. D., Lehman, J. and Kudela, R. (2013). Compound-Specific Amino Acid δ15n Patterns in Marine Algae: Tracer Potential for Cyanobacterial vs. Eukaryotic Organic Nitrogen Sources in the Ocean. *Geochim. Cosmochim. Ac.* 103, 104–120. doi: 10.1016/j.gca.2012.10.037

Mcmahon, K. W. and Mccarthy, M. D. (2016). Embracing Variability in Amino Acid δ15n Fractionation: Mechanisms, Implications, and Applications for Trophic Ecology. *Ecosphere* 7, e01511. doi: 10.1002/ecs2.1511

Michaelis, W., Seifert, R., Nauhaus, K., Treude, T., Thiel, V., Blumenberg, M., et al. (2002). Microbial Reefs in the Black Sea Fueled by Anaerobic Oxidation of Methane. *Science* 297, 1013–1015. doi: 10.1126/science.1072502

Minagawa, M. and Wada, E. (1984). Stepwise Enrichment of 15N Along Food Chains: Further Evidence and the Relation Between δ15n and Animal Age. *Geochim. Cosmochim. Ac.* 48, 1135–1140. doi: 10.1016/0016-7037(84)90204-7

Ohkouchi, N., Chikaraishi, Y., Close, H. G., Fry, B., Larsen, T., Madigan, D. J., et al. (2017). Advances in the Application of Amino Acid Nitrogen Isotopic Analysis in Ecological and Biogeochemical Studies. *Org. Geochem.* 113, 150–174. doi: 10.1016/j.orggeochem.2017.07.009

Orphan, V. J., House, C. H., Hinrichs, K.-U., Mckeegan, K. D. and Delong, E. F. (2001). Methane-Consuming Archaea Revealed by Directly Coupled Isotopic and Phylogenetic Analysis. *Science* 293, 484–487. doi: 10.1126/science.1061338

Paull, C. K., Hecker, B., Commeau, R., Freeman-Lynde, R. P., Neumann, C., Corso, W. P., et al. (1984). Biological Communities at the Florida Escarpment Resemble Hydrothermal Vent Taxa. *Science* 226, 965–967. doi: 10.1126/science.226.4677.965

Petersen, J. M., Kemper, A., Gruber-Vodicka, H., Cardini, U., van der Geest, M., Kleiner, M., et al. (2016). Chemosynthetic Symbionts of Marine Invertebrate Animals are Capable of Nitrogen Fixation. *Nat. Microbiol.* 2, 16195. doi: 10.1038/nmicrobiol.2016.195

Pile, A. J. and Young, C. M. (1999). Plankton Availability and Retention Efficiencies of Cold-Seep Symbiotic Mussels. *Limnol. Oceanogr.* 44, 1833–1839. doi: 10.4319/lo.1999.44.7.1833

Ponnudurai, R., Heiden, S. E., Sayavedra, L., Hinzke, T., Kleiner, M., Hentschker, C., et al. (2020). Comparative Proteomics of Related Symbiotic Mussel Species Reveals High Variability of Host-Symbiont Interactions. *ISME. J.* 14, 649–656. doi: 10.1038/s41396-019-0517-6

Ponnudurai, R., Kleiner, M., Sayavedra, L., Petersen, J. M., Moche, M., Otto, A., et al. (2017). Metabolic and Physiological Interdependencies in the Bathymodiolus Azoricus Symbiosis. *ISME. J.* 11, 463–477. doi: 10.1038/ismej.2016.124

Raggi, L., Schubotz, F., Hinrichs, K. U., Dubilier, N. and Petersen, J. M. (2013). Bacterial Symbionts of Bathymodiolus Mussels and Escarpia Tubeworms From Chapopote, an Asphalt Seep in the Southern Gulf of Mexico. *Environ. Microbiol.* 15, 1969–1987. doi: 10.1111/1462-2920.12051

Riou, V., Bouillon, S., Serrão Santos, R., Dehairs, F. and Colaço, A. (2010). Tracing Carbon Assimilation in Endosymbiotic Deep-Sea Hydrothermal Vent Mytilid Fatty Acids by 13C-Fingerprinting. *Biogeosciences* 7, 2591–2600. doi: 10.5194/bg-7-2591-2010

Rodrigues, C. F., Hilário, A. and Cunha, M. R. (2013). Chemosymbiotic Species From the Gulf of Cadiz (NE Atlantic): Distribution, Life Styles and Nutritional Patterns. *Biogeosciences* 10, 2569–2581. doi: 10.5194/bg-10-2569-2013

Rubin-Blum, M., Antony, C. P., Borowski, C., Sayavedra, L., Pape, T., Sahling, H., et al. (2017). Short-Chain Alkanes Fuel Mussel and Sponge Cycloclasticus Symbionts From Deep-Sea Gas and Oil Seeps. *Nat. Microbiol.* 2, 17093. doi: 10.1038/nmicrobiol.2017.93

Rubin-Blum, M., Antony, C. P., Sayavedra, L., Martinez-Perez, C., Birgel, D., Peckmann, J., et al. (2019). Fueled by Methane: Deep-Sea Sponges From Asphalt Seeps Gain Their Nutrition From Methane-Oxidizing Symbionts. *ISME. J.* 13, 1209–1225. doi: 10.1038/s41396-019-0346-7

Ruff, S. E., Biddle, J. F., Teske, A. P., Knittel, K., Boetius, A. and Ramette, A. (2015). Global Dispersion and Local Diversification of the Methane Seep Microbiome. *P. Natl. Acad. Sci.* 112, 4015–4020. doi: 10.1073/pnas.1421865112

Schonberg, A. and Moubacher, R. (1952). The Strecker Degradation of α-Amino Acids. *Chem. Rev.* 50, 261–277. doi: 10.1021/cr60156a002

Suess, E. (2014). Marine Cold Seeps and Their Manifestations: Geological Control, Biogeochemical Criteria and Environmental Conditions. *Int. J. Earth Sci.* 103, 1889–1916. doi: 10.1007/s00531-014-1010-0

Sun, J., Zhang, Y., Xu, T., Zhang, Y., Mu, H., Zhang, Y., et al. (2017). Adaptation to Deep-Sea Chemosynthetic Environments as Revealed by Mussel Genomes. *Nat. Ecol. Evol.* 1, 121. doi: 10.1038/s41559-017-0121

Takano, Y., Chikaraishi, Y., Imachi, H., Miyairi, Y., Ogawa, N. O., Kaneko, M., et al. (2018). Insight Into Anaerobic Methanotrophy From 13C/12C- Amino Acids and 14C/12C-ANME Cells in Seafloor Microbial Ecology. *Sci. Rep.* 8, 14070. doi: 10.1038/s41598-018-31004-5

Tobler, M., Passow, C. N., Greenway, R., Kelley, J. L. and Shaw, J. H. (2016). The Evolutionary Ecology of Animals Inhabiting Hydrogen Sulfide–Rich Environments. *Annu. Rev. Ecol. Evol. S.* 47, 239–262. doi: 10.1146/annurev-ecolsys-121415-032418

Vokhshoori, N. L., Mccarthy, M. D., Close, H. G., Demopoulos, A. W. J. and Prouty, N. G. (2021). New Geochemical Tools for Investigating Resource and Energy Functions at Deep-Sea Cold Seeps Using Amino Acid δ15n in Chemosymbiotic Mussels (Bathymodiolus Childressi). *Geobiology* 19 (6), 601–617 . doi: 10.1111/gbi.12458

Volland, J. M., Schintlmeister, A., Zambalos, H., Reipert, S., Mozetic, P., Espada-Hinojosa, S., et al. (2018). NanoSIMS and Tissue Autoradiography Reveal Symbiont Carbon Fixation and Organic Carbon Transfer to Giant Ciliate Host. *ISME. J.* 12, 714–727. doi: 10.1038/s41396-018-0069-1

Wagner, A. (2005). Energy Constraints on the Evolution of Gene Expression. *Mol. Biol. Evol.* 22, 1365–1374. doi: 10.1093/molbev/msi126

Wang, X. (2018). *Nutritional Sources Analysis and the Heavy-Metal Enrichment of the Macrofauna From Deep-Sea Chemotrophic Ecosystem Qingdao:* (Institute of Oceanology, Chinese Academy of Sciences).

Wang, F., Wu, Y., Chen, Z., Zhang, G., Zhang, J., Zheng, S., et al. (2019). Trophic Interactions of Mesopelagic Fishes in the South China Sea Illustrated by Stable Isotopes and Fatty Acids. *Front. Mar. Sci.* 5. doi: 10.3389/fmars.2018.00522

Wang, F., Wu, Y., Zhang, L., Jin, J., Chen, Z., Zhang, J., et al. (2022). Improved Method for Measuring the δ15n Compound-Specific Amino Acids: Application on Mesopelagic Fishes in the South China Sea. *Acta Oceanol. Sin.* 41, 30–38. doi: 10.1007/s13131-021-1812-4

Wong, Y. H., Sun, J., He, L. S., Chen, L. G., Qiu, J. W. and Qian, P. Y. (2015). High-Throughput Transcriptome Sequencing of the Cold Seep Mussel Bathymodiolus Platifrons. *Sci. Rep.* 5, 16597. doi: 10.1038/srep16597

Wu, Y., Dittmar, T., Ludwichowski, K.-U., Kattner, G., Zhang, J., Zhu, Z. Y., et al. (2007). Tracing Suspended Organic Nitrogen From the Yangtze River Catchment Into the East China Sea. *Mar. Chem.* 107, 367–377. doi: 10.1016/j.marchem.2007.01.022

Xu, T., Feng, D., Tao, J. and Qiu, J.-W. (2019). A New Species of Deep-Sea Mussel (Bivalvia: Mytilidae: Gigantidas) From the South China Sea: Morphology, Phylogenetic Position, and Gill-Associated Microbes. *Deep-Sea Res. Pt I.* 146, 79–90. doi: 10.1016/j.dsr.2019.03.001

Yamaguchi, Y. T., Chikaraishi, Y., Takano, Y., Ogawa, N. O., Imachi, H., Yokoyama, Y., et al. (2017). Fractionation of Nitrogen Isotopes During Amino Acid Metabolism in Heterotrophic and Chemolithoautotrophic Microbes Across Eukarya, Bacteria, and Archaea: Effects of Nitrogen Sources and Metabolic Pathways. *Org. Geochem.* 111, 101–112. doi: 10.1016/j.orggeochem.2017.04.004

Zhang, L. and Altabet, M. A. (2008). Amino-Group-Specific Natural Abundance Nitrogen Isotope Ratio Analysis in Amino Acids. *Rapid Commun. Mass* Sp. 22, 559–566. doi: 10.1002/rcm.3393

Zhang, L., Lee, W. M., Kreider-Mueller, A., Kuhnel, E., Baca, J., Ji, C., et al. (2021). High-Precision Measurement of Phenylalanine and Glutamic Acid δ15N by Coupling Ion-Exchange Chromatography and Purge-and-Trap Continuous-Flow Isotope Ratio Mass Spectrometry. *Rapid Commun. Mass* Sp. 35, e9085. doi: 10.1002/rcm.9085

Conflict of Interest: The authors declare that the research was conducted in the absence of any commercial or financial relationships that could be construed as a potential conflict of interest.

Publisher's Note: All claims expressed in this article are solely those of the authors and do not necessarily represent those of their affiliated organizations, or those of the publisher, the editors and the reviewers. Any product that may be evaluated in this article, or claim that may be made by its manufacturer, is not guaranteed or endorsed by the publisher.

frontiers | Frontiers in Marine Science

ORIGINAL RESEARCH
published: 18 July 2022
doi: 10.3389/fmars.2022.889022

Stirring the Deep, Disentangling the Complexity: Report on the Third Species of *Thermochiton* (Mollusca: Polyplacophora) From Haima Cold Seeps

Hao Wang[1,2†], *Huijie Liu*[2†], *Xiaowei Wang*[3,4,5], *Junlong Zhang*[2,4,5*], *Boris I. Sirenko*[6], *Chuanyu Liu*[3,4,5], *Dong Dong*[2,4] *and Xinzheng Li*[2,4,5]

[1]School of Marine Science and Engineering, Qingdao Agricultural University, Qingdao, China, [2]Laboratory of Marine Organism Taxonomy and Phylogeny, Institute of Oceanology, Chinese Academy of Sciences, Qingdao, China, [3] Key Laboratory of Ocean Circulation and Waves, Institute of Oceanology, Chinese Academy of Sciences, Qingdao, China, [4]Center for Ocean Mega-Science, Chinese Academy of Sciences, Qingdao, China, [5]Laboratory for Ocean Dynamics and Climate, Pilot National Laboratory for Marine Science and Technology, Qingdao, China, [6]Zoological Institute, Russian Academy of Sciences, St. Petersburg, Russia

OPEN ACCESS

Edited by:
Jian-Wen Qiu,
Hong Kong Baptist University, Hong Kong SAR, China

Reviewed by:
Douglas Eernisse, California State University, Fullerton, United States
Julia Sigwart, Queen's University Belfast, United Kingdom

***Correspondence:**
Junlong Zhang
zhangjl@qdio.ac.cn

[†]*These authors have contributed equally to this work*

Specialty section:
This article was submitted to Deep-Sea Environments and Ecology, a section of the journal Frontiers in Marine Science

Received: *03 March 2022*
Accepted: *13 June 2022*
Published: *18 July 2022*

Citation:
Wang H, Liu H, Wang X, Zhang J, Sirenko BI, Liu C, Dong D and Li X (2022) Stirring the Deep, Disentangling the Complexity: Report on the Third Species of Thermochiton (Mollusca: Polyplacophora) From Haima Cold Seeps. Front. Mar. Sci. 9:889022. doi: 10.3389/fmars.2022.889022

This study documents a new deep-sea chiton from the Haima cold seeps. Thermochiton xui. nov. is the third species of the genus Thermochiton and the first occurrence of this genus in the South China Sea. This species is identified by its morphological characteristics and the molecular sequence of a Thermochiton species is reported for the first time. The placement of the new species is determined in the phylogenetic tree of Ischnochitonidae by Maximum Likelihood (ML) and Bayesian inference (BI) methods, based on the sequences of the mitochondrial cytochrome c oxidase subunit I (COI), 16S ribosomal DNA (16S), and nuclear 28S ribosomal DNA (28S) gene regions. Bayesian evolutionary analysis with an uncorrelated relaxed clock approach indicated that this new species is estimated to have diverged from its most closely related shallow-water ischnochitonid taxa 5.10–10.07 million years ago in the Late Miocene. A regional ocean general circulation model was used to estimate the potential dispersal ability of the three species of Thermochiton. Because it is highly unlikely for one species to have spread between the northwest and southwest Pacific to the localities in which this genus has been found to date, we propose that 'stepping-stone' habitats and/or 'bridge species' were involved in the dispersal and evolution of these cold-seep endemic chitons.

The ZooBank Life Science Identifier (LSID) for this publication is: urn:lsid:zoobank.org:pub:AD93E4BC-2977-405E-B681-D956C5C66D83. And the ISID for Thermochiton xui sp. nov. is: urn:lsid:zoobank.org:act:0C75D2E3-F30E-4970-9BC2-3363B397720C.

Keywords: chiton, *Thermochiton*, Ischnochitonidae, Haima cold seeps, South China Sea, deep-sea, chemosynthetic habitat, numerical model

INTRODUCTION

The Haima cold-seep field, covering 618 km^2, was recently discovered on the northwestern slope of the South China Sea. Within this field, an area of 350 km^2 has had cold seep activity and developed into cold-seep carbonate rocks with crusts and nodules that harbor a distinct biological community (Liang et al., 2017; Zhao et al., 2020). To date, more than 80 species of macrobenthic organisms

have been sampled from the Haima cold seeps, including mostly mollusks, polychaetes, and crustaceans, a few species of echinoderms, and other animals. Since the discovery of the Haima cold seeps, many new molluskan species and the first recorded occurrences of species in the South China Sea have been reported while exploring the benthic communities associated with the cold seeps (Zhang et al., 2016; Zhang and Zhang, 2017; Chen et al., 2018; Sun et al., 2018; Jiang et al., 2019; Xu et al., 2019; Dong et al., 2021). Among them, primarily gastropods and bivalves have been found, with only one reported species of the class Polyplacophora (Dong et al., 2021).

Most polyplacophorans, also called chitons, live in shallow waters, usually in the intertidal zones on rocky substrates. Only a small fraction of chitons have been found in abyssal or bathyal habitats, especially in chemosynthetic environments such as sunken wood, cold seeps, or hydrothermal vents. Until 2010, only 18 chiton species had been found in chemosynthetic areas, of which 16 species were found in cold seeps (Schwabe and Sellanes, 2010). However, new deep-sea species have been discovered with the improvement of exploration technology (Sigwart et al., 2010; Sigwart and Sirenko, 2012; Sirenko and Sellanes, 2016; Sigwart and Chen, 2018; Sirenko, 2020). Saito and Okutani (1990) described a chiton of the order Chitonida from hydrothermal vents in the central Okinawa Trough, East China Sea. They established the genus *Thermochiton* for *Thermochiton undocostatus* Saito & Okutani, 1990 and placed the genus in the family Ischnochitondae. The second member of the genus, *Thermochiton papuaensis*, was reported in deep waters near Papua New Guinea, likely inhabiting communities with chemical activity (Sirenko, 2020). However, both species were described merely by their morphology without any genetic information. Their relationship within the family Ischnochitondae has not been determined by molecular analysis.

Ischnochitonidae is the largest family of Polyplacophora. Kaas and Van Belle (1980) classified the family into 18 genera, comprising approximately 400 species, which contained almost half of the known chitons at the time. Although the taxa were later rearranged (Sirenko, 2006), this large family currently includes 10 genera and approximately 228 species (World Register of Marine Species). Chitons of this family have distinct apophyses, well-developed slits on all valves, insertion plates that are not pectinated, and dorsal surfaces that lack ocelli. Their adanal gills do not extend to the anus. Additionally, all members of the family Ischnochitonidae have a scaly dorsal girdle and varying tegmental sculptures (Kaas and Van Belle, 1987). The inherent paraphyly and lack of well-defined diagnostic morphological features of this family have led to taxonomic controversy. Some molecular studies suggest that the family Ischnochitonidae is not monophyletic (Okusu et al., 2003; Owada, 2018; Irisarri et al., 2020). Even the monophyly of its type genus, *Ischnochiton*, remains doubtful (Owada, 2018; Irisarri et al., 2020). However, most ischnochitonids have only been described by their morphology, and molecular information is scarce. Indeed, the sequences of mitochondrial cytochrome c oxidase subunit I (COI), the most widely used effective DNA barcoding gene marker, have only been published for 24 species of Ischnochitonidae in the NCBI database.

The evolutionary history of geographically separated but closely related species is tangled but fascinating. Chemoautotrophic environments are ideal natural laboratories for studying the spread, connectivity, and evolution. Hydrothermal vents or cold seeps, are essentially isolated islands in the deep sea. As most vent-endemic species are benthic with limited mobility at their adult stage, the larval stage is vital for dispersal and colonization of species obligately living in chemoautotrophic environments (Tyler and Young, 1999; Tyler and Young, 2003). The wide geographic range of distributed species and long-distance dispersal or high connectivity of panmictic populations are achieved *via* long periods of planktonic larval duration (PLD) for swimming larvae (Adams et al., 2012; Fukumori and Kano, 2014; Yahagi et al., 2019). Some vent or seep mollusks, such as *Shinkailepas myojinensis* (Yahagi et al., 2017), *Shinkailepas briandi* (Yahagi et al., 2019), *Bathymodiolus childressi*, and *Thalassonerita naticoidea* (= *Bathynerita naticoidea*) (Arellano et al., 2014), develop long-lived planktotrophic larvae (Warén and Bouchet, 2001; Fukumori and Kano, 2014), which can vertically migrate hundreds of meters to photic and even euphotic zones to hunt for abundant food supplies (Bouchet and Warén, 1994; Arellano et al., 2014). These larvae were considered to float for at least 7–12 months in the pelagic water column before settling, based on the sizes of planktonic and settled larvae, as well as post-settlement juveniles (Arellano et al., 2014; Yahagi et al., 2017). The longer PLD of these species and stronger currents at the sea surface presumably fuel broad-ranged distribution and genetic homogeneity (Bouchet and Warén, 1994; Yahagi et al., 2017). Several crustaceans have developed the same strategy (Teixeira et al., 2011; Beedessee et al., 2013). However, the strategies employed by vent-associated chitons to colonize new territories and expand their distribution have not yet been reported, partly because of their rare occurrence.

During an exploratory cruise of the Haima cold seeps, two specimens of deep-sea chiton were collected and reported as *Leptochiton tenuidontus* Saito & Okutani, 1990 by Dong et al. (2021). This species was misidentified and should be classified as a new species of the genus *Thermochiton*. In this study, we clarify the identification of this new species. Our account is based on analyzing the valve, girdle, and radula morphological characteristics of the chiton, as well as DNA sequencing of the mitochondrial COI, 16S ribosomal DNA (16S), and nuclear 28S ribosomal DNA (28S) gene regions. DNA sequences were used to confirm the arrangement of this *Thermochiton* species within the family Ischnochitondae and to explore its evolutionary relationship with its shallow-water relatives. Further, a numerical model was used to simulate the dispersal range and estimate the potential dispersal ability, thus suggesting the evolutionary pathway of *Thermochiton* species.

MATERIAL AND METHODS

Sample Collection

The samples for this study were obtained during a cruise to the Haima cold seeps in the South China Sea on 19 May 2018 (**Figure 1**). The two individual specimens

were directly preserved in 75% ethanol. The specimens were initially identified at the species level based on their morphology according to identification guidelines (Saito and Okutani, 1990; Saito, 2004; Saito et al., 2008; Sirenko, 2021). The specimens were deposited in the Marine Biological Museum, Chinese Academy of Sciences (MBMCAS), Qingdao, China.

Morphological Observations

The two specimens were identified at the species level under a Zeiss SteREO Discovery.V12 stereo microscope (Zeiss, Wetzlar, Germany). The body length and width were measured, and the number of gills and gill types were observed. Specimens were placed in 7% NaOH and boiled for 10 min, followed by boiling twice in freshwater. Selected valves (head plate, 5th or 2nd plate of the intermediate plates, and tail plate), half of the radula, and a portion of the girdle were glued to the sample stage with conductive glue, gold plated in a vacuum sputter coater, and examined under a Hitachi S-3400N scanning electron microscope (Hitachi, Tokyo, Japan) at an accelerating voltage of 5 kV.

Genetic Study

Total DNA was extracted using a marine animal genomic DNA extraction kit (Tiangen Biotechnology, Beijing, China) according to the instructions of the manufacturer. To explore the genetic distance and relationship of the species to common coastal and deep-sea chitons of the family Ischnochitonidae, the mitochondrial COI, 16S rRNA (16S), and nuclear 28S rRNA (28S) gene regions were sequenced and analyzed.

Polymerase chain reaction (PCR) amplification of the mitochondrial COI gene was carried out using primers LCO1490 (5′-GGTCAACAAATCATAAAGATATTGG-3′) and HCO2198 (5′-TAAACTTCAGGGTGACCAAAAAATCA-3′). The mitochondrial 16S rRNA gene was amplified using primers 16Sa (5'-CGCCTGTTTATCAAAAACAT-3') and 16Sb (5'-CTCCGGTTTGAACTCAGATCA-3'). The nuclear 28S rRNA gene was amplified using primers 28Sa (5'-GACCCGTCTTGAAACACGGA-3') and 28Sb (5'-TCGGAAGGAACCAGCTAC-3'). PCR amplifications were carried out using a total reaction volume of 25 μl, with 12 μl 2×Es Taq MasterMix (CoWin Biosciences Co., Ltd., Beijing, China), 2 μl of template DNA (50 ng/μl), 1 μl of each primer (10 M), and 9 μl of dH_2O. The thermal cycling conditions for PCR amplification were as follows: initial denaturation at 95°C for 3 min, followed by 35 cycles of 95°C (30 s), annealing temperature of 50°C for 1 min, extension at 72°C for 1 min, and a final elongation at 72°C for 10 min. Double-stranded PCR products were purified and sequenced by BGI Tech Solutions Co., Ltd. PCR products were detected by an agarose gel.

The 24 species of the family Ischnochitonidae with available COI, 16S rRNA, and 28S rRNA gene sequences were also included in the analysis (**Table 1**). *Callistochiton jacobaeus* and *Callistochiton antiquus* of the family Callistoplacidae, *Rhyssoplax kurodai* of the family Chitonidae, and *Chaetopleura apiculata* and *Chaetopleura angulata* of the family Chaetopluridae were selected as outgroups based on their current taxonomic relationships.

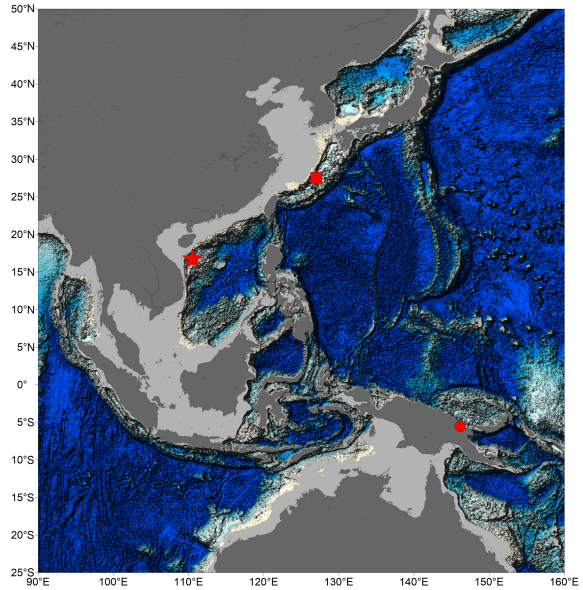

FIGURE 1 | Map of samples sites of species of genus *Thermochiton*. Location of Haima cold seeps was indicated by a pentacle. Type localities of *Thermochiton undocostatus* and *Thermochiton papuaensis* were indicated by square and circle, respectively.

All sequences were aligned using MAFFT v.7 software (Katoh and Standley, 2013) with the G-INS-I algorithm. Alignments were carried out by eye and BLAST analyses of the NCBI database. The online version of Automatic Barcode Gap Discovery (ABGD) (Puillandre et al., 2012) was used to detect barcode gaps and help support species delineation (https://bioinfo.mnhn.fr/abi/public/abgd/abgdweb.html) using four randomly selected COI sequences of the 24 available species of Ischnochitonidae obtained from published studies, excluding outgroups (**Supplementary Table S1**). The analysis settings were as follows: Pmin = 0.001, Pmax = 0.1, Steps = 10, X (relative gap width) = 1.0. Then, the Kimura two-parameter model was used to measure a matrix of pairwise distances (Kimura, 1980). The COI, 16S, and 28S gene sequences from the same individual were concatenated using SequenceMatrix software (Vaidya et al., 2011) to conduct phylogenetic analysis of a combined-gene data set. Best-fitting sequence evolution models were calculated using jModelTest 2.1.10 software (Darriba et al., 2012), deriving the best-fit general time-reversible (GTR)+G model. The maximum likelihood (ML) method was executed using RaxML1.5b1 software (Stamatakis, 2014). The test was executed 1,000 times with the default settings. The support bootstrap scores of nodes were obtained from the best scoring tree after 1,000 bootstrap replications. A Bayesian phylogenetic analysis was carried out using MrBayes v.3.2.6 software (Ronquist et al., 2012). The program was run for 10,000,000 generations, sampling every 1,000 generations.

TABLE 1 | List of species and sequences used in this study for phylogenetic analysis.

Family	Species	COI	16S	28S	Reference
Ischnochitonidae	*Ischnochiton australis*	AY377707	AY377596	AY377670	Okusu et al. (2003)
	Ischnochiton boninensis	LC071647	LC071575	LC071611	Owada (2016)
	Ischnochiton boninensis	AY377709	AY377593	AY377673	Okusu et al. (2003)
	Ischnochiton comptus	LC071627	LC071570	LC071606	Owada (2016)
	Ischnochiton elongatus	AY377708	AY377595	AY377672	Okusu et al. (2003)
	Ischnochiton hakodadensis	LC214409	LC214398	LC214387	Owada (2018)
	Ischnochiton hayamii	LC214410	LC214399	LC214388	Owada (2018)
	Ischnochiton manazuruensis	LC071619	LC071565	LC071601	Owada (2016)
	Ischnochiton paululus	LC214411	LC214400	LC214389	Owada (2018)
	Ischnochiton poppei	LC214412	LC214401	LC214390	Owada (2018)
	Ischnochiton rissoi	AY377706	AY377594	AY377671	Okusu et al. (2003)
	Ischnochiton tridentatus	EF200831			Kelly and Eernisse (2007)
	Ischnochiton tridentatus	EF200834			Kelly and Eernisse (2007)
	Stenoplax alata	LC214413	LC214402	LC214391	Owada (2018)
	Stenoplax alata	AY377711	AY377598	AY377675	Okusu et al. (2003)
	Stenoplax conspicua	EF200968			Kelly and Eernisse (2007)
	Stenoplax mariposa	EF200987			Kelly and Eernisse (2007)
	Stenoplax limaciformis	KC669559			García-Ríos et al. (2014)
	Stenoplax purpurascens	KC669552			García-Ríos et al. (2014)
	Stenoplax floridana	KC669562			García-Ríos et al. (2014)
	Stenosemus albus	KF643687			Layton et al. (2014)
	Lepidozona cooperi	EF200850			Kelly and Eernisse (2007)
	Lepidozona pectinulata	EF200910			Kelly and Eernisse (2007)
	Lepidozona interstincta	EF200871			Kelly and Eernisse (2007)
	Lepidozona radians	EF200957			Kelly and Eernisse (2007)
	Lepidozona coreanica	LC071669	LC071582	LC071618	Owada (2018)
	Lepidozona mertensii	AY377710	AY377597	AY377674	Okusu et al. (2003)
	Thermochiton xui sp. nov.	OM896760	OM892876	OM892875	This study
	Thermochiton xui sp. nov.	OM896759	OM892877	OM892878	This study
Callistoplacidae	*Callistochiton jacobaeus*	LC071667	LC071580	LC071616	Owada (2016)
	Callistochiton antiquus	AY377712	AY377599	AY377676	Okusu et al. (2003)
Chitonidae	*Rhyssoplax kurodai*	LC071668	LC214381	LC071617	Owada (2016)
Chaetopluridae	*Chaetopleura apiculata*	AY377704	AY377590	AY377667	Okusu et al. (2003)
	Chaetopleura angulata	AY377703	AY377591	AY377668	Okusu et al. (2003)
Mopaliidae	*Mopalia cirrata*	EU409065	EU407007		Kelly and Eernisse (2007)
	Mopalia ferreirai	EF159654	EU407015		Kelly and Eernisse (2007)
	Mopalia acuta	EU409064	EU406984		Kelly and Eernisse (2007)

The uncorrelated relaxed clock method was used to estimate the divergence times of the different taxa using BEAST v. 1.10.4 software, based on the Bayesian interference (BI) tree of the concatenated sequences of three genes (Suchard et al., 2018). The earliest fossil record of *Mopalia*, 15–17.2 million years ago (MYA) (Kelly and Eernisse, 2008), was taken as the calibration point. An uncorrelated relaxed lognormal clock was derived for each partition using the GTR substitution model, assuming that the tree prior had a Yule species formation process. This analysis was run for 100 million generations, sampling every 1,000 generations with a 10% burn-in rate. The final result image was rendered using Figtree v1.4.4 software.

Tracer Simulation

The diffusion and advection processes of the biological tracer in the ocean were simulated using a regional ocean general circulation model (OGCM), which was constructed based on the Massachusetts Institute of Technology general circulation model (MITgcm) (Marshall et al., 1997). Our model domain ranged from 25°S to 45°N and from 110°E to 174°E, with a horizontal resolution of 1/10° × 1/10° and 82 z-levels in the vertical. Vertical mixing was represented using the K-Profile Paremeterization (KPP) scheme (Large et al., 1994), and background vertical viscosity and diffusivity were set as 10^{-4} and 10^{-5} m^2 s^{-1}, respectively. The potentially unresolved eddy processes were represented by the parameterizations described by Gent and McWilliams (1990) and Redi (1982), with both layer thickness and isopycnal diffusivity set at 500 m^2 s^{-1}. The initial temperature and salinity of the field were obtained from the climatological monthly mean data for January, which were derived from the Generalized Digital Environmental Model, version 3 (GDEMv3; http://www.

usgodae.org/pub/outgoing/static/ocn/gdem/) dataset. The climatological monthly mean wind stress was calculated from the cross-calibrated multiplatform (CCMP) datasets (Atlas et al., 2011), with a relaxation of the sea surface temperature and salinity to the monthly mean GDEMv3 climatology.

The model was started from an initial state of rest and ran for 100 years. The simulated total kinetic energy of the upper ocean layer reached a quasi-equilibrium state after a 100-year run. Subsequently, the simulated monthly mean temperature, salinity, and currents of the last month were used as the initial states of the following tracer experiments. The horizontal and vertical diffusivities were the same as those in the circulation model. The three localities of *Thermochiton* species were selected as the origins of the model: (1) the central Okinawa Trough, the type locality of *T. undocostatus* Saito et Okutani, 1990 (Saito and Okutani, 1990); (2) Papua New Guinea, the type locality of *T. papuaensis* Sirenko, 2020 (Sirenko, 2020); and (3) the Haima cold seeps in the South China Sea, where our specimens were collected. A tracer experiment was carried out for each origin. At the corresponding model grid of each origin, 100 million floats/m^3 were released at the first model level of 2.5 m water depth. All three experiments ran for three years, with the monthly-mean tracer concentration fields used for analysis.

RESULTS

Systematics

Class Polyplacophora Gray, 1821
Order Chitonida Thiele, 1909
Family Ischnochitonidae Dall, 1889
Genus *Thermochiton* Saito et Okutani, 1990
Thermochiton xui Wang, Zhang & Sirenko sp. nov.
(**Figures 2**-**5**)
rn:lsid:zoobank.org:act:0C75D2E3-F30E-4970-9BC2-3363B397720C

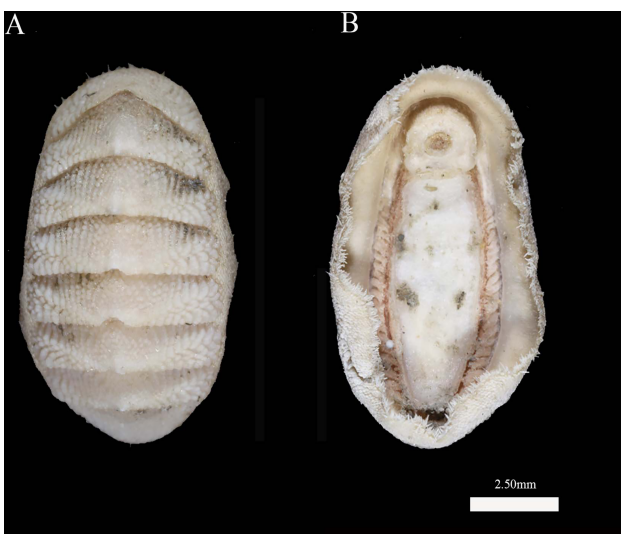

FIGURE 2 | *Thermochiton xui* sp. nov., holotype: MBM229030. **(A)** Dorsal view; **(B)** Ventral view.

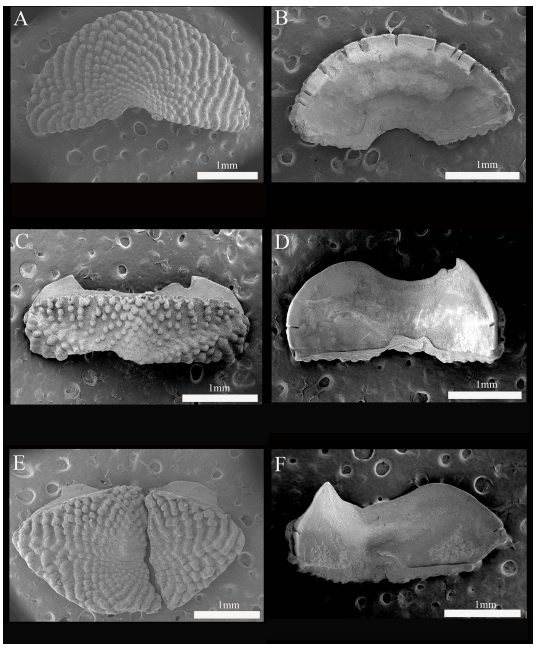

FIGURE 3 | *Thermochiton xui* sp. nov. holotype: MBM229030. **(A)** Head valve, dorsal view; **(B)** Head valve, ventral view; **(C)** Valve III, dorsal view; **(D)** Valve III, ventral view; **(E)** Tail valve, dorsal view; and **(F)** Valve IV, ventral view.

Type Material

Holotype: MBM229030, BL 9.0 mm. Paratype: MBM229031, BL 8.5 mm. All collected from type locality, May 19, 2018, and deposited in the Marine Biological Museum, Chinese Academy of Sciences (MBMCAS), Qingdao.

Type Locality

Haima cold seeps, South China Sea, off southern Hainan Island.

Distribution and Habitat

Only known from the type locality, Haima cold seeps, South China Sea, chemosynthetic habitat at a depth of 1,380–1,390 m.

Etymology

This species is named after Prof. Fengshan Xu for his contributions to Chinese malacology on Polyplacophora. He is the first Chinese author who has published the taxonomy of chitons and has described one genus, *Sinolorica* (= *Loricella* Pilsbry, 1893) and two species of chiton, *Sinolorica scissurata* (= *Loricella scissurata*) and *Deshayesiella sinica* (= *Hanleya sinica*) from the East China Sea (Xu, 1990).

Diagnosis

Animal small, oval to elongated oval in shape, dorsal elevation rather high, and subcarinated. The valves rather elevated, not beaked. Tegmentum white in color. Slit formula 11/1(2)/12. Girdle moderately wide and dorsally covered with dense, imbricating, obliquely set, squarish, curved, and wide scales with large round granules at the distal end and sculpted into approximately 18 longitudinal rows of smaller granules on the

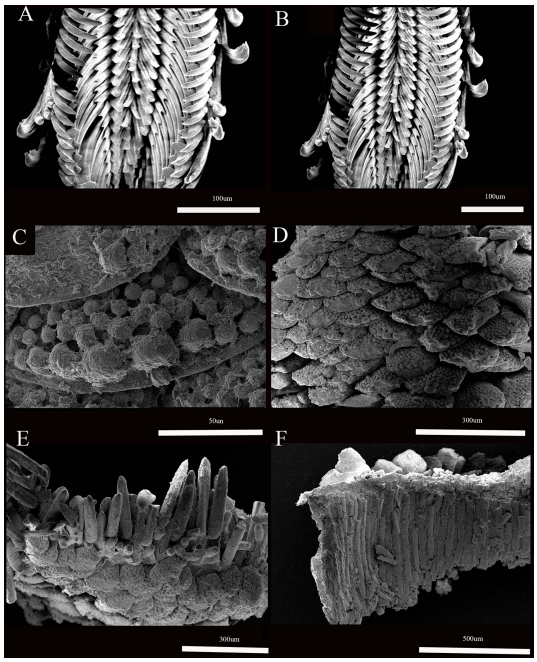

FIGURE 4 | *Thermochiton xui* sp. nov. paratype: MBM229031. **(A, B)** Portion of radula; **(C, D)** Dorsal scales; **(E)** Dorsal scales and marginal spicules; and **(F)** ventral scales.

dorsal side of the scales. Two types of marginal spicules long, smooth, needle-like spicules and short, smooth, blunt-topped spicules. Central tooth of the radula elongated with a wide base. Centro-lateral tooth rough, wedge-shaped, attenuated posteriorly, taller than the central tooth, with a subtriangular blade at the antero-dorsal edge. The top of the lateral central tooth narrow with a sharp, oblique, inward tip. The head of the major lateral tooth of the radula is unicuspidal, bent, sickle-shaped, with an extended base ending with a long, sharp-pointed process directed inside.

Description

Animal elliptical in shape, with a body length of 9.0 mm. Valves rather elevated valves, not beaked, and the side slopes weakly convex. Color of the valves and girdle is white with friable, rusty brown deposits.

Head valve is semicircular, with a straight front slope, and the posterior margin is widely V-shaped and weakly notched in the middle. Intermediate valves rather short compared to their width, rectangular, with the front margin slightly convex, side margins rounded, the front margin slightly angular, the hind margin straight, with no beaks, and lateral areas strongly raised. Tail valve less than semicircular, front margin more or less angular, less wide than the head valve, the length is about half the width, the antemucronal and postmucronal slopes slightly convex, and the mucro central and not swollen.

All the valves in the jugal area delicately sculptured by randomly arranged, oval, flattened granules. Pleural area of intermediate valves covered with randomly arranged, large, and drop-shaped granules. Lateral area covered with elongated granules formed undulating costae. Numerous pores of aesthetes evenly covering both the costae and the interstices between them.

Articulamentum very thin, transparent, and glassy white; apophyses short, very wide, and rounded, coalescing across the small, shallow sinus; slit formula of insertion plates 11/1(2)/12; slit rays barely visible; and the solid teeth short, blunt, and the eaves are narrow. Four of the six intermediate valves with 2 slits on one side, whereas the other sides and other valves with only one slit per side. Ventral tegmental callus well developed.

Girdle rather wide, colored like the tegmentum, and dorsally covered with imbricating obliquely set, curved, wide

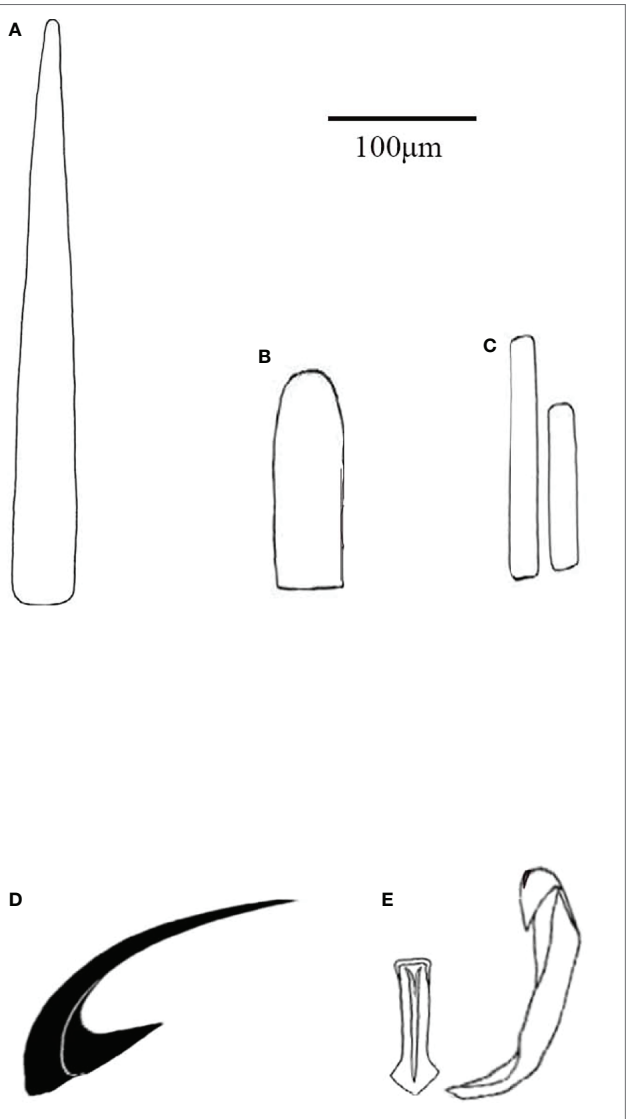

FIGURE 5 | *Thermochiton xui* sp. nov. **(A)** Smooth marginal needle; **(B)** Short blunt-topped marginal spicules; **(C)** Ventral scales; **(D)** Head of major lateral tooth of radula. and **(E)** Central and first lateral teeth of radula.

scales, with large round granules at the distal end and about 18 longitudinal rows of smaller granules on the dorsal side of the scales. Scales near valves straight, but in other places angled in different directions. Some scales with 1–4 short longitudinal ribs near the side margin. Marginal spicules of two types: long, smooth spicules-needles and short, smooth blunt-topped spicules. Ventral side of the girdle is paved with smooth, elongate scales.

Radula 4.1 mm long with 110 transverse rows of mature teeth. Central tooth rectangular, oblong, parallel-sided, keeled medially, with a small blade and a large base. First lateral tooth is roughly wedge-shaped, attenuated posteriorly, taller than the central tooth, with a subtriangular blade at the antero-dorsal edge. Major lateral tooth is thin, long, with a shaft broadened near the base. Head of the major lateral tooth is unicuspid, bent, claw-shaped, with an extended base ending with a long, sharp-pointed process directed inside. Inner small laterals with two spatula-shaped processes and prow-shaped outer small laterals.

A total of 22 gills on each side, extending from valve II to valve VII. The gut containing rusty brown particles of detritus.

Remarks

The new species is the third species within the genus *Thermochiton* and has a very similar morphology to *T. undocostatus* and *T. papuaensis*. The new species differs from *T. undocostatus* by the tegmentum of intermediate valves being covered by granules (vs. undulating costae in *T. undocostatus*) and having two types of marginal spicules: long, smooth spicules-needles and short, smooth blunt-topped spicules (vs. only long, smooth spicules in *T. undocostatus*). *Thermochiton xui* sp. nov. differs from *T. papuaensis* by having granules in the whole tegmentum of intermediate valves (vs. granules only in the jugal area and other areas with undulating costae in *T. papuaensis*); having two types of marginal spicules (vs. three types in *T. papuaensis*: long, smooth spicules and two kinds of ribbed spicules); and the first lateral tooth of the radula being approximately twice as long as the central tooth (vs. the first lateral tooth is approximately the same length as the central tooth in *T. papuaensis*).

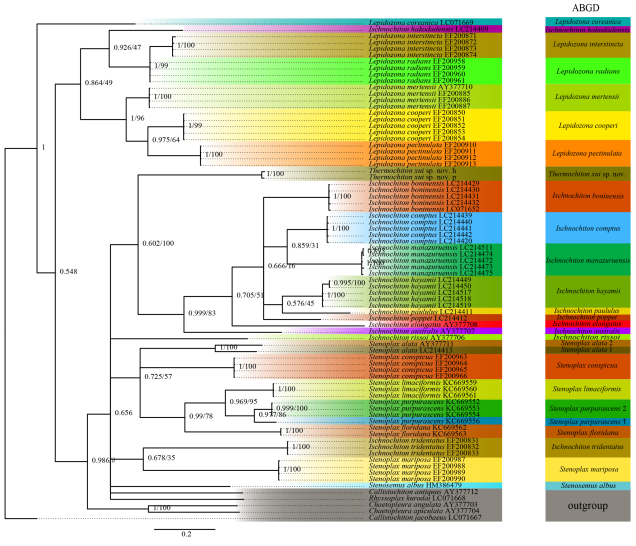

FIGURE 6 | Phylogeny tree of the chitons based on the COI dataset. Numbers above branches refer to BI posterior probability (PP) and ML bootstrap scores (BS). The ABGD based on the COI alignment with the model Kimura (K80) TS/TV (2.0).

Genetic Analysis

The ABGD analysis was performed on the COI gene sequences to determine whether the two specimens of *T. xui* sp. nov. were the same species and to conducted sequence-based species delimitation of the members of the family Ischnochitonidae (**Figure 6**). The ABGD analysis divided the 25 candidate species of chitons into reciprocal clades on the phylogenetic trees. The two specimens collected from the Haima cold seeps belonged to one species, *T. xui* sp. nov., which was consistent with the morphological identification. Additionally, both *Stenoplax alata* and *Stenoplax purpurascens* were respectively divided into two separate species. ML and BI analyses of the concatenated three-gene dataset facilitated the reconstruction of the phylogenetic tree, revealing similar topologies (**Figure 7**). The concatenated tree indicated that the new species was a sister group to most *Ischnochiton* taxa which is one of the four clades of the genus *Ischnochiton*. The species *Ischnochiton rissoi*, *Ischnochiton tridentatus*, and *Ischnochiton hakodadensis* were excluded from this main clade and formed three separate and distant clades. Likewise, the concatenated tree provided consistent support for the non-monophyly of the family Ischnochitonidae. The *Lepidozona* taxa formed a group but also contained *Callistochiton jacobaeus* and *Ischnochiton hakodadensis*. Furthermore, the outgroups were nested within the family Ischnochitonidae.

The evolutionary tree produced using BEAST (**Figure 8**) shows the estimated divergence time for Ischnochitonidae species. According to the analysis of the log files using Tracer 1.7 software, all searches reached convergence, and all effective sample size (ESS) values were greater than 200. The calibrated estimate showed that *T. xui* sp. nov. was separated from most members of the genus *Ischnochiton* in the Late Miocene, roughly 7.31 MYA, with a 95% highest posterior density (HPD) interval of 5.10–10.07 million years. Radiation of the family Ischnochitonidae occurred mainly from the Late Miocene to Pliocene.

Numerical Modeling

The numerical model in this study was designed to explore the evolutionary pathway of *Thermochiton* species and demonstrate how larvae in the three localities were connected by ocean currents. *Thermochiton* larvae were assumed to be passive floating particles in the OGCM to stimulate the spread process during PLD (**Figure 9** and **Supplementary Figures S1–S3**). Even ignoring their time swimming from the bottom to the sea surface and assuming that larvae use the optimal

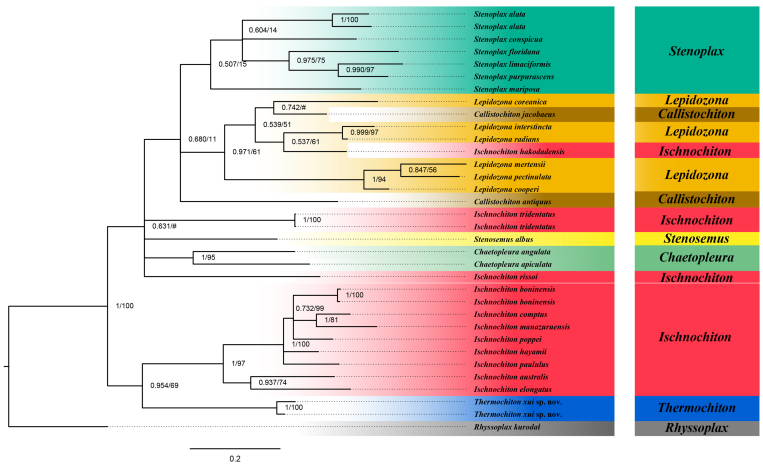

FIGURE 7 | Phylogeny tree based on three genes concatenated sequences. Numbers above branches refer to BI posterior probability (PP) and ML bootstrap scores (BS).

way to spread, i.e., being carried by surface currents, larvae from Papua New Guinea needed at least 15 and 26 months to spread to the Okinawa Trough and Haima cold seeps, respectively (**Supplementary Figure S1**). Meanwhile, larvae from the Haima cold seeps required eight months to spread to the Okinawa Trough (**Supplementary Figure S3**). Notably, the model started in January when northeast (winter) monsoons dominated the South China Sea. Thus, the simulated northeastward surface current would be relatively slower during the first few months than that simulated by a model starting when southwest (summer) monsoons dominated the area. Nevertheless, the simulation ran for 36 months and did not reveal the possibility of the tracer diffusing from the Haima cold seeps or Okinawa Trough to Papua New Guinea (**Supplementary Figures S3**, **S2**).

Although development information about deep-sea chitons is lacking, larvae of shallow-water chitons are mostly lecithotrophic. As a result, deep-sea chitons are more likely spread to the seafloor or deep ocean layer than to float to the surface. Further, the current velocity at the bottom or in the deep ocean layer is much slower than that at the surface, suggesting that deep-sea chitons would need much longer to spread than those floating at the surface.

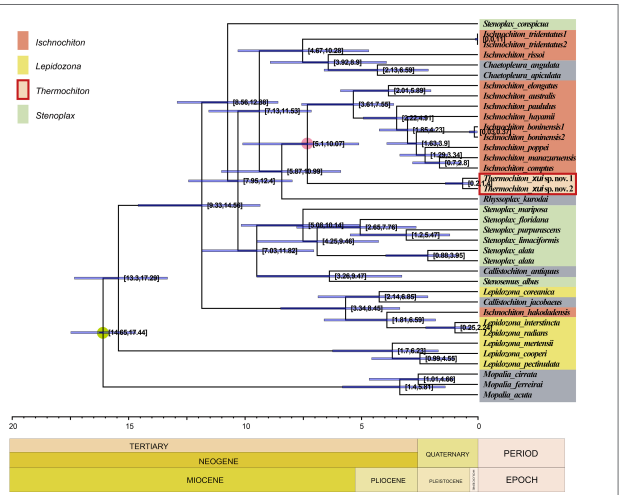

FIGURE 8 | Chronogram of the family Ischnochitonidae obtained with an uncorrelated relaxed clock method (BEAST) on the combined data set (COI, 16S, and 28S genes). Divergent time estimates and 95% highest posterior probabilities were displayed on each node.The green dot indicates fossil calibration point. The red circle indicates split time of *Thermochiton* from its shallow water relatives.

DISCUSSION

The discovery of *T. xui* sp. nov. increased the number of known members of the genus *Thermochiton*. Currently, the three species of the genus likely all live in areas of chemosynthetic activity. The genus *Thermochiton* was established for *T. undocostatus* Saito & Okutani, 1990, a chiton found in hydrothermal vents at the central Okinawa Trough, East China Sea (Saito and Okutani, 1990). The second member of the genus, *T. papuaensis*, was reported near Papua New Guinea and is likely to inhabit communities with chemical activity (Sirenko, 2020). Our new species was sampled from the Haima cold seeps in the South China Sea. The distribution areas of the genus are geographically far removed, located in the southwest and northwest Pacific. The type locality of *T. papuaensis* is approximately 4,637 km away from this sampling site and approximately 4,217 km away from the type locality of *T. undocostatus* (**Figure 1**).

The new species is the only species with molecular information in the genus. It is impossible to analyze the phylogenetic relationship between the three *Thermochiton*

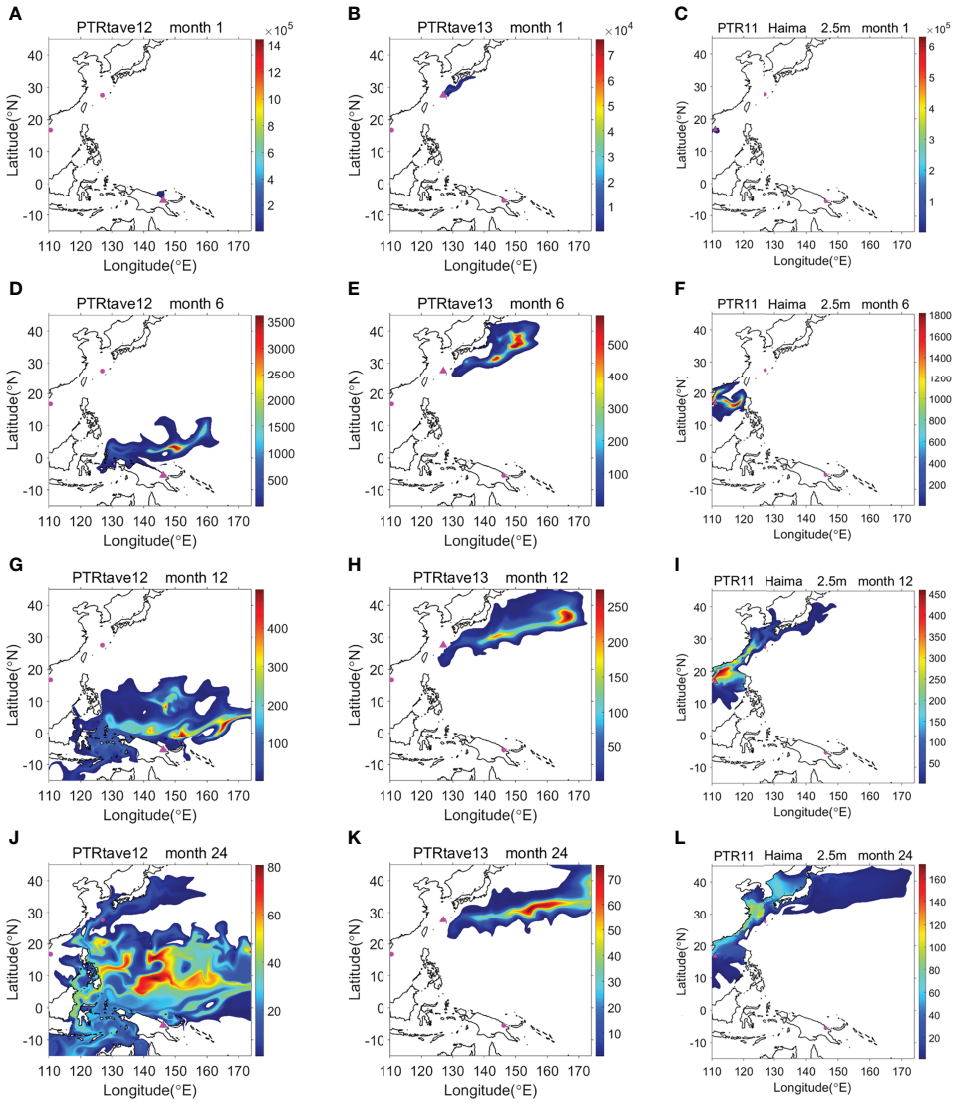

FIGURE 9 | Dispersal path and relative content of chiton larvae released from Papua New Guinea **(A, D, G, J)**, Okinawa Trough **(B, E, H, K)**, and Haima cold seeps **(C, F, I, L)** as modeled by the OGCM for 1 month **(A–C)**, 6 months **(D–F)**, 12 months **(G–I)** and 24 months **(J–L).**

species or infer how their ancestors spread based merely on morphological or molecular information. The modeling results in this study indicated that one *Thermochiton* species is unlikely to have crossed the complex Pacific western boundary currents to reach the three localities in which the genus has been reported. The western Pacific vents in distant basins are potentially connected by the Kuroshio Current (Mitarai et al., 2016). In addition, the South Equatorial Current can distribute vent species more than 4,000 km within the southwest Pacific. Nevertheless, the results of our numerical model suggested that at least 15 months were required for larvae to spread from Papua New Guinea to the Okinawa Trough *via* surface currents. Northward evolutionary migration is highly more likely than southward migration for Pacific deep-sea chitons. The upper prediction of the model reported by Yearsley and Sigwart (2011) estimated no more than 240 days (i.e., 8 months) for the PLD of deep-sea chitons. The deep-sea mollusk with the longest PLD is the cold seep mussel *B. naticoidea*, whose larvae reportedly disperse for 7–12 months at the surface before settling (Arellano et al., 2014). The larvae of the seastar *Mediaster aequalis* can reportedly persist for approximately 13 months before settling (Birkeland et al., 1971). Nevertheless, it was estimated that even the longest PLD could not be expected to exceed 400 days (O'Connor et al., 2007). Thus, one *Thermochiton* species is unlikely to have a sufficiently long PLD and dispersal ability to cross the complex Pacific western boundary currents, even under ideal conditions and with extremely strong surface currents. It is more likely that currents carried the pelagic larvae of their ancestors to spread and radiate into different species along the evolutionary

pathway during colonization. We hypothesize that (1) 'stepping-stones' facilitated their colonization, i.e., suitable habitats for chitons between the southwest and northwest Pacific, such as seeps, vents, sunken wood, or carcasses, and/or (2) evolutionary 'bridge species' existed during their spread, i.e., chitons distributed at 'stepping-stone' sites that have not yet been found or became extinct with the disappearance of these ephemeral habitats. Therefore, additional expeditions are needed to further explore the deep-sea fauna and collect more data in order to reconstruct the evolutionary history of this genus.

Most deep-water chitons belong to the order Lepidopleurida, a basal clade of the class Polyplacophora. Sigwart (2017) suggested that this clade originated at a depth of approximately 500 m and radiated to either deep-sea or coastal areas. Most of the radiation to sunken wood occurred in the Jurassic. Many lepidopleuran chitons diversified during the Cenozoic and invaded the deep sea and different chemosynthetic

TABLE 2 | Summary of deep-sea chitons described from the East and South China Seas.

Taxon	Locality	Depth (m)	Type of area				References
			HV	CS	SW	NC	
Leptochitonidae Dall, 1889							
Leptochiton tenuidontus Saito & Okutani, 1990	Iheya Ridge and off Kikaijima Island, Nansei Islands, East China Sea	1,395–1,442	√	√			Saito and Okutani (1990); Saito et al. (2008)
Leptochiton consimilis Sigwart & Sirenko, 2012	Solomon Islands, Taiwan	912–2,620			√		Sigwart and Sirenko (2012); Sirenko (2018)
Leptochiton habei Saito, 1997	Japan; Vanuatu, Solomon Islands, Taiwan	170–1,314			√		Saito (1997); Sirenko (2001); Sigwart and Sirenko (2012); Sirenko (2018)
Leptochiton longisetosus Sigwart & Sirenko, 2012	Vanuatu, Solomon Islands, Taiwan	492–1,317			√		Sigwart and Sirenko (2012); Sirenko (2018)
Leptochiton taiwanensis Sirenko, 2018	Taiwan	264				√	Sirenko (2018)
Leptochiton torishimensis (Wu & Okutani, 1984)	Izu Islands, Suruga Bay, Tosa Bay, Amami-Oshima Island, Taiwan	170–1,314			√		Wu and Okutani (1984); Saito (1997; 2001a; 2005); Sirenko (2018)
Leptochiton wui Sirenko, 2018	Taiwan, off Tashi	221			√		Sirenko (2018)
Leptochiton sp.	Taiwan, Bashi channel	1,314–1,317			√		Sirenko (2018)
Leptochiton vietnamensis Sirenko, 1998	South China Sea, Andaman Sea, New Caledonia, Philippines, Solomon Islands	651–1,313			√		Sirenko (1998); Sirenko (2001); Schwabe (2006); Sigwart and Sirenko (2012)
Hanleyella japonica Saito, 1997	Japan, Taiwan	85–440				√	Saito (1997; 2011); Sirenko (2018)
Hanleyella henrici Sigwart & Chen, 2018	Okinawa Trough	950–1,178	√				Sigwart and Chen (2018)
Parachiton laevisquamatus Sirenko, 2015	South China Sea	10–300				√	Sirenko (2015)
Nierstraszellidae Sirenko, 1992							
Nierstraszella lineata (Nierstrasz, 1905)	Japan, Taiwan, Philippines, Indonesia, Vanuatu, Solomon Islands	121–1,767				√	Sigwart and Sirenko (2012); Sirenko (2018)
Abyssochitonidae Dell'Angelo & Palazzi, 1989							
Ferreiraella soyomaruae (Wu & Okutani, 1984)	Near south of Japan, Taiwan	1,317–3,100			√		Wu and Okutani (1984); Kaas and Van Belle (1987); Sirenko (1988); Sirenko (2018)
Ferreiraella xylophaga karenae Sirenko, 2001	Near Vanuatu, Solomon Islands, off Taiwan	475–1,314			√		Sirenko (2001); Sigwart and Sirenko (2012); Sirenko (2018)
Protochitonidae Ashby, 1925							
Deshayesiella sinica (Xu, 1990)	Okinawa Trough, East China Sea; off Erimo-misaki, Hokkaido	1,680–2,043				√	Xu (1990); Saito (2012)
Loricidae Iredale & Hull, 1923							
Loricella scissurata (Xu, 1990)	East China Sea, Sagami Bay, Omurodashi Bank, Taiwan, South China Sea, Solomon Islands	187–563				√	Xu (1990); Saito (2005; 2011); Sirenko (2018; 2021)
Ischnochitonidae Dall, 1889							
Thermochiton undocostatus Saito & Okutani, 1990	Okinawa Trough, East China Sea	686–1,497		√	√		Saito and Okutani (1990); Saito et al. (2008)
Thermochiton xui sp. nov.	Haima cold seeps, South China Sea			√			This study
Lepidozona acostata Sirenko, 2016	South China Sea, near Vietnam; East China Sea, near Taiwan	170–760				√	Sirenko (2016a; 2018)
Tripoplax alba (Saito, 2013)	Okinawa Trough, East China Sea	605–611	√				Saito (2013)
Mopaliidae Dall, 1889							
Placiphorella isaotakii Saito, Fujikura& Tsuchida, 2008	Kuroshima Knoll off Yaeyama Islands area	691–692		√			Saito et al. (2008)
Acanthochitonidae Pilsbry, 1893							
Notoplax hilgendorfi Thiele, 1909	Japan, from Hakodate to Amami-Oshima Island, Taiwan	5–450				√	Saito (2001a; 2005); Sirenko (2018)

CS, cold seeps; HV, hot vents: SW, sunken wood; NC, non-chemosynthetic habitat.

habitats. Many other mollusks in hydrothermal vents, seeps, and organic falls have the pattern of Cenozoic radiation in the deep sea (Johnson et al., 2010; Lorion et al., 2013; Taylor et al., 2014). Indeed, our molecular clock analysis revealed that the genus *Thermochiton* originated from a shallow-sea ancestor around 5.10 to 10.07 MYA in the Late Miocene. The genus follows the "onshore to offshore" evolutionary pattern (Jablonski et al., 1983; Vrijenhoek, 2013), but occurred independently of the invasion of lepidopleuran chitons into chemosynthetic habitats.

A total of 23 species of deep-sea chitons have been identified in the bathyal and abyssal zones of the East and South China Seas to date (Kaas, 1979; Saito and Okutani, 1990; Xu, 1990; Saito, 2005; Saito, 2011; Saito, 2013; Sirenko, 2016b; Sigwart and Chen, 2018; Sirenko, 2018). Among them, 15 species live in hydrothermal vents, cold seeps, or sunken wood habitats (**Table 2**). Chemosynthetic areas are the main habitats of deep-sea chitons. Sirenko (2018) discovered 16 chiton species off Taiwan, 13 of which were new occurrences and two were new species, based on two exploration missions in 2000 and 2001. These data significantly increased the deep-sea chiton biodiversity in the East and South China Seas. To date, only four species of deep-sea chitons have been found in the South China Sea (*Leptochiton vietnamensis* Sirenko, 1998; *Parachiton laevisquamatus* Sirenko, 2015; *Loricella. scissurata* (Xu, 1990); *Lepidozona acostata* Sirenko, 2016; and *Thermochiton xui* sp. nov.). Sirenko and Zhang (2019) reported 30 chiton species from the vicinity of Hainan Island. However, the deep sea and numerous islands of the South China Sea have not been adequately sampled. The number of chitons currently recorded in the deep and shallow waters of the South China Sea is far from exhaustive compared with the nearly 100 species of chiton recorded in Japan (Slieker, 2000; Saito, 2001b; Saito, 2017) and the 68 species of chiton found in Vietnam (Sirenko, 2016b). The abundance of chiton species found in other locations suggests that the South China Sea has a high degree of biodiversity waiting to be discovered.

Our phylogenetic analysis based on the concatenated sequences from three gene regions supported the non-monophyly of the family Ischnochitonidae, as well as that of the genera *Ischnochiton*, *Lepidozona*, and *Callistochiton* (**Figure 7**). The outgroups were nested within the clade of the family Ischnochitonidae, similar to the findings reported by Owada (2018). The results suggest that the molecular data are not consistent with the assignment of species to genera and families based on plesiomorphic similarities. Both morphologic and genetic data indicated the complexity of the family Ischnochitonidae. Members of the genus *Connexochiton* Kaas, 1979 resemble those of the genus *Thermochiton*. Members of both genera have rounded granules at the distal end of the dorsal girdle scales, and the heads of the major lateral teeth of the radulae are unicuspidal, bent, and sickle-shaped. However, members of the genus *Thermochiton* have pores of aesthetes distributed throughout the tegmentum with concentric, undulating costae, whereas the pores of aesthetes of members of the genus *Connexochiton* are only distributed in granules. The genus *Subterenochiton* Iredale & Hull, 1924 is similar to members of the genus *Thermochiton* but differs by the presence of flattened, closely set, and same-sized tegmentum granules, as well as a single slit per side in the intermediate valves. The genus *Thermochiton* can be clearly distinguished from most *Ischnochiton* species by the following characteristics: small body size vs. medium to large body size; tegmentum granules raised vs. flat granules; intermediate valves with 2 slits per side vs. 1 slit per side; dorsal scales with granules vs. no granules; head of the major lateral tooth of the radula is unicuspidal vs. bicuspidal. Meanwhile, *Ischnochiton luteoroseus* Suter, 1907, *Ischnochiton granulifer* Thiele, 1909, and *Ischnochiton albinus* Thiele, 1911 also share similarities with members of the genus *Thermochiton*, including rounded granules on the dorsal girdle scales, unicuspidal head of the major lateral tooth of the radula, and a distinct protuberance on the major lateral tooth head. Interestingly, several species of the genus *Lepidozona*, *Ischnochiton*, *Subterenochiton*, and *Callistochiton* have dorsal scales with granules and/or longitudinal ribs, which is similar to members of the genus *Thermochiton*. Thus, these taxa need to be re-examined and more taxon sampling is needed. The current classification system of chitons was established based mainly on the morphology of valves, spicules, and girdle processes. Few taxonomic studies have combined morphology with molecular biology (Sigwart et al., 2010; Irisarri et al., 2020). However, as additional molecular data become available, classification uncertainty will undoubtedly arise. Emerging new data will provide insights into phylogenetic relationships and improve the stepwise systematics approach. For example, the previous morphological classification placed *Ischnochiton. hakodadensis* in the genus *Ischnochiton*, but molecular analysis revealed that the species was nested within the genus *Lepidozona* [(present study and findings reported by Owada (2018)]. The current information is insufficient to suggest any rearrangement of the family Ischnochitonidae; thus, this family remains poorly defined. Integrative taxonomy incorporating molecular data and morphological evidence will help solve this problem (Zhang et al., 2020). More evidence is needed to clarify phylogenetic relationships and improve stepwise systematics of chitons.

DATA AVAILABILITY STATEMENT

The datasets presented in this study can be found in online repositories. The names of the repository/repositories and accession number(s) can be found in the article/**Supplementary Material**.

AUTHOR CONTRIBUTIONS

JZ conceived and designed this project. HW, JZ, and BS performed morphological examination and description. HL and JZ conducted molecular analyses. XW and CL preformed the numerical modeling. DD and XL collected the samples. All

authors listed have made a substantial, direct, and intellectual contribution to the work and approved it for publication.

FUNDING

This work was supported by the Marine S&T Fund of Shandong Province for Pilot National Laboratory for Marine Science and Technology (Qingdao) (No. 2022QNLM050102-2), the National Key Research and Development Program of China (2021YFE0193700), the Strategic Priority Research Program of the Chinese Academy of Sciences (XDB42000000, and XDA22050203), the National Natural Science Foundation of China (31772422, and 42176114), the International Science Partnership Program of the Chinese Academy of Sciences (No. 133137KYSB20200002), and the Senior User Project of RV KEXUE (KEXUE2020GZ01).

ACKNOWLEDGMENTS

The authors are grateful to Editor Prof. Jian-Wen Qiu (Hong Kong Baptist University), Prof. Douglas Eernisse (California State University Fullerton), and an Dr. Julia Sigwart (Queen's University Belfast, United Kingdom), for comments and suggestions on the manuscript. Thanks also to Ms. Shanshan Wang (Institute of Oceanology, Chinese Academy of Sciences) for her assistance with SEM procedures and the photos.

SUPPLEMENTARY MATERIAL

The Supplementary Material for this article can be found online at: https://www.frontiersin.org/articles/10.3389/fmars.2022.889022/full#supplementary-material

REFERENCES

Adams, D. K., Arellano, S. M. and Govenar, B. (2012). Larval Dispersal: Vent Life in the Water Column. *Oceanography* 25 (1), 256–268. doi: 10.5670/oceanog.2012.24

Arellano, S. M., Van Gaest, A. L., Johnson, S. B., Vrijenhoek, R. C. and Young, C. M. (2014). Larvae From Deep-Sea Methane Seeps Disperse in Surface Waters. *Proc. R. Soc B: Biol. Sci.* 281 (1786), 20133276. doi: 10.1098/rspb.2013.3276

Atlas, R., Hoffman, R. N., Ardizzone, J., Leidner, S. M., Jusem, J. C., Smith, D. K., et al. (2011). A Cross-Calibrated, Multiplatform Ocean Surface Wind Velocity Product for Meteorological and Oceanographic Applications. *Bull. Amer. Meteor. Soc* 92 (2), 157–174. doi: 10.1175/2010bams2946.1

Beedessee, G., Watanabe, H., Ogura, T., Nemoto, S., Yahagi, T., Nakagawa, S., et al. (2013). High Connectivity of Animal Populations in Deep-Sea Hydrothermal Vent Fields in the Central Indian Ridge Relevant to Its Geological Setting. *PloS One* 8 (12), e81570. doi: 10.1371/journal.pone.0081570

Birkeland, C., Chia, F.-S. and Strathmann, R. R. (1971). Development, Substratum Selection, Delay of Metamorphosis and Growth in Seastar, *Mediaster Aequalis* Stimpson. *Biol. Bull.* 141 (1), 99–108. doi: 10.2307/1539994

Bouchet, P. and Warén, A. (1994). "Ontogenetic Migration and Dispersal of Deep-Sea Gastropod Larvae," in *Reproduction, Larval Biology and Recruitment in the Deep-Sea Benthos*. Eds. Young, C. M. and Eckelbarger, K. J. (New York: Columbia University Press), 98–117.

Chen, C., Okutani, T., Liang, Q. and Qiu, J. W. (2018). A Noteworthy New Species of the Family Vesicomyidae From the South China Sea (Bivalvia: Glossoidea). *Venus* 76 (1-4), 29–37. doi: 10.18941/venus.76.1-4_29

Darriba, D., Taboada, G. L., Doallo, R. and Posada, D. (2012). Jmodeltest 2: More Models, New Heuristics and Parallel Computing. *Nat. Methods* 9 (8), 772–772. doi: 10.1038/nmeth.2109

Dong, D., Li, X., Yang, M., Gong, L., Li, Y., Sui, J., et al. (2021). Report of Epibenthic Macrofauna Found From Haima Cold Seeps and Adjacent Deep-Sea Habitats, South China Sea. *Mar. Life Sci. Technol.* 3 (1), 1–12. doi: 10.1007/s42995-020-00073-9

Fukumori, H. and Kano, Y. (2014). Evolutionary Ecology of Settlement Size in Planktotrophic Neritimorph Gastropods. *Mar. Biol.* 161 (1), 213–227. doi: 10.1007/s00227-013-2330-5

García-Ríos, C. I., Pérez-Pérez, N. M., Fernández-López, J. and Fuentes, F. A. (2014). Calibrating the Chitons (Mollusca: Polyplacophora) Molecular Clock With the Mitochondrial DNA Cytochrome C Oxidase I Gene. *Rev. Biol. Mar. Oceanogr.* 49 (2), 193–207. doi: 10.4067/s0718-19572014000200003

Gent, P. R. and McWilliams, J. C. (1990). Isopycnal Mixing in Ocean Circulation Models. J. Phys. *Oceanogr.* 20 (1), 150–155. doi: 10.1175/1520-0485(1990)020<0150:imiocm>2.0.co;2

Irisarri, I., Uribe, J. E., Eernisse, D. J. and Zardoya, R. (2020). A Mitogenomic Phylogeny of Chitons (Mollusca: Polyplacophora). *BMC Evol. Biol.* 20 (1), 22. doi: 10.1186/s12862-019-1573-2

Jablonski, D., Sepkoski, J. J., Bottjer, D. J. and Sheehan, P. M. (1983). Onshore-Offshore Patterns in the Evolution of Phanerozoic Shelf Communities. *Science* 222 (4628), 1123–1125. doi: 10.1126/science.222.4628.1123

Jiang, J., Huang, Y., Liang, Q. and Zhang, J. (2019). Description of Two New Species (Bivalvia: Vesicomyidae, Verticordiidae) From a Cold Seep in the South China Sea. *Nautilus* 133 (3-4), 94–101.

Johnson, S. B., Warén, A., Lee, R. W., Kano, Y., Kaim, A., Davis, A., et al. (2010). *Rubyspira*, New Genus and Two New Species of Bone-Eating Deep-Sea Snails With Ancient Habits. *Biol. Bull.* 219 (2), 166–177. doi: 10.1086/BBLv219n2p166

Kaas, P. (1979). On a Collection of Polyplacophora (Mollusca, Amphineura) From the Bay of Biscay. *Bull. Mus. Natl. Hist. Nat. Sect. A Zool.* 4 (1), 1–13.

Kaas, P. and Van Belle, R. A. (1980). *Catalogue of Living Chitons (Mollusca: Polyplacophora)* (Rotterdam: W. Backhuys).

Kaas, P. and Van Belle, R. A. (1987). *Monograph of Living Chitons (Mollusca: Polyplacophora), Volume 3 Ischnochitonidae: Chaetopleurinae and Ischnochitoninae - Pars. Addition to Vols 1 & 2* (Leiden: E. J. Brill).

Katoh, K. and Standley, D. M. (2013). MAFFT Multiple Sequence Alignment Software Version 7: Improvements in Performance and Usability. *Mol. Biol. Evol.* 30 (4), 772–780. doi: 10.1093/molbev/mst010

Kelly, R. P. and Eernisse, D. J. (2007). Southern Hospitality: A Latitudinal Gradient in Gene Flow in the Marine Environment. *Evolution* 61 (3), 700–707. doi: 10.1111/j.1558-5646.2007.00055.x

Kelly, R. P. and Eernisse, D. J. (2008). Reconstructing a Radiation: The Chiton Genus *Mopalia* in the North Pacific. *Invertebr. Syst.* 22 (1), 17–28. doi: 10.1071/is06021

Kimura, M. (1980). A Simple Method for Estimating Evolutionary Rates of Base Substitutions Through Comparative Studies of Nucleotide Sequences. *J. Mol. Evol.* 16 (2), 111–120. doi: 10.1007/BF01731581

Large, W. G., McWilliams, J. C. and Doney, S. C. (1994). Oceanic Vertical Mixing: A Review and a Model With a Nonlocal Boundary Layer Parameterization. *Rev. Geophys.* 32 (4), 363. doi: 10.1029/94rg01872

Layton, K.K., Martel, A.L., and Hebert, P.D. (2014). Patterns of DNA Barcode Variation in Canadian Marine Molluscs. *PloS One* 9 (4), e95003. doi: 10.1371/journal.pone.0095003

Liang, Q., Hu, Y., Feng, D., Peckmann, J., Chen, L., Yang, S., et al. (2017). Authigenic Carbonates From Newly Discovered Active Cold Seeps on the Northwestern Slope of the South China Sea: Constraints on Fluid Sources, Formation Environments, and Seepage Dynamics. *Deep-Sea Res. Part I: Oceanogr. Res. Pap.*, 124, 31-41. doi: 10.1016/j.dsr.2017.04.015

Lorion, J., Kiel, S., Faure, B., Kawato, M., Ho, S. Y. W., Marshall, B., et al. (2013). Adaptive Radiation of Chemosymbiotic Deep-Sea Mussels. *Proc. R. Soc B: Biol. Sci.* 280 (1770), 20131243. doi: 10.1098/rspb.2013.1243

Marshall, J., Hill, C., Perelman, L. and Adcroft, A. (1997). Hydrostatic, Quasi-Hydrostatic, and Nonhydrostatic Ocean Modeling. *J. Geophys. Res. Oceans* 102 (C3), 5733–5752. doi: 10.1029/96jc02776

Mitarai, S., Watanabe, H., Nakajima, Y., Shchepetkin, A. F. and McWilliams, J. C. (2016). Quantifying Dispersal From Hydrothermal Vent Fields in the Western Pacific Ocean. *Proc. Natl. Acad. Sci.* 113 (11), 2976–2981. doi: 10.1073/pnas.1518395113

O'Connor, M. I., Bruno, J. F., Gaines, S. D., Halpern, B. S., Lester, S. E., Kinlan, B. P., et al. (2007). Temperature Control of Larval Dispersal and the Implications for Marine Ecology, Evolution, and Conservation. *Proc. Natl. Acad. Sci.* 104 (4), 1266–1271. doi: 10.1073/pnas.0603422104

Okusu, A., Schwabe, E., Eernisse, D. J. and Giribet, G. (2003). Towards a Phylogeny of Chitons (Mollusca, Polyplacophora) Based on Combined Analysis of Five Molecular Loci. *Org. Div. Evol.* 3 (4), 281–302. doi: 10.1078/1439-6092-00085

Owada, M. (2016). A New Cryptic Species Distinguished From *Ischnochiton Comptus* (Gould 1859) (Polyplacophora: Ischnochitonidae) in Central Honshu, Japan. *Molluscan Res.* 36 (4), 255–263. doi: 10.1080/13235818.2016.1150772

Owada, M. (2018). Phylogenetic Relationships Among Japanese Species of the Genus *Ischnochiton* (Polyplacophora: Ischnochitonidae), Including a New Species. *Zool. Sci.* 35 (3), 281–291. doi: 10.2108/zs170106

Puillandre, N., Lambert, A., Brouillet, S. and Achaz, G. (2012). ABGD, Automatic Barcode Gap Discovery for Primary Species Delimitation. *Mol. Ecol.* 21 (8), 1864–1877. doi: 10.1111/j.1365-294X.2011.05239.x

Redi, M. H. (1982). Oceanic Isopycnal Mixing by Coordinate Rotation. *J. Phys. Oceanogr.* 12 (10), 1154–1158. doi: 10.1175/1520-0485(1982)012<1154:OIMBCR>2.0.CO;2

Ronquist, F., Teslenko, M., van der Mark, P., Ayres, D. L., Darling, A., Höhna, S., et al. (2012). MrBayes 3.2: Efficient Bayesian Phylogenetic Inference and Model Choice Across a Large Model Space. *Syst. Biol.* 61 (3), 539–542. doi: 10.1093/sysbio/sys029

Saito, H. (1997). Deep-Sea Chiton Fauna of Suruga Bay (Mollusca: Polyplacophora) With Descriptions of Six New Species. *Nat. Sci. Mus. Monogr.* 12, 31–58.

Saito, H. (2001a). Chitons (Mollusca: Polyplacophora) Collected by the R/V Kotaka-Maru From Tosa Bay, Western Japan, With Descriptions of Two New Species. *Nat. Sci. Mus. Monogr.* 20, 101–119.

Saito, H. (2001b). Shallow-Water Chitons (Mollusca: Polyplacophora) of Hachijo Island, Izu Islands, Japan. *Mem. Natn. Sci. Mus.* 37, 193–202.

Saito, H. (2004). Phylogenetic Significance of the Radula in Chitons, With Special Reference to the Cryptoplacoidea (Mollusca: Polyplacophora). *Boll. Malacol. 39(Supplement* 5), 83–104.

Saito, H. (2005). Shelf and Bathyal Chitons (Mollusca: Polyplacophora) From the Nansei Islands, Southwestern Japan. *Nat. Sci. Mus. Monogr.* 29, 101–113.

Saito, H. (2011). Chitons (Mollusca: Polyplacophora) From Submarine Banks Off Izu Islands and Bōsō Peninsula, Japan. *Mem. Natn. Mus. Nat. Sci. Tokyo* 47, 65–81.

Saito, H. (2012). Second Specimen of a Rare Deep-Sea Chiton, *Deshayesiella Sinica* (Xu 1990) (Polyplacophora, Lepidopleurida, Protochitonidae) From Northern Japan. *Bull. Natl. Mus. Nat. Sci.* 38, 7–11.

Saito, H. (2013). A New Species of *Lepidozona* (Mollusca, Polyplacophora, Ischnochitonidae) From Okinawa Trough, East China Sea. *Bull. Natl. Mus. Nat. Sci.* 39, 5–10.

Saito, H. (2017). "Class Polyplacophora," in *Marine Mollusks in Japan*, 2nd ed. Ed. Okutani, T. (Tokyo: Tokai University Press), 728–738.

Saito, H., Fujikura, K. and Tsuchida, S. (2008). Chitons (Mollusca: Polyplacophora) Associated With Hydrothermal Vents and Methane Seeps Around Japan, With Descriptions of Three New Species. *Am. Malacol. Bull.* 25 (1), 113–124. doi: 10.4003/0740-2783-25.1.113

Saito, H. and Okutani, T. (1990). Two New Chitons (Mollusca: Polyplacophora) From a Hydrothermal Vent Site of the Iheya Small Ridge, Okinawa Trough, East China Sea. *Venus* 49 (3), 165–179. doi: 10.18941/venusjjm.49.3_165

Schwabe, E. (2006). Chitons (Mollusca, Polyplacophora) Collected During the Thai-Danish Bioshelf Surveys, (1996-2000) in the Andaman Sea, Indian Ocean. *J. Zool. Soc. Wallacea* 2, 19–28.

Schwabe, E. and Sellanes, J. (2010). Revision of Chilean Bathyal Chitons (Mollusca: Polyplacophora) Associated With Cold-Seeps, Including Description of a New Species of Leptochiton (Leptochitonidae). *Org. Div. Evol.* 10 (1), 31–55. doi: 10.1007/s13127-009-0002-6

Sigwart, J. D. (2017). Deep Trees: Woodfall Biodiversity Dynamics in Present and Past Oceans. *Deep-Sea Res. II: Top. Stud. Oceanogr.* 137, 282–287. doi: 10.1016/j.dsr2.2016.06.021

Sigwart, J. D. and Chen, C. (2018). A New Deep Water Chiton (Mollusca: Polyplacophora) From Hydrothermal Vent Ecosystems in the Okinawa Trough, Japan. *Zootaxa* 4531 (3), 430–436. doi: 10.11646/zootaxa.4531.3.7

Sigwart, J. D., Schwabe, E., Saito, H., Samadi, S. and Giribet, G. (2010). Evolution in the Deep Sea: A Combined Analysis of the Earliest Diverging Living Chitons (Mollusca: Polyplacophora: Lepidopleurida). *Invertebr. Syst.* 24 (6), 560–572. doi: 10.1071/is10028

Sigwart, J. D. and Sirenko, B. I. (2012). Deep-Sea Chitons From Sunken Wood in the West Pacific (Mollusca: Polyplacophora: Lepidopleurida): Taxonomy, Distribution, and Seven New Species. *Zootaxa* 9 (3195), 1–38. doi: 10.11646/zootaxa.3195.1.1

Sirenko, B. I. (1988). A New Genus of Deep Sea Chitons *Ferreiraella* Gen. N. (Lepidopleurida, Leptochitonidae) With a Description of a New Ultra-Abyssal Species. *Zool. Zhurnal* 67 (12), 1776–1786.

Sirenko, B. I. (1998). One More Deep Water Chiton Leptochiton Vietnamensis Sp. N. (Mollusca, Polyplacophora) Living and Feeding on Sunken Wood From the South China Sea. *Ruthenica* 8 (1), 1–6.

Sirenko, B. I. (2001). "Deep-Sea Chitons (Mollusca, Polyplacophora) From Sunken Wood Off New Caledonia and Vanuatu," in *Tropical Deep-Sea Benthos*, vol. 22 . Eds. Bouchet, P. and Marshall, B. (France: Muséum National d'Histoire Naturelle), 39–71. doi: 10.18941/venus.65.1-2_27

Sirenko, B. I. (2006). New Outlook on the System of Chitons (Mollusca: Polyplacophora). *Venus* 65 (1-2), 27–49.

Sirenko, B. I. (2015). New Species of *Parachiton* (Mollusca: Polyplacophora) From the South China Sea. *Zoosystematica Ross.* 24 (2), 143–147. doi: 10.31610/zsr/2015.24.2.143

Sirenko, B. I. (2016a). New and Rare Species of the Genus *Lepidozona* (Mollusca: Polyplacophora) From the South China, East China and the Philippine Seas. *Bull. Russ. Far East Malacol. Soc* 20 (2), 28–46.

Sirenko, B. I. (2016b). "Seven-Year Taxonomical Investigation of Chitons in Vietnam," in *in Proceedings of the Conference "Developing Life-Supporting Marine Ecosystems Along With the Asia-Pacific Coast a Synthesis of Physical and Biological Data for the Science-Based Management and Socio-Ecological Policy Making"*. Ed. Dautova, T. N. (Vladivostok-Nha Trang: Dalnauka), 82–86.

Sirenko, B. I. (2018). Taiwanese Deep-Water Chitons (Mollusca: Polyplacophora) and Survey of Chiton Fauna of Taiwan. *Zootaxa* 4422 (3), 301–344. doi: 10.11646/zootaxa.4422.3.1

Sirenko, B. I. (2020). A Second Species of the Genus Thermochiton Saito Et Okutani 1990 (Mollusca: Polyplacophora). *Ruthenica* 30 (1), 7–12. doi: 10.35885/ruthenica.2021.30(1).2

Sirenko, B. I. (2021). Composition of the Genus *Loricella* (Mollusca: Polyplacophora: Loricidae) and the Description of Two New Species. *Zootaxa* 4981 (2), 275–300. doi: 10.11646/zootaxa.4981.2.4

Sirenko, B. I. and Sellanes, J. (2016). Update of the Genus *Leptochiton* (Mollusca: Polyplacophora) in Chilean Deep Waters: Three New Reports and Description of Two New Species. *Zootaxa* 4173 (3), 259–283. doi: 10.11646/zootaxa.4173.3.5

Sirenko, B. I. and Zhang, J. (2019). Chitons (Mollusca: Polyplacophora) of Hainan Island and Vicinity, South China Sea. *Zootaxa* 4564 (1), 1–40. doi: 10.11646/zootaxa.4564.1.1

Slieker, F. J. A. (2000). *Chitons of the World: An Illustrated Synopsis of Recent Polyplacophora* (Italy: Mostra mondiale malacologia, Cupra Marittima).

Stamatakis, A. (2014). RAxML Version 8: A Tool for Phylogenetic Analysis and Post-Analysis of Large Phylogenies. *Bioinformatics* 30 (9), 1312–1313. doi: 10.1093/bioinformatics/btu033

Suchard, M. A., Lemey, P., Baele, G., Ayres, D. L., Drummond, A. J. and Rambaut, A. (2018). Bayesian Phylogenetic and Phylodynamic Data Integration Using BEAST 1.10. *Virus Evol.* 4 (1), vey016. doi: 10.1093/ve/vey016

Sun, Y., Liang, Q., Sun, J., Yang, Y., Tao, J., Liang, J., et al. (2018). The Mitochondrial Genome of the Deep-Sea Tubeworm *Paraescarpia Echinospica* (Siboglinidae, Annelida) and its Phylogenetic Implications. *Mitochondrial DNA B: Res.* 3 (1), 131–132. doi: 10.1080/23802359.2018.1424576

Taylor, J. D., Glover, E. A. and Williams, S. T. (2014). Diversification of Chemosymbiotic Bivalves: Origins and Relationships of Deeper Water Lucinidae. *Biol. J. Linn. Soc* 111 (2), 401–420. doi: 10.1111/bij.12208

Teixeira, S., Cambon-Bonavita, M.-A., Serrão, E. A., Desbruyéres, D. and Arnaud-Haond, S. (2011). Recent Population Expansion and Connectivity in the Hydrothermal Shrimp *Rimicaris Exoculata* Along the Mid-Atlantic Ridge. *J. Biogeogr.* 38 (3), 564–574. doi: 10.1111/j.13652699.2010.02408.x

Tyler, P. A. and Young, C. M. (1999). Reproduction and Dispersal at Vents and Cold Seeps. *J. Mar. Biol. Assoc. U. K.* 79 (2), 193–208. doi: 10.1017/s0025315499000235

Tyler, P. A. and Young, C. M. (2003). Dispersal at Hydrothermal Vents: A Summary of Recent Progress. *Hydrobiologia* 503 (1-3), 9–19. doi: 10.1023/b:hydr.0000008492.53394.6b

Vaidya, G., Lohman, D. J. and Meier, R. (2011). SequenceMatrix: Concatenation Software for the Fast Assembly of Multi-Gene Datasets With Character Set and Codon Information. *Cladistics* 27 (2), 171–180. doi: 10.1111/j.1096-0031.2010.00329.x

Vrijenhoek, R. C. (2013). On the Instability and Evolutionary Age of Deep-Sea Chemosynthetic Communities. *Deep-Sea Res. II - Top. Stud. Oceanogr.* 92, 189–200. doi: 10.1016/j.dsr2.2012.12.004

Warén, A. and Bouchet, P. (2001). Gastropoda and Monoplacophora From Hydrothermal Vents and Seeps: New Taxa and Records. *Veliger* 44, 116–231.

Wu, S. K. and Okutani, T. (1984). The Deepsea Chitons (Mollusca: Polyplacophora) Collected by the R/V Soyo-Maru From Japan. I, Lepidopleuridae. *Venus* 44 (1), 1–31. doi: 10.18941/venusjjm.43.1_1

Xu, F. (1990). New Genus and Species of Polyplacophora (Mollusca) From the East China Sea. *Chin. J. Oceanol. Limnol.* 8 (4), 374–377. doi: 10.1007/BF02849683

Xu, T., Feng, D., Tao, J. and Qiu, J.-W. (2019). A New Species of Deep-Sea Mussel (Bivalvia: Mytilidae: Gigantidas) From the South China Sea: Morphology, Phylogenetic Position, and Gill-Associated Microbes. *Deep-Sea Res. I: Oceanogr. Res. Pap.* 146, 79–90. doi: 10.1016/j.dsr.2019.03.001

Yahagi, T., Fukumori, H., Warén, A. and Kano, Y. (2019). Population Connectivity of Hydrothermal-Vent Limpets Along the Northern Mid-Atlantic Ridge (Gastropoda: Neritimorpha: Phenacolepadidae). *J. Mar. Biol. Assoc. U. K.* 99 (1), 179–185. doi: 10.1017/s0025315417001898

Yahagi, T., Kayama Watanabe, H., Kojima, S. and Kano, Y. (2017). Do Larvae From Deep-Sea Hydrothermal Vents Disperse in Surface Waters? *Ecology* 98 (6), 1524–1534. doi: 10.1002/ecy.1800

Yearsley, J. M. and Sigwart, J. D. (2011). Larval Transport Modeling of Deep-Sea Invertebrates can Aid the Search for Undiscovered Populations. *PLoS One* 6 (8), e23063. doi: 10.1371/journal.pone.0023063

Zhang, S. and Zhang, S. (2017). Description of *Pyropelta Elongata* Sp. Nov. (Gastropoda, Pyropeltidae) From a Methane Seep Area in the South China Sea. *Am. Malacol. Bull.* 35 (1), 51–54. doi: 10.4003/006.035.0106

Zhang, S., Zhang, J. and Zhang, S. (2016). A New Species of *Bathyacmaea* (Gastropoda: Pectinodontidae) From a Methane Seep Area in the South China Sea. *Nautilus* 130 (1), 1–4.

Zhang, S., Zhang, J. and Zhang, S. (2020). Integrative Taxonomy Reveals New Taxa of Trochidae (Gastropoda: Vetigastropoda) From Seamounts in the Tropical Western Pacific. *Deep-Sea Res. I: Oceanogr. Res. Pap.* 159, 103234. doi: 10.1016/j.dsr.2020.103234

Zhao, J., Liang, Q.-Y., Wei, J.-G., Tao, J., Yang, S.-X., Liang, J.-Q., et al. (2020). Seafloor Geology and Geochemistry Characteristic of Methane Seepage of the "Haima" Cold Seep, Northwestern Slope of the South China Sea. *Geochimica* 49 (1), 108–118. doi: 10.19700/j.03791726.2020.01.009

Conflict of Interest: The authors declare that the research was conducted in the absence of any commercial or financial relationships that could be construed as a potential conflict of interest.

frontiers | Frontiers in Marine Science

TYPE Original Research
PUBLISHED 12 August 2022
DOI 10.3389/fmars.2022.960338

OPEN ACCESS

EDITED BY
Clara F. Rodrigues,
University of Aveiro, Portugal

REVIEWED BY
Niels De Winter,
Vrije University Brussel, Belgium
Joachim Reitner,
University of Göttingen, Germany

*CORRESPONDENCE
Dong Feng
dfeng@shou.edu.cn

SPECIALTY SECTION
This article was submitted to Deep-Sea Environments and Ecology, a section of the journal Frontiers in Marine Science

RECEIVED 02 June 2022
ACCEPTED 25 July 2022
PUBLISHED 12 August 2022

CITATION
Wang X, Fan D, Kiel S, Gong S, Liang Q, Tao J, Chen D and Feng D (2022) Archives of short-term fluid flow dynamics and possible influence of human activities at methane seeps: Evidence from high-resolution element geochemistry of chemosynthetic bivalve shells. *Front. Mar. Sci.* 9:960338. doi: 10.3389/fmars.2022.960338

Archives of short-term fluid flow dynamics and possible influence of human activities at methane seeps: Evidence from high-resolution element geochemistry of chemosynthetic bivalve shells

Xudong Wang[1,2], Danling Fan[1], Steffen Kiel[3], Shanggui Gong[1], Qiangyong Liang[4], Jun Tao[4], Duofu Chen[1,2] and Dong Feng[1,2]*

[1]Shanghai Engineering Research Center of Hadal Science and Technology, College of Marine Sciences, Shanghai Ocean University, Shanghai, China, [2]Laboratory for Marine Mineral Resources, Qingdao National Laboratory for Marine Science and Technology, Qingdao, China, [3]Swedish Museum of Natural History, Department of Palaeobiology, Stockholm, Sweden, [4]Ministry of Land and Resources of the People's Republic of China Key Laboratory of Marine Mineral Resources, Guangzhou Marine Geological Survey, Guangzhou, China

The natural dynamics of fluid flow at methane seeps and increasingly human activities influence the biogeochemistry of the microenvironment and further determine the activity of the chemosynthetic communities within these ecosystems. However, ways to reconstruct short-term fluid flow dynamics and to decipher the influence of scientific exploration at seeps are limited. In this study, we present high-resolution trace elements/Ca ratios (Li/Ca, Mg/Ca, Ti/Ca, Mn/Ca, Co/Ca, Cu/Ca, Zn/Ca, Sr/Ca, Zr/Ca, Mo/Ca, Ba/Ca, Th/Ca and U/Ca ratios) from the shells of two species of chemosymbiotic bivalves (the thiotrophic vesicomyid clam *Archivesica marissinica* and the methanotrophic mussel *Gigantidas haimaensis*) from the Haima cold seeps of the South China Sea. We found that the complex distribution patterns of some trace elements (Mg/Ca, Sr/Ca, Mo/Ca and U/Ca ratios) in *G. haimaensis* are largely controlled by mineral composition or age. The observation of Co/Ca and Ba/Ca ratios in both species indicate strong physiological and environmental control on the incorporation of trace elements during the biomineralization process. Besides, the distribution patterns of other trace elements provide information that can be used to discuss open issues such as the loss of trace elements after death of the bivalves, and the possible influence of human activities such as sediment disturbance. Overall, this study emphasizes the potential for using high-resolution element geochemistry of seep bivalve shells to reveal the physiological and environmental factors that control the growth of bivalves, and to elucidate the potential history of fluid discharge at cold seeps.

KEYWORDS

methane seep, bivalve, bioarchive, trace elements, South China Sea

Introduction

The cold seep system is dynamic in both time and space (Suess, 2020). At present, there is a basic understanding of the activity rhythm of cold seep system on a long-time scale (millennia and above, Chen et al., 2019). Yet, increasing evidence points to short-term events such as tides or monsoons also having an influence on methane flux (Himmler et al., 2016; Wang, S. et al., 2020), but the overall frequency of such microenvironmental changes in cold seep systems remains unclear (Leifer et al., 2004; Johansen et al., 2017).

The bivalve shell is an excellent archive to reveal the evolution of their living environment on a relatively short timescale because the lifespan of bivalves can range from several to hundreds of years (Barry et al., 2007; Schöne et al., 2013). As opposed to the soft tissue of bivalves, the corresponding shell is likely to integrate and preserve elements from their environment during their whole life (Immenhauser et al., 2015). Indeed, shell carbonate layers of bivalves can provide insights into various environmental conditions during their lifetime, while soft tissue can only give us instantaneous snapshots at a certain time (Vander Putten et al., 2000; Gillikin et al., 2006; Schöne et al., 2013; Feng et al., 2018; Wang, X. et al., 2020).

Numerous studies have shown that elemental compositions in shell carbonates can provide valuable insights into past environments. Previous studies have successfully established the relationship between Sr/Ca (or Mg/Ca) and temperature, although these relationships may vary greatly among or within species (Branson et al., 2018). An alternative temperature proxy (Sr/Li ratio) was developed (Juárez-Aguilar et al., 2019), and the vital effects of Sr and Li incorporation into aragonite shells can be reduced by normalizing Sr/Ca to Li/Ca. In addition, the shell Mn/Ca ratio (Marali et al., 2017), Ba/Ca ratio (Gillikin et al., 2006; Schöne et al., 2013) and U/Ca (Kim et al., 2015; Poitevin et al., 2020) ratio were also thoroughly investigated as potential indicators of diagenetic trends, weathering intensity, salinity, paleoproductivity, pH and so on. However, the calcifying fluid chemistry and the corresponding mechanistic of shell formation appear to involve complex physiological responses and geochemical controls (e.g., Vander Putten et al., 2000; Schöne et al., 2013; Marali et al., 2017; Markulin et al., 2020). To date, only a few studies explored the high-resolution element geochemistry of deep-sea bivalve shells (Schöne and Giere, 2005; Shirai et al., 2008; Wisshak et al., 2009), and only one of them focused on cold seep areas (Torres et al., 2001). Torres et al. (2001) investigated shells of the vesicomyid clam *Calyptogena kilmeri* from seep sites in Monterey canyon (California, USA) and confirmed that clamshells can be used as paleotracers of fluid seepage events. However, they only investigated the Ba/Ca ratio of this chemoautotrophic bivalve. Lietard and Pierre (2008) performed a high-resolution stable isotope ($\delta^{18}O$ and $\delta^{13}C$) and cathodoluminescence study of lucinid bivalve shells (*Myrtea* aff. *amorpha*) from methane seeps in the Eastern Mediterranean Sea and demonstrated the potential of these methods to reconstruct methane release event, although the influence of metabolic effect could not be completely ruled out.

In the present study, we investigated two species of chemosymbiotic bivalves from the South China Sea. Using microstructure and high-resolution element geochemistry of their shells, the purpose of this study was to reconstruct short-term fluid flow dynamics and to shed light on the short-term microenvironmental changes of cold seep ecosystems.

Materials and methods

Sample collection and preservation

Specimens of two species of seep-restricted, chemosymbiotic bivalves (*Archivesica marissinica*: thiotrophic, infaunal; and *Gigantidas haimaensis*: methanotrophic, epifaunal or semi-infaunal) were collected at the active Haima cold-seep area (water depth: ~1400 m) in the northwestern South China Sea (Figure 1; Liang et al., 2017). Once onboard the ship, the soft tissue and corresponding shell of bivalves were dissected and washed with deionized water to remove salt. The shells were air-dried and placed in a sealed sample bag for analysis.

Shell preparation

It impossible to create a shell chronology for the specimens since the absolute growth rate of seep bivalves is currently unknown. In an attempt to record a longer life history, 4 relatively large individuals with the length between 12.5 and 16.8 cm (*A. marissinica*: C2015 + C2020; *G. haimaensis*: M2020 + M2021) were chosen for this study. The relationships between length, width and height among the two species are almost the same, illustrating that they grew freely and were not limited by additional factors (Table 1). To obtain cross section of bivalves, we used a diamond saw to slice the shells along the axis of maximal growth, following the prevailing practice (Vander Putten et al., 2000; Torres et al., 2001; Markulin et al., 2020). To determine the shell microstructure and facilitate the laser ablation analysis, the cross section of the shells was polished with silicon carbide sandpaper (2000Cw, Ying Qiu Brand).

Analytical procedure

Scanning electron microscopy

A Coxem EM30 PLUS SEM system (South Korea) with an accelerating voltage of 15 kV was used to observe the microstructures of *A. marissinica* and *G. haimaensis* at Shanghai Ocean University. Shell fragments from several

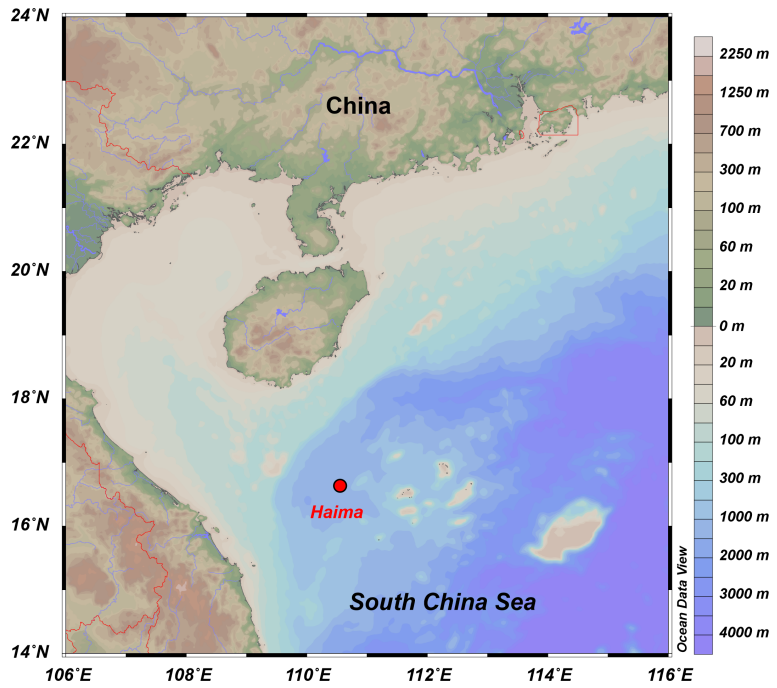

FIGURE 1
Map showing the location of the samples.

sections along the cross sections of each species were sputter-coated with a gold layer prior to observation, and the magnification varied from 969 to 2600 times (Figure 3).

X-ray diffraction

A LabX XRD-6100 X-ray diffractometer system (Shimadzu, Japan) at Shanghai Ocean University was used to analyze the mineral composition of bulk shells (individual microstructures could not be separated since the extremely thin thickness of shell). Approximately 40 mg shell powder was prepared for each sample. The X-ray source was a Cu anode operated at 40 kV and 30 mA using CuKα radiation equipped with a diffracted beam graphite monochromator. The samples were scanned in step scan mode at an interval of 10-80° (2θ), with a step size of 0.02° and a count time of 0.6 s per step (2°/min). The diverging, scattering, and receiving slits were 1.0 mm, 1.0 mm and 0.15 mm, respectively. The carbonate type of shells was identified by using XRD processing software JADE 6.0.

LA-ICP-MS

The concentrations of Li, Mg, Ca, Ti, Mn, Co, Cu, Zn, Sr, Zr, Mo, Ba, Th, and U were determined by means of laser ablation-inductively coupled plasma-mass spectrometry (LA-ICP-MS) in spot analysis mode along the growth axis of the shells near their outside layer (Figures 2C, D). The distance between the two laser spots is about 1mm (Figure 2), although the time span represented by two laser spots between shells or even in same shell, is different (bivalve grow faster when they were young). According to the sample size, the number of laser spots is 153 (C2015),111 (C2020),116 (M2020) and144 (M2021), respectively (Table 1). Analyses were performed at Shanghai Chemlabprop Technology Co., Ltd. using an ESI

TABLE 1 Seep bivalve information including: (1) species; (2) chemoautotrophic type; (3) length, (4) width, (5) height and (6) thickness of shells; (7) sampling time; (8) status when sampling; (9) total laser spots.

Sample ID	Species	Chemoautotrophic type	Length (cm)	Width (cm)	Height (cm)	Thickness (mm)	Sampling time	Status when sampling	Total laser spots
C2015	*Archivesica marissinica*	Thiotrophic clam	16.8	8.4	3.6	2.35	2015.04	Dead	153
C2020			13.5	6.7	2.9	1.92	2020.05	Alive	111
M2020	*Gigantidas platifrons*	Methanotrophic mussel	12.5	6.3	2.7	0.57	2020.05	Alive	116
M2021			16.1	8.1	3.5	0.71	2021.04	Alive	144

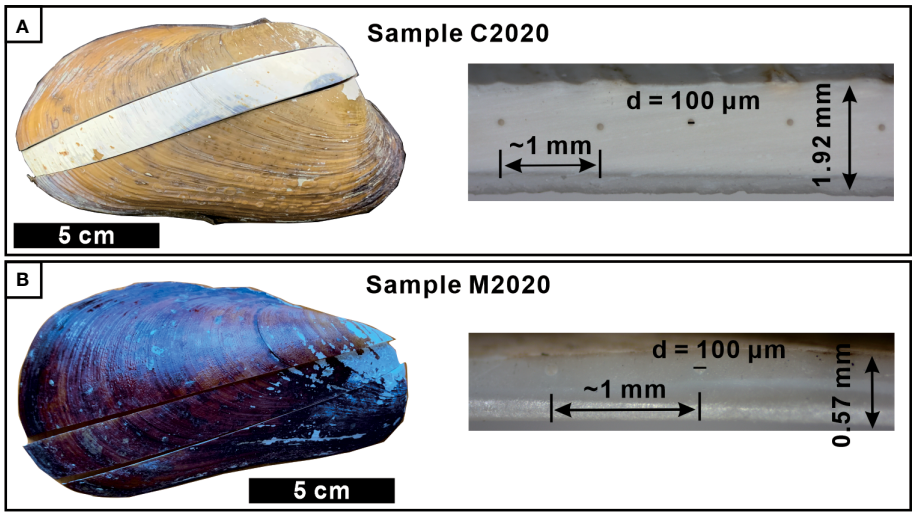

FIGURE 2
Images of typical seep bivalve shells and their cross sections. Clam identified as *Archivesica marissinica* (C2020; **A**) and mussel identified as *Gigantidas haimaensis* (M2020; **B**). The distance between two laser points is about 1 mm.

NWR193 ArF excimer laser ablation system equipped with a TwoVol2 ablation cell operating at 193 nm wavelength connected to an Agilent 7900 quadrupole ICP-MS. High-energy laser pulses hit the sample surface, and high-purity helium (99.999%) was used as the carrier gas at 700 ml/min flow to transfer the ablated material to the ICP for ionization before analysis. Satisfactory sensitivity and sufficiently low levels of oxide formation (ThO/Th < 0.2%) and fractionation effect ($^{232}Th/^{238}U \approx 100\%$) were accomplished by daily optimization, consisting of adjusting the gas flow, sampling depth, and lens setting while ablating the glass standard reference material NIST SRM 612. The ablation was operated using a spot size of 100 μm, an energy density of ~3 J/cm2 and a pulse repetition rate of 15 Hz. The background signal was measured for 10 s prior to each ablation. Ablation time was 50 s, followed by 15 s wash out. The operational conditions of LA-ICP-MS are summarized in Table S1.

To ensure the data quality, NIST SRM 612 glass reference material was used as the quality monitoring standard. The data were exported after being processed with the Iolite 4 software (Paton et al., 2011), and the measured values are shown in Table S2.

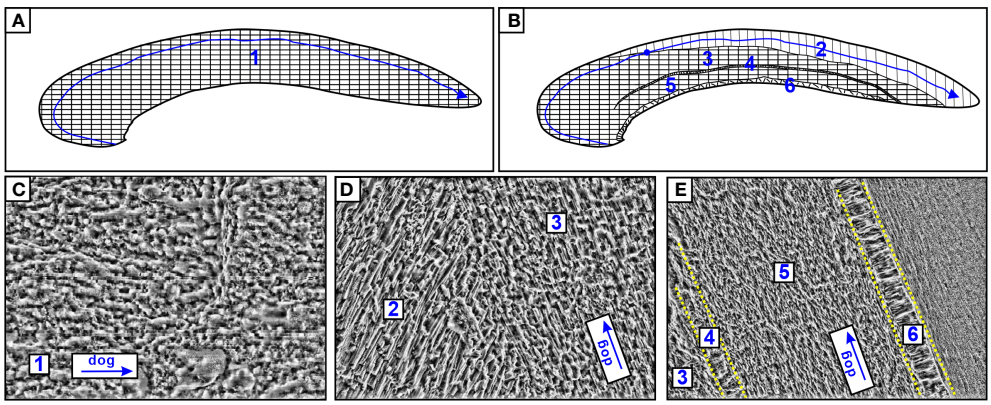

FIGURE 3
Schematic drawing of *A. marissinica* **(A)** and *G. haimaensis* **(B)**. The numbers represent laminated structures (1), outer prismatic layer (2), outer nacre layer (3), myostracum (4), inner nacre layer (5) and simple prismatic layer (6). The blue line with arrow represents the path of the laser spot, the blue point represents the transition position of mineral phase (aragonite to calcite). **(C)** SEM image of *A. marissinica* (C2020); **(D, E)** SEM image of *G. haimaensis* (M2020). dog: direction of growth.

Results

Shell microstructure of the seep bivalves

The thickness of the methanotrophic mussel shell (M2020: 0.57mm; M2021: 0.71mm) was less than one-third that of the thiotrophic clam shell (C2015: 2.35mm; C2020: 1.92mm. Table 1, Figures 2C, D). The microstructure of *A. marissinica* is rather simple since the whole shell is composed of a uniform laminated structure, the orientation of the laminae is consistent with the direction of growth (Figures 3A, C). The shell of *G. haimaensis* can be roughly divided into 5 parts from outside to inside layers (Figure 3): outer (fibrous) prismatic layer → outer nacre layer → myostracum → inner nacre layer → simple prismatic layer (Génio et al., 2012). Specifically, the fibers of the outer prismatic layer are oriented at an oblique angle to the outer nacreous layer. Between the outer and inner nacre layers, there is myostracum - a thin extra layer secreted by virtually all bivalves where they attach the mantle or the muscles to the shell. The inner edge of shell is a simple prismatic layer, a universal microstructure among mussels (family Mytilidae), with the prisms oriented vertically to the inner nacreous layer (Génio et al., 2012).

Carbonate mineral compositions

The mineral compositions of the two seep bivalves correspond to the properties of their microstructure. XRD results of *A. marissinica* show that the shell consists solely of aragonite, while the shell of *G. haimaensis* is composed of calcite and aragonite (Table S3). According to microstructure of the shell and previous research experience (Kennish et al., 1996; Kennish et al., 1998a; Kennish et al., 1998b), it is inferred that the fibrous prismatic layer of *G. haimaensis* is composed of calcite while the other layers are aragonitic (Génio et al., 2012; Immenhauser et al., 2015). The transition from aragonite phase to calcite phase of M2020 and M2021 occurred at laser point 40 and 46, respectively.

Element concentrations

Element results were reported in the form of trace element/calcium (TE/Ca) ratios in Table S4. The Mg/Ca ratio of *G. haimaensis* (~200-14000 μmol/mol, seawater at Sanya Bay: ~4900-5400 μmol/mol, Wu et al., 2014) is significantly higher than that of *A. marissinica* (~100-1200 μmol/mol, pore water at Haima active cold seep area: ~5300-17700 μmol/mol, Wang et al., 2018), which is quite different from the Mg/Ca ratio of their living environments. In addition, the ranges of other element concentrations of the two species were very similar (Figures 4–6).

Discussion

Factors controlling TE/Ca ratios of seep bivalve shells

The factors driving the incorporation of trace elements into bivalve shells are complex and mainly include environmental factors (e.g., temperature, salinity, organic matter, microstructure, nutrition, pollution, etc.) and physiological regulation (e.g., mineral composition, growth rate, etc., Vander Putten et al., 2000; Gillikin et al., 2006; Shirai et al., 2014). Bivalves from shallow and deep-sea are facing different survival pressures. Compared to the shallow bivalves, the living environment for deep sea bivalves is relatively stable and the survival challenge mainly comes from food supply (Wisshak et al., 2009). Although a continuous line of sampling points intuitively suggests a time series with an equal amount of time between each point, the time interval between two sample points in the late stage of growth was much longer than at the beginning of growth, because bivalves grow much faster in their early stage and considerably slower when they get older (Barry et al., 2007). In addition, the faster the growth rate of the bivalve, the less physiological control it has over how much trace elements are incorporated into the shell. Our discussion is based on the relative age framework of the shell and draws on the achievements of previous studies (Vander Putten et al., 2000; Gillikin et al., 2006).

The mineral composition of shell carbonate is controlled by physiological regulation. The Mg/Ca and Sr/Ca ratios show an inverse pattern in *G. haimaensis* and remain constant in *A. marissinica* (Figures 4A2, B2). This is consistent with the fact that most of the derived heterodont bivalves shell (to which the vesicomyids belong) is aragonite and mussel shell (Family mytilids) is the mixture of calcite and aragonite. In *G. haimaensis*, the outer, calcitic layer near the umbones is so thin that it could not be targeted by our sampling method. Thus at a specific position (blue dot in Figure 3B, point 40 for M2020 and point 46 for M2021), our LA-ICP-MS sampling points moved from the aragonitic nacre layer into the calcitic outer layer, resulting in obvious changes in the Mg/Ca and Sr/Ca ratios (Figures 4A2, B2). Aragonite is generally richer in Sr than calcite. However, interestingly, the Sr/Ca ratios of *A. marissinica* is similar to the calcitic part of *G. haimaensis* but much lower than its aragonitic part, highlights the strong physiological control on the incorporation of Sr into seep bivalve shells.

Molybdenum (Mo) enrichment in cold seep systems is a very common and useful trace element proxy (Wang et al., 2019). The behavior of Mo in pore water changes when the H_2S concentration exceeds 11 μM, and Mo in pore water will be scavenged and enter the sediment and then be captured by pyrite, resulting in a sharp decrease in Mo in pore water (Helz

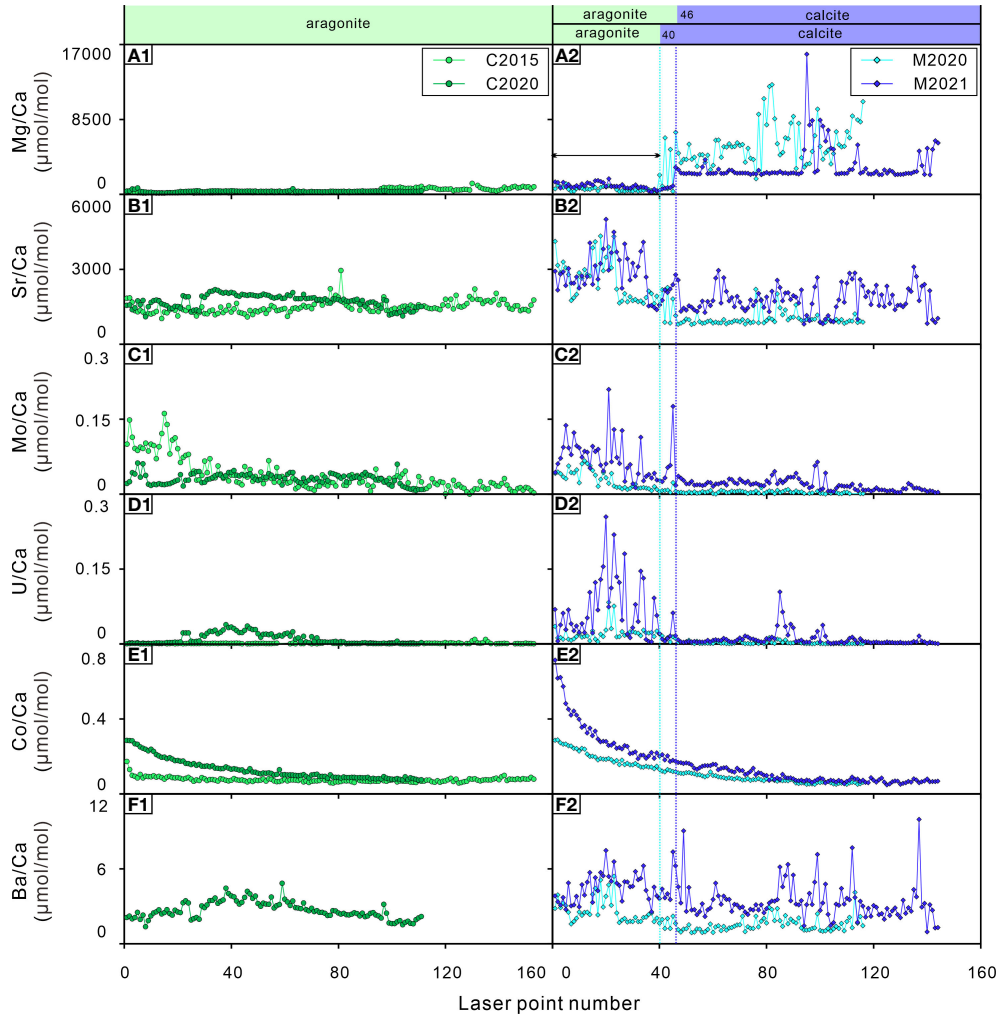

FIGURE 4
Elements/Ca ratios of the bivalve shells. **(A1, A2)** Mg/Ca ratios; **(B1, B2)** Sr/Ca ratios; **(C1, C2)** Mo/Ca ratios; **(D1, D2)** U/Ca ratios; **(E1, E2)** Co/Ca ratios; **(F1, F2)** Ba/Ca ratios. C2015 and C2020 are *A. marissinica*; M2020 and M2021 are *G. haimaensis*. The blue dotted lines indicate the change from aragonite to calcite in *G. haimaensis*.

et al., 1996). In this study, except for C2020, the Mo/Ca ratios of the bivalve shells were higher in their early stage of life and then gradually decreased with occasional peaks. Visually, the Mo/Ca ratio of *G. haimaensis* is probably related to their Mg/Ca and Sr/Ca ratios (i.e. mineral composition). However, the trend of Mo/Ca ratio is inconsistent with the theoretical calculation based on density functional theory (incorporation stability of molybdate anions: calcite > aragonite. Midgley et al., 2020), and there is also no difference of Mo concentration in aragonite versus calcite (Wang et al., 2019). For bivalves, it was found that the incorporation of Mo into the shell is influenced by the growth rate (Tabouret et al., 2012). Therefore, a simple explanation for the Mo pattern observed here is that the bivalves get more control over Mo incorporation with age. However, this is not the case for C2020; possibly, Mo concentration were lower during its early life. Interestingly, there is virtually no difference in Mo concentration between the infaunal (=living within the sediment) *A. marissinica* and the epifaunal *G. haimaensis* (Figures 4C1, C2).

The U/Ca ratios of seep bivalves seem to be closely related to their corresponding Sr/Ca ratios, implying that the incorporation of U into shells could be related to mineral composition (Figure 4, Cravo et al., 2002). It is also found that the U/Ca ratio of marine bivalve shells is higher in the early stage of life but drops below the detection limit in the later stage due to vital effects (Gillikin and Dehairs, 2013). Therefore, as far as the seep-inhabiting species investigated here are concerned, the U/Ca ratios could be regulated by physiological factors, especially among *G. haimaensis*.

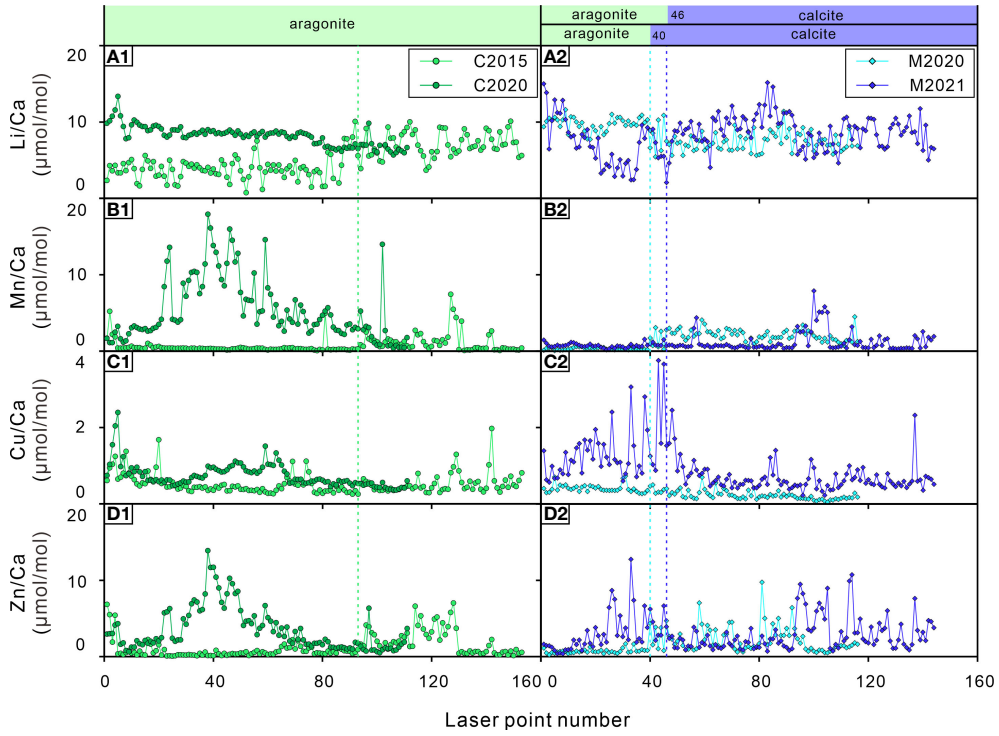

FIGURE 5
Elements/Ca ratios of the bivalve shells. **(A1, A2)** Li/Ca ratios; **(B1, B2)** Mn/Ca ratios; **(C1, C2)** Cu/Ca ratios; **(D1, D2)** Zn/Ca ratios. C2015 and C2020 are *A. marissinica* while M2020 and M2021 are *G. haimaensis*. The blue dotted lines indicate the change from aragonite to calcite in *G. haimaensis*, the green dotted line represents the boundary where elements may be lost for C2015.

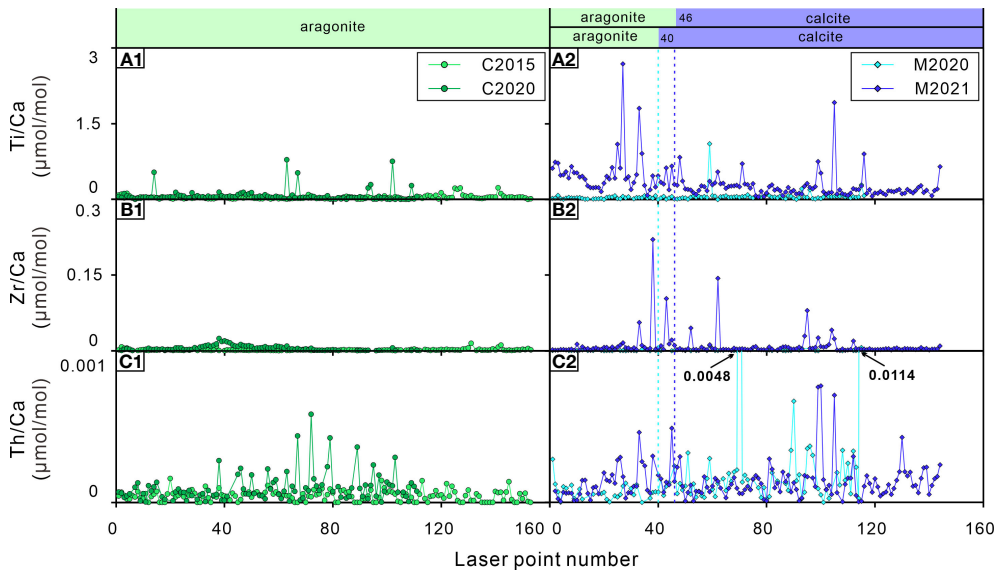

FIGURE 6
Elements/Ca ratios of the bivalve shells. **(A1, A2)** Ti/Ca ratios; **(B1, B2)** Zr/Ca ratios; **(C1, C2)** Th/Ca ratios. C2015 and C2020 are *A. marissinica* while M2020 and M2021 are *G. haimaensis*. The blue dotted lines indicate the change from aragonite to calcite in *G. haimaensis*.

Cobalt (Co) is a biologically essential element (Saito et al., 2004). Co^{2+} competes with Ca^{2+} ions during biomineralization (Bellotto and Miekeley, 2007; Honig et al., 2020). Co is a vital component of vitamin B12 (cyanocobalamin), which is a coenzyme in many cellular processes, including the synthesis of DNA and the oxidation of fatty acids (Blust, 2011; Pouil et al., 2017). There are few exhaustive studies of Co on the physiological effect of bivalves thus far. Previous research indicates that the changes in lipid and sterol metabolism increased with increasing Co^{2+} concentrations, and it is possible that Co^{2+} provokes oxidation damage in mussels (Nechev et al., 2006). Another study showed that the concentration of Co in the clam *Ruditapes philippinarum* increases with increasing CO2 (acidified seawater, Sezer et al., 2018). In a recent study, Honig et al. (2020) found that several TE/Ca ratios differed significantly between age classes, and Co/Ca ratios were usually greater in larvae than in juveniles. It can be determined that the incorporation of Co into shell carbonate is physiologically regulated. With increasing age, the Co/Ca ratios of the shells exponentially decline in both bivalves (Figures 4E1, E2). As far as we know, there is no unambiguous knowledge of this trend. The most likely scenario is that the cobalt-assimilation rate of bivalves slows down with age. Based on this observation, we suppose that the Co/Ca ratios of seep bivalve shells have the potential to be a tool to calculate the age of bivalves at seeps, as long as we obtain the age-confirmed sample and ascertain the function between the age and Co/Ca ratios of seep bivalves. However, the potential of this approach needs to be validated in other seep areas.

The Ba/Ca ratios of shallow-water bivalve shells have been used to reconstruct the primary productivity of their living environment, which is often related to phytoplankton blooms (Vander Putten et al., 2000; Kelemen et al., 2019; Fröhlich et al., 2022), the amplitude of the chlorophyll peaks is often used to explain the peak value of the Ba/Ca ratio of bivalve shells (Goodwin et al., 2013; Doré et al., 2020). Therefore, as long as the Ba/Ca ratio of bivalve shells is not strongly physiologically controlled, the change in Ba in the environment can be reflected in shells because the Ba/Ca ratio of bivalve shells is usually related to the Ba/Ca ratio of environmental water (Gillikin et al., 2006; Goodwin et al., 2013). There are many factors that lead to an increase in Ba in the environment. In addition to autochthonic effects, such as the formation of barite ($BaSO_4$) crystals caused by flocs after phytoplankton decay (Doré et al., 2020), autochthonic effects also include the addition of Ba-rich external fluids to the environment (such as freshwater, groundwater, hydrothermal fluids, upwelling caused by typhoons and storms, etc. Shirai et al., 2008; Goodwin et al., 2013; Markulin et al., 2020), which may lead to changes in salinity in the environment. As mentioned by some previous studies, Ba/Ca ratios in bivalve shells can be used to track salinity (Gillikin et al., 2006; Poulain et al., 2015). The Ba/Ca ratios of C2020 (*A. marissinica*) have a relatively flat distribution pattern with lower values (Ba/Ca ratios of C2015 is below detection limit) while the Ba/Ca ratios of *G. haimaensis* exhibit notable fluctuations with uncertain cycles and large relative amplitudes. The Ba/Ca ratio pattern of *G. haimaensis* appears to be typical for bivalves, as it has been recognized in almost all Ba/Ca ratio profiles of bivalve shells — relatively stable for most of their lifetime interrupted by occasional sharp peaks (Gillikin et al., 2008; Schöne et al., 2013; Poulain et al., 2015; Marali et al., 2017; Markulin et al., 2020). The study site is an area of active seepage with an obvious Ba front in the sediment (the highest concentration of Ba is ~1200 ppm, Liu, S et al., 2020), indicating a considerable Ba supply. Therefore, in our opinion, the peak Ba/Ca ratios of seep bivalves are affected by the discharge of Ba-rich fluids. The same conclusion was reached by Torres et al. (2001), although the peak Ba/Ca ratio in our study (10 μmol/mol) is much lower than theirs (up to 80 μmol/mol). It is necessary to analyze more shells collected from the same cold seep area in the future. If there is strong interindividual reproducibility of the Ba/Ca ratio, then environmental driving factors that control the incorporation of Ba in shells exist.

In summary, due to its monomineralic composition, the distribution of trace elements in *A. marissinica* has its unique advantages in constraining physiological mechanism and reconstructing the changes of microenvironment in the study area. The distribution of trace elements in the bimineralic *G. haimaensis* and other mussel shells is easily affected by mineral composition, as reflected in the Mg/Ca and Sr/Ca ratios, and potentially the U/Ca ratios, too. To solve the issues with bimineralic shells encountered in this study, the application of chemical staining could be used to distinguish aragonite from calcite in future research (Kato et al., 2003). In addition, we propose that the Mo/Ca ratios in the studies bivalves were controlled by age (i.e. growth rate), and probably affected by environmental factors (for C2020). The Co/Ca ratios of seep bivalve shells intuitively indicates that the rate of Co incorporated into the shell carbonate slows down with age, opening the potential to utilize this trend to constrain the age of seep bivalves.

Loss of trace elements in shells after death of the bivalves?

Based on the observation of some TE/Ca ratios of C2015, there is the potential of element loss (decline in concentration) after the bivalve dies. At the time of collection, C2015 was the only dead individual of all four samples. Compared to the other three bivalve shells, the TE/Ca ratios of C2015 often show a flatter distribution pattern (Figure 5). As mentioned earlier, the Mg/Ca and Sr/Ca ratios of seep bivalve shells are mainly

controlled by physiological factors. The mineral composition of C2015 is aragonite, and the ratios of Mg/Ca and Sr/Ca should be relatively stable if there are no other factors involved. This is true for the Sr/Ca ratio but not for the Mg/Ca ratio. After laser point 93, the Mg/Ca ratio of C2015 was significantly increased, implying that Mg may lost before laser point 93 (Figure 4). The same patterns are also observed for the Li/Ca, Mn/Ca, Cu/Ca and Zn/Ca ratios, which all exhibit lower ratios before laser point 93 (green dot line in Figure 5). Furthermore, the decreasing trend of the Co/Ca ratio of C2015 stopped at point 3 (Figure 4E1), which is obviously different from the logarithmic decreasing trend of the other three samples. The Ba/Ca ratios of C2015 were not reported because the content of Ba is lower than the detection limit. Therefore, Co and Ba may also be lost. A possibility is that these trace elements are actually contained in the organic matter within the shell. The presence of organic matter occupies the position of lattice in bivalve shells, thus affect the contents of lattice-bound trace elements. At the same time, trace elements can be adsorbed on organic matter of the shell (Roditi et al., 2000; Vander Putten et al., 2000). It has been observed that organic matter degradation effects the contents of Mn, Mg, Sr and Pb in shells (Takesue et al., 2008). The collected fresh shells obviously contained more organic matter, whereas in C2015, the organic matter had already decayed. It is of course also possible that this phenomenon is caused by individual differences (for example, the M2021 overall has a flatter distribution of Mn/Ca than M2020, whereas M2020 has a much flatter distribution of Cu/Ca compared to M2021), follow-up research is needed on this issue.

The potential influence of human activity on cold seep systems

With the further expansion of human activities to deep-sea cold seep areas, such as fishing, onshore and offshore mining, pollution, and also scientific investigation, these ecosystems are increasingly threatened. For example, epifaunal seep communities on the Hikurangi Margin were disturbed by bottom trawling (Bowden et al., 2013), seep faunas off of northern Papua New Guinea are affected by tailings from onshore mining (Samadi et al., 2015), mining of gas hydrates is explored along continental margins (Song et al., 2014), and trash and other leftovers of human activities are found at increasingly great depth (Schlining et al., 2013). Unfortunately, the deep sea is a slow world, which is not only manifested in the slow growth of various microorganisms, but also in the slow recovery of the environment after being changed (Neves et al., 2015). Now, this tendency has drawn the attention of some countries and international organizations (Van Dover et al., 2012; Danovaro et al., 2020). For example, the Croker Carbonate Slabs in the Irish Sea, as "submarine structures formed by leaking gases", have been designated as a marine protected area (MPA) under the European Commission's Habitats Directive (Judd et al., 2020).

At an active cold seep site in the South China Sea, called 'site F', Wang et al. (2017) found that the concentrations of K, Mg, Sr, Cu, Mo and V increased toward the outer edge of bivalve shells, indicating more abundant concentrations of trace metals in ambient seawater in recent years, which suggests that human activities may interfere with the cold seep area. The studies of tubeworms in cold seep area also found that the top and root of the tubeworms were strongly affected by the environment, causing the anomaly of some redox sensitive elements and rare earth elements (Duperron et al., 2014; Bayon et al., 2020).

A noteworthy phenomenon in this study is that there are abnormal Ti/Ca, Zr/Ca and Th/Ca ratio peaks in bivalve shells C2020, M2020 and M2021, but there are virtually no such peaks in C2015 (Figure 6). As far as we know, there is no report of the biological utilization of elements such as Ti, Zr and Th. Since these are typical elements of terrigenous sediments, one could propose that a drastic increase of these ratios in the bivalve shells was induced by their variability of the bivalves' living environment. Since the discovery of "Haima" cold seeps in 2015, scientific research activities at this site have become an annual event. It is common for ROV cruise to Haima cold seep, and the frequency is increasing year by year (Liang et al., 2017; Wang et al., 2022). When the submersible is maneuvering or sampling, it induces large 'dust clouds', which will slowly settle on the seabed (Figure 7). We suspect that these activities affected the submarine cold seep ecosystem and have been written down into the trace element record of the bivalve shells to a certain extent.

Conclusion and implication

Analysis of high-resolution element geochemistry of shells of two species of seep bivalve from the Haima cold seeps in the South China Sea confirms that these shells are biogeochemical recorder of short-term environmental change and physiological parameters at cold seeps. The incorporation of trace elements such as Mg, Sr, Mo, U, Co, Ba in seep bivalve shells is mainly controlled by physiological and environmental factors; the distribution of Co could potentially be developed into an independent index to estimate the age of seep bivalves. Notwithstanding limitations, our results put forward some open questions concerning the element loss for dead shell (Li-Mn-Cu-Zn) and the influence of human activity on cold seep systems (Ti-Zr-Th). We propose the necessity to investigate seep bivalves on the basis of an absolute age framework and to understand their physiological characteristics in the future, which is a

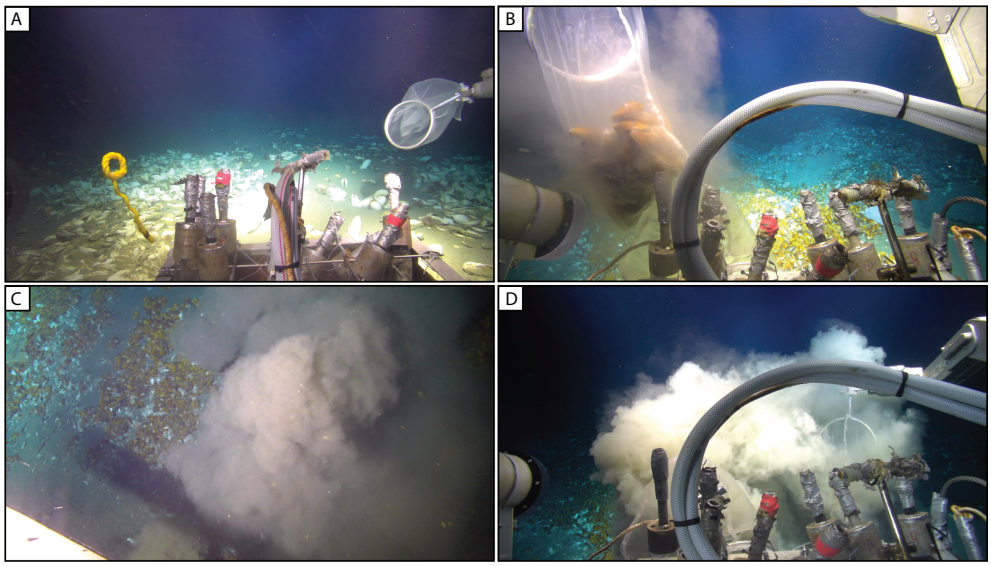

FIGURE 7
Seafloor images showing the 'dust clouds' caused by the ROV during sampling. **(A)** Field of live and dead vesicomyid clams; **(B–D)** large bathymodiolin mussel beds.

prerequisite for further determining the unique potential and effectiveness of this bioarchive in reconstructing environmental information on cold seep systems in a short time scale (years to decades). This study has examined only limited samples that span a relatively short time, our conclusions may thus reflect localized conditions only. Through more measurements over a larger area and longer timespan, the interactions between seep animals and the local environments may be further verified.

Data availability statement

The datasets presented in this study can be found in online repositories. The names of the repository/repositories and accession number(s) can be found in the article/ Supplementary Material.

Author contributions

XW: conceptualization, methodology, data analysis, and writing-original manuscript. DaF: methodology. SK: writing-review & editing. SG: sample collection. QL: sample collection. JT: sample collection. DC: data analysis. DoF: conceptualization, supervision, funding acquisition, and writing-review & editing. All authors contributed to manuscript preparation. All authors contributed to the article and approved the submitted version.

Funding

This study was partially sponsored by the National Natural Science Foundation of China (Grants: 41730528, 42106059, 42225603), Shanghai Sailing Program (Grant: 21YF1416800), special funding for the development of science and technology of Shanghai Ocean University and startup foundation for young teachers of Shanghai Ocean University.

Acknowledgments

The crew and captain of the *Haiyang-6* research vessel and *Haima* ROV are thanked for sample collection. We are grateful to Zice Jia (SHOU) for XRD measurement.

Conflict of interest

The authors declare that the research was conducted in the absence of any commercial or financial relationships that could be construed as a potential conflict of interest.

Publisher's note

All claims expressed in this article are solely those of the authors and do not necessarily represent those of their

affiliated organizations, or those of the publisher, the editors and the reviewers. Any product that may be evaluated in this article, or claim that may be made by its manufacturer, is not guaranteed or endorsed by the publisher.

Supplementary material

The Supplementary Material for this article can be found online at: https://www.frontiersin.org/articles/10.3389/fmars.2022.960338/full#supplementary-material

References

Barry, J. P., Whaling, P. J., and Kochevar, R. K. (2007). Growth, production, and mortality of the chemosynthetic vesicomyid bivalve, calyptogena kilmeri from cold seeps off central California. *Mar. Ecol.* 28, 169–182. doi: 10.1111/j.1439-0485.2007.00119.x

Bayon, G., Lemaitre, N., Barrat, J.-A., Wang, X., Feng, D., and Duperron, S. (2020). Microbial utilization of rare earth elements at cold seeps related to aerobic methane oxidation. *Chem. Geol.* 555, 119832. doi: 10.1016/j.chemgeo.2020.119832

Bellotto, V., and Miekeley, N. (2007). Trace metals in mussel shells and corresponding soft tissue samples: a validation experiment for the use of perna perna shells in pollution monitoring. *Anal. Bioanal. Chem.* 389, 769–776. doi: 10.1007/s00216-007-1420-y

Blust, R. (2011). "Cobalt," in *Fish physiology: Homeostasis and toxicology of essential metals, 1st ed*. Eds. C. M. Wood, A. P. Farrell and C. J. Brauner (Amsterdam: Elsevier), 291–326.

Bowden, D. A., Rowden, A. A., Thurber, A. R., Baco, A. R., Levin, L. A., and Smith, C. R. (2013). Cold seep epifaunal communities on the hikurangi margin, new zealand: composition, succession, and vulnerability to human activities. *PloS One* 8, e76869. doi: 10.1371/journal.pone.0076869

Branson, O., Redfern, S. A. T., Elmore, A. C., Read, E., Valencia, S., and Elderfield, H. (2018). The distribution and coordination of trace elements in krithe ostracods and their implications for paleothermometry. *Geochim. Cosmochim. Acta* 236, 230–239. doi: 10.1016/j.gca.2017.12.005

Chen, F., Wang, X., Li, N., Cao, J., Bayon, G., Peckmann, J., et al. (2019). Gas hydrate dissociation during sea-level highstand inferred from U/Th dating of seep carbonate from the south China Sea. *Geophys. Res. Lett.* 46, 13928–13938. doi: 10.1029/2019GL085643

Cravo, A., Foster, P., and Bebianno, M. J. (2002). Minor and trace elements in the shell of patella aspera (Röding 1798). *Environ. Int.* 28, 295–302. doi: 10.1016/s0160-4120(02)00038-7

Danovaro, R., Fanelli, E., Aguzzi, J., Billett, D., Carugati, L., Corinaldesi, C., et al. (2020). Ecological variables for developing a global deep-ocean monitoring and conservation strategy. *Nat. Ecol. Evol.* 4, 181–192. doi: 10.1038/s41559-019-1091-z

Doré, J., Chaillou, G., Poitevin, P., Lazure, P., Poirier, A., Chauvaud, L., et al. (2020). Assessment of ba/ca in arctica islandica shells as a proxy for phytoplankton dynamics in the northwestern atlantic ocean. *Estuar. Coast. Shelf Sci.* 237, 106628. doi: 10.1016/j.ecss.2020.106628

Duperron, S., Gaudron, S. M., Lemaitre, N., and Bayon, G. (2014). A microbiological and biogeochemical investigation of the cold seep tubeworm escarpia southwardae (Annelida: Siboglinidae): symbiosis and trace element composition of the tube. *Deep-Sea Res. Part I-Oceanogr. Res. Pap.* 90, 105–114. doi: 10.1016/j.dsr.2014.05.006

Feng, D., Peckmann, P., Li, N., Kiel, S., Qiu, J.-W., Liang, Q., et al. (2018). The stable isotope fingerprint of chemosymbiosis in the shell organic matrix of seep-dwelling bivalves. *Chem. Geol.* 479, 241–250. doi: 10.1016/j.chemgeo.2018.01.015

Fröhlich, L., Siebert, V., Walliser, E. O., Thébault, J., Jochum, K. P., Chauvaud, L., et al. (2022). Ba/Ca profiles in shells of pecten maximus – a proxy for specific primary producers rather than bulk phytoplankton. *Chem. Geol* 593, 120743. doi: 10.1016/j.chemgeo.2022.120743

Génio, L., Kiel, S., Cunha, M. R., Grahame, J., and Little, C. T. S. (2012). Shell microstructures of mussels (Bivalvia: Mytilidae: Bathymodiolinae) from deep-sea chemosynthetic sites: Do they have a phylogenetic significance? *Deep-Sea Res. Part I-Oceanogr. Res. Pap.* 64, 86–103. doi: 10.1016/j.dsr.2012.02.002

Gillikin, D., and Dehairs, F. (2013). Uranium in aragonitic marine bivalve shells. *Palaeogeogr. Palaeoclimatol. Palaeoecol.* 373, 60–65. doi: 10.1016/j.palaeo.2012.02.028

Gillikin, D. P., Dehairs, F., Lorrain, A., Steenmans, D., Baeyens, W., and André, L. (2006). Barium uptake into the shells of the common mussel (Mytilus edulis) and the potential for estuarine paleo-chemistry reconstruction. *Geochim. Cosmochim. Acta* 70, 395–407. doi: 10.1016/j.gca.2005.09.015

Gillikin, D. P., Lorrain, A., Paulet, Y.-M., André, L., and Dehairs, F. (2008). Synchronous barium peaks in high-resolution profiles of calcite and aragonite marine bivalve shells. *Geo-Mar. Lett.* 28, 351–358. doi: 10.1007/s00367-008-0111-9

Goodwin, D. H., Gillikin, D. P., and Roopnarine, P. D. (2013). Preliminary evaluation of potential stable isotope and trace element productivity proxies in the oyster crassostrea gigas. *Palaeogeogr. Palaeoclimatol. Palaeoecol.* 373, 88–97. doi: 10.1016/j.palaeo.2012.03.034

Helz, G. R., Miller, C. V., Charnock, J. M., Mosselmans, J. F. W., Pattrick, R. A. D., Garner, C. D., et al. (1996). Mechanism of molybdenum removal from the sea and its concentration in black shales: EXAFS evidence. *Geochim. Cosmochim. Acta* 60, 3631–3642. doi: 10.1016/0016-7037(96)00195-0

Himmler, T., Bayon, G., Wangner, D., Enzmann, F., Peckmann, J., and Bohrmann, G. (2016). Seep-carbonate lamination controlled by cyclic particle flux. *Sci. Rep.* 6, 37439. doi: 10.1038/srep37439

Honig, A., Etter, R., Pepperman, K., Morello, S., and Hannigan, R. (2020). Site and age discrimination using trace element fingerprints in the blue mussel. *J. Exp. Mar. Biol. Ecol.* 522, 151249. doi: 10.1016/j.jembe.2019.151249

Immenhauser, A., Schöne, B. R., Hoffmann, R., and Niedermayr, A. (2015). Mollusc and brachiopod skeletal hard parts: Intricate archives of their marine environment. *Sedimentology* 63, 1–59. doi: 10.1111/sed.12231

Johansen, C., Todd, A. C., and MacDonald, I. R. (2017). Time series video analysis of bubble release processes at natural hydrocarbon seeps in the northern gulf of Mexico. *Mar. Pet. Geol.* 82, 21–34. doi: 10.1016/j.marpetgeo.2017.01.014

Juárez-Aguilar, E. A., Sánchez-Beristain, F., and Bernal, J. P. (2019). Determination of the temperature of precipitation of aragonite in shells of anadara brasiliana (Lamarck, 1819) from playa norte, cazones de herrera (Holocene, veracruz, Mexico) by means of trace element analysis. *J. South Am. Earth Sci.* 91, 71–79. doi: 10.1016/j.jsames.2019.01.007

Judd, A., Noble-James, T., Golding, N., Eggett, A., Diesing, M., Clare, D., et al. (2020). The croker carbonate slabs: extensive methane-derived authigenic carbonate in the Irish Sea–nature, origin, longevity and environmental significance. *Geo-Mar. Lett.* 40, 423–438. doi: 10.1007/s00367-019-00584-0

Kato, K., Wada, H., and Fujioka, K. (2003). The application of chemical staining to separate calcite and aragonite minerals for micro-scale isotopic analyses. *Geochem. J.* 37, 291–297. doi: 10.2343/geochemj.37.291

Kelemen, Z., Gillikin, D. P., and Bouillon, S. (2019). Relationship between river water chemistry and shell chemistry of two tropical African freshwater bivalve species. *Chem. Geol.* 526, 130–141. doi: 10.1016/j.chemgeo.2018.04.026

Kennish, M. J., Lutz, R. A., and Tan, A. S. (1998a). Deep-sea vesicomyid clams from hydrothermal vent and cold seep environments: analysis of shell microstructure. *Veliger* 41, 195–200.

Kennish, M. J., Tan, A. S., and Lutz, R. A. (1996). Shell microstructure of vesicomyid clams from various hydrothermal vent and cold seep environments. *Malacologia* 37, 363–373.

Kennish, M. J., Tan, A. S., and Lutz, R. A. (1998b). Shell microstructure of mytilids (Bivalvia) from deep-sea hydrothermal vents and cold-water sulfide/methane seep environments. *Nautilus* 112, 84–89.

Kim, B., Cheong, D., and Lee, E. (2015).). paleoenvironmental changes in northern Mongolia during the last deglaciation revealed by trace element records in ostracods from lake hovsgol. *Quat. Int.* 384, 169–179. doi: 10.1016/j.quaint.2015.04.041

Leifer, I., Boles, J. R., Luyendyk, B. P., and Clark, J. F. (2004). Transient discharges from marine hydrocarbon seeps: spatial and temporal variability. *Environ. Geol.* 46, 1038–1052. doi: 10.1007/s00254-004-1091-3

Liang, Q., Hu, Y., Feng, D., Peckmann, J., Chen, L., Yang, S., et al. (2017). Authigenic carbonates from newly discovered active cold seeps on the northwestern slope of the south China Sea: Constraints on fluid sources, formation environments, and seepage dynamics. *Deep-Sea Res. Part I-Oceanogr. Res. Pap.* 124, 31–41. doi: 10.1016/j.dsr.2017.04.015

Lietard, C., and Pierre, C. (2008). High-resolution isotopic records (δ18O and δ13C) and cathodoluminescence study of lucinid shells from methane seeps of the Eastern Mediterranean. *Geo-Mar Lett.* 28, 195–203. doi: 10.1007/s00367-008-0100-z

Liu, S., Feng, X., Feng, Z., Xiao, X., and Feng, L. (2020). Geochemical evidence of methane seepage in the sediments of the qiongdongnan basin, south China Sea. *Chem. Geol.* 543, 119588. doi: 10.1016/j.chemgeo.2020.119588

Marali, S., Schöne, B. R., Mertz-Kraus, R., Griffin, S. M., Wanamaker, A. D.Jr., Butler, P. G., et al. (2017). Reproducibility of trace element time-series (Na/Ca,Mg/Ca, Mn/Ca, Sr/Ca, and Ba/Ca) within and between specimens of the bivalve arctica islandica–a LA-ICP-MS line scan study. *Palaeogeogr. Palaeoclimatol. Palaeoecol.* 484, 109–128. doi: 10.1016/j.palaeo.2016.11.024

Markulin, K., Uvanović, H., Mertz-Kraus, R., Schöne, B. R., Kovač, Ž., Arapov, J., et al. (2020). Spatial variations in ba/cashell fingerprints of glycymeris pilosa along the eastern adriatic sea. *Estuar. Coast. Shelf Sci.* 243, 106821. doi: 10.1016/j.ecss.2020.106821

Midgley, S. D., Taylor, J. O., Fleitmann, D., and Grau-Crespo, R. (2020). Molybdenum and sulfur incorporation as oxyanion substitutional impurities in calcium carbonate minerals: A computational investigation. *Chem. Geol.* 553, 119796. doi: 10.1016/j.chemgeo.2020.119796

Nechev, J., Stefanov, K., and Popov, S. (2006). Effect of cobalt ions on lipid and sterol metabolism in the marine invertebrates mytilus galloprovincialis and actinia equina. *Comp. Biochem. Physiol. A-Mol. Integr. Physiol.* 144, 112–118. doi: 10.1016/j.cbpa.2006.02.022

Neves, B. M., Edinger, E., Layne, G. D., and Wareham, V. E. (2015). Decadal longevity and slow growth rates in the deep-water sea pen halipteris finmarchica (Sars, 1851) (Octocorallia: Pennatulacea): implications for vulnerability and recovery from anthropogenic disturbance. *Hydrobiologia* 759, 147–170. doi: 10.1007/s10750-015-2229-x

Paton, C., Hellstrom, J., Paul, B., Woodhead, J., and Hergt, J. (2011). Iolite: Freeware for the visualization and processing of mass spectrometer data. *J. Anal. At. Spectrom.* 26, 2508–2518. doi: 10.1039/C1JA10172B

Poitevin, P., Chauvaud, L., Pécheyran, C., Lazure, P., Jolivet, A., and Thébault, J. (2020). Does trace element composition of bivalve shells record utra-high frequency environmental variations? *Mar. Environ. Res.* 158, 104943. doi: 10.1016/j.marenvres.2020.104943

Pouil, S., Teyssié, J.-L., Rouleau, C., Fowler, S. W., Metian, M., Bustamante, P., et al. (2017). Comparative study of trophic transfer of the essential metals Co and zn in two tropical fish: A radiotracer approach. *J. Exp. Mar. Biol. Ecol.* 486, 42–51. doi: 10.1016/j.jembe.2016.09.005

Poulain, C., Gillikin, D. P., Thébault, J., Munaron, J. M., Bohn, M., Robert, R., et al. (2015). An evaluation of Mg/Ca, Sr/Ca, and Ba/Ca ratios as environmental proxies in aragonite bivalve shells. *Chem. Geol.* 396, 42–50. doi: 10.1016/j.chemgeo.2014.12.019

Roditi, H. A., Fisher, N. S., and Sañudo-Wilhelmy, S. A. (2000). Uptake of dissolved organic carbon and trace elements by zebra mussels. *Nature* 407, 78–80. doi: 10.1038/35024069

Saito, M. A., Moffett, J. W., and DiTullio, G. R. (2004). Cobalt and nickel in the Peru upwelling region: A major flux of labile cobalt utilized as a micronutrient. *Glob. Biogeochem. Cycle* 18, GB4030. doi: 10.1029/2003GB002216

Samadi, S., Puillandre, N., Pante, E., Boisselier, M.-C., Chen, W.-J., Corbari, L., et al. (2015). Patchiness of deep-sea communities in Papua new Guinea and potential susceptibility to anthropogenic disturbances illustrated by seep organisms. *Mar. Ecol.* 36, 109–132. doi: 10.1111/maec.12204

Schlining, K., von Thun, S., Kuhnz, L., Schlining, B., Lundsten, L., Stout, N. J., et al. (2013). Debris in the deep: Using a 22-year video annotation database to survey marine litter in monterey canyon, central california, usa. *Deep-Sea Res. Part I-Oceanogr. Res. Pap.* 79, 96–105. doi: 10.1016/j.dsr.2013.05.006

Schöne, B. R., and Giere, O. (2005). Growth increments and stable isotope variation in shells of the deep-sea hydrothermal vent bivalve mollusk bathymodiolus brevior from the north Fiji basin, pacific ocean. *Deep-Sea Res. Part I-Oceanogr. Res. Pap.* 52, 1896–1910. doi: 10.1016/j.dsr.2005.06.003

Schöne, B. R., Radermacher, P., Zhang, Z., and Jacob, D. E. (2013). Crystal fabrics and element impurities (Sr/Ca, Mg/Ca, and Ba/Ca) in shells of arctica islandica–implications for paleoclimate reconstructions. *Palaeogeogr. Palaeoclimatol. Palaeoecol.* 373, 50–59. doi: 10.1016/j.palaeo.2011.05.013

Sezer, N., Kocaoğlan, H. O., Lacoue-Labarthe, T., and Belivermiş, M. (2018). Acidified seawater increases accumulation of cobalt but not cesium in manila clam ruditapes philippinarum. *J. Environ. Radioact.* 184–185, 114–121. doi: 10.1016/j.jenvrad.2018.01.018

Shirai, K., Schöne, B. R., Miyaji, T., Radarmacher, P., Krause, R. A.Jr., and Tanabe, K. (2014). Assessment of the mechanism of elemental incorporation into bivalve shells (Arctica islandica) based on elemental distribution at the microstructural scale. *Geochim. Cosmochim. Acta* 126, 307–320. doi: 10.1016/j.gca.2013.10.050

Shirai, K., Takahata, N., Yamamoto, H., Omata, T., Sasaki, T., and Sano, Y. (2008). Novel analytical approach to bivalve shell biogeochemistry: A case study of hydrothermal mussel shell. *Geochem. J.* 42, 413–420. doi: 10.2343/GEOCHEMJ.42.413

Song, Y., Yang, L., Zhao, J., Liu, W., Yang, M., Li, Y., et al. (2014). The status of natural gas hydrate research in China: A review. *Renew. Sust. Energ. Rev.* 31, 778–791. doi: 10.1016/j.rser.2013.12.025

Suess, E. (2020). "Marine cold seeps: Background and recent advances," in *Hydrocarbons, oils and lipids: Diversity, origin, chemistry and fate*. Ed. H. Wilkes (Switzerland, Springer International Publishing, Cham), 747–767. doi: 10.1007/978-3-319-90569-3_27

Tabouret, H., Pomerleau, S., Jolivet, A., Pécheyran, C., Riso, R., Thébault, J., et al. (2012). Specific pathways for the incorporation of dissolved barium and molybdenum into the bivalve shell: An isotopic tracer approach in the juvenile great scallop (Pecten maximus). *Mar. Environ. Res.* 78, 15–25. doi: 10.1016/j.marenvres.2012.03.006

Takesue, R. K., Bacon, C. R., and Thompson, J. K. (2008). Influences of organic matter and calcification rate on trace elements in aragonitic estuarine bivalve shells. *Geochim. Cosmochim. Acta* 72, 5431–5445. doi: 10.1016/j.gca.2008.09.003

Torres, M. E., Barry, J. P., Hubbard, D. A., and Suess, E. (2001). Reconstructing the history of fluid flow at cold seep sites from Ba/Ca ratios in vesicomyid clam shells. *Limnol. Oceanogr.* 46, 1701–1708. doi: 10.4319/lo.2001.46.7.1701

Vander Putten, E., Dehairs, F., Keppens, E., and Baeyens, W. (2000). High resolution distribution of trace elements in the calcite shell layer of modern mytilus edulis: Environmental and biological controls. *Geochim. Cosmochim. Acta* 64, 997–1011. doi: 10.1016/S0016-7037(99)00380-4

Van Dover, C. L., Smith, C. R., Ardron, J., Dunn, D., Gjerde, K., Levin, L., et al. (2012). Designating networks of chemosynthetic ecosystem reserves in the deep sea. *Mar. Pol.* 36, 378–381. doi: 10.1016/j.marpol.2011.07.002

Wang, X., Barrat, J.-A., Bayon, G., Chauvaud, L., and Feng, D. (2020). Lanthanum anomalies as fingerprints of methanotrophy. *Geochem. Perspect. Lett.* 14, 26–30. doi: 10.7185/geochemlet.2019

Wang, X., Bayon, G., Kim, J.-H., Lee, D.-H., Kim, D., Guéguen, B., et al. (2019). Trace element systematics in cold seep carbonates and associated lipid compounds. *Chem. Geol.* 528, 119227. doi: 10.1016/j.chemgeo.2019.119277

Wang, X., Guan, H., Qiu, J.-W., Xu, T., Peckmann, J., Chen, D., et al. (2022). Macro-ecology of cold seeps in the south China Sea. *Geosyst. Geoenviron.* 1, 100081. doi: 10.1016/j.geogeo.2022.100081

Wang, X., Li, N., Feng, D., Hu, Y., Bayon, G., Liang, Q., et al. (2018). Using chemical compositions of sediments to constrain methane seepage dynamics: A case study from haima cold seeps of the south China Sea. *J. Asian Earth Sci.* 168, 137–144. doi: 10.1016/j.jseaes.2018.11.011

Wang, X., Li, C., and Zhou, L. (2017). Metal concentrations in the mussel bathymodiolus platifrons from a cold seep in the south China Sea. *Deep-Sea Res. Part I-Oceanogr. Res. Pap.* 129, 80–88. doi: 10.1016/j.dsr.2017.10.004

Wang, S., Wu, S., Du, M., Yang, C., and Wang, X. (2020). A new serial sampler for collecting gas-tight samples from seafloor cold seeps and hydrothermal vents. *Deep-Sea Res. Part I-Oceanogr. Res. Pap.* 161, 103282. doi: 10.1016/j.dsr.2020.103282

Wisshak, M., Neumann, C., Jakobsen, J., and Freiwald, A. (2009). The 'living-fossil community' of the cyrtocrinid cyathidium foresti and the deep-sea oyster neopycnodonte zibrowii (Azores archipelago). *Palaeogeogr. Palaeoclimatol. Palaeoecol.* 271, 77–83. doi: 10.1016/j.palaeo.2008.09.015

Wu, W., Wei, G., Xie, L., and Liu, Y. (2014). Variations of Sr/Ca, Mg/Ca ratios in seawater of the sanya bay and response of coral trace element thermometer. *Mar. Sci.* 38, 46–55. doi: 10.11759/hykx20120706003

frontiers | Frontiers in Marine Science

TYPE Original Research
PUBLISHED 08 September 2022
DOI 10.3389/fmars.2022.957762

OPEN ACCESS

EDITED BY
Hongmei Jing,
Institute of Deep-Sea Science and Engineering (CAS), China

REVIEWED BY
Xiyang Dong,
Third Institute of Oceanography of the Ministry of Natural Resources, China
Xilin Zhang,
Qingdao Institute of Marine Geology (QIMG), China
Youzhi Xin,
China University of Geosciences Wuhan, China

*CORRESPONDENCE
Min Yu
yumin@ouc.edu.cn

†These authors have contributed equally to this work

SPECIALTY SECTION
This article was submitted to Deep-Sea Environments and Ecology, a section of the journal Frontiers in Marine Science

RECEIVED 31 May 2022
ACCEPTED 25 July 2022
PUBLISHED 08 September 2022

CITATION
Zhai X, Shi X, Cheng H, Yao P, Zhao B, Chen L, Liu J, Cao L, Wang M, Fu L, Zhang X-H and Yu M (2022) Horizontal and vertical heterogeneity of sediment microbial community in Site F cold seep, the South China Sea. *Front. Mar. Sci.* 9:957762. doi: 10.3389/fmars.2022.957762

Horizontal and vertical heterogeneity of sediment microbial community in Site F cold seep, the South China Sea

Xinyi Zhai[1†], Xiaochong Shi[1,2,3†], Haojin Cheng[1], Peng Yao[2,4], Bin Zhao[2,4], Lin Chen[2,4], Jiwen Liu[1,2,3], Lei Cao[5], Minxiao Wang[5], Lulu Fu[5], Xiao-Hua Zhang[1,2,3] and Min Yu[1,2,3*]

[1]Frontiers Science Center for Deep Ocean Multispheres and Earth System, and College of Marine Life Sciences, Ocean University of China, Qingdao, China, [2]Laboratory for Marine Ecology and Environmental Science, Qingdao National Laboratory for Marine Science and Technology, Qingdao, China, [3]Institute of Evolution and Marine Biodiversity, Ocean University of China, Qingdao, China, [4]Laboratory of Marine Chemistry Theory and Technology, Ministry of Education, Ocean University of China, Qingdao, China, [5]Center of Deep Sea Research, Institute of Oceanology, Chinese Academy of Sciences, Qingdao, China

Site F is the most vigorous cold seep known on the continental slope of the northern South China Sea. Up to now, the microbial community structures in sediments of Site F based on the high-throughput sequencing of the 16S rRNA genes have been studied extensively. However, few studies investigated the microbial community structures at fine vertical scales of Site F and control stations outside Site F. In this study, a comprehensive investigation of microbial communities in sediments of Site F along the depths varying from 0 to 24 cm below sea floor (cmbsf) of four sampling sites—SRS (Southern Reduced Sediment), NRS (Northern Reduced Sediment), Control 1 (close to Site F), and Control 2 (far from Site F)—was carried out. The high relative abundances of anaerobic methanotrophic archaea (ANME), *Desulfobacterota* [sulfate-reducing bacteria (SRB)], and *Campylobacteria* [sulfur-oxidizing bacteria (SOB)] in SRS and NRS indicated that these two sites were newborn cold seep sites compared with non-seep sites, Control 1, and Control 2. A positive correlation between ANME-1b, ANME-2, and SEEP-SRB and an enrichment of *Sulfurovum* and *Methlomonadaceae* were found in the surface sediments of both SRS and NRS, indicating that the processes of anaerobic oxidation of methane (AOM), sulfur oxidation, and sulfate reduction might occur in seep sites. SRS was enriched with ANME-1b and SEEP-SRB2 with a proposed sulfate-methane transition zone (SMTZ) approximately located at 8 cmbsf. The high abundance of ANME in SRS may due to the high concentration of methane. NRS was enriched with ANME-2, *Desulfatiglans*, *Sulfurovum*, and *Methanosarcinaceae* with a proposed SMTZ at about 10 cmbsf. According to the analyses of microbial community structure and environmental factors, NRS could be described as a notable cold seep reduced sediment site with low sulfate and high H_2S that nourished abundant SEEP-SRB1, ANME-2, *Methanosarcinales*, and *Sulfurovum*, which showed similar distribution

pattern. Our study expands the current knowledge on the differences of microbial communities in cold seep sites and non-seep sites and sheds light on the horizontal and vertical heterogeneity of sediment microbial community in Site F.

KEYWORDS

cold seep, South China Sea, reduced sediments, microbial communities, anaerobic methanotrophic archaea, sulfate-reducing bacteria, sulfur-oxidizing bacteria

Introduction

Deep-sea cold seeps usually refer to the ecosystems located at continental slopes, where dissolved and gaseous methane and reductive fluids emitted from oceanic subsurface (Boetius and Wenzhöfer, 2013; Li et al., 2021). The fluids enriched with hydrocarbons (primarily methane) and hydrogen sulfide sustain distinct microbiomes involved in various reactions in marine sediments, making the cold seep an oasis enriched with key functional groups including methanotrophs, methanogens, hydrocarbon degraders, and sulfate-reducing bacteria (SRB) (Jørgensen and Boetius, 2007; Boetius and Wenzhöfer, 2013; Li et al., 2021). Microorganism-mediated anaerobic oxidation of methane (AOM) is a dominant process at cold seep ecosystems and a major global sink of methane (Knittel et al., 2005; Sun et al., 2020). AOM is often associated with the reduction of sulfate, and the total reaction is $CH_4(aq) + SO_4^{2-} \rightarrow HS^- + HCO_3^- + H_2O$, which is usually performed by a consortium of anaerobic methanotrophic archaea (ANME) and SRB (Hoehler et al., 1994; Cui et al., 2019). ANME, which could be classified into ANME-1, ANME-2, and ANME-3, are found widely distributed in cold seep sediments (Knittel et al., 2005; Vigneron et al., 2013; McKay et al., 2016; Niu et al., 2017; Wu et al., 2018; Cui et al., 2019; Zhang et al., 2020). ANME-1 are divided into ANME-1a and ANME-1b subgroups, whereas ANME-2 are most widely distributed and divided into ANME-2a, ANME-2b, ANME-2c, and ANME-2d subgroups (Orphan et al., 2002; Mills et al., 2003; Knittel et al., 2005).

In general, the syntrophic partners of ANME-1 and ANME-2 are SRB affiliated with *Desulfosarcina*/*Desulfococcus* (DSS; within the *Desulfobacteraceae*) or *Desulfobulbus* (DBB; within the *Desulfobulbaceae*) (Orphan et al., 2001a; Orphan et al., 2001b; Orphan et al., 2002; Boetius et al., 2000; Jørgensen and Boetius, 2007; Zhang et al., 2020). It was found that ANME-1 were associated to SEEP-SRB2 (within the *Desulfuribacteraceae*) (Ruff et al., 2016); ANME-2 were associated to SEEP-SRB1 (members of DSS), SEEP-SRB2, and SEEP-DBB (members of DBB) (Orphan et al., 2001a; Pernthaler et al., 2008; Kleindienst et al., 2012; Green-Saxena et al., 2014; Ruff et al., 2016); and ANME-3 were associated with DBB and SEEP-SRB1 (Niemann et al., 2006; Lösekann et al., 2007; Schreiber et al., 2010). Furthermore, ANME-1 may perform AOM process *via* reversal of the methanogenic pathway without a bacterial partner (Orphan et al., 2002; Knittel et al., 2005; Stokke et al., 2012; Cho et al., 2017). Sulfur-oxidizing bacteria (SOB) also inhabit widely in cold seep sediments, many of which are affiliated with *Campylobacterota* and *Gammaproteobacteria* (Feng et al., 2018; Sun et al., 2020; Li et al., 2021). SOB play an important role in sulfide oxidation, which occurs in the near-surface sediment and supplies sulfate to the layers below (Li et al., 2021). Sulfate diffuses from above and methane rises from below, resulting in a region where sulfate and methane coexist called the sulfate-methane transition zone (SMTZ) (Borowski et al., 1996). The microbial consortia of ANME and SRB involved in AOM and sulfate reduction are often found in SMTZ (Boetius et al., 2000; Orphan et al., 2002).

Since the first cold seep discovered in the South China Sea (SCS) in 2004, more than 40 cold seeps were found on the continental margins of the SCS (Chen et al., 2005; Feng et al., 2018). Among them, Site F (22°06.922N; 119°17.130E) is the first intensely vigorous cold seep known on the continental slope of the northern SCS (Feng and Chen, 2015; Wang et al., 2021). Site F is found extremely active and characterized by an authigenic carbonate mound, which interspersed with cold seeps and benthic communities as well as surrounded by shell bed features and reduced sediments (Wang et al., 2021). In Site F, sufficient cold seep fluids are migrating along and escaping at the bottom of the authigenic carbonate mound, resulting in presence of the newly formed reduced sediment patches (Wang et al., 2021).

Up to now, a series of studies focused on the microbial communities in sediments of Site F have been carried out with high-throughput sequencing based on the 16S rRNA genes. It was found that *Sulfurovum* was the dominated microorganisms in the surface sediments, whereas *Deltaproteobacteria*, *Methanomicrobia*, and *Dehalococcoidia* were abundant in the subsurface (Sun et al., 2020). In addition, *Nitrosopumilus* was also found dominant and type I methanotrophs was found

conducted aerobic methane oxidization in Site F sediments (Jing et al., 2020). In the SMTZ, the high relative abundance of ANME-1b may perform AOM in collaboration with ANME-2c and *Desulfobacteraceae* (Cui et al., 2019). Studies on Jiaolong cold seep closed to Site F revealed that *Sulfurimonas*, *Sulfurovum*, and ANME-1 dominated the surface sediment layers, whereas SEEP-SRB1, ANME-2, ANME-1, and ANME-3 dominated the deeper sediment layers (Wu et al., 2018; Li et al., 2020; Li et al., 2021). It was found that ANME, especially ANME-2a-2b, as well as SOB and SRB were dominant microorganisms in the SMTZ of Jiaolong (Li et al., 2021). However, the conclusions varied among studies because of the inconsistency of sampling locations and depths. Many studies were limited by the number of sampling stations and few studies investigated stations apart from the cold seeps as control. In addition, the microbial community structures and metabolic potentials along the fine vertical scales of these seeps are still unknown (Jing et al., 2020).

In this study, we investigated the microbial communities of sediment samples among four sites around Site F by high-throughput sequencing based on the 16S rRNA gene amplicons. Our study aimed the following: to (i) determine and compare the difference of microbial communities in the cold seep sites and non-seep control sites along the horizontal and vertical directions at fine vertical scales and to infer the SMTZ depths of cold seep sites; (ii) to investigate the relationship of SRB, SOB, ANME, and other methane-metabolizing microbes to depict the ecological integrity of cold seep sites; and (iii) to improve the understanding of microbial biogeochemical processes in cold seeps of SCS.

Materials and methods

Sample collection and environmental characterization

Samples were collected from Site F cold seep in the SCS during the scientific cruise of R/V "*Kexue*" organized by the Institute of Oceanology, Chinese Academy of Sciences in June, 2021. The four sampling sites are SRS, NRS, Control 1, and Control 2 (Figure 1A). SRS is the reduced sediment site at southeastern periphery of authigenic carbonate mound and about 50 m from the known seepage, and NRS is the reduced sediment site at northern periphery of the authigenic carbonate mound and about 120 m from the seepage. Control 1 is on the south near Site F and about 85 m from the seepage, whereas Control 2 is on the southwest far from Site F and about 320 m from the seepage (Wang et al., 2021). Sediment samples from these sites were collected by Discover manned submersible dives 261, 263, 267, 268, and 271, respectively, with pushcore equipment. The cores were washed with sterile water and kept closed before sampling. After sampling, the cores were closed again and taken on board. The core was opened on board, and the sediment inside was pushed up from the bottom of the core. When the sample emerged at the top end of the core, subsample was taken for every 2 cm with a stainless-steel cutter, and considered as one sample. To analyze the concentration of methane in sediment methane, 3 ml of sample was transferred with a 5-ml cutoff syringe to a 22-ml serum vial containing 3 ml of NaOH (2 mol /L) (purged with 99.999% N_2), crimp sealed, and stored at 4°C for subsequent next measurement (Zhuang et al., 2019). In addition, the pore waters were extracted with Rhizons samplers (The Netherlands) inserted into the pre-drilled holes in PVC tubes and attached to vacuum test tubes by 23G needles under N_2 atmosphere (Zhao et al., 2017). Notably, site SRS was sampled twice by two dives and named as SRS 1 and SRS 2. All sampling depths ranged from 12 to 22 cm below sea floor (cmbsf). A total of 53 sediment samples were obtained, named as SRS 1_0-20, SRS 2_0-22, NRS_0-20, Control 1_0-12, and Control 2_0-22. All the samples were stored in sterile sampling bags and were immediately frozen at −80°C.

Methane concentrations were measured using a gas chromatograph (GC; SRI Instruments) equipped with a HayeSep column and a flame ionization detector by injecting 500 µl of headspace gas, and the analytical precision was better than 1.5% (Zhuang et al., 2019). The sulfate concentration in pore waters was determined with a Dionex ICS-3000 ion chromatography (USA) on 1:200 diluted aliquots in Milli-Q water, and the relative standard deviation of duplicate analyses was less than 1% (Zhao et al., 2017).

DNA extraction and PCR amplification

Microbial community genomic DNA was extracted from sediment samples using the FastDNA® Spin Kit for Soil (MP Biomedicals) and a FastPrep-24 cell disrupter (MP Biomedicals) according to manufacturer's instructions. The extracted DNA was checked on 1% agarose gel, and DNA concentration and purity were determined with NanoDrop 2000 UV-vis spectrophotometer (Thermo Scientific, Wilmington, USA). The hypervariable region V4 of prokaryotic (bacterial and archaeal) 16S rRNA genes was amplified with primer pairs 515FmodF (5′-GTGYCAGCMGCCGCGGTAA-3′) and 806RmodR (5′-GGACTACNVGGGTWTCTAAT-3′) by an ABI GeneAmp® 9700 PCR thermocycler (ABI, CA, USA) (Walters et al., 2015). The PCR amplification of 16S rRNA gene was performed as follows: initial denaturation at 95°C for 3 min; 29 cycles of denaturing at 95°C for 30 s, annealing at 55°C for 30 s, extension at 72°C for 45 s; single extension at 72°C for 10 min and end at 10°C. The PCR mixtures contain 5× *TransStart* FastPfu buffer of 4 µl, 2.5 mM dNTPs of 2 µl, forward primer of (5 µM) 0.8 µl, reverse primer of (5 µM) 0.8 µl, *TransStart* FastPfu DNA Polymerase of 0.4 µl, bovine serum albumin (BSA) of 0.2 µl, template DNA of 10 ng, and finally

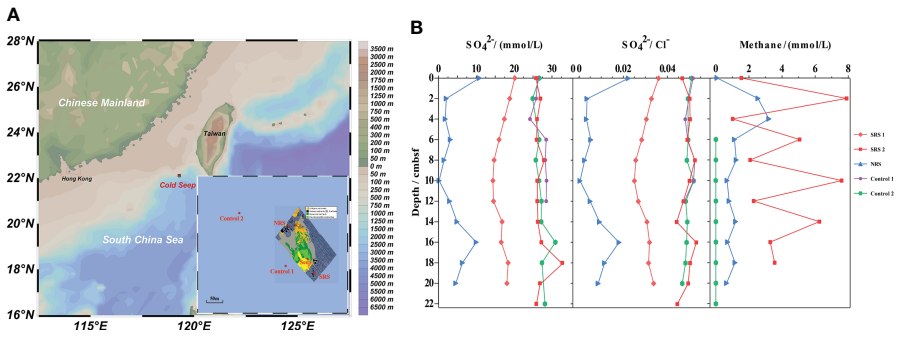

FIGURE 1
The locations and environmental characteristics of sampling sites. **(A)** The locations of sampling sites. Seabed features associated with cold seep activity at Site F referred to Wang et al. (2021). **(B)** The chemical properties of sediment samples.

ddH_2O of up to 20 μl. PCR reactions were performed in triplicate. The PCR product was extracted from 2% agarose gel and purified using the AxyPrep DNA Gel Extraction Kit (Axygen Biosciences, Union City, CA, USA) according to the manufacturer's instructions and quantified using Quantus™ Fluorometer (Promega, USA).

Sequencing and reads processing

Purified amplicons were pooled in equimolar and paired-end sequenced on an Illumina NovaSeq PE250 platform (Illumina, San Diego, USA) according to the standard protocols by Majorbio Bio-Pharm Technology Co. Ltd. (Shanghai, China). The raw reads have been deposited into the NCBI Sequence Read Archive (SRA) database (Accession Number: PRJNA827936).

The raw 16S rRNA gene sequencing reads were demultiplexed, quality-filtered by fastp version 0.20.0 (Chen et al., 2018), and merged by FLASH version 1.2.7 (Magoč and Salzberg, 2011) with the following criteria: (i) the 300 bp reads were truncated at any site receiving an average quality score of <20 over a 50-bp sliding window, and the truncated reads shorter than 50 bp and containing ambiguous characters were discarded; (ii) only overlapping sequences longer than 10 bp were assembled according to their overlapped sequence. The maximum mismatch ratio of overlap region is 20%, and reads that could not be assembled were discarded; (iii) samples were distinguished by barcoding (exact matches) and primers (allowing 2-nucleotide mismatches). Operational taxonomic units (OTUs) with 97% similarity cutoff (Edgar, 2013) were clustered using UPARSE version 7.1 (Edgar, 2013), and chimeric sequences were identified and removed. The taxonomy of each OTU representative sequence was analyzed by RDP Classifier version 2.2 (Wang et al., 2007) against the 16S rRNA gene database (Silva v138) (http://www.arb-silva.de) using confidence threshold of 70% (Quast et al., 2013).

Quantitative PCR

Quantitative PCR was performed to quantify the abundance of total bacterial and archaeal 16S rRNA gene with the specific primer sets 967R/1046R (Sogin et al., 2006) and 967F/1060R (Cadillo-Quiroz et al., 2006), respectively. A 20-μl reaction system contained 10 μl of SYBR Premix ExTaq II (2×), 0.4 μl of ROX Reference Dye II (50×) (TaKaRa, Tokyo, Japan), 0.4 μl (0.8 μl for archaea; 10 μM) of primers, and 2 μl of template. For bacterial 16S rRNA gene, the thermal cycling steps consisted of an initial denaturation at 95°C for 5 min, 40 cycles of 95°C for 30 s, 53°C for 1 min, and 72°C for 15 s and a final extension at 72°C for 10 min. For archaeal 16S rRNA gene, the thermal cycling steps contain an initial denaturation at 95°C for 30 s, 40 cycles of 95°C for 5 s, 50°C for 30 s, and 72°C for 30 s and a final extension at 72°C for 5 min. All assays with negative controls were conducted in triplicate, using a QuantStudio 5 System (Thermo Fisher Scientific). Standard curves were generated by PCR amplification of a 10-fold serial dilution of plasmids containing target gene fragments. The amplification curves showed good linear relationships (R^2 > 0.999) and the amplification efficiencies >0.90.

Data analysis and statistics

The analyses of microbial diversity were performed with the "vegan" package in R software. Chao1 and Shannon indices of α-diversity based on similarities (ANOSIM) were chosen to display microbial community richness and community diversity, respectively. The distribution patterns of microbial

communities were analyzed by non-metric multidimensional scaling (NMDS) and hierarchical clustering of β-diversity based on Bray–Curtis distances. The relationship between the community structures at the OTU level and the environmental variables was displayed by distance-based redundancy analysis (db-RDA) based on Bray–Curtis distances. The line charts showing sulfate and methane concentrations, bar graphs showing microbial community composition at various taxonomic levels, as well as ternary plot showing the distribution and relative abundance of the top 50 genera between sediment sites were performed by Originpro 2021 software (https://www.originlab.com).

Co-occurrence network analyses were conducted in R software with "igraph" and "Hmisc" packages. The co-occurrence patterns were generated with the top 50 abundant microbial genera, as well as the top 50 abundant bacterial and archaeal genera across all samples to reduce network complexity. Co-occurrence paired with a Spearman's correlation coefficient >0.7 or<−0.7 and a P-value<0.01 (Benjamini and Hochberg adjusted) was considered as a valid relationship. Gephi 0.9.2 software (http://gephi.org) was used for network visualization (Jacomy et al., 2009).

Results

Environmental characteristics

The sulfate concentration in porewater of most sediment samples and the methane concentration of SRS 2, NRS, and Control 2 were determined (Figure 1B). The SO_4^{2-}/Cl^- value could show the exact sulfate concentration by eliminating the influence of salinity. Site NRS exhibited an obvious lower. SO_4^{2-}/Cl^- value than SRS and Control 2 at all depths. Meanwhile, SO_4^{2-}/Cl^- value in NRS decreased with depths and was almost 0 at 10 cmbsf, whereas that in Control 2 remained comparatively constant. As for the content of methane, Control 2 remained almost 0 at all depths, whereas in NRS, increased obviously from 0 to 4 cmbsf and then decreased to stabilization. Despite great variations with depths, SRS 2 exhibited a superiority of methane than NRS in general.

Horizontal α-diversity patterns and general microbial abundances

A total of 3,194,466 reads were generated after quality control, discard of singletons, and then rarefaction. The sequencing statistics of all samples were showed in Table S1. Each sample was rarefied and clustered into 26,046 OTUs at a 97% similarity level (22,802 bacterial OTUs and 3,162 archaeal OTUs) for further analyses. Chao1 and Shannon indices indicated the microbial community richness and diversity of different sampling sites. Figures 2A, B show that Chao1 and Shannon indices varied among sites, ranging from 3,786.8 to 4,224.9 and 5.06 to 6.95, respectively. In general, there was significant differences in richness and diversity among seep sites (SRS and NRS) and non-seep sites (Control 1 and Control 2). Sites SRS and NRS, especially NRS, had lower richness and diversity indices compared with Control 1 and Control 2. In addition, the Shannon indices of SRS 1, SRS 2, and NRS did not show significant difference.

Quantitative PCR showed that the abundances of bacterial 16S rRNA gene were about 1.0 order of magnitude higher than that of archaea in SRS and Controls; however, the opposite result was found in NRS (Figure 2C). The bacterial and archaeal 16S rRNA gene abundances decreased at 0–4 cmbsf, and a sharp increase of archaeal abundance was observed at 6–12 cmbsf in SRS 1 and SRS 2. In NRS, the abundance of bacteria increased below 14 cmbsf, and the archaeal abundances were relatively high at all depths. In general, the abundances of archaeal 16S rRNA gene showed more distinguishable among sites than that of bacteria.

Horizontal and vertical β-diversity patterns

NMDS and hierarchical clustering based on Bray–Curtis distances are performed to visualize the differences and relationship of the microbial communities in the 53 samples along the sites and depths (Figures 2D, E). Samples from each site were distinguished with each other at OTU level of the total prokaryotes (stress = 0.067), bacteria (stress = 0.067), and archaea (stress = 0.1018) (Figures 2D, E and Figures S1, S2). Samples from SRS 1 and SRS 2 clustered together and had similar microbial compositions. Moreover, bacterial and archaeal communities from sites Control 1 and Control 2 were clustered together and were apart from SRS and NRS. Hierarchical clustering also revealed that the sediment samples clustered by site other than depth. However, there were still slight vertical clusters observed within each site, and assemblages of sediments clustered with 10 cmbsf as the boundary (<10 and >10 cmbsf) in general.

Horizontal and vertical microbial community compositions

The relative abundances of major microbial communities of the 53 samples along the sampling sites and vertical depths were analyzed at the levels of phylum, class, order, and family (Figure 3). The dominant groups varied significantly among sites. At the phylum level, 92 phyla were observed. *Chloroflexi* (0.5%–48.1%), *Halobacterota* (0.3%–42.6%), and *Desulfobacterota* (6.6%–20.9%) were dominant groups in SRS;

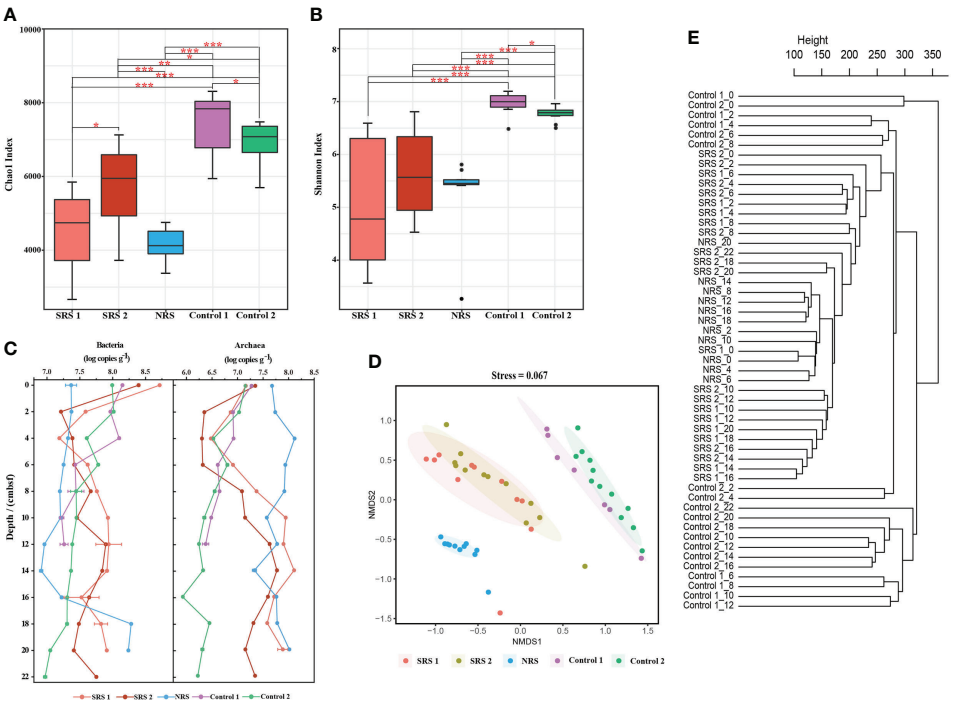

FIGURE 2
The α-diversity and β-diversity indices, as well as 16s rRNA gene abundance of all samples. **(A)** Horizontal Chao1 index at the OTU level. **(B)** Horizontal Shannon index at the OTU level. **(C)** Horizontal and vertical changes of bacterial and archaeal 16S rRNA gene abundance. **(D)** Non-metric multidimensional scaling ordination of microbial communities based on the Bray–Curtis dissimilarity. **(E)** Hierarchical clustering of microbial communities based on the Bray–Curtis distances. * 0.01 ≤ P value ≤ 0.05; ** 0.001 ≤ P value ≤ 0.01; *** P value ≤ 0.001.

Campylobacterota (7.6%–61.0%), *Chloroflexi* (8.6%–19.4%), and *Desulfobacterota* (7.5%–19.7%) were dominant groups in NRS; and *Proteobacteria* (6.7%–29.3% and 10.7%–33.7%, respectively), *Planctomycetota* (8.7%–20.2% and 8.2%–31.6%, respectively), and *Chloroflexi* (5.4%–25.2% and 5.0%–21.0%, respectively) were dominant groups in both Control 1 and Control 2. However, Control 1 contained more *Desulfobacterota* (7.5%–19.7%), whereas Control 2 contained more *Actinobacteriota* (3.1%–15.3%). In addition, 250 classes, 594 orders, and 944 families were observed. Within all sequences of each sample, *Campylobacterales* (0.7%–43.4%), *Anaerolineales* (composed of *Anaerolineaceae*, 0.3%–39.7%), and ANME (mainly composed of ANME-1b, 0.01%–39.4%) were dominant groups in SRS; *Campylobacterales* (mainly composed of *Sulfurovaceae*, 5.9%–57.5%), *Anaerolineales* (composed of *Anaerolineaceae*, 0.8%–15.0%), *Methanosarciniales* (0.7%–11.8%), and *Desulfobulbales* (4.4-9.7%) were dominant groups in NRS; and *Gammaproteobacteria* (2.9%–22.1% and 4.5%–20.6%, respectively), *Anaerolineae* (0.8%–16.0% and 0.5%–11.5%, respectively), and *Alphaproteobacteria* (3.0%–8.8% and 6.2%–15.1%, respectively) were dominant groups in both Control 1 and Control 2. However, proportions of microbial communities in Control 1 and Control 2 differed at the family level, for example, Control 2 contained more *Pirellulaceae* (3.1%–9.2%), *Nitrosopumilaceae* (0.5%–17.6%), and *Scalinduaceae* (0.03%–13.6%). Microbial composition of different sites also showed comparative differences at the same depth. In the shallow sediments above 6 cmbsf, SRS and NRS were mainly composed of *Campylobacterales*, whereas Controls were mainly composed of *Nitrosopumilales*. In the sediments deeper than 6 cmbsf, SRS were mainly composed of *Anaerolieales* and ANME-1b, and NRS were mainly composed of *Campylobacterales*, whereas Controls did not show a dominant group.

The abundance and distribution of microorganisms involved in methane and sulfur metabolisms were analyzed in detail (Figure 4). ANME were more abundant in SRS (0.04%–42.5%) and NRS (0.6%–11.7%) and almost not available in Control 1 (0%–0.006%) and Control 2 (0%–0.035%). ANME showed higher relative abundances in SRS (0.04%–42.5%) and were mainly composed of ANME-1b (0.01%–39.4%). Nevertheless, more ANME-2a-2b (0.4%–3.8%) and ANME-2c (0.2%–4.7%) compared with ANME-1 (0.01%–4.1%) were observed in NRS. As for methylotrophs and methanogens, they also showed higher sequence abundances in SRS and NRS compared with Control 1 and Control 2. *Methylomonadaceae* (0.01%–12% and 0.5%–7.4%, respectively) and *Methanosarcinaceae* (0.02%–5.4%

10.3389/fmars.2022.957762

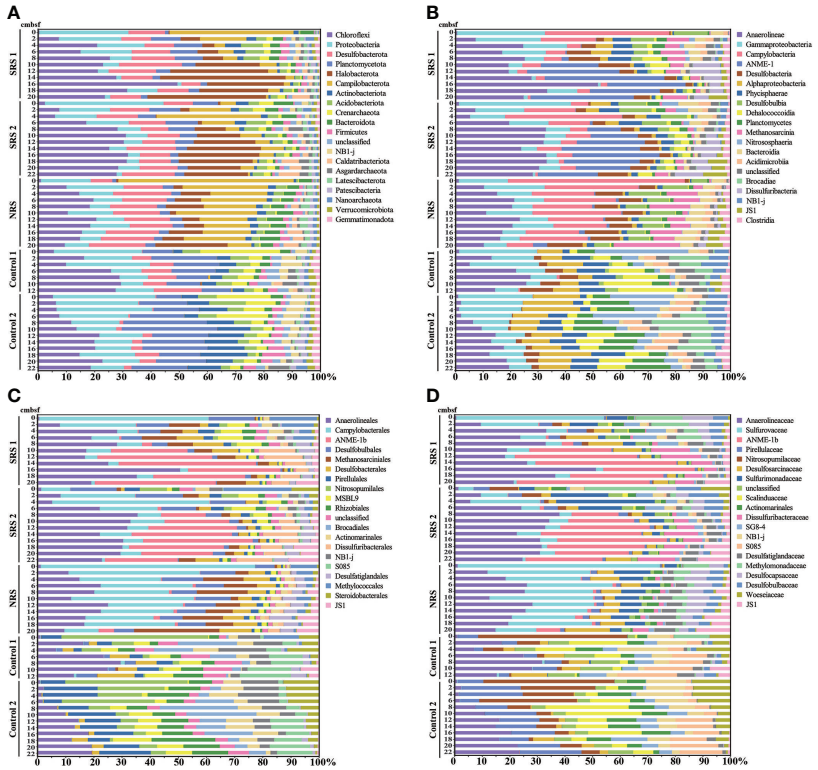

FIGURE 3
Microbial community compositions in all samples. **(A)** Microbial community compositions of the top 20 phyla. **(B)** Microbial community compositions of the top 20 classes. **(C)** Microbial community compositions of the top 20 orders. **(D)** Microbial community compositions of the top 20 families.

and 0.1%–0.3%, respectively) were dominant methylotrophs and methanogens in SRS and NRS. Few methanogens were found in Controls, but methylotrophs were identified, such as *Methloligellaceae* (0.9%–2.7%) and *Methylomirabilaceae* (0.01%–0.9%) in Control 2 and *Methloligellaceae* (0.32%–1.07%) and *Methylomonadaceae* (0.12%–0.45%) in Control 1. The phylum *Campylobacterota* were abundant in SRS (0.7%–43.4%) and NRS (7.6%–61%) and not affluent in Control 1 (0.04%–0.36%) and Control 2 (0.003%–0.009%). At the genus level, *Sulfurovum* was the most abundant genus belonging to *Campylobacterota* in SRS and NRS, followed by *Sulfurimonas*. Similarly, the phylum *Desulfobacterota* was enriched in SRS (6.5%–20.7%) and NRS (6.8%–17.5%), but almost not available in Control 1 (0.09%–12.7%) and Control 2 (0.07%–7.5%). For SRB, SEEP-SRB2 was the most abundant genus in SRS, followed by SEEP-SRB1. *Desulfatiglans* and SEEP-SRB1 were abundant in NRS, whereas unclassified *Syntrophobacterales* were abundant in Control 1 and Control 2. Above all, the distribution and abundance of ANME, methylotrophs, methanogens, SOB, and SRB showed clear differences among sampling sites. It is suggested that a great series of active biogeochemical reactions might occur in SRS and NRS, including sulfur oxidation, sulfate reduction, anaerobic and aerobic oxidation of methane, and even methane production.

Microbial community compositions also varied along depths in each sampling site. In NRS, ANME-1, ANME-2, SEEP-SRB1, and SEEP-SRB2 all reached to the minimum at 10 cmbsf and started to increase with depths. Considering that the concentration of sulfate is almost 0 at 10 cmbsf, the SMTZ was proposed to locate at 10 cmbsf in NRS. Meanwhile, the abundances of *Sulfurovum* and *Methlomonadaceae* were peaked in surface sediment and decreased with depths in NRS, whereas *Methanosarcinaceae* showed the opposite result. In SRS, the abundances of ANME-1, SEEP-SRB1, and SEEP-SRB2 were low above 8 cmbsf and increased rapidly at 8–10 cmbsf, and the abundances of ANME-2a-2b also showed slight increase at 8 cmbsf. Interestingly, ANME-2a-2b, SEEP-SRB1, and SEEP-SRB2 all decreased below 12 cmbsf. There might be a positive correlation between ANME and SEEP-SRB, and the proposed SMTZ was approximately at 8 cmbsf in SRS. In addition, the

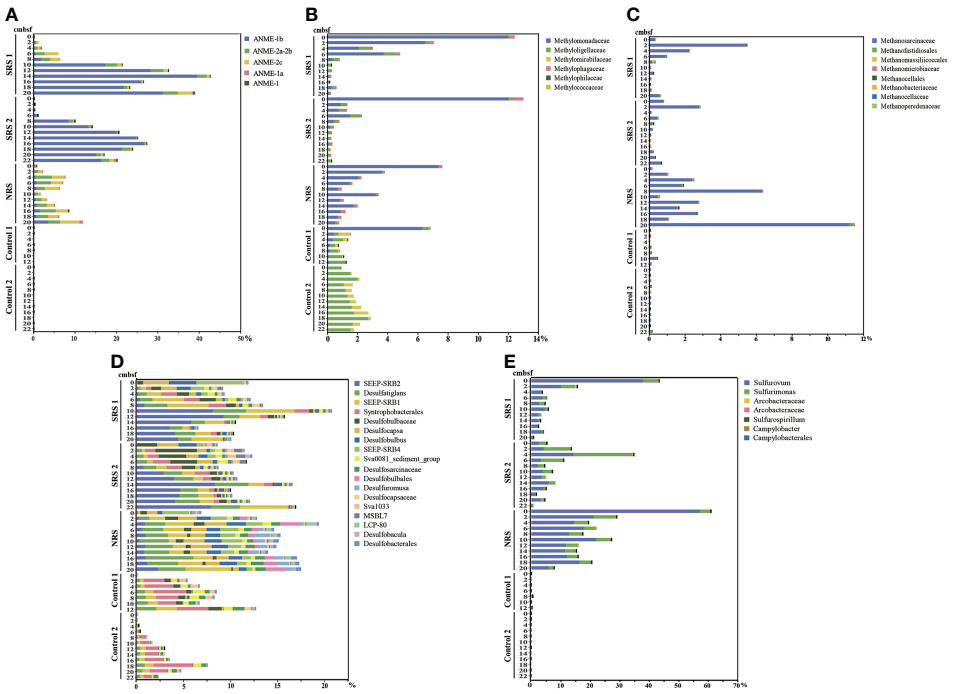

FIGURE 4
The abundances of main functional microbial groups in all samples. **(A)** Main genera of the ANME group. **(B)** Main genera of the methylotrophs group. **(C)** Main genera of the methanogens group. **(D)** Main genera of the SRB in the phylum *Desulfobacterota*. **(E)** Main genera of the SOB in the phylum *Campylobacterota*.

abundances of *Sulfurovum* and *Sulfurimonas*, as well as methylotrophs especially *Methylomonadaceae*, were peaked in surface sediment and decreased with depths in SRS.

Differences of microbial groups between seep sites and control sites

The distribution and relative abundance of microbial groups were different among sampling sites (Figures 5A, B). As shown in the ternary plot, *Anaerolineaceae* was the most abundant genus across all samples, whereas *Sulfurovum* and *Sulfurimonas* were enriched in NRS, and ANME-1b was enriched in SRS (Figure 5A). Few ANME was found in Control 1 and Control 2. In addition, all the top 15 genera were found to have significant differences ($p< 0.01$) between different sites in multi-group comparison stamp (Figure 5B). It could also be seen that *Sulfurovum* and *Sulfurimonas*, especially *Sulfurovum*, were enriched in NRS sediments, indicating sulfur oxidation in NRS. ANME-1b and SEEP-SRB2 were enriched in SRS, whereas SEEP-SRB1 and *Desulfatiglans* were enriched in both SRS and NRS. In general, the composition and distribution of ANME and SOB showed significant differences and might indicate different biogeochemical processes between seep sites (SRS and NRS) and non-seep sites (Control 1 and Control 2).

Microbial co-occurrence networks

Co-occurrence networks were conducted to show the relationships of the top 50 microbial genera (Figure 6A), as well as the top 50 bacterial and the top 50 archaeal genera among all sediment samples (Figure S3). These three networks were all consisted of 49 nodes and 201 edges. ANME-1b was mainly associated with ANME-3, SEEP-SRB2, and *Methyloprofundus*; ANME-2a-2b was mainly associated with *Nitrosopumilaceae* and B2M28; ANME-2c was mainly associated with ANME-1b, ANME-2a-2b, ANME-3, *Methyloprofundus*, and *Methanogenium*. SEEP-SRB1 and SEEP-SRB2 were mainly associated with *Desulfatiglans* and JS1; SEEP-SRB2 was mainly associated with ANME-1b, ANME-2c, and *Methyloprofundus*; SEEP-SRB4 and *Desulfobulbus* were mainly associated with *Candidatus Nitrosopumilus* and *Candidatus Scalindua*.

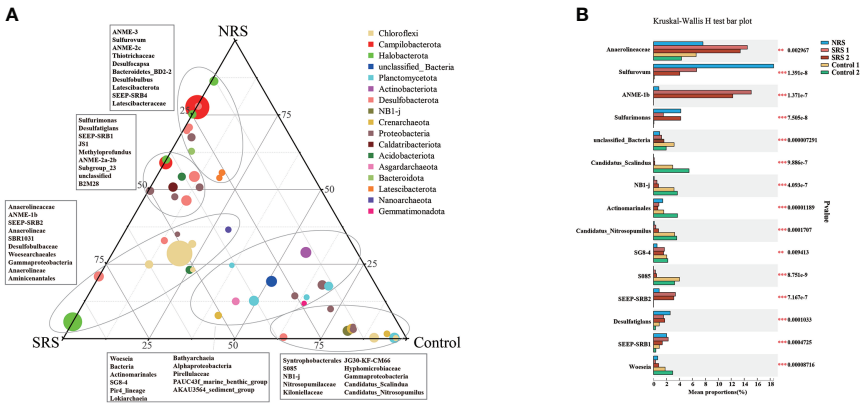

FIGURE 5
Distribution and relative sequence abundance of microbial groups between sampling sites. **(A)** Ternary plot showing the distribution and relative sequence abundance of the top 50 genera in all samples. Taxonomic affiliations were indicated by colors, whereas the size of the symbol indicated the relative sequence abundance of each genus. **(B)** Multi-group comparison stamp showing the relative sequence abundance and distribution differences of the top 15 genera in all samples. ** 0.001 ≤ P value ≤ 0.01; *** P value ≤ 0.001.

Sulfurovum and *Sulfurimonas* were mainly associated with *Desulfobulbus*, *Desulfocapsa*, and *Thiotrichaceae*. Our results found that ANME displayed a close relationship with SRB, especially ANME-1b with SEEP-SRB2.

Influence of environmental factors on microbial communities

The predictor variables of sulfate, SO_4^{2-}/Cl^-, and methane in SRS 2, NRS, and Control 2 were analyzed for db-RDA based on Bray–Curtis distances to understand the influence of environmental factors on microbial communities (Figure 6B). The results showed that sulfate, SO_4^{2-}/Cl^-, and methane explained 22.89% (15.75% by first axis and 7.14% by second axis) of the variation in community distribution. It seemed that sulfate and methane affected microbial community structure at the OTU level to the similar extent. Sulfate concentration showed obvious negative correlations with NRS samples compared with SRS 2 and Control 2 samples. In addition, methane concentration showed positive correlations with Control 2 samples and negative correlations with SRS 2 and NRS samples.

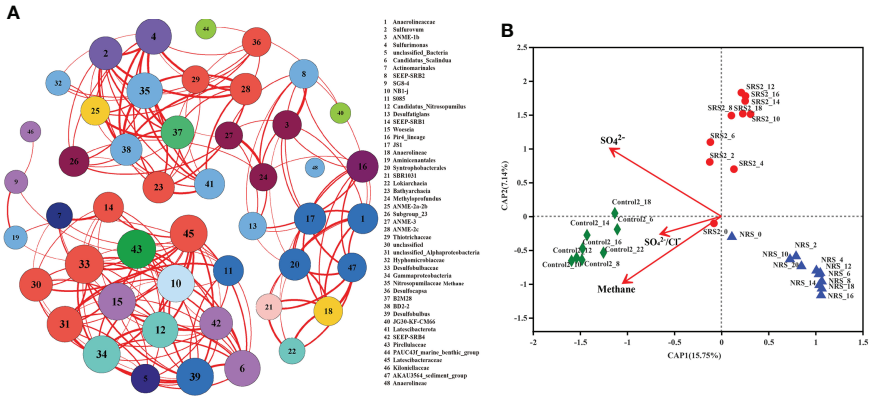

FIGURE 6
The relationship and environmental variables of microbial groups between sampling sites. **(A)** Co-occurrence networks of the top 50 genera in all samples with a Spearman's correlation coefficient >0.7 or<−0.7 and a P-value<0.01. The size of each node indicates degree of connectivity and the color indicates the phylum that the genus affiliated to. The thickness of each line indicates strength of correlation. **(B)** Db-RDA the relationship of sulfate and methane changes and microbial community at the OTU level based on Bray–Curtis distances.

Discussion

Horizontal investigations of microbes revealed two dissimilar newborn cold seep sites

The microbial community compositions of the 53 samples exhibited an obvious discrepancy along four sites. Microbial community compositions and multi-group comparison showed that phyla *Halobacterota*, *Campylobacterota*, and *Desulfobacterota* were enriched in SRS and NRS. *Halobacterota* were mainly composed of ANME-1b, whereas *Campylobacterota* and *Desulfobacterota* represented the groups of SOB and SRB, respectively. Cold seeps supported an enormous biomass of microbial life, which was nourished by oxidation of methane, higher hydrocarbons, and sulfide (Jørgensen and Boetius, 2007). Many studies have showed that deep-sea cold seep sediments contained abundant ANME, SRB, SOB, and methane-oxidizing bacteria (MOB) (Sun et al., 2020). In our study, these microorganisms could be the indicators that differed SRS and NRS from Control 1 and Control 2 as cold seep sites. In Control 1 and Control 2, *Alphaproteobacteria*, *Dehalococcoidia*, *Phycisphaerae*, and *Planctomycetes* were abundant, all of which were found to show high abundances in SCS deep-sea sediments (Zhang et al., 2021). Especially, our findings of abundant *Dehalococcoidia* and sulfate concentration were consistent with previous results that *Dehalococcoidia* mediating reductive dehalogenation and potential sulfate reduction were commonly observed in sulfate-replete and deep anoxic sediments in the SCS (Graw et al., 2018; Jochum et al., 2018). In addition, abundant *Syntrophobacterales* in SRB also hinted Control 1 and Control 2 contain adequate sulfate even as non-seep sites.

Bacteria and archaea in the four sites showed obvious site-tendentious distribution pattern. Except for the difference between cold seep sites and non-seep sites, interestingly, cold seep sites SRS and NRS showed distinct microbial compositions. SRS was well marked by high abundance of ANME-1b of *Halobacterota*, whereas NRS was well marked by that of *Sulfurovum* of *Campylobacterota* (Figure 5A). The dominant microbial communities in cold seep Site F sediments varied between previous studies. For example, Sun et al. (2020) found that *Campylobacterota* and *Deltaproteobacteria* were enriched in cold seep sediment, whereas Cui et al. (2019) found that ANME-1b were the dominant microbial communities (Cui et al., 2019; Sun et al., 2020). It could be seen that the microbial compositions varied with sampling sites in Site F, which could be attributed to different maturity of the sediments influenced by distances to the seeps and the availability of organic carbon (Jing et al., 2020). In addition, it was found that the presence of reduced sediment patches resulted from cold seep fluids migrating along the bottom of the authigenic carbonate mound and escaping at its boundary (Wang et al., 2021). The reduced sediment areas were newly formed because of the *in situ* measured upward advection of methane-rich fluids, the ongoing AOM processes producing sulfide or pyrite, and non-existent animal aggregations, which needed more time to settle down (Wang et al., 2021). Our study of microbial compositions in the reduced sediments SRS and NRS showed potential AOM processes because of the enriched methane-metabolizing microbes. As a result, we could infer that SRS and NRS were dissimilar newborn cold seep sites with distinct microbial communities.

Vertical investigations of microbes revealed the SMTZs of two cold seep sites

In NRS, ANME-2 were the dominant microorganisms, and the abundances of ANME (especially ANME-2) and SRB showed consistent tendency along depths, suggesting the positive correlation between ANME-2 and SEEP-SRB. In addition, it was found that ANME-2a-2b dominated in the high-sulfate sediments and upper layers of estimated SMTZ and was replaced by ANME-1b in the bottom layers of estimated SMTZ (Niu et al., 2017). Our result showed that the abundance of ANME-2 was positively related to the sulfate concentration, especially at 10 cmbsf, where the sulfate concentration is almost 0. Therefore, the SMTZ in NRS was inferred to locate at 10 cmbsf. In addition, the sulfate concentration showed an increased trend below 10 cmbsf and reached maximum at about 16 cmbsf. This phenomenon was also found in Site F before (Sun et al., 2022), and the increased sulfate might be attributed to the reoxidation of H_2S in the deeper layers of the sediment. Correspondingly, SOB showed a higher abundance at about 18 cmbsf, which may be responsible for the reoxidation of H_2S.

In SRS, the high sequence abundance of ANME could be explained by pretty high level of methane (Figure 1B). ANME in SRS were mainly composed of ANME-1b, which was consistent with many studies (Knittel et al., 2005; Ruff et al., 2016; Niu et al., 2017; Wu et al., 2018; Cui et al., 2019). Our results of ANME-1b were consistent with previous studies that ANME-1 were dominated in the deeper, anoxic, sulfide-rich sediments, and the methanogenic zone even showed high relative abundance in SMTZ (especially bottom layers) as well (Ruff et al., 2016; Niu et al., 2017). Considering ANME-1b, SEEP-SRB1, and SEEP-SRB2, the proposed SMTZ in SRS was approximately at 8 cmbsf. In addition, the strong association between ANME-1b and SEEP-SRB2 showed by co-occurrence network was in correspondence with the finding, and ANME-1 was associated with SEEP-SRB2 in Pomonte methane seep, Italy (Ruff et al., 2016). In SMTZ, ANME-1 was found to perform AOM with

ANME-2, SEEP-SRB1, SEEP-SRB2, and even *Desulfobacteraceae* as syntrophic partners (Wu et al., 2018; Cui et al., 2019; Dong et al., 2020). Our results proved the positive correlation between ANME and SEEP-SRB. However, the correlation between ANME and *Desulfobacteraceae* was not found because of the low abundance of *Desulfobacteraceae* in SRS. In addition, fluorescence *in situ* hybridization and other research have found cell numbers of ANME-1 increased with sediment depths and frequently existed as single cells, indicating that ANME-1 can also perform AOM process without an archaeal or bacterial partner (Orphan et al., 2002; Knittel et al., 2005; Stokke et al., 2012; Maignien et al., 2013). In deep-sea cold seep sediments with high concentrations of hydrocarbon gases, ANME-1 might participate in AOM process *via* reversal of the methanogenic pathway alone and utilize electron acceptors other than sulfate (Harrison et al., 2009; Lloyd et al., 2011; Cho et al., 2017; Bowles et al., 2019; Vigneron et al., 2019). In SRS, the abundant ANME-1b was not ruled out to perform AOM alone.

Methylotrophs *Methylomonadaceae*, belonging to the order *Methylococcales*, is type I aerobic methanotrophs and was found to mainly conduct aerobic methane oxidization in Site F sediments (Broman et al., 2020; Jing et al., 2020). This might account for the high abundance of *Methylomonadaceae* in the surface sediment of SRS and NRS. The exact opposite vertical distribution pattern of ANME and methylotrophs in SRS and NRS proved that methane was produced in anoxic sediments and diffused upward and was oxidized successively by ANME and aerobic methylotrophs in the surface sediment. As for SOB in SRS and NRS, the distributions of *Sulfurovum* and *Sulfurimonas* were consistent with previous reports that *Campylobacterota*, including *Sulfurovum*, were microaerobic and abundant in the surface sediments of cold seeps (Wu et al., 2018; Sun et al., 2020).

Variations and relationships of functional groups depicted the ecological integrity of NRS

Compared with SRS, the low abundance of total ANME in NRS might be attributed to the low concentration of methane. ANME-2 was enriched in NRS, and it had distinct methane-oxidizing and electron-transporting pathways from ANME-1 (Wang et al., 2014). It was reported that ANME-2a shared similarities with *Methanosarcinales* and performed a reversal of H_2-independent methanogenesis (Wang et al., 2014). Meanwhile, complete metabolic pathway converting methane to acetate identified in ANME-2a suggested that acetate produced by ANME-2a support the heterotrophic communities as a carbon source in cold seep ecosystem (Yang et al., 2020). The *Methanosarcinales* are tolerant to low levels of oxygen and usually predominant in environments with high acetate concentrations (Conklin et al., 2006). It was found that *Methanosarcinales* constituted a major component of methanogenic archaea in sediments of Haima cold seep, including plenty of methylotrophic *Methanosarcinales* distributed along all depths and a few acetogenotrophic *Methanosarcinales* within the methanogenic zone (Niu et al., 2017). In addition, methylotrophic and acetogenotrophic *Methanosarcinales* were also found predominant in sediments of Site F along all depths (Jing et al., 2020). Therefore, it can be speculated that ANME-2 and *Methanosarcinales* enriched in NRS cooperated to implement the active conversion between methane and acetate, which was also supported by the consistent vertical distribution tendency of them. In addition, methanogens were generally unable to assimilate sulfate and able to use sulfide as the sole sulfur source. For example, *Methanococcales*, usually inhabited anaerobic environments with high levels of sulfide (Liu et al., 2012). This could explain the consistency between high abundance of *Methanosarcinales* and low sulfate concentration in NRS. Moreover, we smelt smelly H_2S in NRS sediment samples, suggesting high concentration of sulfide in NRS although we did not measure.

Our result of co-occurrence network showed that ANME-1b was associated strongly with SEEP-SRB2, which was consistent with the finding conducted in Haima cold seep (Zhang et al., 2020). In addition, there were proportional abundances of SEEP-SRB1, ANME-2, and *Methanosarcinales* in NRS. It was reported that *Methanosarcinales* favored the growth of SRB by avoiding competition for the same substrate, and ANME-2a could produce acetate that might be a candidate electron shuttle between ANME-2 and SRB in AOM (Jing et al., 2020; Stams and Valentine, 2000; Plugge and Reeburgh, 2009; Yang et al., 2020). Above findings could explain the coincident distribution of *Methanosarcinales*, ANME-2, and SEEP-SRB1, which might coexist without competition and metabolize methane through acetate production and utilization in the cold seep environment. Compared with SRS, there was more *Desulfatiglans* in NRS. *Desulfatiglans* could oxidize acetate and pass the reducing equivalents to methanogens (Jochum et al., 2018), and it might be the reason that *Desulfatiglans* and *Methanosarcinaceae* were both abundant in NRS. Meanwhile, *Desulfatiglans* could produce acetate, which might be an important metabolic strategy for the microorganisms in sulfate-limited subsurface sediments and could be proved by the low sulfate concentration in NRS (Jochum et al., 2018).

SRB could produce acetate and hydrogen sulfide, which transferred upward for flourish of SOB in surface layers (Li et al., 2021). SOB played a role in sulfide oxidation, acetate assimilation, and carbon fixation in cold seep sediments (Li et al., 2021). Compared with SRS, NRS contained more SOB, especially *Sulfurovum* along the depths. *Sulfurovum* was microaerobic, and its distribution might imply differences of oxygen concentration among sites. In addition, the enrichment of SOB in NRS might be due to the inferred high concentration of sulfide, especially

H_2S. H_2S might be released by methane oxidization and sulfate reduction (Sun et al., 2020). These might indicate comparative sulfate reduction in NRS.

Conclusions

In this study, a comprehensive investigation of sediment microbial communities of different sampling sites and depths in cold seep Site F was carried out. Both bacteria and archaea exhibited an obvious site-tendentious distribution pattern. The microbial community compositions and abundances of AMNE, *Desulfobacterota* (SRB), and *Campylobacteria* (SOB) indicate that SRS and NRS are newborn cold seep sites compared with non-seep sites Control 1 and Control 2. The close relationship between ANME-1b and SEEP-SRB2 was found in both SRS and NRS; however, the two cold seep sites have distinct microbial compositions. NRS can be described as notable cold seep reduced sediment with low sulfate and high H_2S, nourishing abundant SEEP-SRB1, ANME-2, *Methanosarcinales*, and *Sulfurovum*, which showed similar distribution. The variations and relationships of microorganisms involved in methane and sulfur metabolisms depicted the ecological integrity of NRS commendably. Our study sheds light on the heterogeneity of different cold seep sites from the aspect of microbiology and expands current knowledge on the potential roles of microorganisms in cold seeps.

Data availability statement

The datasets presented in this study can be found in online repositories. The names of the repository/repositories and accession number(s) can be found in the article/Supplementary Material.

Author contributions

MY and X-HZ designed the experiments and analyzed the data. XZ performed most of the experiments, analyzed the data, prepared the figures and tables, and wrote the manuscript. XS attended the cruise, collected the samples and analyzed the data. HC performed the quantitative PCR analysis. PY, BZ, LiC, and LF analyzed the sulfate concentration. LeC and MW analyzed the methane concentration. MY, X-HZ, PY, and JL revised the manuscript. All the authors edited and approved the manuscript.

Funding

This work was supported by the Fundamental Research Funds for the Central Universities (202172002 and 202072003) and the National Natural Science Foundation of China (41730530, 91751202, and 41976137).

Acknowledgments

We acknowledge the Senior User Project of the R/V KEXUE (KEXUE2021GH01) for this cruise and all of the scientists and crews from Institute of Oceanology, Chinese Academy of Sciences, for their assistance with sampling during the cruise.

Conflict of interest

The authors declare that the research was conducted in the absence of any commercial or financial relationships that could be construed as a potential conflict of interest.

Publisher's note

Supplementary material

The Supplementary Material for this article can be found online at: https://www.frontiersin.org/articles/10.3389/fmars.2022.957762/full#supplementary-material

References

Boetius, A., Ravenschlag, K., Schubert, C. J., Rickert, D., Widdel, F., Gieseke, A., et al. (2000). A marine microbial consortium apparently mediating anaerobic oxidation of methane. *Nat.* 407, 623–626. doi: 10.1038/35036572

Boetius, A., and Wenzhöfer, F. (2013). Seafloor oxygen consumption fuelled by methane from cold seeps. *Nat. Geosci.* 6, 725–734. doi: 10.1038/ngeo1926

Borowski, W. S., Paull, C. K., and Ussler, W. (1996). Marine pore-water sulfate profiles indicate *in situ* methane flux from underlying gas hydrate. *Geology.* 24, 655–658. doi: 10.1130/0091-7613(1996)024<0655:MPWSPI>2.3.CO;2

Bowles, M. W., Samarkin, V. A., Hunter, K. S., Finke, N., Teske, A. P., Girguis, P. R., et al. (2019). Remarkable capacity for anaerobic oxidation of methane at high

methane concentration. *Geophys Res. Lett.* 46, 12192–12201. doi: 10.1029/2019GL084375

Broman, E., Sun, X., Stranne, C., Salgado, M. G., Bonaglia, S., Geibel, M., et al. (2020). Low abundance of methanotrophs in sediments of shallow boreal coastal zones with high water methane concentrations. *Front. Microbiol.* 11. doi: 10.3389/fmicb.2020.01536

Cadillo-Quiroz, H., Brauer, S., Yashiro, E., Sun, C., Yavitt, J., and Zinder, S. (2006). Vertical profiles of methanogenesis and methanogens in two contrasting acidic peatlands in central new York state, USA. *Environ. Microbiol.* 8, 1428–1440. doi: 10.1111/j.1462-2920.2006.01036.x

Chen, D. F., Huang, Y. Y., Yuan, X. L., and Iii, L. (2005). Seep carbonates and preserved methane oxidizing archaea and sulfate reducing bacteria fossils suggest recent gas venting on the seafloor in the northeastern south China Sea. *Mar. Pet Geol.* 22, 613–621. doi: 10.1016/j.marpetgeo.2005.05.002

Chen, S., Zhou, Y., Chen, Y., and Gu, J. (2018). Fastp: An ultra-fast all-in-one fastq preprocessor. *Bioinformatics.* 34, i884–i890. doi: 10.1093/bioinformatics/bty560

Cho, H., Hyun, J. H., You, O. R., Kim, M., Kim, S. H., Choi, D. L., et al. (2017). Microbial community structure associated with biogeochemical processes in the sulfatemethane transition zone (SMTZ) of gas-hydrate-bearing sediment of the ulleung basin, East Sea. *Geomicrobiol J.* 34, 207–219. doi: 10.1080/01490451.2016.1159767

Conklin, A., Stensel, H., Ferguson, D., et al. (2006). Growth kinetics and competition between methanosarcina and *Methanosaeta* in mesophilic anaerobic digestion. *Water Environ Res* 78, 486–496. doi: 10.2175/106143006X95393

Cui, H., Su, X., Chen, F., Holland, M., Yang, S., Liang, J., et al. (2019). Microbial diversity of two cold seep systems in gas hydrate-bearing sediments in the south China Sea. *Mar. Environ. Res.* 144, 230–239. doi: 10.1016/j.marenvres.2019.01.009

Dong, X., Rattray, J. E., Campbell, D. C., Webb, J., Chakraborty, A., Adebayo, O., et al. (2020). Thermogenic hydrocarbon biodegradation by diverse depth-stratified microbial populations at a scotian basin cold seep. *Nat. Commun.* 11, 5825–5825. doi: 10.1038/s41467-020-19648-2

Edgar, R. C. (2013). UPARSE: Highly accurate OTU sequences from microbial amplicon reads. *Nat. Methods* 10, 996–998. doi: 10.1038/nmeth.2604

Feng, D., and Chen, D. (2015). Authigenic carbonates from an active cold seep of the northern south China Sea: New insights into fluid sources and past seepage activity. *Deep Sea Res. Part II: Topical Stud. Oceanography.* 122, 74–83. doi: 10.1016/j.dsr2.2015.02.003

Feng, D., Qiu, J. W., Hu, Y., Peckmann, J., Guan, H., Tong, H., et al. (2018). Cold seep systems in the south China Sea: An overview. *J. Asian Earth Sci.* 168, 3–16. doi: 10.1016/j.jseaes.2018.09.021

Graw, M. F., D'Angelo, G., Borchers, M., Thurber, A. R., Johnson, J. E., Zhang, C., et al. (2018). Energy gradients structure microbial communities across sediment horizons in deep marine sediments of the south China Sea. *Front. Microbiol.* 9. doi: 10.3389/fmicb.2018.00729

Green-Saxena, A., Dekas, A. E., Dalleska, N. F., and Orphan, V. J. (2014). Nitrate-based niche differentiation by distinct sulfate-reducing bacteria involved in the anaerobic oxidation of methane. *ISME J.* 8, 150–163. doi: 10.1038/ismej.2013.147

Harrison, B. K., Zhang, H., Berelson, W., and Orphan, V. J. (2009). Variations in archaeal and bacterial diversity associated with the sulfate-methane transition zone in continental margin sediments (Santa Barbara basin, California). *Appl. Environ. Microbiol.* 75, 1487–1499. doi: 10.1128/aem.01812-08

Hoehler, T. M., Alperin, M. J., Albert, D. B., and Martens, C. S. (1994). Field and laboratory studies of methane oxidation in an anoxic marine sediment: Evidence for a methanogen-sulfate reducer consortium. *Global Biogeochem Cycles.* 8, 451–463. doi: 10.1029/94GB01800

Jørgensen, B. B., and Boetius, A. (2007). Feast and famine-microbial life in the deep-sea bed. *Nat. Rev. Microbiol.* 5, 770–781. doi: 10.1038/nrmicro1745

Jacomy, M., Bastian, M., and Heymann, S. (2009) *Gephi: An open source software for exploring and manipulating networks*. Available at: https://gephi.org/.

Jing, H., Wang, R., Jiang, Q., Zhang, Y., and Peng, X. (2020). Anaerobic methane oxidation coupled to denitrification is an important potential methane sink in deep-sea cold seeps. *Sci. Total Environ.* 748, 142459. doi: 10.1016/j.scitotenv.2020.142459

Jochum, L. M., Schreiber, L., Marshall, I. P. G., Jørgensen, B. B., Schramm, A., and Kjeldsen, K. U. (2018). Single-cell genomics reveals a diverse metabolic potential of uncultivated *Desulfatiglans*-related *Deltaproteobacteria* widely distributed in marine sediment. *Front. Microbiol.* 9. doi: 10.3389/fmicb.2018.02038

Kleindienst, S., Ramette, A., Amann, R., and Knittel, K. (2012). Distribution and *in situ* abundance of sulfate-reducing bacteria in diverse marine hydrocarbon seep sediments. *Environ. Microbiol.* 14, 2689–2710. doi: 10.1111/j.1462-2920.2012.02832.x

Knittel, K., Lösekann, T., Boetius, A., Kort, R., and Amann, R. (2005). Diversity and distribution of methanotrophic archaea at cold seeps. *Appl. Environ. Microbiol.* 71, 467–479. doi: 10.1128/AEM.71.1.467-479.2005

Li, W. L., Dong, X., Lu, R., Zhou, Y. L., Zheng, P. F., Feng, D., et al. (2021). Microbial ecology of sulfur cycling near the sulfate-methane transition of deep-sea cold seep sediments. *Environ. Microbiol.* 23, 6844–6858. doi: 10.1111/1462-2920.15796

Liu, Y., Beer, L. L., and Whitman, W. B. (2012). Methanogens: a window into ancient sulfur metabolism. *Trends Microbiol.* 20 (5), 251–258. doi: 10.1016/j.tim.2012.02.002

Li, H., Yang, Q., and Zhou, H. (2020). Niche differentiation of sulfate- and iron-dependent anaerobic methane oxidation and methylotrophic methanogenesis in deep sea methane seeps. *Front. Microbiol.* 11. doi: 10.3389/fmicb.2020.01409

Lloyd, K. G., Alperin, M. J., and Teske, A. (2011). Environmental evidence for net methane production and oxidation in putative ANaerobic MEthanotrophic (ANME) archaea. *Environ. Microbiol.* 13, 2548–2564. doi: 10.1111/j.1462-2920.2011.02526.x

Lösekann, T., Knittel, K., Nadalig, T., Fuchs, B., Niemann, H., Boetius, A., et al. (2007). Diversity and abundance of aerobic and anaerobic methane oxidizers at the haakon mosby mud volcano, barents Sea. *Appl. Environ. Microbiol.* 73, 3348–3362. doi: 10.1128/aem.00016-07

Magoč, T., and Salzberg, S. L. (2011). Flash: Fast length adjustment of short reads to improve genome assemblies. *Bioinformatics.* 27, 2957–2963. doi: 10.1093/bioinformatics/btr507

Maignien, L., Parkes, R. J., Cragg, B., Niemann, H., Knittel, K., Coulon, S., et al. (2013). Anaerobic oxidation of methane in hypersaline cold seep sediments. *FEMS Microbiol. Ecol.* 83, 214–231. doi: 10.1111/j.1574-6941.2012.01466.x

McKay, L., Klokman, V. W., Mendlovitz, H. P., LaRowe, D. E., Hoer, D. R., Albert, D., et al. (2016). Thermal and geochemical influences on microbial biogeography in the hydrothermal sediments of guaymas basin, gulf of California. *Environ. Microbiol. Rep.* 8, 150–161. doi: 10.1111/1758-2229.12365

Mills, H. J., Hodges, C., Wilson, K., Macdonald, I. R., and Sobecky, P. A. (2003). Microbial diversity in sediments associated with surface-breaching gas hydrate mounds in the gulf of Mexico. *FEMS Microbiol. Ecol.* 46, 39–52. doi: 10.1016/s0168-6496(03)00191-0

Niemann, H., Lösekann, T., de Beer, D., Elvert, M., Nadalig, T., Knittel, K., et al. (2006). Novel microbial communities of the haakon mosby mud volcano and their role as a methane sink. *Nat.* 443, 854–858. doi: 10.1038/nature05227

Niu, M., Fan, X., Zhuang, G., Liang, Q., and Wang, F. (2017). Methane-metabolizing microbial communities in sediments of the haima cold seep area, northwest slope of the south China Sea. *FEMS Microbiol. Ecol.* 93, 10.1093. doi: 10.1093/femsec/fix101

Orphan, V. J., Hinrichs, K. U., Ussler, W.3rd, Paull, C. K., Taylor, L. T., Sylva, S. P., et al. (2001a). Comparative analysis of methane-oxidizing archaea and sulfate-reducing bacteria in anoxic marine sediments. *Appl. Environ. Microbiol.* 67, 1922–1934. doi: 10.1128/aem.67.4.1922-1934.2001

Orphan, V. J., House, C. H., Hinrichs, K. U., McKeegan, K. D., and DeLong, E. F. (2001b). Methane-consuming archaea revealed by directly coupled isotopic and phylogenetic analysis. *Science.* 293, 484–487. doi: 10.1126/science.1061338

Orphan, V. J., House, C. H., Hinrichs, K. U., McKeegan, K. D., and DeLong, E. F. (2002). Multiple archaeal groups mediate methane oxidation in anoxic cold seep sediments. *Proc. Natl. Acad. Sci. U. S. A.* 99, 7663–7668. doi: 10.1073/pnas.072210299

Pernthaler, A., Dekas, A. E., Brown, C. T., Goffredi, S. K., Embaye, T., and Orphan, V. J. (2008). Diverse syntrophic partnerships from deep-sea methane vents revealed by direct cell capture and metagenomics. *Proc. Natl. Acad. Sci. U. S. A.* 105, 7052–7057. doi: 10.1073/pnas.0711303105

Quast, C., Pruesse, E., Yilmaz, P., Gerken, J., Schweer, T., Yarza, P., et al. (2013). The SILVA ribosomal RNA gene database project: Improved data processing and web-based tools. *Nucl. Acids Res.* 41, 590–596. doi: 10.1093/nar/gks1219

Ruff, S. E., Kuhfuss, H., Wegener, G., Lott, C., Ramette, A., Wiedling, J., et al. (2016). Methane seep in shallow-water permeable sediment harbors high diversity of anaerobic methanotrophic communities, Elba, Italy. *Front. Microbiol.* 7. doi: 10.3389/fmicb.2016.00374

Schreiber, L., Holler, T., Knittel, K., Meyerdierks, A., and Amann, R. (2010). Identification of the dominant sulfate-reducing bacterial partner of anaerobic methanotrophs of the ANME-2 clade. *Environ. Microbiol.* 12, 2327–2340. doi: 10.1111/j.1462-2920.2010.02275.x

Sogin, M. L., Morrison, H. G., Huber, J. A., Mark Welch, D., Huse, S. M., PR, N., et al. (2006). Microbial diversity in the deep sea and the underexplored "rare biosphere". *Proc. Natl. Acad. Sci. U. S. A.* 103, 12115–12120. doi: 10.1073/pnas.0605127103

Stams, A. J., and Plugge, C. M. (2009). Electron transfer in syntrophic communities of anaerobic bacteria and archaea. *Nat. Rev. Microbiol.* 7, 568–577. doi: 10.1038/nrmicro2166

Stokke, R., Roalkvam, I., Lanzen, A., Haflidason, H., and Steen, I. H. (2012). Integrated metagenomic and metaproteomic analyses of an ANME-1-dominated

community in marine cold seep sediments. *Environ. Microbiol.* 14, 1333–1346. doi: 10.1111/j.1462-2920.2012.02716.x

Sun, Y., Niu, M. Y., Liu, Q., Zhuang, G. C., and Wang, F. P. (2022). Diversity and distribution of microorganisms in the sediment of Formosa cold seep in south China Sea. *Acta Microbiol. Sin.* 62, 2001–2020. doi: 10.13343/j.cnki.wsxb.20220345

Sun, Q. L., Zhang, J., Wang, M. X., Cao, L., Du, Z. F., Sun, Y. Y., et al. (2020). High-throughput sequencing reveals a potentially novel sulfurovum species dominating the microbial communities of the seawater-sediment interface of a deep-sea cold seep in south China Sea. *Microorganisms.* 8, 687. doi: 10.3390/microorganisms8050687

Valentine, D. L., and Reeburgh, W. S. (2000). New perspectives on anaerobic methane oxidation. *Environ. Microbiol.* 2, 477–484. doi: 10.1046/j.1462-2920.2000.00135.x

Vigneron, A., Alsop, E. B., Cruaud, P., Philibert, G., King, B., Baksmaty, L., et al. (2019). Contrasting pathways for anaerobic methane oxidation in gulf of Mexico cold seep sediments. *mSystems.* 4, e0009–18. doi: 10.1128/mSystems.00091-18

Vigneron, A., Cruaud, P., Pignet, P., Caprais, J. C., Cambon-Bonavita, M. A., Godfroy, A., et al. (2013). Archaeal and anaerobic methane oxidizer communities in the Sonora margin cold seeps, guaymas basin (Gulf of California). *ISME J.* 7, 1595–1608. doi: 10.1038/ismej.2013.18

Walters, W., Hyde, E. R., Berg-Lyons, D., Ackermann, G., Humphrey, G., Parada, A., et al. (2015). Improved bacterial 16S rRNA gene (V4 and V4-5) and fungal internal transcribed spacer marker gene primers for microbial community surveys. *mSystems.* 1 (1), e00009–e00015. doi: 10.1128/mSystems.00009-15

Wang, B., Du, Z., Luan, Z., Zhang, X., and Yan, J. (2021). Seabed features associated with cold seep activity at the Formosa ridge, south China Sea: Integrated application of high-resolution acoustic data and photomosaic images. *Deep Sea Res. Part I Oceanographic Res. Papers.* 177, 103622. doi: 10.1016/j.dsr.2021.103622

Wang, Q., Garrity, G. M., Tiedje, J. M., and Cole, J. R. (2007). Naive Bayesian classifier for rapid assignment of rRNA sequences into the new bacterial taxonomy. *Appl. Environ. Microbiol.* 73, 5261–5267. doi: 10.1128/aem.00062-07

Wang, F.-P., Zhang, Y., Chen, Y., He, Y., Qi, J., Hinrichs, K.-U., et al. (2014). Methanotrophic archaea possessing diverging methane-oxidizing and electron-transporting pathways. *ISME J.* 8, 1069–1078. doi: 10.1038/ismej.2013.212

Wu, Y., Qiu, J.-W., Qian, P.-Y., and Wang, Y. (2018). The vertical distribution of prokaryotes in the surface sediment of jiaolong cold seep at the northern south China Sea. *Extremophiles.* 22, 499–510. doi: 10.1007/s00792-018-1012-0

Yang, S., Lv, Y., Liu, X., Wang, Y., Fan, Q., Yang, Z., et al. (2020). Genomic and enzymatic evidence of acetogenesis by anaerobic methanotrophic archaea. *Nat. Commun.* 11, 3941. doi: 10.1038/s41467-020-17860-8

Zhang, T., Xiao, X., Chen, S., Zhao, J., Chen, Z., Feng, J., et al. (2020). Active anaerobic archaeal methanotrophs in recently emerged cold seeps of northern south China Sea. *Front. Microbiol.* 11. doi: 10.3389/fmicb.2020.612135

Zhang, Y., Yao, P., Sun, C., Li, S., Shi, X., Zhang, X. H., et al. (2021). Vertical diversity and association pattern of total, abundant and rare microbial communities in deep-sea sediments. *Mol. Ecol.* 30, 2800–2816. doi: 10.1111/mec.15937

Zhao, B., Yao, P., Bianchi, T. S., Xu, Y., Liu, H., Mi, T., et al. (2017). Early diagenesis and authigenic mineral formation in mobile muds of the changjiang estuary and adjacent shelf. *J. Mar. Syst.* 172, 64–74. doi: 10.1016/j.jmarsys.2017.03.001

Zhuang, G.-C., Xu, L., Liang, Q., Fan, X., Xia, Z., Joye, S. B., et al. (2019). Biogeochemistry, microbial activity, and diversity in surface and subsurface deep-sea sediments of south China Sea. *Limnol Oceanogr.* 64, 2252–2270. doi: 10.1002/lno.11182

frontiers | Frontiers in Marine Science

TYPE Original Research
PUBLISHED 18 January 2023
DOI 10.3389/fmars.2023.1087411

OPEN ACCESS

EDITED BY
Yu Zhang,
Shanghai Jiao Tong University, China

REVIEWED BY
Liqiang Zhao,
Guangdong Ocean University, China
Zhi Liao,
Zhejiang Ocean University, China

*CORRESPONDENCE
Chaolun Li
lcl@qdio.ac.cn

SPECIALTY SECTION
This article was submitted to Marine Molecular Biology and Ecology, a section of the journal Frontiers in Marine Science

RECEIVED 02 November 2022
ACCEPTED 04 January 2023
PUBLISHED 18 January 2023

CITATION
Zhou L, Li M, Zhong Z, Chen H, Wang M, Lian C, Wang H, Zhang H, Cao L and Li C (2023) Toxicological effects of cadmium on deep-sea mussel *Gigantidas platifrons* revealed by a combined proteomic and metabolomic approach.
Front. Mar. Sci. 10:1087411.
doi: 10.3389/fmars.2023.1087411

Toxicological effects of cadmium on deep-sea mussel *Gigantidas platifrons* revealed by a combined proteomic and metabolomic approach

Li Zhou[1], Mengna Li[1,2,3], Zhaoshan Zhong[1], Hao Chen[1], Minxiao Wang[1,2], Chao Lian[1], Hao Wang[1], Huan Zhang[1], Lei Cao[1] and Chaolun Li[1,2,3,4,5]*

[1]Center of Deep Sea Research, Institute of Oceanology, Chinese Academy of Sciences, Qingdao, China, [2]Key Laboratory of Marine Ecology and Environmental Sciences, Qingdao, China, [3]University of Chinese Academy of Sciences, Beijing, China, [4]South China Sea Institute of Oceanology, Chinese Academy of Sciences, Guangzhou, China, [5]Laboratory for Marine Ecology and Environmental Science, Qingdao National Laboratory for Marine Science and Technology, Qingdao, China

Introduction: Marine metal contamination caused by deep-sea mining activities has elicited great concern from both social and scientific communities. Among the various metals deep-sea organisms might encounter, cadmium (Cd) is a widely detected metal that in very small amounts is nonetheless capable of severe toxicity. Yet due to both remoteness and technical challenges, insights into the effects of metal exposure resulting from mining activities upon deep-sea organisms are limited.

Methods: Here, we investigated Cd's toxicological effects on deep-sea mussels of *Gigantidas platifrons* exposed to 100 or 1000 g/L of Cd for 7 days; an integrated approach was used that incorporated proteomics and metabolomics along with traditional approaches (metal concentrations, metal subcellular distribution, and anti-oxidative and immune-related biochemical indexes).

Results and Discussion: Results showed that Cd exposure caused significant Cd's accumulation in mussel gills and redistribution of Cd among subcellular compartments, with cellular debris being the primary binding site. Although anti-oxidative enzymes activities (superoxide dismutase and catalase) were not significantly altered in mussel gills of both exposed groups, the markedly increased level of glutathione S-transferase detected via proteomic technique clearly evinced that deep-sea mussels suffered from oxidative stress under Cd exposure. Besides, altered activities of acid phosphatase and alkaline phosphatase assayed by traditional methods along with the predominant presence of largely altered immune-related proteins detected by proteomic data strongly revealed an immune response of deep-sea mussels elicited by Cd. In addition, results of proteomics combined with those of non-targeted metabolomics demonstrated that Cd could exert toxicity by disrupting cytoskeleton structure, ion homeostasis, and primary metabolisms of energy, lipid, and nucleotide in deep-sea mussels. As

demonstrated in this study, proteomics and metabolomics can be used in tandem to provide valuable insights into the molecular mechanisms of deep-sea organisms' response to Cd exposure and for helping to discover potential biomarkers for application during deep-sea mining assessments.

KEYWORDS

metal, toxicology, Mytilidae, deep-sea, omics, environment monitor

1 Introduction

The deep-sea floor harbors a wealthy of valuable mineral resources which are necessary components of a variety of low-carbon energy technologies, such as solar panels, wind turbines, and geothermal capture systems (Carlsson and Gade, 1986). As mineral resources on land are gradually depleted and deep-sea equipment and technology are further developed, deep-sea mineral resources have emerged as a new target for extraction and acquisition by humans, with deep-sea mining now entering a highly active period. The contract numbers for exploring deep-sea mineral resources has soared, from just seven in 2010 to thirty-one in 2021, of which seven mining contracts are for the exploration of hydrothermal areas (ISA).

However, deep-sea mining is a large-scale human activity. In the process of transporting metal minerals from hundreds or even thousands of meters of seabed up to the water surface, a mining operation will inevitably result in the release of toxic substances including copper, cadmium, zinc, lead, and iron. When excessive amounts of these metals are absorbed by local organisms, it can cause acute or chronic damage to deep-sea species, inhibiting their growth and reproduction, affecting the local food chain, and eventually leading to ecosystem shutdown (Boschen et al., 2013; Hauton et al., 2017; Martins et al., 2017). Hindered by both its remoteness and technical challenges, the deep sea is the least explored biome on the planet. As a result, there is very little knowledge of how deep-sea mining impacts deep-sea organisms in terms of their physiology and population dynamics. To establish guidelines and frameworks for sustainable mining practices as soon as possible, it is imperative that metal toxicological research of deep-sea organisms be conducted, which provide a timely empirical basis that can also inform theory for the establishment of sensitive biomarkers for the monitoring of deep-sea mining activities.

The deep-sea bivalve *Gigantidas platifrons* is a cosmopolitan mussel that can be found in most deep-sea chemosynthetic ecosystems of the West Pacific Ocean. As stationary filter feeders, individuals of this species live in the benthic environment, where pollutants are deposited and accumulated (Zhou et al., 2020; Zhou et al., 2021). These mussels are very sensitive to environmental fluctuations and can serve as sentinels to monitor the deep-sea environment (Zhou et al., 2020; Zhou et al., 2021). Among the various metals deep-sea life may come into contact with, Cd is a nonessential element in deep-sea mussels' physiology, which can be readily absorbed, transported, and accumulated in their bodies (Company et al., 2010; Zhou et al., 2021). Furthermore, Cd does not biodegrade and can persist in organisms for a long time, causing serious toxic effects *via* trace amounts on organisms at their physiological, cellular, subcellular and molecular levels. Experimental studies with deep-sea organisms under metal exposure have shown that Cd could cause general cellular injury, impair lysosomal and plasma membrane integrity, induce oxidative stress and overproduction of reactive oxygen species (ROS), disrupt cellular osmoregulation as well as disordering core metabolic pathways of amino acids, carbohydrates, and lipids (Company et al., 2019; Zhou et al., 2021). In deep-sea hydrothermal ecosystems, Cd levels tend to be high, capable of reaching 1.5 μM and 3950 ppm in hydrothermal fluids and metallic mineral deposits, respectively (Zeng, 2011).

Previously, researchers have investigated the toxic effects of deep-sea mining upon deep-sea fauna by using shallow-water taxa as proxies for deep-sea taxa (Brown et al., 2017b; Mestre et al., 2019; Pinheiro et al., 2021). However, such studies are controversial because they ignore the complexity of the deep-sea environment and species differences between organisms in shallow and deep water habitats (Brown et al., 2017a). A recent study of deep-sea organisms exposed to metals found that the expression of some traditional metal-related biochemical indexes (e.g., metallothioneins) or metabolites (e.g., D-allose) were not significantly induced or exhibited a pattern opposite to that found in shallow-water (Zhou et al., 2021), implying that deep-sea organisms might undergo different biochemical and molecular responses when exposed to metals. Besides, when compared with the vast amount of toxicological research in costal organisms, corresponding research on deep-sea organisms far from comprehensive and limited to the responses of a known class of toxicity-responsive genes or particular enzyme activity (Company et al., 2010; Bougerol et al., 2015; Martins et al., 2017). The response mechanisms of deep-sea organisms induced by stress from different metals are not exactly the same, and they depend on a complex genomic regulatory network involving multiple genes and pathways (del Rio, 2016; Wong et al., 2015). Therefore, systematical toxicological work carried out using multiple approaches at once, to unravel these biological effects and responsive mechanisms, can truly reflect the ongoing and expected life processes in those parts of the deep sea incurring mining perturbations.

Recently, with dramatic advances in high-throughput molecular tools, 'omic' technologies including proteomics and metabolomics have been extensively used in toxicological studies of marine environments (Sanchez et al., 2011; Xu et al., 2019). Proteomics theoretically characterizes the entire protein pool at the organelle,

cellular or tissue level, and is capable of detecting significantly different expressed proteins (DEPs) caused by exogenous factors in organisms (Tomanek, 2011; Campos et al., 2012). Meanwhile, metabolomics systematically examines the entire range of endogenous low-molecular weight metabolites (< 1000 Da) in biological samples (Ji et al., 2015). It offers the opportunity to compare the metabolites and then detect alterations in their expression profiles in organisms. When used in tandem, proteomics and metabolomics could provide plenty of information concerning the molecular responses of living organisms to contamination. In combination, these two 'omic' approaches would ideally complement each other, offering opportunities to decode novel molecular mechanisms involved in stress response, and being useful for discovering reliable biomarkers of metal exposure and its effects. To our best knowledge, however, no attempt has yet been made to study the toxic effects of metals on deep-sea organisms simultaneously at the protein and metabolite levels.

In this study, to gain a comprehensive understanding of the underlying toxicological effects associated with metal exposure in deep-sea organisms, the deep-sea mussel *G. platifrons* was selected as the model organism and exposed to cadmium (100 and 1000 μg/L) for 7 days, and the response of the treated deep-sea mussels then evaluated using both traditional toxicological methods (i.e., metal accumulation, metal subcellular distribution, biochemical indexes) and 'omic' techniques (proteomics and metabolomics). The objectives of this study were (i) to determine the subcellular distribution and biochemical response of *G. platifrons* gill tissue under Cd stress; (ii) to identify key proteins/metabolites that are differentially expressed in *G. platifrons* under Cd stress, and their involved essential pathways; (iii) to uncover the molecular mechanisms by which *G. platifrons* responds to Cd. This study will contribute to bridging a glaring knowledge gap regarding the potential impacts of deep-sea mining on deep-sea organisms, as well as identifying some important responsive candidate biomarkers associated Cd stress for the monitoring of deep-sea mining.

2 Material and methods

2.1 Experimental design

Mussels of *G. platifrons* were collected from the seabed of the South China Sea at seawater depths below 1119 m, by using the remotely operated vehicle *Faxian* (ROV Faxian), it mounted to the research vessel *Kexue*. ROV *Faxian* brought the mussels to the sea surface after first placing them in an insulated container. Once aboard, mussels were immediately transferred to a specially designed aquarium system, used for culturing deep-sea organisms. In this system, mussels were cultured in surrounding seawater at 4°C with a pressure of 1 atm. Water was half-renewed daily and any dead mussels were immediately discarded. Mussels received methane gas twice a day for 30 min, as a food and energy source.

Following acclimatization period of 48 hours, thirty mussels (93.2 ± 5.65 mm in shell length) were randomly placed in the three high-density polypropylene tanks (10 mussels per tank; rearing density: one mussel per liter of seawater). Mussels were exposed to nominal 100 μg/L or 1000 μg/L of Cd for 7 days, with clean filtered seawater serving as a control. The exposure concentrations of Cd chosen in this study reflect those in deep-sea environments (Zeng, 2011). Cadmium was prepared with $CdCl_2 \cdot 2.5H_2O$ (Sigma-Aldrich, analytical grade). The exposed concentrations were environmentally relevant and reported for hydrothermal systems (Zeng, 2011). The filtered seawater and exposed metal solution were renewed thoroughly on a daily basis. During this exposure experiment, other conditions were consistent with those of the acclimatization period, and no mussel mortality was observed.

All of thirty mussels were sacrificed after 7 days of exposure. Immediately after dissecting each with plastic tools, the mussel gills were flash frozen in liquid nitrogen, and then stored at –80°C for further analysis. Mussel gill of each individual was separated into five sets for their metal contents' determination, metal subcellular distribution, biochemical analysis, and metabolic and proteomic assessments.

2.2 Metal content and metal subcellular distribution

To quantify the gills' Cd accumulation, inductively coupled plasma mass spectrometry was used as previously described (ICP-MS, Thermo-Scientific iCAPQc, Bremen, Germany) (Zhou et al., 2020). A detailed description of these procedures can be found in the Supplementary Material (S1.1).

Metal subcellular distribution in mussel gills was determined according to a well-established protocol reported in several studies (Wallace and Luoma, 2003; Pan and Wang, 2008; Yu et al., 2013; Ma and Wang, 2020). Briefly, each gill tissue sample was individually homogenized in a freshly prepared 30 mM Tris-NaCl buffer (pH 8.0, 0.15 M NaCl, 5 mM 2-mercaptoehanol, with 0.1 mM of freshly prepared phenylmethylsufonyl fluoride) using an Ultra-Turrax homogenizer (Jing Xin, China) for 30 sec. The homogenized tissue was first fractionated by centrifugation at 1450× *g* for 15 min. The collected pellets were digested in 1 N NaOH. After the mixture had been heated at 80°C for 10 min in a water bath, a second centrifugation at 5000× *g* for 10 min was carried out. Next, the metal-rich granule fraction (MRG) was obtained from the pellets, while cellular debris was obtained from the supernatant. A third centrifugation at 100 000× *g* for 60 min was performed on the supernatant from the first centrifugation. From this, the resulting pellet resulting was treated as the organelle fraction, and a 10-min water bath at 80°C was used to heat the ensuing supernatant. After doing another centrifugation at 50 000× *g* for 30 min, the heat-sensitive protein fraction (HSPF) was obtained from the supernatant, while metallothionein-like protein fraction (MTLP) was derived from the pellet. All procedures were conducted at 4°C unless otherwise stated. The experiment was conducted with blank samples lacking any tissue addition. Following the freeze-drying of each fraction, the fractions were digested with 2 mL of 15.6 M HNO_3 at 80°C for 48 h. The obtained digested mixture was then diluted to 5 mL with deionized water and the Cd concentration in each fraction likewise measured according to the above procedure. The percentages of Cd metal in each fraction were defined as the metal subcellular distributions.

2.3 Biochemical measurements

Six biochemical indexes—acid phosphatase (ACP), alkaline phosphatase (AKP), superoxide dismutase (SOD), catalas (CAT), reduced glutathione (GSH) and lipid peroxidation (LPO)—were measured in the mussel gill samples. All these biochemical indexes were quantified using commercial kits from the Nanjing Jiancheng Bioengineering Institute (China). AKP and ACP activity were determined according to the method King (1965). SOD was measured by the method of McCord and Fridovich (1969). CAT activity was quantified by the method of Goth (1991). Reduced GSH was determined following the method of Jollow et al. (1974). LPO was assessed by the method of Korobeĭnikova (1989). A detailed description of these procedures can be found in the Supplementary Material (S1.2).

2.4 Proteomic analysis

Three mussel gill tissues were pooled into one biological replicate, and three biological replicates were analyzed for each group. This analysis using 4D Label free proteomics was conducted in collaboration with Jingjie PTM BioLabs (Hangzhou, China) (Ding et al., 2022). The main procedures included protein extraction, protein alkylation, trypsin digestion, LC-MS/MS analysis, and the bioinformatics analysis. Briefly, a lysis buffer containing 8 M urea and 1% protease inhibitor cocktail was used to extract the mussel gill proteins, which were then digested with trypsin. The tryptic peptide was dissolved in mobile phase A of liquid chromatography, and separated by a NanoElute ultra-high-performance liquid chromatography system (Bruker, Germany). Protein profiles were generated by timsTOF Pro (Bruker Daltonics) mass spectrometry after separation with the ultra-performance liquid system. The resulting MS/MS data was analyzed using the MaxQuant search engine (v1.6.15.0). Tandem mass spectra were searched against deep-sea mussel *G. platifrons* genome data concatenated with the reverse decoy database. The reference genome of *G. platifrons* employed in this study was originally published by Sun et al. (2017) and updated by Wang et al. (GenBank accession no. JAOEFJ000000000, unpublished data). The FDR (false discovery rate) was adjusted to < 1%.

Proteins with a fold-change > 1.2 or < 0.83 *and* a $P < 0.05$ were designated as being significantly differentially expressed. These proteins were classified and grouped using Gene Ontology (GO) and KEGG databases. A detailed description of these procedures can be found in the Supplementary Material (S1.3).

2.5 Non-target metabolomic profiling analysis

Metabolites in mussel gills were extracted as previously described (Zhou et al., 2021). After that, an ultrahigh performance liquid chromatography instrument (UHPLC) (1290 Infinity LC, Agilent Technologies, Santa Clara, CA, USA), equipped with a quadruple time-of-flight mass spectrometer (AB Sciex TripleTOF 6600), was used to generate the untargeted metabolic profiles. This analysis was supported by Shanghai Applied Protein Technology Co., Ltd, APTBIO. The procedures involved are described in detail in the Supplementary Material (S1.4).

2.6 Data analysis

The statistical analysis was implemented in SPSS v19 software for Windows (IBM, Armonk, NY, USA). For biochemical indices and metal concentrations, their means and standard deviations were calculated. Before their formal statistical analysis, data of fitted residuals were checked for homogeneity of variance and normality. Analyses of variance (ANOVA) and Kruskal–Wallis tests were applied to parametric and nonparametric variables, respectively. When a significant difference among the three groups was detected, or Tukey's range test or Mann–Whitney *U* tests were respectively applied in pairwise manner to identify which treatment or control groups differed from each other.

3 Results

3.1 Metal accumulation and subcellular metal distribution in deep-sea mussel gills under Cd exposure

Accumulated Cd concentrations and the corresponding subcellular Cd distribution in mussel gills are depicted in Figure 1. Mussel gills can significantly accumulate Cd from the surrounding environment, with the higher Cd exposure concentration resulting in a higher Cd concentration in mussel gills (Figure 1A). Cd concentrations within the subcellular fractions (i.e., MTLP, organelle, HSPF, MRG, cellular debris) of the mussel gills were also significantly impacted by exposure concentration (Figure 1B). In the control group, HSPF harbored the most Cd. As the exposure concentration increased, Cd was transferred to MTLP, organelle, and cellular debris, the last being where Cd was predominantly stored in deep-sea mussels.

3.2 Biochemical responses of deep-sea mussel gills under Cd exposure

Most biochemical parameters analyzed in this study were affected by the exposure concentrations of Cd (Figure 2). The activity of ACP decreased as the concentration of Cd increased. Conversely, AKP activity and the levels of GSH and LPO all increased with an increased Cd concentration. The activity of SOD or CAT did not differ significantly among the treatments and control group. The ACP activity and LPO level were statistically similar in both low- and high-dose group. The GSH level only raised in mussel gills of the high-dose group, being approximately three times higher that of the control group.

3.3 Proteomic profiles of deep-sea mussel gills under Cd exposure

A total of 5260 quantifiable proteins were identified in the deep-sea mussel gills (Supplementary Materials S2.1). Of those, in the low dose-Cd exposure group, 162 were significantly differentially expressed proteins (DEPs) consisting of 87 up-regulated (53.7%)

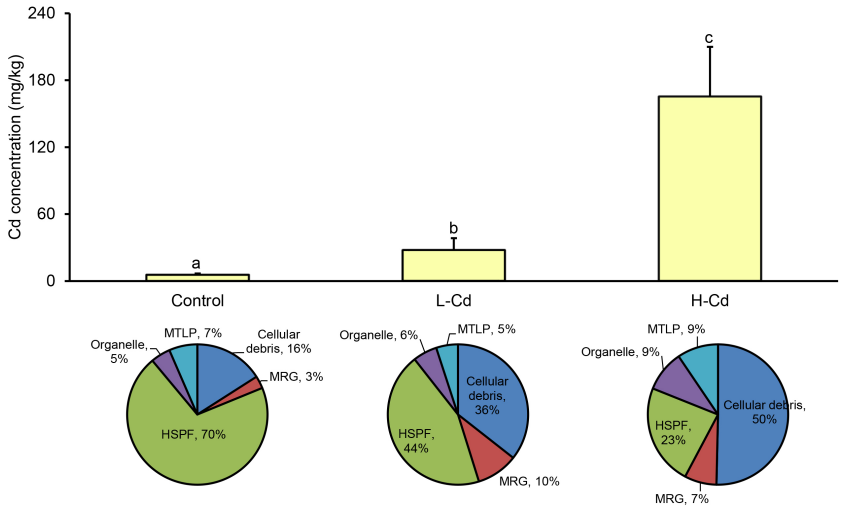

FIGURE 1
Mean metal concentrations (mg/kg) and subcellular distribution of Cd in gills of the deep-sea mussel *Gigantidas platifrons* after 7 days of exposure to 100 or 1000 μg/L Cd (n = 10 per group, mean ± SD). Values followed by the same letter are not statistically different ($P > 0.05$) between the treatment groups. Pie charts show subcellular distribution of Cd in the gills of *G. platifrons*. L-Cd: 100 μg/L Cd; H-Cd: 1000 μg/L Cd; MTLP: metallothionein-like protein; MRG: metal-rich granules; HSPF: heat-sensitive protein.

and 75 down-regulated (46.3%) induced DEPs; in the high dose-Cd exposure group 222 DEPs were found induced, these consisting of 144 up-regulated (64.9%) and 78 down-regulated (35.1%) DEPs (Figure 3A). Venn diagram analysis showed that 47 DEPs were altered in common (30 down-regulated and 17 up-regulated) by the two Cd-exposure treatments (Figure 3B). Detailed information on all significantly regulated proteins is provided in Table 1 and Supplementary Materials Table S1.

The DEPs were classified into three categories based on their GO annotations: biological process (BP), molecular function (MF), and cellular component (CC). Under the BP category, most DEPs were involved in cellular process, biological regulation, and metabolic process in both treatment groups. In the MF category, most DEPs detected were involved in catalytic activity and binding in both treatment groups. In the CC category, most DEPs were located in cell and intracellular, in both treatment groups (Figure 3C). A detailed description of the GO enrichment results for the DEPs is provided in Table S2 of the Supplementary Materials.

The most representative KEGG pathways for the down- and up-regulated DEPs are shown in Figure 4. In the low-dose Cd exposed group, O-glycan biosynthesis, apoptosis, the wnt signaling pathway, and protein processing in the endoplasmic reticulum were the most statistically significant pathways for the up-regulated DEPs. For the down-regulated DEPs, the most significant pathway was galactose metabolism. In the high dose-Cd exposure group, both mismatch repair and spliceosome were significantly enriched for the up-regulated DEPs; vitamin digestion and absorption, linoleic acid metabolism, glycolysis/gluconeogenesis and necroptosis pathway were enriched for the down-regulated DEPs.

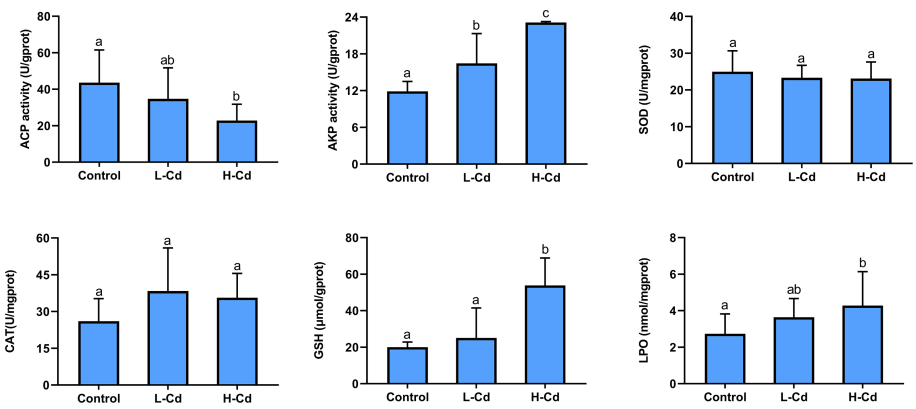

FIGURE 2
The activity of acid phosphatase (ACP), alkaline phosphatase (AKP), superoxide dismutase (SOD) and catalase (CAT), and the levels of glutathione (GSH), and lipid peroxidation (LPO) in the gills of *Gigantidas platifrons* after 7 days of exposure to 100 or 1000 μg/L Cd (n = 10 per group, mean ± SD). Values followed by the same letter are not statistically different ($P > 0.05$) between the treatment groups.

10.3389/fmars.2023.1087411

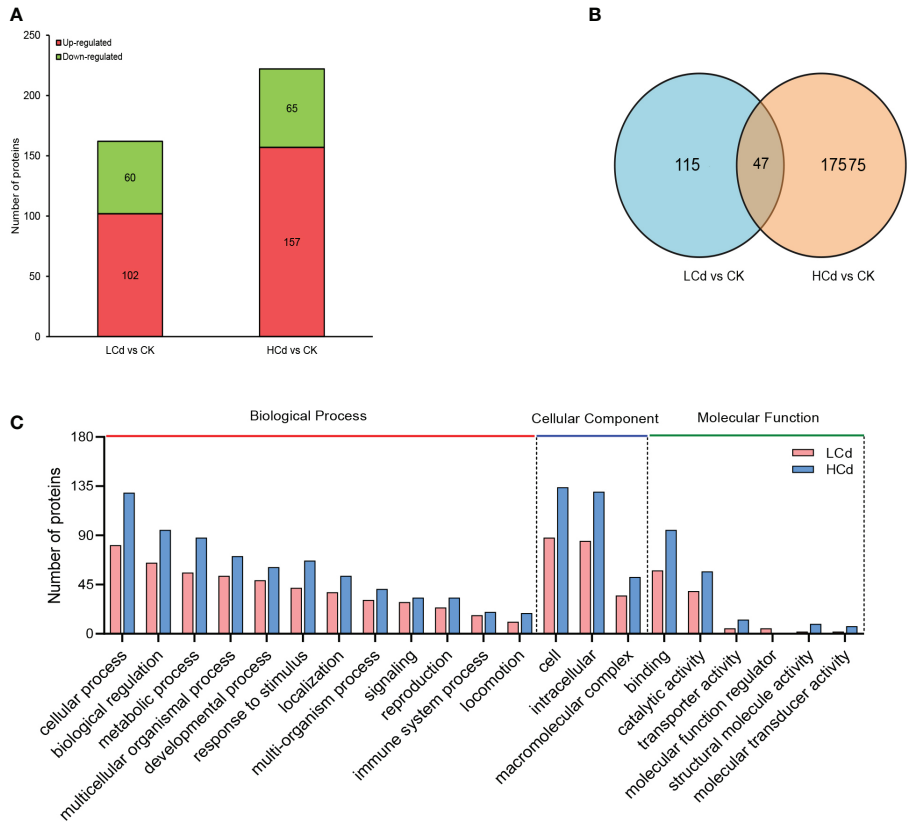

FIGURE 3
Quantitative proteomics data. **(A)** Significantly up- and down-regulated proteins in mussel gills of low- and high-dose groups compared with the control group. **(B)** Venn diagram showing the number of DEPs (differently expressed proteins) uniquely and commonly altered in the groups exposed to 100 and 1000 μg/L of Cd. **(C)** The GO (Gene Ontology) classification of proteins that were expressed in 100 and 1000 μg/L groups indicated by pink and blue bars, respectively.

TABLE 1 The key differentially expressed proteins (DEPs) responsive to cadmium in deep-sea mussel gills.

Protein accession	Accession no.	Protein description	Fold change	
			100 μg/L	1000 μg/L
Detoxification				
yibei_GLEAN_10021621	XP_022337663.1	microsomal glutathione S-transferase 3-like	3.1235	
yibei_GLEAN_10017956	XP_025111853.1	microsomal glutathione S-transferase 1-like isoform X2		1.8265
yibei_GLEAN_10021632	QBM06404.1	microsomal glutathione S-transferase 3 isoform b		1.6278
yibei_GLEAN_10005609	XP_011428128.1	cytochrome P450 2C31		0.7681
Stress response				
yibei_GLEAN_10004579	XP_021349090.1	heat shock 70 kDa protein 12A-like	2.5479	3.909
yibei_GLEAN_10020804	XP_011432755.1	major vault protein	1.834	
yibei_GLEAN_10012195	XP_021376559.1	heat shock 70 kDa protein 12A-like	0.6002	
yibei_GLEAN_10023865	BAD99026.1	heat shock protein 70		2.2481
yibei_GLEAN_10020983	CAH04106.1	heat shock protein 70		1.4894
yibei_GLEAN_10011520	XP_021376559.1	heat shock 70 kDa protein 12A-like		1.2724
yibei_GLEAN_10005694	XP_005097388.1	10 kDa heat shock protein, mitochondrial-like		0.7902
yibei_GLEAN_10008543	XP_021349090.1	heat shock 70 kDa protein 12A-like		0.5919

(Continued)

TABLE 1 Continued

Protein accession	Accession no.	Protein description	Fold change	
yibei_GLEAN_10005890	ANN45953.1	byssal HSP-like protein 1		1.2349
yibei_GLEAN_10029721	XP_021352707.1	glutamate receptor-like		1.5127
yibei_GLEAN_10025891	XP_021355385.1	putative glutamate synthase [NADPH]		1.3247
yibei_GLEAN_10030644	BAF63637.1	glucose-regulated protein 94		1.2191
Cytoskeleton				
yibei_GLEAN_10033077	XP_021377767.1	unconventional myosin-XVI-like isoform X10	0.6599	
yibei_GLEAN_10025956	XP_022295584.1	IST1 homolog	0.8093	
yibei_GLEAN_10020375	XP_022323498.1	kinesin-like protein KIF28P isoform X1	1.4335	
yibei_GLEAN_10015354	XP_019919334.1	dynein heavy chain 6, axonemal-like isoform X3	1.2369	
yibei_GLEAN_10026715	XP_011446273.1	dynein intermediate chain 2, ciliary isoform X2	1.2518	
yibei_GLEAN_10021778	XP_022339665.1	leupaxin-like isoform X2	0.8168	
yibei_GLEAN_10002721	XP_022306398.1	ribosome biogenesis protein WDR12 homolog		1.5925
yibei_GLEAN_10009294	XP_022340059.1	tektin-3-like isoform X1		1.8697
yibei_GLEAN_10012024	XP_025114800.1	tubulin beta chain-like		3.3209
yibei_GLEAN_10012532	NP_001292292.1	tubulin beta chain-like		1.7281
yibei_GLEAN_10018803	.	tektin-3-like isoform X2		1.7148
yibei_GLEAN_10020493	XP_021370513.1	dynein heavy chain 10, axonemal-like isoform X2		1.3877
yibei_GLEAN_10022711	XP_011416301.1	tektin-1		1.4629
yibei_GLEAN_10025426	XP_022293672.1	dynein heavy chain 5, axonemal-like isoform X2		1.6873
yibei_GLEAN_10032206	XP_022317078.1	WD repeat-containing protein 63-like isoform X3		1.5104
yibei_GLEAN_10027407	XP_011436383.1	tubulin-specific chaperone A		0.8061
yibei_GLEAN_10034641	XP_022338092.1	translationally-controlled tumor protein homolog		1.2166
yibei_GLEAN_10019514	XP_021340611.1	zinc finger ZZ-type and EF-hand domain-containing protein 1-like isoform X2		1.6331
Immune response				
yibei_GLEAN_10034298	XP_018092523.1	baculoviral IAP repeat-containing protein 7-B isoform X3	1.2636	1.2075
yibei_GLEAN_10035199	AJQ21543.1	stimulator of interferon protein 2	1.3678	1.2846
yibei_GLEAN_10011188	XP_021353098.1	AP-2 complex subunit alpha-2-like	1.2202	1.216
yibei_GLEAN_10015328	XP_021359219.1	interleukin enhancer-binding factor 2 homolog	1.5721	1.5939
yibei_GLEAN_10031808	XP_021373459.1	superkiller viralicidic activity 2-like 2	1.2801	1.5276
yibei_GLEAN_10027593	XP_021353442.1	E3 ubiquitin-protein ligase TRIM56-like	0.6072	0.5192
yibei_GLEAN_10017550	XP_022338572.1	nuclear transport factor 2-like	0.7733	0.6733
yibei_GLEAN_10025664	AKQ70855.1	shell fibrous prismatic cathepsin-like protein 1	0.214	0.1018
yibei_GLEAN_10018923	AJQ21549.1	c-Jun N-terminal kinase	1.2152	
yibei_GLEAN_10009572	XP_012866152.1	deoxynucleoside triphosphate triphosphohydrolase SAMHD1	4.0582	
yibei_GLEAN_10017095	AKS48146.1	protease inhibitor-like protein-B1	0.5625	
yibei_GLEAN_10013055	XP_021342211.1	tumor suppressor candidate 3-like	1.2308	
yibei_GLEAN_10019488	OPL21754.1	forkhead k2-like box protein	1.3562	
yibei_GLEAN_10029659	XP_021342748.1	alpha-L-fucosidase-like isoform X4		1.3694
yibei_GLEAN_10027085	XP_021378597.1	poly [ADP-ribose] polymerase 14-like isoform X1		1.3365
yibei_GLEAN_10018578	XP_025114852.1	probable ATP-dependent RNA helicase DDX17		1.2475

(Continued)

TABLE 1 Continued

Protein accession	Accession no.	Protein description	Fold change	
yibei_GLEAN_10034369	AJQ21489.1	galectin 1		0.7879
yibei_GLEAN_10029806	XP_022300022.1	alpha-L-fucosidase-like isoform X1		0.7722
yibei_GLEAN_10026261	XP_022329082.1	osteoclast-stimulating factor 1-like		0.7388
yibei_GLEAN_10028825	XP_021374846.1	pleckstrin homology domain-containing family A member 1-like		0.6247
yibei_GLEAN_10017110	XP_022293912.1	tyrosine-protein kinase JAK2-like isoform X2		0.3699
Energy metabolism				
yibei_GLEAN_10032781	XP_011448800.1	aldose 1-epimerase isoform X1	0.6914	0.6916
yibei_GLEAN_10006843	XP_022321339.1	isocitrate dehydrogenase [NAD] subunit beta, mitochondrial-like	0.7722	0.8028
yibei_GLEAN_10027755	XP_021355538.1	enolase 4-like isoform X4	1.2627	
yibei_GLEAN_10031289	OWF54443.1	Phosphoglucomutase-1	0.8085	
yibei_GLEAN_10030873	XP_027899350.1	NADH dehydrogenase [ubiquinone] 1 alpha subcomplex subunit 5	0.6991	
yibei_GLEAN_10011053	XP_021368351.1	cinnamyl alcohol dehydrogenase 8-like isoform X2		0.4288
yibei_GLEAN_10018823	AOR07076.1	mitochondrial ATP synthase subunit d precursor		1.2296
yibei_GLEAN_10011582	XP_021348297.1	V-type proton ATPase 16 kDa proteolipid subunit		1.8389
yibei_GLEAN_10017617	XP_011424185.1	phosphoenolpyruvate carboxykinase, cytosolic [GTP] isoform X1		0.6209
Lipid metabolism				
yibei_GLEAN_10017128	XP_011453569.1	phosphoethanolamine N-methyltransferase 3 isoform X1	1.438	
yibei_GLEAN_10030036	XP_021369900.1	monoglyceride lipase-like isoform X1	1.541	
yibei_GLEAN_10022257	XP_022301267.1	acetoacetyl-CoA synthetase-like	1.4266	
yibei_GLEAN_10032607	XP_011425291.1	phospholipase B1, membrane-associated-like		0.4038
Ion homeostasis				
yibei_GLEAN_10022970	XP_011450059.1	EF-hand calcium-binding domain-containing protein 5-like isoform X1	1.7475	1.8024
yibei_GLEAN_10013077	XP_025088321.1	sodium- and chloride-dependent taurine transporter-like	2.1074	
yibei_GLEAN_10002833	PFX23011.1	Calmodulin	0.3819	
yibei_GLEAN_10015019	XP_022310738.1	calmodulin-like protein 4		0.7516
yibei_GLEAN_10018664	XP_022315953.1	EF-hand calcium-binding domain-containing protein 6-like isoform X2		1.7431
yibei_GLEAN_10019514	XP_021340611.1	zinc finger ZZ-type and EF-hand domain-containing protein 1-like isoform X2		1.6331
yibei_GLEAN_10024939	XP_021377425.1	androglobin-like isoform X6		1.5648
yibei_GLEAN_10011582	XP_021348297.1	V-type proton ATPase 16 kDa proteolipid subunit		1.8389
yibei_GLEAN_10034360	XP_021370577.1	sodium-dependent phosphate transport protein 2B-like isoform X1		1.4312
yibei_GLEAN_10028951	XP_023930119.1	phosphate carrier protein, mitochondrial		1.2895
yibei_GLEAN_10006225	XP_021372793.1	calcium-binding mitochondrial carrier protein SCaMC-2-like		0.7521

3.4 Metabolic profiles of deep-sea mussel gills under Cd exposure

Compared with the control group, 21 and 68 metabolic features were significantly altered in the low dose- and high dose-Cd exposure groups, respectively (Table 2). These differential metabolic profiles demonstrated that deep-sea mussels relied on differing metabolic strategies when exposed to Cd at different exposure concentrations. Importantly, only eight metabolites in total were commonly altered by both Cd exposure treatments. The metabolite classes identified included amino acids, carbohydrates, nucleotides, and lipids, as well as others. KEGG enrichment analysis demonstrated seven pathways (ABC transporters, protein digestion and absorption, aminoacyl-tRNA biosynthesis, valine, leucine and isoleucine biosynthesis, choline metabolism in cancer, glycine, serine and threonine metabolism, and mineral absorption) were commonly enriched when comparing each of the Cd-exposed group with the control group (Figure 3S). Specially, pathways of lysine degradation, fructose

10.3389/fmars.2023.1087411

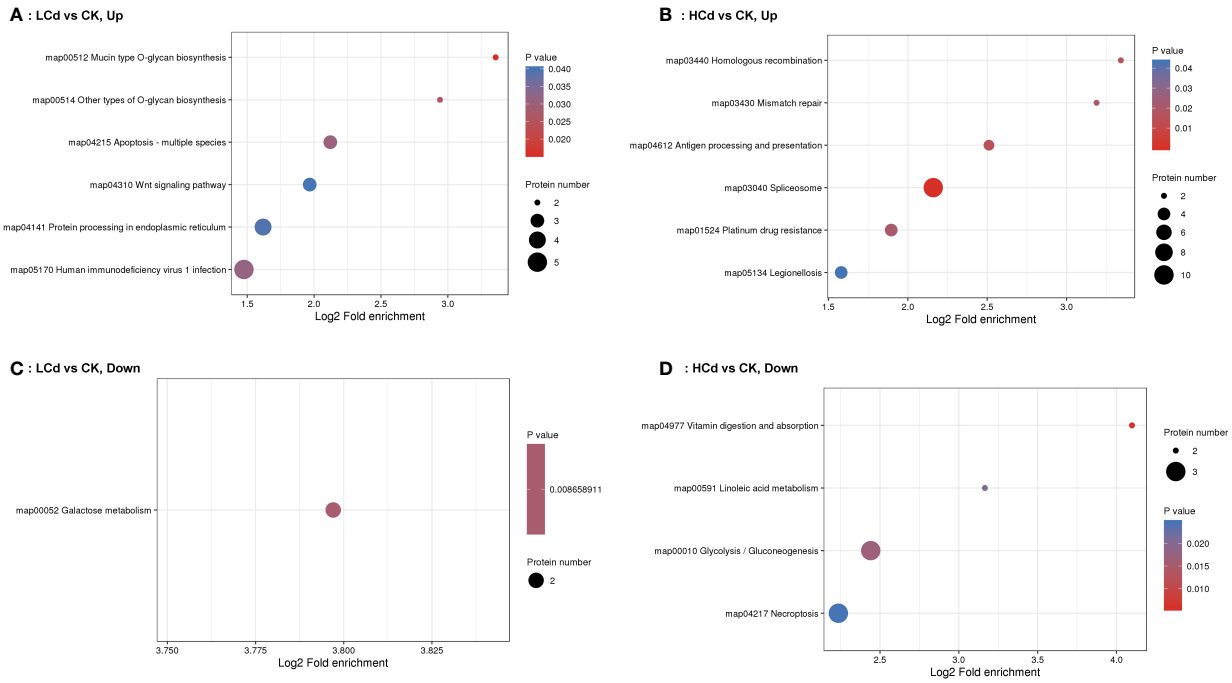

FIGURE 4
KEGG pathway enrichment analyses of up and low-regulated differentially expressed proteins (DEPs) detected in gill mussels of *Gigantidas platifrons* treated with LCd (100 μg/L Cd) or HCd (1000 μg/L Cd). **(A)** up-regulated DEPs, LCd; **(B)** up-regulated DEPs, HCd; **(C)** down-regulated DEPs, LCd; **(D)** down-regulated DEPs, HCd.

TABLE 2 Significantly expressed metabolites in the studied deep-sea mussel in response to a low and high dose of cadmium exposure (Note: Symbol ↑ indicates the metabolite is upregulated;Symbol ↓ indicates the metabolite is downregulated).

Metabolites	Lcd vs Ck	Trend	HCd vs Ck	Trend
Amino acid & derivatives	L-Threonine	↑	Beta-Alanine	↑
	Allocystathionine	↑	D-Proline	↑
	Betaine	↓	L-Threonine	↑
	L-Glutamate	↓	L-Isoleucine	↑
			L-Histidine	↑
			L-Tyrosine	↑
			L-Alanine	↑
			L-Phenylalanine	↑
			Glycine	↑
			Allocystathionine	↑
			Tyramine	↑
			Phenyllactic acid	↑
			L-Pipecolic acid	↑
			Linoleic acid	↓
			Betaine	↓
Carbohydrates	D-Mannose	↓	Beta-D-Fructose 6-phosphate	↓
	Erythritol	↓	N-Acetylglucosamine 1-phosphate	↓
	Alpha-D-Glucose	↓	L-Malic acid	↓

(Continued)

10.3389/fmars.2023.1087411

TABLE 2 Continued

Metabolites	Lcd vs Ck	Trend	HCd vs Ck	Trend
	D-Allose	↓	N-Acetylmannosamine	↓
			D-Glucose 6-phosphate	↓
			UDP-N-acetylglucosamine	↓
			D-Mannose-6-phosphate	↓
			UDP-D-Galactose	↓
			N-Acetyl-D-Glucosamine 6-Phosphate	↓
			Argininosuccinic acid	↓
			N-Acetyl-D-glucosamine	↓
			Ribulose 5-phosphate	↑
			D-Lyxose	↑
Nucleotides & derivatives	Inosine 5'-monophosphate	↓	Allopurinol riboside	↑
	Xanthine	↑	Deoxyguanosine	↑
			Adenosine 2',3'-cyclic monophosphate	↑
			2-Hydroxyadenine	↑
			Guanosine	↑
			Adenosine 3'-monophosphate	↑
			Hypoxanthine	↑
			Xanthine	↑
			Thymine	↑
			Thymidine	↑
			Inosine	↑
			2'-Deoxyuridine	↑
			2'-Deoxyinosine	↑
			Deoxyinosine	↑
			Adenine	↑
			1-Methyladenosine	↑
			Deoxyguanosine	↑
			2-Deoxyribose 5-phosphate	↑
			Adenosine monophosphate	↓
			Guanosine 5'-monophosphate	↓
			S-Methyl-5'-thioadenosine	↓
Lipids	PGD2	↑	PGD2	↑
	Glycerophosphocholine	↑	Glycerol 3-phosphate	↑
	21-hydroxypregnenolone	↑	Valeric acid	↑
	15-Deoxy-delta-12,14-PGJ2	↑	1-Palmitoyl-sn-glycero-3-phosphocholine	↑
			1-O-Octadecyl-sn-glyceryl-3-phosphorylcholine	↑
			1-O-(cis-9-Octadecenyl)-2-O-acetyl-sn-glycero-3-phosphocholine	↑
			1-Stearoyl-2-hydroxy-sn-glycero-3-phosphocholine	↑

(Continued)

TABLE 2 Continued

Metabolites	Lcd vs Ck	Trend	HCd vs Ck	Trend
			Phthalic acid Mono-2-ethylhexyl Ester	↑
			Adrenic Acid	↓
			gamma-L-Glutamyl-L-glutamic acid	↓
			cis-9-Palmitoleic acid	↓
Others	L-Pipecolic acid	↑	Choline	↑
	Stearidonic Acid	↑	Stearidonic Acid	↑
	Diacetyl	↑	5-L-Glutamyl-L-alanine	↑
	Diethyltoluamide	↑	Propionic acid	↑
	2-Ethoxyethanol	↑	Acamprosate	↑
	Glutaric acid	↓	Citraconic acid	↓
	2-Oxoadipic acid	↓	Muramic acid	↓
			Glutaric acid	↓

and mannose metabolism, proximal tubule bicarbonate reclamation were uniquely enriched in low-dose group, and pathways of purine metabolism, glucosinolate biosynthesis, mTOR signaling pathway, amino sugar and nucleotide sugar metabolism were enriched in high-dose group (Figure 3S).

4 Discussion

4.1 Metal subcellular distribution and detoxification

The accumulation of Cd in deep-sea mussels increased with increasing exposure concentrations, indicating that deep-sea mussels are robust indicator organisms of environmental changes caused by metal pollution (Martins et al., 2017; Zhou et al., 2021). The subcellular compartmentalization of metals reflects dynamic processes that occur during metal accumulation and provides insights into temporary metal-binding ligands and the detoxification process in organisms (Wallace et al., 2003; Pan and Wang, 2008). As the exposure concentrations increased, the proportion of Cd in its major binding site (HSPF) significantly decreased, whereas Cd's proportions in other fractions (mainly cellular debris) increased correspondingly. A similar pattern was also found in the scallop *Chlamys nobilis* under Cd or Zn exposure (Pan and Wang, 2008). This phenomenon is called the spillover effect, namely because once the major binding pool is saturated and its binding capacity now exceeded, metal(s) may subsequently become associated with other fractions (Pan and Wang, 2008). Cellular debris contains tissue fragments, cell membranes, and other cellular components without any known function. Under Cd exposure, newly accumulated Cd in deep-sea mussel gills tended to bind to less sensitive fractions in cellular debris, preventing it from binding to sensitive fractions in the cell and thus decreasing Cd's toxicity (Lucu and Obersnel, 1996). Interestingly, there was a very small proportion of Cd (< 9%) eliminated into MTLP, whether in the control or either exposure group, suggesting that MTLP could play a minor role in Cd detoxification. This result is in line with previous findings that MTLP is probably not relied upon for a major metal detoxification strategy in deep-sea bivalves (Hardivillier et al., 2004; Zhou et al., 2021).

Apart from detoxification by binding with cellular debris other than MTLPs, deep-sea mussels also can express detoxification enzymes for adaption and survival under Cd stress. In this study, exposure to Cd resulted in the significant up-regulation of glutathione transferases (GSTs) in deep-sea mussel gills. The GSTs are phase II detoxification enzymes responsible for catalyzing the conjugation of glutathione into electrophilic compounds that eventually lead to their excretion (McDonagh and Sheehan, 2006). GSTs also play a role in defense against oxidative stress by metabolizing reactive products formed during lipid peroxidation (Canesi et al., 1999). Furthermore, another detoxification enzyme, cytochrome P450 2C31 (CYP450 [2C31]), was found uniquely down-regulated in deep-sea mussels of high dose-Cd exposure group. In a toxicological study with clam *Mactra chinensis* exposed to Cd, CYP450 (2C31) was inhibited by a low Cd concentration (0.69 mg/L), yet induced by high Cd exposure concentrations (1.38 and 2.76 mg/L) (Zhang et al., 2016). The current results bring forth new and relevant information regarding the metal detoxification response of deep-sea mussels.

4.2 Stress response associated with Cd exposure

Oxidative stress is a major mechanism underpinning Cd toxicity, because its overload could disrupt the redox balance at a cellular scale and stimulate the generation of ROS (Valko et al., 2005). To counter oxidative stress, an antioxidant cascade that includes SOD, CAT, and GSH could be invoked. Among these antioxidants, SOD is responsible for the disproportionation of superoxide anions into hydrogen peroxide and dioxygen, meanwhile CAT can act as a scavenger of hydrogen peroxide. This SOD-CAT system provides the first line of defense against Cd toxicity (Li et al., 2011). However, in the current

study, both SOD and CAT activity were inactivated in either Cd exposure treatment, implying that they might not be suitable for use as sensitive biomarkers in deep-sea mussels during the monitoring of Cd pollution. Altered GSH levels could also be serve as a biomarker for oxidative stress (Valko et al., 2005). Actually, the patterns of change in GSH tend to differ under different experimental conditions: GSH was reportedly depleted substantially during acute Cd exposure while being markedly augmented following chronic Cd exposure (Liu et al., 2009). Our results show that exposure to a low dose of Cd slightly raised the GSH in deep-sea mussels whereas a high dose of it significantly induced GSH in them. Besides, as a major consequence of Cd-induced oxidative stress (Liu et al., 2009), LPO was increased exclusively in deep-sea mussels belonging to the high-dose group. The altered GSH and increased LPO together suggest oxidative stress in mussels of the high-dose group. According to the biochemical data, a low dose of Cd exposure seems unlikely to have caused overt changes to the mussel's cellular oxidative status and lipid peroxidation. Nevertheless, the markedly augmented level of GST detected *via* the proteomic technique clearly evidenced that these deep-sea mussels in the low dose-Cd exposure group also incurred oxidative stress. Therefore, the proteome can convey a more complete picture of the biochemical changes that deep-sea mussels undergo when faced with Cd stress, and it is more sensitive than traditional approaches for discovering novel biomarkers.

From the proteomic profiles, Cd exposure altered 11 proteins that are linked to stress responses. Among these proteins, major vault protein (MVP) was uniquely induced in deep-sea mussel gills of low-dose group. MVP is the main component of the ubiquitous, vault particles that exceed the size of ribosomes. Although the exact role of MVP remains unclear, research has shown that vault complexes are involved in cellular responses to environmental toxins by directly binding and excreting conjugated metabolites, thereby precluding a metal's accumulation and toxic effects (Berger et al., 2009). In addition, because MVP can play a strong regulatory role in apoptosis by binding to several stress-induced effectors of signaling cascades, it has been proposed as a candidate target for modulating apoptosis resistance in aging modulation and cancer treatments (Lara et al., 2011). The up-regulated expression of MVP in mussels exposed to Cd's low dose suggested an anti-apoptotic response to offset potential toxic effects of Cd. Expression of seven stress-related proteins belonging to the class of heat shock protein 70 (HSP70) family were significantly altered in deep-sea mussel gills of both Cd-exposure groups. HSP70 is a group of highly conserved and abundant proteins that help organisms deal with abiotic stressors (heat shock, salinity change, acidification and contaminants) by refolding, sorting, translocating, and degrading deformed proteins, as well as being co-chaperones and regulating the biologically active form of other proteins (Kim and Schöffl, 2002; Chaudhary et al., 2019; Yusof et al., 2022). A field investigation of deep-sea mussel *Bathymodiolus azoricus* from Atlantic hydrothermal vents confirmed that that this species could express and induce a mixture of constitutive heat-shock protein isoforms, ranging from 64 and 76 kDa, enabling it to survive despite toxic vent fluids (Pruski and Dixon, 2007). Accordingly, HSP70 can be set up as a general stress biomarker in deep-sea mussels to monitor deep-sea environmental changes caused by Cd leakage during mining activities.

4.3 Cytoskeleton changes associated with Cd exposure

Eighteen proteins associated with cytoskeleton were altered by Cd exposure. In constituting the system of fibrillar structures in the cytoplasm of eukaryotic cells, the cytoskeleton is primarily composed of three types of fibrils: microtubules, actin filaments, and intermediate filaments. These fibrils could serve as 'weak' elements during episodes of metal stress, inducing the expression of several molecular chaperones, including small HSP and HSP70, to protect the cytoskeleton (Liang and MacRae, 1997). Besides, there is compelling evidence that cytoskeletal proteins could be among the first targets of oxidative stress and that they participate in the homeostasis of oxidative stress (Dalle-Donne et al., 2001). Given that cytoskeletal proteins are crucial for a cell's structure and intracellular organization, any disruption in the architecture of one of the three cytoskeletal networks is liable to cause adverse effects to cells' integrity and functioning (Fletcher and Mullins, 2010). Cytoskeletal injuries in bivalves induced by metal pollution have been repeatedly confirmed (Gomes et al., 2013; Xu et al., 2016). And these cytoskeletal-related DEPs are generally contain actins, tubulins, and myosins in marine bivalves (Xu et al., 2019), a finding consist with our study's results. Consequently, the significantly altered cytoskeletal proteins demonstrate that oxidative stress and subsequent disturbed cytoskeleton and cell structures can be induced by Cd in deep-sea mussels.

4.4 Immune response associated with Cd exposure

The immune system of deep-sea mussels was also affected by their exposure to Cd, as evinced by the altered ACP and AKP activity as well as the thirty regulated proteins (17 DEPs in the low-dose group, 20 DEPs in the high-dose group) involved in the GO term "immune system process". Both ACP and AKP are ubiquitous enzymes in organisms that hydrolyze phosphate-containing compounds and therefore can serve as effective biomarkers of immune responses to environmental contamination (Mazorra et al., 2002). AKP activity is reliably indicative of cell membrane's integrity and is involved in the osmoregulation (Lovett et al., 1994), immune defense (Revel et al., 2019), and calcification process of bivalves (Hohagen and Jackson, 2013). Any perturbation (i.e., altered temperature, increased exposure to metals, microplastics exposure) to the membrane properties could result in AKP's altered activity (Jiang et al., 2012; Huang et al., 2021; Sun et al., 2021). In the present study, a significant increase in AKP activity resulted from increasing the Cd exposure concentrations, this implying a strong immune response of mussels under Cd exposure to resist metal toxicity, or disturbance in osmoregulation from disrupted membrane integrity. ACP has been proven to be associated with lysosomal functionality (Pampanin et al., 2002). Upon entering body, toxic chemicals such as metals can be sequestered within the lysosome, causing increased toxicity and eventually affecting the permeability, integrity or structure of the lysosome (Moore, 1994). Under certain circumstances when lysosomes become overburdened, hydrolases burst out of their leaky membranes and are released into

the extracellular environment, with the possibility of cause cellular injury or even death (Kohler et al., 2002). Hence, the decreased ACP activity in mussels of the high-dose group might due to enzyme escape from damaged lysosomes (Jiang et al., 2012).

When studying the effects of metals on the immune functioning of marine bivalves, researchers have mainly examined total and differential hemocyte counts and phagocytic activity (Hoher et al., 2012). By using proteomics, we discerned the predominant presence of largely altered immune-related proteins in deep-sea mussel gills under Cd stress. These significantly expressed proteins have never been reported before in deep-sea invertebrates in response to metal exposure. For instance, interleukin enhancer-binding factor 2 (ILF2) homolog, stimulator of interferon genes (STING) protein 2, and E3 ubiquitin-protein ligase TRIM56-like were the three of the most prominently regulated proteins in deep-sea mussels when exposed to either Cd treatment, indicating that Cd can disturb the immune homeostasis in deep-sea mussels. As one of the six categories of cytokines that are inducible immune regulatory proteins, interleukin could play pivotal roles in modulating cell communication, growth, development, and differentiation to maintain immune system homeostasis (Yang et al., 2022). Although there are few reports of interleukin and its analogues in invertebrates, ILF has been reported to exist in invertebrates where it functions as regulator in some innate immune responses by affecting the Toll signaling pathway and cell apoptosis (Venier et al., 2011; Yang et al., 2022). As for STING, it is well known for inducing the generation of interferon and proinflammatory cytokines. Being an endoplasmic reticulum membrane protein anchored by several transmembrane domains at its N-terminal region, STING can function as a cGMP-AMP synthase downstream signal adapter in the innate immune cytosolic DNA-sensing pathway (McKnight et al., 2020; Zhang et al., 2020). Concerning E3 ubiquitin-protein ligase TRIM56, it can promote the function of STING by binding to the latter's C-terminal domain and serve as a powerful modulator of innate immunity (Tsuchida et al., 2010). Overall, the significant alterations of the aforementioned biochemical indexes and molecules strongly suggest that multiple mechanisms are involved in mobilizing the immune response against Cd stress in the studied mussel species.

4.5 Alteration of energy metabolism associated with Cd exposure

Metals can impair energy homeostasis in marine organisms because the latter require more energy for mounting one or more stress responses, detoxification steps, or damage repair mechanisms (Sokolova et al., 2012). Glycolysis is the process of decomposing glucose into pyruvate and lactate, leading to the generation of ATP (Satyanarayana, 2021). Herein, five glycolysis-related proteins (phosphoglucomutase-1, enolase 4-like isoform X4, aldose 1-epimerase isoform X1, cinnamyl alcohol dehydrogenase 8-like isoform X2, and phosphoenolpyruvate carboxykinase) were found to be significantly changed in both Cd-exposure groups. Of them, four proteins were down-regulated significantly, suggesting inhibition of glycolysis in deep-sea mussels from exposure to low or high doses of Cd. Concurrently, metabolomics data revealed that all metabolites (α-D-glucose, β-D-fructose 6-phosphate, D-glucose 6-phosphate) associated with glycolysis were down-regulated, which further confirmed that Cd exposure inhibited glycolysis in deep-sea mussels, as noted above. Previous research with the sea cucumber *Apostichopus japonicas* revealed that its glycolysis could be promoted in the initial phase of exposure to Cd, but then became inhibited as the duration of metal stress was prolonged. Inhibition effects tend to occur earlier if the exposure concentrations are higher (Li et al., 2016). In addition, we also detected isocitrate dehydrogenase (IDH) as commonly down-regulated in both Cd-exposure groups. IDH is an indispensable enzyme that regulates the citric acid cycle (TCA), catalyzing the conversion of isocitrate to oxalosuccinate and then to α-ketoglutarate (Satyanarayana, 2021). Thus the decreased IDH and glycolysis-associated proteins together suggests that Cd toxicity is able to impair the energy metabolism in deep-sea mussels.

Notably, we found disparate effects of Cd on the oxidative phosphorylation of deep-sea mussels in the different treatment groups. Linked to the mitochondrial electron transport chain (ETC), oxidative phosphorylation is the major source of ATP production that takes place in the mitochondria of aerobic organisms. In the low-dose group, the NADH dehydrogenase [ubiquinone] 1 alpha subcomplex subunit 5 (NDUFA5), which is responsible for converting NAD from reduced form (NADH) into oxidized form (NAD^+) during oxidative phosphorylation, was down-regulated relative to the control group. This reduction in NDUFA5 might have been caused by the reduced IDH activity in the TCA cycle. Metals can reportedly influence key enzymes such as IDH in the TCA cycle, leading to less generated NADPH and NADH, which can then negatively affect the normal function of ETC and ultimately lead to lower ATP production (Sun et al., 2022). In the high-dose group, however, we found that NDUFA5 was unaltered, but all the proteins associated with oxidative phosphorylation (mitochondrial ATP synthase subunit d precursor and V-type proton ATPase 16 kDa proteolipid subunit) were up-regulated and related to ATP synthase, implying an increased demand for ATP production in deep-sea mussels. Increased oxidative phosphorylation was reported in the rock fish *Sebastes schlegelii* under arsenic exposure and the mussel *Mytilus galloprovincialis* under nano-Ag exposure, both revealing a process of energetic re-adjustment to counteract the effects of arsenic toxicity (Gomes et al., 2013; Xu et al., 2019). In particular, to compensate for the diminished energy supply caused by the inhibition of glycolysis and the TCA, deep-sea mussels bolstered amino acid levels in their body to protect themselves from more damage caused by high-dose Cd exposure (Table 2). By serving as precursors for acetyl CoA and glucose synthesis, amino acids can also be degraded and utilized as energy sources in the body (Satyanarayana, 2021). Using metabolomics, a similar phenomenon has been extensively documented in marine bivalves when they are exposed to toxic chemicals (Viant et al., 2003; Zhou et al., 2021). Overall, our findings clearly show that Cd could alter mitochondrial metabolism and thereby risk impairment of ATP generation in deep-sea mussel gills. Collectively, these changes in energy metabolism coupled with a disordered cytoskeleton and lipid peroxidation would lead to stark physical changes in the membrane, affecting the respiratory, oxidative and calcium buffer capacity of mitochondria in gills of deep-sea mussels (Gomes et al., 2013).

4.6 Alteration of lipid and nucleotide metabolisms associated with Cd exposure

As the principal concentrated fuel reserve of organisms, lipids play important roles in maintaining cellular structure and regulating cellular metabolism (Satyanarayana, 2021). Alterations to lipid metabolism reportedly serve as protective strategies of organisms in response to environmental stress (Liu et al., 2016; Meng et al., 2018; Zhou et al., 2021). A metal exposure study using blue mussel *Mytilus edulis* demonstrated that Cd could significantly disturb its lipid metabolism by changing lipid structures and the fatty acid composition in mussels (Fokina et al., 2013). Furthermore, a metal exposure experiment with the crab *Chiromantes dehaani* showed that Cd could disturb lipid metabolism by weakening the ability of lipid digestion, transportation and synthase, thereby affecting the normal growth and development of that organism (Liu et al., 2016). Here, two proteins associated with lipid metabolism, phosphoethanolamine N-methyltransferase 3 isoform X1 and monoglyceride lipase-like isoform X1, were found uniquely up-regulated in low-dose group. Monoglyceride lipase catalyzes the final step of phospholipid and triglyceride breakdown by hydrolyzing monoacylglycerols into fatty acids and glycerol molecules (Aschauer et al., 2016). These products can be used for energy production or synthetic reactions. Hence, the up-regulated monoglyceride lipase-like isoform X1 is further evidence of a disturbed energy homeostasis in deep-sea mussels caused by Cd exposure. In plants, phosphoethanolamine N-methyltransferase has been suggested as one key bottleneck for the *de novo* synthesis of phosphatidylcholine, the chief component of plasma membrane phospholipids in most eukaryotes, which has been shown to be up-regulated under abiotic stress conditions (Jost et al., 2009). We also observed augmented levels of glycerophosphocholine in the metabolic profiles of mussels in the low-dose group. Glycerophosphocholines are critical components of biological membranes and contribute to lipid bilayer asymmetry. Therefore, those up-regulated proteins and metabolites in mussels of the low dose-Cd exposure group might together reflect an alteration of biological membranes. In the high dose-Cd exposure group, the phospholipase B1 membrane-associated-like was down-regulated exclusively. Phospholipase B1 (PLB1) can hydrolyze ester linkages on membrane phospholipids and liberate fatty acids (Chayakulkeeree et al., 2011). It is involved in membrane homeostasis and remodeling in fungi (Siafakas et al., 2007) and could be modulated under various environmental and physiological conditions (Mukherjee et al., 2003). As gleaned from the metabolic profiles, fatty acids including adrenic acid, cis-9-palmitoleic acid, and valeric acid were up- or down-regulated. One explanation for those altered proteins and metabolites is that deep-sea mussels may modify their cell membrane's composition in order to maintain/rebuild its stability and integrity. Another possibility is that Cd exposure resulted in damaged membranes of deep-sea mussels due to lipid peroxidation (He et al., 2020). Therefore, our results demonstrate that Cd has the potential to alter the membrane state of mussel gills, directly or indirectly, by disrupting membrane lipid biosynthesis and fatty acid composition.

Perturbed nucleotide metabolism is often reported in bivalves exposed to pollutants (Jones et al., 2008; Fasulo et al., 2012; Zhou et al., 2021). In the current study, a total of 21 nucleotides or their derivatives (Table 2) were found altered in mussels of high-dose group, with only two nucleotides changed in low-dose group, indicating dose-dependent toxicity effects of Cd. As structural components of DNA, RNA as well as many coenzymes, the availability of nucleotides underpins diverse metabolic reactions (Satyanarayana, 2021). Changed nucleotides profiles could be linked to neurotransmitter processes and cell signaling given that nucleosides (e.g., guanosine and adenosine), bases (e.g., guanine and adenine), and their metabolic products (e.g., xanthine and hypoxanthine) can be discharged into the extracellular space as intercellular signaling molecules (Rathbone et al., 1999). Apart from their function as signaling molecules, adenine and its analogues and inosine can also act as immunomodulatory molecules, exerting cellular protective and multiple anti-inflammatory effects in organisms (Haskó et al., 2000). That these purine metabolites increased in deep-sea mussels suggests their immune and inflammatory responses were enhanced under Cd exposure. Changing nucleotide profiles may also have contributed to peroxisome proliferation in rats (Ringeissen et al., 2003). As common oxidative organelles in eukaryotes, peroxisomes can function to protect the cell from toxic substances, contributing to the detoxification process of organisms. Thus, the increased levels of nucleotides identified in this study may point to elevated antioxidant enzyme activities and other catalytic activities during the metal detoxification process (Leonard et al., 2014).

4.7 Ion homeostasis associated with Cd exposure

Calcium binding proteins (CaBPs) have been identified as molecular targets for cadmium binding and cadmium toxicity. Due to the similarity between Cd^{2+} and Ca^{2+} in both structure and size, Cd^{2+} can not only enter cells *via* the Ca^{2+} uptake pathway but also compete with Ca^{2+} for the binding sites in CaBPs, in this way inhibiting the calcium influx of organisms (Choong et al., 2014), which can eventually affect cellular Ca^{2+} homeostasis. Here, CaBPs of the EF-Hand superfamily (EF-CaBPs) including calmodulin, calmodulin-like protein 4, EF-hand calcium-binding domain-containing protein 5-like isoform X1, EF-hand calcium-binding domain-containing protein 6-like isoform X2, and zinc finger ZZ-type and EF-hand domain-containing protein 1-like isoform X2, were all significantly altered in both Cd exposure groups. EF-CaBPs regulate all aspects of cellular calcium signaling pathways by binding to Ca^{2+}, including Ca^{2+} gating control, modulation of the amplitude and duration of Ca^{2+} signals, and transduction of Ca^{2+} signals into biochemical responses (Girard et al., 2015). Therefore, the abnormal expression of EF-CaBPs indicated that Ca^{2+}-triggered signaling could be involved in how deep-sea mussels overcome a metal challenge.

Deep-sea mussel gills are in direct contact with the ambient environment, and serve as an important organ for regulating cellular osmoregulation. We found that certain membrane transport proteins belonging to the solute carrier (SLC) family, such as sodium- and chloride-dependent taurine transporter-like in low-dose Cd-exposed group and sodium-dependent phosphate transport protein 2B-like isoform X1, phosphate carrier protein, and calcium-binding mitochondrial carrier protein SCaMC-2-like were significantly altered in high dose-Cd exposure group. Specifically, for these treated deep-sea mussels of high-dose group, the 16 kDa proteolipid (subunit c) of V-ATPase involved in translocating protons across lipid bilayers was significantly up-regulated. V-ATPase is capable of ensuring

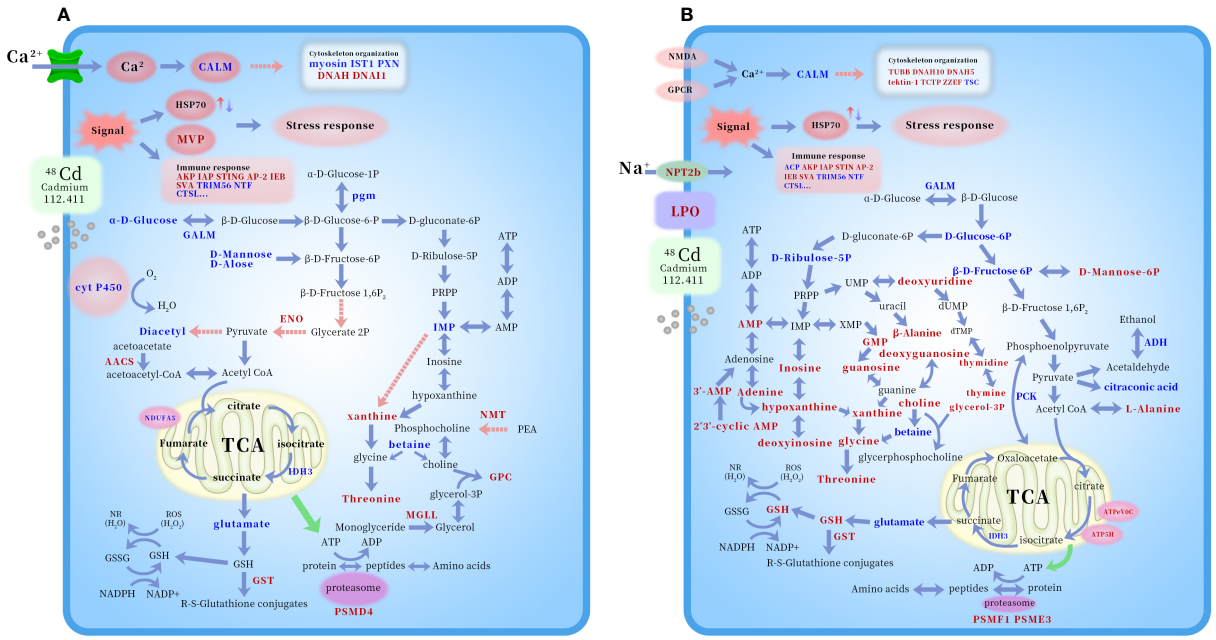

FIGURE 5
Potential mechanism schematic of Cd toxicology on deep-sea mussel *G. platifrons* according to KEGG (100μg/L Cd, A and 1000μg/L Cd, B). The altered proteins and metabolites were shown by marking the names in red (up-regulated) or blue (down-regulated) color. Abbreviations: ACP, acid phosphatase; AKP, alkaline phosphatase; IAP, baculoviral IAP repeat-containing protein 7-B isoform X3; STING, stimulator of interferon protein 2; AP-2, AP-2 complex subunit alpha-2-like; IEB, interleukin enhancer-binding factor 2 homolog; SVA, superkiller viralicidic activity 2-like 2; TRIM56, E3 ubiquitin-protein ligase TRIM56-like; NTF, nuclear transport factor 2-like; CTSL: shell fibrous prismatic cathepsin-like protein 1; Myosin, unconventional myosin-XVI-like isoform X10; IST1, IST1 homolog; PXN, leupaxin-like isoform X2; DNAH, dynein heavy chain 6, axonemal-like isoform X3; DNAI1, dynein intermediate chain 2, ciliary isoform X2; TUBB, tubulin beta chain-like; DNAH10, dynein heavy chain 10, axonemal-like isoform X2; DNAH5, dynein heavy chain 5, axonemal-like isoform X2; TCTP, translationally-controlled tumor protein homolog; ZZEF, zinc finger ZZ-type and EF-hand domain-containing protein 1-like isoform X2; TSC, tubulin-specific chaperone A; 3′-AMP, Adenosine 3′-AMP monophosphate; 2′,3′-cyclic AMP, Adenosine 2′,3′-cyclic monophosphate; D-Ribulose-5P, Ribulose 5′-phosphate; PRPP, phosphoribosyl diphosphate; ATP5H, mitochondrial ATP synthase subunit d precursor; ATPeV0C, V-type proton ATPase 16 kDa proteolipid subunit; IDH3, isocitrate dehydrogenase [NAD] subunit beta, mitochondrial-like; NDUFA5, NADH dehydrogenase [ubiquinone] 1 alpha subcomplex subunit 5; ADH, cinnamyl alcohol dehydrogenase 8-like isoform X2; GPC, Glycerophosphocholine; PEA, phosphoethanolamine; Cyt P450, cytochrome P450 2C31; GST, glutathione S-transferase; HSP70, heat-shock protein 70 family; CALM. Calmodulin; pgm, Phosphoglucomutase-1; GALM, aldose 1-epimerase isoform X1; ENO, enolase 4-like isoform X4; AACS, acetoacetyl-CoA synthetase-like; NMT, phosphoethanolamine N-methyltransferase 3 isoform X1; MGLL, monoglyceride lipase-like isoform X1; PCK, phosphoenolpyruvate carboxykinase, cytosolic [GTP] isoform X1; NMDA, glutamate receptor ionotropic; NPT2b, sodium-dependent phosphate transport protein 2B-like isoform X1; GPCR, 5-hydroxytryptamine receptor 7; PSMD4, 26S proteasome non-ATPase regulatory subunit 4-like; PSMF1, Proteasome inhibitor PI31 subunit; PSME3, proteasome activator complex subunit 3-like.

intracellular pH homeostasis, protecting cells against endogenous oxidative stress induced by divalent heavy metals, and inhibiting ROS production (Techo et al., 2020). Similar findings were found for the shrimp *Litopenaeus vannamei* under copper exposure (Guo et al., 2021). Meanwhile, the metabolic profiles of deep-sea mussels exposed to a high dose of Cd revealed that large amounts of amino acids were significantly induced. Previous research has shown that marine invertebrates such as deep-sea mussels can utilize intracellular amino acids to maintain their osmolality in balance with their surroundings (Zhou et al., 2021). Collectively then, the accumulated amino acids, dysregulated SLCs, and V-ATPase (subunit c) further suggest that Cd disturbed the ion exchange function of gills in the studied deep-sea mussel.

5 Conclusion

This study took a holistic perspective, incorporating both traditional approaches and 'omic' techniques to study the toxicological effects of Cd upon a keystone deep-sea bivalve *Gigantidas platifrons*. To do this, *G. platifrons* was exposed for 7 days to Cd at concentrations of 100 or 1000 μg/L, and metal accumulation, metal distribution in the subcellular compartments, anti-oxidative and immune-related biochemical parameters, and protein and metabolic profiles were evaluated as response variables. Under Cd exposure, the deep-sea mussel *G. platifrons* heavily accumulated Cd in its gills, where this Cd tended to bind to cellular debris other than MTLP, suggesting that MTLP might not be a major detoxification strategy in deep-sea bivalves. Parallel proteomic and metabolomics analyses revealed that the two doses of Cd evoked similar cellular responses, namely the elicitation of stress and immune responses and the disruption of the cytoskeleton structure, ion homeostasis, and primary metabolism processes in deep-sea mussels. A potential toxicological mechanism of Cd on deep-sea organisms is schematically illustrated in Figure 5. Overall, with deep-sea mining activities predicted to significantly impact marine ecosystems, the current results provide much-needed critical insights into how deep-sea organisms respond to metals as well as contributing to global information for identifying early responses of deep-sea organisms to metal pollution.

Data availability statement

The datasets presented in this study can be found in online repositories. The names of the repository/repositories and accession number(s) can be found in the article/Supplementary Material.

Author contributions

LZ contributed to conception, methodology, software, writing of the study. ML, ZZ, HC, and CL carried out the experiments. MW, HW, HZ, and LC organized the database. CLL directed the manuscriptrevision. All authors contributed to the article and approved the submitted version.

Funding

This research was financially supported by the National Key R&DProgram of China (2022YFC2804003), the Strategic Priority Research Program of the Chinese Academy of Sciences (grant number XDB42020401), the National Natural Science Foundation of China (grant number 42276153, 41906103, 41906124,42030407), the Key Research Program of Frontier Sciences, CAS (ZDBS-LY-DQC032), the Open Research Project of National Major Science & Technology Infrastructure (RV KEXUE) (grant number NMSTI-KEXUE2017K01).

Acknowledgments

The authors thank to Lingling Sun for metal analyzing.

Conflict of interest

The authors declare that the research was conducted in the absence of any commercial or financial relationships that could be construed as a potential conflict of interest.

Publisher's note

Supplementary material

The Supplementary Material for this article can be found online at: https://www.frontiersin.org/articles/10.3389/fmars.2023.1087411/full#supplementary-material

References

Aschauer, P., Rengachari, S., Lichtenegger, J., Schittmayer, M., Das, K. M. P., Mayer, N., et al. (2016). Crystal structure of the saccharomyces cerevisiae monoglyceride lipase Yju3p. *Biochim. Biophys. Acta (BBA) Mol Cell Biol. Lipids* 1861, 462–470. doi: 10.1016/j.bbalip.2016.02.005

Berger, W., Steiner, E., Grusch, M., Elbling, L., and Micksche, M. (2009). Vaults and the major vault protein: novel roles in signal pathway regulation and immunity. *Cell. Mol. Life Sci.* 66, 43–61. doi: 10.1007/s00018-008-8364-z

Boschen, R. E., Rowden, A. A., Clark, M. R., and Gardner, J. P. (2013). Mining of deep-sea seafloor massive sulfides: a review of the deposits, their benthic communities, impacts from mining, regulatory frameworks and management strategies. *Ocean Coast. Manage.* 84, 54–67. doi: 10.1016/j.ocecoaman.2013.07.005

Bougerol, M., Boutet, I., LeGuen, D., Jollivet, D., and Tanguy, A. (2015). Transcriptomic response of the hydrothermal mussel *Bathymodiolus azoricus* in experimental exposure to heavy metals is modulated by the pgm genotype and symbiont content. *Mar. Genomics* 21, 63–73. doi: 10.1016/j.margen.2014.11.010

Brown, A., Thatje, S., and Hauton, C. (2017a). The effects of temperature and hydrostatic pressure on metal toxicity: insights into toxicity in the deep sea. *Environ. Sci. Technol.* 51, 10222–10231. doi: 10.1021/acs.est.7b02988

Brown, A., Wright, R., Mevenkamp, L., and Hauton, C. (2017b). A comparative experimental approach to ecotoxicology in shallow-water and deep-sea holothurians suggests similar behavioural responses. *Aquat. Toxicol.* 191, 10–16. doi: 10.1016/j.aquatox.2017.06.028

Campos, A., Tedesco, S., Vasconcelos, V., and Cristobal, S. (2012). Proteomic research in bivalves: Towards the identification of molecular markers of aquatic pollution. *J. Proteomics* 75, 4346–4359. doi: 10.1016/j.jprot.2012.04.027

Canesi, L., Viarengo, A., Leonzio, C., Filippelli, M., and Gallo, G. (1999). Heavy metals and glutathione metabolism in mussel tissues. *Aquat. Toxicol.* 46, 67–76. doi: 10.1016/S0166-445X(98)00116-7

Carlsson, K.-H., and Gade, G. (1986). Metabolic adaptation of the horseshoe crab, *Limulus polyphemus*, during exercise and environmental hypoxia and subsequent recovery. *Biol. Bull.* 171, 217–235. doi: 10.2307/1541919

Chaudhary, R., Baranwal, V. K., Kumar, R., Sircar, D., and Chauhan, H. (2019). Genome-wide identification and expression analysis of Hsp70, Hsp90, and Hsp100 heat shock protein genes in barley under stress conditions and reproductive development. *Funct. Integr. Genomics* 19, 1007–1022. doi: 10.1007/s10142-019-00695-y

Chayakulkeeree, M., Johnston, S. A., Oei, J. B., Lev, S., Williamson, P. R., Wilson, C. F., et al. (2011). SEC14 is a specific requirement for secretion of phospholipase B1 and pathogenicity of cryptococcus neoformans. *Mol. Microbiol.* 80, 1088–1101. doi: 10.1111/j.1365-2958.2011.07632.x

Choong, G., Liu, Y., and Templeton, D. M. (2014). Interplay of calcium and cadmium in mediating cadmium toxicity. *Chemico Biol Interact.* 211, 54–65. doi: 10.1016/j.cbi.2014.01.007

Company, R., Antunez, O., Cosson, R. P., Serafim, A., Shillito, B., Cajaraville, M., et al. (2019). Protein expression profiles in *Bathymodiolus azoricus* exposed to cadmium. *Ecotoxicol Environ. Saf.* 171, 621–630. doi: 10.1016/j.ecoenv.2019.01.031

Company, R., Serafim, A., Cosson, R. P., Fiala-Medioni, A., Camus, L., Serrao-Santos, R., et al. (2010). Sub-Lethal effects of cadmium on the antioxidant defence system of the hydrothermal vent mussel *Bathymodiolus azoricus*. *Ecotoxicol Environ. Saf.* 73, 788–795. doi: 10.1016/j.ecoenv.2010.01.003

Dalle-Donne, I., Rossi, R., Milzani, A., Di Simplicio, P., and Colombo, R. (2001). The actin cytoskeleton response to oxidants: from small heat shock protein phosphorylation to changes in the redox state of actin itself. *Free Radical Biol. Med.* 31, 1624–1632. doi: 10.1016/S0891-5849(01)00749-3

del Rio, G. F. (2016). *Transcriptomic approach of the response to metals in the hydrothermal mussel bathymodiolus azoricus.* (Doctoral dissertation, Université Pierre et Marie Curie-Paris VI).

Ding, P., Xu, Y., Li, L., Lv, X., Li, L., Chen, J., et al. (2022). Intracellular complement C5a/C5aR1 stabilizes β-catenin to promote colorectal tumorigenesis. *Cell Rep.* 39, 110851. doi: 10.1016/j.celrep.2022.110851

Fasulo, S., Iacono, F., Cappello, T., Corsaro, C., Maisano, M., D'Agata, A., et al. (2012). Metabolomic investigation of *Mytilus galloprovincialis* (Lamarck 1819) caged in aquatic environments. *Ecotoxicol Environ. Saf.* 84, 139–146. doi: 10.1016/j.ecoenv.2012.07.001

Fletcher, D. A., and Mullins, R. D. (2010). Cell mechanics and the cytoskeleton. *Nature* 463, 485–492. doi: 10.1038/nature08908

Fokina, N. N., Ruokolainen, T. R., Nemova, N. N., and Bakhmet, I. N. (2013). Changes of blue mussels *Mytilus edulis l.* lipid composition under cadmium and copper toxic effect. *Biol. Trace Element Res.* 154, 217–225. doi: 10.1007/s12011-013-9727-3

Girard, F., Venail, J., Schwaller, B., and Celio, M. R. (2015). The EF-hand Ca^{2+}-binding protein super-family: a genome-wide analysis of gene expression patterns in the adult mouse brain. *Neuroscience* 294, 116–155. doi: 10.1016/j.neuroscience.2015.02.018

Gomes, T., Pereira, C. G., Cardoso, C., and Bebianno, M. J. (2013). Differential protein expression in mussels *Mytilus galloprovincialis* exposed to nano and ionic Ag. *Aquat. Toxicol.* 136, 79–90. doi: 10.1016/j.aquatox.2013.03.021

Goth, L. (1991). A simple method for determination of serum catalase activity and revision of reference range. *Clinica Chimica Acta* 196, 143–151. doi: 10.1016/0009-8981(91)90067-M

Guo, H., Chen, T., Liang, Z., Fan, L., Shen, Y., and Zhou, D. (2021). iTRAQ and PRM-based comparative proteomic profiling in gills of white shrimp litopenaeus vannamei under copper stress. *Chemosphere* 263, 128270. doi: 10.1016/j.chemosphere.2020.128270

Hardivillier, A., Leignel, V., Denis, F., Uguen, G., Cosson, R., and Laulier, M. (2004). Do organisms living around hydrothermal vent sites contain specific metallothioneins? the case of the genus bathymodiolus (Bivalvia, mytilidae). *Comp. Biochem. Physiol. C Toxicol Pharmacol.* 139, 111–118.

Haskó, G., Kuhel, D. G., Németh, Z. H., Mabley, J. G., Stachlewitz, R. F., Virág, L., et al. (2000). Inosine inhibits inflammatory cytokine production by a posttranscriptional mechanism and protects against endotoxin-induced shock. *J. Immunol.* 164, 1013–1019. doi: 10.4049/jimmunol.164.2.1013

Hauton, C., Brown, A., Thatje, S., Mestre, N. C., Bebianno, M. J., Martins, I., et al. (2017). Identifying toxic impacts of metals potentially released during deep-sea mining–a synthesis of the challenges to quantifying risk. *Front. Mar. Sci.* 4. doi: 10.3389/fmars.2017.00368

He, E. K., Qiu, R. L., Cao, X. D., Song, L., Peijnenburg, W. J. G. M., and Qiu, H. (2020). Elucidating toxicodynamic differences at the molecular scale between ZnO nanoparticles and $ZnCl_2$ in *Enchytraeus crypticus via* nontargeted metabolomics. *Environ. Sci. Technol.* 54, 3487–3498. doi: 10.1021/acs.est.0c00663

Hohagen, J., and Jackson, D. J. (2013). An ancient process in a modern mollusc: early development of the shell in *Lymnaea stagnalis*. *BMC Dev. Biol.* 13. doi: 10.1186/1471-213X-13-27

Hoher, N., Kohler, A., Strand, J., and Broeg, K. (2012). Effects of various pollutant mixtures on immune responses of the blue mussel (*Mytilus edulis*) collected at a salinity gradient in Danish coastal waters. *Mar. Environ. Res.* 75, 35–44. doi: 10.1016/j.marenvres.2011.11.003

Huang, W., Wang, X. H., Chen, D. Y., Xu, E. G., Luo, X., Zeng, J. N., et al. (2021). Toxicity mechanisms of polystyrene microplastics in marine mussels revealed by high-coverage quantitative metabolomics using chemical isotope labeling liquid chromatography mass spectrometry. *J. Hazard Mater* 417. doi: 10.1016/j.jhazmat.2021.126003

Jiang, H. X., Yang, H. M., Kong, X. H., Wang, S. P., Liu, D. Q., and Shi, S. J. (2012). Response of acid and alkaline phosphatase activities to copper exposure and recovery in freshwater fish *Carassius auratus gibelio* var. *Life Sci. J Acta Zhengzhou Univ. Overseas Edition* 9, 233–245.

Ji, C. L., Cao, L. L., and Li, F. (2015). Toxicological evaluation of two pedigrees of clam *Ruditapes philippinarum* as bioindicators of heavy metal contaminants using metabolomics. *Environ. Toxicol. Pharmacol.* 39, 545–554. doi: 10.1016/j.etap.2015.01.004

Jollow, D., Mitchell, J., Zampaglione, N. A., and Gillette, J. (1974). Bromobenzene-induced liver necrosis. protective role of glutathione and evidence for 3, 4-bromobenzene oxide as the hepatotoxic metabolite. *Pharmacology* 11, 151–169. doi: 10.1159/000136485

Jones, O. A. H., Dondero, F., Viarengo, A., and Griffin, J. L. (2008). Metabolic profiling of *Mytilus galloprovincialis* and its potential applications for pollution assessment. *Mar. Ecol. Prog. Ser.* 369, 169–179. doi: 10.3354/meps07654

Jost, R., Berkowitz, O., Shaw, J., and Masle, J. (2009). Biochemical characterization of two wheat phosphoethanolamine n-methyltransferase isoforms with different sensitivities to inhibition by phosphatidic acid. *J. Biol. Chem.* 284, 31962–31971. doi: 10.1074/jbc.M109.022657

Kim, B. H., and Schöffl, F. (2002). Interaction between arabidopsis heat shock transcription factor 1 and 70 kDa heat shock proteins. *J. Exp. Bot.* 53, 371–375. doi: 10.1093/jexbot/53.367.371

King, J. (1965). "The hydrolases-acid and alkaline phosphatases," in *Practical clinical enzymology*. Ed. J. King (London: Van Nostrand Company Ltd), 191–208.

Kohler, A., Wahl, E., and Soffker, K. (2002). Functional and morphological changes of lysosomes as prognostic biomarkers of toxic liver injury in a marine flatfish (*Platichthys flesus* (L.)). *Environ. Toxicol. Chem.* 21, 2434–2444. doi: 10.1002/etc.5620211124

Korobeĭnikova, E. N. (1989). Modification of the determination of lipid peroxidation products in a reaction with thiobarbituric acid. *Laboratornoe delo*, 8–10.

Lara, P. C., Pruschy, M., Zimmermann, M., and Henriquez-Hernandez, L. A. (2011). MVP and vaults: a role in the radiation response. *Radiat. Oncol.* 6. doi: 10.1186/1748-717X-6-148

Leonard, J. A., Cope, W. G., Barnhart, M. C., and Bringolf, R. B. (2014). Metabolomic, behavioral, and reproductive effects of the synthetic estrogen 17 alpha-ethinylestradiol on the unionid mussel *Lampsilis fasciola*. *Aquat. Toxicol.* 150, 103–116. doi: 10.1016/j.aquatox.2014.03.004

Liang, P., and MacRae, T. H. (1997). Molecular chaperones and the cytoskeleton. *J. Cell Sci.* 110, 1431–1440. doi: 10.1242/jcs.110.13.1431

Li, L., Tian, X., Yu, X., and Dong, S. (2016). Effects of acute and chronic heavy metal (Cu, cd, and zn) exposure on sea cucumbers (*Apostichopus japonicus*). *BioMed. Res. Int.* 2016.

Liu, Z. Q., Lv, W. W., Huang, Y. H., Fan, B., Li, Y. M., and Zhao, Y. L. (2016). Effects of cadmium on lipid metabolism in female estuarine crab, *Chiromantes dehaani*. *Comp. Biochem. Physiol. C Toxicol Pharmacol.* 188, 9–16.

Liu, J., Qu, W., and Kadiiska, M. B. (2009). Role of oxidative stress in cadmium toxicity and carcinogenesis. *Toxicol. Appl. Pharmacol.* 238, 209–214. doi: 10.1016/j.taap.2009.01.029

Li, Z. H., Zlabek, V., Velisek, J., Grabic, R., Machova, J., Kolarova, J., et al. (2011). Acute toxicity of carbamazepine to juvenile rainbow trout (Oncorhynchus mykiss): Effects on antioxidant responses, hematological parameters and hepatic EROD. *Ecotoxicol Environ. Saf.* 74, 319–327. doi: 10.1016/j.ecoenv.2010.09.008

Lovett, D. L., Towle, D. W., and Faris, J. E. (1994). Salinity sensitive alkaline-phosphatase activity in gills of the blue crab, *Callinectes sapidus* rathbun. *Comp. Biochem. Physiol. B Biochem Mol. Biol.* 109, 163–173.

Lucu, Č., and Obersnel, V. (1996). Cadmium influx across isolated carcinus gill epithelium interaction of lanthanum and calcium with cadmium influxes. *J. Comp. Physiol. B* 166, 184–189. doi: 10.1007/BF00263981

Martins, I., Goulart, J., Martins, E., Morales-Román, R., Marín, S., Riou, V., et al. (2017). Physiological impacts of acute Cu exposure on deep-sea vent mussel *Bathymodiolus azoricus* under a deep-sea mining activity scenario. *Aquat. Toxicol.* 193, 40–49. doi: 10.1016/j.aquatox.2017.10.004

Ma, L., and Wang, W.-X. (2020). Subcellular metal distribution in two deep-sea mollusks: Insight of metal adaptation and detoxification near hydrothermal vents. *Environ. pollut.* 266, 115303. doi: 10.1016/j.envpol.2020.115303

Mazorra, M. T., Rubio, J. A., and Blasco, J. (2002). Acid and alkaline phosphatase activities in the clam *Scrobicularia plana*: kinetic characteristics and effects of heavy metals. *Comp. Biochem. Physiol. Part B: Biochem. Mol. Biol.* 131, 241–249.

McCord, J. M., and Fridovich, I. (1969). Superoxide dismutase an enzymic function for erythrocuprein (hemocuprein). *J. Biol. Chem.* 244, 6049–6055. doi: 10.1016/S0021-9258(18)63504-5

McDonagh, B., and Sheehan, D. (2006). Redox proteomics in the blue mussel *Mytilus edulis*: carbonylation is not a pre-requisite for ubiquitination in acute free radical-mediated oxidative stress. *Aquat. Toxicol.* 79, 325–333. doi: 10.1016/j.aquatox.2006.06.020

McKnight, K. L., Swanson, K. V., Austgen, K., Richards, C., Mitchell, J. K., McGivern, D. R., et al. (2020). Stimulator of interferon genes (STING) is an essential proviral host factor for human rhinovirus species a and c. *Proc. Natl. Acad. Sci. U.S.A.* 117, 27598–27607. doi: 10.1073/pnas.2014940117

Meng, X.-L., Li, S., Qin, C.-B., Zhu, Z.-X., Hu, W.-P., Yang, L.-P., et al. (2018). Intestinal microbiota and lipid metabolism responses in the common carp (*Cyprinus carpio* l.) following copper exposure. *Ecotoxicol Environ. Saf.* 160, 257–264. doi: 10.1016/j.ecoenv.2018.05.050

Mestre, N., Auguste, M., De Sá, L., Fonseca, T., Cardoso, C., Brown, A., et al. (2019). Are shallow-water shrimps proxies for hydrothermal-vent shrimps to assess the impact of deep-sea mining? *Mar. Environ. Res.* 151, 104771.

Moore, M. N. (1994). *Reactions of molluscan lysosomes as biomarkers of pollutant-induced cell injury. contaminants in the environment. a multidiscplinary assessment of risks to man and other organisms* (Boca Raton: CRC Press, Lewis Publishers), 111–123.

Mukherjee, P. K., Chandra, J., Kuhn, D. M., and Ghannoum, M. A. (2003). Differential expression of *Candida albicans* phospholipase b (PLB1) under various environmental and physiological conditions. *Microbiology-Sgm* 149, 261–267. doi: 10.1099/mic.0.25829-0

Pampanin, D. M., Ballarin, L., Carotenuto, L., and Marin, M. G. (2002). Air exposure and functionality of *Chamelea gallina* haemocytes: effects on haematocrit, adhesion, phagocytosis and enzyme contents (vol 131, pg 605, 2002). *Comp. Biochem. Physiol. A Mol Integr. Physiol.* 133, 199–199. doi: 10.1016/S1095-6433(02)00114-9

Pan, K., and Wang, W. X. (2008). The subcellular fate of cadmium and zinc in the scallop *Chlamys nobilis* during waterborne and dietary metal exposure. *Aquat. Toxicol.* 90, 253–260. doi: 10.1016/j.aquatox.2008.09.010

Pinheiro, M., Oliveira, A., Barros, S., Alves, N., Raimundo, J., Caetano, M., et al. (2021). Functional, biochemical and molecular impact of sediment plumes from deep-sea mining on *Mytilus galloprovincialis* under hyperbaric conditions. *Environ. Res.* 195, 110753. doi: 10.1016/j.envres.2021.110753

Pruski, A. M., and Dixon, D. R. (2007). Heat shock protein expression pattern (HSP70) in the hydrothermal vent mussel *Bathymodiolus azoricus*. *Mar. Environ. Res.* 64, 209–224. doi: 10.1016/j.marenvres.2007.01.003

Rathbone, M. P., Middlemiss, P. J., Gysbers, J. W., Andrew, C., Herman, M. A. R., Reed, J. K., et al. (1999). Trophic effects of purines in neurons and glial cells. *Prog. Neurobiol.* 59, 663–690. doi: 10.1016/S0301-0082(99)00017-9

Revel, M., Lagarde, F., Perrein-Ettajani, H., Bruneau, M., Akcha, F., Sussarellu, R., et al. (2019). Tissue-specific biomarker responses in the blue mussel mytilus spp. exposed to a mixture of microplastics at environmentally relevant concentrations. *Front. Environ. Sci.* 7.

Ringeissen, S., Connor, S. C., Brown, H. R., Sweatman, B. C., Hodson, M. P., Kenny, S. P., et al. (2003). Potential urinary and plasma biomarkers of peroxisome proliferation in the rat: identification of n-methylnicotinamide and n-methyl-4-pyridone-3-carboxamide by ^{1}H nuclear magnetic resonance and high performance liquid chromatography. *Biomarkers* 8, 240–271. doi: 10.1080/1354750031000149124

Sanchez, B. C., Ralston-Hooper, K., and Sepulveda, M. S. (2011). Review of rRecent proteomic applications in aquatic toxicology. *Environ. Toxicol. Chem.* 30, 274–282. doi: 10.1002/etc.402

Satyanarayana, U. (2021). *Biochemistry, 6e-e-book* (Netherlands, Elsevier Health Sciences).

Siafakas, A. R., Sorrell, T. C., Wright, L. C., Wilson, C., Larsen, M., Boadle, R., et al. (2007). Cell wall-linked cryptococcal phospholipase B1 is a source of secreted enzyme and a determinant of cell wall integrity. *J. Biol. Chem.* 282, 37508–37514. doi: 10.1074/jbc.M707913200

Sokolova, I. M., Frederich, M., Bagwe, R., Lannig, G., and Sukhotin, A. A. (2012). Energy homeostasis as an integrative tool for assessing limits of environmental stress

tolerance in aquatic invertebrates. *Mar. Environ. Res.* 79, 1–15. doi: 10.1016/j.marenvres.2012.04.003

Sun, Q. Y., Li, Y., Shi, L. J., Hussain, R., Mehmood, K., Tang, Z. X., et al. (2022). Heavy metals induced mitochondrial dysfunction in animals: Molecular mechanism of toxicity. *Toxicology* 469, 153136. doi: 10.1016/j.tox.2022.153136

Sun, Y., Liu, Y., Yu, X. B., Wang, T., Wang, Q., Yao, W. Z., et al. (2021). Combined effects of ration levels and temperature on immune responses of the triangle sail mussel *Hyriopsis cumingii*. *Aquacult Res Toxicology*. 469, 153136.

Techo, T., Jindarungrueng, S., Tatip, S., Limcharoensuk, T., Pokethitiyook, P., Kruatrachue, M., et al. (2020). Vacuolar h^+-ATPase is involved in preventing heavy metal-induced oxidative stress in saccharomyces cerevisiae. *Environ. Microbiol.* 22, 2403–2418. doi: 10.1111/1462-2920.15022

Tomanek, L. (2011). Environmental proteomics: changes in the proteome of marine organisms in response to environmental stress, pollutants, infection, symbiosis, and development. *Ann. Rev. Mar. Sci.* 3, 373–399. doi: 10.1146/annurev-marine-120709-142729

Tsuchida, T., Zou, J. A., Saitoh, T., Kumar, H., Abe, T., Matsuura, Y., et al. (2010). The ubiquitin ligase TRIM56 regulates innate immune responses to intracellular double-stranded DNA. *Immunity* 33, 765–776. doi: 10.1016/j.immuni.2010.10.013

Valko, M., Morris, H., and Cronin, M. T. D. (2005). Metals, toxicity and oxidative stress. *Curr. Medicinal Chem.* 12, 1161–1208. doi: 10.2174/0929867053764635

Venier, P., Varotto, L., Rosani, U., Millino, C., Celegato, B., Bernante, F., et al. (2011). Insights into the innate immunity of the Mediterranean mussel *Mytilus galloprovincialis*. *BMC Genomics* 12. doi: 10.1186/1471-2164-12-69

Viant, M. R., Rosenblum, E. S., and Tjeerdema, R. S. (2003). NMR-based metabolomics: a powerful approach for characterizing the effects of environmental stressors on organism health. *Environ. Sci. Technol.* 37, 4982–4989. doi: 10.1021/es034281x

Wallace, W. G., Lee, B. G., and Luoma, S. N. (2003). Subcellular compartmentalization of cd and zn in two bivalves. i. significance of metal-sensitive fractions (MSF) and biologically detoxified metal (BDM). *Mar. Ecol. Prog. Ser.* 249, 183–197. doi: 10.3354/meps249183

Wallace, W. G., and Luoma, S. N. (2003). Subcellular compartmentalization of cd and zn in two bivalves. II. significance of trophically available metal (TAM). *Mar. Ecol. Prog. Ser.* 257, 125–137. doi: 10.3354/meps257125

Wong, Y. H., Sun, J., He, L. S., Chen, L. G., Qiu, J. W., and Qian, P. Y. (2015). High-throughput transcriptome sequencing of the cold seep mussel *Bathymodiolus platifrons*. *Sci. Rep.* 5, 16597. doi: 10.1038/srep16597

Xu, L., Ji, C., Wu, H., Tan, Q., and Wang, W.-X. (2016). A comparative proteomic study on the effects of metal pollution in oysters *Crassostrea hongkongensis*. *Mar. pollut. Bull.* 112, 436–442. doi: 10.1016/j.marpolbul.2016.07.009

Xu, L. L., Lu, Z., Ji, C. L., Cong, M., Li, F., Shan, X. J., et al. (2019). Toxicological effects of as (V) in juvenile rockfish *Sebastes schlegelii* by a combined metabolomic and proteomic approach. *Environ. pollut.* 255. doi: 10.1016/j.envpol.2019.113333

Yang, B. B., Lin, S. H., Li, B., Wei, Z., Li, Q. Q., Shen, X. L., et al. (2022). Interleukin enhancer binding factor 2 (IEBF 2) was involved in the regulation of the antibacterial immune reactions in fresh water crayfish, *Procambarus clarkii*. *Dev. Comp. Immunol.* 126. doi: 10.1016/j.dci.2021.104226

Yu, X. J., Pan, K., Liu, F. J., Yan, Y., and Wang, W. X. (2013). Spatial variation and subcellular binding of metals in oysters from a large estuary in China. *Mar. pollut. Bull.* 70, 274–280. doi: 10.1016/j.marpolbul.2013.02.036

Yusof, N. A., Masnoddin, M., Charles, J., Thien, Y. Q., Nasib, F. N., Wong, C. M. V. L., et al. (2022). Can heat shock protein 70 (HSP70) serve as biomarkers in Antarctica for future ocean acidification, warming and salinity stress? *Polar Biol.*, 1–24.

Zeng, Z. (2011). *Submarine hydrothermal geology (in Chinese)* (Beijing: Science Press).

Zhang, J., Li, H., Qin, Y., Ye, S., and Liu, M. (2016). Identification of functional genes involved in Cd^{2+} response of Chinese surf clam (*Mactra chinensis*) through transcriptome sequencing. *Environ. Toxicol. Pharmacol.* 41, 113–120. doi: 10.1016/j.etap.2015.11.006

Zhang, H., You, Q. D., and Xu, X. L. (2020). Targeting stimulator of interferon genes (STING): A medicinal chemistry perspective. *J. Medicinal Chem.* 63, 3785–3816. doi: 10.1021/acs.jmedchem.9b01039

Zhou, L., Cao, L., Wang, X., Wang, M., Wang, H., Zhong, Z., et al. (2020). Metal adaptation strategies of deep-sea bathymodiolus mussels from a cold seep and three hydrothermal vents in the West pacific. *Sci. Total Environ.* 707, 136046. doi: 10.1016/j.scitotenv.2019.136046

Zhou, L., Li, M., Zhong, Z., Chen, H., Wang, X., Wang, M., et al. (2021). Biochemical and metabolic responses of the deep-sea mussel *Bathymodiolus platifrons* to cadmium and copper exposure. *Aquat. Toxicol.*, 10584. doi: 10.1016/j.aquatox.2021.105845

frontiers | Frontiers in Marine Science

TYPE Original Research
PUBLISHED 23 January 2023
DOI 10.3389/fmars.2023.1068916

OPEN ACCESS

EDITED BY
Elva G. Escobar-Briones,
National Autonomous University of Mexico, Mexico

REVIEWED BY
Zhilei Sun,
Qingdao Institute of Marine Geology (QIMG), China
Xiaoshou Liu,
Ocean University of China, China

*CORRESPONDENCE
Chaolun Li
lcl@qdio.ac.cn

SPECIALTY SECTION
This article was submitted to Deep-Sea Environments and Ecology, a section of the journal Frontiers in Marine Science

RECEIVED 13 October 2022
ACCEPTED 09 January 2023
PUBLISHED 23 January 2023

CITATION
Wang H, Wang X, Cao L, Zhong Z, Luan Z and Li C (2023) Macrofauna community of the cold seep area at Site F, South China Sea.
Front. Mar. Sci. 10:1068916.
doi: 10.3389/fmars.2023.1068916

Macrofauna community of the cold seep area at Site F, South China Sea

Haining Wang[1,2,3], Xiaocheng Wang[2], Lei Cao[3], Zhaoshan Zhong[3], Zhendong Luan[3,4,5] and Chaolun Li[1,3,4]*

[1]Key Laboratory of Marine Ecology and Environmental Sciences, Institute of Oceanology, Chinese, Academy of Sciences, Qingdao, China, [2]National Marine Environmental Monitoring Center, Dalian, China, [3]Deep Sea Research Center, Institute of Oceanology, Chinese Academy of Sciences, Qingdao, China, [4]Center for Ocean Mega-Science, Chinese Academy of Sciences, Qingdao, China, [5]Key Laboratory of Marine Geology and Environment, Institute of Oceanology, Chinese Academy of Sciences, Qingdao, China

A cold seep is one of the typical deep-sea chemical energy ecosystems and a hotspot for studying unique life processes and biogeochemical cycles in the deep sea. Macrofauna, which is one of the most important components of the cold seep ecosystem, has not been thoroughly studied. We examined the macrofauna community at Site F using images collected in 2016 by an imaging and laser profiling system and biological samples collected in 2020 and 2021 by TV grab and a remotely operated vehicle. In total, 41 species were found. The overall number of macrofauna identified at Site F (20,000 m^2) reached 252,943 individuals, and the biomass reached 726.15 kg by dry weight. As the dominant species, *Gigantidas platifrons* and *Shinkaia crosnieri* reached their highest densities of 629 and 396 individuals/m^2, respectively. The comparisons between different stations revealed that the diversity and density, even the biomass of dominant species, were much higher in the south than in the north at Site F in 2020. Correlation analysis showed that methane had a positive effect on macrofauna density. Compared with *S. crosnieri*, *G. platifrons* seems to be more adapted to the harsh cold seep environment. Methane consumption rates of the dominant species show that macrofauna are important in influencing seafloor methane fluxes. Our findings provide valuable insights into the ecology, community structure, and biota-environment interaction in the cold seep at Site F.

KEYWORDS

macrofauna, cold seep, density, body length, distribution, methane consumption

1 Introduction

Cold seeps are environments where emissions of methane, sulfide, or other reduced chemicals occur from the seafloor at near-ambient temperatures (Vanreusel et al., 2009; Levin et al., 2016). They are commonly called "oases" because they contain a large number of symbiont-bearing invertebrates (Laubier, 1993; Carney, 1994). These invertebrate communities are found at seeps on active and passive continental margins throughout the

world's oceans (Sibuet and Olu, 1998; Cordes et al., 2009). In general, seeps that support many chemosynthetic organisms (Levin, 2005; Cordes et al., 2010), such as symbiont-containing bathymodiolin mussels or vestimentiferan tubeworms, often host communities with high abundances and biomass but low diversity compared to surrounding non-seep habitats (Menot et al., 2010). Meanwhile, some non-symbiotic macrobenthos and vagrants are also attracted by the cold seeps because of their high food availability and habitat heterogeneity (Levin et al., 2016; Zhao et al., 2020). The macrofauna inhabiting cold seeps are distinct from those in other areas of the deep sea, and so they should be recognized as a distinct component of biodiversity and protected (Levin et al., 2016; Amon et al., 2017). As one of the most investigated components of the cold seep ecosystem, macrofauna have great ecological importance and obvious significance. Some of them are considered ecosystem engineers because they influence the sediment environment by providing physical structure and modulating geochemistry through oxygenation (pumping) and ion uptake activities (Levin, 2005). However, these macrofauna have not been thoroughly studied, and little is known about their numbers, habitats, and relationships with surrounding environments. As a critical tool for promoting sustainable management of marine resources, habitat mapping of these macrofauna at seeps plays an important role (Cochrane and Lafferty, 2002; Degraer et al., 2008). Therefore, it is essential to comprehensively describe the species, density, biomass, and so on of macrofauna at cold seeps. However, because of the high heterogeneity of cold seeps, it is difficult to obtain complete information in a traditional way (Levin et al., 2000; Wang et al., 2021). With the development of camera and video technologies, imaging technologies have become the obvious method to characterize these communities and have proven helpful in dense habitats (Sen et al., 2016).

The Formosa Ridge is located on the northern continental margin of the South China Sea, offshore of southwestern Taiwan (Figure 1). Exposed gas hydrates on the seafloor were found in this area (Zhang et al., 2017). Site F, located on the Formosa Ridge, was first recognized as an active cold seep in 2007 (Lin et al., 2007). Previous studies have focused on geological and biogeochemical backgrounds (Feng et al., 2015; Zhang et al., 2017; Wang et al., 2018; Cao et al., 2021), where epifauna were collected and identified (Li, 2015; Li, 2017; Zhao et al., 2020). For example, Cao et al. (2021) identified the chemical gradients (mainly methane and oxygen) from the flourishing center to the periphery of Site F. However, there have been fewer studies on spatial distribution and density until a transect survey was conducted by a remotely operated vehicle (ROV) in 2018 (Zhao et al., 2020). This study showed the highest densities of dominant species such as *G. platifrons* and *S. crosnieri* could reach 273 and 300 individuals/m^2, respectively. The similarity between the macrobenthos in the South China Sea cold seeps and the Okinawa Trough hydrothermal vents indicated a high degree of connectivity. Despite this, the total quantity, biomass, and distribution of macrofauna, in addition to the interaction between the environment and biota at the entire Site F are not well documented. Otherwise, few studies have systematically and exhaustively examined the macrofauna community at cold seeps.

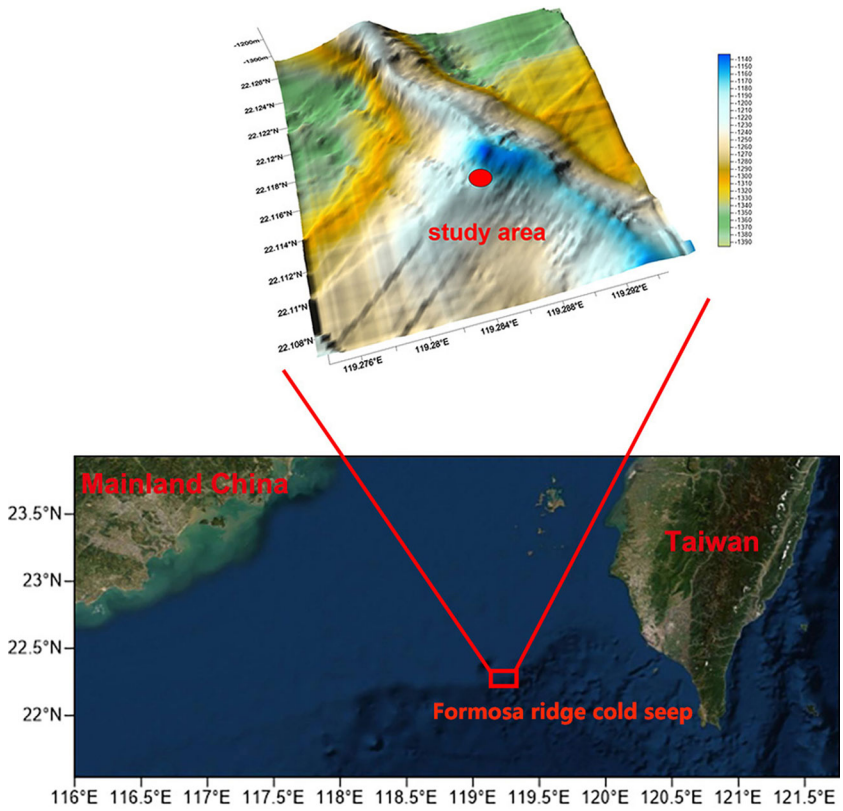

FIGURE 1
Location of the cold seep sites surveyed at Formosa ridge. Topographic map shows the tectonic features. The study area is delimited by the red dot.

For example, quantitative mosaics and videos collected by laser line-scan, multibeam backscatter, and bathymetry, together with video records and other methods, were used to map the habitats and species distributions of cold seeps because of the high habitat heterogeneity (MacDonald et al., 2003; Sen et al., 2016). Astrom et al. (2018) used photographs to examine the diversity, abundance, and biomass of infaunal communities at high-Arctic cold seeps. Alternatively, seafloor images were also used by Sen et al. (2019) to compare the megafauna community between seep and non-seep background sites at the Svanefjell seep. However, it is still a challenge to completely describe the biodiversity, spatial distribution, and interannual variation of cold seep macrofauna communities.

Because the understanding of biomass, spatial distribution, and the controlled factors of macrofauna is the basis for further understanding the cold seep ecosystem, we examined macrofauna communities at Site F through analyses of images and biological samples in 2016, 2020, and 2021. An imaging and laser profiling system was used to collect images, and a TV grab and an ROV were used to collect biological samples . Our goal was to show the density, biomass, and distribution of macrofauna throughout the site to the greatest degree possible. This will be truly helpful for understanding the community structure of Site F. The length-weight relationships and distribution of body length for the dominant species *G. platifrons* and *S. crosnieri* are useful in comparing the growth of these two species in different areas and at different times. Geochemical measurements were used to gain an understanding of how abiotic features relate to the macrofauna communities.

2 Materials and methods

2.1 Image collection and analysis

The R.V. *Kexue* conducted a photographic survey of the Formosa Ridge during a research cruise in 2016 . *Faxian*, an ROV equipped with an L1000 imaging and laser profiling system which was designed and supplied by Cathx Ocean Ltd., was used to obtain all images. This system was equipped with a still camera, two LED lights with outputs of 7,000 and 28,000 lumens, and two green line lasers. All original images associated with geographic coordinates were captured at a rate of nine frames per second. The mosaic was pieced together using these coordinates and the same object identifier in adjacent images (Figure 2) (Wang et al., 2019). PTGui software was used for the initial splice, and Adobe Photoshop was used for the subsequent image optimization. Then, for statistical convenience, the mosaic was divided uniformly by 200 x 200 tiles (19,516 small pictures with an area of about 1 m^2, except the blank). All visible macrofauna in the mosaic were counted and identified to the lowest taxonomic level possible. To compare the spatial distribution and density of macrofauna, the whole cold seep area was divided into a 10 m by 10 m grid. Geographic information and the density of macrofauna in each grid were used to perform cluster analysis to verify the similar occurrence of macrofauna. Meanwhile, a non-metric multidimensional scaling (NMDS) approach was used to compare the similarity between different groups. All these analyses were performed using Primer v.6. To calculate the mean body length in each grid, 20 to 50 individuals of the dominant species (*G. platifrons* and *S. crosnieri*) were chosen at random.

2.2 Sample collection and environmental detections

To compare the spatial difference and interannual variation of macrofauna (compared to the 2016 data, mainly from the south and north of Site F), TV grab operations (including GA, GB, and GC monitored twice at each station) were taken by the R.V. *Kexue* at Site F in 2020. All macrofauna collected by TV grab were counted. The Shannon–Weiner index was calculated to compare the species diversity at different stations. Meanwhile, environmental factors at each station were also identified. Benthic environmental variables (methane and dissolved oxygen) were measured by the Seabird SBE 43 dissolved oxygen sensor (DO) (Sea-Bird Electronics, Inc., Washington, USA) and the CONTROS HydroC® CH_4 sensor (Kongsberg Gruppen, Norway) installed in the ROV tool sled (Cao et al., 2021). The manipulator arm performed every *in situ* detection as it approached the target sites. Pearson correlation analysis was used to identify correlations between environmental factors (methane and DO) and the dominant species.

2.3 Biomass measurement

The body length and weight (wet and dry) of *G. platifrons* and *S. crosnieri* were measured in 50 specimens, respectively, to model the

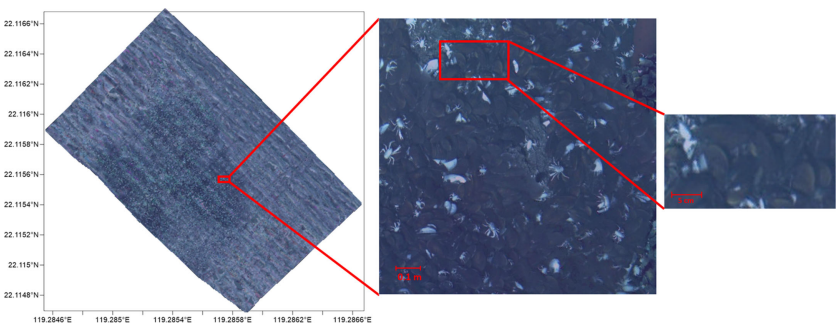

FIGURE 2
Mosaic (20,000 m^2) of the seep community at Site F cold seep in 2016; two high-resolution images used to identify macrofauna are shown in the inset. The outline represents the area where images were obtained.

relationship between length and weight. Dry weights were measured after at least 48 hours in a freeze dryer. For *G. platifrons*, the dry weight was calculated only after the shell was removed. For *S. crosnieri*, the shell length of the head and the whole-body length were all recorded. Because of the inconvenient measurement, the whole-body length appears worse in modeling. So, the shell lengths of the head were used as the body length of *S. crosnieri*. These data were used to model the following standard equation:

$$W = aL^b$$

where W is the weight (g) and L is the body length (or the shell, for *G. platifrons*), measured with a vernier caliper, in mm.

2.4 The methane consumption of the dominant species

To assess the metabolism in the *G. flatirons* community, the relationship between oxygen consumption and body weight of mytilids was determined according to this equation (Khripounoff et al., 2017):

$$R = 21.2 \times W^{-0.19}$$

where R is the oxygen consumption, and W is the dry body weight of *G. platifrons*. W is calculated by the equation given in Section 2.3. L is the mean body length of *G. platifrons* measured from the mosaic. The methane consumption of *G. platifrons* was calculated by the relationship in metabolic gas flux (per mol CH_4 consumed, the *G. platifrons* consumed ~1.2 mol O_2) (Kochevar et al., 1992). Meanwhile, the mean methane consumption rate (1.98 μmol/h) of *S. crosnieri* as estimated by Watsuji et al. (2014) at 12.0 MPa was used.

3 Results

3.1 Background environments

Methane concentrations at Site F varied quickly and were unstable, ranging from 237.25 ppm to 15,000 ppm with a mean of 4120.88 ppm (Supplementary Table 1). The variation in concentration of dissolved oxygen was relatively smaller, ranging from 2.89 mg/L to 3.16 mg/L with a mean of 3.07 mg/L. The substrates at Site F contained hard (central authigenic carbonates) and soft (peripheral muddy) sea bottoms. Large mussel beds, lobster clusters, and shell debris were found on hard substrates formed by authigenic carbonates (Figure 2). In addition to authigenic carbonates, there was a large, soft argillaceous environment, including reduced sediments and muddy sea bottoms.

3.2 Species composition and density

In this survey, 41 species or categories, including Mollusca (12), Porifera (3), Annelida (9), Echinodermata (4), Arthropoda (9), Cnidaria (3), and Vertebrata (1) were found in the mosaic and TV grabs. There were 34 taxa identified as species or genera, and others were the higher taxa (Supplementary Table 2). There were 17 categories collected or identified through this method, including Cnidaria (*Anthomastus* sp., *Caryophyllia* sp., and *Alvinactis* sp.), Mollusca (*Conchocele bisecta*, *Solemya* sp., *Enigmaticolus inflatus* sp. nov., cf. *Abyssochrysos* sp., and *Chaetoderma* sp.), Arthropoda (*Lysianassoidea* sp., and *Pleurocryptella fimbriata*), Annelida (*Lepidonotopodium* sp., *Branchinotogluma* sp., *Lamellibrachia* sp., *Glycera* sp., *Nereis* sp., and *Capitellidae* sp.), and Enteropneusta (cf. *Balanoglossus*) . Among them, there were 10 newly recorded species.

The quantity of macrofauna in the whole mosaic (20,000 m^2) reached as high as 252,943 individuals. *G. platifrons* and *S. crosnieri* were the dominant species at Site F, with 215,339 and 37,422 individuals, respectively. Clustering analysis revealed a 77.5% similarity between the four groups ($r = 0.995$, $P < 0.01$) and was used to verify the similarity of macrofauna occurrence in each grid (Figure 3A, B). The densities (individuals/100 m^2) of Groups 1 through 4 were as follows: Group 1, 3,584–17,806; Group 2, 1,075–3,108; Group 3, 106–815; and Group 4, 0–133. According to the spatial distribution of each grid at the cold seep in Site F, we discovered a pattern of patchy distribution of macrofauna in which the most abundant areas (Group 1) were concentrated in the center of the entire site , followed by Groups 2, 3, and 4 (Figure 3C).

The density of macrofauna at Site F was greater than that of the surrounding seabed, especially for dominant species. *G. platifrons* and *S. crosnieri* reached their highest densities of 560 and 396 individuals/m^2, respectively. Their density distributions in every grid are shown in Figure 4. *G. platifrons* mostly covered a large area and had the highest population density in the north, while *S. crosnieri* was not widely distributed and had the highest population density in the south (Figure 4). These locations, which had a dense population of the dominant species, possessed visibly active seepages (such as the release of strings of bubbles from the seabed). In contrast, areas without any sign of seepage, such as shell debris and exposed carbonate rocks, had a relatively lower density of the dominant species. In comparison with *G. platifrons* and *S. crosnieri*, the abundance of *Munidopsis* sp. at these locations was not high, with 861 individuals and a maximum density of 45 individuals/m^2. Other macrofauna densities in the mosaic were considerably lower than those of *G. platifrons* and *S. crosnieri*. *Lithodes longispina*, *Ophidiidae* sp., *Benthesicymus* sp., and *Henricia* sp. Populations reached 103, 55, 23, and 19 individuals/m^2, respectively. In the meantime, the dominant species collected by TV grab in 2020 were counted to calculate the species density (Supplementary Table 1). TV grab collections showed that the highest densities of *G. platifrons*, *Histampica* sp., *Bathyacmaea lactea*, *Phymorhynchus buccinoides*, and *Provanna glabra* reached 629, 28, 56, 17, and 78 individuals/m^2, respectively. The grabs in three stations showed that *G. platifrons* in GA (356 individuals/m^2) and GB (336 and 330 individuals/m^2) were similar in density, while *S. crosnieri* in GB (29 and 129 individuals/m^2) was higher than GA (25 individuals/m^2). Compared with GA and GB, the densities of *G. platifrons* (289 and 629 individuals/m^2) and *S. crosnieri* (225 and 271 individuals/m^2) in GC were relatively high. The Shannon–Weiner index of GC (1.15) was the highest, followed by GB (0.66) and GA (0.49).

To assess the biomass of the dominant species, we calculated its wet and dry weight. For *G. platifrons*, flesh wet weight accounted for 20.78 ± 30.37% of total weight. Flesh dry weight accounted for 3.98 ±

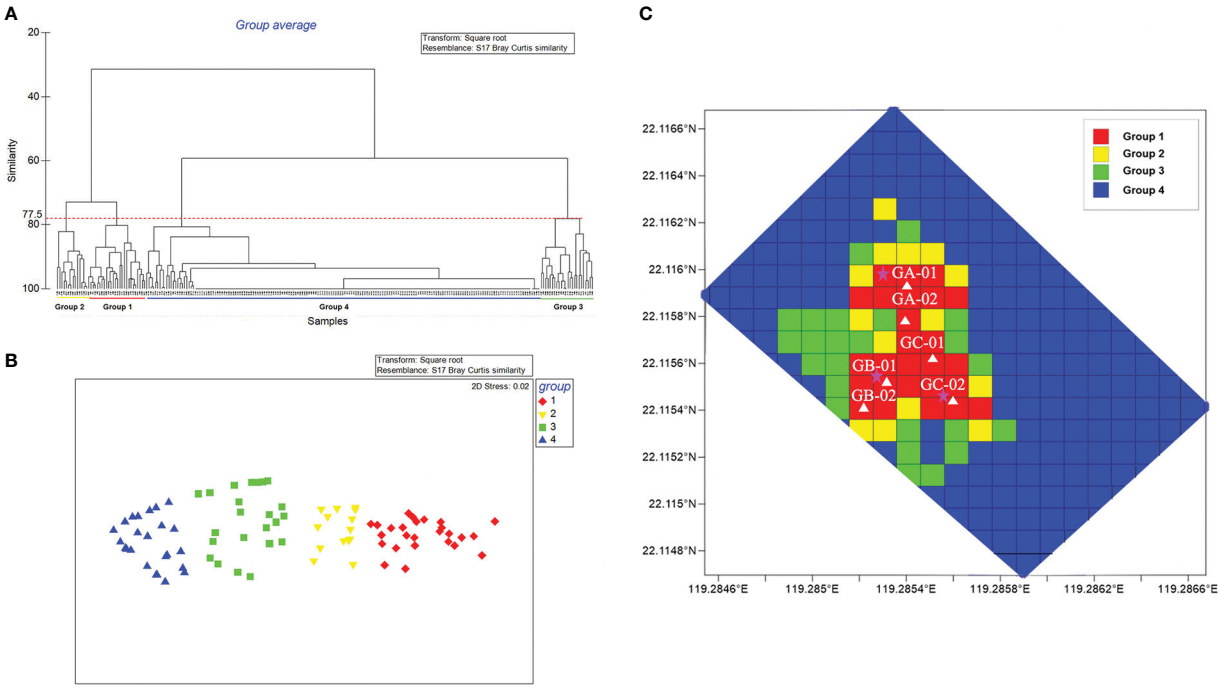

FIGURE 3
Cluster analysis of different grids from the mosaic. **(A)** Four groups (Groups 1 to 4) had a similarity of 77.5%. **(B)** Multidimensional scaling plots of different groups. **(C)** Spatial distribution of each grid at Site F. The ranges of density (individuals/100 m^2) of each group are as follows: Group 1, 3584–17806; Group 2, 1075–3108; Group 3, 106–815; and Group 4, 0–133.The white triangles represent the TV grab and environmental detection stations. The vent sites are indicated by pentagrams.

5.08% of total weight and 19.07 ± 11.46% of flesh wet weight. Dry weight accounted for 32.82 ± 13.80% of wet weight in *S. crosnieri*. None of the data shows an obvious trend of change with the variation in body length. Meanwhile, the length-to- weight ratios of *G. platifrons* and *S. crosnieri* fit well (Table 1). The mean body lengths of these two species calculated from the mosaic were 74.44 mm and 39.08 mm, respectively. Therefore, their respective mean dry weights in the mosaic were 2.71 g and 3.81 g. Based on the total number of the two species, the dry biomass of Site F reached 726.15 kg. Otherwise, the ratio of dry weight to wet weight was used to calculate the biomass (dry weight) of the three stations in 2020. The highest and lowest total mean biomass per station were 1.62 kg dry weight/m^2 (dw/m^2) and 16.42 kg wet weight/m^2 (ww/m^2) at GC and 0.43 kg dw/m^2 and 6.83 kg ww/m^2at GB.

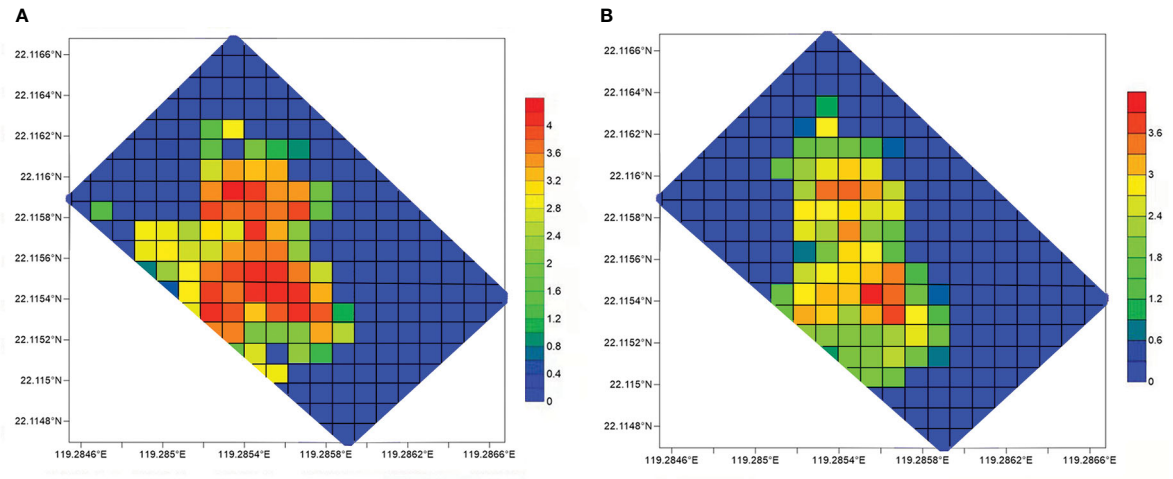

FIGURE 4
Density (log base 10) distribution of **(A)** *G. platifrons* and **(B)** *S. crosnieri* in every grid. The highest density of these two species reached 15,452 and 6,868 individuals/100 m^2, respectively.

TABLE 1 The relationships between length and weight of *G. platifrons* and *S. crosnieri*. .

Species	*n*	Length-weight (wet)	R^2	Length-weight (dry)	R^2
G. platifrons	50	W = exp (−10.79) *L^2.29	0.9179	W = exp (−9.59) *L^1.60	0.8974
S. crosnieri	50	W = exp (−10.16) *L^ 3.43	0.9166	W = exp (−9.66) *L^3.00	0.9372

W, weight (g); L, length (mm); n, number of individuals used to model the relationships.

A patch distribution pattern of macrofauna was found at the Site F cold seep (Figures 4 and 5). Almost all macrofauna, such as *G. platifrons, S. crosnieri*, *Lithodes longispina*, and most of the *Ophidiidae* sp., were found living on or around the hard substrates. Meanwhile, some common species (*B. lactea*, *P. buccinoides*, *Alvinocaris longirostris*, and several species of Polynodiae) at Site F were also found on hard substrates through the TV grab and the ROV camera. According to grab operations in different substrates, the macrofauna in soft substrates, even in reduced sediments (only four types of macrofauna were found), had relatively low diversity and density when compared to hard substrates. *Munidopsis* sp. was found on carbonate rocks and the exterior (mainly a mix of mussels and shells) of the *G. platifrons* –*S. crosnieri* community. A phenomenon we observed was that *Munidopsis* sp. and *S. crosnieri* did not exist in large numbers (>30 individuals/m^2) at the same location. An abundance of *S. crosnieri* was found at Site F, but no significant numbers of *Munidopsis* sp. In addition, two species of sponges, *Esperiopsis* sp. and *Stlocordyla* sp., were abundant (the highest density reached 578 individuals/m^2) and widely distributed in carbonate rocks.

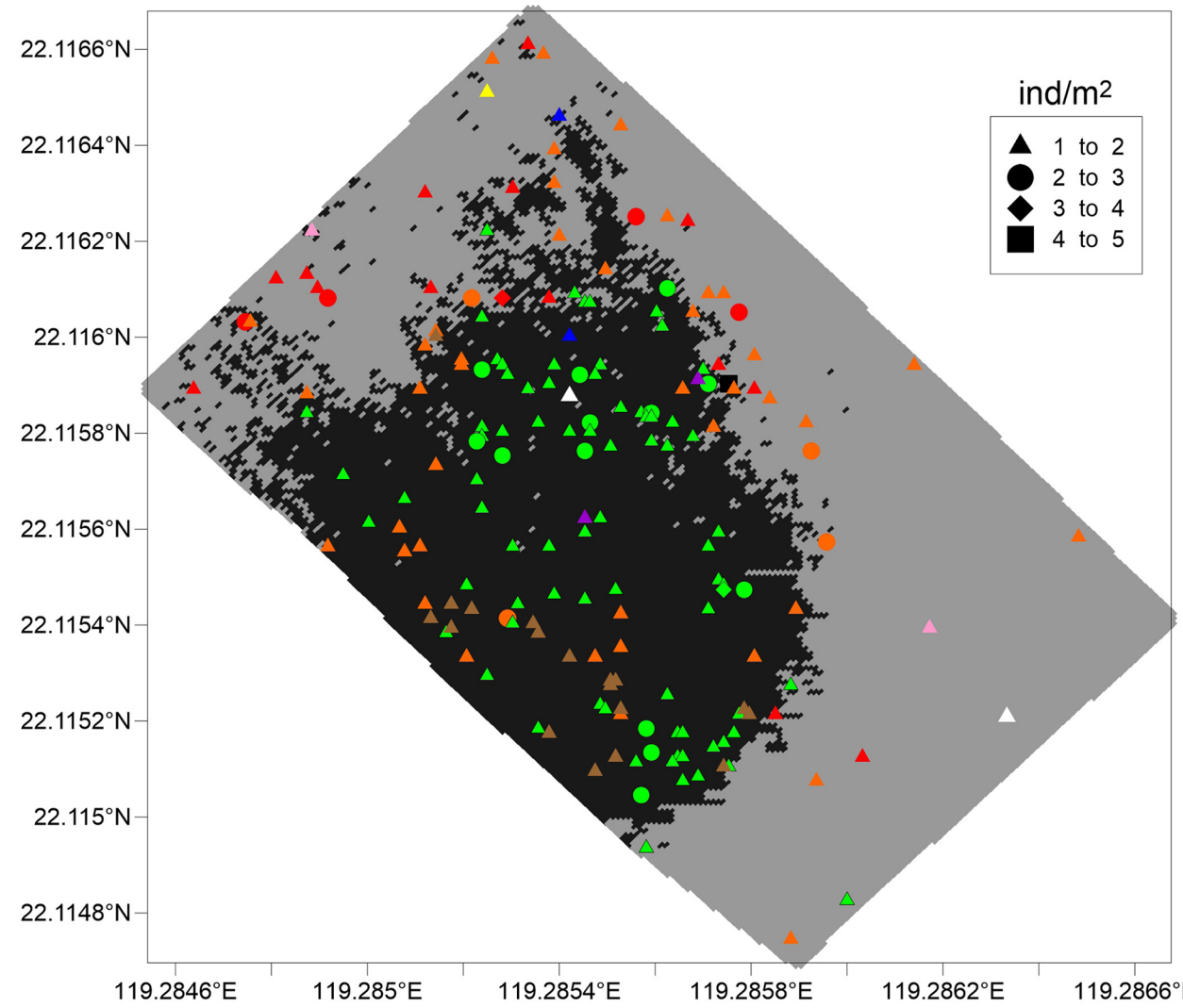

FIGURE 5
Spatial distribution of other macrofauna in the mosaic, including *Lithodes Longispina* (green), *Benthesicymus* sp. (red), Ophidiidae sp. (orange), cf. *Semperella jiaolongae* (yellow), cf. *Bathypolypus* (blue), cf. *Bathyteuthoida* (purple), *Asteroidea* (brown), *Histampica* sp. (pink), and cf. *Cidaridae* (white). The outline represents the area where images were obtained. Large patches of black and gray represent hard and soft bottoms, respectively.

3.3 Interannual variation in body length of the dominant species in different areas

The body length of the dominant species was measured to compare the age composition in different areas. The mean body lengths of *G. platifrons* and *S. crosnieri* we found in the mosaic in 2016 reached 35.89 to 94.15 mm and 24.26 to 55.35 mm, respectively. The central area was almost covered by the larger *G. platifrons*, while the larger *S. crosnieri* were abundant only in the southeast (Figure 6). Obvious signs of seepage were found in these two locations. To compare the interannual variation in body length, samples were taken from three stations (Supplementary Table 1). The average body length and weight in GA were higher as compared to those in the other locations. Individuals with a smaller body length (< 20 mm) and no signs of seepage were absent. Using the normal distribution of body length in 2016 and 2020, we analyzed the body length at these three stations (Figure 7). The average body length of *G. platifrons* and *S. crosnieri* in GA was significantly increased. Their length ranges were noticeably narrower. In contrast, the mean body length of *G. platifrons* in GB and GC decreased dramatically, with the former dropping from 70–80 mm to 30–40 mm and the latter dropping from 80–90 mm to 30–40 mm. The proportion of medium and small body lengths in both areas increased significantly.

3.4 The correlation between methane, oxygen, and dominant species

The concentration of methane showed a strong positive correlation with the density of *G. platifrons* (r = 0.895, $P < 0.05$) and *S. crosnieri* (r = 0.833, $P = 0.08$), while DO showed a strong negative correlation with *G. platifrons* (r = –0.908, $P < 0.05$) and *S. crosnieri* (r = –0.823, $P = 0.08$).

The oxygen consumption calculated from the 2.71 g dry weight of *G. platifrons* was 17.54 μmol/(g dry weight by h). *G. platifrons* consumed 14.62 μmol/(g dry weight by h) of CH_4. Therefore, with a dry weight of 2.71 g and a quantity of 215,339 individuals, the *G. platifrons* in the whole of Site F (2,000 m^2) consumed 204.74 mol of methane per day. Methane consumption of *S. crosnieri* at the entire Site F was 1.78 mol/d by 37,422 individuals.

4 Discussion

4.1 Seep community compositions in Site F

For the Site F cold seep, 41 species of macrofauna were found in our study. Compared with 42 chemosynthesis-based ecosystems in the northwest Pacific (range 2–38), including cold seeps in Sagami Bay, Nankai Trough, and so on, the species richness of Site F was high (Nakajima et al., 2014; Zhao et al., 2020). A previous study proved the strong influences among seepage activity and density, species evenness, and taxonomic composition of macrofauna (Levin et al., 2017). The relatively young carbonate rocks at Site F (Feng et al., 2018) suggested that past seep activity may have contributed to the relatively high species diversity. In addition to the previously reported macrofauna from the Formosa cold seep (Dong and Li, 2015; Li, 2017; Zhang et al., 2020; Zhao et al., 2020), we also found some new or newly recorded species. This indicates that species richness in this area remains under-sampled. It is worth noting that almost half of the species were found through TV grabs. Most of these were new or newly recorded species. Thus, further research on traditional physical collection could help in the discovery of possible new species.

Density-wise, Bivalvia, mainly *G. platifrons*, and Crustacea, particularly *S. crosnieri*, dominated community composition at Site F. The highest densities of these two species in the mosaic reached 560

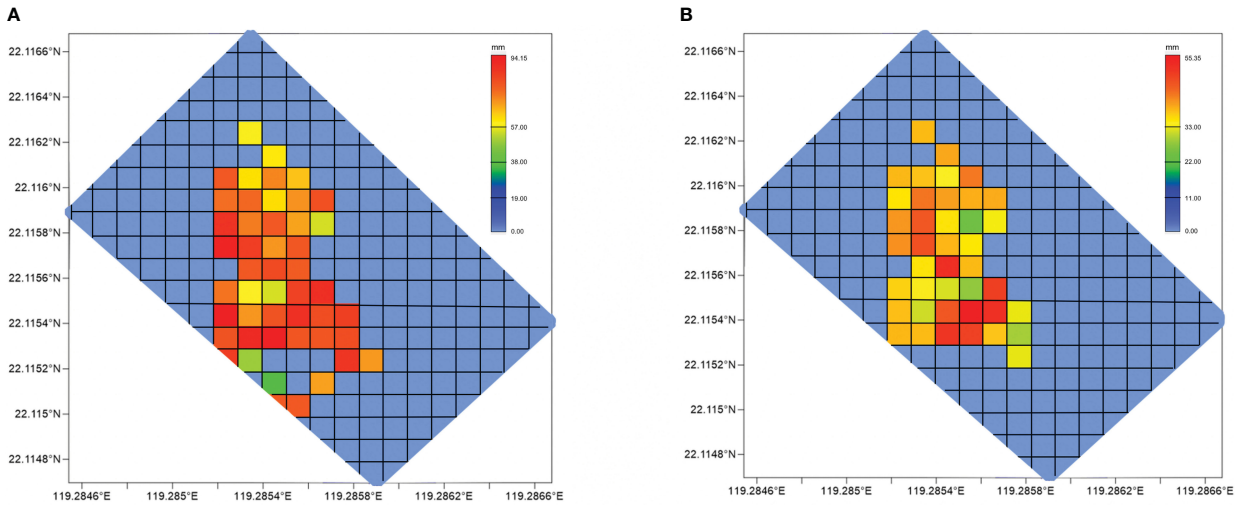

FIGURE 6
Body length distribution of **(A)** *G. platifrons* and **(B)** *S. crosnieri* in every grid. The maximum body length of these two species reached 94.15 and 55.35 mm, respectively.

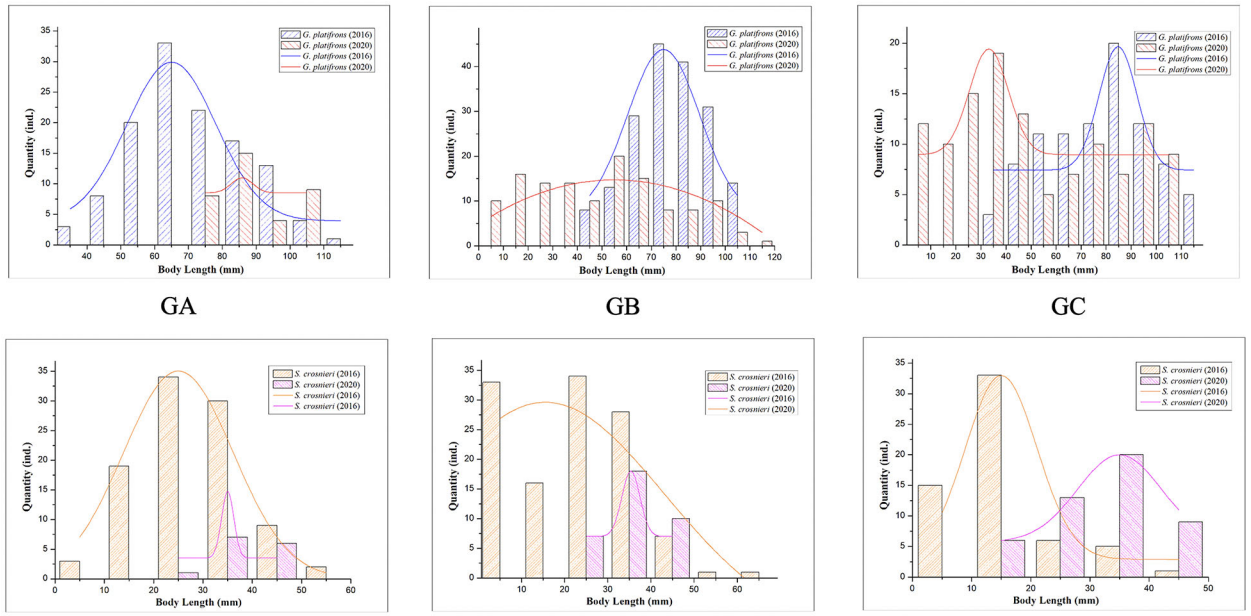

FIGURE 7
Interannual variation of organism length in three areas (GA, GB, and GC). The bar charts and curves are the actual quantity of different body length ranges and normally fitted curves, respectively.

and 396 individuals/m^2, respectively. Our research found a higher density of *G. platifrons* (629 individuals/m^2) with our TV grab in 2020. This was more than double what Zhao et al. (2020) had previously reported. However, there were still a substantial number of individuals that had not been collected. Therefore, the density of *G. platifrons* and *S. crosnieri* at Site F has been greatly underestimated. The total mean biomass at Site F was low when compared with other cold seeps, including the Monterey Bay (0.7–2.05 kg ash-free dry mass/m^2), the Gulf of Mexico (0.47–3.13 kg ash- free dry mass/m^2), and the Peru Trench (30 kg ww/m^2) (Olu et al., 1996; Bergquist et al., 2003; Barry et al., 2007). One cold seep dominated by vesicomyid at the Regab pockmark (0.77–2.03 kg dw/m^2) (Decker et al., 2012) had the closest amount of biomass. However, because of the undersampling of the dominant species, the biomass at Site F was underestimated.

4.2 Distribution pattern of macrofauna and environment at Site F

Site F had both hard (central authigenic carbonates) and soft (peripheral muddy) substrates. This pattern may be a result of the succession of cold seeps. When seepage begins in an area, microbial mats form and methanogenesis occurs, creating carbonates (Levin, 2005). Then, the fauna began to gather. As time goes on, the outermost mussel beds decompose into shell debris.

Almost all the macrofauna were found on or around the hard substrates (mainly the authigenic carbonates), and their relatively high density was always found at the locations where there were obvious signs of seepage. Authigenic carbonates appeared to be a major factor contributing to the higher macrofaunal diversity and abundance (Sen et al., 2019). This is mainly because these structures (e.g., cracks, outcrops) formed by authigenic carbonates can enhance habitat heterogeneity and might be used as the migration pathway for seepage. For example, small clusters of *S. crosnieri* can be found living in the cracks formed by authigenic carbonates. These cracks might be used as the dominant migration pathway for cold seep fluid transportation and provide sufficient energy and shelter for the overlying fauna. Some macrofauna, such as some top predators (*L. longispina*, Ophidiidae sp., *Henricia* sp.) and some small species (like *Histampica* sp. and some Gastropoda) were also observed in the vicinity of carbonates (Figure 5) because the high biomass communities formed by *G. platifrons* and *S. crosnieri* could provide more food sources. Some studies also found that the prevalence of provannid snails, pyropeltid limpets, and polynoid polychaetes occurred on carbonates in common with another hard substrate vent, seep, and whale fall communities in the Pacific (Bergquist et al., 2007; Levin and Le Bris, 2015). *L. longispina* has been observed feeding on *G. platifrons* and possibly *S. crosnieri* (Li, 2017). *Bathyacmaea lactea*, a type of limpet, may consume biofilm on mussel shells (Chen et al., 2019). As for soft substrates, even in the reduced sediments, there was a lack of macrofauna. Only three species (*Solemya* sp., *Glycera* sp., and *Chaetoderma* sp.) were discovered in locations where oxidizing and reducing sediments were mixed. Sulfide in reduced sediments, a vital energy source, is important for the regulation of sulfide-dependent symbiont-bearing species (Cao et al., 2021). Despite the fact that it has been proven that animals can adapt to the toxic sulfide (Grieshaber and Volkel, 1998), relatively high concentrations may prevent biological adaptations. Otherwise, habitat suitability, geochemical differences, fluid flow, and seepage rates also had an effect on species distribution (Roy et al., 2007; Rybakova et al., 2013; Sen et al., 2018).

Overall, a distinct patchy distribution pattern of macrofauna was found in the mosaic, where the most abundant areas were clustered in

the center of the entire cold seep area. Strong spatial differences in faunal composition and large aggregations characterized the megafauna pattern at the seep site (Astrom et al., 2018). Other cold seep ecosystems with patchy faunal distributions include the pockmark Regab, a cold seep near Baltimore Canyon, the northern Peruvian margin, and so on (Olu et al., 1996; Menot et al., 2010; Bourque et al., 2017). To clarify the spatial differences at Site F, we analyzed the macrofauna composition by comparing five stations in the south and north. Predictable successional processes were occurring within the *G. platifrons* –*S. crosnieri* communities. The density, biomass, and diversity of the associated macrofauna all decreased in the north. Narrowed body length ranges, a lack of juveniles (Figure 7), and the disappearance of the cold seep vent may indicate that the northern region was in the final stages of the cold seep eruption and on the way to extinction. In the south, however, high densities and biomass of macrofauna were discovered. An obvious cold seep vent was found in this area in 2020, which may have contributed to a rise in local primary productivity. Some local macrofauna, such as *B. lactea*, *P. glabra*, and *Histampica* sp., were abundant in the south, especially in the southeast. Therefore, in 2020, the macrofauna in the north at Site F was declining, whereas the southern macrofauna was thriving .

4.3 The interaction between environmental factors and dominant species

The dominant species in the cold seep area had strong connections with methane and DO concentrations. *In in situ* environment detection and macrofauna collection were critical for better understanding these connections. However, the variation in these environmental factors, especially methane, was relatively different in the cold seep area (Cao et al., 2021). Indeed, a number of studies have shown that the concentration of methane can vary greatly in a short period of time, even by an order of magnitude (Davide et al., 2013; Bayrakci et al., 2014). This undoubtedly increased the difficulty of detection. Data from several stations were used to understand the interaction between environmental factors and dominant species. *G. platifrons* and *S. crosnieri* in central areas that had relatively high concentrations of methane were found to have comparatively higher densities (Supplementary Table 1). *G. platifrons* and *S. crosnieri* obtained energy through symbiosis with methane-oxidizing bacteria and were limited to areas where chemical flux was sufficient for endosymbiont nutrition (Sibuet and Olu, 1998). This may also suggest that high methane concentrations have some positive effects on these two species. As for DO, we attributed the negative correlation to oxygen consumption by life processes. Other environmental factors, including temperature, pH, salinity, and depth, were also applied in correlation analysis and showed insignificant correlations. In addition, to better understand the biological-environmental relationships, more sampling sites and environmental factors (such as fluid flow, seepage rate, and so on) needed to be included in future investigations.

The consumption of methane (204.74 and 1.78 mol/d) at the entire Site F by the dominant species *G. platifrons* and *S. crosnieri* was estimated. The equation between oxygen consumption and body weight of mytilids was used to calculate the oxygen consumption of *G. platifrons*. The conditions for this equation were that the dry weight of bivalves should be 0.03- 4 g (Khripounoff et al., 2017). The dry weight of *G. platifrons* at Site F was predominantly in the range of 0.03–2.36 g. Meanwhile, the similar temperature of the habitat could also reduce the estimation error because temperature is the most important factor affecting oxygen consumption. Since it was assumed that mytilids were solely responsible for oxygen consumption , the oxygen consumption of *G. platifrons* may be overestimated. As for the relationship between methane and oxygen, the presence of related species (*Gigantidas* sp.) at Site F and the Gulf of Mexico added credibility to the estimation of methane consumption. For assessing the influence of dominant species on methane flux, the methane flux (60-1,598 mol/d) at the whole of Site F (20,000 m^2) was estimated according to Mau et al. (2020). Methane consumption by the dominant species accounted for 12.93% of the maximum methane flux at Site F. Although the methane flux was underestimated (ignoring any methane that remained in bubbles), the consumption of methane by macrofauna on the seafloor cannot be ignored.

5 Conclusions

The combination of habitat mapping and physical collection is an important method for characterizing seafloor ecosystems. Imagery provided an opportunity to identify the structure, composition, and temporal change of macrofauna communities on a larger scale. Our quantitative evidence of images and TV grab data revealed the number, body length, biomass, and distribution of the dominant species living in the cold seep area at Site F. Combined with porewater geochemistry (e.g., dissolved oxygen and methane concentrations), a high-resolution map of macrofauna could be used to estimate population dynamics. Methane consumption by macrofauna indicates that they play an important role in affecting methane fluxes. Seepage and authigenic carbonate exerted strong control over the diversity, taxonomic composition, and density of macrofauna at Site F. However, habitat suitability, geochemical differences, fluid flow, and seepage rate probably also played other roles in enhancing the richness and density of macrofauna, although this could not be specifically explained in our study. Therefore, more sampling is needed for further research. An enhanced understanding of methane flux and associated sediment geochemistry, coupled with the composition of the macrofauna community, could benefit the ecosystem modelling relating to the macrofauna structure and function of cold seeps. All of our data contributed to ecosystem modeling, which is key to promoting sustainable management of the deep seas.

Data availability statement

The raw data supporting the conclusions of this article will be made available by the authors, without undue reservation.

Author contributions

Conceptualization, HW and CL; data curation, HW, and ZL; formal analysis, HW; funding acquisition, CL; investigation, HW, LC, and ZZ; methodology, HW and CL; validation, HW; writing—original draft, HW; writing—review and editing, CL and XW. All authors contributed to the article and approved the submitted version.

Funding

This work was supported by the National Natural Science Foundation of China (42030407 and 42076091).

Acknowledgments

The samples and data were collected by R.V. *Kexue*. We thank Lei Cao and Chao Lian for their help in environmental data collection. We appreciate the help of Minxiao Wang, Xin Zhang, and Zhendong Luan in data analysis.

Conflict of interest

The authors declare that the research was conducted in the absence of any commercial or financial relationships that could be construed as a potential conflict of interest.

Publisher's note

Supplementary material

The Supplementary Material for this article can be found online at: https://www.frontiersin.org/articles/10.3389/fmars.2023.1068916/full#supplementary-material

References

Amon, D. J., Gobin, J., Van Dover, C. L., Levin, L. A., Marsh, L., and Raineault, N. A. (2017). Characterization of methane-seep communities in a deep-Sea area designated for oil and natural gas exploitation off Trinidad and Tobago. *Front. Mar. Sci.* 4. doi: 10.3389/fmars.2017.00342

Astrom, E. K. L., Carroll, M. L., Ambrose, W. G.Jr., Sen, A., Silyakova, A., and Carroll, J. (2018). Methane cold seeps as biological oases in the high-Arctic deep sea. *Limnol. Oceanogr.* 63, S209–S231. doi: 10.1002/lno.10732

Barry, J. P., Whaling, P. J., and Kochevar, R. K. (2007). Growth, production, and mortality of the chemosynthetic vesicomyid bivalve, calyptogena kilmeri from cold seeps off central California. *Mar. Ecol. an Evol. Perspect.* 28 (1), 169–182. doi: 10.1111/j.1439-0485.2007.00119.x

Bayrakci, G., Scalabrin, C., Dupré, S., Leblond, I., Tary, J.-B., Lanteri, N., et al. (2014). Acoustic monitoring of gas emissions from the seafloor. part II: a case study from the Sea of marmara. *Mar. Geophys. Res.* 35 (3), 211–229. doi: 10.1007/s11001-014-9227-7

Bergquist, D. C., Eckner, J. T., Urcuyo, I. A., Cordes, E. E., Hourdez, S., Macko, S. A., et al. (2007). Using stable isotopes and quantitative community characteristics to determine a local hydrothermal vent food web. *Mar. Ecol. Prog. Ser.* 330, 49–65. doi: 10.3354/meps330049

Bergquist, D. C., Ward, T., Cordes, E. E., McNelis, T., Howlett, S., Kosoff, R., et al. (2003). Community structure of vestimentiferan-generated habitat islands from gulf of Mexico cold seeps. *J. Exp. Mar. Biol. Ecol.* 289 (2), 197–222. doi: 10.1016/s0022-0981(03)00046-7

Bourque, J. R., Robertson, C. M., Brooke, S., and Demopoulos, A. W. J. (2017). Macrofaunal communities associated with chemosynthetic habitats from the U.S. Atlantic margin: A comparison among depth and habitat types. *Deep Sea Res. Part II: Topical Stud. Oceanogr.* 137, 42–55. doi: 10.1016/j.dsr2.2016.04.012

Cao, L., Lian, C., Zhang, X., Zhang, H., Wang, H., Zhou, L., et al. (2021). *In situ* detection of the fine scale heterogeneity of active cold seep environment of the Formosa ridge, the south China Sea. *J. Mar. Syst.* 218, 103530. doi: 10.1016/j.jmarsys.2021.103530

Carney, R. S. (1994). Consideration of the oasis analogy for chemosynthetic communities at gulf of Mexico hydrocarbon vents. *Geo Marine Lett.* 14 (2-3), 149–159. doi: 10.1007/BF01203726

Chen, C., Watanabe, H. K., Nagai, Y., Toyofuku, T., Xu, T., Sun, J., et al. (2019). Complex factors shape phenotypic variation in deep-sea limpets. *Biol. Lett.* 15 (10), 20190504. doi: 10.1098/rsbl.2019.0504

Cochrane, G. R., and Lafferty, K. D. (2002). Use of acoustic classification of sidescan sonar data for mapping benthic habitat in the northern channel islands, California. *Continental Shelf Res.* 22 (5), 683–690. doi: 10.1016/S0278-4343(01)00089-9

Cordes, E. E., Bergquist, D. C., and Fisher, C. R. (2009). Macro-ecology of gulf of Mexico cold seeps. *Ann. Rev. Mar. Sci.* 1, 143–168. doi: 10.1146/annurev.marine.010908.163912

Cordes, E. E., Cunha, M. R., Galeron, J., Mora, C., Olu-Le Roy, K., Sibuet, M., et al. (2010). The influence of geological, geochemical, and biogenic habitat heterogeneity on seep biodiversity. *Mar. Ecol. an Evol. Perspect.* 31 (1), 51–65. doi: 10.1111/j.1439-0485.2009.00334.x

Davide, E., Giuditta, M., Francesco, F., Stephen, M., Giuseppe, E., Luca, G., et al. (2013). Monitoring of gas and seismic energy release by multiparametric benthic observatory along the north Anatolian fault in the Sea of marmara (NW Turkey). *Geophys. J. Int.* 196 (2), 850–866. doi: 10.1093/gji/ggt436

Decker, C., Caprais, J.-C., Khripounoff, A., and Olu, K. (2012). First respiration estimates of cold seep vesicomyid bivalves from *in situ* total oxygen uptake measurements. *Comptes Rendus Biologies* 335 (4), 261–270. doi: 10.1016/j.crvi.2012.03.002

Degraer, S., Verfaillie, E., Willems, W., Adriaens, E., Vincx, M., and Lancker, V. V. (2008). Habitat suitability modelling as a mapping tool for macrobenthic communities: An example from the Belgian part of the north Sea. *Continental Shelf Res.* 28 (3), 0–379. doi: 10.1016/j.csr.2007.09.001

Dong, D., and Li, X. (2015). Galatheid and chirostylid crustaceans (Decapoda: Anomura) from a cold seep environment in the northeastern south China Sea. *Zootaxa* 4057 (1), 91–105. doi: 10.11646/zootaxa.4057.1.5

Feng, D., Cheng, M., Kiel, S., Qiu, J.-W., Yang, Q., Zhou, H., et al. (2015). Using bathymodiolus tissue stable carbon, nitrogen and sulfur isotopes to infer biogeochemical process at a cold seep in the south China Sea. *Deep Sea Res. Part I Oceanogr. Res. Papers* 104, 52–59. doi: 10.1016/j.dsr.2015.06.011

Feng, D., Qiu, J.-W., Hu, Y., Peckmann, J., Guan, H., Tong, H., et al. (2018). Cold seep systems in the south China Sea: An overview. *J. Asian Earth Sci.* 168, 3–16. doi: 10.1016/j.jseaes.2018.09.021

Grieshaber, M. K., and Volkel, S. (1998). Animal adaptations for tolerance and exploitation of poisonous sulfide. *Annu. Rev. Physiol.* 60, 33–53. doi: 10.1146/annurev.physiol.60.1.33

Khripounoff, A., Caprais, J. C., Decker, C., Le Bruchec, J., Noel, P., and Husson, B. (2017). Respiration of bivalves from three different deep-sea areas: Cold seeps, hydrothermal vents and organic carbon-rich sediments. *Deep Sea Res. Part II: Topical Stud. Oceanogr.* 142, 233–243. doi: 10.1016/j.dsr2.2016.05.023

Kochevar, R. E., Childress, J. J., Fisher, C. R., and Minnich, E. (1992). The methane mussel: roles of symbiont and host in the metabolic utilization of methane. *Mar. Biol.* 112, 389–401. doi: 10.1007/978-94-024-0884-3_3

Laubier, L. (1993). La vie aux frontières du possible: Les oasis animales des grandes profondeurs marines. *Sciences* (1969) 93(2-3): 99–115.

Levin, L. A. (2005). "Ecology of cold seep sediments: Interactions of fauna with flow, chemistry and microbes," in *Oceanography and Marine Biology - An Annual Review*, Vol. 43 . Eds. R. N. Gibson, R. J. A. Atkinson and J. D. M. Gordon(Boca Raton, FL: CRC Press), 1–46. doi: 10.1201/9781420037449.ch1

Levin, L. A., Baco, A. R., Bowden, D. A., Colaco, A., Cordes, E. E., Cunha, M. R., et al. (2016). Hydrothermal vents and methane seeps: Rethinking the sphere of influence. *Front. Mar. Sci.* 3. doi: 10.3389/fmars.2016.00072

Levin, L. A., James, D. W., Martin, C. M., Rathburn, A. E., Harris, L. H., and Michener, R. H. (2000). Do methane seeps support distinct epifaunal assemblages? observations on community structure and nutrition from the northern California slope and shelf. *Mar. Ecol. Prog. Ser.* 208, 21–39. doi: 10.3354/meps208021

Levin, L. A., and Le Bris, N. (2015). The deep ocean under climate change. *Science* 350 (6262), 766–768. doi: 10.1126/science.aad0126

Levin, L. A., Mendoza, G. F., and Grupe, B. M. (2017). Methane seepage effects on biodiversity and biological traits of macrofauna inhabiting authigenic carbonates. *Deep Sea Res. Part II: Topical Stud. Oceanogr.* 137, 26–41. doi: 10.1016/j.dsr2.2016.05.021

Li, X. (2015). Report on two deep-water caridean shrimp species (Crustacea: Decapoda: Caridea: Alvinocarididae, acanthephyridae) from the northeastern south China Sea. *Zootaxa* 3911 (1), 130–138. doi: 10.11646/zootaxa.3911.1.8

Li, X. (2017). Taxonomic research on deep-sea macrofauna in the south China Sea using the Chinese deep-sea submersible *Jiaolong*. *Integr. Zool.* 12 (4), 270–282. doi: 10.1111/1749-4877.12254

Lin, S., Lim, Y., Liu, C. S., Yang, T. F., Chen, Y. G., Machiyama, H., et al. (2007). Formosa Ridge, a cold seep with densely populated chemosynthetic community in the passive margin, southwest of Taiwan. *Geochimica Et Cosmochimica Acta* 71 (15), A582. doi: 10.1007/s11001-017-9339-y

MacDonald, I. R., Sager, W. W., and Peccini, M. B. (2003). Gas hydrate and chemosynthetic biota in mounded bathymetry at mid-slope hydrocarbon seeps: Northern Gulf of Mexico. *Marine Geology* 198(1-2), 133–158. doi: 10.1016/s0025-3227(03)00098-7.

Mau, S., Tu, T. H., Becker, M., Ferreira, C., Chen, C. N., Lin, L. H., et al. (2020). Methane seeps and independent methane plumes in the south China Sea offshore Taiwan. *Front. Mar. Sci.* 7. doi: 10.3389/fmars.2020.00543

Menot, L., Galeron, J., Olu, K., Caprais, J.-C., Crassous, P., Khripounoff, A., et al. (2010). Spatial heterogeneity of macrofaunal communities in and near a giant pockmark area in the deep gulf of Guinea. *Mar. Ecol. an Evol. Perspect.* 31 (1), 78–93. doi: 10.1111/j.1439-0485.2009.00340.x

Nakajima, R., Yamakita, T., Watanabe, H., Fujikura, K., Tanaka, K., Yamamoto, H., et al. (2014). Species richness and community structure of benthic macrofauna and megafauna in the deep-sea chemosynthetic ecosystems around the Japanese archipelago: An attempt to identify priority areas for conservation. *Divers. Distrib.* 20, 1160–1172. doi: 10.1111/ddi.12204

Olu, K., Duperret, A., Sibuet, M., Foucher, J. P., and FialaMedioni, A. (1996). Structure and distribution of cold seep communities along the Peruvian active margin: Relationship to geological and fluid patterns. *Mar. Ecol. Prog. Ser.* 132 (1-3), 109–125. doi: 10.3354/meps132109

Roy, K. O.-L., Caprais, J. C., Fifis, A., Fabri, M. C., Galeron, J., Budzinsky, H., et al. (2007). Cold-seep assemblages on a giant pockmark off West Africa: Spatial patterns and environmental control. *Mar. Ecol. an Evol. Perspect.* 28 (1), 115–130. doi: 10.1111/j.1439-0485.2006.00145.x

Rybakova, E., Galkin, S., Bergmann, M., Soltwedel, T., and Gebruk, A. (2013). Density and distribution of megafauna at the håkon mosby mud volcano (the barents Sea) based on image analysis. *Biogeosciences* 10 (5), 3359–3374. doi: 10.5194/bg-10-3359-2013

Sen, A., Ondréas, H., Gaillot, A., Marcon, Y., Augustin, J.-M., and Olu, K. (2016). The use of multibeam backscatter and bathymetry as a means of identifying faunal assemblages in a deep-sea cold seep. *Deep Sea Research Part I: Oceanographic Research Papers* 110, 33–49. doi: 10.1016/j.dsr.2016.01.005.

Sen, A., Astrom, E. K. L., Hong, W.-L., Portnov, A., Waage, M., Serov, P., et al. (2018). Geophysical and geochemical controls on the megafaunal community of a high Arctic cold seep. *Biogeosciences* 15 (14), 4533–4559. doi: 10.5194/bg-15-4533-2018

Sen, A., Chitkara, C., Hong, W. L., Lepland, A., Cochrane, S., di Primio, R., et al. (2019). Image based quantitative comparisons indicate heightened megabenthos diversity and abundance at a site of weak hydrocarbon seepage in the southwestern barents Sea. *PeerJ* 7, e7398. doi: 10.7717/peerj.7398

Sibuet, M., and Olu, K. (1998). Biogeography, biodiversity and fluid dependence of deep-sea cold-seep communities at active and passive margins. *Deep Sea Res. Part Ii Topical Stud. Oceanogr.* 45 (1-3), 517–567. doi: 10.1016/s0967-0645(97)00074-x

Vanreusel, A., Andersen, A. C., Boetius, A., Connelly, D., Cunha, M. R., Decker, C., et al. (2009). Biodiversity of cold seep ecosystems along the European margins. *Oceanography* 22 (1), 110–127. doi: 10.5670/oceanog.2009.12

Wang, H., Fu, X., Zhao, C., Luan, Z., and Li, C. (2021). A deep learning model to recognize and quantitatively analyze cold seep substrates and the dominant associated species. *Front. Mar. Sci.* 8. doi: 10.3389/fmars.2021.775433

Wang, X., Liu, B., Qian, J., Zhang, X., Guo, Y., Su, P., et al. (2018). Geophysical evidence for gas hydrate accumulation related to methane seepage in the taixinan basin, south China Sea. *J. Asian Earth Sci.* 168, 27–37. doi: 10.1016/j.jseaes.2017.11.011

Wang, B., Song, Y., and Du, Z. (2019). A submarine imaging and laser profiling system and its application to cold seep site investigation off southwestern Taiwan. *Mar. Geol. Lett.* 35 (11), 60–65. doi: 10.16028/j.1009-2722.2019.11009

Watsuji, T.-o., Yamamoto, A., Takaki, Y., Ueda, K., Kawagucci, S., and Takai, K. (2014). Diversity and methane oxidation of active epibiotic methanotrophs on live *Shinkaia crosnieri*. *Isme J.* 8 (5), 1020–1031. doi: 10.1038/ismej.2013.226

Zhang, X., Du, Z., Luan, Z., Wang, X., Xi, S., Wang, B., et al. (2017). *In situ* raman detection of gas hydrates exposed on the seafloor of the south China Sea. *Geochem. Geophys. Geosystems* 18 (10), 3700–3713. doi: 10.1002/2017gc006987

Zhang, S., Zhang, S., and Chen, H. (2020). Enigmaticolus inflatus sp. nov., a new buccinid species from a methane seep area in the south China Sea (Gastropoda: Neogastropoda). *Zootaxa* 4728 (3), 385–389. doi: 10.11646/zootaxa.4728.3.8

Zhao, Y., Xu, T., Law, Y. S., Feng, D., Li, N., Xin, R., et al. (2020). Ecological characterization of cold seep epifauna in the south China Sea. *Deep Sea Res. Part I Oceanogr. Res. Papers* 163, 103361. doi: 10.1016/j.dsr.2020.103361

Frontiers in Marine Science

Explores ocean-based solutions for emerging global challenges

The third most-cited marine and freshwater biology journal, advancing our understanding of marine systems and addressing global challenges including overfishing, pollution, and climate change.

Discover the latest Research Topics

See more →

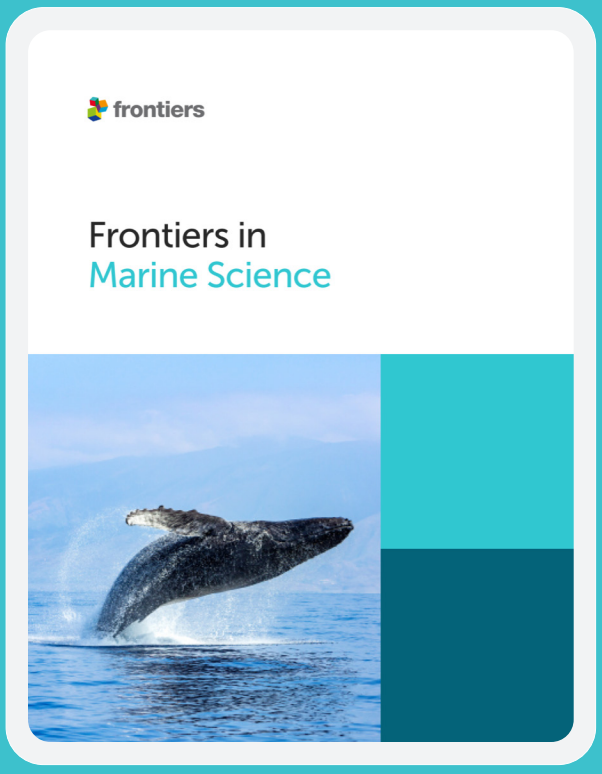

Frontiers

Avenue du Tribunal-Fédéral 34
1005 Lausanne, Switzerland
frontiersin.org

Contact us

+41 (0)21 510 17 00
frontiersin.org/about/contact